THE VOLCANIC AND GEOCHEMICAL EVOLUTION OF A TRACHYDACITE-DOMINATED ISLAND ARC CENTRE: EFATÉ ISLAND GROUP, VANUATU ARC, SW PACIFIC

Alison Mary Raos, B.Sc. (Hons)

Submitted in fulfilment of the requirements for the degree of Doctor of Philosophy

CODES

UNIVERSITY OF TASMANIA

April 2001

STATEMENT OF AUTHENTICITY & AUTHORITY OF ACCESS

This thesis contains no material that has been accepted for a degree or diploma by the University or any other institution, except by way of background information and duly acknowledged in the thesis. To the best of my knowledge and belief this thesis contains no material previously published or written by another person except where due acknowledgment is made in the text of the thesis.

This thesis may be made available for loan and limited copying in accordance with the *Copyright Act 1968*.

alison Raos. 4 · April · 2001

Alison Raos

ABSTRACT

The Efaté Island Group is a trachydacite-dominated volcanic centre in the Vanuatu island arc, southwest Pacific. This centre is part of the Central Chain of islands that form the active Vanuatu arc, and is related to current subduction of the Australian Plate beneath the Pacific Plate. The volcanic succession at Efaté comprises a bimodal association of voluminous trachydacitic volcaniclastic deposits, and younger basaltic lavas and pyroclastic deposits associated with small volume volcanic cones. This association is the record of a major explosive caldera eruption that occurred in the Vanuatu arc about one million years ago.

The oldest known deposits at Efaté are the ~1 Ma, semi-consolidated, trachydacitic pumice breccias and shard-rich sand and silt beds of the Efaté Pumice Formation. The base of the formation is not exposed, but it has a total thickness of about 500 m in the centre of Efaté Island and a total bulk volume of approximately 85 km^3.

The lowermost unit of the Efaté Pumice Formation is dominated by thick to very thick beds of massive and stratified pumice breccia that are variably interbedded with fine-grained shard-rich sand and silt. These beds are referred to as the Efaté Pumice Breccias. The facies characteristics of the Efaté Pumice Breccias indicate deposition principally by water-supported turbidity currents and debris flows in deep marine environments. The nature of the clast population, coupled with facies characteristics, further suggest that the submarine volcaniclastic mass-flows were *directly* generated by concurrent explosive magmatic eruptions from a volcanic caldera.

A sharp, conformable surface separates the Efaté Pumice Breccias from the overlying Rentabau Tuffs. These are characterised by very regularly bedded and well-sorted, fine-grained shard-rich sand and silt facies. Beds are typically massive, to locally stratified and cross-stratified, and convolute bedded intervals occur throughout the sequence. The clast population is generally >95 % volcaniclastic, but fossil foraminifera are a ubiquitous and important non-volcanic component. The Rentabau Tuffs are interpreted to represent a change in explosive activity from magmatic to hydromagmatic fragmentation of the trachydacite magmas due to flooding of vent areas by seawater. Deposition of the Rentabau Tuffs occurred by the passage of steady turbidity currents generated directly from explosive eruptions, by post-eruptive remobilisation of unconsolidated material, and by fallout from the eruption column.

Vent locations and environments for the eruption that generated the Efaté Pumice Formation remain unknown. However, sparse paleocurrent indicators and grain-size variations point to a source to the north of Efaté. Environments are more difficult to interpret but the restricted nature of the Efaté Pumice Formation and the lack of evidence of subaerially produced components in all beds, indicate that vents were probably submarine, although the eruption column may have breached the sea surface.

Following eruption of the Efaté Pumice Formation, late stage basaltic magmas were erupted initially from submarine vents, and continued eruptions produced small volume (3-6 km^3) emergent volcanoes, mainly consisting of stratified lavas with minor pyroclastic deposits and volcaniclastic breccias and conglomerates.

This bimodal association is related to the successive emptying of a strongly compositionally zoned, shallow crustal magma chamber. The trachydacite magmas that were erupted to form the Efaté Pumice Formation were generated by prolonged fractional crystallisation involving plagioclase, olivine, clinopyroxene and Ti-magnetite, from basaltic parental magmas that were continually supplied from the mantle wedge. The Basalt Volcanoes Formation lavas and pyroclastic facies were eventually erupted from the core and lower parts of this magma chamber.

The Basalt Volcanoes Formation lavas can be divided into three different suites on the basis of their temporal and geochemical variability. Overall these lavas have transitional tholeiitic/calcalkaline affinities, anomalously high Sr, appreciably elevated P and strikingly low Zr contents relative to 'normal' southern Vanuatu arc basalts. Sr-Nd isotopes of the Basalt Volcanoes Formation lavas are akin to central, collision-affected Vanuatu arc lavas, and Pb isotopes are transitional between the central and 'normal' southern Vanuatu arc rocks, in keeping with the position of the Efate Island Group between these segments of the Vanuatu arc.

Parental basaltic magmas were generated by partial melting of a mantle wedge source beneath Efaté. It is hypothesised that this mantle wedge source had been previously metasomatised by ephemeral carbonatite melts that elevated levels of Sr and P in the subsequent partial melts, but not the high field strength elements such as Zr and Nb. The generation of the carbonatite melts may be related to variations in local tectonics where the detachment of the subducting slab and subduction of a seamount is occurring and has probably persisted for at least ~3 Ma. In addition, the freezing of ascending primitive melts related to an earlier west-dipping subduction regime, may have caused local areas of enrichment notably in K, and Rb, within the mantle wedge source of the Efaté basalts. These features are reflected in the unusual geochemical signature of the Basalt Volcanoes Formation lavas, relative to the central and 'normal' southern parts of the Vanuatu arc.

ACKNOWLEDGMENTS

Firstly, many thanks to Drs Tony Crawford and Jocelyn McPhie for suggesting the volcanic geology of the Efaté Island Group as a topic for investigation. It has been a very interesting and rewarding journey to work side-by-side with two researchers whose principal areas of interest rarely coincide, and whose approaches are so different. The ideas presented in this thesis have benefited greatly from lengthy discussions with both Tony and Jocelyn over the years. In particular, I would like to thank Tony for his extreme patience in assisting me to come to grips with the complexities of island arc petrogenesis, and Jocelyn for continually challenging my assumptions and encouraging me to develop my critical thinking skills.

Financial support for this project came from an Australian Research Council large grant, awarded to Dr Tony Crawford for research in the Vanuatu arc. I was awarded a School of Science and Technology scholarship from the University of Tasmania to facilitate the research.

The staff and associates of the Vanuatu Department of Geology, Mines and Water Resources (DGMWR) in Vila are gratefully thanked for logistical support during field studies. I would also like to give a special note of thanks to the DGMWR director Stanley Temakon, and to my various field assistants Victor Rory, Maurice Stephens, Thomas, Tony and Siri. Doug Hutchison, Steve Rogers, Neil Nimoho and Chantal Malalo provided help with reference materials, computers and communications at DGMWR headquarters in Vila. Charley Douglas (ORSTOM Port Vila) also assisted in preparing some samples for shipping to Tasmania. In 1996 Jean-Philippe Eissen (ORSTOM France) was kind enough to assist me with some sampling in the central cliffs area of Efaté by dangling precariously off a rope in high winds.

Simon Stephens prepared thin sections for this research, and Phil Robinson, Ashley Townsend and Zongshou Yu performed various whole rock geochemical analyses at the University of Tasmania. The expert and friendly assistance of Nilar Hlaing and Katie McGoldrick is happily acknowledged for sample preparation. Radiogenic isotopes were analysed by Roland Maas at La Trobe University. K-Ar dates were determined by the Argon Mass Spectrometry Laboratory at the Institute of Geological and Nuclear Science, Lower Hutt, New Zealand. I analysed mineral grains and glasses on "Madame Cameca" in the Central Science Laboratory at the University of Tasmania under the always helpful and very much appreciated guidance of Dr David Steele.

Mark Duffett and Andrew Fitzpatrick kindly assisted me with extracting the geophysical data for the Efaté Island Group and preparing the images presented in this thesis.

During a short mission on the research vessel L'Atalante in 1996, I had encouraging discussions about my research with Michel Monzier, Jean-Philippe Eissen, Christine Laporte, and Jeff Witter. Discussions with various members of the volcanology and petrology groups in the School of Earth Sciences also helped me with directions for this research.

A giant thank you to June Pongratz, Peter Cornish, Michael Blake, Christine Higgins, Di Steffens, Lyn Starr and Darren Turner for the countless small things that added up to a smooth and mostly hitch-free existence within the School of Earth Sciences. Thanks also to Dr Jean McClenaghan, Phil Robinson and Kathi Stait for managing to find work for me at the end of my scholarship.

The companionship and camaraderie of the various graduate students in the School of Earth Sciences from 1995-2000 is duly acknowledged and greatly valued. I wish to extend extra special thanks to Alicia Verbeeten, Robina Sharpe, Cathryn Gifkins, Mark Doyle, Andrew Rae, Briony Sinclair, and Rohan Wolfe, and also (importantly) to my office buddies Catherine Reid, Steve Hunns, Russell Fulton, and Bill Wyman.

The enthusiasm and commitment of the first year geology students from 1996-1999 was a constant reminder to me of my reasons for persisting.

Finally, an enormous thank you to my parents Mark and Nea, especially for looking after me through the last few difficult months. To scott, and all the members of the Raos and Howard families for their unfailing love and support.

TABLE OF CONTENTS

STATEMENT OF AUTHENTICITY & AUTHORITY OF ACCESS i

ABSTRACT ii

ACKNOWLEDGEMENTS iv

TABLE OF CONTENTS vi

LIST OF FIGURES xi

LIST OF TABLES xiv

CHAPTER ONE

Introduction: High-silica volcanism in island arcs

HIGH-SILICA VOLCANISM IN ISLAND ARCS 1
VOLCANISM IN ISLAND ARC ENVIRONMENTS 2
SYN-ERUPTIVE VOLCANICLASTIC DEPOSITS IN SUBMARINE ENVIRONMENTS 3
AIMS OF THE THESIS 5
FIELD AREA, FIELDWORK AND LABORATORY STUDIES 6
EFATÉ ISLAND GROUP 6
Stratigraphy 7
Structure 8
Geophysics 10
Magnetic 10
Radiometrics 10
ORGANISATION OF THE THESIS 12

CHAPTER TWO

Regional Geology: Evolution of the Vanuatu island arc

INTRODUCTION 13
TECTONIC FRAMEWORK 13
SOUTHWESTERN PACIFIC 13
VANUATU ISLAND ARC (NEW HEBRIDES ISLAND ARC) 14
TECTONIC EVOLUTION OF THE VANUATU ARC 17
Vitiaz Arc System (38 - ~10 Ma) 17
Arc breakup and rotation (~10 - 8 Ma) 17
Recent history and present arc (8 Ma - Present) 19
TECTONIC POSITION OF EFATÉ ISLAND 19
GEOLOGICAL HISTORY OF THE VANUATU ARC 19
Western Belt 22
Eastern Belt 23
Central Chain 24
CALDERA VOLCANOES OF THE VANUATU ARC 28
GECHEMICAL CHARACTERISTICS OF THE VANUATU ARC 29
Western Belt 31
Mineralogy 31
Chemistry 31
Eastern Belt 32

Mineralogy 32
Chemistry 32
Central Chain 32
Mineralogy 33
Chemistry 33

CHAPTER THREE

Syn-eruptive submarine pumice breccias from explosive trachydacitic eruptions, Efaté Pumice Breccias: Facies characteristics and genetic and depositional controls

INTRODUCTION 35
METHODS AND APPROACH 36
EFATE PUMICE BRECCIAS 36
AGE AND DISTRIBUTION 37
LITHOFACIES 40
Coarse-grained facies association 40
Components and composition 40
Grain-size characteristics 41
Texture and sedimentary structures 43
Massive pumice breccia (MPB) 43
Stratified pumice breccia (SPB) 44
Cross-stratified pumice breccia (XPB) 44
Massive lithic breccia (MLB) 45
Fine-grained facies association 45
Components and composition 45
Grain-size characteristics 47
Texture and sedimentary structures 47
Massive shard-rich sand and silt (MAS) 47
Stratified shard-rich sand (SAS) 50
Cross-stratified shard-rich sand (XAS) 50
Pumice gravel lenses (PGL) 52
INTERNAL STRATIGRAPHY 52
Section 1 52
Section 2 57
Section 3 59
Section 4 59
Section 5 59
Section 6 61
Section 7 64
Section 8 64
Other exposures 67
REGIONAL VARIATION OF THE EFATÉ PUMICE BRECCIAS 68
ORIGIN OF THE EFATÉ PUMICE BRECCIAS 68
ORIGIN OF CLASTS 68
ERUPTION STYLE AND VENT SETTING 70
TRANSPORT AND DEPOSITIONAL PROCESSES AND ENVIRONMENTS 72
Sedimentary environments 72
Sedimentation processes 72
Initiation of mass flows 73
Duration of eruption and deposition 74
DISCUSSION 74
MODEL FOR ERUPTION AND EMPLACEMENT OF EFATÉ PUMICE BRECCIAS 78
CONCLUSIONS 81

CHAPTER FOUR

Sedimentology of the Rentabau Tuffs: shard-rich sand and silt facies associated with voluminous pumice-rich mass flows

INTRODUCTION 82
THE RENTABAU TUFFS 82
AGE AND DISTRIBUTION 82
COMPONENTS AND COMPOSITION 83
Glassy particles 83
Crystals 85
Other clast types 85
Fossil assemblage 85
POST-DEPOSITIONAL ALTERATION PROCESSES 87
Clay development 87
Carbonate cements and replacement textures 87
Manganese cements and replacement textures 88
LITHOFACIES CHARACTERISTICS 88
Massive shard-rich sand 89
Laminated shard-rich sand 89
Ripple-laminated shard-rich sand 90
Convolute-bedded shard-rich sand and silt 91
Massive shard-rich silt 91
Pumice-rich fine gravel 91
INTERNAL STRATIGRAPHY 92
Section 1 92
Section 2 (Forari clays) 94
Section 3 94
Section 4 (Forari clays) 97
Section 5 99
Section 6 99
Regional variation of the Rentabau Tuffs 102
ORIGIN OF THE RENTABAU TUFFS 102
FRAGMENTATION PROCESSES AND SOURCE OF PYROCLASTS 102
VENT SETTING - SUBMARINE VS. SUBAERIAL ERUPTION? 105
TRANSPORT AND DEPOSITION PROCESSES 106
Turbidity currents and debris flows 107
Fallout 108
Bottom currents and soft-sediment deformation 109
Duration of deposition 109
Summary 110
COMPARISON WITH SUBAQUEOUS, SHARD-RICH DEPOSITS 110
CONCLUSIONS 113

CHAPTER FIVE

Basalt Volcanoes Formation, Efaté Island Group, Vanuatu: petrology and geochemistry

INTRODUCTION 114
BASALT VOLCANOES FORMATION 115
AGE AND DISTRIBUTION 115
VOLCANO MORPHOLOGY AND SETTING 115
LITHOLOGIES OF THE BASALT VOLCANOES FORMATION 116
Lavas 117
Intrusions 117
Breccia and conglomeratic facies 117
PETROLOGY 119
PETROGRAPHY 119
Mainland Efaté (MLS) - Older Sequence 120
Offshore Islands (OSS and HKRS) - Younger Sequence 122

Phenocryst mineral chemistry 124
Plagioclase 124
Olivine 126
Clinopyroxene 126
Ti-magnetite 128
GEOCHEMISTRY 128
Major element geochemistry 128
Trace elements 134
Sr, Nd and Pb isotope geochemistry 137
SUMMARY 139
DISCUSSION 139
Sr enrichment - slab melting? 140
Sr enrichment - subducted sediment component? 142
Sr enrichment - plagioclase accumulation? 143
Other possibilities? 145
Phosphorus enrichments? 145
INTER-SUITE VARIATIONS 146
SPECULATIVE PETROGENETIC MODEL 147
IMPLICATIONS 149
CONCLUSIONS 149

CHAPTER SIX

Geochemical characteristics of the Efaté Pumice Formation, Vanuatu: Petrogenesis of a dacitic magma chamber in an island arc environment

INTRODUCTION 150
PETROLOGY OF THE EFATÉ PUMICE FORMATION 151
PETROGRAPHY 151
Plagioclase 151
Pyroxene 153
Ti-magnetite 153
Accessory phases 155
GEOCHEMISTRY 155
Glass chemistry 155
Juvenile clast whole-rock chemistry 157
Major elements 157
Trace elements 160
Sr, Nd and Pb isotope geochemistry 163
SUMMARY 165
PETROGENESIS OF TRACHYDACITE MAGMAS AT EFATÉ 166
FRACTIONAL CRYSTALLISATION 166
Problems with the closed system fractional crystallisation model 172
Summary 172
MAGMA CHAMBER PROCESSES 173
PETROGENETIC MODEL 175
CONCLUSIONS 175

CHAPTER SEVEN

Conclusions: Evolution of a trachydacite-dominated island arc centre

IGNEOUS PETROGENESIS 176
ERUPTION STYLE AND DEPOSITIONAL MECHANISMS 177
STAGE 1 179
Eruption event 179
Depositional processes 179
STAGE 2 179
Eruption event 179

Depositional processes 180
STAGE 3 180
Eruption event 180
Depositional processes 182
IMPLICATIONS AND FUTURE RESEARCH 182
Geochemistry 182
Volcanology 182

REFERENCES 184

APPENDICES

APPENDIX A: Sample list and sample locations A1
APPENDIX B: Bulk volume estimates for Efaté Island Group volcanic formations A7
APPENDIX C: Granulometric and component analysis techniques A8
APPENDIX D: Clay mineralogy of altered Rentabau Tuffs A12
APPENDIX E: Basalt Volcanoes Formation petrography A14
APPENDIX F: Analytical methods for whole rock geochemistry A20
APPENDIX G: BVF mineral chemistry: electron microprobe analytical results A24
APPENDIX H: BVF groundmass compositions: electron microprobe analytical results A46
APPENDIX I: Results of plagioclase addition to BVF parent calculations A48
APPENDIX J: EPF mineral chemistry: electron microprobe analytical results A52
APPENDIX K: EPF glass chemistry: electron microprobe analytical results A62
APPENDIX L: Results of major element modelling from BVF to EPF A81

LIST OF FIGURES

CHAPTER ONE

Figure 1.1 Geological map of the Efaté Island Group 9
Figure 1.2 Geophysics of the Efaté Island Group: magnetic and radiometric data 11

CHAPTER TWO

Figure 2.1 Bathymetry and tectonic map of the southwest Pacific 15
Figure 2.2 Geology and tectonics of the Vanuatu arc 16
Figure 2.3 Tectonic reconstruction of the southwest Pacific 18
Figure 2.4 Seismic profile along the Vanuatu arc 20
Figure 2.5 Summarised stratigraphy of the Vanuatu arc 21
Figure 2.6 Evolution of the Vanuatu arc in schematic cross-section 27
Figure 2.7 Geochemical variation in the Vanuatu arc 30

CHAPTER THREE

Figure 3.1 Distribution of the Efaté Pumice Breccias 38
Figure 3.2 Photomicrographs of pumice breccia textures 42
Figure 3.3 Coarse-grained facies of the Efaté Pumice Breccias 46
Figure 3.4 Grain size histograms and component abundances 48
Figure 3.5 Sorting characteristics of the Efaté Pumice Breccias 49
Figure 3.6 Fine-grained facies of the Efaté Pumice Breccias 51
Figure 3.7 Graphic log: Section 1(a) 53
Figure 3.8 Graphic log: detail of Section 1(a) - lower 8 m 54
Figure 3.9 Photo mosaic: Section 1(b) 55
Figure 3.10 Graphic logs: Section 1(b) 56
Figure 3.11 Graphic log: Section 2 58
Figure 3.12 Graphic log: Section 3 and Section 4 60
Figure 3.13 Graphic log: Section 5(a) 62
Figure 3.14 Graphic log: Section 5(b) 63
Figure 3.15 Graphic log: Section 6 and Section 7 65
Figure 3.16 Graphic log: Section 8 66
Figure 3.17 Regional variations in the Efaté Pumice Breccias 69
Figure 3.18 Comparison of some non-welded pumice breccias facies 79
Figure 3.19 Model of eruption and deposition for Efaté Pumice Breccias 80

CHAPTER FOUR

Figure 4.1 Section locations and distribution of the Rentabau Tuffs 84
Figure 4.2 Photomicrographs of the Rentabau Tuffs 86
Figure 4.3 Graphic log: Section 1 93
Figure 4.4 Graphic log: Section 2 95
Figure 4.5 Graphic log: Section 3 96
Figure 4.6 Graphic log: Section 4 98
Figure 4.7 Graphic log: Section 5 100
Figure 4.8 Graphic log: Section 6 101
Figure 4.9 Regional variations in the Rentabau Tuffs 103
Figure 4.10 Model for eruption and deposition processes for the Rentabau Tuffs 111

CHAPTER FIVE

Figure 5.1 Facies of the BVF 118
Figure 5.2 Photomicrographs of BVF lavas and intrusions 121
Figure 5.3 Photomicrographs of BVF lavas and intrusions 123
Figure 5.4 Mineral compositions of BVF: histograms 127
Figure 5.5 CaO and NiO covariation diagrams of olivine core compositions: BVF 127
Figure 5.6 Quadrilateral compositions and CaO and NiO covariation diagrams for clinopyroxene cores 127
Figure 5.7 Discrimination diagrams for BVF whole-rock data 132
Figure 5.8 Major element covariation diagrams plotted against MgO: BVF 133
Figure 5.9 Trace element covariation diagrams plotted against MgO: BVF 135
Figure 5.10 REE and multi-element diagrams: BVF 136
Figure 5.11 Standard Sr-Nd-Pb radiogenic isotope covariation diagrams: BVF 138
Figure 5.12 Adakite discrimination diagrams: BVF 141
Figure 5.13 Sr vs. $^{87}Sr/^{86}Sr$ diagram 141
Figure 5.14 Schematic representation of BVF petrogenesis 148

CHAPTER SIX

Figure 6.1 Plagioclase phenocryst composition diagrams: EPF 154
Figure 6.2 Pyroxene phenocryst composition diagrams: EPF 154
Figure 6.3 Variation of EPF glass compositions 154
Figure 6.4 Discrimination diagrams for Efaté Island Group volcanics 158
Figure 6.5 Major element covariation diagrams plotted against SiO_2: EPF 159
Figure 6.6 Trace element covariation diagrams plotted against SiO_2: EPF 161
Figure 6.7 REE and multi-element diagrams: EPF 162
Figure 6.8 Standard Sr-Nd-Pb radiogenic isotope covariation diagrams: EPF 164
Figure 6.9 Log-element versus log-Rb plots for Efaté Island Group magmas 167
Figure 6.10 Schematic diagram of petrogenesis of the EPF 174

CHAPTER SEVEN

Figure 7.1 Geochemical evolution of the Efaté Island Group magmas 178
Figure 7.2 Eruption history of the Efaté Island Group volcanoes..... 181

APPENDICES

Figure D.1 PIMA output spectra for some Rentabau Tuffs sample..... A13
Figure G.1 Ti-magnetite compositions for BVF lavas..... A25
Figure I.1 Plots of plagioclase addition to Tanna basalt, TA93 ..... A49
Figure I.2 Plots of plagioclase addition to Tanna basaltic andesite, Tan5C A50
Figure I.3 Plots of plagioclase addition to Tanna andesite, Tan3B A51
Figure J.1 Ti-magnetite compositions for EPF volcaniclastic samples..... A53

LIST OF TABLES

CHAPTER TWO

Table 2.1 Caldera volcanoes of the Vanuatu arc 28

CHAPTER THREE

Table 3.1 Facies of the Efaté Pumice Breccias 39

Table 3.2 Facies descriptors used for the Efaté Pumice Breccias 40

Table 3.3 Features of pumiceous subaqueous volcaniclastic deposits 76

CHAPTER FOUR

Table 4.1 Facies of the Rentabau Tuffs 89

Table 4.2 Characteristics of some subaqueous pyroclast-rich successions 112

CHAPTER FIVE

Table 5.1 Phenocryst modal abundances for Basalt Volcanoes Formation 122

Table 5.2 Representative mineral analyses for Basalt Volcanoes Formation 125

Table 5.3 Whole-rock geochemical analyses for Basalt Volcanoes Formation 129

Table 5.4 Sr-Nd-Pb isotope data for Basalt Volcanoes Formation 137

Table 5.5 Groundmass compositions for Basalt Volcanoes Formation 144

CHAPTER SIX

Table 6.1 Representative mineral analyses for Efaté Pumice Formation 152

Table 6.2 Representative glass analyses for Efaté Pumice Formation 155

Table 6.3 Whole-rock geochemical analyses for Efaté Pumice Formation 156

Table 6.4 Variety of clast types analysed for whole-rock geochemistry 157

Table 6.5 Sr-Nd-Pb isotope data for Efaté Island Group volcanics 165

Table 6.6 Fractional crystallisation models for Efaté Island Group volcanics 169

Table 6.7 Trace element test results for D = 0 170

Table 6.8 Trace element test results for calculated D values 170

Table 6.9 K_D values used to calculated D_{bulk} 171

APPENDICES

Table A.1 List of Efaté Pumice Formation samples A1

Table A.2 List of Basalt Volcanoes Formation samples A5

Table B.1 Bulk volume estimates for volcanic lithological units A7

Table C.1 Average grain sizes for representative pumice breccias A8

Table C.2 Errors for replicate sieve analyses (example) A8
Table C.3 Results of granulometric analysis, Efaté Pumice Breccias A9
Table C.4 Results of point counting, Efaté Pumice Breccias A10
Table D.1 Clay mineral content of some Rentabau Tuffs samples A12
Table E.1 Petrography of Basalt Volcanoes Formation samples A15
Table F.1 X-ray fluorescence instrument operating conditions, major elements A21
Table F.2 X-ray fluorescence instrument operating conditions, trace elements A21
Table F.3 Comparison of XRF and ICP-MS results A22
Table F.4 Radiogenic isotope results and errors A23
Table G.1 Electron microprobe operating conditions for BVF mineral analysis A24
Table G.2 Plagioclase compositions for BVF lavas A26
Table G.3 Olivine compositions for BVF lavas A35
Table G.4 Clinopyroxene compositions for BVF lavas A40
Table G.5 Ti-magnetite compositions for BVF lavas A43
Table H.1 Electron microprobe operating conditions for BVF groundmass analysis A46
Table H.2 Groundmass compositions for MLS sample AR153 ..... A47
Table H.3 Groundmass compositions for OSS sample AR184 ..... A47
Table H.4 Groundmass compositions for HKRS sample AR198 ..... A47
Table I.1 Initial rock and plagioclase compositions for addition calculations A48
Table J.1 Electron microprobe operating conditions for EPF mineral analysis A52
Table J.2 Plagioclase compositions for EPF lavas A54
Table J.3 Orthopyroxene compositions for EPF lavas A57
Table J.4 Clinopyroxene compositions for EPF lavas A59
Table J.5 Ti-magnetite compositions for EPF lavas A61
Table K.1 Electron microprobe operating conditions for EPF glass analysis A62
Table K.2 Major element chemistry of EPF juvenile glasses A63
Table K.3 Major element chemistry of glass inclusions in EPF plagioclases A80
Table L.1 Major element fractionation models A81

Chapter One

INTRODUCTION

High-silica volcanism in island arcs

HIGH-SILICA VOLCANISM IN ISLAND ARCS

Volcanic arcs are of two types: (1) continental margin arcs, and (2) intra-oceanic or island arcs. The respective geochemical and volcanological characteristics of the two types of arc reflect the primary controls on magma genesis and evolution in these different environments. In particular, the abundance of intermediate to silicic magmas compared with basaltic compositions in continental (and microcontinental) arcs is most readily explained largely by assimilation of continental crust, accompanied by differentiation due to fractional crystallisation (Ewart, 1982; Davidson, 1992; Hamilton, 1995).

Arc volcanism is overwhelmingly dominated by volcanic products of andesitic composition, and although volumetrically subordinate, particularly in immature arcs, dacitic and rhyolitic magmatism is well represented in many modern intra-oceanic arc environments. The genesis of dacitic and rhyolitic magmas in island arcs is frequently attributed to fractional crystallisation, since the effects of assimilating continental crust are removed in these environments (*e.g.* Wheller, 1986; Wood *et al.*, 1995; Gertisser & Keller, 2000). However, fractionation models commonly fail to adequately explain the genesis of large-volume silicic magma chambers and the presence of rhyolitic compositions in many island arcs (Wood *et al.*, 1995).

The presence of high-silica magmas in island arcs leads to highly explosive eruptions from caldera volcanoes occurring in both subaerial and submarine environments. Although the transport and deposition processes of subaerial products from such eruptions are generally well understood (*e.g.* Smith, 1960; Sparks, 1976; Wright *et al.*, 1981; Wilson & Walker, 1982; Walker, 1983), the same is not true for submarine products (Fiske, 1969; Sparks *et al.*, 1980; Yamada, 1984; Cashman & Fiske, 1990; Cas & Wright, 1991). In island arcs in particular, the record of major explosive eruptions is likely to be preserved best in submarine volcanic successions (Fisher & Schmincke, 1984a). Submarine deposits from caldera eruptions are being increasingly recognised throughout the rock record, but deposit characteristics are enormously variable and thus the transport and deposition mechanisms can be difficult to interpret (*e.g.* Vessell & Davies,

1981; Soh *et al.*, 1989; Mángano & Buatois, 1997; Stow *et al.*, 1998; Allen & McPhie, 2000). Furthermore, the question as to whether or not highly explosive eruptions can occur and be sustained underwater is still hotly debated (Burnham, 1983; Kokelaar *et al.*, 1985; Fiske & Cashman, 1987; Cashman & Fiske, 1991; Kano *et al.*, 1996).

The non-welded, pumice-rich, volcaniclastic deposits of the Efaté Island Group in the immature Vanuatu island arc were rapidly emplaced in submarine environments and are related to a large-scale eruption of evolved trachydacite magma. Dacitic products are not unique to the Efaté Island Group within the Vanuatu arc, but only at Efaté do dacitic products have such a large volume and overwhelmingly dominate over more mafic compositions, and only at Efaté are dacitic, volcaniclastic products deposited in exclusively submarine environments.

Volcanism in island arc environments

A wide variety of volcanic activity is recognised in island arc environments. Magma compositions range from picritic and primitive basalts through to rhyolites, and the relative abundances of these magmas change with temporal evolution of the arc. The complete spectrum of styles of both subaerial and subaqueous volcanism is represented in arc and back-arc environments. In general, magma composition is one of the strongest controls in determining volcano type and eruption style in arcs. However, the abundance of hydrous minerals in the volcanic products provides evidence of the high volatile contents of arc magmas, which further contributes to the highly explosive nature of volcanic eruptions in arcs (Gill, 1981).

In young island arcs, basaltic and basaltic andesite magmatism is important in the earliest stages of arc development. Small volume seamounts and stratocones are typical products of basaltic magmatism in island arcs. Basaltic centres may also construct large shield volcanoes characterised by broad, low aspect ratio platforms built predominantly by low viscosity lavas. Examples of immature arcs which include such volcanoes are the Tonga-Kermadec and the Izu-Bonin-Mariana arc systems in the Pacific Ocean, and the South Sandwich arc in the southern Atlantic Ocean (Gill, 1981).

Andesitic magmas more commonly produce stratocones built of lavas interbedded with pyroclastic deposits, and locally reworked volcanic sediments (Hackett & Houghton, 1989). Composite cones and small calderas are thus the typical volcanoes seen in arcs. In the intra-oceanic arc environment, andesitic centres initiate as seamounts and subsequently form volcanic islands. Pillow lava, hyaloclastite and peperite are particularly important facies in the submarine environment on andesitic and basaltic seamount volcanoes (McPhie *et al.*, 1993; McPhie, 1995; Sohn, 1995). Volcanoes have steep slopes approximating or exceeding the angle of repose (from 33-36°) (Walker,

1982). An example of an andesite-dominated island arc is the Lesser Antilles arc in the Caribbean Sea (Baker, 1968).

As island arcs mature, thickening of the crust causes magma compositions to become more silicic, principally by the enhanced opportunity for magmas to pool, cool and fractionate, coupled with assimilation of this thickened crustal material (Chester, 1993). Dacitic and rhyolitic magmas in island arcs are commonly associated with highly explosive, large-scale, caldera-forming eruptions (*e.g.* Krakatau, Carey *et al.*, 1996; Mandeville *et al.*, 1996b). Welded and non-welded pyroclastic deposits dominate the volcanic products from these types of centres. High aspect ratio lavas and domes are associated with dacitic and rhyolitic caldera volcanoes and also with andesitic to dacitic composite cones. The best examples of mature to microcontinental arcs hosting these types of volcanoes include the Japan arc, the Taupo Volcanic Zone at the southern extension of the Tonga-Kermadec arc, the Central American and Mexican arcs, and the western part of the Sunda arc (Hamilton, 1995).

The presence of several caldera volcanoes is an unusual feature of the immature intra-oceanic Vanuatu arc. The calderas have been the source of the most differentiated products in the arc with compositions ranging from basalt and evolved andesite to dacite (*e.g.* Robin *et al.*, 1993a; Monzier *et al.*, 1994; Robin *et al.*, 1994a; Robin *et al.*, 1995). Local tectonic controls might explain the presence of these structures in the Vanuatu arc (Crawford *et al.*, 1988).

Syn-eruptive volcaniclastic deposits in submarine environments

The record of volcanic activity in island arc environments is substantially preserved in adjacent submarine environments (Davidson, 1992). This is because much of the volcanic activity occurs under water and most of the subaerial eruptive processes are capable of delivering volcanic products to and beyond shorelines (Fisher & Schmincke, 1984a).

Although weathering and erosion of subaerial and shallow marine volcanoes also contributes to volcaniclastic deposits offshore, pyroclastic activity is the principal source of volcanic clasts in submarine environments. Surface weathering and erosion occur concurrently with volcanic processes and unconsolidated volcaniclastic deposits are easily remobilised by aeolian, fluvial and submarine influences. Particle type, the volume of material supplied, and the processes operating during transport and deposition all influence the nature of the resulting deposits (Cas & Wright, 1987; McPhie *et al.*, 1993).

Volcaniclastic deposits that are *directly* generated and influenced by concurrent volcanic activity, but partly transported and deposited by conventional sedimentary processes, are not adequately accounted for by existing sedimentary or volcanological facies models.

In particular, the impact of explosive eruptions on sedimentary processes is not widely appreciated (*e.g.* Fisher, 1984). Such eruptions occur commonly in island arcs, producing large volumes of debris which are rapidly, though spasmodically, introduced into ambient sedimentary systems. In cases where delivery of pyroclasts into sedimentary systems occurs concurrently with supply from active volcanism, resulting transport and depositional processes are classed as *syn-eruptive*.

Pyroclasts from explosive eruptions typically range widely in size, shape, density and temperature. Explosive fragmentation of magmas produces particles which vary from a few microns (particularly so for hydromagmatic eruptions) to a few metres across. Clast shapes are principally influenced by fragmentation mechanisms, though shape modification by abrasion and disaggregation during transport also occurs. Juvenile pyroclasts range from extremely vesicular, fragile, low density and chemically reactive glassy clasts, to dense, solid, glassy or crystalline lava fragments. Non-juvenile clasts include vent-derived country rock fragments and accidental lithic fragments that may be volcanic or non-volcanic. Clasts can be extremely hot and/or partially molten, or cool and rigid when deposited.

Transport of pyroclasts by primary volcanic processes can occur in several ways. Particles may be entrained and suspended in an eruption column or cloud and deposited by fallout through the air and/or water column. Eruption column collapse and/or "boiling over" of pyroclasts at subaerial volcanic vents can produce hot, gas-supported pyroclastic density currents. Subaerial pyroclastic currents that transgress shorelines may mix with seawater to become water-supported density currents (*e.g.* Fiske & Matsuda, 1964; Yamada, 1973; Cas, 1983). Pyroclastic currents may also be generated directly from underwater vents, probably at shallow depths, and similar fluid mixing processes may occur (Cas & Wright, 1991; Kano *et al.*, 1996).

Hybrid volcaniclastic deposits result when fragmentation, transport and deposition are controlled by both volcanic and sedimentary processes. This syn-eruptive category of volcaniclastic deposits is well represented in both subaerial and subaqueous volcanic settings and especially so in island arcs (McPhie *et al.*, 1993). The character and evolution of volcaniclastic sedimentation processes occurring in volcanic environments, particularly submarine environments, are complex. Revision of conventional facies models, and in some cases the creation of new ones, is required to adequately interpret these syn-eruptive volcaniclastic deposits.

Some of the calderas of the Vanuatu arc are partly or fully submerged, and consequently much of their products have been deposited in submarine environments (Monzier *et al.*, 1994; Robin *et al.*, 1994a; Robin *et al.*, 1994b; Eissen & CALVA scientific team, 1997; Iizasa *et al.*, 1998). At this stage, little is known about the submarine volcaniclastic deposits in this island arc.

AIMS OF THE THESIS

This thesis describes and interprets the physical volcanology, sedimentology and geochemical characteristics of the volcanic rocks of the Efaté Island Group, Vanuatu arc, southwest Pacific, with particular emphasis on the Efaté Pumice Formation. The principal aims of this thesis are:

- to describe in detail the volcano-sedimentological facies and facies relationships of the Efaté Pumice Formation
- to propose a model for particle formation, transport and deposition of the Efaté Pumice Formation

Subaqueous volcaniclastic sedimentation is common in island arcs, yet little is known about the transport and depositional processes, or the facies characteristics of the resulting deposits since access to deep subaqueous environments is commonly difficult and expensive. Most facies models for marine volcaniclastic successions come from the rock record and not from geologically young, or *in situ* sequences. The Efaté Pumice Formation provides a unique opportunity to look at facies characteristics and facies relationships present in a young, syn-eruptive, marine volcaniclastic succession and consequently give an insight into transport and depositional mechanisms and environments.

In additional, the presence of large volumes of silicic volcanic debris at Efaté remains poorly explained and further aims of this thesis are:

- to describe in detail the petrographic and geochemical characteristics of the Efaté Pumice Formation and the Basalt Volcanoes Formation
- to discuss the geochemical links between these spatially related, but compositionally different formations
- to propose a geochemical model for the magmatic evolution in the Efaté region that is consistent with the wider tectonic context of the Vanuatu arc

The Efaté Island Group lies in the transition zone between two tectonically and geochemically distinct areas within the Vanuatu arc (Chapter Two), so characterisation of this centre is crucial to understanding the arc as a whole. Important geochemical similarities and differences of the Efaté Island Group with respect to other parts of the Vanuatu arc are presented and explored. The relationship between the late stage basalts of the Basalt Volcanoes Formation and the earlier Efaté Pumice Formation is also investigated geochemically.

By uniting the results of the investigation, the final goal of this thesis is:

- to reconstruct the evolution of this trachydacite-dominated, intra-oceanic arc volcanic centre

Caldera volcanism is represented throughout the Vanuatu arc but most prevalent in the zone extending north from the Efaté Island Group. This thesis presents the first detailed model for the volcanic and geochemical evolutionary history of the Efaté Island Group.

FIELD AREA, FIELD WORK AND LABORATORY STUDIES

The Efaté Island Group is centred at 17°40'S and 168°20'E in the southwest Pacific (Fig. 1.1). Efaté is the administrative centre of the Vanuatu island nation and the fourth largest island in the archipelago with an area of ~770 km^2 (Ash *et al.*, 1978). Fieldwork was carried out over two two-month field seasons in July-August, 1995 and 1996. River and coastal traverses were the focus of field work, to identify and study in detail the best exposed sections of Efaté Pumice Formation, resulting in 14 detailed sections logged at 1:25 scale. Samples of both Efaté Pumice Formation sediments and Basalt Volcanoes Formation were collected for sedimentological and geochemical analysis. A short mission on the scientific research vessel L'Atalante in 1996 produced new bathymetry maps in the Efaté region (Eissen & CALVA scientific team, 1997).

Samples were principally analysed at the University of Tasmania (Appendix A). Conventional grain-size analyses of suitable volcaniclastic sediments were performed at Monash University, Melbourne, and the University of Tasmania. Shape characteristics of glassy particles were investigated using the environmental scanning electron microscope (E-SEM) at the University of Tasmania. Petrological investigations were conducted on thin sections of samples from the Efaté Pumice Formation, and the Basalt Volcanoes Formation. Geochemical analyses were performed using X-ray fluorescence (XRF), inductively coupled plasma mass spectrometry (ICP-MS), and electron microprobe techniques at the University of Tasmania. Two new K-Ar age determinations were performed on samples from the Efaté Pumice Formation at the Institute for Geological and Nuclear Sciences, New Zealand. Radiogenic isotope ratios were determined using the facilities at La Trobe University, Melbourne.

EFATÉ ISLAND GROUP

Previous studies of the Vanuatu arc have generally neglected detailed sedimentological and geochemical studies of the volcanic rocks of the Efaté Island Group. Other investigations in the Efaté region have focussed on mineral resources (Abrard & Aubert

de la Rue, 1938; Aubert de la Rue, 1939; Bernard & Obellianne, 1963; Warden, 1970; Girschik, 1995), fossil fauna assemblages (Abrard, 1947), the nature of the soils (Quantin, 1972; Quantin, 1992), geothermal potential (Marks, 1983; Anderson *et al.*, 1986; Bath, 1986), seismic and tectonic history (Malahoff, 1970; Neef & Veeh, 1977; Lecolle *et al.*, 1990; Mellors *et al.*, 1991; Chatelain & Grasso, 1992; Chatelain *et al.*, 1993; Prévot *et al.*, 1994; Calmant *et al.*, 1995), and the petrology of Efaté Island Group (Lacroix, 1940; Coulon *et al.*, 1979).

Mawson (1905) proposed the first stratigraphy for the Efaté Island Group and the current stratigraphic framework is based on his early observations. Obellianne (1958) also described in some detail the geology of these islands and produced the first detailed 1:100,000 scale geological map with eight lithostratigraphic subdivisions. A detailed mapping exercise undertaken by the British Geological Survey in the 1960s and 1970s led to publication of the first coloured geological map of Efaté and nearby islands, together with an accompanying report (Ash *et al.*, 1974; Ash *et al.*, 1978).

Stratigraphy

The Efaté Island Group consists of two major volcanic sequences, overlain by reef-forming limestone (Fig. 1.2 Mawson, 1905; Obellianne, 1958; Ash *et al.*, 1978). This simple stratigraphy is broken down into three formations. The oldest deposits on Efaté belong to the trachydacitic pumice breccia and shard-rich sand and silt facies of the ~1 Ma *Efaté Pumice Formation (EPF)*. This succession is interpreted to have been generated by caldera volcanism, and deposited subaqueously (Mawson, 1905; Obellianne, 1958; Ash *et al.*, 1978). No attempt has been made yet to determine the mode of sedimentation of these units, nor has the location of their volcanic source vents been identified. The Pleistocene to Recent (~0.7-0 Ma) *Basalt Volcanoes Formation (BVF)* is restricted to the north of Efaté and includes two periods of volcano growth. On Efaté, the older basalt sequence consists of subaqueous to subaerial basaltic lavas, breccias and conglomerates associated with small, now dissected composite cones, unconformably overlie the EPF. Offshore on the islands of Nguna, Pele and Emau more recent subaerial basaltic activity, including lava effusion and pyroclastic activity. The fringing *Reef Limestone Formation (RLF)*, consisting of detrital and reef carbonate, is the dominant exposed lithology and unconformably onlaps both the EPF and the BVF on Efaté. Deposition of the limestone began in the late Pleistocene (~0.3 Ma) and reef growth is recorded in a series of terraces that developed during broadly domal uplift of Efaté, Hat, Lelepa and Moso islands. Modern deposits of the Efaté Island Group include fluvial and alluvial sediments, and fringing coral reefs that extend up to 1 km from the coast (Fig. 1.1).

Uplift and exposure following emplacement of the oldest basalt sequences on Efaté has provided a rare and excellent opportunity to examine the facies characteristics of the thick, trachydacitic, submarine volcaniclastic sediments.

Structure

Efaté is geologically young and structurally simple. A detailed outline of the structure is available in Ash *et al.* (1978). The major structural features are normal faults associated with localised uplift of the Vanuatu arc platform in the region (Fig. 1.1). Bedding in the EPF and surfaces of the RLF are tilted radially away from the island's centre with shallow dips generally not exceeding 10°. However, limestone plateaux in the interior of Efaté and on Moso Island are horizontal.

East-southeast trending normal faults associated with horst block development mark the dominant and most recently occurring structural orientation on the island. Longer faults (7-10 km) with wider inter-fault spacings (2-3 km), give way to closely spaced (<1 km), down-stepping, normal fault blocks bounded by shorter (3-4 km), arcuate, faults north of Mount MacDonald. Faults within the poorly consolidated EPF variably penetrate through the overlying RLF. However, within the RLF the surface expression of the faults is more marked towards the interior of the island. Ash *et al.* (1978) interpreted these features as indicating differential uplift of the island along common reactivated structures. On the limestone platforms, faults are less numerous and only locally important.

The Teouma Graben is a large structure that bisects the island and dies off to the north. Graben margins are defined by north trending fault scarps extending for over 20 km. Uplift is greater to the west where topography rises to 647 m on Mount MacDonald. Other off-trend structures include the northeast trending, uplifted horst block that forms a 4-6 km-wide promontory in the southwest of the island. An east-northeasterly trending fault, located northeast of the Teouma Graben, may be a surface expression of a deep-seated, arcuate, crustal fracture system that closes to the north, and along which the northern basaltic centres are aligned (Malahoff, 1970).

Small (1-3 km) normal faults on the northern offshore islands show no regional preferred orientation and are probably related to volcano development rather than uplift. However, steep high-angle cliffs form the northern coasts of Pele and Emau, and the northeastern coast of Nguna. This feature is a fault scarp marking a major structural trace along which parts of the volcanoes have collapsed (Obellianne, 1958; Malahoff, 1970; Ash *et al.*, 1978).

Existing bathymetric data for areas offshore of the Efaté Island Group show a pronounced kink or re-entrant structure along the Vanuatu trench-line, immediately northwest of Efaté. The origin of the Efaté re-entrant is still in question but is likely the result of impingement of the ORSTOM Seamount against the trench in this area (Chase &

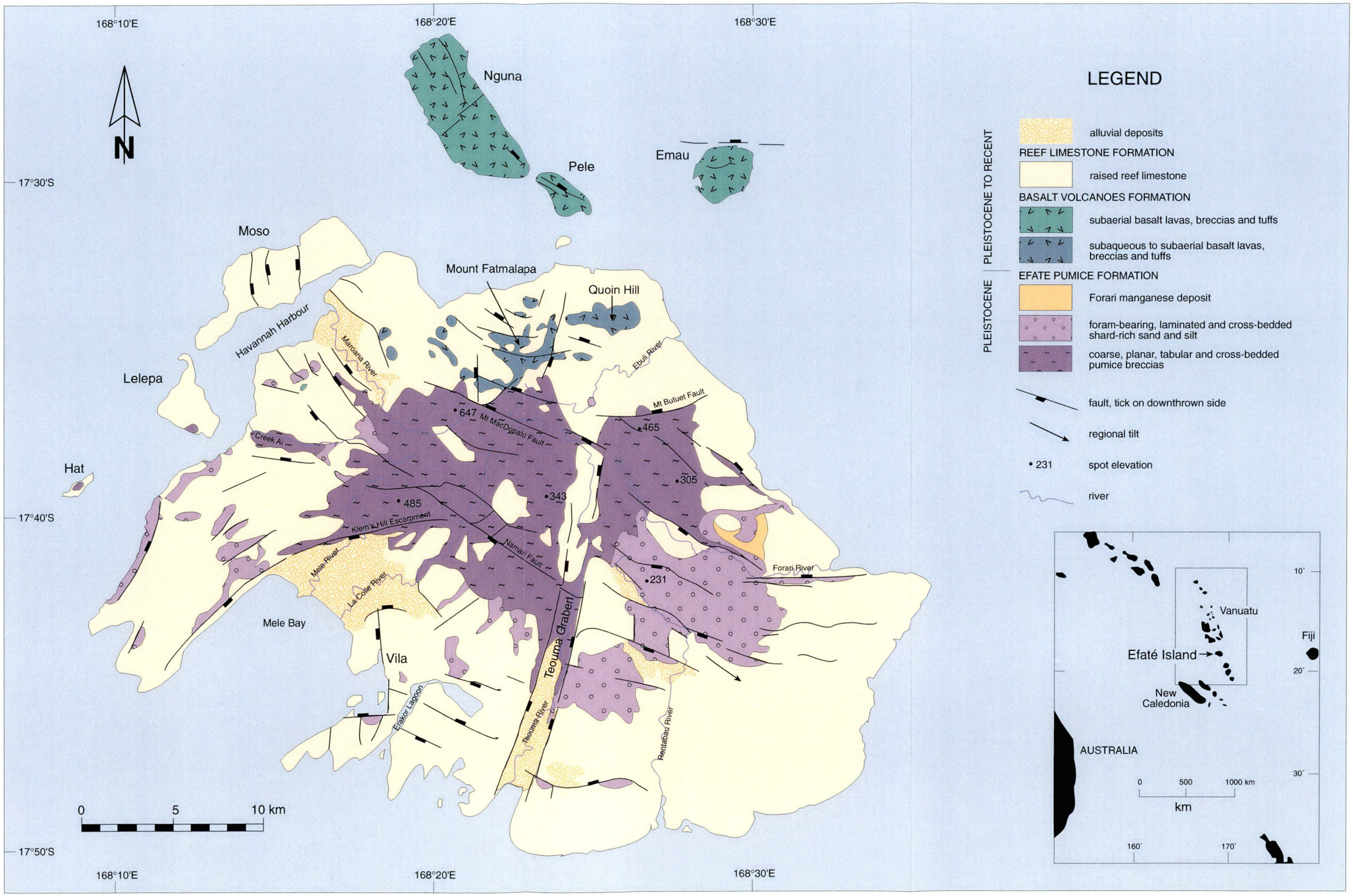

Figure 1.1. Geology and structure of the Efaté Island Group, Vanuatu arc, southwestern Pacific. Modified from Ash *et al.* (1974; 1978).

Seekins, 1988; Chatelain & Grasso, 1992). New data acquired during the 1996 CALVA scientific cruise identified two southwest trending, fault-controlled submarine canyons shedding from the western coast of Efaté, Lelepa and Hat Islands, into the fore-arc region. South of the Kuwae caldera, similar southwest trending canyons are 1-2 km wide with depths from 200-400 m (Eissen & CALVA scientific team, 1997).

Geophysics

The Australian Geological Survey Organisation (AGSO) published newly acquired magnetic and radiometric data for Efaté Island in 1995. A brief summary of the main observations and interpretations of the data follows. Airborne surveys acquired data from east-west oriented flight lines, with line spacings at 400 m intervals onshore and 800 m intervals offshore, and with 100 m nominal ground clearance (Vanuatu Department of Geology, Mines and Water Resources, 1995).

Magnetics

Reduced to pole magnetic data are draped over a digital elevation model with a linear stretch and a sun-shading applied to enhance relative magnetic highs and accentuate the dominant structural features (Fig. 1.2). Several striking magnetic anomalies are apparent within the new data (Fig. 1.2). The basaltic islands of Nguna, Pele and Emau give a strong magnetic response, as do the basaltic centres at Mount Fatmalapa and Quoin Hill in northern Efaté. A similar magnetic high occurs offshore to the east of Quoin Hill and may be the response of a now submerged and degraded basaltic centre that was active at the same time, but not uplifted. The area hosting the Forari manganese mine on the eastern side of the island also lies coincident with a high magnetic anomaly. The relative intensity of the anomaly indicates that there may be a basaltic centre at depth, underneath the volcaniclastic and limestone cover. Other relative magnetic highs, trending northeast, occur in the southwestern part of the Efaté Island Group and probably reflect block faulting in the basement. Areas where the EPF crops out give a characteristically low magnetic response. Localised magnetic highs within outcropping areas of the EPF might indicate mafic intrusions at depth, or alternatively, shallower depths to basement lithologies (Nash & Rankin, 1995).

Radiometrics

A ternary diagram depicting the three-channel radiometric data is given in Figure 1.2. A broad correlation exists between the radiometric response and the surface geology of Efaté. Particularly significant is the K-channel response that coincides with the outcropping EPF. Localised areas of elevated K-channel response within the EPF occur on topographic highs adjacent to major fault structures; for example, in the fault bounded Creek Ai region to the west, adjacent to a major fault escarpment immediately north of Vila, and on the western boundary fault of the Teouma Graben. The anomalies

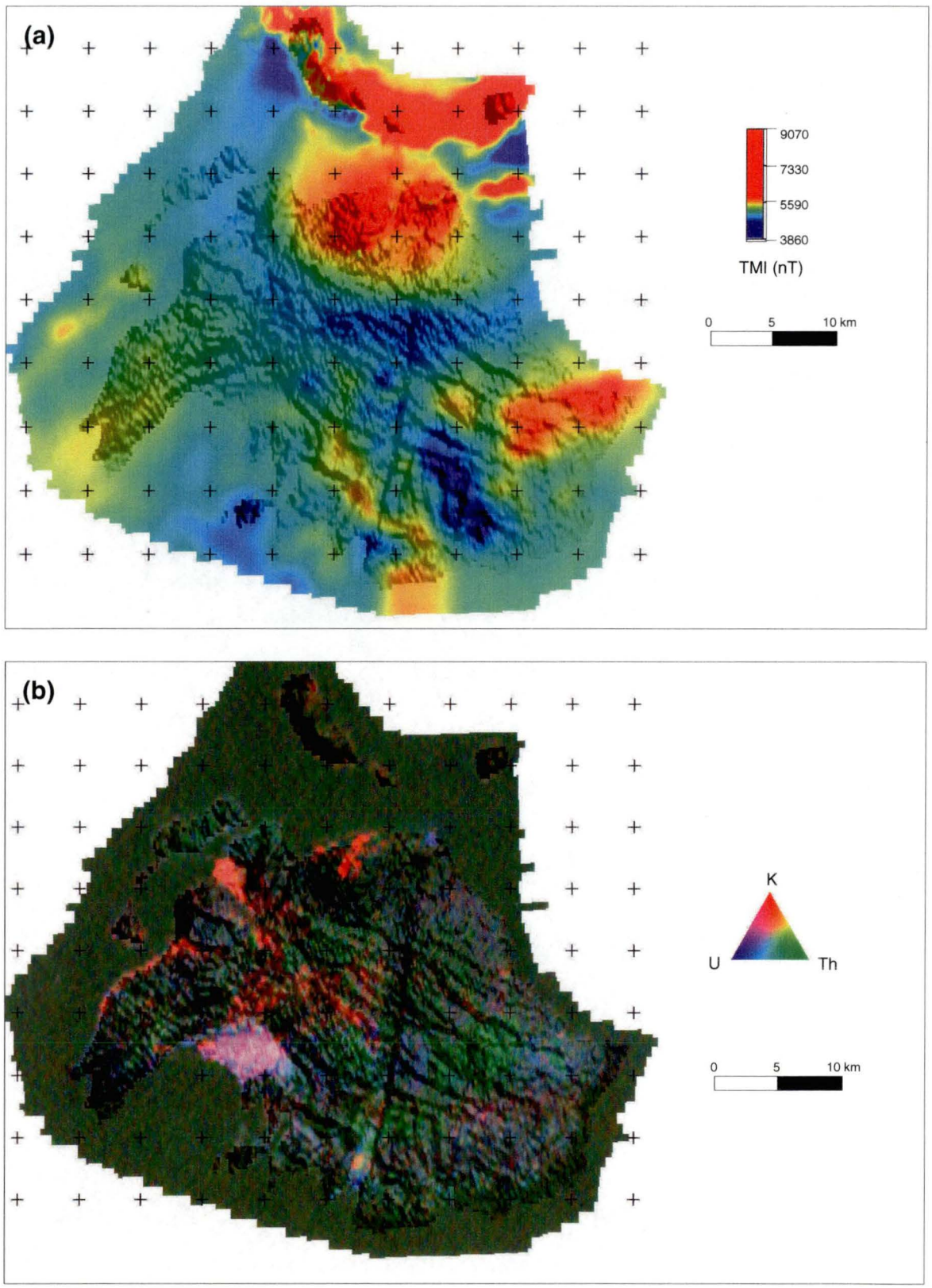

Figure 1.2. Geophysical characteristics of the Efaté Island Group. (a) Reduced to pole, total magnetic intensity data are draped over a digital elevation model for Efaté Island, with a histogram linear stretch and a northeast sunshading applied. These filters highlight the dominant northwest-southeast structural trend. Also note the strong relative magnetic highs (red) in the north that coincide with the outcropping Basalt Volcanoes Formation. (b) Radiometric data with linear autoclip stretch applied to K- and U-channel signals, and linear stretch applied to Th-channel signal. Note strong K-channel response (red) for Efaté Pumice Formation in western Efaté. Data released by theVanuatu Department of Geology, Mines and Water Resources (1995).

may be reflecting primary chemical signatures of the trachydacitic pumiceous volcaniclastic deposits, or more likely, incipient clay alteration in the volcaniclastic deposits caused by tropical weathering processes. A small K-channel anomaly on top of Mt Fatmalapa probably reflects an alteration halo and soil anomaly associated with an area of known epithermal gold occurrences (Martin, 1988). Strong responses are also evident in alluvial flats. U-channel and Th-channel responses are strongest in alluvial areas although slightly elevated U-channel signals occur over limestone platforms. A small U-channel anomaly on the northeast coast may be the result of changed surface chemistry due to the activity of geothermal waters at hot springs (Hochstein, 1977; Ash *et al.*, 1978; Bath, 1986).

ORGANISATION OF THE THESIS

The thesis combines two main themes: physical volcanology and geochemistry. Chapter Two gives an overview of the tectonic setting and geological history of the Vanuatu arc. The physical characteristics of the volcaniclastic deposits of the EPF are described in Chapters Three (Efaté Pumice Breccias) and Four (Rentabau Tuffs) and an interpretation of the volcano-sedimentary evolution and emplacement mechanisms is presented for each unit. Chapter Five gives a description of the volcanology and geochemistry of the BVF and compares and contrasts this with other Vanuatu arc centres, and explores the effects of local tectonic controls on magma genesis. Chapter Six discusses the geochemical evolution of the EPF trachydacites, their relationship to the post-caldera basaltic volcanism, and their context within the arc. The last chapter is a synthesis of the main conclusions of the study and a model for the magmatic and volcanological evolution of the Efaté Island Group is presented.

Chapter Two

REGIONAL GEOLOGY

Evolution of the Vanuatu island arc

INTRODUCTION

The Vanuatu (formerly New Hebrides) island arc has been the focus of detailed geological enquiry for several decades. The earliest recorded geological observations were made my European explorers in the 17th and 18th centuries (Robin *et al.*, 1993b), but the first highly detailed investigation was undertaken by Sir Douglas Mawson (1905). In the 1930s the economic mineral potential of the islands was explored principally by the French geologist Aubert de la Rue (1937; 1956), and these studies led to a greater understanding of the geology of the Vanuatu archipelago. French industry geologists produced the first geological maps of the islands in the 1950s, and a systematic mapping exercise to produce 1:100,000 scale geological maps of the separate islands was carried out by British Overseas Survey geologists from 1959-1979 (Greene *et al.*, 1988b). Since the 1980s detailed geochemical, seismological and geochronological investigations have further consolidated general understanding regarding the evolution of the Vanuatu arc, and the tectonics of the southwestern Pacific region (*e.g.* Kroenke, 1984a; Auzende *et al.*, 1988; Chatelain *et al.*, 1992; Chatelain *et al.*, 1993; Auzende *et al.*, 1995; Crawford *et al.*, 1995; Maillet *et al.*, 1995; Monzier *et al.*, 1997; Pelletier *et al.*, 1998; Turner *et al.*, 1999). Two large volumes, produced as the result of scientific cruises and ocean drilling in the area, report on structural, seismic, petrological, sedimentological, paleontological properties, and the economic potential of the central part of the Vanuatu arc (Greene & Wong, 1988; Greene *et al.*, 1994b).

TECTONIC FRAMEWORK

Southwestern Pacific

The southwestern Pacific is a geologically, tectonically and structurally complex region where the Pacific and Indo-Australian plates are converging. The major plate

boundary is marked by a narrow chain of Tertiary to Recent volcanic island arcs which extend northwest to south from Papua New Guinea and the Solomon Islands through Vanuatu, Fiji, Tonga and the Kermadec Islands to New Zealand (Greene *et al.*, 1988b). Subduction zones, spreading ridges and major fault zones are situated adjacent to one another in the area and record the multi-stage tectonic evolution of this region (Auzende *et al.*, 1995).

In the Vanuatu sector, plate convergence is complicated by the presence of nearby active spreading centres that separate two subduction zones with opposite convergence (Fig. 2.1). Subduction is east-directed under the New Britain-Solomon Islands-Vanuatu Island Arc system and west-directed along the Tonga-Kermadec trench. A newly recognised but no longer active intra-oceanic arc known as the Hunter Ridge links these two opposite-facing subduction zones (Verbeeten, 1996).

Active spreading centres in this region occur between Vanuatu and Fiji and between Fiji and the Tonga Ridge. The North Fiji Basin consists of several young spreading centres with associated sinistral transform faulting, and east of Fiji, spreading occurs in the Lau Basin, a marginal basin associated with the Tongan-Lau subduction system (Auzende *et al.*, 1988).

Vanuatu Island Arc (New Hebrides Island Arc)

The Vanuatu arc is a 1000 km-long, approximately 200 km wide, northwest trending, partially emergent volcanic ridge located in the southwestern Pacific (Fig. 2.2). It is a Tertiary to Recent feature formed in response to subduction at the Pacific-Indo-Australian plate boundary. The arc comprises the islands of the Republic of Vanuatu and extends from Matthew and Hunter Islands in the south, to the Santa Cruz Islands (Solomon Islands) in the north (Carney *et al.*, 1985; Greene *et al.*, 1988b; Macfarlane *et al.*, 1988; Robin *et al.*, 1993b).

Three morphological elements make up the Vanuatu arc: the trench, the arc-ridge complex and the back-arc region. The arc-ridge complex comprises the emergent part of the arc and includes the Central Chain of active volcanic islands (submarine and subaerial volcanoes), the now uplifted, inactive volcanic islands of the Eastern and Western Belts, and locally developed submarine sedimentary basins in the central part of the arc. Parallel to and west of the arc-ridge complex lies the Vanuatu Trench (New Hebrides Trench), a 6000 m-deep (on average) depression which is absent to the west of Espiritu Santo and Malekula Islands. Here the arc is colliding with the locally east-west trending d'Entrecasteaux Zone (DEZ), an arcuate series of submerged ridges and basins now generally accepted to be an extension of the Loyalty Ridge (Greene *et al.*, 1988a; Robin *et al.*, 1993b; Greene & Collot, 1994;

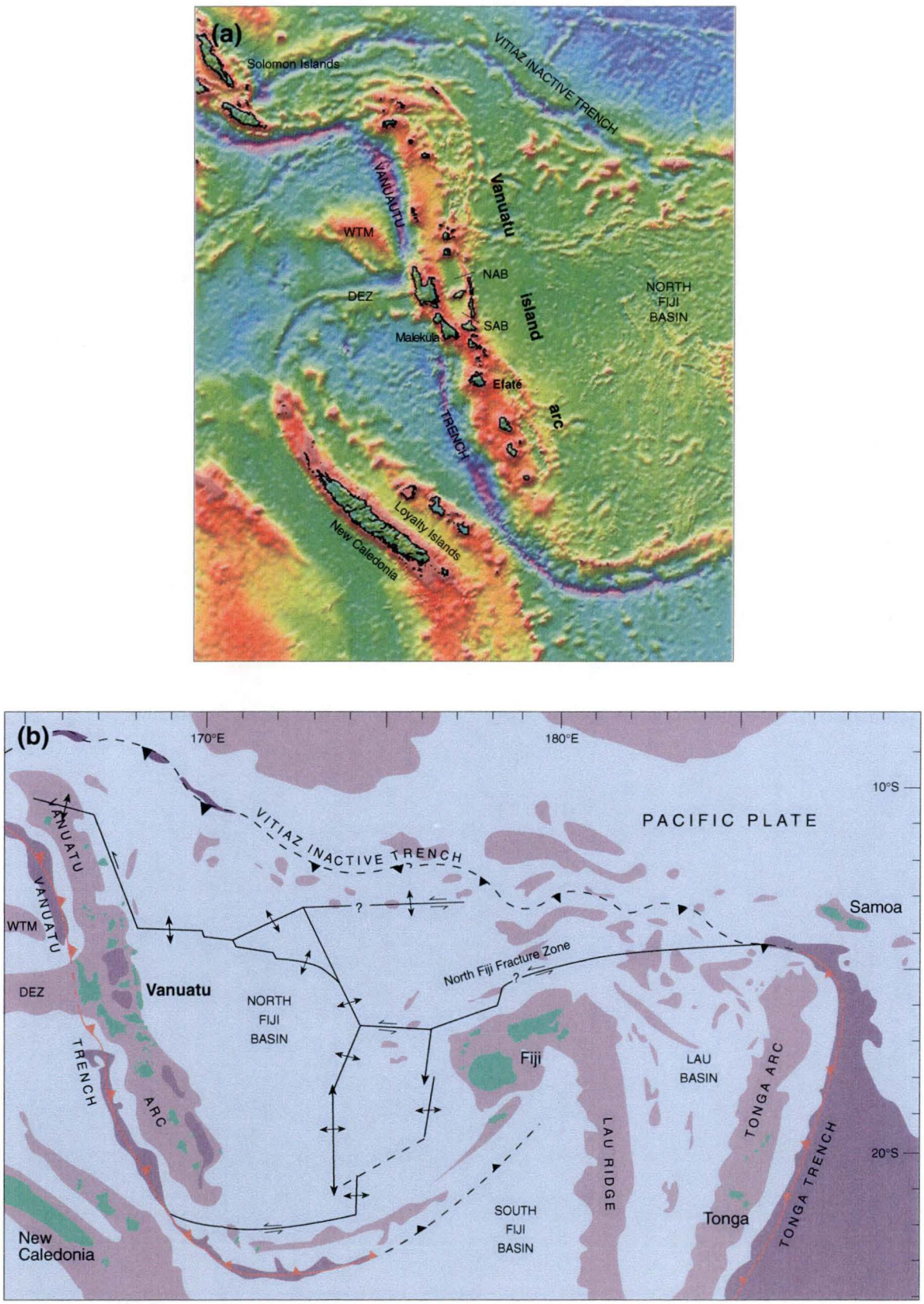

Figure 2.1. (a) False colour bathymetry map of the Vanuatu island arc and immediate environs. Features to note include the Vitiaz Trench, West Torres Massif (WTM), arcuate d'Entrecasteaux Zone (DEZ), the North and South Aoba Basins (NAB and SAB), and the kink in the Vanuatu trench line between Efaté and Malekula Islands, causing an offset in the dominant arc trend. Modified from Smith and Sandwell (1997). (b) Tectonic map of the southwest Pacific area with major bathymetric features highlighted. Bathymetry marked as follows: landmasses 0-7 km (pale green), 0-2 km depths (medium blue), 2-3 km depths (pale blue), 3+ km depths (dark blue). Modified from Maillet *et al.* (1995), with North Fiji Basin spreading axes from Auzende *et al.* (1995), and the trace of the Hunter Ridge inactive arc from Verbeeten (1996).

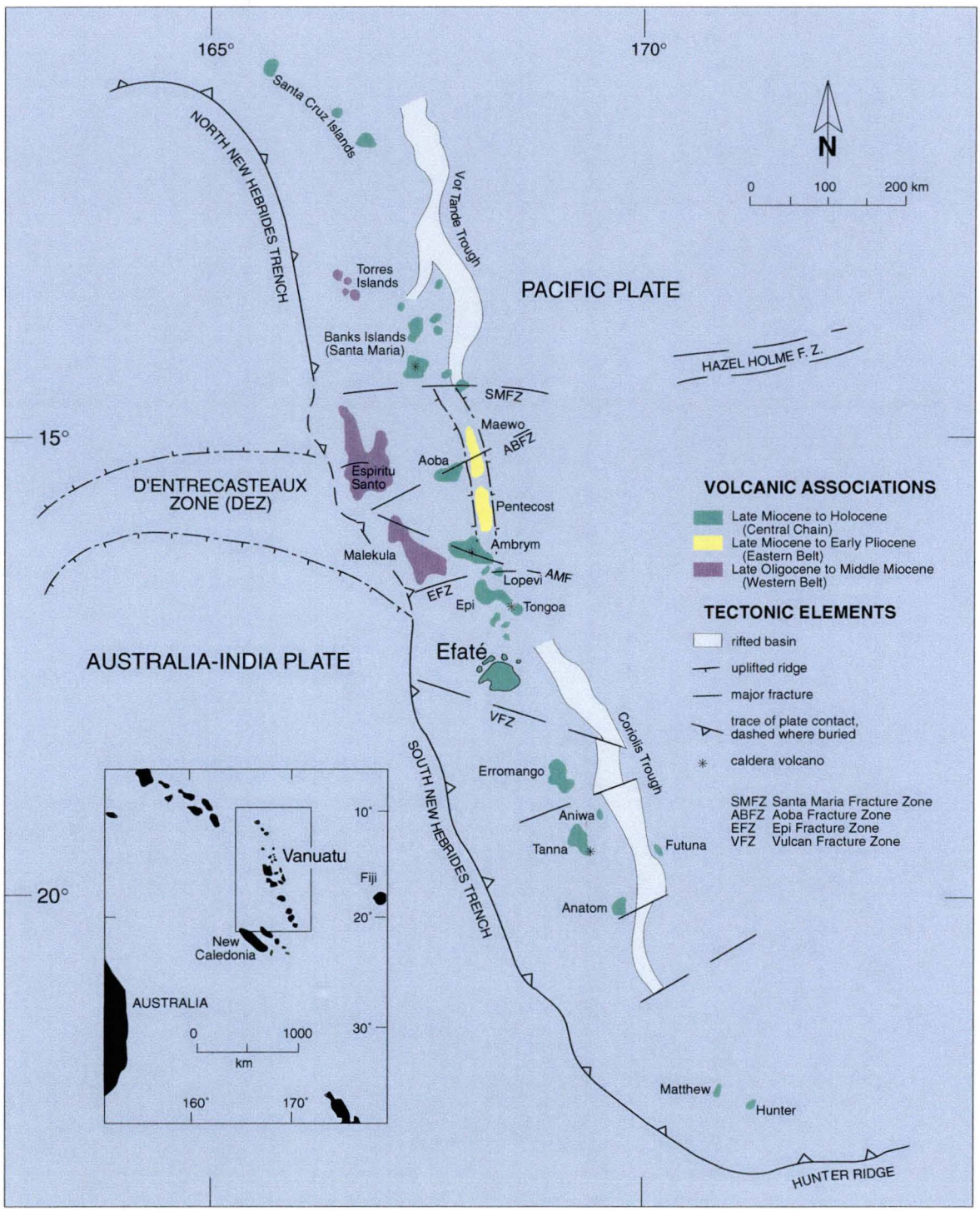

Figure 2.2. Regional geological and tectonic map of the Vanuatu island arc. Modified from Macfarlane *et al.* (1988) and incorporating information from Monzier *et al.* (1991), Robin *et al.* (1993a, b), Monzier *et al.* (1994), Robin *et al.* (1994a), Robin *et al.* (1995), and Verbeeten (1996).

Aitchison *et al.*, 1995). A mostly continuous, eastward-dipping Benioff Zone, inclined at 70°, underlies the Vanuatu arc and delineates the site of active subduction of the Indo-Australian plate beneath the Pacific plate. The Vot Tande and Coriolis Troughs are ~30 km-wide extensional rifts lying to the east of the arc-ridge complex in the immediate back-arc region. Futuna Island is probably a slice of uplifted arc crust separated from the main arc platform by late Neogene rifting of the Coriolis Trough (Robin *et al.*, 1993b).

TECTONIC EVOLUTION OF THE VANUATU ARC

Although the timing and duration of tectonic events in the southwestern Pacific are contentious, there is general agreement regarding the sequence of these events (Gill *et al.*, 1984; Kroenke, 1984c; Carney *et al.*, 1985; Macfarlane *et al.*, 1988). A cartoon depicting the events described below is presented in Figure 2.3 (Kroenke, 1984c).

Vitiaz Arc System (38 - ~10 Ma)

The Vitiaz trench, a broadly west-northwest trending feature which lies to the north of Vanuatu and Fiji, is interpreted to mark the site of west-dipping subduction of the Pacific plate beneath the Indo-Australian plate active from ~38 to 10 Ma (Carney *et al.*, 1985; Macfarlane *et al.*, 1988; Robin *et al.*, 1993b). The early history of the Vanuatu arc is thought to have occurred along this fossil Vitiaz trench line. At that time, volcanic islands from Manus, the Solomon Islands, Vanuatu, Fiji and possibly Tonga were arranged in a co-linear fashion to form the Vitiaz arc. The timing of initiation of the Vitiaz arc remains unconstrained but basement rocks preserved in the Fijian and Tongan sections are Late Eocene. Late Oligocene sedimentary rocks in Vanuatu contain clasts of these basement lithologies (Gill *et al.*, 1984).

Arc breakup and rotation (~10 - 8 Ma)

At ~10 Ma, the Ontong Java Plateau (a now inactive, large submarine igneous province) arrived at the Vitiaz Arc trench in the Solomon Islands region, and effectively halted subduction by choking the subduction system. This forced a reversal of subduction polarity along the Solomon-Vanuatu-Fiji sector from west-directed to east-directed. Perhaps in response to this collision, opening of the North Fiji Basin at about the same time caused a clockwise rotation of the Vanuatu portion of the pre-existing Vitiaz arc, and anticlockwise rotation of the Fijian segment (Greene *et al.*, 1988a; Robin *et al.*, 1993b).

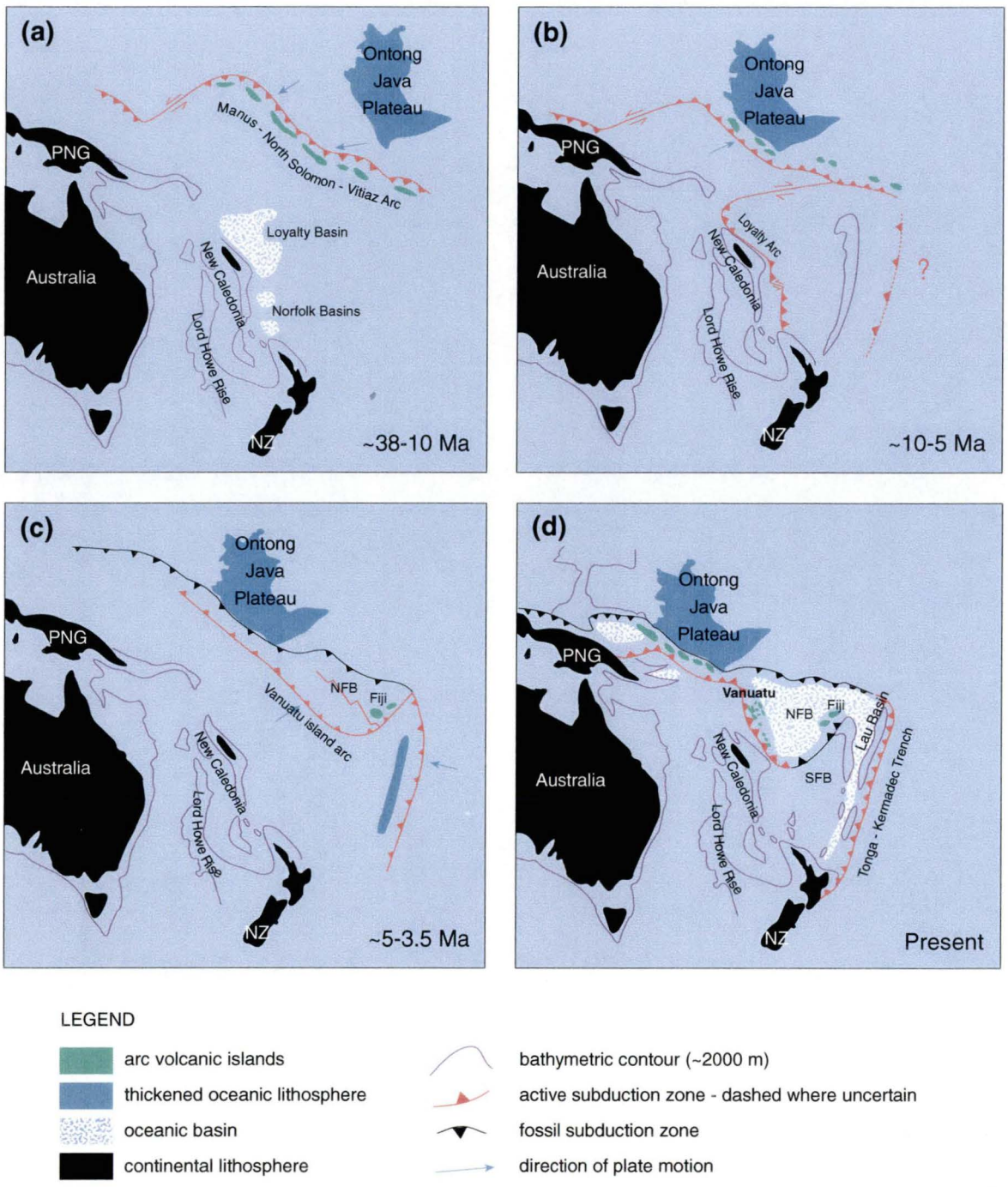

Figure 2.3. Tectonic reconstruction of the southwest Pacific: (a) the earliest phase of Vanuatu arc evolution occurred with southwest-directed subduction along the Eocene Vitiaz arc; (b) incipient collision of the Ontong Java Plateau followed, and choked the existing subduction system, forcing a reversal of subduction polarity (also coinciding with early development of the Loyalty island arc); (c) opening of the North Fiji Basin occurred in response to the collision and caused a clockwise rotation of the Vanuatu segment; (d) the present day configuration of the southwest Pacific plate margin. Acronyms read as follows: PNG = Papua New Guinea, NZ = New Zealand, NFB = North Fiji Basin, SFB = South Fiji Basin. Modified from Kroenke (1984c) and incorporating information from Macfarlane *et al.* (1988), Auzende *et al.* (1995) and Verbeeten (1996).

Recent history and present arc (8 Ma - Present)

Following collision of the Ontong Java Plateau, east-dipping subduction of the Indo-Australian plate under the Pacific plate was established and continues to the present day. Since ~3.5 Ma the Vanuatu arc has been colliding with the DEZ which has moved northwards along the arc, from at least as far south as Efaté, to its present position immediately west of Malekula and Espiritu Santo Islands (Greene & Collot, 1994).

Tectonic position of Efaté Island

The Efaté Island Group sits at an important position within the arc. An area of higher relief on the seafloor east of the active southern Vanuatu arc volcanoes is probably the submarine extension of arc basement from the time of activity of the Western Belt (remnant Vitiaz arc, Fig. 2.1 a). Efaté lies directly at the point between this older arc basement and the modern arc volcanoes. The basement to the Efaté Island Group is still unknown, but Western Belt arc basement may floor the modern arc deposits of Efaté. Chemical characteristics of the magmas produced at Efaté may reflect contributions from this thickened crust.

Several detailed seismic investigations have shown that there is a marked seismic gap extending and broadening from Ambrym, southward to Efaté, and is at its broadest below the Efaté Island Group (Fig. 2.4 Monzier *et al.*, 1997). No intermediate focus earthquakes occur under these islands, in contrast to abundant intermediate depth seismicity in the adjacent collision zone (Chatelain & Grasso, 1992; Chatelain *et al.*, 1992; Prévot *et al.*, 1994; Monzier *et al.*, 1997). Chatelain *et al.* (1992) interpreted this to represent detachment of the descending slab at this position. The geochemistry and the nature of magmatism at Efaté are clearly quite different from other Vanuatu arc centres and probably reflect this local tectonic variation (see Chapter Five). Rapid uplift of the Efaté Island Group, as recorded in the ages of limestone terraces, occurred at least partially in response to slab detachment and possibly the subduction of a seamount (Lecolle *et al.*, 1990; Chatelain & Grasso, 1992; Chatelain *et al.*, 1992).

GEOLOGICAL HISTORY OF THE VANUATU ARC

The Vanuatu arc is divided into three provinces with distinctive magma compositions, ages and evolution (Fig. 2.2, Greene *et al.*, 1988b). The early history of the arc is recorded in the rocks of the Western and Eastern Belts. The more recent and current volcanic activity of the arc occurs along the Central Chain islands. A simplified stratigraphic column is given in Figure 2.5 and a summary of the important

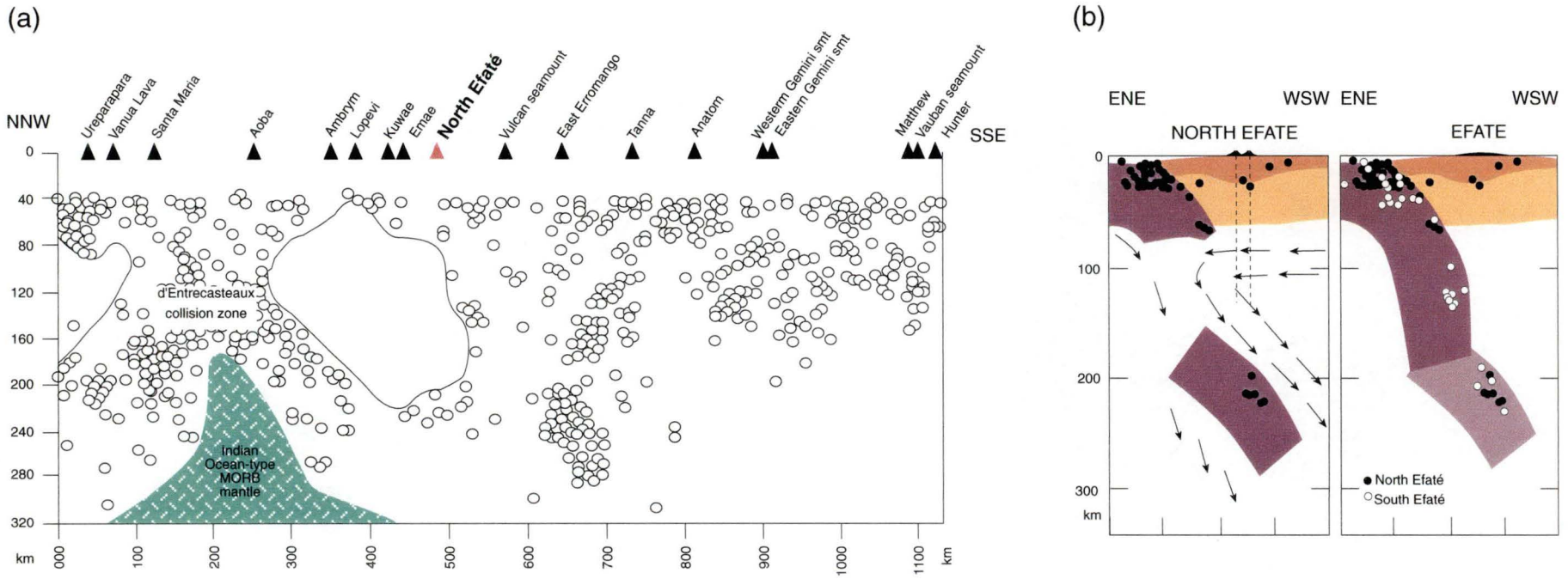

Figure 2.4. (a) Seismic profile of shallow and intermediate depth events recorded from 1961-1988 along the Vanuatu arc (N160°E). Open circles indicate earthquakes recorded by more than 20 stations. Aseismic gaps under the arc volcanoes are highlighted. Invasion of Indian Ocean type MORB beneath the central part of the arc is reflected in the isotopic signature of central Vanuatu arc magmas (Crawford *et al.*, 1995; Turner *et al.*, 1999). (b) Schematic interpretation of the position of the sinking slab from the Australian plate beneath the Efaté region of the Vanuatu arc. Cross sections are oriented N70°E. The North Efaté section originates at 17°51'S/167°22'E and is drawn from a swath width of 30 km. The Efaté section originates at 18°18'S/167°25'E and has a swath width of 70 km. The swath width of the Efaté section encompasses the north Efaté section. Seismic events for North Efaté are represented by black circles, and by white circles for the remainder of the Efaté section. Dashed lines indicate inferred magma ascent pathways. Modified from Monzier *et al.* (1997).

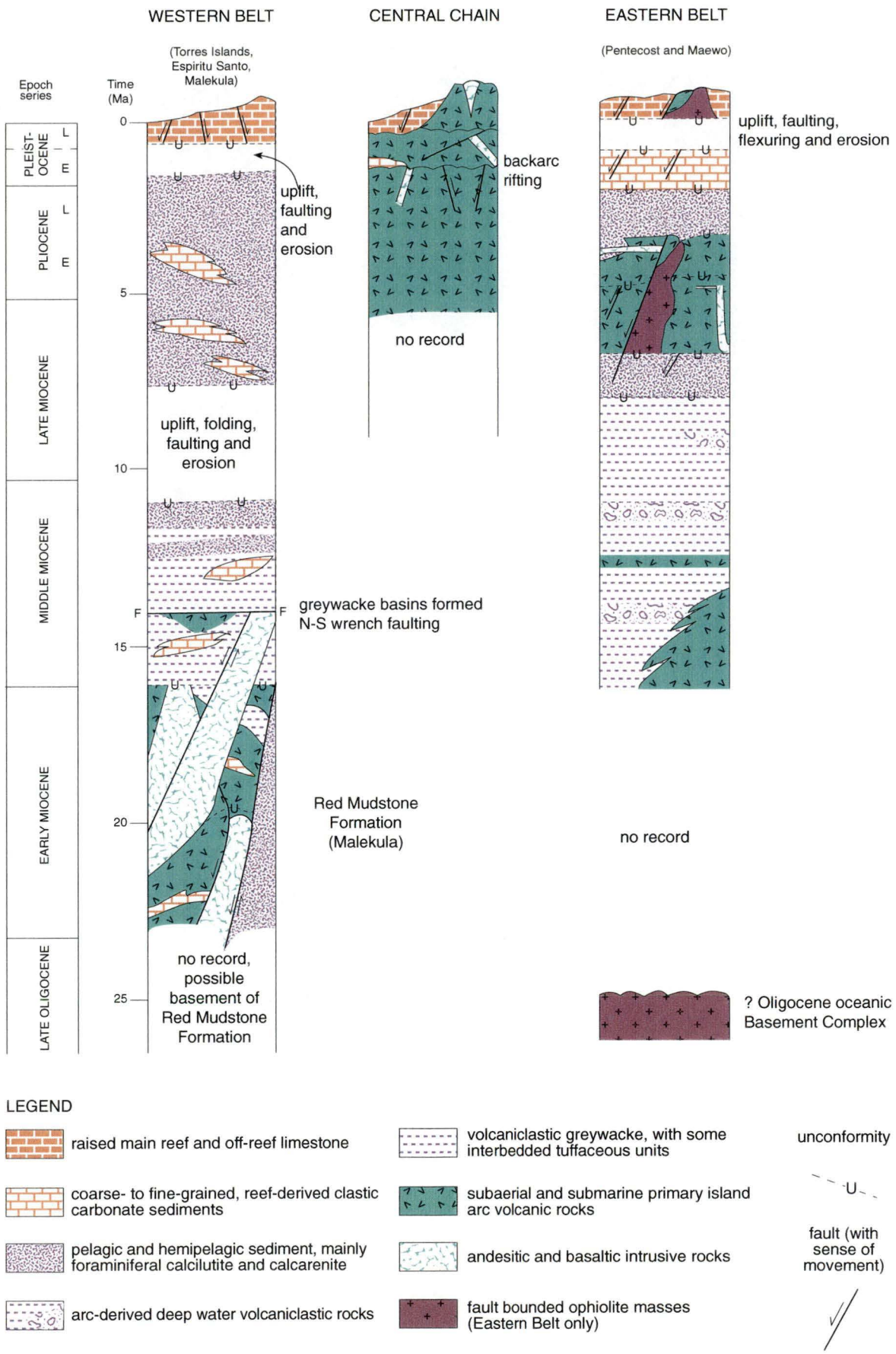

Figure 2.5. Summarised stratigraphy of principal geological units, correlated across the Vanuatu arc. Modified from Macfarlane *et al.* (1988).

geological events occurring throughout the evolution of the Vanuatu arc in Figure 2.6 (Greene *et al.*, 1988b).

Western Belt

The Western Belt includes the two large islands of Malekula and Espiritu Santo located in the central part of the Vanuatu arc, and the northernmost Torres Group of islands. The oldest rocks exposed in the Western Belt are strongly altered, deformed and metamorphosed Oligocene sedimentary rocks found in northwestern Malekula. These rocks are interpreted as either ocean floor deposits, or an uplifted deep water volcaniclastic facies correlate of a dominantly volcanic package with which they are in fault contact (Mitchell, 1970; Carney *et al.*, 1985; Robin *et al.*, 1993b).

Extensive submarine and minor subaerial volcanism with associated basin sedimentation and local reef growth occurred in all areas of the Western Belt. The locus of volcanism and direction of sediment transport appear to have shifted from east to west along the Vitiaz arc with time (Robin *et al.*, 1993b). Volcanic facies include submarine pillow lavas and massive volcanic breccias, subaerial lavas, autobreccias, primary and reworked pyroclastic deposits and both subaerial and submarine coarse- and fine-grained volcaniclastic mass-flow facies. These lithologies are well represented in the Western Belt and are intercalated with carbonate reef facies and minor mixed and epiclastic sedimentary facies (Carney *et al.*, 1985; Macfarlane *et al.*, 1988; Robin *et al.*, 1993b).

The earliest record of arc volcanism is found in the Torres Group. The sequence is dominated by submarine volcanic facies at the base, with upward transitions to shallow marine and subaerial volcanic, volcaniclastic and sedimentary facies demonstrating the eventual emergence of these volcanic centres (Greenbaum *et al.*, 1975). Radiometric dates give an oldest age for these rocks at 39-37 Ma (Eocene/Oligocene boundary), but fossil ages from included limestone clasts are much younger, ranging from 25-20 Ma. These conflicting results have yet to be resolved (Robin *et al.*, 1993b).

The most vigorous period of volcanic activity occurred from 25-11 Ma associated with shallow, southwest-directed subduction along the Vitiaz arc (Fig. 2.6). Several shallow marine to subaerial centres are recognised on Espiritu Santo and others in Malekula (Mitchell, 1966; Jones, 1967; Robinson, 1969; Mitchell, 1970; Mallick & Greenbaum, 1977). Late-stage subvolcanic intrusions occur on both Espiritu Santo and Malekula, and are a characteristic feature of volcanism in the Western Belt. Three stages of intrusion spanning 21-14 Ma have been recognised on Espiritu Santo (Mallick & Greenbaum, 1977; Carney *et al.*, 1985). The dykes and intrusions follow north- and northeast-trending regional structures. Continuous sedimentation in adjacent basins, enhanced by uplift in the Middle Miocene, is recorded in the

submarine volcanogenic mass-flow successions on Espiritu Santo and Malekula (Jones, 1967; Mitchell, 1970).

By Late Miocene and Early Pliocene time, progressive subsidence and marine transgression resulted in hemipelagic sedimentation on angular unconformity surfaces in Espiritu Santo and shallow marine carbonate, epiclastic and lagoonal sedimentation in a time-equivalent position on Malekula. A subsequent period of uplift and regression towards the end of the Plio-Pleistocene (followed by extremely rapid uplift after collision of the Vanuatu arc with the DEZ after 2 Ma) generated a series of fringing reef limestone terraces in the Western Belt (Mitchell, 1970; Taylor, 1992).

Eastern Belt

Rocks of the Eastern Belt are exposed on Pentecost and Maewo Islands in the central part of the Vanuatu arc. These islands are elongate in an arc-parallel direction (north-northwest) and are geologically distinctive as they contain the only occurrence of ophiolitic rocks in the arc (Mallick & Neef, 1974).

Metamorphosed ophiolitic rocks are the oldest exposed rocks in the Eastern Belt and are found only on Pentecost Island. This Basement Complex is in fault contact with younger lithologies and has been emplaced as horst blocks along the length of the island. Radiometric age determinations give a metamorphic age around 35-28 Ma (Mallick & Neef, 1974). Lithologies include metamorphosed and altered harzburgite, serpentinite, dunite, banded feldspathic peridotite, basalt and dolerite that are cut by gabbroic dykes and stocks. The ultramafic assemblage also contains schistose epidote and amphibolite blocks and rafts. The ultramafic rocks of the Basement Complex are overlain by basaltic submarine pillow lavas that have mid-ocean-ridge-basalt (MORB) geochemical affinities (Mallick & Neef, 1974). The origin of the Basement Complex is currently the subject of some investigation; two current interpretations suggest that this ophiolite complex represents either Oligocene ocean crust that was basement to the Eastern Belt, or early North Fiji Basin ocean crust. Subsequent upthrusting or backthrusting, probably related to the DEZ collision, emplaced the ophiolitic basement into the Eastern Belt (Robin *et al.*, 1993b). Recent results from an ongoing geochemical-geochronological study by Crawford *et al.* (1998) indicate that these ophiolitic rocks might be back-arc basin crust of the present North Loyalty Basin; they are definitely not Late Tertiary North Fiji Basin basement.

During the Miocene and prior to the subduction polarity reversal, mass-flow clastic sedimentation produced thick successions of turbidites with overall fining-upward trends on both Maewo and Pentecost. Many of the units are fossiliferous. The coarsest units are polymictic conglomerates and breccias that grade up into tuffaceous siltstones and sandstones. Provenance studies of volcanogenic clasts from the coarsest units indicate an Eocene to Middle Miocene Fijian source rather than a

local source for these sedimentary rocks. Carbonate sedimentation is important at the top of the succession, and limestone units are intercalated with pumiceous tuff beds (Robin *et al.*, 1993b).

Volcanic activity began in the Eastern Belt towards the end of the Miocene (~7 Ma) and continued strongly into Pliocene time, post-dating the subduction polarity reversal at ~10 Ma (Greene *et al.*, 1988b). At least two periods of dominantly submarine volcanism are recognised on both islands. On Maewo the oldest volcanic rocks have been dated at 7-5 Ma by fossil faunal assemblages, supported by a K-Ar date of 7 Ma on a pillow lava (Carney, 1988). K-Ar dates on the oldest volcanic rocks from Pentecost give an age range from 6-3 Ma, which agrees with fossil ages from the same succession (Mallick & Neef, 1974).

The earliest volcanic units on both islands are largely submarine pillow basalts, associated hyaloclastite, and intrusions. On Pentecost, the top of this sequence is dominated by intercalations of massive volcanic breccia with thick volcaniclastic turbidite and carbonate-rich sedimentary sequences. Shallow marine to subaerial eruptions occurred in the second phase of volcanism on Maewo accompanied by fine-grained volcaniclastic and carbonate sedimentation in the north (Carney, 1988). Submarine pillow lavas continued to be emplaced on Pentecost in the second eruptive period. Basaltic lavas are interbedded with carbonate clastic facies in the upper part of the stratigraphy, indicating that volcanic edifices here were shoaling (Mallick & Neef, 1974).

Emplacement of the ophiolitic Basement Complex on Pentecost occurred concurrently with uplift and erosion of the Eastern Belt in Late Pliocene time. This episode was followed by subsidence of the islands and shallow water sedimentation, including reef growth. Limestone terraces on both Maewo and Pentecost developed from Late Pleistocene to Holocene times in response to uplift of the Eastern Belt. This uplift is probably related to collision of the DEZ with the central Vanuatu arc, and concurrent with uplift in the Western Belt (Robin *et al.*, 1993b).

Central Chain

Initiation of volcanic activity along the Central Chain of islands overlaps with the latest events occurring in the Eastern Belt in the late Miocene (~6 Ma), following clockwise rotation of the arc, and the reversal of subduction polarity from west-directed to east-directed at about 10-8 Ma (Greene *et al.*, 1988b). Extensive magmatic activity developed along the length of the arc from the Plio-Pleistocene to the present and is characterised by a remarkably regular spacing of volcanic centres. The six southernmost centres, including the Mons Gemini and Vulcan seamounts, are about 85 km apart on average. Further north, the spacing of volcanoes is less regular, reflecting disruption by local collisional tectonics (Robin *et al.*, 1993b).

Shallow submarine volcanism on Erromango, dating from 5.8-5.3 Ma, is the oldest known in the Central Chain (Robin *et al.*, 1993b). This activity produced basaltic and andesitic pyroclastic deposits and subordinate pillow lavas. Extensive subaerial basaltic to basaltic andesite volcanism was dominant by Early to Middle Pliocene time, as was activity at Vot Tande in the far north of the arc. By the Late Pliocene, volcanic activity was widespread on the southern islands. Erromango had several active centres, producing large volumes of andesitic lava and pyroclastic deposits, some of which were associated with caldera collapse. On Tanna, subaerial basaltic volcanism dominated, whereas submarine basaltic lava eruptions and subvolcanic intrusions dominated at Futuna (Carney & Macfarlane, 1979).

Volcanic activity extended along the length of the Central Chain during the Pleistocene. In the southern part of the Central Chain, large basaltic stratocones were built on Tanna and Anatom. Contemporaneous explosive andesitic volcanism generated pyroclastic deposits, and also resulted in caldera collapse on Anatom (Robin *et al.*, 1993b). Thick sequences of submarine dacitic to rhyolitic volcaniclastic debris, associated with caldera collapse, were deposited in the Efaté region at ~1 Ma, followed by late-stage (0.7 Ma) submarine to emergent basaltic stratocone development dominant in the north (Ash *et al.*, 1978). Pillow basalts and submarine andesitic pyroclastic deposits were emplaced between 0.7 and 0.4 Ma in the Epi-Tongoa region (Warden, 1967). In the North Aoba Basin from ~1.8 Ma, large basaltic shield volcanoes grew forming Aoba and Ambrym Islands. These volcanic centres are aligned along major faults thought to be associated with the DEZ collision (Eggins, 1993; Robin *et al.*, 1993a; Robin *et al.*, 1993b). At the same time, large subaerial stratovolcanoes were developing in the Banks Islands. Eroded centres at Santa Maria (Gaua), Vanua Lava, Mota Lava and Mota are basaltic whereas volcanic remnants on Merig consist of an association of andesitic intrusive plugs and volcanic breccias. A large, less eroded basalt to basaltic andesite composite cone forms the island of Ureparapara (Ash *et al.*, 1980). The evolutionary histories of the active submarine volcanic centres of the Vanuatu arc are poorly known due to their location. Monzier *et al.* (1993) noted that most of the seamounts in the southern part of the arc were less than 2-3 Ma with the exception of the Vauban seamount which is significantly older (Late Miocene).

Sedimentation patterns in the North Aoba Basin show that volcanic activity has slowed from the Late Pleistocene to the present day, during which time the arc has narrowed to its present shape (Greene *et al.*, 1994a). Holocene andesitic volcanism in the southernmost part of the arc generated the islands of Matthew and Hunter. Subaerial basaltic to andesitic cone-building pyroclastic activity on Erromango continued, whereas on Tanna volcanic activity changed from cone-building pyroclastic eruptions to effusion of basalt lavas, and following that, caldera-related andesitic lava extrusions (Colley & Ash, 1971; Carney & Macfarlane, 1979). Further

north, subaerial basaltic eruptions built composite cones on three islands north of Efaté (Ash *et al.*, 1978). In the Shepherd Group of islands, subaerial eruptions produced several basaltic pyroclastic cones, including the currently active Lopevi volcano (Warden, 1967). A major basaltic andesite-dacite pyroclastic eruption of the Kuwae caldera occurred about 1425 A.D. and subaqueous pyroclastic cone activity followed caldera collapse (Crawford *et al.*, 1988; Monzier *et al.*, 1994; Robin *et al.*, 1994b). On the shield volcanoes of Aoba and Ambrym, composite basaltic stratocone growth, fissure eruptions and caldera-collapse replaced shield-forming lava eruptions (Monzier *et al.*, 1991; Eggins, 1993; Robin *et al.*, 1993a). Subaerial pyroclastic activity associated with stratocone growth and subsequent caldera collapse occurred on both Santa Maria (Gaua) and Vanua Lava islands in the Banks Group. Basaltic to basaltic andesite compositions were important on Santa Maria, and more andesitic compositions dominated at Vanua Lava. Cinder cones and composite cones built up by both ash and lava emissions followed caldera collapse on these islands, and basaltic cone building was also continuing on Mota Lava and Mere Lava (Mallick & Ash, 1975).

Currently active volcanism within the Vanuatu arc occurs at several locations. All of the following eruption activity records are reported in Simkin and Siebert (1994). In the northern part of the arc, explosive eruptions are historically known for centres on Vanua Lava and Mere Lava. Mount Garet on Santa Maria (Gaua) Island was most recently active in early 1982. Semi-permanent lava lakes occur in the craters of Ben Bow and Marum post-caldera cinder cones on Ambrym, which have also been locations for explosive ash and lava eruptions historically. Historical eruptions on Lopevi Island volcano in the Shepherd Group include basaltic lavas, explosive ash emissions, and small volume pyroclastic flows. The ignimbrite-forming ~1425 A.D. eruption of the Kuwae caldera is reported in local folklore and its signal has been recognised in Greenland icecore (*e.g.* Monzier *et al.*, 1994). Post-dating the cataclysmic Kuwae eruption, the submarine volcanoes of Epia, Epib, and Karua have all been active in the last 70-100 years, with the tip of Karua emerging from time to time (*e.g.* Crawford *et al.*, 1988). To the south, the Eastern Gemini Seamount has been active as recently as 1996 (GVN Bulletin, 21:04). Yasur andesitic cinder cone volcano on Tanna Island has been in continual eruption since Captain Cook visited in 1774. Vigorous Strombolian explosions shower the crater and the cone with fluidal bombs, and occasional Vulcanian hydromagmatic activity generates ash emissions which blanket the volcano and surrounds (Robin *et al.*, 1993b). Explosive magmatic, phreatic and lava eruptions on both Matthew and Hunter Islands at the southern tip of the arc have been reported in the last 200 years.

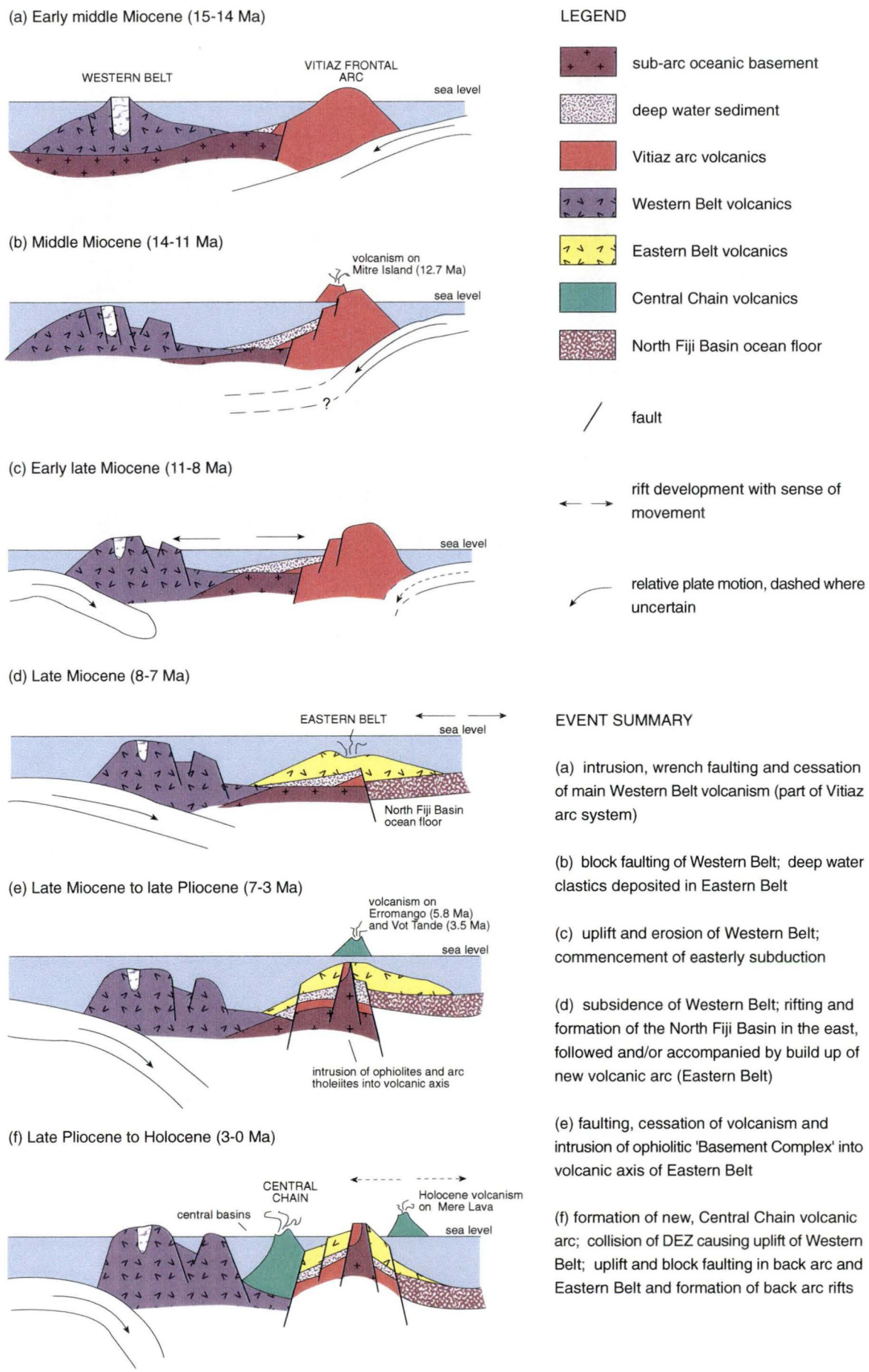

Figure 2.6. Model of the evolution of the Vanuatu arc. Modified from Carney *et al.* (1985) and Macfarlane *et al.* (1988).

Caldera volcanoes of the Vanuatu arc

A particular feature of the Vanuatu arc is the presence of several caldera volcanoes in the Central Chain of islands (Fig. 2.2). This type of activity is uncommon in young island arcs, and even within the Vanuatu arc basaltic lava extrusions and small volume pyroclastic eruptions are dominant. Recent studies have identified subaerial ignimbrites associated with caldera collapse at Santa Maria (Robin *et al.*, 1993b; Robin *et al.*, 1995), Tanna (Robin *et al.*, 1994a), Ambrym (Monzier *et al.*, 1991; Robin *et al.*, 1993a), and the Kuwae caldera between Epi and Tongoa Islands (Monzier *et al.*, 1994; Robin *et al.*, 1994b). There have been several other possible caldera structures identified in bathymetric studies in the Epi-Tongoa-Efaté region and further seafloor mapping in these areas should clarify the abundance and significance of calderas in the Vanuatu arc (Crawford *et al.*, 1988). The characteristic features of major caldera collapse centres in the Central Chain are described in Table 2.1, and compared with deposits from the Efaté Island Group.

Table 2.1. Caldera volcanoes of the central chain, Vanuatu island arc.

VOLCANO	AGE	SIZE	CHARACTERISTICS
Santa Maria	~2000 B.P.	8.5 x 6 km	*dominantly basalt to andesite/dacite* hydromagmatic surge and fall deposits, ash- and scoria-flow deposits, non-welded pyroclastic flow deposits bulk volume: 6.5-7 km^3 sequence thickness: at least 60 m (Mallick & Ash, 1975; Robin *et al.*, 1995)
Ambrym	<2000 years	12-km-wide	*dominantly basalt to dacite* hydromagmatic surge and fall deposits, non-welded pyroclastic flow deposits bulk volume: 60-80 km^3 sequence thickness: ~500 m (Monzier *et al*, 1991; Robin *et al*, 1993a)
Kuwae	~ 1425 A.D.	12 x 6 km	*basaltic andesite to dacite* hydromagmatic surge and fall deposits, non-welded pyroclastic flow deposits, densely welded ignimbrites bulk volume: 32-39 km^3 sequence thickness~150 m thick (Monzier *et al.*, 1994; Robin *et al*, 1994b)
Tanna	Late Plio-Pleistocene	undefined	*dominantly basaltic andesite to andesite* hydromagmatic surge and fall deposits, non-welded pyroclastic flow deposits, densely welded ignimbrites bulk volume: no estimate sequence thickness: <100 m (Carney & Macfarlane, 1979; Robin *et al.*, 1994a)
Efaté	~ 1 Ma	undefined	*trachydacite* subaqueous pumiceous sediment gravity flow deposits, shard-rich sand and silt turbidites bulk volume: 84 km^3 sequence thickness at least 500 m (this study, Mawson, 1905; Obellianne, 1958; Ash *et al.*, 1978)

Caldera volcanism in the Vanuatu arc is most typically associated with basaltic and basaltic andesite products, with subordinate dacite. The voluminous deposits of the EPF are uniformly trachydacitic in composition, and represent the products of a

significant explosive eruption in this region (Chapters Two and Three). Even compared with the next closest centre, Kuwae, Efaté shows marked compositional differences. The pyroclastic deposits from the Kuwae caldera-forming eruption change from basalt to basaltic andesite hydromagmatic fall and surge deposits low in the sequence, to non-welded and densely welded dacitic ignimbrites higher in the sequence (Robin *et al.*, 1994b). On Ambrym, the lowermost part of the caldera sequence is dominated by non-welded but indurated, dacitic, pumiceous pyroclastic flow deposits, with abundant accidental basaltic clasts. In the upper sequences, which are much thicker and more widespread, basaltic compositions dominate, and hydromagmatic fall and surge deposits are more common (Robin *et al.*, 1993a). Compositions of non-welded and welded ignimbrites, and hydromagmatic ash and scoria deposits from Tanna range from basalt/basaltic andesite to dacite (Robin *et al.*, 1994a). Mafic scoria-flow and ash fall deposits form the bulk of the pyroclastic deposits on Santa Maria. Dacitic obsidian blocks have also been reported but their geological significance and context remain unclear (Robin *et al.*, 1995).

The pyroclastic deposits of the Efaté region (the EPF) are also distinctive in having been deposited in the submarine environment (Chapters Three and Four). In all other Vanuatu arc caldera centres, the caldera-related deposits are products of subaerial eruptions and at least partly emplaced subaerially. Interestingly, episodes of hydromagmatic fragmentation are common in many of these eruptions (*e.g.* Robin *et al.*, 1993a; Robin *et al.*, 1994b).

GEOCHEMICAL CHARACTERISTICS OF THE VANUATU ARC

Chemical affinities of the volcanic rocks from the three Vanuatu arc provinces were defined initially by Mallick (1973) and reflect tectonic changes occurring throughout the history of the Vanuatu arc. The earlier arc-wide summaries focussed on describing the principal mineralogical and chemical differences among rocks of the three belts (Mitchell & Warden, 1971; Mallick, 1973; Colley & Warden, 1974), eventually resulting in a generally consistent tectonic model for the arc system (*e.g.* Colley & Warden, 1974; Kroenke, 1984c; Macfarlane *et al.*, 1988). More recent investigations have concentrated on the Central Chain volcanoes, and hence the nature of the current subduction system (Barsdell *et al.*, 1982; Dupuy *et al.*, 1982; Eggins, 1993; Crawford *et al.*, 1995; Monzier *et al.*, 1997; Peate *et al.*, 1997). Figure 2.7 shows the variation of Vanuatu arc igneous geochemistry.

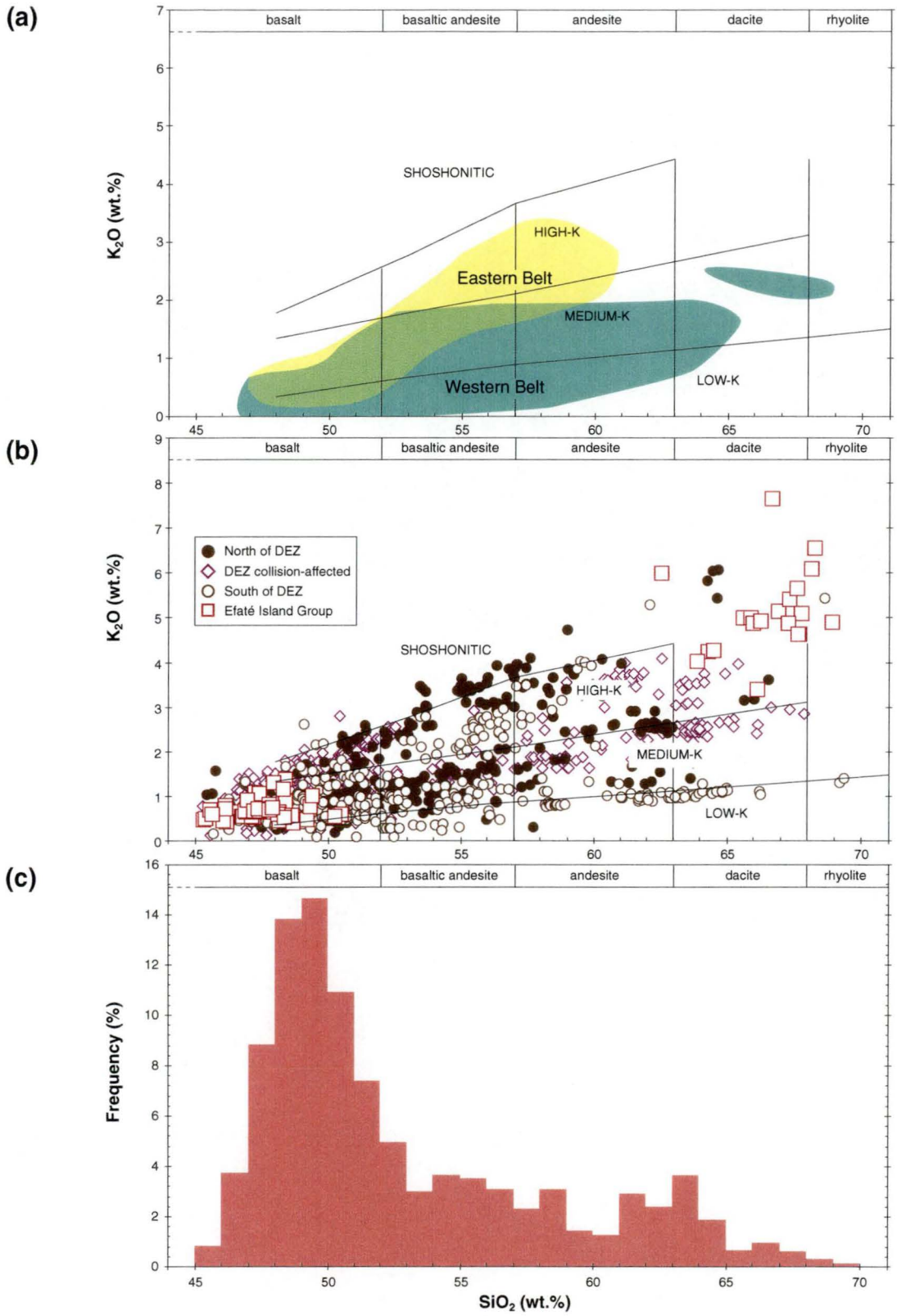

Figure 2.7. Geochemical characteristics of Vanuatu arc volcanic rocks. (a) Western Belt rocks have low- to medium-K trends, in contrast to medium- to high-K trends shown by Eastern Belt rocks on the K_2O vs. SiO_2 (weight %) bivariate plot of Peccerillo and Taylor (1976); fields from Macfarlane *et al.* (1988). (b) This diagram also highlights the compositional diversity of the currently active Central Chain magmas. Low-K, medium-K, high-K and weakly shoshonitic suites are all represented throughout the Vanuatu arc. Note the strongly bimodal nature of Efaté Island Group rocks. (c) Histogram of SiO_2 contents in Vanuatu arc magmas (1000+ analyses) illustrating the dominance of basaltic over more evolved andesite or dacite compositions in this immature island arc. Data sources include: Gorton (1977); Dupuy *et al.* (1982); Barsdell and Berry (1990); Eggins (1993); Peate *et al.* (1997); Monzier *et al.* (1997).

Western Belt

Upper Oligocene - Middle Miocene rocks of the Western Belt (including the Torres Group, Malekula, and Espiritu Santo) are characterised by a predominance of calc-alkaline andesite compositions. Basalts and high-silica dacites and rhyolites are less abundant. Typical rock types are volcaniclastic, with coherent volcanic units being locally important and best represented by late-stage subvolcanic intrusions, particularly on Malekula and Espiritu Santo. Intrusions of microgabbro, hornblende-microdiorite and gabbro-diorite have been reported. Western Belt rocks show zeolite facies metamorphism and consequently alteration minerals such as chlorite, zeolite, calcite and pyrite are locally important.

Mineralogy

Western Belt volcanic rocks are distinguished by their plagioclase-phyric nature and the abundance of hornblende-bearing lithologies. Hornblende is rare or absent elsewhere in the Vanuatu arc so its appearance in these rocks is striking. On Espiritu Santo, pyroxene-phyric basalt and two pyroxene + plagioclase-phyric andesite, and hornblende-phyric andesite are the commonest rock types. Pyroxene-phyric andesite, with hornblende-rich xenoliths, occurs as lavas on Malekula. Intrusions occurring primarily as dykes include clinopyroxene + hornblende + labradorite microdiorite and hornblende + olivine + augite microgabbro with minor plagioclase. A two pyroxene-phyric andesite and a pale hornblende-phyric andesite are the dominant lava types in the Torres Group.

Chemistry

Carney *et al.* (1985) pointed out the transitional arc tholeiitic to calc-alkaline characteristics of Western Belt volcanic rocks. The basalts are typically high-alumina to tholeiitic basalts, whereas the andesitic rocks are more commonly calc-alkaline. No detailed petrogenetic studies have been published on the Western Belt, however a brief overview is presented in Macfarlane *et al.* (1988).

Available analyses of the freshest lavas and intrusions from the Western Belt plot in the medium- and low-K_2O fields on a K_2O versus SiO_2 diagram (Fig. 2.7). Limited trace element data show Ti/Zr ratios in the range 107-180, and <13 ppm Rb for Lower Miocene basalt. These features are typical of arc tholeiitic lavas but Western Belt lavas show no marked Fe-enrichment or enrichment of light rare earth elements (LREE) which is also expected in arc tholeiites. These features suggest that Western Belt rocks have transitional arc tholeiite/calc-alkaline characteristics and are chemically similar to the Lau Ridge rocks and the lower-K_2O suite in the currently active Vanuatu arc (Macfarlane *et al.*, 1988).

Eastern Belt

In contrast to the Western Belt, the Eastern Belt (Maewo, Pentecost) arc volcanic rocks are dominantly tholeiitic submarine basaltic lavas, with subordinate volcaniclastic facies. The Upper Miocene to Lower Pliocene pillow lavas are still fresh enough in places to retain glassy groundmasses. Some rocks with picritic compositions occur on Maewo. Seawater alteration has had a pronounced effect on rock chemistry in some areas. The older suite of Early Oligocene ophiolitic rocks described in earlier sections will not be discussed here. Brief accounts of the chemistry of this suite can be found in Mallick and Neef (1974) and Crawford *et al.* (1998).

Mineralogy

Arc rocks of the Eastern Belt are dominantly mafic phase-phyric basalts. Phenocryst phases from Maewo pillow basalts include olivine and clinopyroxene with subordinate labradorite. Hornblende and orthopyroxene phenocrysts are rare. The lavas of Pentecost include plagioclase + clinopyroxene-phyric basalt and a lesser two pyroxene andesite (Colley & Warden, 1974; Mallick & Neef, 1974; Carney, 1988).

Chemistry

Basalt and basaltic andesite lavas from the arc phase of volcanism in the Eastern Belt fall into medium-K_2O to high-K_2O fields on a K_2O versus SiO_2 plot (Fig. 2.7), and less common, more strongly differentiated calc-alkaline andesites have high-K_2O affinities. Although these rocks have medium to high-K_2O contents based on major element analyses, trace element abundances are not typical for rocks normally associated with these suites. Rb (<26 ppm) and Ba (136 ppm on average) contents of the Eastern Belt arc lavas are low, and La/Ba, La/Nb and La/Th ratios more closely resemble those expected in low-K_2O arc suites. This contrast may be due in part to alteration of the analysed lavas (Gill *et al.*, 1984; Macfarlane *et al.*, 1988).

Central Chain

The nature of the active Central Chain volcanism is an ongoing area of interest and several recent papers have drawn on and reviewed available data, and generated new ideas about the arc tectonics and evolution (*e.g.* Monzier *et al.*, 1997). The Central Chain has been active since Upper Miocene and Early Pliocene time and includes the Banks Islands, Aoba, Ambrym, Epi-Tongoa and the Shepherd Group, Efaté, Erromango, Tanna, Anatom and in the southernmost extension of the arc, Matthew and Hunter Islands. Most of the volcanism in the active Central Chain is subaerial with notable exceptions being the Mons Gemini, Vulcan and Vauban Seamounts. A consequence of this is that primary subaerial facies are widespread, as

are primary and secondary volcaniclastic units. These subaerial units commonly rest on submarine volcanic sequences.

Mineralogy

Rocks of the Central Chain range in composition up to rhyodacites although basaltic and basaltic andesite magma compositions dominate. Ankaramitic and picritic basalts have been recognised in the Banks Group and on Ambrym, Aoba and Western Epi. The typical rock type for Central Chain is a holocrystalline, feldspar-phyric, olivine + pyroxene-bearing basalt to basaltic andesite. The most primitive ankaramitic and picritic rocks from Central Chain volcanoes have over 50% clinopyroxene and/or olivine phenocrysts respectively, with trace amounts of plagioclase (Barsdell & Berry, 1990; Della-Pasqua, 1997). Other primitive basalts contain labradorite + forsteritic olivine + clinopyroxene and more differentiated basalts and basaltic andesites are two pyroxene + plagioclase-phyric with or without forsteritic olivine. Hornblende is rare or absent in most Central Chain volcanic rocks, however mafic hornblende gabbro xenoliths occur in Ureparapara pyroclastic deposits (Colley & Warden, 1974).

The most silicic compositions in the Central Chain are dacitic pyroclastic deposits from Efaté, Epi and Tanna. Phenocrysts of andesine, labradorite and rarely sanidine, with both clino- and orthopyroxene are sparsely scattered in a highly vesicular, glassy groundmass within pyroclastic fragments. Coherent lithologies commonly occurring as clasts within pyroclastic breccias, have similar phenocryst assemblages, and glassy to microcrystalline groundmasses.

Chemistry

Central Chain magmas are much more compositionally diverse than those of the Western and Eastern Belts, although a broadly 'normal' suite of low-K_2O magmatism has been suggested by Macfarlane *et al.*, (1988). Magmas in the active arc fall into several different geochemical suites, ranging from low-K tholeiitic, medium-K calc-alkaline, to high-K alkaline and high-Mg andesite magmas, with different suites also existing at individual centres (*e.g.* Tanna, Epi, Ambrym Robin *et al.*, 1993b Fig. 2.7).

The 'normal' pattern of Central Chain volcanism is characterised by a low-K_2O magmatic suite, with separate centres showing deviations to higher-K_2O values for the most silica-rich samples (Fig. 2.7). This 'normal' suite is typically represented by basalts with low- to medium-K_2O abundances, showing light rare earth element (LREE) enrichment, coupled with fairly flat heavy rare earth element (HREE) patterns, low high field strength element (HFSE) abundances, and $^{86}Sr/^{87}Sr$ ratios varying from 0.7030-0.7032 (Macfarlane *et al.*, 1988; Crawford *et al.*, 1995; Peate *et al.*, 1997).

In the more tectonically and structurally complex central part of the arc, where collision with the DEZ occurs, high-K_2O compositions dominate. Elsewhere in the arc however, there is no clear association between high-K_2O magmas and arc tectonics (Robin *et al.*, 1993b). The primitive ankaramitic and picritic lavas of Santa Maria, Aoba, Ambrym and Epi also occur in, or close to, the DEZ. Strontium isotopic ratios in the range 0.7036-0.7043 are much higher than those reported for 'normal' Central Chain lavas. Differing Pb-Sr-Nd isotopic signatures have been attributed to mantle source variations in the collision zone, influenced by mixing with an Indian Ocean DUPAL-type mantle source (Crawford *et al.*, 1995).

A distinctly different group of lavas exists at the southern termination of the arc, where it sweeps around to the east below 22°S. The islands of Matthew and Hunter consist of a high-Mg andesite suite of lavas, with the more mafic end-members showing high-Ca boninitic affinities, distinctly different from the 'normal' Central Chain lavas as described above. Monzier *et al.* (1993) suggested that an elevated heat source caused partial melting of a shallow level, refractory, hydrated mantle source to generate the parental boninite magmas. This heat source was provided by rising mantle diapirs associated with the propagation of a major North Fiji Basin back-arc spreading axis into the Vanuatu subduction zone. The chemical and mineralogical characteristics of this suite are very similar to those of Hunter Ridge boninites which are found further to the east and were generated in a similar fashion (Monzier *et al.*, 1993; Verbeeten, 1996; Monzier *et al.*, 1997).

Chapter Three

SYN-ERUPTIVE SUBMARINE PUMICE BRECCIAS FROM EXPLOSIVE TRACHYDACITIC ERUPTIONS: EFATÉ PUMICE BRECCIAS

Facies characteristics and genetic and depositional controls

INTRODUCTION

The lowermost unit of the Efaté Pumice Formation (herein referred to as the Efaté Pumice Breccias) is an excellent example of a non-welded, pumice-rich volcaniclastic unit deposited in a submarine setting. The Efaté Pumice Breccias are composed of ~85 % trachydacitic pumice clasts and are the record of a major felsic explosive eruption in the Vanuatu arc.

Interpreting the origin of thick, non-welded, submarine volcaniclastic successions, like the Efaté Pumice Breccias, is difficult since volcaniclastic sediments derived directly from originally hot gas/pyroclast dispersions that admix with seawater (*i.e.* syn-eruptive deposition), may be transported and deposited by processes essentially identical to those that remobilise and redeposit unconsolidated pyroclastic aggregates stored temporarily in either subaerial or subaqueous environments (*i.e.* post-eruptive deposition, Fisher, 1984; Schmincke & van den Bogaard, 1991; McPhie *et al.*, 1993). Distinguishing syn-eruptive, water-supported volcaniclastic mass flows that are *directly* generated from explosive eruptions from other subaqueous volcaniclastic mass flows involves careful evaluation of the nature and abundance of juvenile particles, and the significance of lithic clasts and intraclasts (McPhie *et al.*, 1993).

This chapter addresses: (1) the nature (deep vs. shallow) of depositional environments of the Efaté Pumice Breccias; (2) the transport and depositional processes that delivered the pumice-rich sediments to these environments; (3) the vent environments and eruption processes that generated the pyroclasts; (4) criteria that distinguish syn-eruptive and post-eruptive deposits; and (5) contrasts between these deposits and subaerial non-welded pumice breccias.

METHODS AND APPROACH

The Efaté Pumice Breccias are described in terms of their lithofacies characteristics. Field work involved detailed logging of the best available outcrops at various scales, dependent upon the quality of outcrop and the complexity of the volcano-sedimentary units and structures present. Photo mosaics of key sections (and inaccessible sections) provided base maps for some stratigraphic logs. Bulk samples were collected for granulometric and component analyses; raw data are presented and techniques described in Appendix C. Clasts from the coarsest units were hand picked for geochemical analysis (Chapter Six). Some representative cobbles and boulders, and parts of very large boulders sourced from the Efaté Pumice Breccias, were collected from creek beds and beaches for textural analysis, particularly in sections where overhanging cliffs (the most likely source of the clasts) were inaccessible. Clast shapes are described qualitatively from hand specimens, binocular microscope studies, thin section analysis and SEM images of clasts. Some semi-consolidated samples were examined in large thin sections providing information on grain-to-grain relationships and internal textural features of grains in coarser grained facies. However, most data on the pumice breccias and related beds come from outcrop scale observations. The petrography of the Efaté Pumice Breccias is presented here, and glass and crystal chemistry is given in Chapter Six.

EFATE PUMICE BRECCIAS

Age and distribution

The Efaté Pumice Breccias include the lowermost part of the Efaté Pumice Formation (EPF), which also comprises the conformably overlying Rentabau Tuffs (Chapter Four). Ash *et al.* (1978) assigned a Plio-Pleistocene age to the EPF based on fossil faunas in the Rentabau Tuffs, and a K-Ar date of 1.6 Ma on a trachydacite (latite) lava clast from a pumice breccia bed in the Mele (Bokua) River. New dates on juvenile glassy clasts obtained for this study place the Efaté Pumice Breccias in the earliest Pleistocene (Jones & AGSO Timescale Calibration and Development Project, 1995). A pumice clast (AR206, Mele River) from near the lowermost exposed part of the sequence yielded an age of 1.10±0.02 Ma. Sample AR064 from a pumice breccia bed ~3 m below the conformable contact with the Rentabau Tuffs was dated at 0.96±0.02 Ma. The implications of the age range determined by radiometric dating are discussed later in this chapter.

The Efaté Pumice Breccias have been mapped in detail by Obelliane (1958) and Ash *et al.* (1978) and the best exposed sections have been investigated for this project (Fig. 3.1). The Efaté Pumice Breccias are exposed extensively on Efaté and also on the western offshore islands of Hat and Lelepa. Current outcrops cover at least 160 km^2, and have maximum thicknesses up to 400 m in valleys around Mount Macdonald. A minimum volume estimate for the Efaté Pumice Breccias based on current outcrop is ~65 km^3 (Fig. 3.1, Appendix B). A more reasonable minimum estimate would include at least another 15 km^3 from areas covered by limestone (Mawson, 1905).

Thick tropical vegetation limits exposure of the pumice breccia beds and rugged topography means several sections are inaccessible. West of the Teouma Graben, in central Efaté, deep canyons cut through the EPF and where preserved, onlapping limestone forms high plateaux. Cliffs up to 500 m high variably expose sections through the Efaté Pumice Breccias and the overlying Rentabau Tuffs. Cliff sections, up to 100 m high, occur in valleys of the Mele River, La Colle River, Creek Ai and unnamed western tributaries of the Teouma River. East of the Teouma Graben, the topography is much flatter, lower and gently rolling, and exposure is restricted to small outcrops in valleys. Coastal cliffs in southwestern Efaté, Hat and Lelepa Islands expose the uppermost portions of the Efaté Pumice Breccias, and the contact with the Rentabau Tuffs.

Ash *et al.* (1978) defined a marker horizon of thinly bedded to laminated shard-rich sand and silt within the Efaté Pumice Breccias called the Bokua Tuffs (or Bokua Clays where altered). This interval generally comprises discontinuous lenses a few metres thick (up to 20 m thick) in the Mele (Bokua) River valley (Ash *et al.*, 1978). Except for a 3 m-thick interval in the Mele River, fine-grained shard-rich sediment beds thicker than 1 m were not observed in mapped traverses. In fact, thin intervals of similar shard-rich sediment occur interbedded with the pumice breccias throughout the succession. The limited nature of exposure, near uniform appearance of the pumice breccia beds, lateral variation of facies over several tens of metres and abundance of normal faults meant that correlation of fine-grained facies among the sections was not possible. The Bokua Tuffs have therefore been included within the Efaté Pumice Breccias in this thesis.

Lithofacies

The Efaté Pumice Breccias comprise flat-lying, unconsolidated, poorly to moderately sorted, very thickly bedded, massive and cross-stratified, trachydacitic pumice breccia beds. This unit has been divided into eight principal facies (Table 3.1), distinguished on the basis of grain-size, sedimentary structures and composition (Table 3.2). Coarse-grained facies are dominated by gravel (>2 mm), and fine-grained facies by sand (<2 mm). Bed thicknesses are described following Ingram (1954).

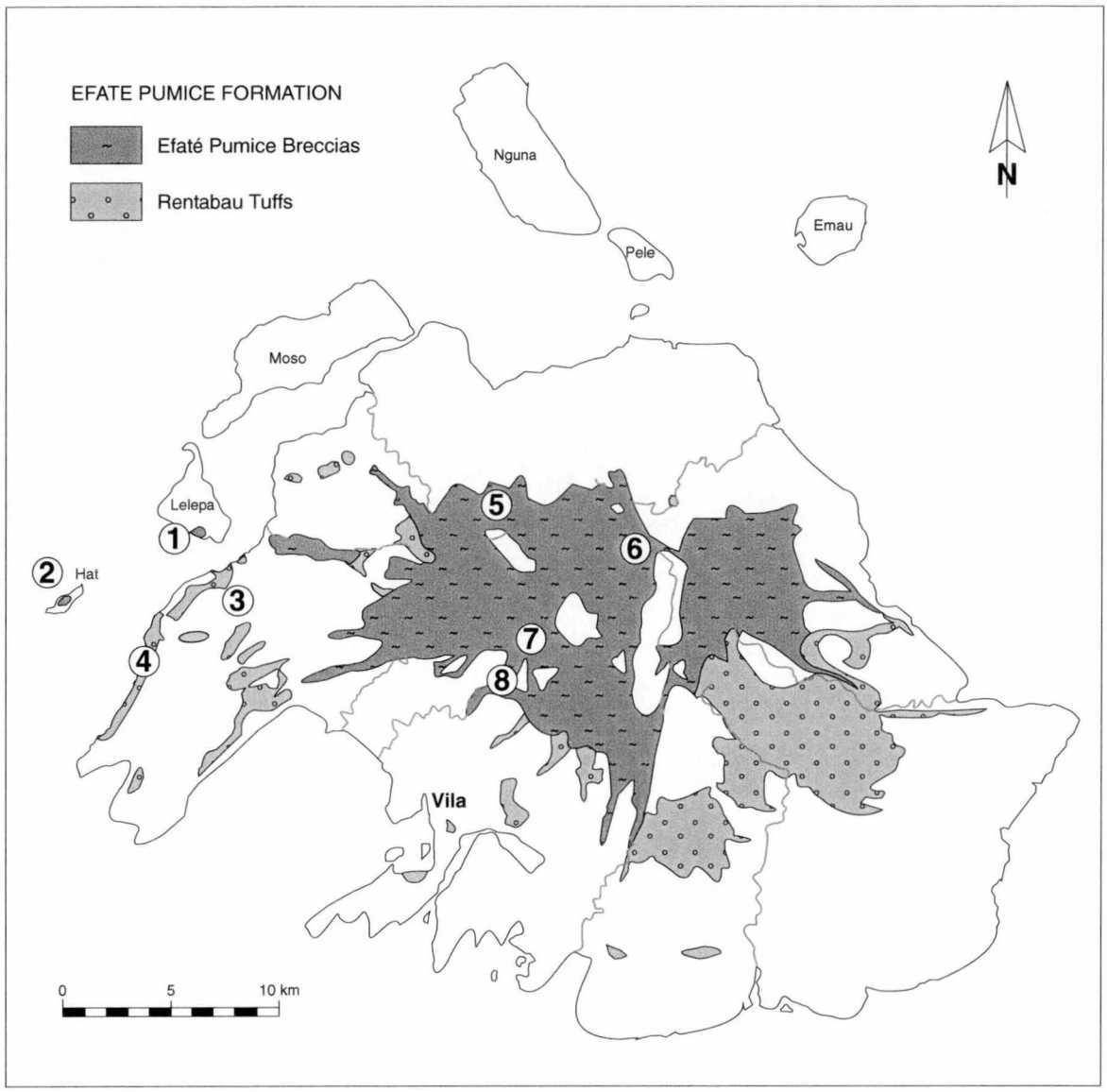

Figure 3.1. Regional distribution of the Efaté Pumice Breccias with measured section locations. (1) Lelepa Island, (a) cliff section and (b) Fele's Cave section (grid reference: KA039507); (2) Hat Island (grid reference: JA981475); (3) Mangalui Quarry (grid reference: KA044474); (4) southern Efaté coastal cliff section (grid reference: KA023455); (5) interior cliffs section (a: grid reference: KA176532; b: grid reference: KA177530); (6) Upper Teouma River valley (grid reference: KA240461); (7) La Colle River north (grid reference: KA186422); (8) La Colle River south (grid reference: KA171430). Modified from Ash *et al.* (1974; 1978).

Table 3.1. Summarised facies descriptions for the principal facies of the Efaté Pumice Breccias.

LITHOFACIES	BED THICKNESS	GENERAL DESCRIPTION	DEPOSITIONAL PROCESSES
coarse grained facies			
massive pumice breccia	0.5-5.0 m	clast-supported, moderately sorted, fines-poor, pumice breccia, massive to normally or inverse graded close to bed contacts; planar, tabular, laterally continuous beds with sharp and erosional, to gradational bases; may have lithic-rich basal layer locally	high-density gravelly turbidity currents
MPB	thick to very thick		
stratified pumice breccia	0 2-5 0 m	clast-supported, moderately to well sorted, fines-poor pumice breccia; planar stratified and locally normally and inversely graded, planar, tabular, laterally continuous beds with sharp bases	high-density gravelly turbidity currents
SPB	medium to very thick		
cross-stratified pumice breccia	0.5-5.0 m	clast-supported, moderately sorted, fines-poor, pumice breccia, internally stratified and cross-stratified discontinuous beds with sharp generally erosive bases	high-density gravelly turbidity currents
XPB	thick to very thick		
massive lithic breccia	0.5-1.0 m	matrix-supported, poorly sorted polymictic lithic breccia; lensoidal bed geometries, commonly gradational upper contacts and sharp bed bases	debris flows
MLB	thick		
fine grained facies			
massive shard-rich sand and silt	thin to very thin	shard-rich, well sorted, massive silt and fine sand, some planar, tabular beds with sharp bases, commonly draping beds and may show injection structures and soft-sediment deformation features at upper contacts; indurated and locally carbonate veined	suspension fallout deposition
MAS			sandy turbidity currents and suspension fallout
stratified shard-rich sand and gravelly sand	thin to very thin	shard-rich, well sorted gravelly sand to silt; planar, tabular beds with sharp bases; planar stratified and laminated; commonly contain single grain thickness layers, crystal-rich layers common	traction plus suspension sedimentation
SAS			low-density sandy turbidity currents
cross-stratified shard-rich sand and gravelly sand	thin to very thin	shard-rich, well sorted gravelly sand to silt; planar, tabular beds with sharp bases; commonly contain granular pumice stringers or single-grain thickness layers; crystal rich layers common	traction sedimentation
XAS			low-density sandy turbidity currents
pumice gravel lenses	one to a few grains thick	well sorted granular pumice lenses, typically one to a few grains thick; lenticular beds with sharp contacts	traction sedimentation
PGL			turbidity currents

Table 3.2. Facies descriptors (used as codes) and explanations for beds in the Efaté Pumice Breccias.

FACIES DESCRIPTOR	EXPLANATION	
MPB	massive pumice breccia	
SPB	stratified pumice breccia	
XPB	cross-stratified pumice breccia	
MLB	massive lithic breccia	
MAS	massive shard-rich sand	
SAS	stratified shard-rich sand	
XAS	cross-stratified shard-rich sand	
PGL	pumice gravel lenses	
SUBDESCRIPTORS	COARSE-GRAINED FACIES	FINE-GRAINED FACIES
vf	2-4 mm	<1/8 mm
f	4-8 mm	1/8-1/4 mm
m	8-16 mm	1/4-1/2 mm
c	16-32 mm	1/2-1 mm
vc	>32 mm	1-2 mm
n	normally graded bed	
i	inversely graded bed	

Coarse-grained facies association

This association includes the massive pumice breccia facies (MPB), the stratified pumice breccia facies (SPB), the cross-stratified pumice breccia facies (XPB) and the massive lithic breccia facies (MLB).

Components and composition

Coarse-grained, pale coloured (grey, white, buff) facies dominate Efaté Pumice Breccias. Components are dominantly angular pumice clasts with variable abundances of perlitic, weakly porphyritic obsidian, and dense porphyritic lava clasts in a minor matrix of glass shards and crystals. The glassy components are uniformly trachydacitic (Chapter Six, Fig. 6.4) and the crystal population comprises plagioclase, ortho- and clinopyroxene, Ti-magnetite and accessory apatite and ilmenite (see Chapter Six). Other components include intraclasts of finer-grained lithologies, and rare limestone, rounded to subangular scoria fragments and hydrothermally altered intraclasts of fine to medium pumice breccia.

Angular, ragged-ended, elongate tube pumice, and subordinate irregular and round vesicle pumice make up to 85 % by volume of the Efaté Pumice Breccias (Fig. 3.2 a and e). Tube pumice clasts may contain internally folded tube vesicles, and elongate, very fibrous clasts may rarely show *in situ* brittle fractures perpendicular to long vesicle walls (Fig. 3.2 b). Subrounded pumice clasts are important in breccia beds in Mangalui Quarry close to the contact with the Rentabau Tuffs (Section 3). Tube pumice fragments are dominantly aphyric, but rarely contain large (2-3 mm), sieve-textured, plagioclase phenocrysts (Fig. 3.2 c). Phenocrysts in irregular and round vesicle pumices typically occur as crystal aggregates include large (2-7 mm), euhedral plagioclase (3-7 %)

with clear to brown glassy inclusions, smaller (0.5-2 mm) pyroxene, and tiny (50-500 μm), subhedral Ti-magnetite grains. Very fine (<50 μm) accessory apatite and ilmenite needles may occur as inclusions in plagioclase. Discrete plagioclase and pyroxene crystals are smaller (0.5-1.5 mm), subhedral to euhedral, and plagioclase crystals commonly have clear, non-vesicular glassy rims.

Other glassy particles account for at least 5-10 % of the Efaté Pumice Breccias. These components include angular, weakly plagioclase + pyroxene-phyric obsidian clasts with well-developed classical perlite and curviplanar clast margins (1-5 %) and blocky, angular to subangular, grey to dark grey lava clasts (≤2 %).

The lava clasts are still dominantly glassy, flow banded and plagioclase-phyric; flow bands are defined by magnetite microlites (Fig. 3.2 d and e). The matrix (≤10 %, <4 mm) contains cuspate, bubble-wall and blocky glass shards with sharp angular margins (Fig. 3.2 f), as well as, clear, honey-coloured and brown, non-vesicular and weakly vesicular glass fragments, which are generally perlitised (splintery fragments and round perlite cores). Pale yellow, honey-coloured and light to dark brown glass fragments are important in samples from Creek Ai and the Mele River (AR025, AR096, AR041, AR043).

Lithic breccia beds contain rounded to subrounded, hematite-altered, plagioclase + pyroxene-phyric scoria clasts, pumice breccia clasts, clasts of semi-consolidated, massive and laminated shard-rich sand, and bioclastic limestone fragments. The pumice breccia clasts are typically rounded, indurated and may be incipiently altered, and are identical in composition to their pumice breccia host sediment. The semi-consolidated massive and laminated sands are compositionally identical to fine grained facies within the succession. These clasts are typically elongate parallel to internal bedding, with long axes up to 30 cm, and rounded edges and ends. Limestone clasts are characterised by strongly abraded margins and highly irregular shapes that reflect original biogenic forms (fossil corals), to subrounded blocky clasts of bioclastic sandstone and siltstone.

Grain-size characteristics

The coarse-grained facies are dominated by moderately to well sorted, coarse to very coarse pumice pebble breccias that are typically fines-poor (<1-10 % sand matrix). Conventional grain size analysis by sieving was not possible for samples from these facies, due to the fragility of the finely vesicular tube pumice clasts. However, an approximate average grain size of 2-3 cm was determined from measuring the longest exposed dimensions of representative pumice and lithic grains in beds from key sections (Appendix C).

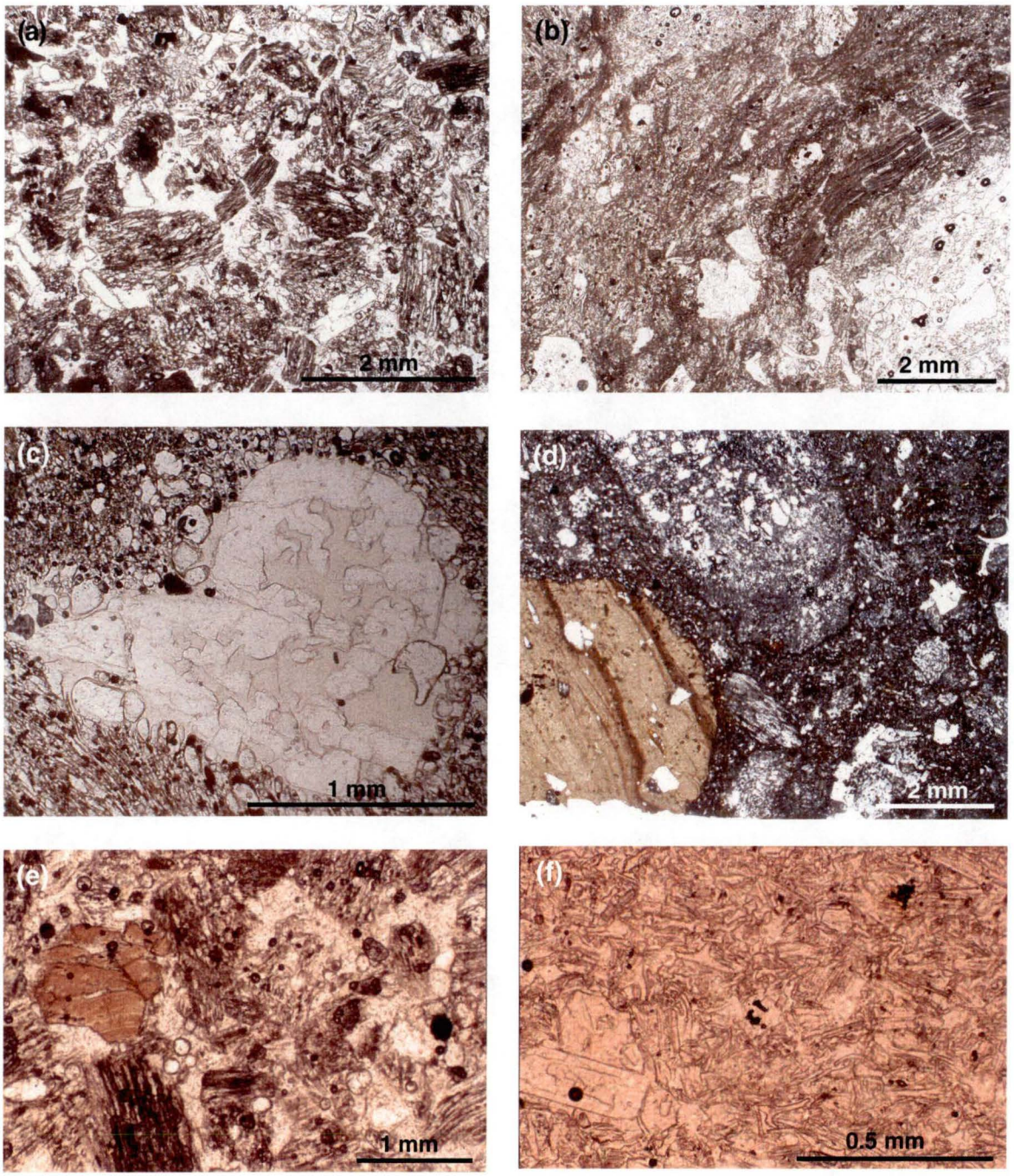

Figure 3.2. Photomicrographs of the Efaté Pumice Breccias. (a) Clast-supported fabric in a fine pumiceous sand, note *in situ* brittle fracture in elongate tube pumice clast at centre. Sample AR064. (b) Randomly oriented tube pumice clasts and plagioclase crystals in matrix of finer glass shards. Sample AR084. (c) Large, sieve-textured plagioclase phenocryst with irregular glassy inclusions in tube pumice clast, thin section oriented approximately perpendicular to elongate vesicle direction. Sample AR070. (d) Plagioclase-phyric, flow banded perlite core and large subrounded tube pumice clast. Sample AR232. (e) Pumice breccia with abundant tube pumice clasts, flow banded lava fragments and bubble-wall shards. Sample AR064. (f) Glass shard-rich bed with euhedral plagioclase phenocryst. Note abundant elongated cuspate shards. Sample LI961.All photomicrographs taken in plane polarised light.

Texture and sedimentary structures

Well-developed planar stratification characterises the coarse grained facies of the Efaté Pumice Breccias. Thick to very thick beds are typically internally massive (MPB) although diffuse stratification is locally important (SPB). Cross-stratified beds with high-angle discordant surfaces and oversteepened dune foresets (XPB) are well exposed at Fele's Cave on Lelepa Island. Isolated scour-and-fill structures are locally important and normal grading occurs in many beds.

Massive pumice breccia (MPB)

Description - This facies is a dominantly massive, clast-supported, moderately sorted, fines-poor pumice breccia with minor angular perlitic obsidian clasts (Fig. 3.3 a). Although most beds are massive, some are internally normally or inversely graded close to upper and lower bed contacts respectively. Beds are commonly thick to very thick (0.5-5.0 m), planar, tabular, and laterally continuous with sharp, erosive to non-erosive lower contacts. Lithic-rich layers ~1-3 cm-thick are locally present at the bases of beds.

Bedding-parallel aligned tube pumice clasts from massive pumice breccia beds at the base of sections on Hat Island and the western tributaries of the Teouma River have wrinkled vesicle walls and clast margins (Fig.3.3 b). Clasts oriented at higher angles to bedding, or which are round vesicle rather than tube vesicle varieties, do not to show the same texture.

Occurrence - The massive pumice breccia facies is volumetrically the most important facies of the Efaté Pumice Breccias. It occurs in all sections and exposures studied.

Interpretation - Deposition of massive beds may result from *en masse* freezing of highly concentrated sediment dispersions (Lowe, 1982; Ghibaudo, 1992), progressive aggradation from steady turbidity currents (Kneller, 1995; Kneller & Branney, 1995), or debris-flow processes (Shanmugam, 1997). Lithic-rich basal layers in this facies may result from suspension fallout of the densest clasts during deposition from turbulent currents (Lowe, 1982). Normally graded intervals commonly result from traction plus suspension fallout within waning turbidity currents (Allen, 1982; Lowe, 1982; Shanmugam, 1997), whereas inversely graded intervals at the base of otherwise massive beds may form from suspension sedimentation and high particle fallout rates (Hiscott, 1994b; Kneller, 1995).

The wrinkled texture in some pumice clasts indicates that they have been weakly compressed. The three beds in which this texture was found are frequently submerged by seawater or high river levels. Incipient post-depositional compaction may result from the combined effects of overburden pressure and non-brittle deformation of hydrated glass (Federman, 1984; Branney & Sparks, 1990). Incipient hydration of glassy particles caused by the continual interaction with cool fluids (freshwater and seawater) could

render them more susceptible to deformation than clasts in exposed beds (Adams, 1984; Federman, 1984; Friedman & Long, 1984; O'Keefe, 1984).

Stratified pumice breccia (SPB)

Description – This facies comprises clast-supported, moderately to well sorted, fines-poor, pumice breccia in medium to very thick (0.2-5.0 m), planar, tabular, laterally continuous beds (Fig. 3.3 c). The beds have diffuse to strongly developed internal planar stratification (5-20 cm-thick), with sharp, typically non-erosive bases and may be upward fining. Isolated scour-and-fill structures may occur on stratified intervals.

Occurrence - A ubiquitous facies found in all sections studied but subordinate to the massive pumice breccia facies.

Interpretation – Internal planar stratification and isolated scour-and-fill structures develop from tractional sedimentation under turbulent currents (Allen, 1982). Traction will develop in turbidity currents as particle-concentration drops, due to variations in flow steadiness or dilution during run-out (Lowe, 1982; Ghibaudo, 1992; Hiscott, 1994a; Kneller, 1995; Kneller & Branney, 1995). Upward fining may result from traction plus suspension sedimentation and high particle fallout rates within turbidity currents (Lowe, 1982; Kneller, 1995; Shanmugam, 1997).

Cross-stratified pumice breccia (XPB)

Description - This facies is a clast-supported, moderately sorted, fines-poor, pumice breccia, characterised by thick to very thick (0.5-5.0 m), internally stratified and cross-stratified, discontinuous beds with sharp, erosive bases (Fig. 3.3 d). Upward fining occurs within some beds, and within single internal strata. Dune foresets vary from 0.2-1 m high but wavelengths are difficult to determine due to lensoidal bed geometries and lateral gradation into horizontally stratified facies. Oversteepening of foresets is seen in beds exposed in the Fele's Cave section.

Occurrence - This facies occurs in the cliff sections on Lelepa Island, some of the interior cliff sections and locally in river traverses.

Interpretation – Bed load traction sedimentation is indicated for the development of cross-stratification, and traction plus suspension fallout for normal grading within beds (Lowe, 1982; Pickering *et al.*, 1986; Ghibaudo, 1992). These conditions may develop in decelerating high-concentration turbidity currents as they lose capacity (Lowe, 1982; Hiscott, 1994a; Kneller, 1995). Cross-stratification in sediments coarser than sand is rare (see Pickering *et al.*, 1986), but low-density pumice pebbles are probably hydrodynamically similar to siliciclastic sand grains (Manville *et al.*, 1998), and may

therefore develop bedforms that are uncharacteristic of 'normal' coarse-grained deep water facies.

Massive lithic breccia (MLB)

Description - This facies forms thick (0.5-1.0 m), massive beds of matrix-supported, poorly sorted, polymictic (rarely monomictic) lithic breccia (Fig. 3.3 e). Beds commonly have lensoidal geometries over 10-30 m, gradational upper contacts and sharp to gradational bed bases. Clasts are typically boulders and cobbles that range from very angular to well rounded, governed by the parent lithology and account for up to 50 % by volume. Clasts include elongate, shard-rich sand and silt with rounded margins, limestone fragments with highly irregular shapes and abraded or rounded margins, very angular to subangular and subrounded glassy and partly crystalline blocky lava clasts, and rare, rounded scoria clasts. The matrix component is a medium- to fine-grained pumice breccia, with rare sand sized crystals and glassy particles.

Occurrence – This facies occurs only in Sections 2 and 5 (interior cliffs and Hat Island), and is not a major constituent of the sections. Dark clasts in inaccessible Section 5 are probably monomictic lava fragments (perlitic obsidian?).

Interpretation – Very coarse-grained, massive, matrix-supported sediments commonly result from debris flow deposition (*e.g.* Soh, 1989; Ballance & Gregory, 1991; Malone, 1995). Large clasts are supported principally by matrix strength and deposition occurs by *en masse* frictional freezing (Lowe, 1982; Einsele, 1991; Stow, 1994).

Fine-grained facies association

This association includes the massive shard-rich sand and silt facies (MAS) the stratified shard-rich sand facies (SAS), the cross-stratified shard-rich sand facies (XAS) and the pumice gravel lens facies (PGL).

Components and composition

The interbedded sand and silt facies of the Efaté Pumice Breccias are dominantly composed of non-abraded glass shards, tube pumice clasts and subordinate crystal fragments. Trachydacitic glass shards include Y-shaped, cuspate and platy bubble wall shards, and less abundant blocky shards with sharp clast margins, and account for 80-90 % by volume (Fig. 3.2 f). Angular, anhedral fragments of feldspar, clino- and orthopyroxene and Ti-magnetite make up the remaining crystal fraction. Although crystals are less abundant overall than the glassy fragments, they are commonly concentrated in crystal-rich layers. Pumice clasts are typically aphyric with long tubular vesicles and ragged terminations. The finest grained beds are generally indurated, and

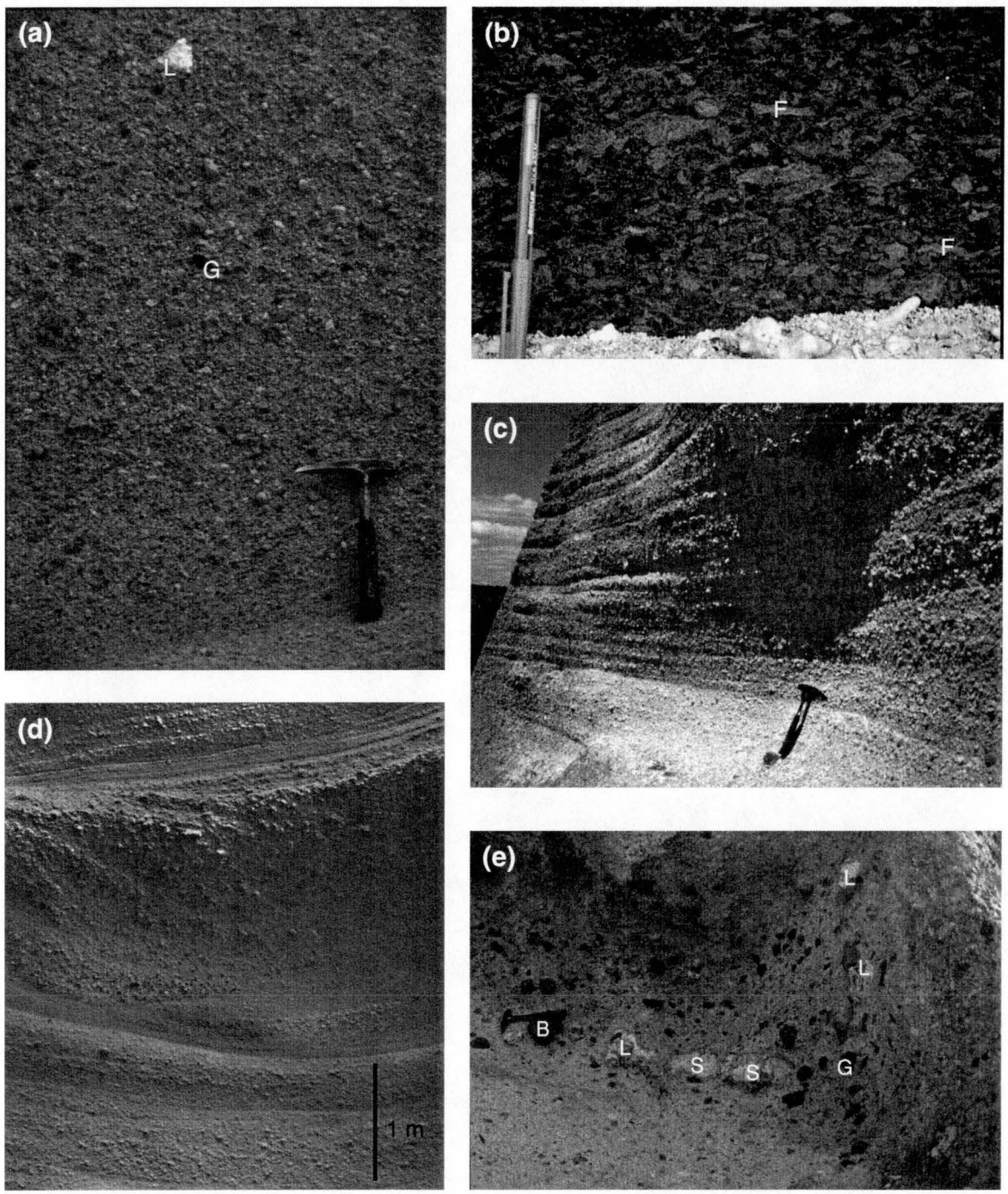

Figure 3.3. Coarse-grained facies of the Efaté Pumice Breccias: (a) massive pumice breccia (MPB) facies, Hat Island [JA981475], (b) massive pumice breccia (MPB) facies with compressed pumice clasts. Lelepa Island [KA038507], (c) stratified pumice breccia (SPB) facies, Hat Island [JA981475], (d) cross-stratified pumice breccia (XPB) facies, Lelepa Island [KA039507], and (e) massive lithic breccia (MLB) facies, Hat Island [JA981475]. Grid references are given in square brackets. L = limestone clast, S = laminated sand/mud intraclast, B = blocky, partly crystalline lava clast, G = perlitically fractured lava clast, F = flattened pumice (fiamme). Hammer is 33 cm long and ballpoint pen is 14 cm long.

react with dilute HCl. Calcite veinlets oriented perpendicular to bedding occur in a fine massive silt bed on Lelepa Island.

Grain-size characteristics

The fine-grained facies are typified by gravelly sand, sand and rarely silt beds. Results of granulometric analysis of samples from Mangalui Quarry, Lelepa Island and Hat Island are shown in Figure 3.4. These diagrams show that the samples have an average medium to coarse (Md_ϕ = 0-1.4) sand particle size and are typically well-sorted deposits (σ_ϕ = 0.95-1.80). However, sample AR036 has a bimodal grain size distribution and includes a sub-population of granules (2-4 mm). These samples from the fine-grained facies have sorting characteristics that fall mostly within the overlap area between the fines-depleted flow and pyroclastic fall fields on Walker's (1983) Md_ϕ vs. σ_ϕ diagram for subaerial pyroclastic deposits (Fig. 3.5). Outsize pumice clasts (2 cm) occur rarely as single grains, but may be abundant in very thin lenses (PGL) within fine-grained facies.

Texture and sedimentary structures

Planar stratification is ubiquitous in the fine-grained facies and commonly includes low-angle truncations of bedding, and single-grain thickness lenses of pumice granules a few centimetres to decimetres long. Normal grading is common in thin beds, and angle-of-repose cross-stratification and inverse grading occur locally. Long wavelength ripples and internal scours occur in some beds, and flame structures and load casts are locally important. Type examples of the fine-grained facies are illustrated in Figure 3.6.

Massive shard-rich sand and silt (MAS)

Description - Shard-rich, well sorted, massive silt and fine sand beds and lenses characterise this facies. Beds are thin to very thin, and have tabular geometries with sharp bases, or else form lenses draping over irregular surfaces. These beds locally develop flame structures into overlying coarser beds and may have load casts at upper contacts (Fig. 3.6 a). This facies is typically indurated and locally carbonate veined.

Occurrence - This facies is widespread in the Efaté Pumice Breccias but is volumetrically minor. It is commonly associated with stratified and cross-stratified fine grained facies.

Interpretation - Massive sand beds may be deposited by *en masse* freezing of highly concentrated sediment dispersions (Lowe, 1982; Ghibaudo, 1992), progressive aggradation from steady turbidity currents (Kneller, 1995; Kneller & Branney, 1995), or debris flow processes (Shanmugam, 1997), or perhaps by very rapid suspension fallout (Allen, 1982).

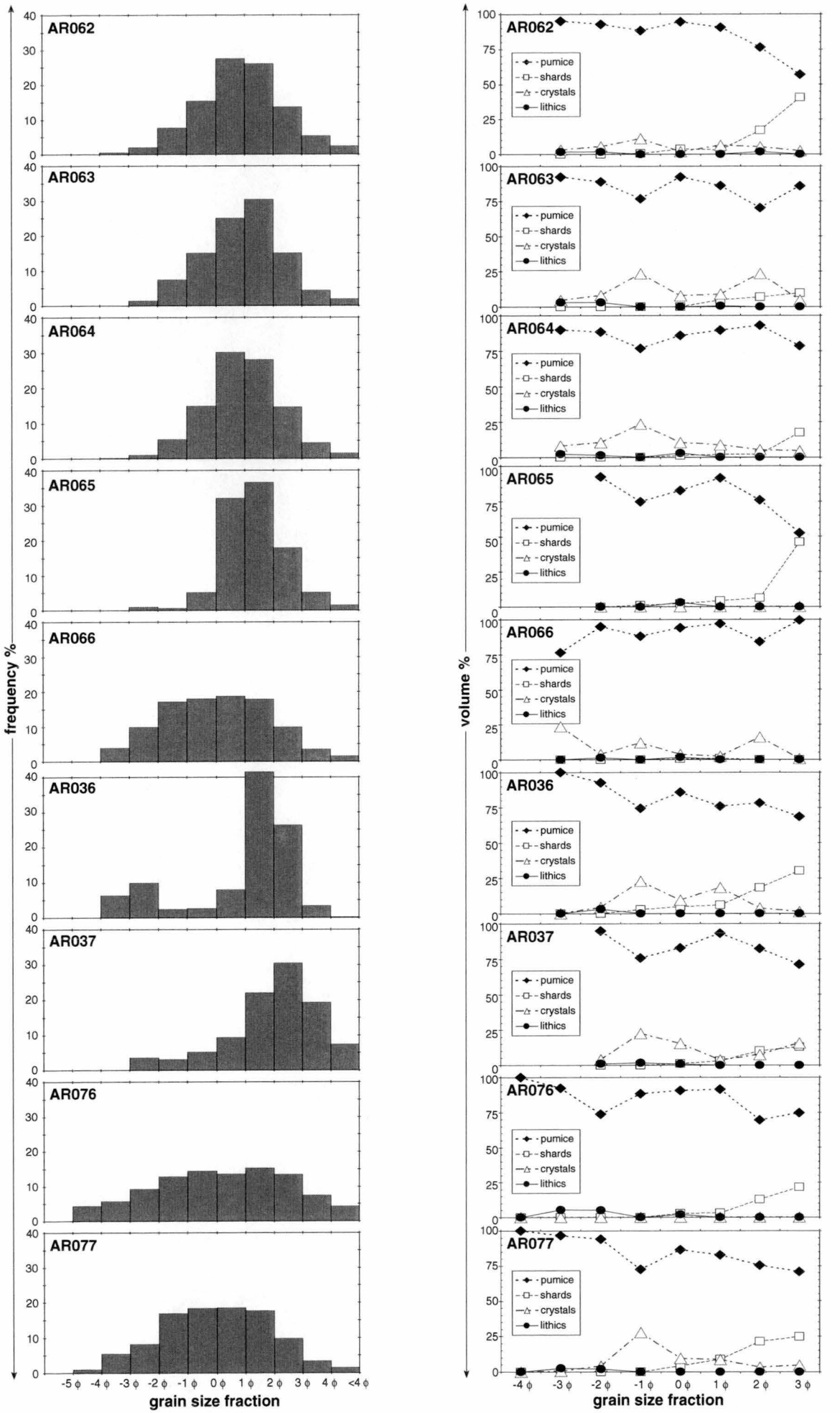
AR062
AR063
AR064
AR065
AR066
AR036
AR037
AR076
AR077
frequency %
volume %
pumice
shards
crystals
lithics
-5 ϕ -4 ϕ -3 ϕ -2 ϕ -1 ϕ 0 ϕ 1 ϕ 2 ϕ 3 ϕ 4 ϕ <4 ϕ
-4 ϕ -3 ϕ -2 ϕ -1 ϕ 0 ϕ 1 ϕ 2 ϕ 3 ϕ
grain size fraction
grain size fraction

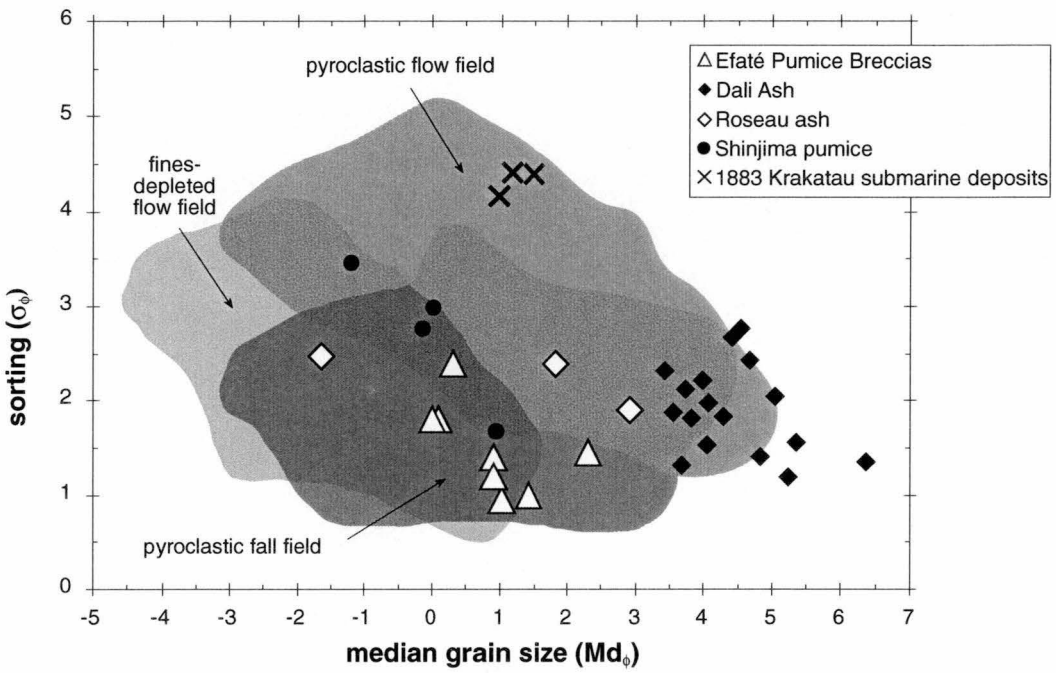

Figure 3.5. Plot of median grain size (Md_ϕ) vs. graphic standard deviation (σ_ϕ) for some well known subaqueous pumiceous deposits and the Efaté Pumice Breccias. Also plotted are fields defined by Walker (1983) for pyrolcastic flow, fines-depleted pyroclastic flow and pyroclastic fall deposits. Modified from Kano *et al.* (1996), and incorporating subaerial pyroclastic flow, fines-depleted flow and fall fields of Walker (1983).

Stratified shard-rich sand (SAS)

Description - This facies comprises shard-rich, well-sorted, coarse sand to silt. Beds are thin to very thin, internally planar stratified and laminated, and have sharp, planar bases with tabular geometries (Fig. 3.6 b). Upper contacts may be gradational into massive shard-rich sand and silt or cross-stratified shard-rich sand facies. Single-grain-thickness layers of angular pumice granules, or angular to subangular crystals, are common. In Section 6, very thinly beds of shard- and crystal-rich sand are inversely graded with crystals and blocky glass shards concentrated at the base and very coarse pumice sand grains and granules at the top.

Occurrence - This facies occurs throughout the Efaté Pumice Breccias commonly gradationally interbedded with coarse stratified pumice breccias, or with intervals of the massive and cross-stratified shard-rich facies.

Interpretation – Planar stratified sand may be deposited by tractional sedimentation under upper or lower flow regime conditions, or by traction plus suspension sedimentation from turbidity currents (Allen, 1982; Lowe, 1982). Deposition of some coarser layers probably represents suspension fallout of the denser particles. The inverse size grading in beds in Section 6 actually represents density grading of particles (Fiske & Matsuda, 1964).

Cross-stratified shard-rich sand (XAS)

Description - The cross-stratified shard-rich sand facies comprises well-sorted, coarse sand to silt beds with tabular geometries and sharp, planar or irregular, erosive bases (Fig. 3.6 c). Beds are thin to very thin and sedimentary structures include uni-directional, angle-of-repose cross beds, climbing ripples and isolated or weakly developed ripple sets. Ripple amplitude varies from 3-10 cm but wavelengths are much more variable (~8 cm to >40 cm for isolated ripples). Beds may contain single-grain-thickness layers of pumice granules, and crystal rich layers are common.

Occurrence - This is a volumetrically minor facies. The best exposures occur on Lelepa Island and in the upper Teouma River valley. This facies always occurs interbedded with the stratified and massive fine-grained facies.

Interpretation – Angle-of-repose cross-stratification is produced by tractional sedimentation in response to the migration of ripple bedforms in sand (Allen, 1982). Isolated and irregular ripples may form due to bottom current action (Stow, 1994; Shanmugam *et al.*, 1995).

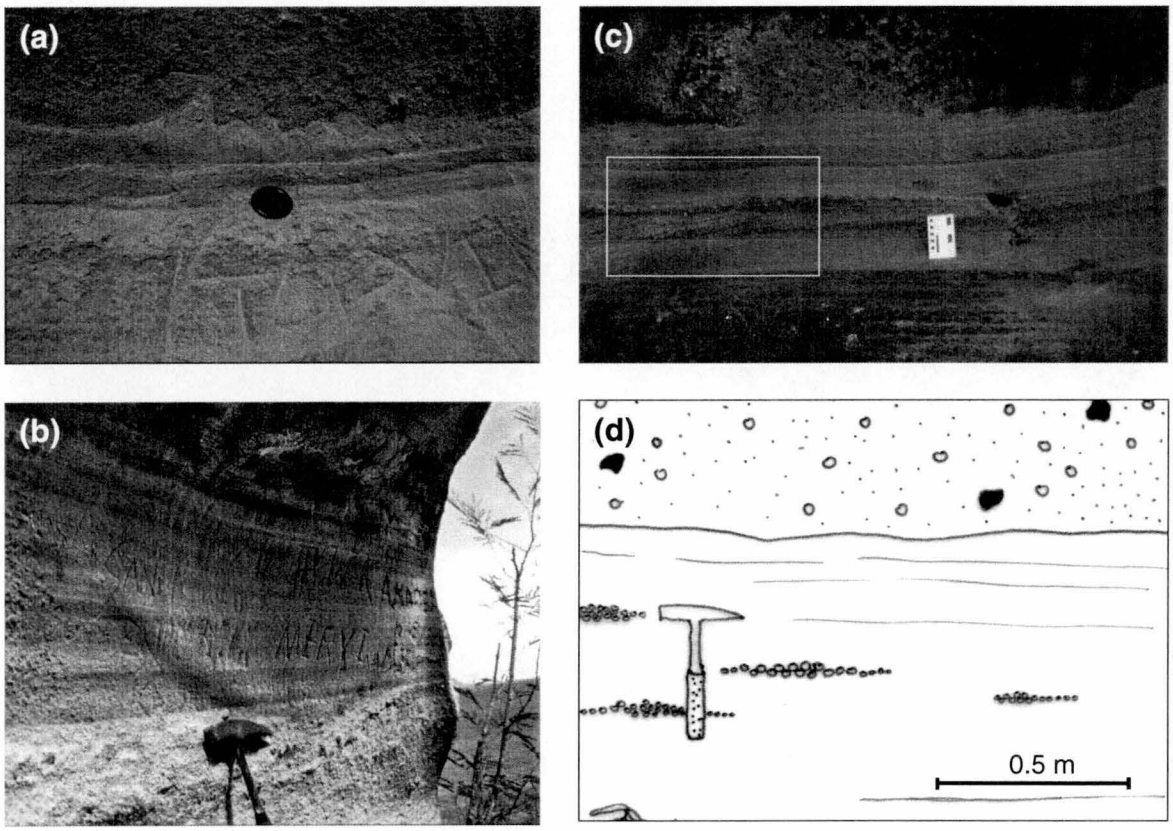

Figure 3.6. Fine-grained facies of the Efaté Pumice Breccias: (a) massive shard-rich sand and silt (MAS) facies, Lelepa Island [KA039507], note loading structures developed at contact with overlying uppermost bed of MPB; (b) stratified shard-rich sand and silt (SAS) facies, Lelepa Island [KA039507]; (c) cross-stratified shard-rich sand and silt (XAS) with trains of pumice clasts on ripple avalanche-slip faces (inset), current direction from right to left, Lelepa Island [KA039507]. Also note lateral transition into planar stratification towards right of photograph; (d) pumice gravel stringer (PGS) facies, occurring as pumice trails within MAS facies, field sketch, La Colle River [KA186442]. Lens cap diameter is 60 mm, hammer head is 18 cm long.

Pumice gravel lenses (PGL)

Description - This facies is characterised by lenses of well-sorted, subangular pumice grains, generally smaller than 10 mm, and have thicknesses from one to a few grains thick (Fig. 3.6 d). Pumice lenses have sharp contacts, are generally less than 30 cm-long, and are always contained in much finer grained facies.

Occurrence - This facies is present in all sections that include the fine-grained facies, however it is volumetrically very minor overall.

Interpretation –Pumice lenses within the fine grained facies may represent lags of coarse, low density particles deposited together with smaller clasts of similar density (Allen, 1982; Manville *et al.*, 1998). Alternatively they may represent deposition from unsteady currents or fluctuations in the clast population of the depositing current (Kneller & Branney, 1995).

Internal stratigraphy

Graphic logs of sections through the Efaté Pumice Breccias, and facies maps of key exposures are given in Figures 3.7-3.16. These show the vertical, and in some cases lateral facies relationships and provide a framework for interpretation of the depositional systems. Grid references for section locations refer to 1:50,000 scale digital maps (based on the World Geodetic Spheroid 1984, UTM zone 59) and are given in square brackets.

Section 1.

On Lelepa Island [KA039507] excellent cliff exposures show marked lateral and vertical variations in facies. Section 1a exposes ~35 m though the Efaté Pumice Breccias and contains examples of most facies (Figs 3.7 and 3.8). Section 1 (b) shows that abrupt lateral facies changes are locally important within the generally monotonous Efaté Pumice Breccias (Figs 3.9 and 3.10).

The lowermost 15 m of Section 1 (a) consists of a succession of thickly to very thickly bedded, planar, tabular, coarse pumice breccias (facies MPB and SPB), with intercalated thinner (0.3-0.5 m) beds of shard-rich sand and silt (facies MAS, SAS and XAS). At the base of the section, two massive pumice breccia beds contain wrinkled tube pumice clasts aligned parallel to bedding (Fig. 3.8 c). Tube pumice clasts in these beds that have other orientations are unaffected, as are round or irregular vesicle pumice clasts. The thickest pumice breccia beds generally have a lithic- and crystal-rich basal layer, one to several grains thick, which grade rapidly upwards (Fig. 3.8 b). Bed bases change laterally over several metres from sharp and erosional, to gradational, to indistinct. Massive beds

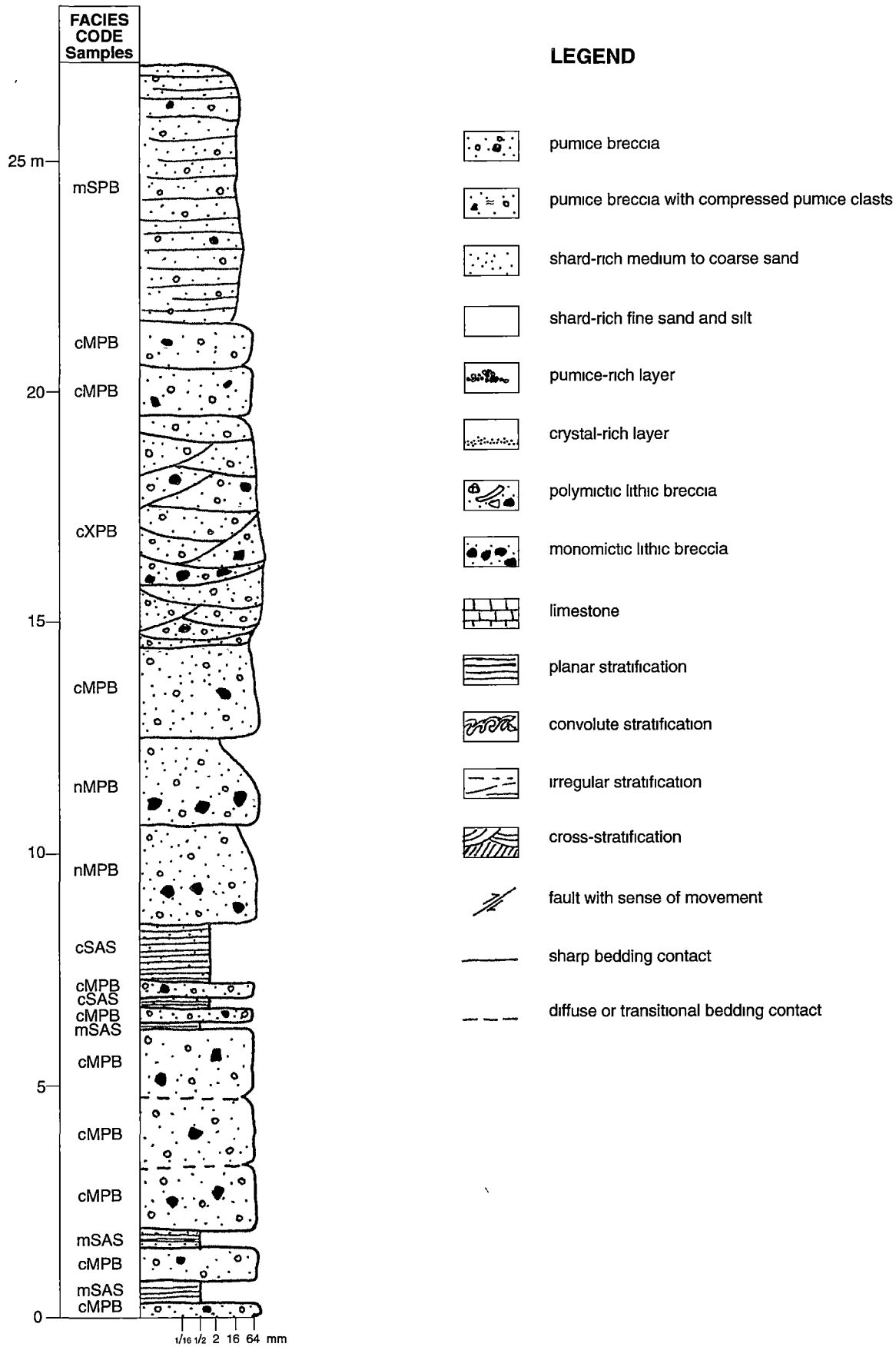

Figure 3.7. Graphic log of Section 1(a), Lelepa Island [KA038507]. Most of the eight facies described in the text and summarised in Table 3.1 occur at this locality. Facies codes are explained in Table 3.2. Legend applies to all graphic logs presented in Chapter Three.

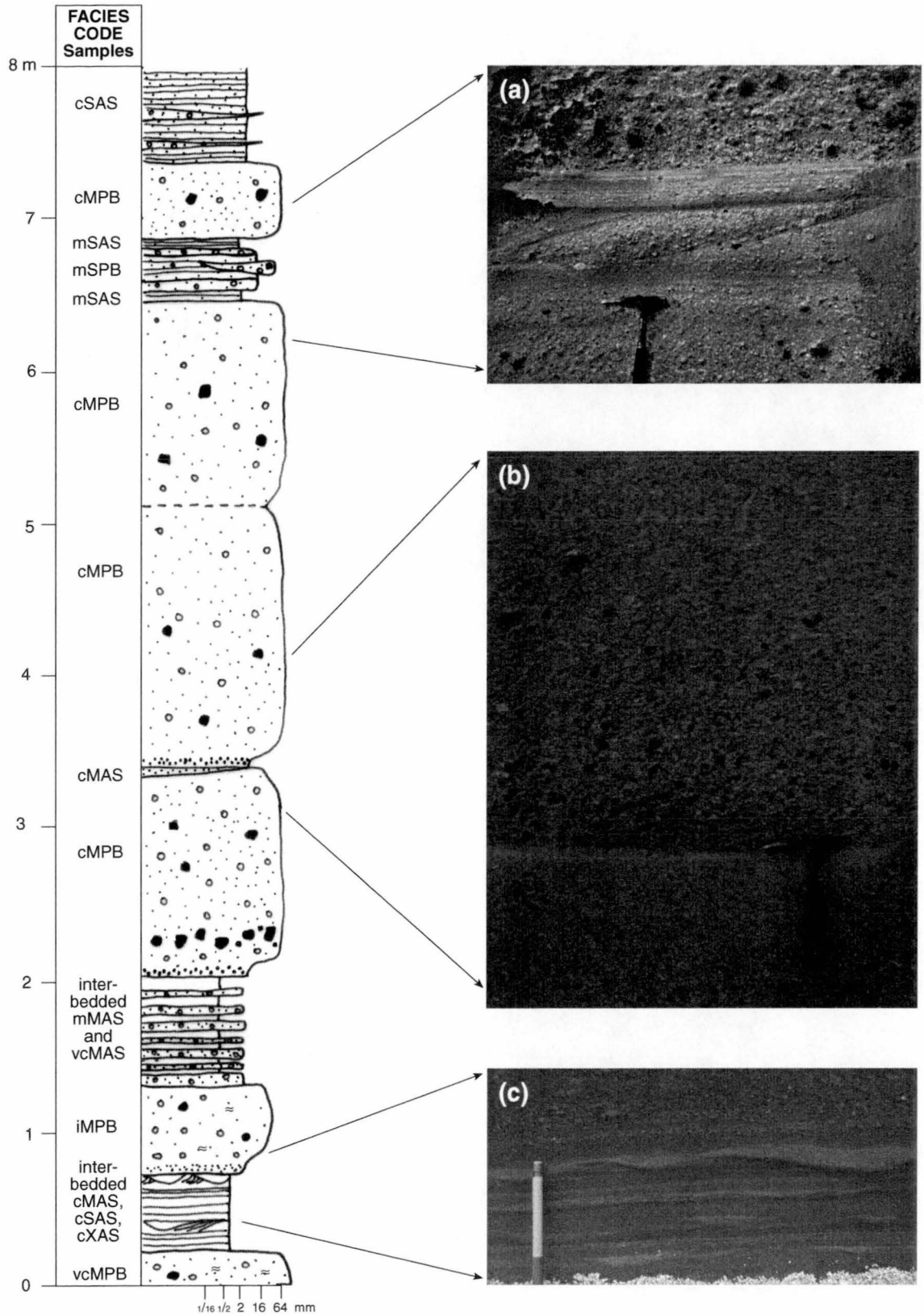

Figure 3.8. Larger scale graphic log of lower 8 m of Section 1(a). Note variety of sedimentary structures within both coarse grained facies and fine grained facies. Illustrated at right: (a) isolated scour-and-fill structure, (b) thin bed of sand between two MPB beds, and (c) laminated fine sands, interbedded with massive beds and angle-of-repose cross-beds, with scours draped over by shard-rich massive silt. Hammer is 33 cm long (head is 18 cm), pencil is 8 mm wide. Facies codes are given in Table 3.2. Legend as for Fig. 3.7.

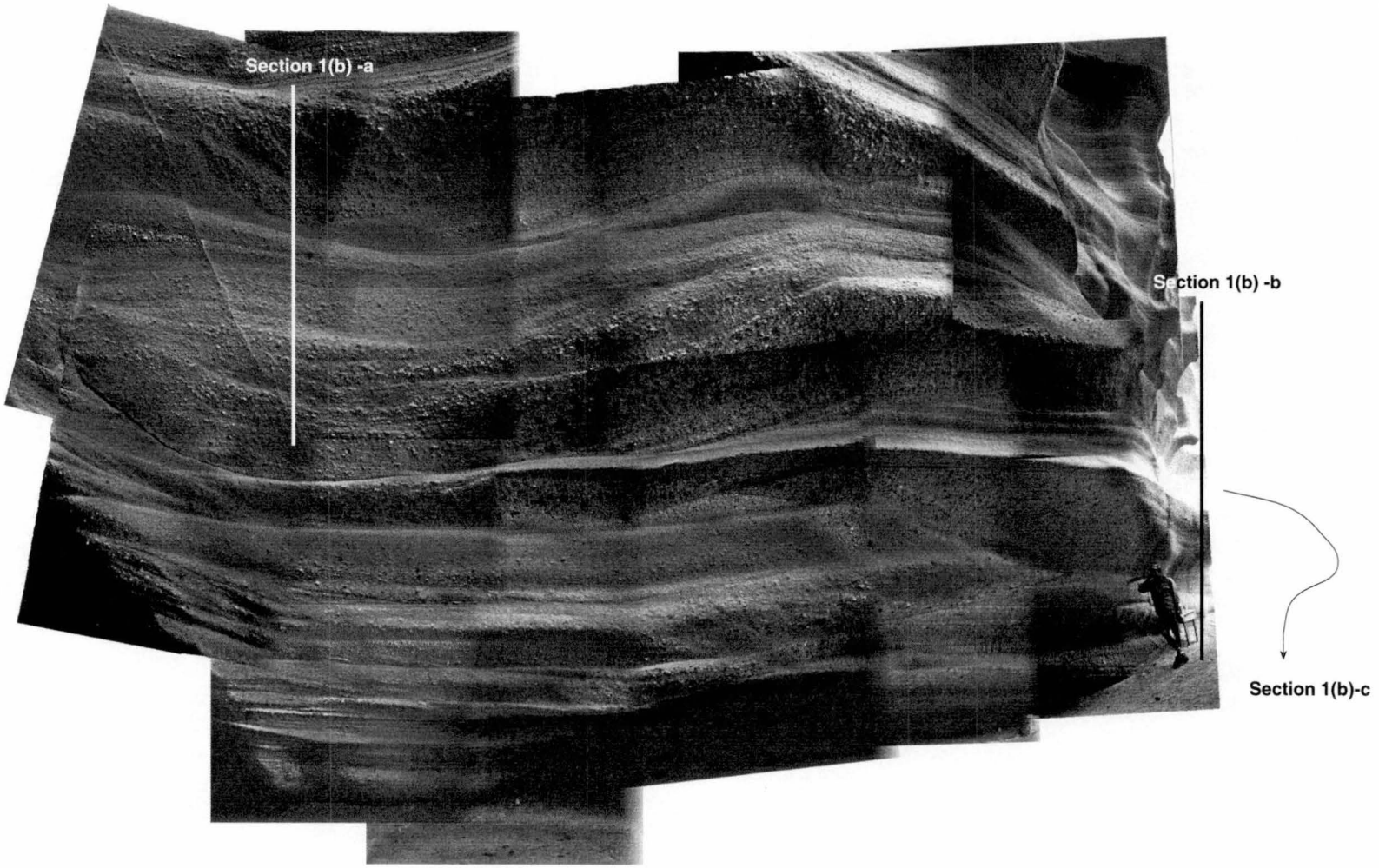

Figure 3.9. Photo mosaic of Section 1(b) Fele's Cave entrance, Lelepa Island [KA039507]. Note the rapid lateral changes in stratification and facies, and common internal scours. The positions of the three 5 m-thick logs presented in Figure 3.10 are indicated on this imag; note that the third log is not within this section and occurs about 3 m below and behind the cave entrance.

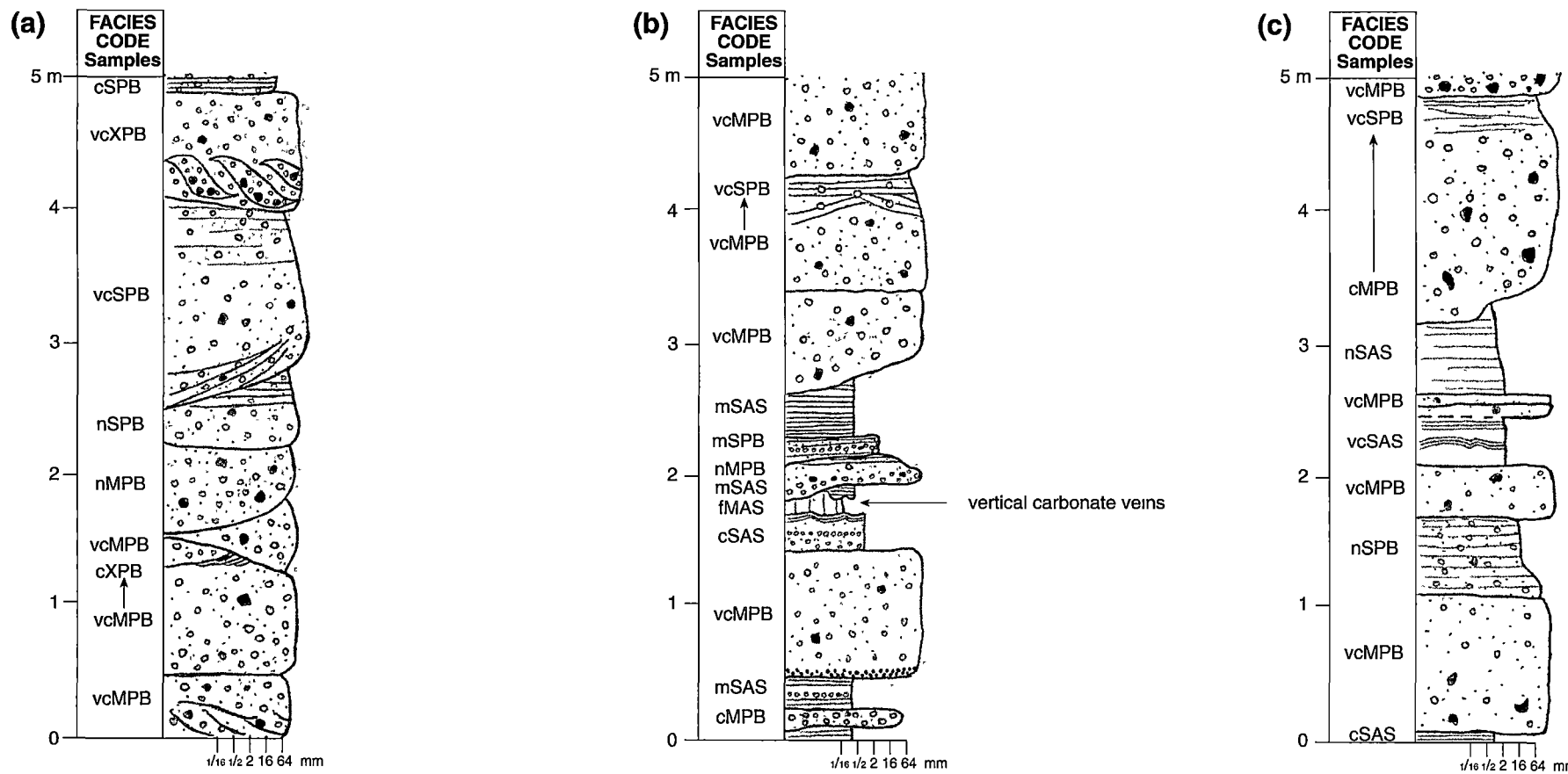

Figure 3.10. Graphic logs of three 5 m-thick sections from Section 1(b), Fele's Cave, Lelepa Island [KA039507]: (a) section from cave entrance showing irregularly bedded and deeply scoured very coarse pumice breccia facies (see also Fig. 3.9.), (b) interbedded coarse and fine grained facies at the cave entrance, (c) shows typical relationships of beds in area where tabular geometries dominate. Facies codes are given in Table 3.2. Legend as for Figure 3.7. Arrows indicate gradational transitions between two facies types.

commonly have gradational contacts with overlying beds of the SPB facies and the uppermost parts of massive beds may be normally graded. Beds also show gradational lateral variations in grain-size over several metres. Stratified pumiceous sand layers are locally preserved between breccia beds but in most cases are truncated by erosion surfaces. Thinner (0.3-0.5 m) beds of fine and medium SPB facies are typically normally graded and include internal scour-and-fill structures (Fig. 3.8 a).

The intercalated fine shard-rich sand and silt show six vertical sequences of massive, stratified and cross-stratified shard-rich sand (MAS, SAS and XAS), capped by massive shard-rich silt (vfMAS) that fills scours and drapes ripples. In fine-grained intervals higher in the section, inverse and normally graded beds of coarse massive shard-rich sand (MAS with pumiceous lenses) are interbedded with medium stratified shard-rich sand (SAS). Flame structures and load casts are weakly developed at contacts with overlying pumice breccia beds. Paleocurrent directions determined from ripple foresets indicate that the dominant sediment transport direction was to the southwest.

These beds are succeeded by 5-6 m of medium to thick, and very thick beds of the cross-stratified pumice breccia facies (XPB). Erosional contacts between beds are abundant and beds commonly have weakly developed diffuse internal stratification and cross-stratification, and may fine upwards. The dominant transport direction implied by foresets is towards the south. The upper part of the section includes a second 2 m interval of thickly bedded MPB facies, capped a by 6-7 m interval of medium bedded, coarse stratified pumice breccia facies (SPB, Fig. 3.7).

Figure 3.9 shows the entrance to Fele's Cave (Section 1 b). This figure highlights the common presence of both high-angle and low-angle erosional contacts between beds, and gradational lateral changes from facies XPB to facies SPB from west to east. Section 1 (b) is stratigraphically equivalent to the interval dominated by the XPB facies in Section 1 (a), and includes the first of the three 5 m-thick sections (Fig. 3.10). Variations in the clast population are also apparent with at least two internally stratified beds (SPB) that contain up to 5 % dark, perlitic obsidian clasts. The other two sections have vertical sequences containing thin to medium interbeds of fine-grained facies. Upper contacts between the fine-grained facies and the coarse pumice breccia beds vary from sharp and conformable, to gradational or erosional or irregular.

Section 2.

A 30 m cliff section (Section 2) at Hat Island [JA981475], exposes shallowly tilted (123/2/SW) pumice breccia facies of the Efaté Pumice Breccias, and fine-grained, shard-rich sand and silt of the Rentabau Tuffs (Chapter Four). Unconformably onlapping reef limestone caps the sequence (Fig. 3.11). Dominant facies are planar, very thickly bedded, massive and stratified pumice breccias (MPB and SPB), and all contacts are sharp and

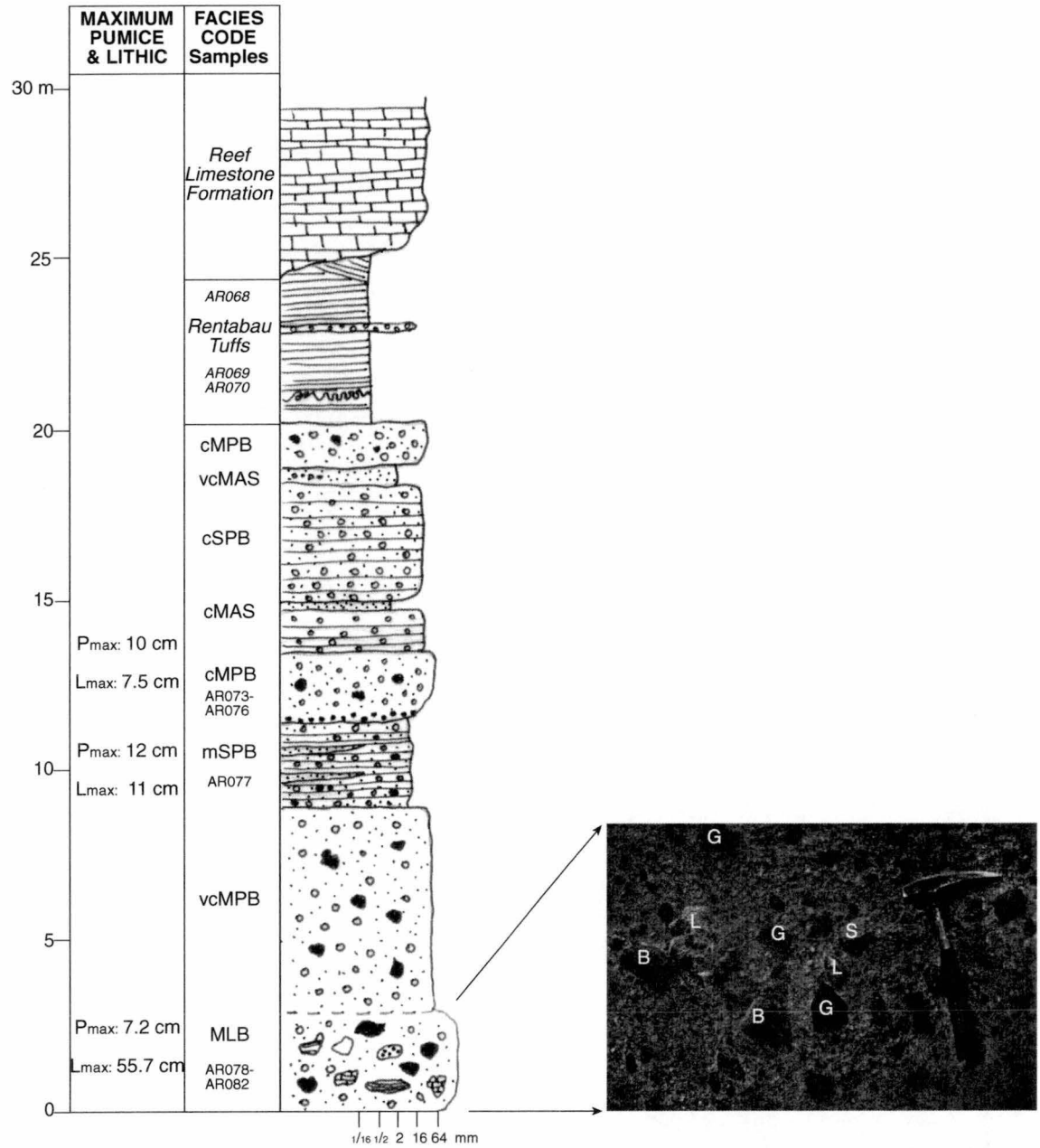

Figure 3.11. Graphic log of Section 2, Hat Island [JA981475]. Facies codes in first column are explained in Table 3.2. Maximum pumice and lithic sizes refer to the maximum exposed dimension of the largest clast in the bed. Photograph at right shows clast types and matrix-supported nature of MLB lithic concentration zone at base of section. Hammer is 33 cm long, L =limestone clast, S = laminated sand/mud intraclast, B = blocky hemicrystalline lava clast, G = perlitically fractured lava clast. Legend as for Figure 3.7.

conformable. The base of the section comprises a 2.8 m-thick massive lithic breccia bed (MLB) that grades upwards into facies cMPB but its base is not exposed. This lithic breccia contains clasts as large as 55 cm-long. Higher in the section, intervals of facies SPB contain low-angle truncation surfaces and variably grade into very fine-grained pumice breccia laterally. Minor thin to medium beds of facies coarse massive shard-rich sand (MAS), commonly containing lenses of pumice granules (PGL), occur between intervals of facies SPB.

Section 3.

Section 3 at Mangaliu Quarry [KA044474] comprises thick beds of mostly fine to very fine pumice breccia facies with sharp, conformable contacts (Fig. 3.12 a). The lowermost beds of the section are unconformably onlapped by limestone that partly envelopes the pumice deposits. Single, thick to very thick beds of medium massive pumice breccia (MPB) make up about half of the section and are interbedded with similarly thick beds of fine and medium stratified pumice breccia (SPB). Single, normally graded beds of SPB and MPB occur locally. Minor intercalations of coarse massive and stratified shard-rich sand occur towards the top of the succession. Pumice clasts in Section 3 breccia beds tend to be slightly more rounded than elsewhere. At this locality the Efaté Pumice Breccias are in fault contact with the overlying Rentabau Tuffs.

Section 4.

Section 4 is from a 35 m-high waterfall cliff [KA023455] that exposes the uppermost parts of the Efaté Pumice Breccias and the overlying Rentabau Tuffs on the southwest coast of mainland Efaté (Fig. 3.12 b). Well bedded shard-rich sands and silts of the Rentabau Tuffs conformably overlie the pumice breccias with sharp contact. Very thick beds of massive pumice breccia facies (MPB) dominate and some include locally developed very diffuse, bedding-parallel, stratification planes. Fine-grained intervals comprise conformable beds of massive and stratified very coarse sand and very fine pumice breccia (MAS, SAS, vfMPB, SPB). As at Hat Island, all contacts are sharp and conformable.

Section 5.

The interior of Efaté Island is characterised by inaccessible vertical cliffs (300-500 m-high) which variably expose thick sections of the Efaté Pumice Breccias. Graphic logs were constructed from photographs of cliffs taken from a helicopter, and visually estimated grain-size and lithofacies characteristics are best approximations only.

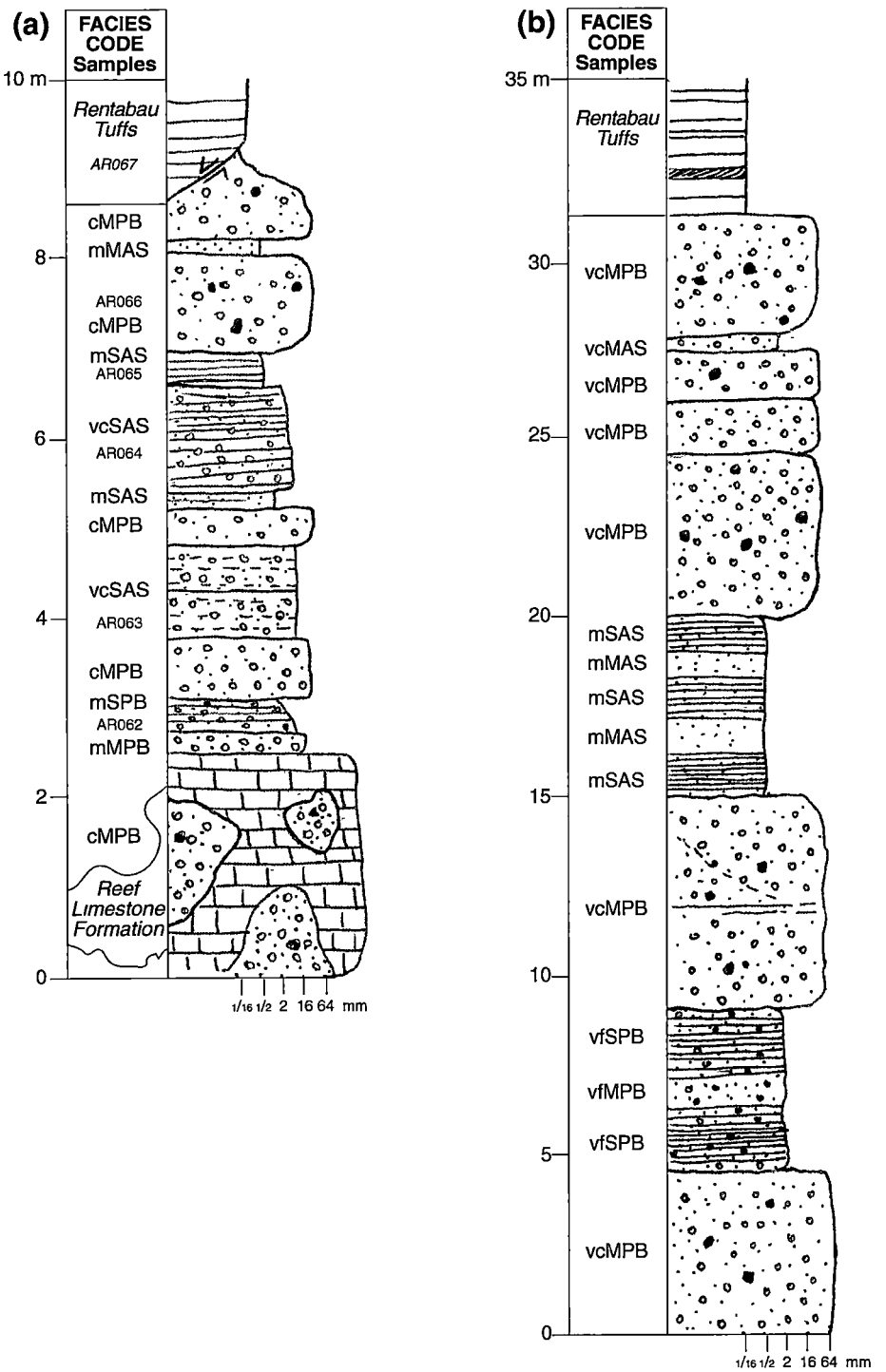

Figure 3.12. Graphic log of (a) Section 3, Mangalui Quarry [KA044474], and (b) Section 4, southwest coast of Efaté [KA044474]. Note that base of Section 2 is covered by an onlapping veneer of limestone, which locally masks pumice breccia facies. Facies codes are explained in Table 3.2. Legend as for Figure 3.7.

The small interval exposed in Section 5 (a) [KA176532] consists of very thick beds of facies coarse massive and stratified pumice breccia (MPB, SPB) with sharp contacts (Fig. 3.13). The basal very thick bed is dominantly a coarse to very coarse, massive pumice breccia (MPB), but grades normally from a layer of monomictic, matrix-supported, very coarse massive lithic breccia (MLB) at the bottom and inversely into the same facies at the top. The lithic clasts are very coarse, black and angular, and probably include both glassy and hemicrystalline lava clasts. The finer-grained interval overlying this unit includes a medium bed of massive pumice breccia (MPB) that has a low-angle, erosional, truncation surface near its upper contact. A bed of massive pumice breccia sits above another low-angle truncation surface overlying this interval at the top of the exposure.

Section 5 (b) [KA240461] has a wider variation in facies both vertically and laterally. It is presented as a single graphic log constructed from two sections laterally separated by 10-15 m (Fig. 3.14). The lower part of the section comprises conformable, thick to very thick beds of massive and stratified pumice breccia (MPB, SPB). Diffuse and discontinuous layering occurs in facies MPB. A thick normally graded bed of clast-supported MLB occurs in this sequence. Clasts appear to be dominantly pale grey and white, pumice blocks (>256 cm), with some darker grey lithic clasts but visual resolution was not good enough to confirm this. The upper part of the section is more complex and dominated by facies SPB. Internal stratification in very thick beds grades from well developed to diffuse, and randomly distributed pumice gravel lenses (PGL) occur throughout. The lowermost metre of this portion of the section shows lateral gradation, and interfingering of stratified pumice breccia beds with very coarse cross-stratified shard-rich sand (XAS).

Section 6.

Section 6 is a 1.5 m measured section from a gorge wall of one of the deeply gullied tributaries of the Teouma River, west of the Teouma Graben [KA240461]. Although this section is much smaller than most of the others presented here, local features within the fine-grained facies are different (Fig. 3.15 a). The fine-grained interval is enclosed by thick (perhaps very thick) beds of massive coarse pumice breccia (MPB). The lowermost bed contains abundant (~25 %) bedding-parallel aligned tube pumice clasts with wrinkled clast margins and vesicle walls. As for similar beds in Section 2, other pumice clasts do not have the same texture.

Above the lower MPB bed, a thin interval of planar, very thinly bedded, very coarse shard- and crystal-rich sand to very fine pumice breccia (SAS, SPB), have single beds with reverse size grading. Particles are actually density graded from dark crystal- and blocky shard-rich bases, to more pumice-rich tops, commonly containing outsize pumice

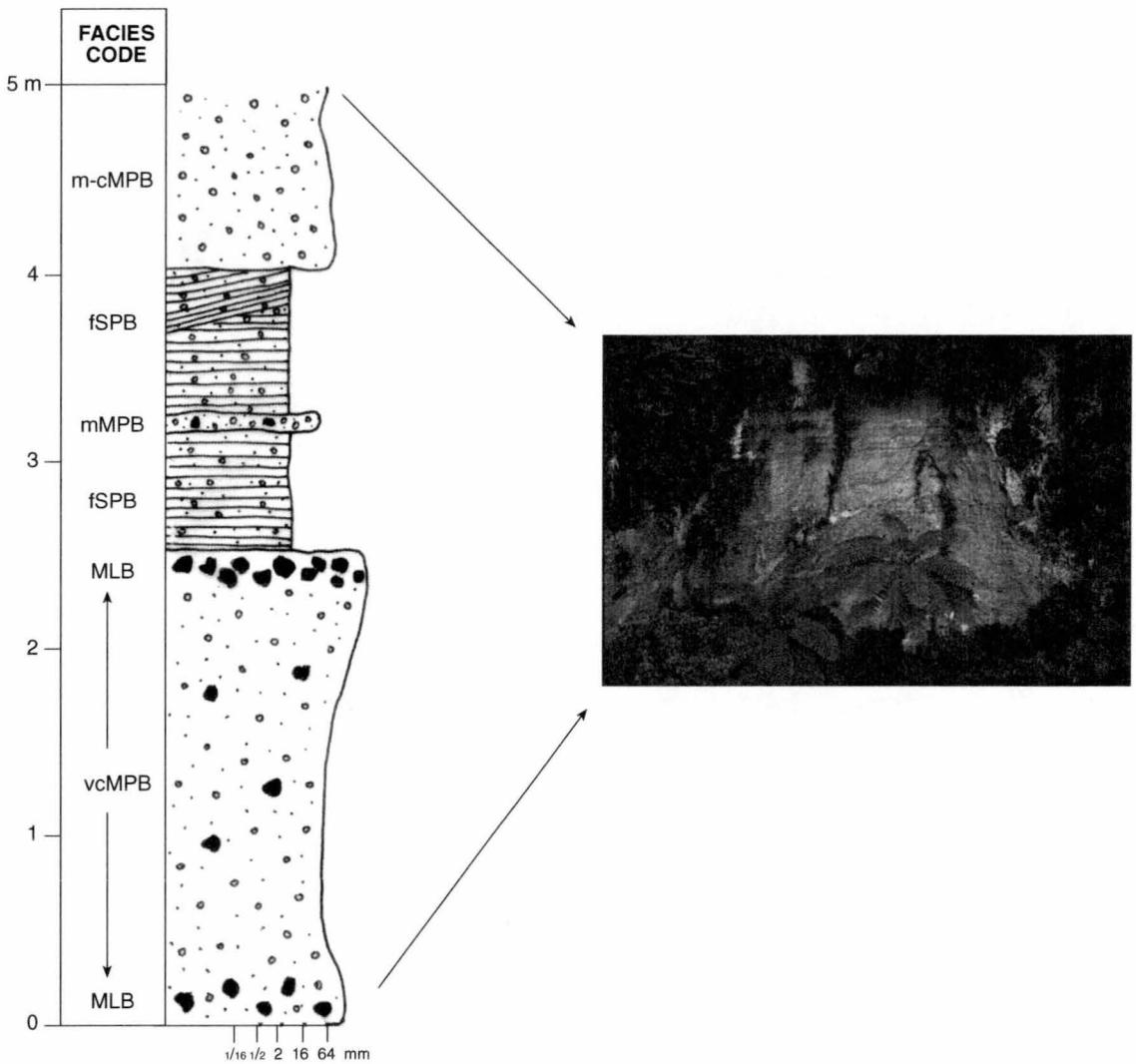

Figure 3.13. Graphic log of Section 5(a), illustrated in photograph at right [K176532]. Facies codes are given in Table 3.2. Legend as for Figure 3.7. Arrows indicate gradational transitions between two different facies.

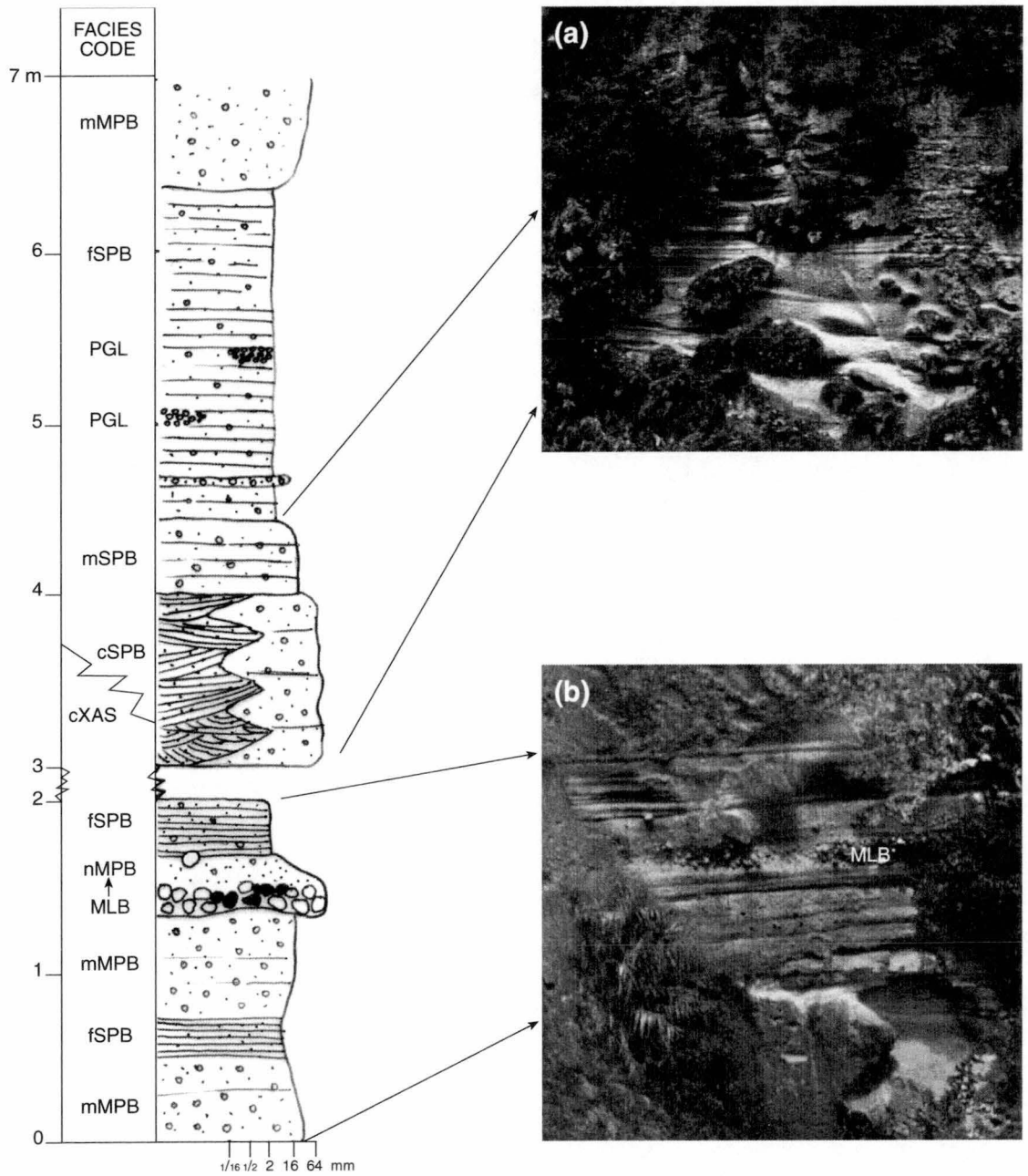

Figure 3.14. Graphic log of Section 5(b) [KA177530]. Note interfingering of facies cXAS and cSPB above 3 m mark, illustrated at right in (a). In illustration (b) note MLB bed and large outsize (pumice?) clast at top of bed. Facies codes are explained in Table 3.2. Legend as for Fig. 3.7.

clasts up to 2 cm. Overlying these density graded sand and very fine breccia couplets, is an interval of planar laminated, medium to fine, shard-rich sand (SAS) with complex internal scours, that are variably filled or lined by pumice granules (facies PGL). Laminae are defined by alternating crystal-rich and shard-rich layers, but in the middle of the interval single laminae are reverse graded from crystal-rich bases to pumice shard-rich tops. The entire fine-grained interval is upward-fining overall, and massive shard-rich silt caps the interval. Syn-sedimentary normal faults with bed-scale off-sets occur in the fine-grained interval immediately below the contact with the upper pumice breccia bed, and poorly developed shard-rich mud flame structures intrude into the overlying breccia bed.

Section 7.

Fine and coarse massive pumice breccia and shard-rich sand beds (MPB, MAS) dominate Section 7 from the La Colle River valley [KA186422] (Fig. 3.15 b). The basal bed of facies MAS has randomly distributed but ubiquitous pods and lenses of pumice granules and pebbles and rare outsize lithic clasts (PGL). Overlying this bed with a sharp conformable contact is a thick bed of essentially matrix-free, very well-sorted, fine MPB, with randomly distributed coarser lithic clasts. This bed grades upward into coarse MAS which has an erosional contact with the succeeding very thick coarse MPB bed. An elongate clast of laminated shard-rich sand (SAS) is present in this bed. A second bed of coarse MPB overlies an erosional contact with this layer and also truncates a bed of cross-stratified shard-rich sand (XAS), occurring discontinuously between these beds. The lower-most part of the second coarse MPB bed contains foreset stratification of mega-ripples defined by angle-of-repose fine pumice pebble trains that dip north (PGL).

Section 8.

Two sections from the La Colle River valley, separated laterally by 10 m show gradational to diffuse contacts between facies and well-developed grading in many beds (Fig. 3.16). Section 8 (a) shows a gradational upward transition and overall fining of grain size from massive to stratified pumice breccia beds (MPB, SPB). Locally abundant pods of coarser pumice grains (PGL) occur in facies SPB. A very thick overlying bed of the coarse MPB facies has a diffuse contact with a successive bed of inversely graded SPB. Another thicker inversely graded bed overlies this with conformable contact and is succeeded by a diffusely stratified bed of SPB. By contrast, contacts between beds in Section 8 (b) are sharper, but beds are normally to inversely graded, and pumice gravel lenses (PGL) commonly occur in the stratified facies.

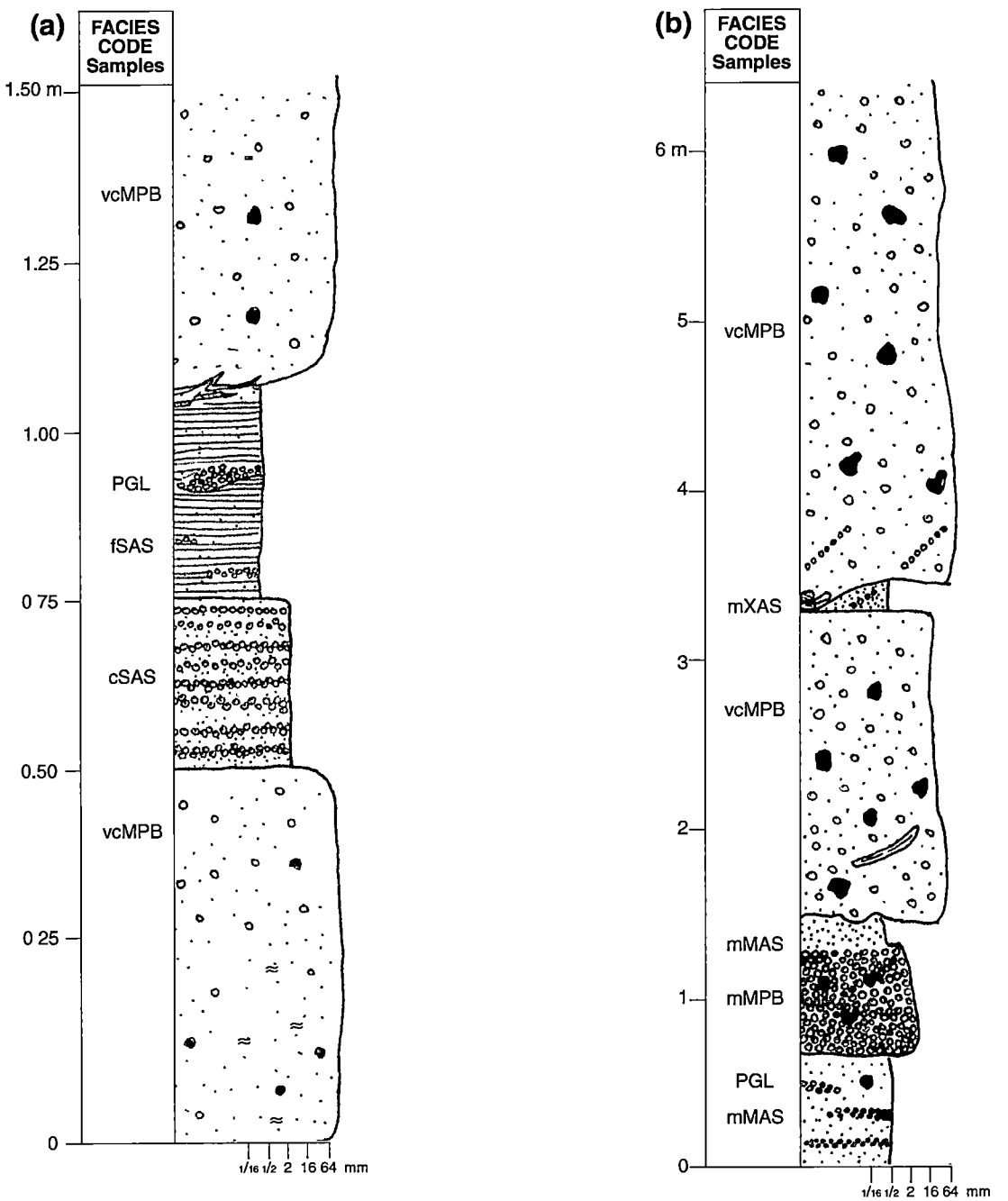

Figure 3.15. Graphic logs of (a) Section 6, upper Teouma River [KA240461], and (b) Section 7, La Colle River [KA186442]. Facies codes explained in Table 3.2. Legend as for Fig. 3.7.

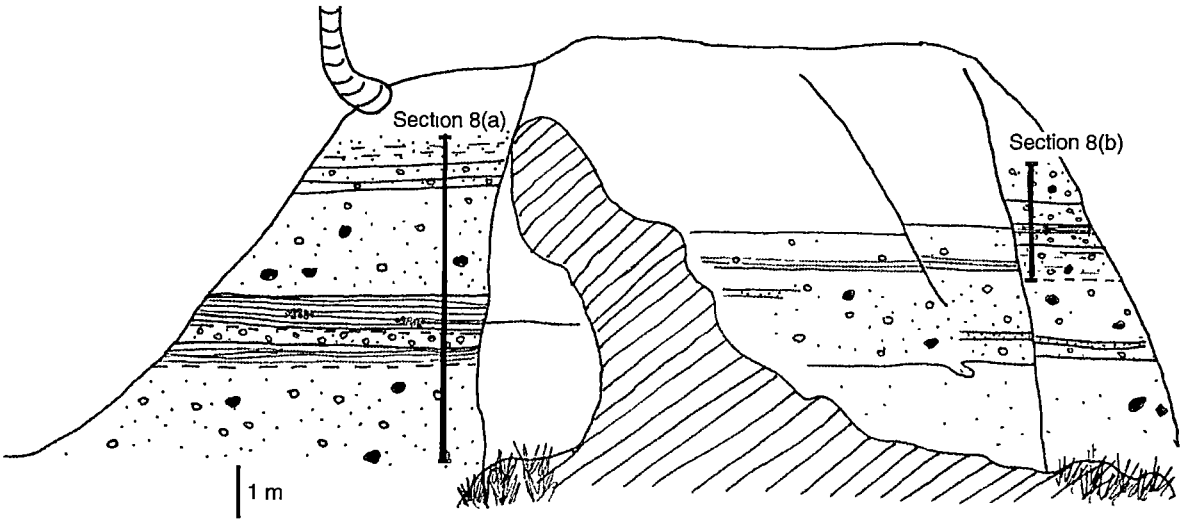

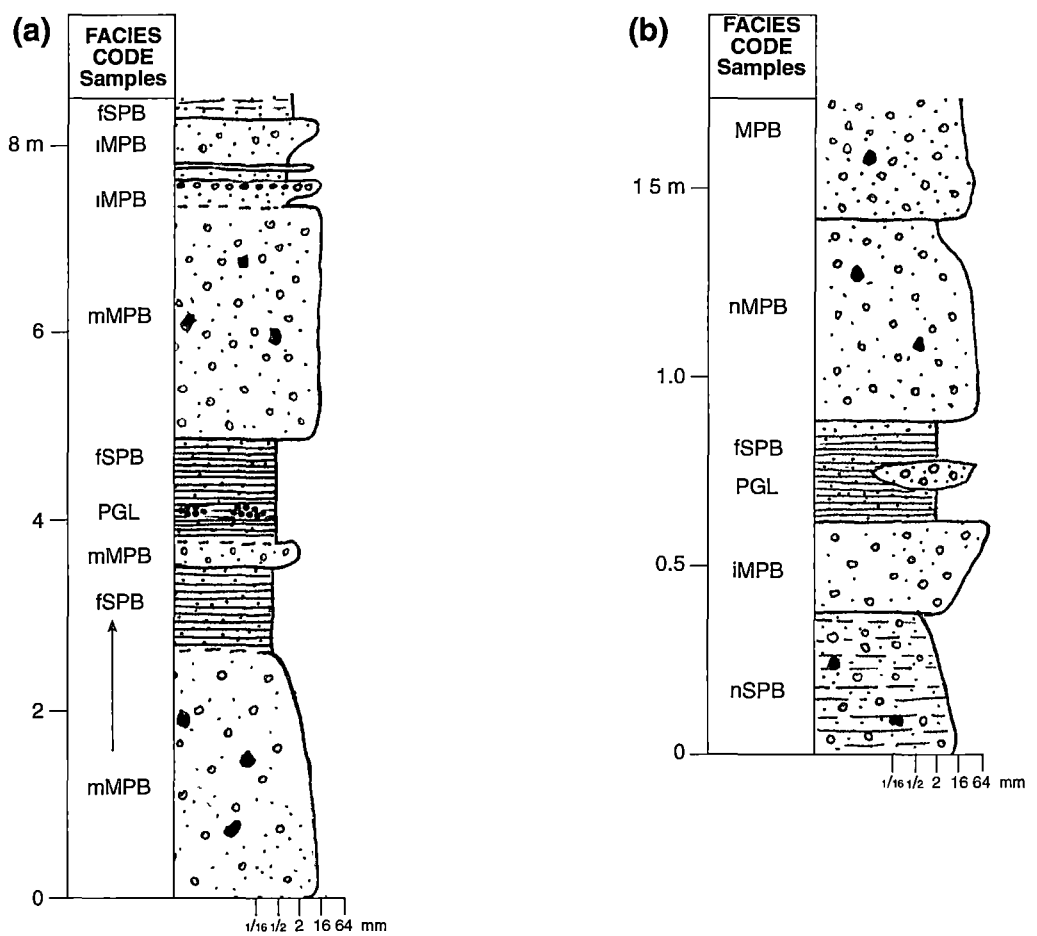

Figure 3.16. Graphic logs and facies outcrop map from Section 8, La Colle River (south) [KA171434]. At topis a field sketch showing the positions of Section 8(a) and Section 8(b). Facies codes explained in Table 3.2. Legend as for Fig. 3.7. Arrow indicates gradational transitions between facies.

Other exposures

Good, accessible exposure is rare in the deep canyons of the Mele, La Colle and Teouma Rivers and Creek Ai. However several high cliffs show that most beds in the Efaté Pumice Breccias are very coarse-grained, massive and greater than 10-15 m-thick. Medium to thin (5-15 mm) layers of massive or laminated shard-rich sand and silt that pinch out laterally over 5-10 m, define boundaries between otherwise indistinguishable intervals of thickly bedded massive pumice breccia. In the upper Teouma River valley, the contact between fine-grained shard-rich sand and a very thick pumice breccia bed is highly irregular and clearly erosional.

Some differences in facies associations and sedimentary structures are present in small exposures in banks of the Mele River and Creek Ai. Beds of massive and laminated shard-rich facies (MAS and SAS) occur in a ~15 m-long lens up to 3 m thick in the Mele River [KA133469], but the upper and lower contacts of this interval are obscured. Elsewhere fine-grained intervals are generally less than 0.5 m thick and these beds are likely to be the Bokua Tuffs of Ash *et al.* (1978). Fine-grained facies in bank exposures in Creek Ai have well-developed ball-and-pillow structures at an upper contact with an overlying pumice breccia bed (MPB). The tops of the ball-structures are truncated by an erosional surface that the pumice breccia bed unconformably rests on. This indicates soft-sediment deformation and intraformational erosion during emplacement of these facies.

Large (3-5 m), angular boulders in the Namarai River [KA228442] have textures quite different from the eight principal facies of the Efaté Pumice Breccias. Sample AR049 is a semi-lithified and incipiently altered fine to very fine pumice breccia with up to 16 % crystals (mainly euhedral plagioclase). Tube pumice clasts (4-10 mm) have wispy terminations, wrinkled and compressed vesicle walls, and may wrap around phenocrysts. The matrix dominantly comprises clay (altered glass ?), with compressed pumice shards (0.5-2 mm), large (1-2 mm), euhedral plagioclase, rounded, resorbed clinopyroxene crystals (3-5 mm), and minor subhedral Ti-magnetite. These features indicate that the glassy pumice clasts were plastically deformed and therefore still hot when emplaced, causing incipient welding. This sample can be interpreted as being formed by a hot pyroclastic flow. Sample AR049 has a eutaxitic texture defined by elongate, dark glassy lenses separated by irregular, sub-parallel, wispy bands of white clay (altered glass ?). The glassy lenses consist of perlitically fractured, porphyritic brown glass with up to 12 % euhedral phenocrysts of plagioclase, lesser pyroxene and Ti-magnetite. Wispy, clay-altered bands may be deformed around phenocrysts and may contain rare, star-shaped cavities (~2 mm). The origin of this rock is more difficult to interpret. It could be a welded pyroclastic flow in which compacted pumice lenses were preferentially altered to clay, while areas rich in glass shards, so densely welded as to form coherent glass, remained unaltered. Alternatively it may be a glassy lava clast that

originally contained pumiceous bands that were preferentially compacted and altered to clay. Star-shaped cavities are lithophysae related to devitrification of the originally pumiceous bands (Bigger & Hanson, 1992; McPhie *et al.*, 1993). The euhedral nature of the phenocrysts suggests that effusion by lavas, rather than explosive fragmentation and deposition from pyroclastic flows, generated this rock.

Regional variation of the Efaté Pumice Breccias

Figure 3.17 shows the variation in the dominant facies throughout the Efaté Pumice Breccias. Coarser grained facies and massive beds dominate overall. The deposits are overwhelmingly dominated by pumice clasts, and other clasts are only important in a few locations, and are often restricted to certain beds, although they are more abundant in Section 5. Since beds are difficult to trace laterally across the island due to their uniform appearance, this diagram is a fairly loose portrait of the Efaté Pumice Breccias.

ORIGIN OF THE EFATÉ PUMICE BRECCIAS

Origin of clasts

Pumice fragments may be generated in two ways: by the explosive fragmentation of a vesiculating magma and by passive fragmentation (autobrecciation and/or quench fragmentation) of vesicular lavas and domes. Explosive eruptions driven by magmatic volatiles can produce large volumes (10s to 1000s km^3) of finely fragmented pumice (and glass shards), whereas pumiceous domes or lavas rarely produce more than a few km^3 of pumice (Wilson & Walker, 1981; Newhall & Self, 1982; Cas *et al.*, 1990). Pumice fragments spalled from vesiculating dome/lava carapaces may be several metres across (Mahood, 1980; Mahood, 1981; Houghton & Wilson, 1989), but pumice clasts produced in explosive eruptions are typically much smaller (several tens of centimetres at most Klug & Cashman, 1996). The Efaté Pumice Breccias contain a large volume of pumiceous debris (at least 65 km^3), and pumice clasts have an average clast size of ~30 mm and upper size limit of about 20 cm. This size constraint coupled with the bulk volume of pumice fragments, suggest that the mechanism of formation of pumice fragments within the Efaté Pumice Breccias was most likely from an explosive eruption of considerable magnitude. The majority of glassy clasts have ruptured bubble walls indicating that fragmentation by explosive expansion of volatiles in "dry" magmatic eruptions was the dominant clast forming process (Heiken & Wohletz, 1991; Cashman & Mangan, 1994; Gardner *et al.*, 1996; Klug & Cashman, 1996; Sahagian, 1999).

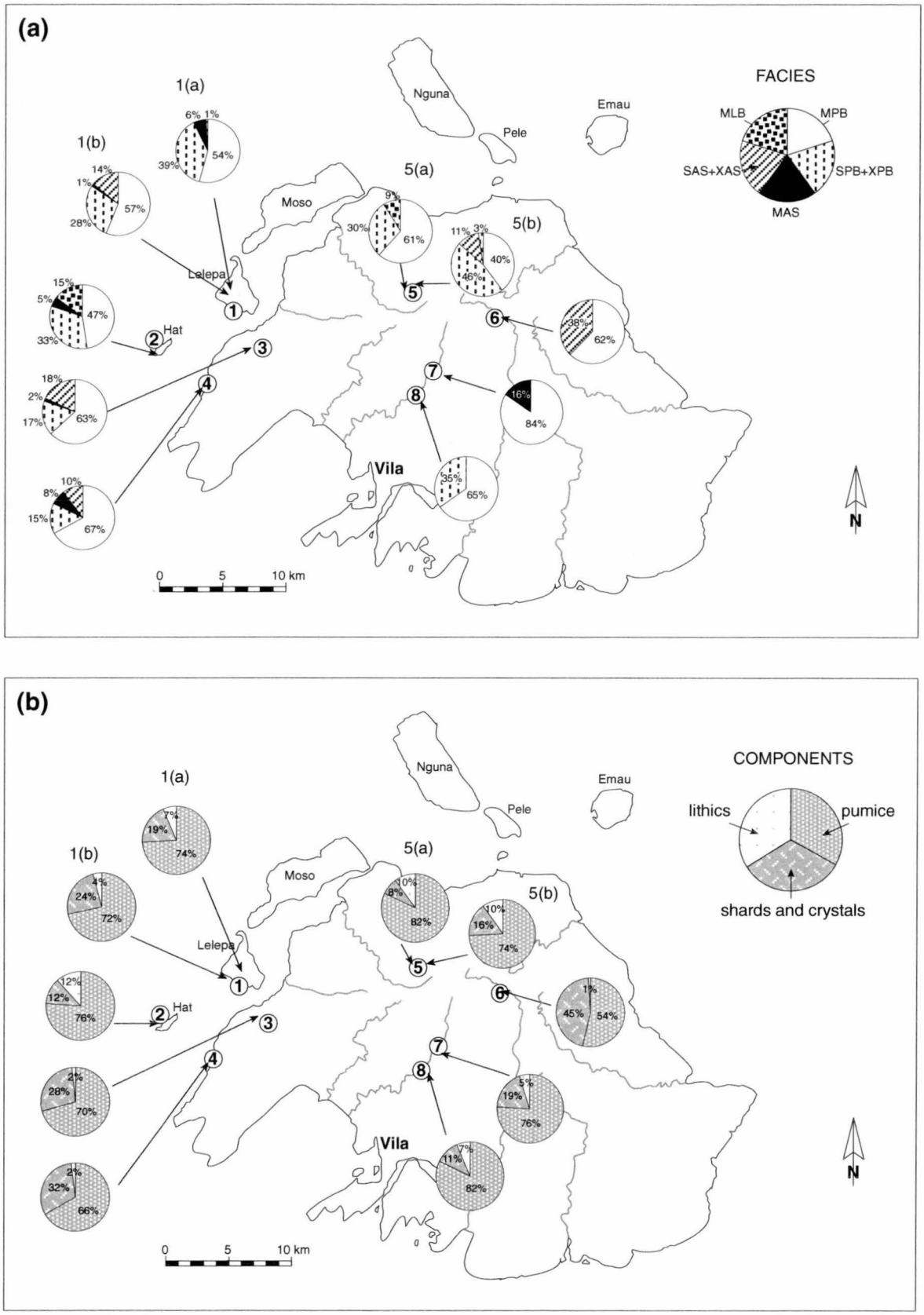

Figure 3.17. Regional variation of (a) principal facies, and (b) overall clast content of the Efaté Pumice Breccias expressed and percentage abundances and based on measured section locations. Section 1 (a), 27 m; Section 1 (b), 15 m; Section 2, 20 m; Section 3, 9 m; Section 4, 32 m; Section 5 (a), ~5 m; Section 5 (b), ~7 m; Section 6, 1.5 m; Section 7, 6,5 m; Section 8, 10 m.

Blocky perlite cores and splintery sheath fragments are a component of the matrix of many breccias, particularly in lithic-rich layers, and clast margins of perlitic obsidian cobbles and boulders are commonly sharp and curviplanar. The clast margins may represent original macroperlite fracture traces (*e.g.* Yamagishi & Goto, 1991). These features indicate that the perlite developed prior to incorporation of the obsidian clasts in the Efaté Pumice Breccias. Although the perlitic obsidian clasts are geochemically identical to pumice and glass shards in the Efaté Pumice Breccias, they were probably derived from pre-existing near-vent trachydacite lavas and domes that were fragmented by explosions and/or further disintegrated during transport and deposition. These clasts are therefore not juvenile components.

Rounded and subrounded clasts of semi-consolidated pumice breccia and shard-rich sand and silt are intraformational clasts derived by erosion of existing beds during the passage of sediment-laden currents (Lowe, 1982). Elongate clasts of shard-rich sand with stratification parallel to bedding may have been incorporated by undercutting of distributary channel banks during transport (Einsele, 1991; Stow, 1994). Limestone clasts and scoria fragments in lithic breccia beds are a very minor component and were probably accidentally incorporated into sediment currents.

Eruption style and vent setting

Large-scale eruptions producing volumes of pumice-rich silicic tephra similar to that of the Efaté Pumice Breccias are usually associated with caldera collapse and plinian eruption columns (*e.g.* Krakatau, Toba Ninkovich *et al.*, 1978; Carey *et al.*, 1996). Caldera volcanism is well-represented in the Vanuatu arc (Chapter Two), and products from the Kuwae caldera are compositionally most similar to the Efaté Pumice Breccias. The Kuwae pyroclastic deposits are related to a 12x6 km caldera that produced at least 39 km^3 of dominantly dacitic tephra (Monzier *et al.*, 1994; Robin *et al.*, 1994b). The eruptions that formed the Efaté Pumice Breccias (and overlying Rentabau Tuffs) must have been more substantial than the Kuwae eruption, yet source vents and vent-proximal facies for the Efaté Pumice Breccias have not been located.

Proximal facies generated by large-scale explosive eruptions commonly comprise beds containing very large vent-derived, lithic particles several metres across (Smith, 1988; Riggs *et al.*, 1997), yet the maximum clast dimensions of accidental lithic clasts (not intraclasts) in the Efaté Pumice Breccias rarely exceed 30 cm. However, paleocurrent indicators suggest that the source of sediment currents (vent) was to the north-northeast, probably offshore. Since this eruption occurred ~1 Ma, it is likely that caldera margins are now buried. However, recently and currently active faults in the north of the Efaté Island Group and offshore have semicircular, concentric patterns and may be reactivated on old caldera faults.

Volcanic vents in island arc settings are commonly submerged, and partially or fully submerged calderas occur in many island arcs (*e.g.* Krakatau, Indonesia; Rabaul, New Britain arc; Santorini, Hellenic arc; Aira caldera, Japan arc), including the Vanuatu arc (Robin *et al.*, 1994a; Robin *et al.*, 1994b). Explosive fragmentation of silicic magmas due to volatile expansion is hindered at water depths greater than three kilometres since confining pressures exceed the pressure of the critical point of water thus preventing explosive expansion (McBirney, 1963; Fisher, 1984; Cas, 1992). All historical, silicic subaqueous explosive eruptions (*e.g.* Myojin Knoll, 1952-3, Fiske *et al.*, 1998), have occurred in water depths of only a few hundred metres. It is recognised that while vesiculation of magma can occur in relatively deep water (several kilometres), *sustained explosive eruption* of a vesiculating magma is theoretically unlikely in water depths greater than 500-1000 m (McBirney, 1963).

The Efaté Pumice Breccias have facies characteristics that indicate that they were clearly deposited in submarine environments (see below), but vent environments are more difficult to determine. Explosive activity from subaqueous vents commonly involves abundant hydromagmatic explosions as external water gains access to magmas (Sheridan & Wohletz, 1981; Wohletz, 1983; Kokelaar *et al.*, 1985; Kokelaar, 1986). The Efaté Pumice Breccias contains >80 % of clasts generated by "dry" magmatic fragmentation, and very few finely fragmented clasts with fractured surfaces indicating interaction with external water (*e.g.* blocky, equant shapes with arcuate fracture-bounded surfaces, Wohletz, 1983). However, this does not preclude derivation of the pyroclasts from submarine vents as energetic discharge may prevent water gaining access to vents, and submarine eruption columns may remain protected from interaction with seawater by a steam carapace (Kano *et al.*, 1996).

Facies of the Efaté Pumice Breccias offer few clues to vent environments. The presence of limestone clasts in lithic breccia beds indicates volcaniclastic debris flows at least transgressed shallow/shelf environments (*e.g.* Cousineau, 1994). However, the Efaté Pumice Breccias generally lack clasts that would unequivocally indicate that eruptions were subaerial (or breached the sea surface) such as charred vegetation. The Roseau Ash contains charred wood fragments (2 cm) in volcaniclastic submarine debris flow deposits more than 250 km from source (Carey & Sigurdsson, 1980; Whitham, 1989). Furthermore, pyroclasts retain no evidence that definitively indicates subaqueous derivation which might include quench rims on glassy clasts (*e.g.* Kano *et al.*, 1996).

Limited but weak evidence indicates that the eruption that produced the Efaté Pumice Breccias may have been partly subaerial. Cas and Wright (1991) concluded that submarine pyroclastic flows only retain enough heat to form welded deposits in rare circumstances. Welded pumice breccia lithologies from large (3+ m) boulders in the Namarai River and float from the Mele River (see 'Other exposures' above, also reported in Ash *et al.*, 1978) suggest that deposition of some units was probably subaerial. The

stratigraphic status of these lithologies is unknown but the large size of the Namarai boulders indicates that these clasts are unlikely to have travelled very far from source (Allen, 1970; Einsele *et al.*, 1996).

One problem with a subaerial interpretation is the limited extent of the Efaté Pumice Breccias. Large-scale, explosive, silicic, subaerial eruptions commonly produce plinian eruption columns and associated widespread submarine ash fallout layers (Ninkovich *et al.*, 1978; Schmincke & van den Bogaard, 1991). No record of the Efaté Pumice Breccias (or EPF in general) is recognised regionally within the Vanuatu arc, although the submarine volcanic record includes ash beds as old as ~2 Ma (Baker *et al.*, 1994; Goud Collins, 1994; Baker & Condliffe, 1996). Dispersal of pyroclastic debris from subaqueous eruptions may be more restricted due to the damping effects of water on the eruption column (Cousineau, 1994). Thus vent environments for the Efaté Pumice Breccias remain equivocal.

TRANSPORT AND DEPOSITIONAL PROCESSES AND ENVIRONMENTS

Sedimentary environments

A below storm-wave-base marine setting is envisaged for deposition of the Efaté Pumice Breccias. Several key criteria point to submarine rather than terrestrial deposition. The conformably overlying Rentabau Tuffs contain marine fossils and this unit was deposited in submarine environments. Sedimentary structures including massive and stratified, planar, tabular beds, indicate the dominance of high-concentration turbidity current deposition of coarse- and fine- grained facies, further constraining deposition to below-storm-wave base environments. Furthermore, the Efaté Pumice Breccias lack features that might normally be expected to form in shallow marine or terrestrial environments. The pumice breccias contain no terrestrial plant or animal fossils and no evidence of hummocky cross-stratification, or bi-directional cross-stratification with low-angle truncation surfaces indicating deposition in shallow shelf environments. Limestone clasts sourced from shelf environments are generally confined to debris flow-deposited lithic breccia beds (see below) and may be transported far from source (Stow, 1994).

Sedimentation processes

Deposition of coarse gravelly sediments in deep marine successions is commonly attributed to high-concentration mass-flow processes occurring on submarine fans (Postma, 1984; Einsele, 1991; Boiano, 1997). These deposits are typically massive and vary from clast-supported to matrix-supported depending on the major particle support mechanisms (Lowe, 1982; Ghibaudo, 1992; Lomas, 1992). The dominance of massive and planar stratified breccia beds within the Efaté Pumice Breccias indicates that they

were principally deposited from high-density, gravelly, volcaniclastic turbidity currents. Massive divisions of beds can be generated by deposition from turbulent currents with high particle concentration and gradational contacts with graded and stratified intervals favour this interpretation (Lowe, 1982). The development of the graded and stratified intervals probably reflects a loss of capacity (decrease in particle concentration) of the sediment current as deposition proceeded (Hiscott, 1994a). Tractional structures such as cross-bedding indicate that some volcaniclastic currents were fully turbulent, allowing dune bedforms to develop.

The generally fines-poor nature of the Efaté Pumice Breccias may be explained by efficient elutriation of these particles from coarse-grained turbidity currents during transport (*e.g.* Druitt, 1995). This elutriated fine sediment then became detached from the parent flow, generating low-density, fine, shard-rich turbidity currents that deposited between successive high-density flows (*e.g.* Busby-Spera, 1986). Fine shard-rich sediments at the base of Section 1 have classical Bouma T_{abce} sequences, demonstrating the importance of this mechanism (Bouma, 1962).

Transport and deposition of massive matrix-supported lithic breccias involved debris flows rather than turbidity currents. Internal matrix strength and dispersive pressure within cohesive debris flows would provide enough buoyancy to transport large, dense lithic clasts in a finer grained matrix dominated by pumice granules and fine pebbles (*e.g.* Pickering *et al.*, 1989; Stow, 1994).

Initiation of mass flows

Fiske and Matsuda (1964), Niem (1977), and Yamada (1973) attributed the deposition of submarine pyroclast-rich units to syn-eruptive, water-supported, volcaniclastic mass flows based on the dominance of pyroclasts, the fines-poor nature of massive beds, and the presence of doubly graded sequences. Such features also occur in facies of the Efaté Pumice Breccias, and the texturally unmodified nature of the pumice clasts and glass shards further indicates that reworking was minimal. Deposition of the majority of the Efaté Pumice Breccias was probably also essentially syn-eruptive.

However, pumice is a low-density geological material that commonly floats (*e.g.* Iyer & Karisiddaiah, 1988; White *et al.*, 1997). Whitham and Sparks (1986) demonstrated that initially hot pumice rapidly absorbs water, making it readily available for entrainment in water-supported currents. In addition, tube pumice will be preferentially concentrated in water-supported flows due to its high permeability (Fiske, 1969). Thus water-supported volcaniclastic mass flows may be directly generated by turbulent mixing of gas/pyroclast dispersions with seawater, either from submarine eruption columns or from subaerial pyroclastic density currents that transgress shorelines (*e.g.* Cas & Wright, 1991; Stix, 1991).

The complex internal stratigraphy throughout the Efaté Pumice Breccias suggests that sedimentation was generally rapid and chaotic, in response to successive or pulsing mass flows, which might be expected for pumiceous successions directly generated by large-scale, contemporaneous eruptions (*e.g.* Yamada, 1973). Pumice breccia beds with slightly rounded clasts may have been locally reworked and/or remobilised prior to deposition. Internal erosion features within fine-grained beds also indicate that bottom currents were locally active between successive pumiceous mass-flow currents. The presence of semi-consolidated intraclasts suggests that some time elapsed between deposition of some units.

Facies characteristics and facies associations of the Efaté Pumice Breccias indicate deposition in medial to distal environments from vent areas. Busby-Spera (1986) described proximal to distal facies associations in the subaqueously emplaced, Monarch rhyolite ash-flow tuff, and concluded that interbeds of fine-grained sediments elutriated from coarse, volcaniclastic mass flows, were best preserved in the most distal facies. All sections of the Efaté Pumice Breccias contain fine-grained interbeds interpreted to have formed in a similar fashion, and maximum pumice clast sizes in all areas are generally less than 50 mm. In addition, very large (few m) lithic clasts, and coarse lithic lag breccias are absent.

Duration of eruption and deposition

Facies characteristics of the Efaté Pumice Breccias indicate that these volcaniclastic sediments were rapidly emplaced contemporaneously with explosive magmatic eruptions. Caldera-forming eruptions akin to those envisaged for generation of the Efaté Pumice Breccias commonly last from hours to a few weeks at most (Ledbetter & Sparks, 1979; Newhall & Self, 1982; Carey *et al.*, 1996). Ash *et al.* (1978) described burrows in Bokua Tuff beds immediately below an erosion surface overlain by a very coarse pumice breccia bed in the Mele River. This together with the presence of semi-consolidated intraclasts, indicate that there were lulls in eruptive activity during deposition of the Efaté Pumice Breccias. This may explain in part age range represented by the two new K-Ar age determinations. Sample AR206 (1.1±0.02 Ma) comes from a bed low in the succession and probably below this disconformity, whilst sample AR064 (0.96±0.02 Ma) comes from the very top of the pumice breccia succession. Therefore, deposition of the Efaté Pumice Breccias may have involved two or more explosive eruption cycles. However, the homogeneous geochemical composition of the Efaté Pumice Breccias (and Rentabau Tuffs) dictates that such time breaks must not have been significant.

DISCUSSION

Since Fiske (1969) recognised the importance of pumice in submarine successions, many examples of non-welded subaqueous pumice breccias have been documented. These

include syn-eruptive deposits that are: (1) known to have been generated from subaerial pyroclastic flows that entered the sea (Roseau Ash, Whitham, 1989; Krakatau, Mandeville *et al.*, 1996); (2) believed to have been directly generated by submarine eruptions (Wadaira tuff, Fiske & Matsuda, 1964; Sumisu Rift pumice breccias, Nishimura *et al.*, 1991; Shinjima Pumice, Kano *et al.*, 1996); and (3) deposits for which vent environments remain equivocal (Ohanapecosh Formation, Fiske, 1963; Onikobe caldera deposits, Yamada, 1973; Stanley Group, Niem, 1977; Dali Ash, Wright & Mutti, 1981; Monarch ash flow tuff, Busby-Spera, 1986). The main characteristics of these deposits are summarised in Table 3.3.

The Efaté Pumice Breccias share features in common with most of these deposits. Thick, massive to normally or density graded beds are common, as are overlying or interbedded fine glass shard-rich sand or silt. Deposits generated from the 1883 Krakatau pyroclastic flows that entered the sea cannot be distinguished from contemporaneous subaerial pyroclastic flow deposits on the basis of grain size or sorting characteristics. This contrasts with most other subaqueous deposits that tend to be fines-poor, suggesting that the 1883 flow did not admix greatly with seawater. Water is a very efficient medium for grain size sorting particularly in turbulent flows (Cousineau, 1994; Druitt, 1995). Sorting characteristics for the coarsest beds in the Efaté Pumice Breccias could not be determined by conventional granulometric analysis, but these beds are overwhelmingly clast-supported with generally <8-10 % matrix of sand. However, the fine-grained facies in the Efaté Pumice Breccias are well sorted (Fig. 3.5). Also plotted on this diagram are sorting characteristics of the 1883 Krakatau submarine facies, the Dali Ash, the Roseau ash and the Shinjima pumice (Kano *et al.*, 1996). The Efaté Pumice Breccias are generally better sorted than all of these units and have characteristics transitional between Shinjima pumice and the Dali ash, perhaps reflecting the stage of development of the transporting currents.

The biggest variation between Efaté Pumice Breccias and other sequences is the thickness of this unit and the presence of multiple beds with intercalated shard-rich beds and no intervening hemipelagic intervals. Yamada (1973) described similarly complex internal stratigraphy for deposits in the Onikobe caldera and interpreted this to represent rapid emplacement from an eruption that produced multiple flows of pyroclastic debris, and/or overlapping flows and local disruption of flow lobes.

Documented examples of syn-eruptive pumice breccias are typically very thin (<100 m) or separated by intervals of hemipelagic sediment. The Efaté Pumice Breccias, by contrast, are extremely thick (up to 350 m) and uninterrupted, and most similar in this respect to pumice breccias from the Mineral King Caldera Complex and the Ohanapecosh Formation. These thick successions probably represent deposition in rapidly developed volcaniclastic aprons around source vents (Fiske, 1963; Busby-Spera, 1986).

Table 3.3. Characteristics of some non-welded, syn-eruptive, subaqueous, pumice breccia successions.

DEPOSIT	AGE	THICKNESS	FACIES CHARACTERISTICS AND COMPONENTS	INTERPRETATION AND REFERENCES
1883 Krakatau deposit Indonesia	1883 A.D.		*pumiceous beds* dominantly massive, matrix-supported, poorly-sorted pumice, obsidian, lithics, crystals in a sand to silt vitric matrix *overlain by ash beds* well sorted, laminated, ± low angle cross-bedding glass shards, crystals	*deposition contemporaneous with SUBAERIAL eruption* a true subaqueous pyroclastic flow (maintained its integrity as a gas-supported transporting system) basal dense part sank, and less dense overflow travelled across the ocean surface fine grained laminated vitric sand deposited from low-concentration, water-supported mass-flows Mandeville *et al.* (1996a)
Roseau Ash Domenica, Lesser Antilles arc	30 000 years B P.	at least 4 7 m thick (range: 0 9->4 5 m) extends up to 250 km from source	*pumiceous beds* massive, poorly sorted pumice and lithic breccias, upward fining, graded (reverse and normal) rounded pumice, radiolarian tests, minor sponge spicules, minor wood fragments	*deposition contemporaneous with SUBAERIAL eruption* high-concentration, water-supported, turbidity currents and debris flows Carey & Sigurdsson (1980), Whitham (1989)
Wadaira Tuff Bed D Japan	Miocene	8-15 m – upper ash-beds ≤45 m – pumiceous bed	*pumiceous bed* massive, dense lithic components concentrated at base dacitic pumice, crystals, glassy lithics in ash matrix *overlain by ash beds* massive to internally density graded, upward thinning and fining cycle **(double grading)** pumice shards, crystal fragments, dense glassy dacite clasts	*deposition contemporaneous with eruption* massive pumiceous bed deposited from a cold, subaqueous pyroclastic (debris?) flow, doubly graded ash beds deposited by turbidity currents deposit formed by collapse of an entirely subaqueous eruption column Fiske and Matsuda (1964)
Shinjima Pumice Shinjima Island, Kagoshima Bay, SW Japan	last several thousand years	40 m thick	*pumiceous beds* very thick beds, diffusely stratified, fines-depleted, sharp to transitional bases, upward-coarsening of pumice clasts pumice, minor crystals and glass shards, rare obsidian and mudstone	*deposition contemporaneous with eruption* deposition by cold, water-supported mass-flows deposit formed by collapse of an entirely subaqueous eruption column Kano *et al* (1996)
ODP Leg 126 pumice breccias Sumisu Rift, Izu-Bonin arc	Plio-Pleistocene	tens of meters thick	*volcaniclastic beds* subordinate structureless pumiceous gravels and breccias grade upward into fine laminated and graded vitric sands and silts rhyolitic pumice and ash, fossil fragments *entire sequence* upward fining overall (five volcaniclastic cycles/episodes separated by thin layers of hemipelagic muds)	*deposition contemporaneous with eruption* deposition by sediment gravity flows; direct settling, re-sedimentation and bottom-current reworking implied for some layers eruption probably submarine (nearby vents) Nishimura *et al.*, (1991), Nishimura *et al* (1992)
Miyazawa Formation Onikobe Basin Deposits Japan	Miocene (?)	25-50 m – upper ash-beds 60-100 m – pumiceous beds	*pumiceous beds* massive lower division, some density grading apparent parallel bedded division, strong density grading pumice, crystals, andesite and scoria lithics in ash matrix *overlain by ash beds* parallel laminated coarse and fine tuff, massive very fine tuff pumice shards, crystals *entire sequence* upward thinning and fining cycle **(double grading)**	*deposition contemporaneous with eruption* deposition of entire sequence by turbidity currents (subaqueous equivalent of a subaerial pyroclastic flow) eruption probably subaerial or shallow subaqueous Yamada (1973)

Table 3.3. (cont.). Characteristics of some non-welded, syn-eruptive, subaqueous, pumice breccia successions.

DEPOSIT	AGE	THICKNESS	FACIES CHARACTERISTICS AND COMPONENTS	INTERPRETATION AND REFERENCES
Stanley Group	Mississippian	1-10 m – upper ash-beds	*pumiceous beds* massive lower division, some density grading apparent	*deposition contemporaneous with eruption* deposition of coarse, pumiceous beds by density currents (mass-flows)
Oklahoma / Arkansas		1-25 m – pumiceous beds	parallel bedded division, strong density grading pumice, crystals, shale rip-up clasts in ash matrix *overlain by ash beds* massive and locally laminated coarse and fine tuff, bubble wall and cuspate shards, crystals, rare shale clasts and carbonised organic matter *entire sequence* upward thinning and fining cycle (**double grading**)	fine ash deposited by fallout and reworked by bottom currents eruption probably subaerial or shallow subaqueous Niem (1977)
Dali Ash	Tertiary	2 5 m – upper ash-beds	*pumiceous bed* generally massive, laminated crystal-rich basal layer, normally graded at	*syn- or post-eruptive deposition - unknown* deposition of massive division by high-concentration turbidity currents
Island of Rhodes, Greece		5 m – pumiceous bed	upper contact, bubble wall and sickle-shaped shards, crystals, rare marine fossils *overlain by ash beds* normally graded, laminated, cross-laminated and minor massive beds bubble wall and cuspate shards, crystals	fine ash deposited by dilute turbidity currents eruption character unknown Wright and Mutti (1981)
Monarch rhyolite ash-flow tuff (Mineral King Caldera Complex)	Triassic	27 m – upper ash-beds ≤600 m – pumiceous beds	*pumiceous beds* generally massive, normally graded or bedded in upper parts, interbeds of fine shard-rich tuff pumice, crystals, rip-up clasts in ash matrix *overlain by ash beds*	*deposition contemporaneous with eruption* deposition of pumice rich beds by non-turbulent, high-concentration mass-flows, deposition of ash by suspension fallout shallow marine or subaerial eruption
California			massive, thin-bedded or parallel laminated bubble wall and pumice shards, crystals	Busby-Spera (1986)
Ohanapecosh Formation	Eocene and Oligocene	~3000 m pumice beds· 3-60 m-thick	*pumiceous beds* generally massive, locally stratified and graded, fine and coarse pumice tuff breccias	*syn-and post-eruptive deposition* massive beds deposited by syn-eruptive cold, gas(?)+water-supported mass-flows stratified and graded pumice beds deposited by volcaniclastic turbidity currents
Mount Rainer National Park, Washington		ash beds 0 1-0 6 m-thick	tube pumice, glassy lithic clasts in fine ash and crystal matrix (matrix commonly ~70 % vol.) *interbedded ashes* very well-sorted, graded and laminated, locally massive non-vesicular glass shards, minor micro-vesicular glassy particles	ash beds deposited mostly by rapid fallout shallow marine to subaerial eruptions Fiske (1963)

The facies characteristics of non-welded submarine emplaced pumice breccias, including the Efaté Pumice Breccias represent transport and deposition by water-supported, mass flows, particularly turbidity currents. Figure 3.18 compares facies models developed for deposits from some subaqueously emplaced non-welded pumice breccias (all of these deposits are typically clast-supported), with a generalised (representative) sequence from the Efaté Pumice Breccias, and an established facies model for a subaerial pyroclastic flow (ignimbrite) deposit. Syn-eruptive deposition by water-supported, subaqueous pyroclastic density currents produces the double grading in sequences from the Tokiwa Formation, and the Onikobe caldera, Japan (Fiske & Matsuda, 1964;Yamada, 1973). Intervals within the Efaté Pumice Breccias succession, represented by the idealised sequence in Figure 3.18, show a similarly upward fining sequence but tractional features imparted by turbulent currents are better developed and double grading is rare. In contrast, a bed from the Shirahama Group, Japan shows overall upward fining and no evidence of traction. In this deposit, extreme bimodality in clast size, with pumice clasts 8-10 times larger than coexisting lithic fragments, is interpreted to represent very efficient hydraulic sorting of clasts during fallout from a subaqueous eruption column (Cashman & Fiske, 1990; Cashman & Fiske, 1991). Lithic components in the coarse deposits of the Efaté Pumice Breccias are typically much larger than co-existing pumice clasts indicating that fallout mechanisms were not important for deposition of these beds.

Non-welded, subaerial ignimbrites also have generally massive bedding and weakly developed density grading of particles, but these deposits are commonly matrix-supported, and retain evidence of hot emplacement such as thermal colouration, charred wood, and gas escape pipes. The matrix component of subaerial ignimbrites contains abundant fine ash, and fallout ash commonly caps massive ignimbrite beds.

In summary, key criteria for the recognition of syn-eruptive subaqueous volcaniclastic mass-flow deposits, like the Efaté Pumice Breccias, include: the presence of thick successions of texturally unmodified pyroclastic debris that lack significant intervals of hemipelagic sediments (indicating rapid emplacement); massive to stratified, planar, tabular, clast-supported pumice-rich beds that are generally poor in fine particles; associated shard-rich ash beds with doubly graded sequences; and the dominance of pyroclasts over other particle types.

Model for eruption and emplacement of Efaté Pumice Breccias

A model for the eruption and deposition of the Efaté Pumice Breccias is presented in Figure 3.19. Lavas were initially extruded from submarine vents and hot trachydacitic magma was rapidly quenched, forming domes with glassy outer margins. Vesiculating trachydacite magmas were explosively erupted from shallow, submarine vents located to the north of Efaté, and continuous collapse of this submarine eruption column *directly*

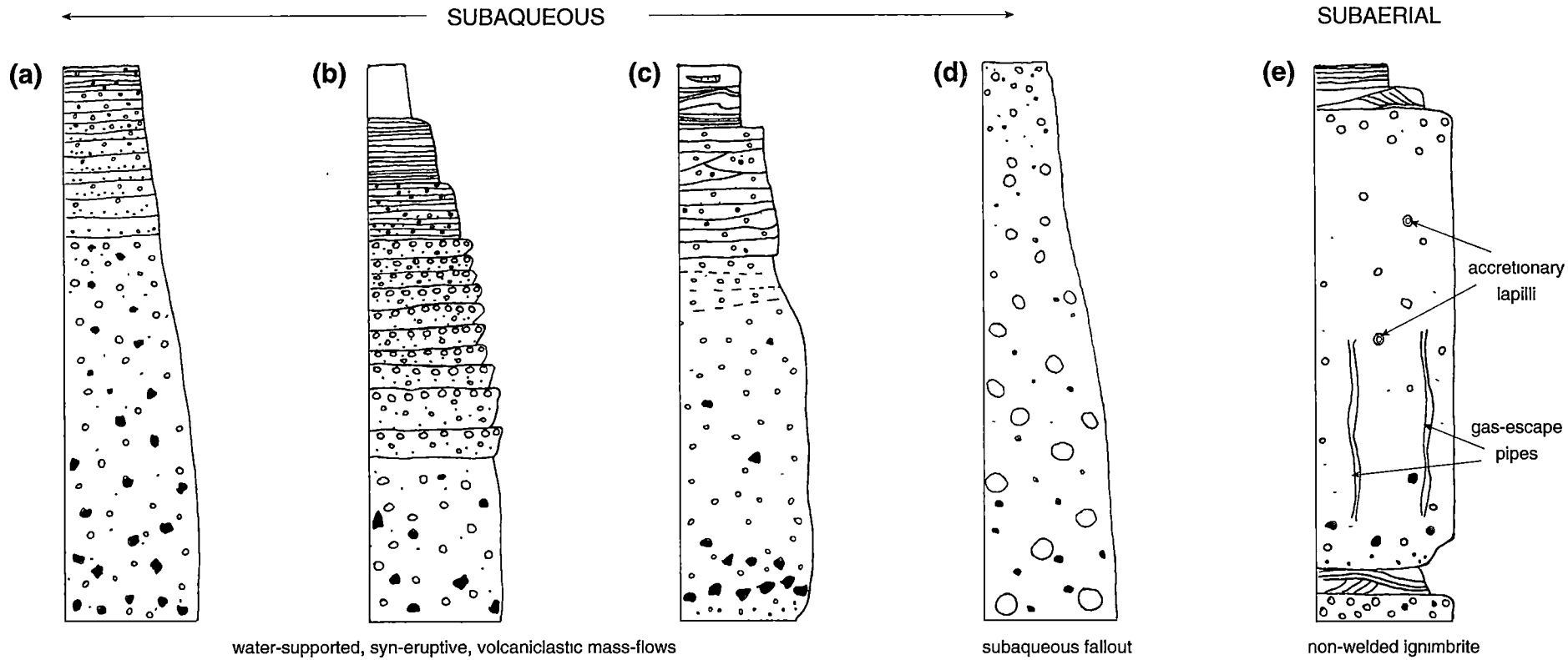

Figure 3.18. Comparison of facies models for non-welded pumice breccias. (a) A doubly graded sequence , deposited by a syn-eruptive, water-supported pyroclastic density current, generated by a contemporaneous submarine eruption. Tokiwa Formation, Japan (Fiske & Matsuda, 1964). (b) A coarser grained, doubly graded sequence, with an upper layer of massive volcanic ash, deposited by syn-eruptive, water-supported, pyroclastic turbidity currents from contemporaneous eruptions at either subaerial or sublacustrine vents. Onikobe caldera, Japan (Yamada, 1973). (c) Idealised sequence from the syn-eruptive Efaté Pumice Breccias, Vanuatu arc (this study). (e) Upward fining bed with bimodal distribution of pumice and lithic clasts interpreted to have formed by submarine fallout of pyroclasts from a contemporaneous submarine eruption column, Shirahama Group, Japan (Fiske & Cashman, 1987; Cashman & Fiske, 1990). (d) Facies model for a non-welded ignimbrite. Special features include the presence of gas-escape pipes, accrectionary lapilli and a pumice-rich zone towards the top (Sparks *et al.*, 1973).

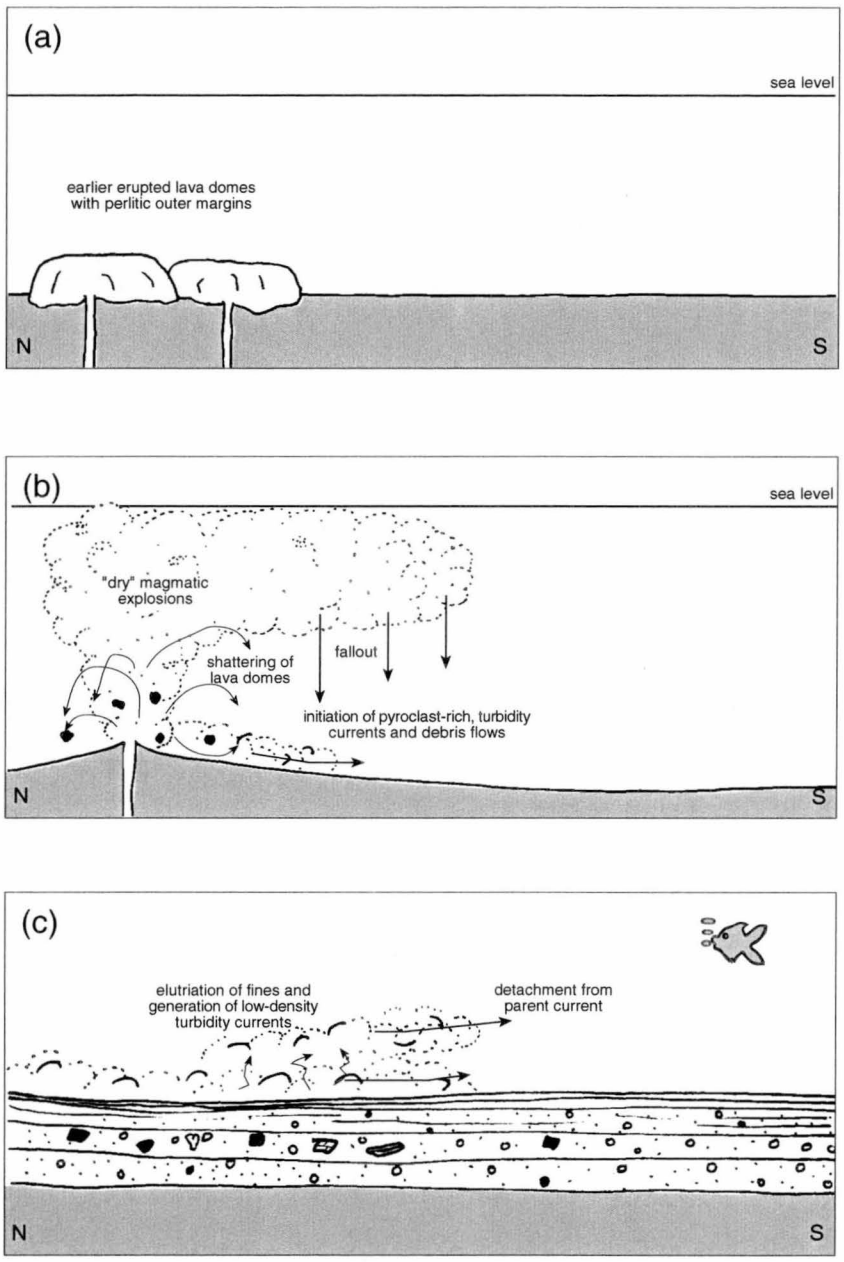

Figure 3.19. Model for eruption and emplacement of the Efaté Pumice Breccias. (a) Early eruption of trachydacite domes, probably in shallow submarine to subaerial environmnets. Rapid quenching plus hydration of the glassy lavas caused pervasive perlitic fracturing in the outermost parts of the domes. (b) Explosive expansion of magmatic volatiles causes a large magnitude eruption of highly vesicular pumice clasts and finer glass shards. The eruption occurs in shallow submarine to subaerial environments, near the existing lava domes causing them to shatter and become incorporated as accidental lithics in mass flows generated by the collapse of the eruption column. (c) Mass flows were generated by ingestion of seawater which transformed initially hot, gas-pyroclast dispersions in to syn-eruptive, cold, water-supported mass-flows (turbidity currents and debris flows) of pumice-rich sediment. Elutriation of fine pyroclasts during transport generated fine-grained , low-density turbidity currents that deposited shard-rich beds between successive, coarse mass flows.

generated cold, high-density, pumiceous turbidity currents by turbulent mixing with seawater. Hot pumice clasts, in particular the highly permeable tube pumice clasts, rapidly ingested water, allowing them to become incorporated in the turbidity currents. These currents deposited the Efaté Pumice Breccias. Elutriation of fine glass shards occurred during transport, leading to the generation of fine-grained, low-density turbidity currents that ultimately became detached from the parent flows. Debris flows, perhaps related to vent clearing episodes, deposited the coarsest lithic rich facies. The Efaté Pumice Breccias may have rapidly accumulated in depocentres, leading to a very thick and regionally confined succession (*e.g.* Cousineau, 1994).

CONCLUSIONS

The facies and facies associations of the Efaté Pumice Breccias were produced by a succession of volcaniclastic turbidity currents depositing in below storm-wave-base submarine environments. These turbidity currents were mostly generated directly from contemporaneous explosive magmatic eruptions by the turbulent mixing of initially hot, pyroclastic debris with seawater, leading to transformation into water-supported volcaniclastic mass flows that subsequently formed syn-eruptive deposits. Structures including stratification, cross-stratification and grading developed as currents lost capacity and traction sedimentation overtook suspension plus fallout sedimentation. Turbulence during transport elutriated fine particles from gravelly pumiceous flows, generating low-density turbidites that are interbedded with coarse-grained facies. The eruptions occurred at shallow (≤1000 m) submarine (and perhaps locally subaerial) vents located to the north of Efaté.

Chapter Four

SEDIMENTOLOGY OF THE RENTABAU TUFFS

Shard-rich sand and silt beds associated with voluminous submarine pumice-rich mass flows

INTRODUCTION

The Rentabau Tuffs conformably overlie the Efaté Pumice Breccias and record the final stages of trachydacitic volcanism in the Efaté Island Group. The Rentabau Tuffs are up to 70 m thick and predominantly comprise glass shards, with subordinate crystals and rare but ubiquitous marine foraminifera fossils. Although many thin and widespread silicic ash layers are attributed to subaerial plinian eruptions, and dispersal from atmospheric plumes (Schmincke & van den Bogaard, 1991; Stow, 1994), the origin of thick accumulations of subaqueously deposited, pyroclast-rich sediment, like the Rentabau Tuffs, is more difficult to interpret (Fisher, 1984; Fisher & Schmincke, 1984b; Suthren, 1985; Cas & Wright, 1991; Cas, 1992).

The Rentabau Tuffs are semi-consolidated, generally well preserved, lack evidence of diagenetic or welding compaction textures, and a submarine depositional environment is constrained by the presence of foraminifera fossils. Unresolved problems that are addressed in this chapter include: (1) the interpretation of the transport and depositional processes operating during deposition of the Rentabau Tuffs; (2) whether the Rentabau Tuffs represent syn-eruptive deposits directly generated from concurrent volcanic eruptions, or immediately post-eruptive sedimentation of temporarily stored volcaniclastic debris; (3) whether the volcanic vents were subaerial or subaqueous; (4) the interpretation of the style of eruption that generated the pyroclasts; and (5) the relationship of the Rentabau Tuffs with the underlying Efaté Pumice Breccias.

THE RENTABAU TUFFS

Age and distribution

The Rentabau Tuffs occur stratigraphically above the Efaté Pumice Breccias over a sharp, conformable contact, forming the uppermost package of the EPF. Biostratigraphic ages determined from fossil foraminifera assemblages in the Rentabau Tuffs deposits are Plio-

Pleistocene (Messinian and Zanclean stages, Ash *et al.*, 1978; Jones & AGSO Timescale Calibration and Development Project, 1995). The Rentabau Tuffs are penecontemporaneous with the underlying 1.1 Ma Efaté Pumice Breccias, based on contact relationships and the uniform geochemical composition of the two units, which indicates that they were erupted from the same magma batch (Chapter Six). A bulk minimum volume estimate for the Rentabau Tuffs is ~3 km^3 based on current outcrop patterns (Appendix B, Fig. 4.1). This is a conservative estimate given that much of the unit is covered by the RLF (*e.g.* Mawson, 1905). West of the Teouma Graben, the Rentabau Tuffs vary in thickness from a few metres to ~30 m. Exposures occur at the tops of the interior cliffs just west of the summit of Mount MacDonald, along the southwestern coast of the island, and at Hat Island. In eastern Efaté, the Rentabau Tuffs reach a minimum thickness of 70 m in the middle reaches of the Rentabau River (Ash *et al.*, 1978), but vertical sections are typically less than 10 m thick in small fault scarps and cuttings.

Ash *et al.* (1978) defined the clay-altered weathering products of the Rentabau Tuffs as the Forari clays, and treated them separately. In this chapter, units which were classified by Ash *et al.* (1978) as Forari clays are included in the Rentabau Tuffs, since clay alteration occurs to varying degrees throughout all sections described below.

Components and composition

Compositionally, the Rentabau Tuffs are very similar to the pumice breccias they overlie (Chapters Three and Six). Clasts are dominantly trachydacitic, glassy particles, crystals and crystal fragments. Significant additional components are marine fossil foraminifera in many of the beds (Fig. 4.2). Although the fossils are a very minor constituent, generally accounting for less than 2 % by volume of single beds, their presence provides evidence that the depositional environment of the Rentabau Tuffs was submarine.

Glassy particles

Glassy particles generally account for >90 % of the clast population in all facies and include tube pumice and bubble wall, cuspate and blocky shards in decreasing order of abundance (Fig. 4.2 a and b). Pumice clasts have both ragged and fracture-bounded terminations and bubble wall, cuspate and blocky shards are angular with well-defined clast margins. Rare blocky shards with convex-outward curviplanar margins associated with jigsaw-fit splintery fragments probably represent perlite cores and their spalled outer sheathes. Post-depositional alteration of glass marked by speckled, impure carbonate partially replacing individual shards, preserves the original clastic textures (Fig. 4.2 c and d), but partial or complete alteration of glass to halloysite is texturally

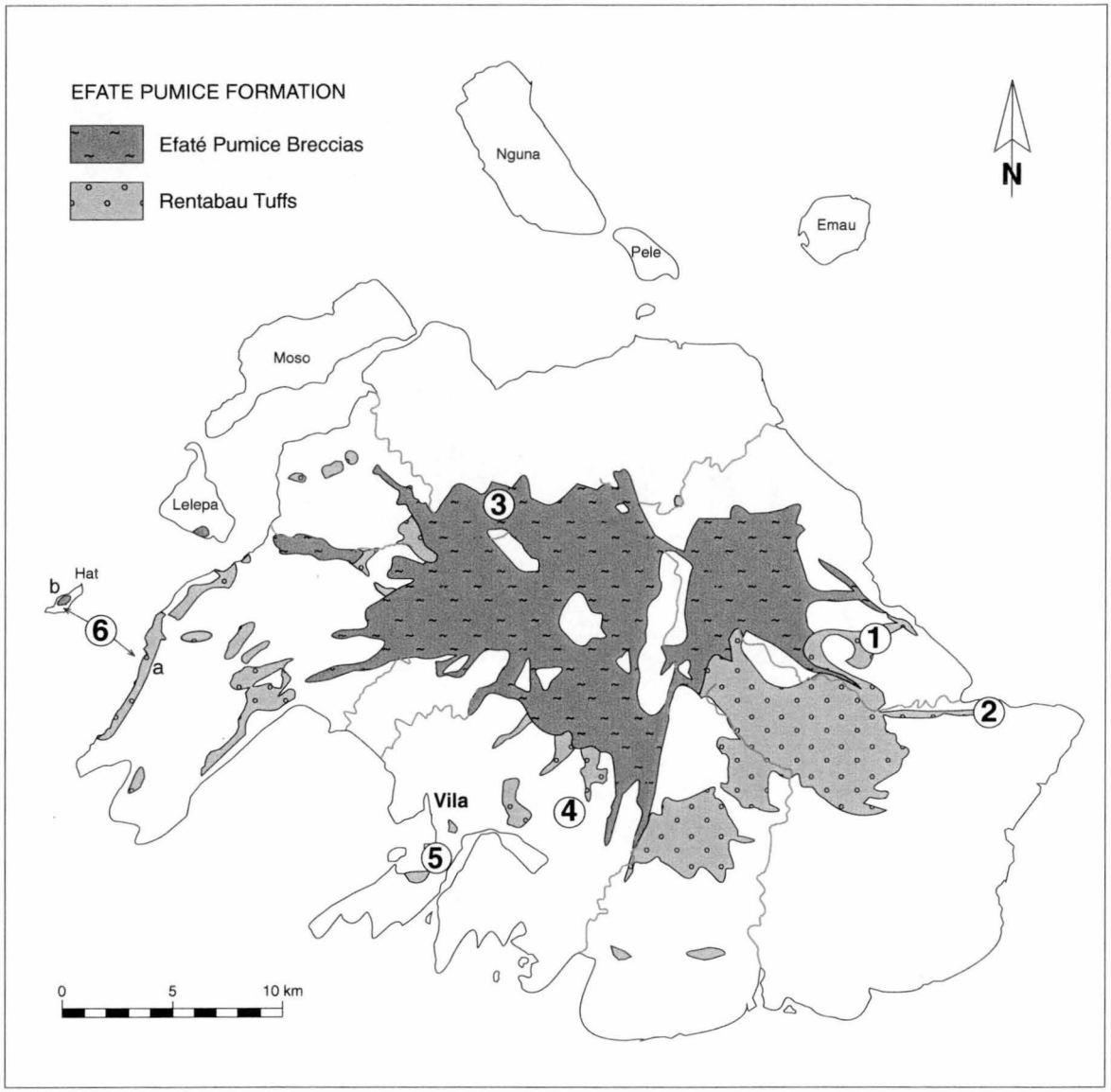

Figure 4.1. Regional distribution of the Rentabau Tuffs with measured section locations. (1) Elu River cliff section, (grid reference: KA355474); (2) road cutting close to old Forari manganese mine, (grid reference: KA413429); (3) interior cliff section, (grid reference: KA171514); (4) Bofua Municipal Tip site, deeply weathered trench section, (grid reference: KA225372); (5) Vila wharf section, (grid reference: KA153357); (6a) southern Efaté coastal cliff section, (grid reference: KA023455); (6b) Hat Island cliff section, (grid reference: JA981475). Modified from Ash *et al.* (1974; 1978)

destructive. Locally important secondary replacement of clay-altered, originally glassy, shard-rich facies by hydrated manganese oxides overprints the clay alteration features.

Crystals

Crystals and crystal fragments include plagioclase, ortho- and clinopyroxene and Ti-magnetite. Crystal abundances vary within facies and are generally low (up to ~10 %) except in the laminated shard-rich sand and silt beds, where crystals may account for up to 70 % of components in very thin, crystal-rich laminae (Fig. 4.2 e). Plagioclase (0.5-2 mm) and pyroxene (0.1-1 mm) crystals vary from euhedral in the coarser sandy beds, to fractured, anhedral grains in the finer silty beds. Most Ti-magnetites (<0.1 mm) are concentrated as discrete euhedral to subhedral crystals in the finest facies, and may have Fe-oxide alteration haloes. In the very coarse sand and fine breccia beds, crystals generally occur as phenocrysts in pumice clasts, but plagioclase may also occur as discrete large (2-4 mm) crystals mantled by ragged glassy rims. Accessory apatite needles may be present and are common inclusions in plagioclase.

Other clast types

Rare lithic clasts include large (8 cm), rounded bioclastic limestone clasts, occurring within beds subjacent to a limestone contact, as well as rare, well rounded scoria clasts commonly displaying weakly developed, narrow (<10 mm) Fe-oxide alteration haloes within the host sediment (Fig. 4.5, Section 2). Subrounded clasts of moderately sorted, very fine pumice breccia/shard-rich sand (up to 2 cm) are locally important within some beds of very similar sediment (Fig. 4.4, Section 1).

Fossil assemblage

Foraminifera tests are an important component of the clast population and vary in abundance amongst samples but generally comprise less than 2 % by volume (Fig. 4.2 f). Samples in this study were generally too sparsely populated and fossils recovered were not well enough preserved to identify species confidently, or to provide unequivocal constraints on water depth. *Orbulina universa* and examples of the benthic genera *Anomalinoides* were tentatively identified in sample ELUR10a, while recrystallised organic remains in sample AR101 probably include bryozoa fragments in addition to the 3-5 % foraminifera fossils (P. Quilty pers. comm.). Foraminifera species identified by Coleman (cited in Ash *et al.*, 1978) include *Globigerinoides ruber, Globigerinoides conglobatus, Orbulina universa* and *Globigerina dutertrei.* These planktic foraminifera species probably belong to deep sea or open water fauna assemblage, and provide a minimum below-storm-wave-base constraint on the depositional setting of the Rentabau Tuffs (Todd, cited in Ash *et al.*, 1978).

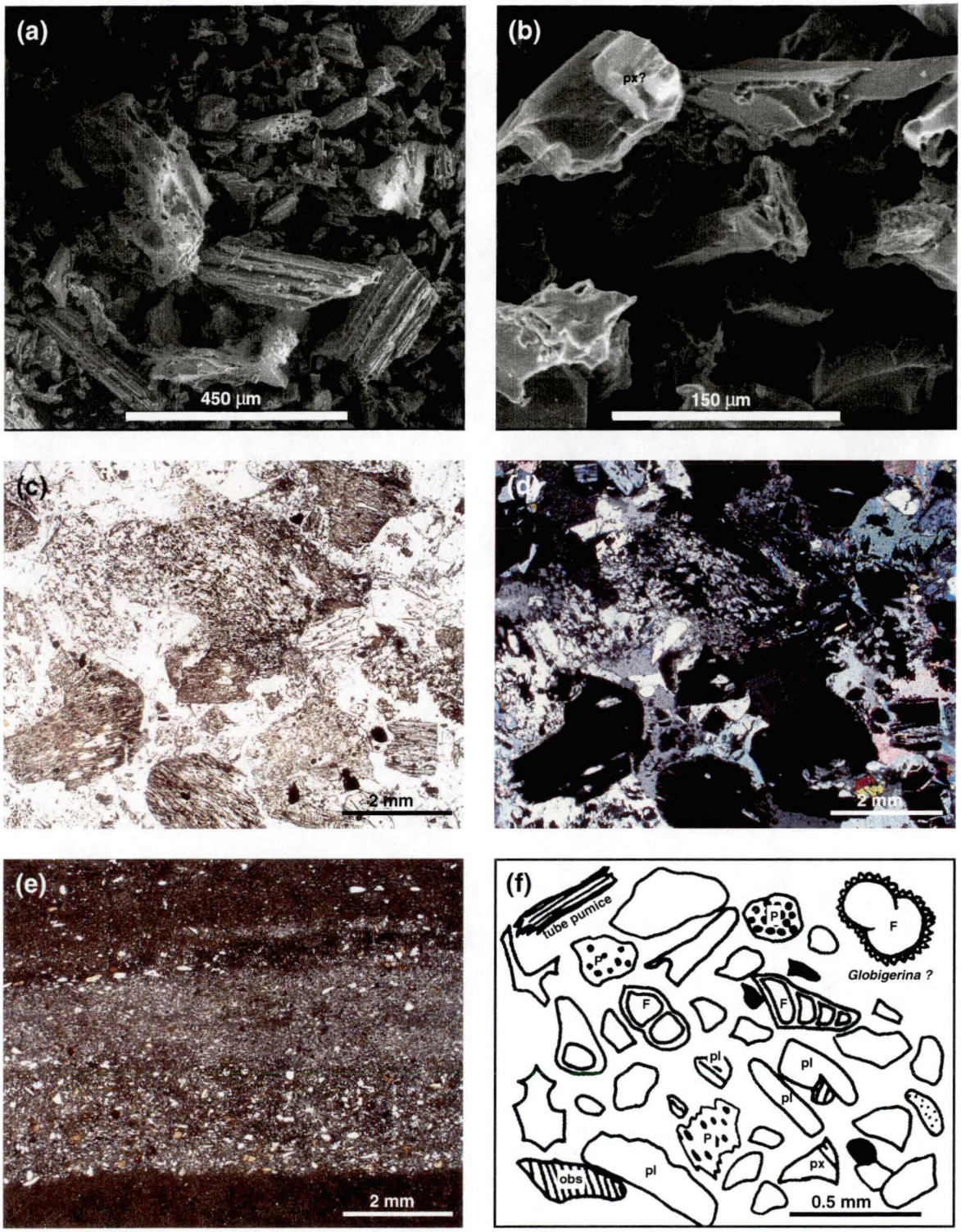

Figure 4.2. Componentry of the Rentabau Tuffs. (a) Scanning electron microscope (SEM) image of glass shards in sample AR307. Note abundant tube pumice shards. (b) SEM image of glass shards and a crystal in sample ELUR2. Shards are more blocky to cuspate than those in (a) and bubble walls are relatively thick. Note euhedral pyroxene (px?) crystal shape. Photomicrographs in (c) and (d) show carbonate cement textures in sample AR052 from the Efaté Pumice Breccias in plane polarised and cross polarised light respectively. These are very similar to carbonate cements in the Rentabau Tuffs. Pumice, cuspate and blocky shards are generally preserved but incipient replacement by speckly (impure?) carbonate occurs along elongate vesicle walls in tube pumices. (e) Crystal- and shard-rich lamina in sample AR016. Crystal phases in the shard-rich base are dominantly plagioclase, with minor pyroxene (pale yellow) and Ti-magnetite. Brown clasts are blocky glass shards. Enclosing dark layers comprise inipiently clay-altered shard rich silt. (f) Sketch of microscope field of view of sample AR101. Note variety of fossil foraminifera (F). Pumice (P) and other glass shards, including a flow banded obsidian fragment (obs), are the most abundant components, with subordinate plagioclase (pl), pyroxene (px), and Ti-magnetite crystals. Pore space is filled by a speckled (impure?) carbonate cement.

Post-depositional alteration processes

Volcanic glass is metastable and subject to rapid syn- and post-depositional alteration in subaerial, subaqueous and diagenetic environments (*e.g.* Walton, 1975; Federman, 1984; Sturchio *et al.*, 1986; Zhou & Fyfe, 1989; Casey & Bunker, 1990; Capaccioni & Conglio, 1995; de' Gennaro *et al.*, 1999). Studies of natural glasses in abyssal environments show that basic tephras are more chemically reactive than felsic tephras, unless such glasses are exposed to elevated temperature and/or pressure conditions associated with circulating hydrothermal fluids or deep burial (Friedman & Long, 1984; Zhou & Fyfe, 1989; Ghiara & Petti, 1996). Alteration of glassy particles in the Rentabau Tuffs occurred in both subaerial and submarine environments.

Clay alteration

Although the Rentabau Tuffs were deposited in a submarine environment, alteration to clay affected the glassy sediments only after uplift and exposure to tropical weathering. Original glassy textures are obliterated, but crystals are generally preserved. Larger pumice fragments are also variably preserved which may be a function of grain size compared with glass shards. Halloysites are the dominant authigenic clays in the Rentabau Tuffs (Appendix D, Quantin, 1972; Ash *et al.*, 1978; Quantin *et al.*, 1984; Quantin *et al.*, 1991; Girschik, 1995) and halloysite has long been recognised as a common product of rapid weathering of volcanic rocks, especially glassy rocks and sediments (Aomine & Wada, 1962; Loughnan, 1982; Quantin *et al.*, 1988; Hodder *et al.*, 1990; Kawano *et al.*, 1997). Quantin (1972; 1992), and Quantin *et al.* (1984) studied the *in situ* development of halloysite and hydrated halloysite in the EPF in detail and attributed clay formation to low temperature, circulating groundwater and accelerated weathering rates in the tropical subsoil of Efaté.

Carbonate cements and replacement textures

Carbonate cements are variably developed in the Rentabau Tuffs. Strongly indurated beds generally react with dilute hydrochloric acid, although carbonate is hard to recognise in thin section. In strongly cemented samples, pore spaces are completely sealed by carbonate and incipient replacement of glassy fragments by carbonate may occur, although glass shard outlines are preserved (Fig. 4.2 c and d). Carbonate cementation and incipient replacement of the glass probably took place in shallow or emergent environments, where low-temperature, carbonate-rich, circulating fluids, sourced from the onlapping limestones, percolated through the volcaniclastic pile and deposited in pore spaces. Carbonate recrystallisation in tropical shallow water environments is related to changing pH conditions in circulating groundwater. Acids produced by biological sulfate reduction dissolve existing carbonate, eventually increasing alkalinity and Ca saturation in circulating fluids, and causing re-precipitation of carbonate in sediment pore spaces

(Walter & Burton, 1990; Reid *et al.*, 1992; Walter *et al.*, 1993). Replacement of the volcanic glass probably occurred by diffusion processes across the glass/fluid boundary (Adams, 1984). Carbonate cements are also locally developed in the Efaté Pumice Breccias.

Manganese cements and replacement textures

A manganese orebody was mined at Forari from 1962-1977. Non-economic manganese occurs scattered throughout the Rentabau Tuffs, or in lateritic soils, principally at or near the contact with the onlapping reef limestones in the eastern part of Efaté Island (Warden, 1970; Warden, 1971; Ash *et al.*, 1978). Hydrated manganese oxide (todorokite) occurs as a cement in sample AR002 and is texturally destructive. Original crystal fragments are totally preserved, and pumice grains ranging from 1-3 mm are variably preserved. Massive manganese oxide occurs in pore space, as do single and coalesced radial clusters of acicular crystals, which also encroach upon glassy clasts. Hein *et al.* (1990) attributed similar features in manganese deposits from the Tonga Ridge to localised precipitation of manganese from pore water and seawater, heated by hydrothermal fluids close to submarine volcanic vents. For the Rentabau Tuffs, a similar mineralising event probably occurred in submarine environments but supergene enrichment in the subaerial weathering zone may also have been important (Warden, 1971).

Lithofacies characteristics

In contrast to the pumice breccias described in the preceding chapter, the Rentabau Tuffs are dominated by well sorted, shard-rich sand and silt facies. In southern and western Efaté, bedding is remarkably uniform, grain sizes are consistently fine, and components are dominantly glass shards and crystal fragments. Further north, and in sections east of the Teouma Graben, more variation in bed geometry, grain size and composition is apparent. Single beds typically have consistent thicknesses and are laterally continuous with sharp bases and tops, and tabular geometries. The deposits are characterised by medium and thin, to very thin beds of pumice shard-rich sand and/or very fine breccia, and massive, laminated, and cross-laminated shard-rich silt, with rare to locally important pumice breccia lenses. Fine pumice breccia beds occur locally, as do bioclastic limestone lenses and mixed limestone/shard-rich beds. Microcrystalline or sparry calcite and hydrated manganese oxide cements occur locally. Characteristics of the six principal facies are summarised in Table 4.1 and described in detail below. Locally important features and distinctly different beds/facies are described where they occur within particular sections. All facies contain rare fossil foraminifera tests and are generally well sorted, but may contain outsize pumice clasts up to ~3 cm but typically 6-10 mm.

Table 4.1. Facies of the Rentabau Tuffs

FACIES NAME	BED THICKNESS / GEOMETRY	SEDIMENTARY STRUCTURES	PROCESSES
massive shard-rich sand	very thin to medium beds tabular (sharp, conformable contacts)	structureless beds	mass flows,
laminated shard-rich sand	medium to very thick beds of internally laminated sand tabular (sharp, conformable contacts)	internally thickly laminated, rare low-angle truncation surfaces	mass flows, bottom current reworking
ripple-laminated shard-rich sand	medium to thick beds tabular (sharp, conformable contacts) rarely lenticular	wavy and undulose ripples (typically isolated), climbing ripples, local trough cross-lamination	bottom current reworking, mass flows
convolute-bedded shard rich sand and silt	variable, generally medium to thick intervals generally tabular intervals (discordant contacts)	contorted bedding, irregular folds	soft sediment deformation, slumping
massive shard-rich silt	medium to thick beds tabular (sharp, conformable contacts)	structureless beds	mass flows
pumice-rich fine breccia	thin to thick beds tabular (sharp, conformable contacts) locally lenticular (erosional contacts)	generally massive beds, internal scours common, clast-supported fabric, normal grading at upper contacts	mass flows

Massive shard-rich sand

Description - Medium to very thin beds of moderately to well-sorted, massive, shard-rich sand characterise this facies. Bed bases are sharp and conformable but erosive basal contacts, sole marks and load-casts are also locally important. This facies tends to be more indurated than others in the Rentabau Tuffs, and massive sand beds commonly form narrow (3-5 cm) ledges in the succession. Rare, discrete, 8-15 mm pumice clasts occur randomly within this facies and ~5 cm-thick, medium to fine pumice breccia lenses are found in a bed on Hat Island. This facies comprises ~92 % glass shards with subordinate crystals (3-6 %) and up to 3 % marine foraminifera tests.

Occurrence - This facies is ubiquitous, but sand grain size, bed thicknesses and fossil content vary from locality to locality. Thin (2-5 cm) beds of laminated shard-rich sand may separate beds of massive shard-rich sand.

Interpretation - Deposition of massive beds may result from *en masse* freezing or rapid suspension fallout from highly concentrated sediment dispersions (Lowe, 1982; Ghibaudo, 1992), progressive aggradation from steady turbidity currents (Kneller, 1995; Kneller & Branney, 1995), debris flow processes (Shanmugam, 1997).

Laminated shard-rich sand

Description - This facies typically comprises medium to very thick (0.1-1.2 m), even, continuous, tabular beds of internally laminated, well-sorted, crystal- and glass shard-rich sand. Thin (2-5 cm) planar tabular beds are locally important. Bed bases and tops

are sharp, planar and typically conformable. Two types of internal lamination are present: (1) alternating, non-graded, glass shard-rich (~95 %) and crystal-rich (≤70 %) laminae, and (2) normally graded 2-5 mm-thick laminae, with medium to coarse crystal-rich bases and fine to very fine shard-rich tops. No regular distribution pattern exists for the type of laminae present within a bed and both types may occur over intervals as small as several centimetres. Low-angle (≤1°) discontinuity surfaces occur randomly within some beds. Outsize pumice clasts (~3 cm) commonly occur within this facies. This facies commonly contains 2-5 % marine foraminifera fossils.

Occurrence – The laminated shard-rich sand facies occurs in all sections and is a volumetrically important facies. It is commonly interbedded with the massive shard-rich sand facies and the convolute-bedded shard-rich sand and silt facies. This facies may pass laterally into the ripple-laminated shard-rich sand facies.

Interpretation - Deposition of laminated sand may result from suspension settling of clasts through the water column (Allen, 1982; Fisher & Schmincke, 1984a). Laminated sands can also result from traction plus fallout sedimentation processes occurring under lower flow regime conditions (Allen, 1982; Lowe, 1988). These conditions commonly exist for deposition from low-density turbidity currents (Bouma, 1962; Einsele, 1991), or alternatively, in bottom currents that rework the sediments (Shanmugam *et al.*, 1995). The alternating shard- and crystal-rich laminae result from hydraulic sorting of these particles through suspension fallout, whereas graded laminae probably reflect deposition by tractional sedimentation, related to turbidity currents or bottom currents.

Ripple-laminated shard-rich sand

Description - This facies consists of laterally continuous, 10-50 cm-thick, tabular, or rarely lenticular beds of internally ripple-laminated glass shard- and crystal-rich sand. Ripple bedforms vary from wavy or undulose, to locally well-developed climbing ripples and trough cross-laminae. Ripple amplitudes are generally 6-8 cm with wavelengths 20-25 cm. Planar cross-stratification is absent. Laminae are defined by alternating shard-rich (>90 %) and crystal-rich (>70 %) layers. Bed bases vary from sharp and flat, to undulose. Bed tops are either sharp, or gradational. This facies may contain up to 2 % marine foraminifera fossils. Outsize pumice clasts up to 15 mm may occur within this facies.

Occurrence - This facies is commonly interbedded with both laminated shard-rich sand facies and convolute-bedded shard-rich sand and silt facies and occurs in most sections. This facies may grade laterally and/or upwards into the laminated shard-rich sand facies.

Interpretation - Ripple bedforms result from tractional sedimentation in turbulent currents under upper flow regime conditions (Allen, 1982; Lowe, 1982; Ghibaudo, 1992). Swaley

and undulose bedforms could form in sediments reworked by bottom currents (Shanmugam *et al.*, 1995), or from poorly developed traction within a depositing current. Climbing ripples are commonly diagnostic of suspension sedimentation occurring within turbidity currents, or may develop under standing waves in high-energy sedimentary environments (Bouma, 1962; Stow & Piper, 1984; Piper & Stow, 1991; Shanmugam, 1997).

Convolute bedded shard-rich sand and silt

Description - This facies is characterised by contorted and irregularly folded laminated shard-rich sands. The scale of folds and bedding contortions varies from a few cm up to 10-20 cm. Laminae alternate between being crystal-rich and shard-rich. Foraminifera tests (<2 %) may be present. Bases and tops of the convolute-bedded intervals (30-60 cm) are sharp and regular, and are commonly discordant with enclosing bedding.

Occurrence - This facies is consistently represented in many outcrops, particularly on the southwestern coastal cliffs. It is best developed in the western and southern areas.

Interpretation - This type of bedding is the result of deformation of semi-consolidated sediment during slumping along basal shear surfaces (Stow, 1994). Slumping on submarine slopes may be due to several factors, including the gradient of the slope, high sedimentation rates and seismic activity (Schwartz, 1982; Barnes & Lewis, 1991).

Massive shard-rich silt

Description - This facies is characterised by medium to thick (10-50 cm) beds of massive, well sorted, shard-rich, crystal-poor silt and/or clay. Bed bases and tops are sharp, regular and conformable. Massive silt beds are overwhelmingly compositionally uniform comprising ~98 % glass shards with rare marine fossil foraminifera.

Occurrence - This facies is most important in sections in the southwest and southern part of the island.

Interpretation - Massive silt beds may result from deposition by *en masse* freezing or rapid suspension fallout from highly concentrated sediment dispersions (Lowe, 1982; Ghibaudo, 1992), progressive aggradation from steady-state turbidity currents (Kneller, 1995; Kneller & Branney, 1995), or debris flow processes (Shanmugam, 1997).

Pumice-rich fine breccia

Description - This facies is characterised by thick to thin beds of fine to very fine, moderately sorted, pumice breccia. Angular to sub-angular pumice clasts with ragged

terminations are the dominant (~80 %) components in this facies and rarely exceed 2 cm. Beds typically have a clast-supported fabric, with a medium to coarse sand matrix consisting of glass shards (~18 %) and crystals (1-2 %). Sorting is moderate, and beds have planar, tabular geometries. Bedding is generally massive, although internal scours and normal grading in the uppermost parts of beds occur locally. Bed bases and tops are sharp and conformable. Rare marine foraminifera tests may be present.

Occurrence - This facies is important in the northern cliffs section (Section 4), and east of the Teouma Graben (Section 1). It is commonly interbedded with very thin beds of massive shard-rich sand.

Interpretation - Coarse-grained massive beds may result from deposition by *en masse* freezing of highly concentrated sediment dispersions (Lowe, 1982; Ghibaudo, 1992), progressive aggradation from steady-state turbidity currents (Kneller, 1995; Kneller & Branney, 1995), or debris flow processes (Shanmugam, 1997). Graded intervals may be produced by the development of traction plus suspension sedimentation within the depositing sediment-laden current (Lowe, 1982). Internal scouring may be caused by local flow unsteadiness in the depositing current (Allen, 1982).

Internal stratigraphy

Reconnaissance of inaccessible cliff top exposures of the Rentabau Tuffs indicates that measured sections from six localities outlined below are generally representative of the unit and so provide a broad overview of the regional variation. The sections show the remarkable overall consistency in facies of the Rentabau Tuffs. Grid references for section locations refer to 1:50,000 scale digital maps (based on the World Geodetic Spheroid 1984, UTM zone 59) and are given in square brackets.

Section 1.

An 8 m high section through a portion of the Rentabau Tuffs in which pumice granules and pebbles are an important component, is exposed in a small fault scarp along the Elu River [KA335474], approximately 2 km from the coast (Fig. 4.3). The basal 1.5 m of the section comprises medium beds of the massive shard-rich sand facies, irregularly interbedded with thin layers of the laminated shard-rich sand facies. The bulk of Section 1 however, consists of thick (0.5-1 m) beds of the massive to graded and internally scoured, pumice-rich fine breccia facies. Massive pumiceous beds may show a lateral gradation from coarse shard-rich sand to very fine pumice breccia over a few metres. Normal grading in some beds passes upward into medium to very coarse laminated shard-rich sand layers up to 40 cm-thick. Low-angle truncations within beds occur over a few metres laterally. A lenticular bed of cross-laminated and internally scoured very fine pumice breccia occurs towards the top of the section. Two thirds of the

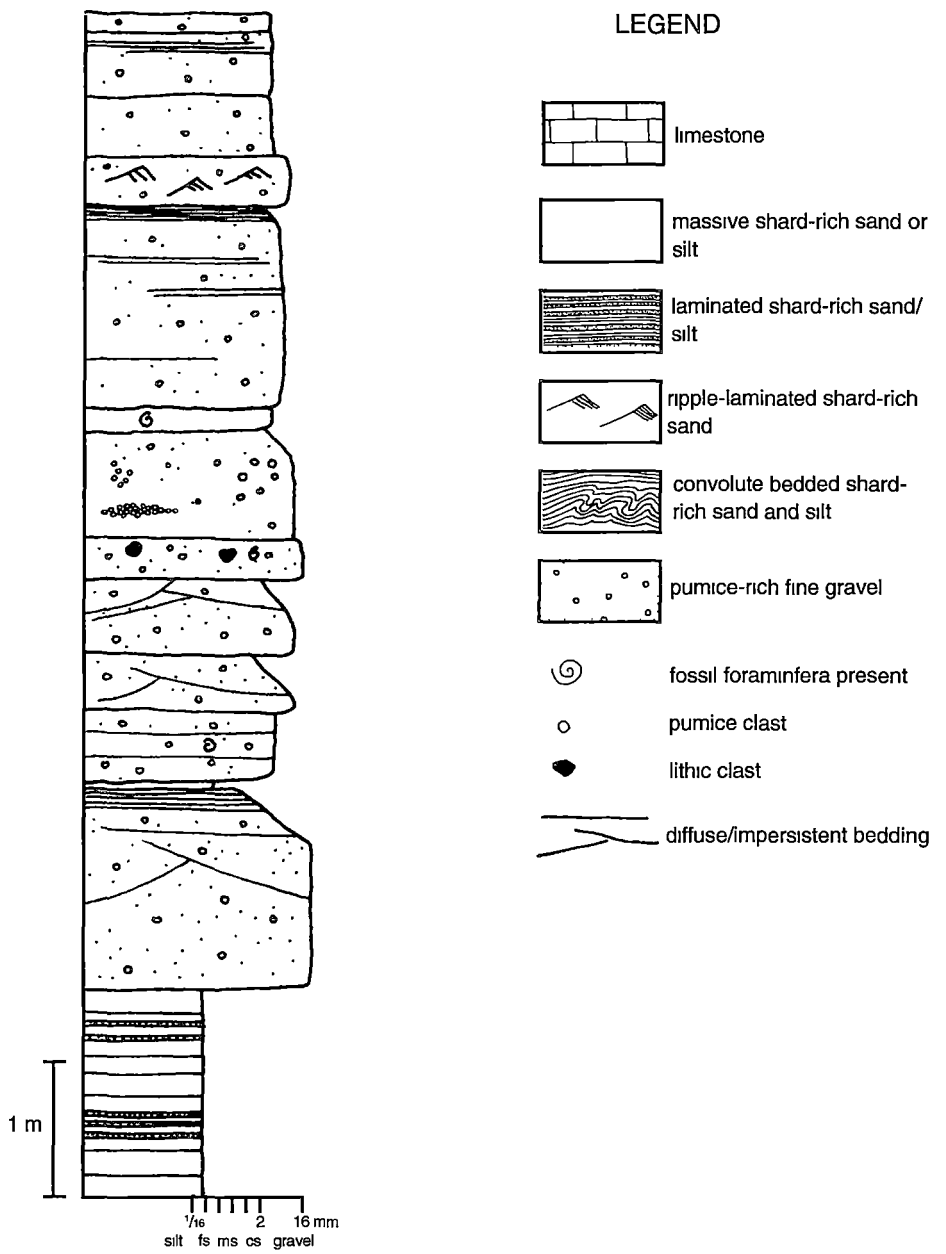

Figure 4.3. Graphic log for Section 1. Elu River (grid reference: KA355474). Legend at right also refers to Figs 4.4-4.8. Note abundance of pumice-rich very fine gravel beds, normal grading and internal scouring, which is in contrast to other sections of the Rentabau Tuffs.

way up the section, patchy carbonate and manganese oxide cements have produced a pseudoclastic texture in coarse to very coarse shard-rich sand to very fine breccia. Sample ELUR10a from this interval also contains a rare, rounded clast (~20 mm) of massive medium to coarse shard-rich sand. Clay development is patchy, and glassy particles are variably preserved.

Section 2. (Forari clays)

A recent cutting on the circum-island road, near the old Forari manganese mine [KA413429], exposes planar, continuous beds of the Rentabau Tuffs (Fig. 4.4). Small post-depositional thrust faults disrupt the continuity of several beds in the middle of the cutting. An irregular, unconformable contact with the overlying Reef Limestone Formation (RLF) is clearly exposed here. Alteration of the glassy clasts to halloysite clays possibly masks original grain size characteristics, but crystals are unaffected. Manganese oxides occur in veins and as spots in a 0.3 m-wide alteration zone within the clay-altered Rentabau Tuffs, immediately below the limestone contact.

The massive shard-rich sand facies dominates in Section 2, with laminated shard-rich sand comprising most of the remaining beds. Pumice-rich fine and very fine breccia beds also occur in the section. A facies unique to Section 2 consists of a single, inversely graded, greenish-grey bed with 15-20 % *Globigerina (?)* tests (2-4 mm), in a finer matrix of shard-rich coarse sand. Grading is indicated by an upward increasing abundance of foraminifera tests. The presence of this bed signals a hiatus in deposition of glass-shard rich sediment that may be related to a lull in supply. Although not recognised in other sections for this investigation, Ash *et al.* (1978) report similar beds elsewhere. A rounded limestone cobble (8 cm), and two well-rounded, mafic scoria pebbles (5-6 cm), occur at contacts between beds of laminated and massive shard-rich sand. Deformation of laminated bedding immediately below the dense limestone clast is probably due to loading compaction. The scoria clasts are exotic lithics and may have floated on the sea surface for some time, and travelled some distance, before becoming water-logged and sinking into the accumulating Rentabau Tuffs (*e.g.* Whitham & Sparks, 1986; Manville *et al.*, 1998).

Section 3.

In Section 3, from the interior cliffs [KA171514], the Rentabau Tuffs conformably overlie 5-10 m-thick beds of medium- to fine-grained Efaté Pumice Breccia (Fig. 4.5). The contact between the stratigraphic units is conformable, and approximately 20 m of the Rentabau Tuffs is exposed in this section. The dominant facies are massive, laminated, ripple-bedded and convolute-bedded, medium to very coarse grained, glass shard-rich and crystal-bearing sand.

The lowermost part of the section consists of regular ~10 cm-thick beds of the massive shard-rich sand facies. Beds alternate between medium and very coarse sand, contain

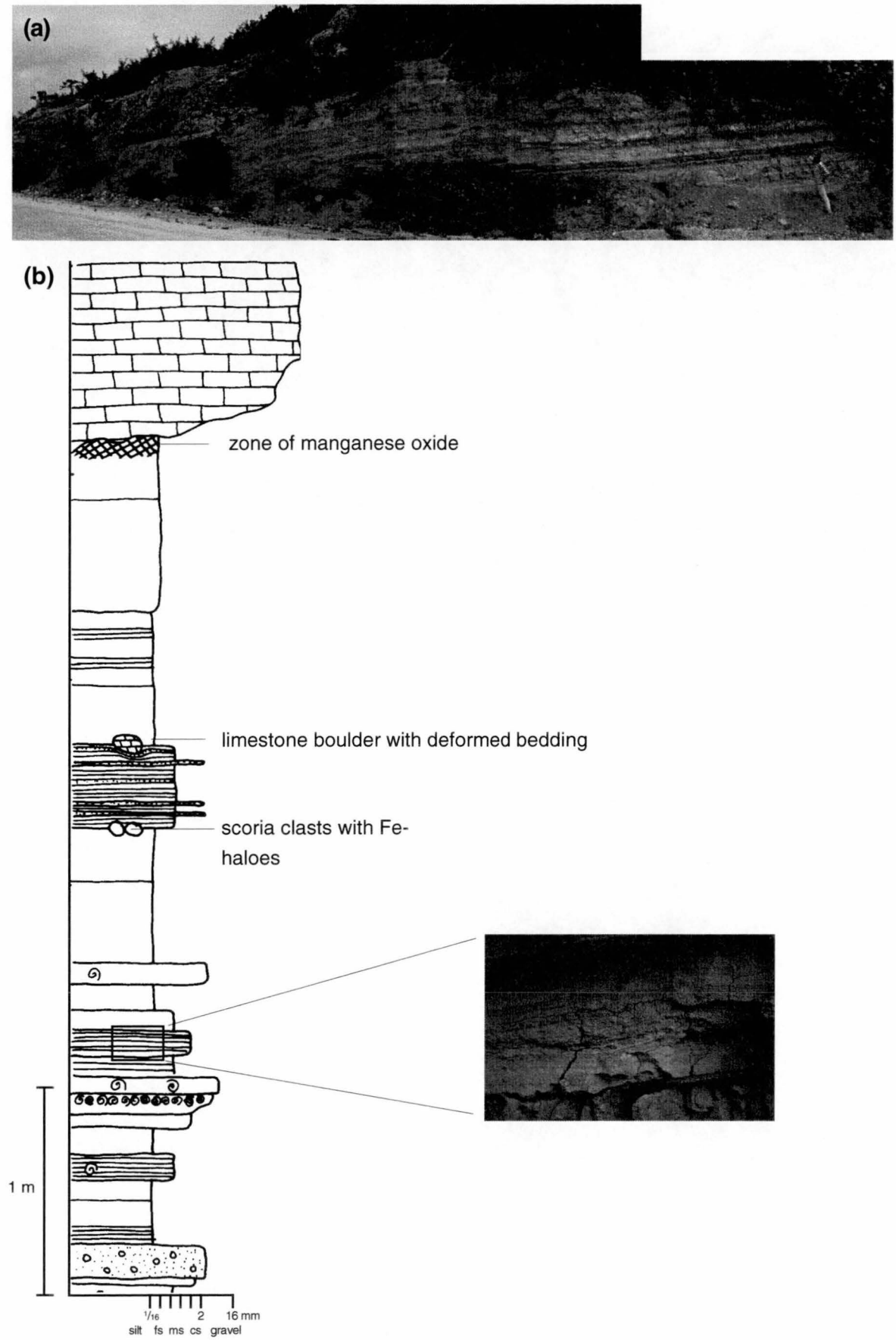

Figure 4.4. Section 2. Road cutting near Forari Mine, (grid reference: KA413429). (a) View of section showing locally fault-disrupted even, continuous, tabular beds, and an unconformable contact with the overlying Reef Limestone Formation. (b) Graphic log shows that the section dominantly comprises massive shard-rich sand beds with lesser laminated shard-rich sand beds (inset, pencil is 14.5 cm long). Note also subordinate beds of pumice-rich fine gravel and a unique inversely graded fossil-rich bed towards base of section. Legend as per Fig. 4.3.

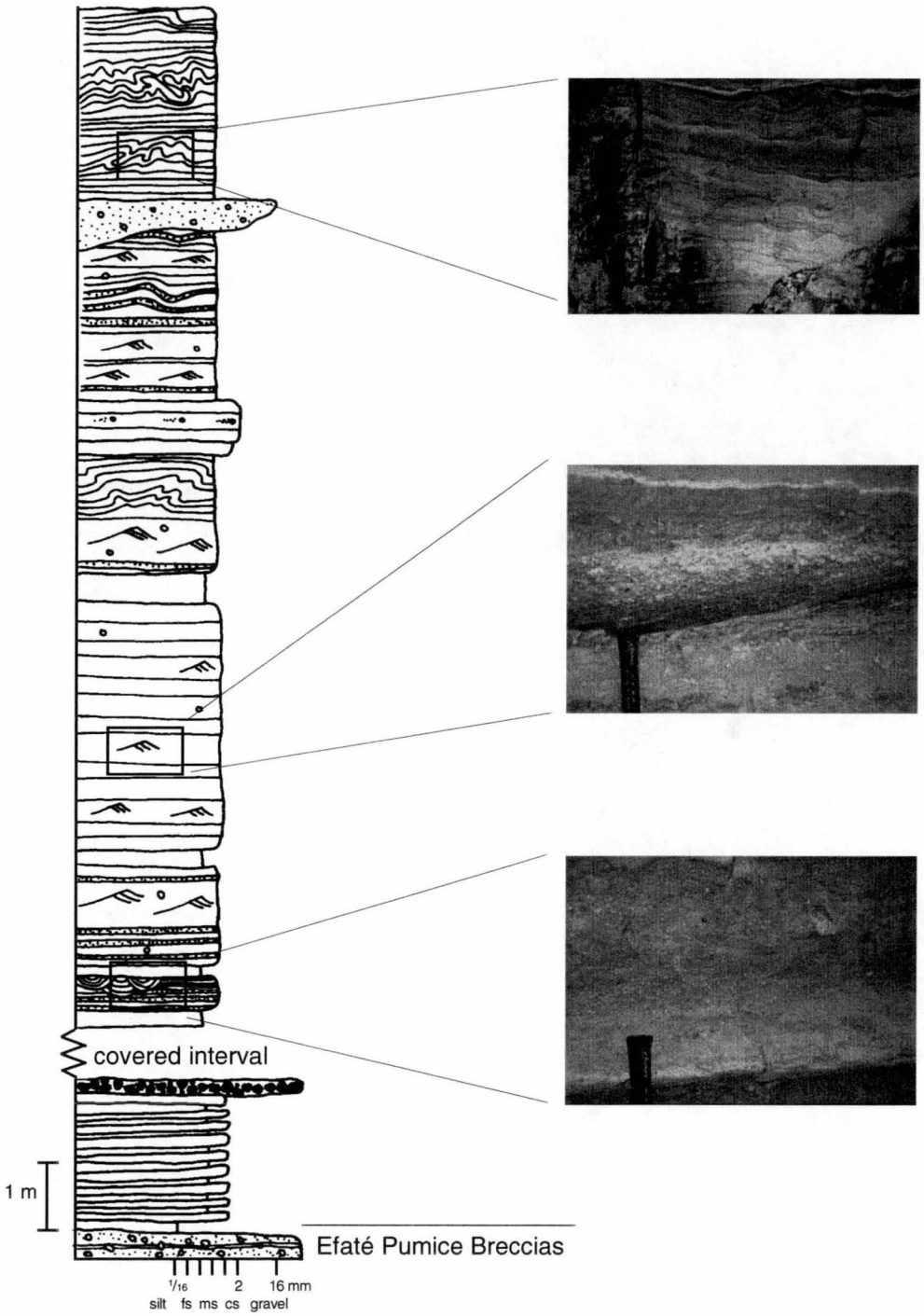

Figure 4.5. Graphic log of Section 3. Interior cliffs (grid reference: KA171514). This section is dominated by thin to medium beds of massive, laminated, and ripple-laminated shard-rich sand. Intervals of convolute-bedded shard-rich sand are also common. Unusual features of this section include a thin lithic breccia bed, and rare occurrence of trough cross-laminated sands near base of sequence (inset). Also note lensoidal, pumice-rich very fine gravel bed towards top. Laminae in uppermost photograph ~4 mm thick. Hammer handle approximately 3.5 cm wide. Legend as per Fig. 4.3.

moderately abundant (~10 %) outsize pumice pebbles (up to 3 cm), and rare (<1 %) perlitic obsidian clasts (1-5 mm), and are separated by indurated thin to very thin interbeds of massive, fine to very fine sand (not shown on log, Fig. 4.5). These massive sand beds are overlain by a unique conformable, thin (8 cm), lithic breccia bed comprising sub-angular to sub-rounded 3-6 cm clasts of perlitic obsidian, and dark grey, hollocrystalline, porphyritic volcanic (lava?) clasts, with subordinate pumice. This breccia bed represents deposition by high-concentration turbidity currents generated by different mechanisms to those interpreted for the bulk of the Rentabau Tuffs (see below).

Occurring above a covered area in the section, the laminated and cross-laminated shard-rich sand facies are important and commonly show lateral transitions from one to the other over less than 1 m, indicating that unsteady currents operated during deposition. Ripple forms are generally irregular but wavy ripples dominate and trough cross-stratification is locally important. The section cuts obliquely through ripples so no current directions could be determined, but forms are uni-directional. The massive shard-rich sand facies is randomly interbedded with the ripple-laminated sand facies in the middle of the section, and the upper half of the section comprises abundant intervals of the convolute-bedded shard-rich sand facies. Irregular folds, load casts and erosional surfaces associated with contorted bedding are abundant in these beds.

Beds of the pumice-rich fine breccia facies in the upper part of the section are generally massive but obsidian fragments (~3 cm) associated with cigar-shaped lenses of slightly coarser material are randomly present within one bed. A discontinuous lens of yellow fine pumice breccia occurs 3-4 m from the top of the section and has erosional contacts. The matrix component of this bed comprises a mixture of shard-rich sand and sand-sized detrital limestone clasts, and reacts with dilute HCl.

Section 4. (Forari clays)

Trenches at the Bofua Municipal Tip [KA225372] expose 10 and 15 m longitudinal sections 3-4 m high through the modern soil profile into deeply weathered (clay-altered) Rentabau Tuffs (Section 4, Fig. 4.6). Although the glassy components are almost completely altered to halloysite and other hydrated clays (see discussion below), the bedding characteristics are still preserved. The beds are tabular, massive, and internally laminated, and folded. Bedding contacts are sharp and conformable, but local thrust faults cause offsets on the scale of a few centimetres to 0.5 m. One small thrust terminates in a 0.5-.75 m-wide network of 1-5 mm-wide veinlets of Fe-rich halloysite (Fig. 4.6 a). Well-developed folds in a layer of laminated yellow clay imply a transport direction consistent with that of the thrust orientations (towards 130°).

Weathering has produced clays varying from brown to yellow, white, red and green. Mottled red/green clay dominates the lower half of the section. In the uppermost part, the beds grade laterally from massive to laminated facies. Mottling of beds and lateral

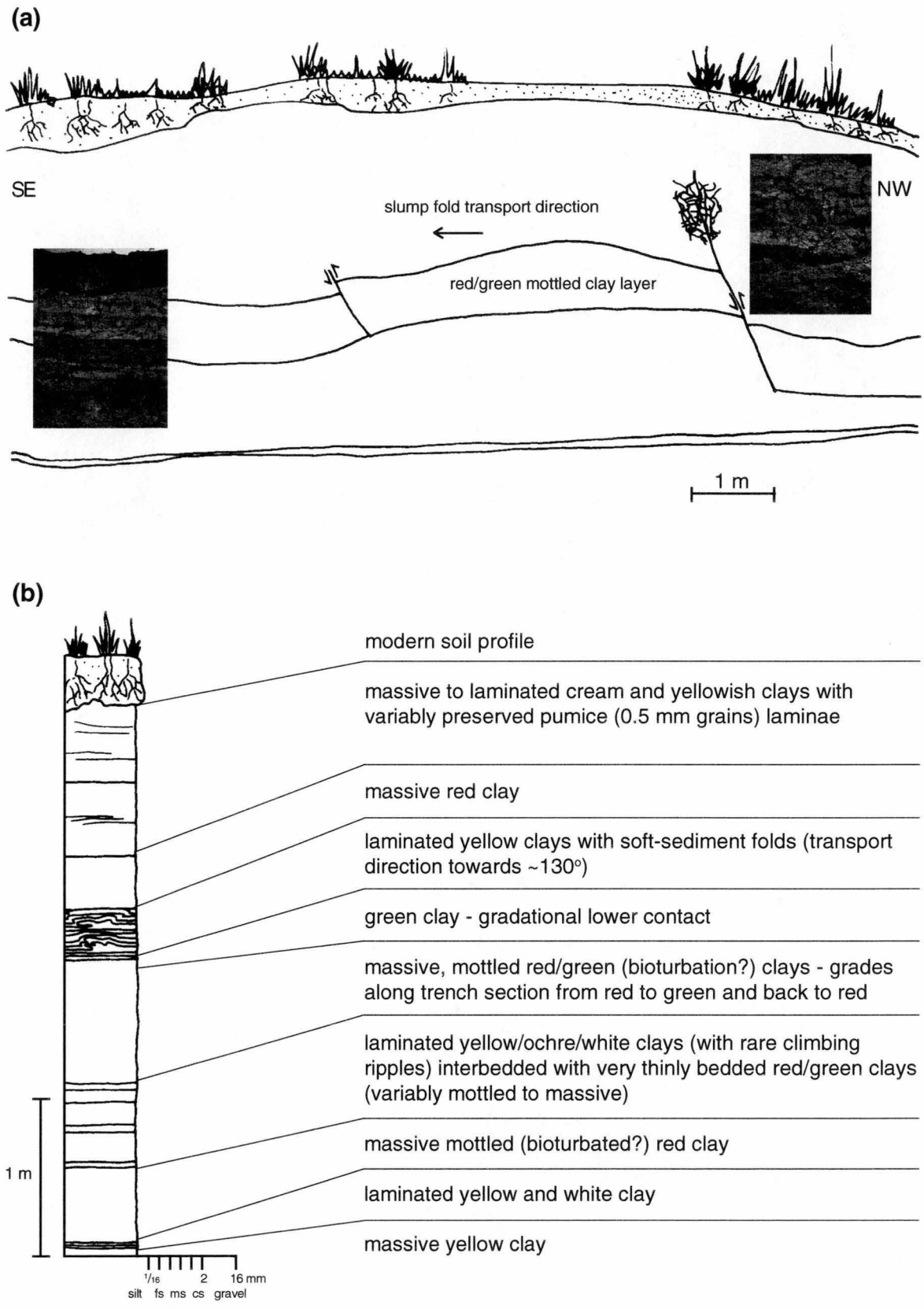

Figure 4.6. Section 4. Bofua Municipal Tip (grid reference: KA225372). (a) Long section through trench showing bedding (photo), small offsets by thrust faults and veinlet network at fault termination (photo). Hammer is 33 cm long. (b) Graphic log of clay-altered facies in the trench wall. Legend as per Fig. 4.3.

gradation of facies may be due in part to modern bioturbation associated with soil development. Pumice sand and granule layers one-to-several-grains-thick occur within these beds. All layers have manganese oxide in veins and along bedding planes. Plant rootlet casts and degraded wood fragments are common in the uppermost layers, approaching the modern soil profile.

Section 5.

A fault scarp cliff on the main wharf road at Vila Harbour [KA153357] exposes a 10 x 20 m section though laminated, ripple-bedded and massive shard-rich semi-consolidated very fine sand (Section 5, Fig. 4.7). Grain sizes in all beds rarely exceed very fine sand, however, rare, outsize (≤ 3 cm), subangular to subrounded pumice clasts are randomly present throughout the section.

The lowermost parts of the section principally consist of very thick and medium beds of the laminated shard-rich sand facies containing rare, internal low-angle truncations over several tens of centimetres. Medium beds of the massive shard-rich sand facies are also important. In the middle and the upper half of the section the rippled-laminated shard-rich facies is more common. Wavy and undulose ripples are abundant, as are isolated sets of climbing ripples. Ripple foresets indicate sediment transport towards the south (~185). The convolute-bedded facies is represented by weakly developed soft-sediment deformation structures such as contorted ripples, folds, load casts and flame structures. In Section 5 the convolute-bedded facies is typically gradational from laminated and ripple-laminated facies both laterally and vertically, and sharp discordant shear surfaces are absent. Interbeds of the massive shard-rich sand facies within the section are generally more indurated than other facies, and contain rare fossil foraminfera. The massive beds may have irregular, but conformable lower contacts, in contrast to the sharp, flat to undulose bases of the laminated or ripple-laminated facies.

Section 6.

Section 6 includes two nearby occurrences of Rentabau Tuffs, one towards the top of the fault scarp on the southwestern coast of Efaté [KA023455] (Fig. 4.8, Section 6 a), and the other section offshore on Hat Island [JA981475] (Fig. 4.8, Section 6 b). Sections were partly reconstructed from photographs due to difficulties accessing these outcrops. In this western area, the contact with the underlying pumice breccias is knife-sharp and non-erosional. Intervals of convolute laminae occur in Section 6 a. Overall the sections are monotonously well bedded, with 10-30 cm beds dominating.

In Section 6 a (Efaté), beds up to 60 cm-thick of the massive shard-rich silt/clay facies dominate and may contain fossil foraminifera (trace amounts). These are interbedded with ledge-forming, indurated thinner (≤ 10 cm) beds of the laminated shard-rich sand facies, or rarely thin massive beds. The indurated beds are not obviously different in grain size from the thick massive beds. Ripple-laminated shard-rich sand beds are also

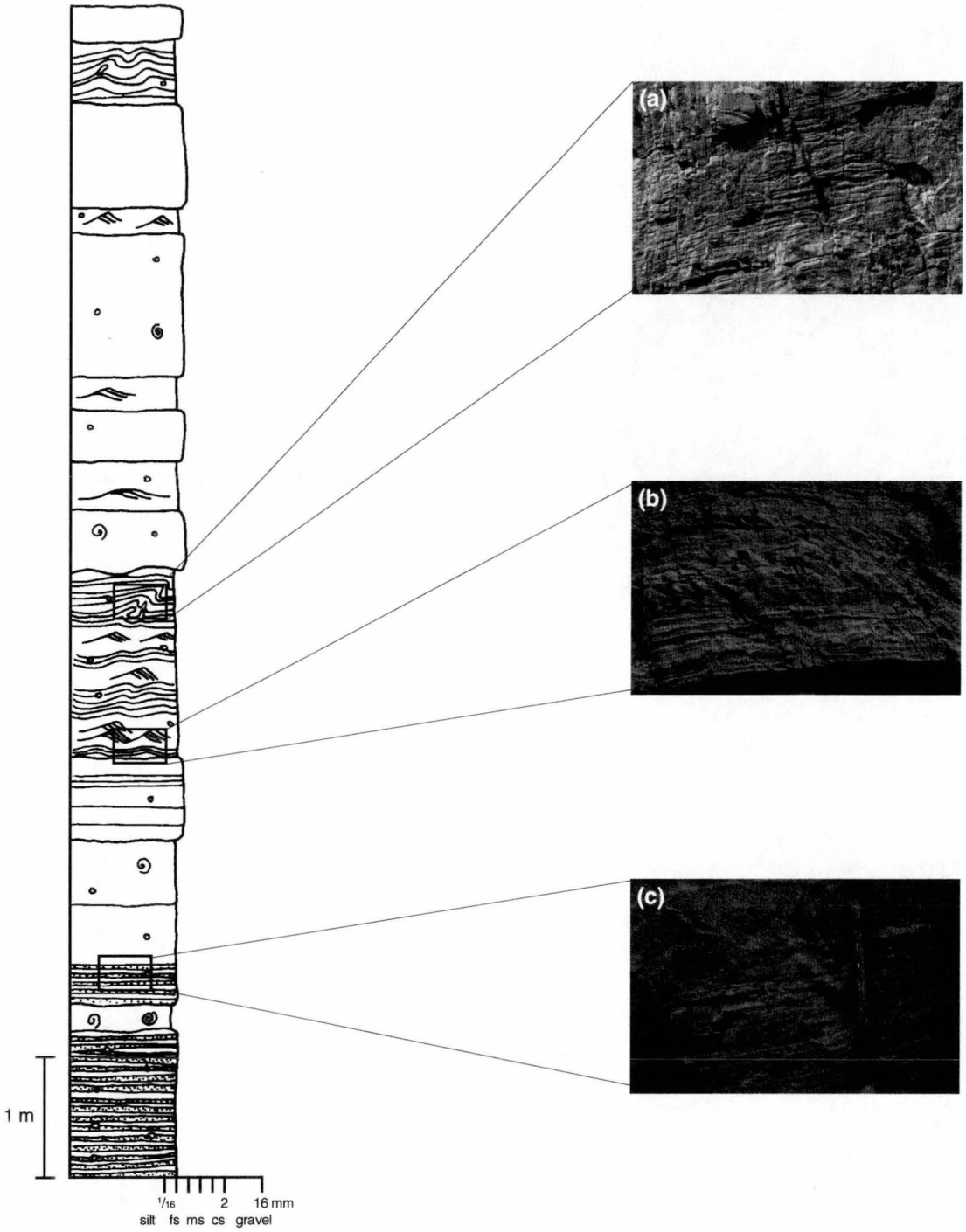

Figure 4.7. Graphic log of Section 5. Vila wharf, (grid reference: KA153357). (a) Detail of soft-sediment deformation features of the convoluted-bedded shard-rich and silt facies. Note contorted ripple bedforms with uneven lamina thicknesses. Field of view ~3 m-wide. (b) Detail of climbing ripple lamination at base of bed, transport direction from left to right (towards 185°). Ripple amplitude approximately 8-10 cm. (c) Detail of laminated facies containing thin lenses of outsize pumice clasts, pencil is 14.5 cm long. Legend as per Fig. 4.3.

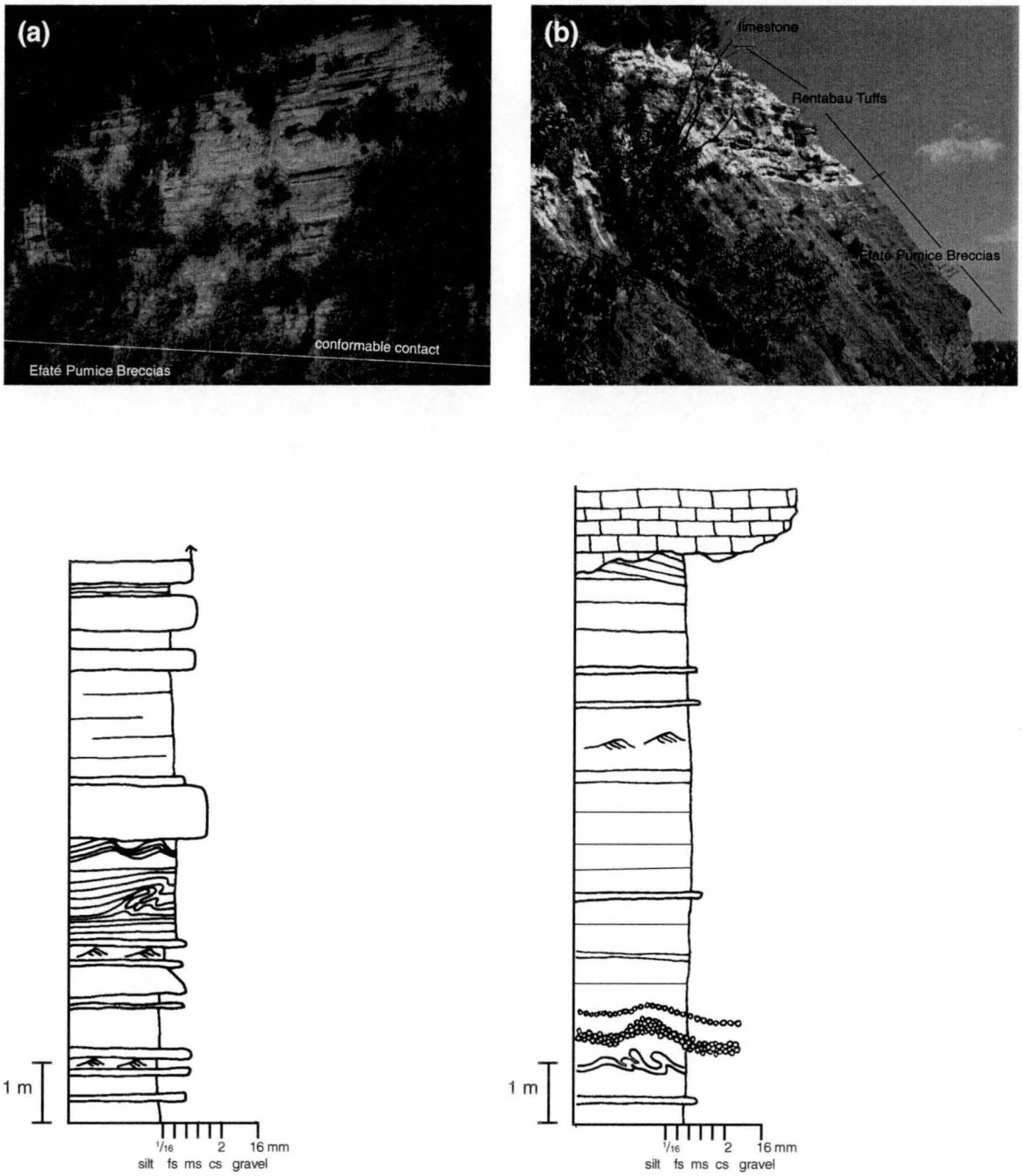

Figure 4.8. Graphic logs of Section 6. (a) View and graphic log of Section 6 a. Southwestern Efaté, (grid reference: KA023455). This section is dominated by massive shard-rich sand and silt with rare ripple-laminated and convolute-bedded shard-rich sand and silt. Note sharp, regular contact with underlying Efaté Pumice Breccias. (b) View and graphic log of Section 6 b. Hat Island, (grid reference: JA981475). This section comprises almost exclusively medium and thin beds of massive shard-rich very fine sand. Rare pumice-rich gravel lenses and ripple-laminated shard-rich sand are also present. Note knife-sharp, regular contact with underlying Efaté Pumice Breccias (grey), and unconformable contact with onlapping limestone. Legend as per Fig. 4.3.

scattered throughout the section, and foresets indicate south-southwest current transport directions (towards 212). At least one interval of the convolute-bedded shard-rich facies occurs in the middle of the section.

Section 6 b (Hat Island) is composed of similarly fine-grained beds but also includes rare lenses or 3-5 cm-thick, wavy beds of fine pumice breccia. A thin (<20 cm) interval of convoluted-bedded shard-rich sand occurs immediately below the pumice beds. Medium beds of massive shard-rich very fine sand make up to ~90 % of the section. Ripple-laminated shard-rich sands are also rare but indurated ledges are common. Bedding dips shallowly to the southwest (estimated at 123/2/SW), except towards the top of the section where bed orientations above a low-angle truncation surface are horizontal. Encrusting Reef Limestone Formation unconformably overlies the Rentabau Tuffs in Section 6 b.

Regional variation of the Rentabau Tuffs

Figure 4.9 shows the variation in facies, grain size and components of the Rentabau Tuffs. Massive facies are dominant in all sections except Section 3, indicating that mass-flow processes are the most important mechanisms for sediment dispersal for this unit (*e.g.* turbidity currents, debris flows, see below). Generally finer grain size in the Rentabau Tuffs in southern areas indicate more distal depositional environments, also shown by the decreasing crystal abundances in these areas. Fine grain sizes in Section 2 may be an artefact of alteration of glassy particles to clays. The Rentabau Tuffs are compositionally uniform with glassy clasts dominating in all sections with fossil foraminifera a minor but generally ubiquitous component. Lithic clasts are notably lacking in Sections 5 and 6 and are rare elsewhere. Current directions indicated by ripple foresets, and rarely by folded slumped sediment are consistently towards the south. In summary, a general picture of sediment dispersal from a source to the north of Efaté is indicated for the Rentabau Tuffs by decreasing grain sizes, decreasing crystal and lithic abundances towards the south/southwest, and paleocurrent data.

ORIGIN OF THE RENTABAU TUFFS

Fragmentation processes and source of pyroclasts

Explosive fragmentation of vesiculating magma can generate large volumes (1000s km^3) of pumice, cuspate, blocky and bubble-wall glass shards and crystals (Heiken & Wohletz, 1991; Klug & Cashman, 1996). The Rentabau Tuffs consist almost exclusively of such clasts and are related to a major explosive volcanic eruption. The dominance of

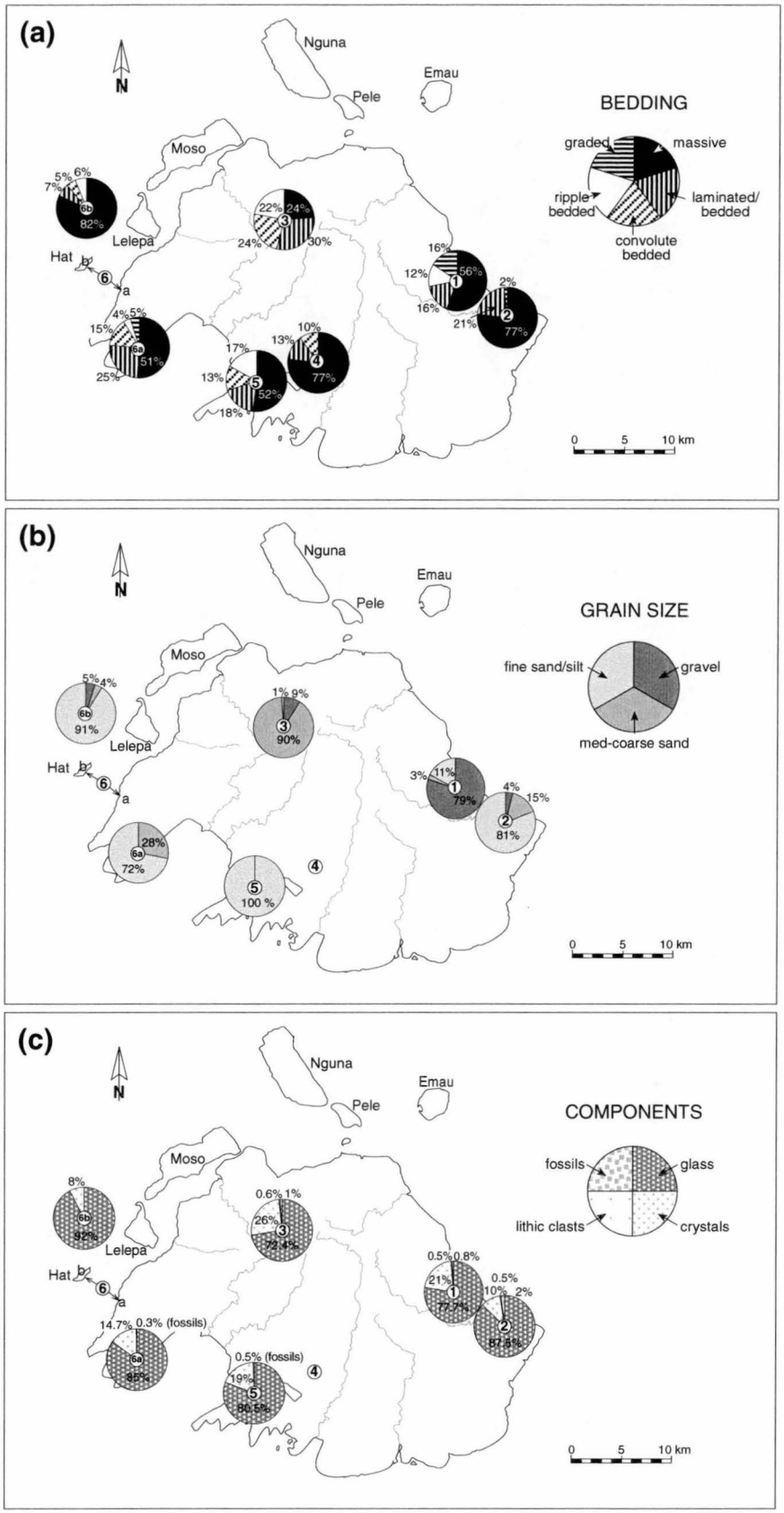

Figure 4.9. (a) Dominant bedding styles, (b) grain size and (c) component variations expressed as percentage abundances, based on measured sections. Section 1, 9.6 m; Section 2, 4.2 m; Section 3, 16 m; Section 4, 3.5 m; Section 5, 10 m; Section 6a, 9.5 m; Section 6b, 9 m. Grain size estimates for Section 2 are based principally on crystal content as the degree of secondary clays variably masks the original glassy particle grain sizes characteristics. Glass content for Section 2 estimated from average abundances in unaltered beds. Extensive secondary clay alteration in Section 4 has completely destroyed fine glass shard textures and no grain size or component data are given for this section.

mechanically unmodified pyroclasts in the Rentabau Tuffs indicates that reworking following fragmentation was minimal.

The Rentabau Tuffs are compositionally identical to the Efaté Pumice Breccias and likely to have been erupted from the same magma batch (Chapter Six). The Rentabau Tuffs therefore represent the final stages of deposition from the eruption that generated the Efaté Pumice Breccias. The transition between the two units is marked by a knife-sharp, non-erosive, conformable contact, and an abrupt change in particle size from very coarse to very fine. At least three processes can account for the abrupt change in grain size between these units and the dominance of pyroclastic sand and silt in the Rentabau Tuffs: (1) the elutriation of fine glassy particles from the very coarse pumiceous mass flows that produced the Efaté Pumice Breccias; (2) eventual fallout of the finest pyroclasts entrained in the gas thrust or umbrella region of an eruption column; or perhaps (3) external water gained access to the vent causing hydromagmatic fragmentation of the vesiculating magma and thus a dramatic reduction in pyroclast size (*e.g.* Sheridan & Wohletz, 1981; Wohletz, 1983; Kaminski & Jaupart, 1998).

Sigurdsson and Carey (1989) demonstrated that up to 40 % of the finest grain size fractions may have been lost by elutriation from subaerial pyroclastic flows that entered the sea. This fine fraction was then deposited as thin (generally <20 cm) fallout beds. Busby-Spera (1986) suggested that fines winnowed from coarse-grained, submarine erupted, volcaniclastic mass flows were deposited in thin beds between coarser facies in distal environments. Medium to thin interbeds of glass-shard rich sand within the Efaté Pumice Breccias may have been generated in this way (Chapter Three). However, the Rentabau Tuffs are generally too thick (~20 m average unit thickness) to support a similar interpretation, and if the Rentabau Tuffs did result from fallout of the finest entrained material, a gradational contact with the Efaté Pumice Breccias might be expected (Fiske & Matsuda, 1964). Furthermore, the presence of multiple beds and a variety of facies provide evidence for multiple successive depositional events for this unit.

Similarly, fine fallout ash from subaerial explosive eruption columns commonly produces only thin ash layers (generally <10 cm and >0.5 m) except in the most proximal regions (Schmincke & van den Bogaard, 1991). Distal fine fallout-plus-mass-flow-deposited ash beds from the Tokiwa Formation, believed to have been produced by eruptions that were entirely submarine, are up to 15 m thick (Fiske & Matsuda, 1964). Except for a lithic breccia bed in Section 3, there is little evidence to support a proximal environment for the bulk of the Rentabau Tuffs.

A final consideration for generation of the Rentabau Tuffs involves a change in eruption style from "dry" explosive, magmatic fragmentation, which dominated during eruption of the underlying Efaté Pumice Breccias (Chapter Three), to hydromagmatic fragmentation. Hydromagmatic fragmentation is an effective mechanism for generating and depositing

large volumes of fine pyroclasts and is interpreted to have played a role in all other Vanuatu arc caldera eruptions (Self & Sparks, 1978; Wohletz *et al.*, 1989; Robin *et al.*, 1994a; Robin *et al.*, 1994b; Robin *et al.*, 1995). Pyroclasts generated by hydromagmatic fragmentation vary widely in vesicularity (Wohletz, 1983; Wohletz, 1987), and can be highly vesicular if interaction with external water occurred near peak vesiculation (Houghton & Wilson, 1989). The island arc setting of the Efaté Island Group provides ample opportunity for external water to access vents and interact with magmas; sea-water can also readily access submerged vents.

The principal evidence for hydromagmatic fragmentation of the Rentabau Tuffs is the overwhelming dominance of fine particles (<2 mm). Clast morphologies of the Rentabau Tuffs vary, and although pumice dominates over blocky and platy glass shards, particles commonly have fracture-bounded surfaces (Fig. 4.2). Such surfaces are generated by rapid quenching due to contact with external water, rather than bubble-wall rupture by magmatic fragmentation processes (Sheridan & Wohletz, 1981; Wohletz, 1983; Fisher & Schmincke, 1984a).

In summary, a change from magmatic to hydromagmatic fragmentation of trachydacite magmas in the Efaté region can best explain the abrupt change in grain size between the Efaté Pumice Breccias and the Rentabau Tuffs. However, deposition of the finest pyroclasts from fallout cannot be ruled out and it is likely that both processes were involved.

Vent setting – submarine vs. subaerial eruption?

One important consideration for the eruption of the Rentabau Tuffs (and the Efaté Pumice Breccias) is whether the vent was subaerial or submarine, since this will affect both the style and regional impact of the eruption (Sigurdsson *et al.*, 1980; Whitham, 1989; Cas, 1992). Bathymetric investigations in the Efaté region have not identified an obvious caldera structure that relates to emplacement of the EPF, although an overall concentric fault pattern is evident in the Efaté Island Group and immediately offshore (Ash *et al.*, 1978; Chase & Seekins, 1988; Crawford *et al.*, 1988; Greene *et al.*, 1988). The source vent (or vents) for the Rentabau Tuffs, and the Efaté Pumice Breccias, probably lay to the north of Efaté.

Although it is known that vesiculation of silicic magmas can occur in water depths up to at least 3000 m (Waters *et al.*, 1996; Waters & Binns, 1998), explosive expansion and fragmentation of such magma is generally believed to be hindered by hydrostatic pressure in depths greater than about 500-1000 m (McBirney, 1963; Burnham, 1983; Fisher, 1984).

The facies of the Rentabau Tuffs provide good evidence of a submarine *depositional* environment but they provide no evidence of the vent setting. Fiske and Matsuda (1964)

proposed that double grading, whereby beds are internally density graded and fine upwards overall, may indicate deposition from contemporaneous submarine explosive eruptions, but this style of sedimentation is lacking in the Rentabau Tuffs. Fiske (1963) suggested that beds dominated by hydromagmatically fractured pyroclasts in the Ohanapecosh Formation resulted from eruptions occurring at submarine vents. In this case, a submarine eruption interpretation is favoured due to the large volume (>12 km^3) of hydromagmatic pyroclast-rich beds, indicating that extensive hydromagmatic activity occurred, probably in response to continual flooding of vents by seawater. However, water can also gain access to subaerial vents via aquifers or in littoral areas, so the presence of hydromagmatic pyroclasts alone does not constrain the vent environment, particularly for smaller volume deposits like the Rentabau Tuffs (Wohletz, 1983; Wohletz & Sheridan, 1983; Kokelaar, 1986; Ayres *et al.*, 1991).

The vent setting for the Rentabau Tuffs is unresolved. Hydromagmatic fragmentation reflecting the flooding of vents by external water could have occurred in either submarine or subaerial environments. However, several factors may favour a submarine eruption interpretation for the Rentabau Tuffs. Deposition of the Rentabau Tuffs (and the Efaté Pumice Breccias) is restricted to the Efaté Island Group. Explosive subaerial eruptions commonly produce plumes which can disperse fine ash over extensive areas (Schmincke & van den Bogaard, 1991), but ash layers from this eruption have not been identified in sediment cores from the Vanuatu arc (Chapter Three, Baker *et al.*, 1994; Goud Collins, 1994; Baker & Condliffe, 1996). A single, centimetre-thick dacite ash bed identified in ODP hole 380A has chemistry that indicates derivation from eruptions at the Kuwae caldera, rather than Efaté (Baker *et al.*, 1994). The Rentabau Tuffs also lack any charred organic remains, which would definitively indicate that eruptions occurred on land. Charred wood fragments (2 cm) were found in submarine debris flows of the Roseau Ash more than 250 km from source (Carey & Sigurdsson, 1980; Whitham, 1989). The Rentabau Tuffs do not contain any accretionary lapilli which are a common product of subaerial fallout, and particularly so in hydromagmatic eruptions (Reimer, 1983; Fisher & Schmincke, 1984a; McPhie *et al.*, 1993). Accretionary lapilli generated in subaerial eruptions are commonly preserved in submarine volcaniclastic sediments (Soh *et al.*, 1989; Stow *et al.*, 1998), but strong current action in the water column may disaggregate delicate accretionary lapilli (Fisher & Schmincke, 1984a). Although some factors indicate that submarine eruption of the Rentabau Tuffs was likely, the vent setting remains equivocal.

TRANSPORT AND DEPOSITION PROCESSES

A submarine depositional environment for the Rentabau Tuffs is constrained by the presence of fossil foraminifera in most beds. The presence of massive and laminated

beds, and generally southerly current indicators in ripple laminated intervals imply that deposition, dominated by mass-flow and suspension fallout processes, occurred in low energy environments below storm-wave-base (Lowe, 1982). The monotonous and extremely regular bedding of the Rentabau Tuffs, especially in the southwest, and the dominance of fine grain sizes, is reminiscent of deep marine, non-channelised, turbidite successions (*e.g.* Bouma, 1962; Walker, 1984b). Bedforms and facies associations in the Rentabau Tuffs have none of the hallmarks of deposition in tidal or storm wave-dominated environments, such as bi-directional cross-bedding, hummocky cross-stratification, abundant erosional bed bases, wedge-shaped bed geometries, shallow-water fossils, or coarsening upwards cycles (Walker, 1984a; Elliot, 1986; Johnson & Baldwin, 1986).

Turbidity currents and debris flows

Turbidity currents have long been recognised as an important mechanism of delivering sand and mud to deep-water environments (Bouma, 1962; Lowe, 1982; Walker, 1984b; Stow, 1994; Einsele *et al.*, 1996), and were the major transport and depositional mechanisms involved in sedimentation of the Rentabau Tuffs. Kneller (1995) suggested that the variety of deposits interpreted to result from turbidity current deposition could be explained in terms of current acceleration, current steadiness, and progressive aggradation under the passing turbulent current. This model is particularly useful for interpreting the deposition of thick massive sand beds not easily explained by classical turbidite models (Bouma, 1962; Lowe, 1982; Kneller & Branney, 1995).

Concurrent hydromagmatic eruptions could continuously supply volcaniclastic sediment without significant breaks. This process should produce quasi-steady depletive currents, depositing massive beds, that fine down-current, and/or thick intervals of climbing-rippled sand (Kneller, 1995). Changes in rate of supply due to non-uniform eruption character or waning eruption intensity, and resultant surging currents are likely to produce intervals containing tractional bedforms, such as the laminated and rippled sand facies. Traction may also develop from flow transformation and flow expansion (Fisher, 1983).

The turbidity currents may have been directly generated from mixing of pyroclast/gas dispersions with seawater, either in submarine environments or at the air/water interface if the eruption was subaerial, by remobilisation of pyroclasts temporarily stored in a volcaniclastic apron around the eruptive centre, or by transformation of vertical sediment plumes (see below). The uniform composition and the lack of admixing of pyroclasts with abundant hemipelagic components require that the Rentabau Tuffs were rapidly emplaced after eruption.

Debris flows, however, are also known to produce massive beds in deep-sea sediments (Shanmugam & Moiola, 1995; Shanmugam, 1997). Debris flows are characterised by high

sediment concentration, and particle support and transport mechanisms include matrix pore pressure, dispersive pressure, frictional strength, and matrix-fluid cohesion (Lowe, 1982; Postma, 1986; Stow, 1994). In practice, features of deep-marine massive sand beds such as floating or rafted outsize clasts can be equally well explained by progressive aggradation in turbidity currents (Kneller & Branney, 1995), or matrix strength and laminar flow in debris flows (Shanmugam, 1997). Deposition of the Rentabau Tuffs by turbidity currents is favoured due to the association of the massive beds with laminated and ripple-bedded sand and silt. In addition, debris flows may ingest water during transport and transform into turbidity currents down-current (Stow, 1994).

General differences in the facies associations of Rentabau Tuffs occur in Sections 1 and 3. The presence of coarser-grained sediments, lenticular beds, internal scouring and moderately well developed trough cross-laminated beds in these sections implies higher-energy transport and deposition, and rapidly changing flow regime conditions within depositing currents (Fisher, 1983). Such processes commonly occur in high-density turbidity currents confined within submarine channels (Einsele, 1991). The presence of a lithic-dominated breccia bed in Section 1 also indicates that strong, competent currents operated here, at least temporarily. This breccia bed may have been derived from a vent-clearing episode during eruption of the Rentabau Tuffs, or may be remobilised material from the brecciated margin of a proximal lava dome.

Fallout

Fine ash produced by volcanic eruptions is commonly entrained in eruption columns/clouds and eventually deposited by suspension settling of particles governed by Stokes's Law and resulting in normally (plus density) graded deposits (Fisher & Schmincke, 1994). This can occur in both subaerial and submarine environments. Vertical grading of any kind is largely absent in the Rentabau Tuffs except within single laminae in the laminated shard-rich sand facies. In particular, marked vertical density grading of dense lithic and pumice clasts, interpreted to be diagnostic of fallout from submarine eruption columns, is not present (Cashman & Fiske, 1990; Cashman & Fiske, 1991). Traction plus fallout from turbidity currents or bottom currents can explain these features.

Sediment traps recorded fallout rates of tephra in the South China Sea from the 1991 Pinatubo eruption at two to three orders of magnitude greater than predicted by Stokes's Law settling (Wiesner *et al.*, 1995). Although Weisner *et al.* (1995) explained this phenomenon by particle aggregation leading to increased fallout rates, Carey (1997) suggested that vertical, gravity-driven, particle-laden plumes can accelerate the settling of volcanic ash to the seabed. The plumes develop from the destabilisation of a rapidly accumulating ash layer at the air/seawater interface, due to the differential settling rates of particles in the two media.

Dispersal of pyroclasts from a submarine eruption column may also lead to the concentration of particles in the upper parts of the water column, and such layers may become unstable and generate similar vertical sediment plumes (*e.g.* Fiske *et al.*, 1998). Particle-laden gravity plumes probably transform down-slope into turbidity currents by turbulent mixing and reflection on reaching the seafloor (Carey, 1997; Stow *et al.*, 1998).

Bottom currents and soft-sediment deformation

Tractional bedforms, particularly isolated or swaley ripples (Fig. 4.7 b) and low-angle truncation surfaces within laminated intervals, may result from localised bottom current reworking of the sediment rather than turbidity current deposition (Flood & Shor, 1988; Shanmugam *et al.*, 1995).

The convolute bedded shard-rich sand and silt facies resulted from slumping of semi-consolidated sediment on the submarine slope. Earthquakes accompanying active volcanism, and high sedimentation rates during deposition are probably important mechanisms for triggering sediment slumping in the Rentabau Tuffs (*e.g.* Niem, 1977; Stow, 1994).

The Rentabau Tuffs probably represent deposition in medial to distal environments. Although grain size characteristics largely reflect fragmentation mechanisms (Self & Sparks, 1978; Houghton & Wilson, 1989), coarser facies are confined to Section 1 and a lithic breccia bed in Section 2. In proximal areas, facies might be expected to include large, ballistically ejected, country rock fragments and such clasts are notably absent in the Rentabau Tuffs (Cas *et al.*, 1990). In addition, the lithic breccia bed in Section 2 is very thin (8 cm), indicating distal deposition (Pickering *et al.*, 1986).

Duration of deposition

The Rentabau Tuffs are composed principally of texturally unmodified pyroclasts, and bedding is not punctuated by intervals of hemipelagic sediment, indicating that these sediments were rapidly emplaced following eruption and that reworking was minimal.

The biggest compositional variation between the Efaté Pumice Breccias and the Rentabau Tuffs is the minor presence of fossil foraminifera in the latter. These fossils provide evidence of the subaqueous setting of the Rentabau Tuffs, and therefore also for the Efaté Pumice Breccias, but they may provide a further constraint on duration of sedimentation events between the two stratigraphic units. Deposition of the Efaté Pumice Breccias occurred contemporaneously with, and shortly after, a major explosive eruption that may have lasted hours to days (Chapter Three). This rapid accumulation of volcaniclastic sediment probably displaced local faunas. Foraminiferal communities will re-establish within a few days to a week (P. Quilty, pers. comm., Akimoto, 1994), and thus deposition of the Rentabau Tuffs probably occurred over some weeks to months following the eruption.

Bioturbation only occurs in strongly altered beds in Section 4 where it is probably related to modern subaerial faunas. All other beds lack any evidence of bioturbation indicating that (1) sediments accumulated too rapidly for burrowing organisms to have an impact, (2) bioturbated horizons did exist but have since been stripped away by erosion and later deposition of the RLF, or (3) that the sediments were emplaced above the carbonate compensation depth (indicated by preservation of foraminifera), but below water depths at which burrowing organisms are intensely active. The unconformable contact with the overlying RLF and the variability of thicknesses of the Rentabau Tuffs indicates that significant erosion may have occurred during uplift.

Summary

The facies and facies relationships in the Rentabau Tuffs indicate that shard-rich sand and silt was deposited in deep marine environments by turbidity currents consisting of pyroclasts generated by hydromagmatic fragmentation during the final stages of a lare explosive eruption in the Efaté region. A model of the eruption, transport and deposition processes interpreted to have generated the Rentabau Tuffs is given in Figure 4.10.

COMPARISON WITH SUBAQUEOUS, SHARD-RICH DEPOSITS

Thick successions of ash-dominated submarine volcaniclastic sediments are rarely reported (Ninkovich *et al.*, 1978; Fisher, 1984; Schmincke & van den Bogaard, 1991; Baker *et al.*, 1994). Thick subaqueous ash beds commonly overlie deposits of coarser-grained pumiceous mass flows but such ash-dominated intervals are generally thinner than the Rentabau Tuffs (*e.g.* Niem, 1977; Wright & Mutti, 1981; Cousineau, 1994). However, much thicker sequences (>1 km) of subaqueous pyroclast-rich deposits related to explosive silicic volcanism are known from some ancient successions (*e.g.* Ohanapecosh Formation, Fiske, 1963; Snowy River Volcanics, Bull & Cas, 1991; Mount Read Volcanics, Allen & Cas, 1990; McPhie *et al.*, 1993; White & McPhie, 1997).

Table 4.2 summarises the characteristics and preferred interpretations of subaqueous pyroclast-rich successions that are most similar to the Rentabau Tuffs. These deposits include the Wadaira Tuff Bed D, Japan, (Fiske & Matsuda, 1964), volcaniclastic sediments in the Miyazawa Formation, Japan, (Yamada, 1973), the Stanley Group, southern USA, (Niem, 1977), and the Saint-Victor Formation, Quebec, (Cousineau, 1994), the Dali Ash, Greece, (Wright & Mutti, 1981), and the Monarch rhyolite ash-flow tuff, California, (Busby-Spera, 1986).

Sedimentation of the entire volcaniclastic facies association in each case is ascribed to rapid emplacement following a single eruptive episode (or sedimentation event, Dali

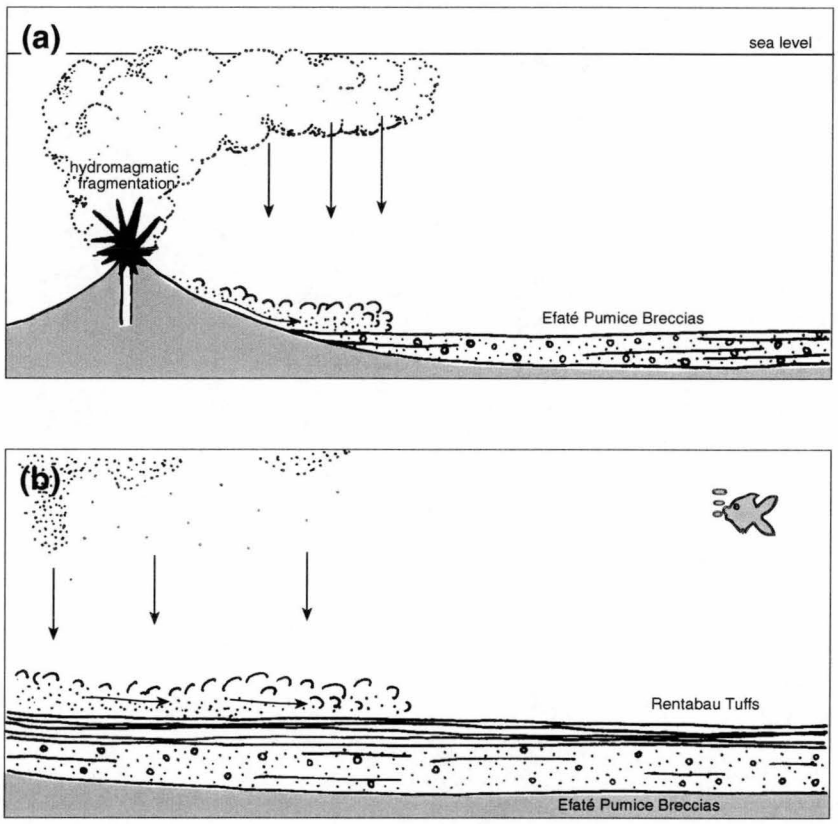

Figure 4.10. Model for eruption and deposition of the Rentabau Tuffs. (a) Hydromagmatic explosion and eruption of trachydacite magma occurs at submarine vents. (b) Deposition of fine-grained, shard-rich sediments by turbidity currents consisting of cold pyroclastic debris, principally generated by mixing of seawater and the collapsing eruption column. Vertical plumes of pyroclastic debris periodically detach from the spreading eruption column in the upper parts of the water column and transform into turbidity currents on reflection at the seafloor. Slumping of this uncosolidated pyroclastic sediment generates the convolute-bedded intervals, and probably initiates further turbidity currents.

Table 4.2. Characteristics of some subaqueous pyroclast-rich successions.

DEPOSIT	AGE	THICKNESS	FACIES CHARACTERISTICS AND COMPONENTS	INTERPRETATION AND REFERENCES
Wadaira Tuff Bed D	Miocene	8-15 m – ash-dominated	*ash-dominated*	*deposition contemporaneous with eruption*
		≤45 m – pumiceous bed	massive to internally density graded, upward thinning and fining cycle (**double grading**)	massive pumiceous bed deposited from a cold, subaqueous pyroclastic (debris?) flow, doubly graded ash beds deposited by turbidity currents
			pumice shards, crystal fragments, dense glassy dacite clasts	deposit formed by collapse of an entirely subaqueous eruption column
Japan			*pumiceous bed*	
			massive, dense lithic components concentrated at base	Fiske and Matsuda (1964)
			dacitic pumice, crystals, glassy lithics in ash matrix	
Miyazawa Formation	Miocene (?)	25-50 m – ash-dominated	*ash-dominated*	*deposition contemporaneous with eruption*
Onikobe Basin			parallel laminated coarse and fine tuff, massive very fine tuff (upper division)	deposition of entire sequence by turbidity currents
Deposits		60-100 m – pumiceous beds	pumice shards, crystals	(subaqueous equivalent of a subaerial pyroclastic flow)
			pumiceous beds	eruption probably subaerial or shallow subaqueous
			massive lower division, some density grading apparent	
			parallel bedded division, strong density grading	
Japan			pumice, crystals, andesite and scoria lithics in ash matrix	
			entire sequence	
			upward thinning and fining cycle (**double grading**)	Yamada (1973)
Stanley Group	Mississippian	1-10 m – ash-dominated	*ash-dominated*	*deposition contemporaneous with eruption*
			massive and locally laminated coarse and fine tuff,	deposition of coarse, pumiceous beds by density currents (mass-flows)
		1-25 m – pumiceous beds	bubble wall and cuspate shards, crystals, rare shale clasts and carbonised organic matter	fine ash deposited by fallout and reworked by bottom currents
				eruption probably subaerial or shallow subaqueous
Oklahoma /			*pumiceous beds*	
Arkansas			massive lower division, some density grading apparent	
			parallel bedded division, strong density grading	
			pumice, crystals, shale rip-up clasts in ash matrix	
			entire sequence	Niem (1977)
			upward thinning and fining cycle (**double grading**)	
Dali Ash	Tertiary	2 5 m – ash-dominated	*ash-dominated*	*syn- or post-eruptive deposition - unknown*
		5 m – pumiceous bed	normally graded, laminated, cross-laminated and minor massive beds	deposition of massive division by high-concentration turbidity currents
			bubble wall and cuspate shards, crystals	fine ash deposited by dilute turbidity currents
			pumiceous bed	eruption character unknown
Island of Rhodes,			generally massive, laminated crystal-rich basal layer, normally graded at upper	
Greece			contact,	Wright and Mutti (1981)
			bubble wall and sickle-shaped shards, crystals, rare marine fossils	
Monarch rhyolite	Triassic	27 m – ash-dominated	*ash-dominated*	*deposition contemporaneous with eruption*
ash-flow tuff		≤600 m – pumiceous beds	massive, thin-bedded or parallel laminated	deposition of pumice rich beds by non-turbulent, high-concentration mass-flows,
Mineral King			bubble wall and pumice shards, crystals	deposition of ash by suspension fallout
Caldera Complex			*pumiceous beds*	shallow marine or subaerial eruption
			generally massive, normally graded or bedded in upper parts, interbeds of fine	
California			shard-rich tuff	Busby-Spera (1986)
			pumice, crystals, rip-up clasts in ash matrix	
Saint-Victor	Ordovician	2-15 m – ash-dominated	*ash-dominated*	*deposition contemporaneous with eruption*
Formation			normal grading, parallel lamination, density grading and dish structures	deposition of massive division by debris flow
		1-20 m – pumiceous bed	upward thinning and fining cycle (**double grading**)	fine ash deposited by high-concentration and dilute turbidity currents
			pumice and cuspate shards, crystals	eruption probably mostly submarine
			pumiceous bed	
Quebec			massive to normally graded in upper parts, weakly density graded	
			pumice, felsic and intermediate volcanic clasts, mudstone rip-up clasts	Cousineau (1994)

Ash). The resulting deposits typically show fining and thinning upward sequences and well-developed density grading. These features are considered diagnostic of deposition from subaqueous eruptions (Fiske & Matsuda, 1964; Cousineau, 1994). However, Yamada (1973) argued that the same features may simply indicate deposition from pumice- and shard-rich turbidity currents. Thinning and fining upwards cycles are not apparent within the Rentabau Tuffs at outcrop scale, and neither is density grading due to the well sorted nature of facies overall. This probably reflects differences in transport and depositional styles for the Rentabau Tuffs, but may also be related to clast formation processes.

Facies models for all of the deposits outlined in Table 4.2 assume that eruptions were essentially magmatic, but pyroclasts in the Rentabau Tuffs were probably largely generated in hydromagmatic explosions. Hydromagmatic activity commonly occurs at silicic, shallow submarine (or sublacustrine) vents leading to the production of abundant ash with a narrow range of fine clast sizes (Bond & Sparks, 1976; Heiken, 1987; Houghton & Wilson, 1989; Wohletz *et al.*, 1989; Wilson & Houghton, 1990; Houghton *et al.*, 1995; Smith & Houghton, 1995; Fiske *et al.*, 1998). Despite the potential for abundant deposits of silicic hydromagmatic ash in submarine environments, there are few existing models catering for such situations (Fiske, 1963; Cas *et al.*, 1990). This may be due in part to difficulties of recognising the hydromagmatic origin of highly vesicular clasts in ancient successions (*e.g.* Hatepe ash, Houghton & Wilson, 1989). The 1952-53 eruption of Myojinsho Dome involved hundreds of separate hydromagmatic explosions, each potentially generating discrete submarine volcaniclastic mass-flows of fine pyroclast-rich debris (Fiske *et al.*, 1998). Ash-rich deposits generated in this way may not show thinning and fining upwards sequences, but instead, lateral fining, as mass flows ran out with distance from source (Kneller, 1995).

CONCLUSIONS

The Rentabau Tuffs are fine-grained pyroclast-rich sediments deposited in deep submarine environments. They are genetically related to the underlying Efaté Pumice Breccias and represent a change in eruption style from magmatic to hydromagmatic fragmentation of trachydacite magma. Quasi-steady turbidity currents deposited thin to thick beds of glass shard-rich massive, laminated and ripple-bedded sand and silt, continually supplied by contemporaneous hydromagmatic eruptions. Slumping of material on the submarine slopes, probably initiated by ground tremors, formed intervals of convolute bedded volcaniclastic sand. Eruptive vents are no longer exposed and some evidence suggests that vent environments were submarine, but this interpretation remains equivocal.

Chapter Five

BASALT VOLCANOES FORMATION, EFATE ISLAND GROUP, VANUATU

Post-caldera basaltic stratovolcanoes: Petrology and geochemistry

INTRODUCTION

Although the volcanic geology of the Efaté Island Group is dominantly dacitic (Chapters Three, Four and Six), younger basaltic volcanoes are significant in the northern part of the island group. The geochemistry of the basaltic lavas offers some insight into the petrogenetic evolution of this Vanuatu arc volcanic centre, as the complicating effects of advanced differentiation are largely absent.

The geochemistry of island arc magmas is controlled by the various processes governing melt generation and the subsequent history of the magmas on ascent and residence in crustal magma chambers. Models of melt generation beneath island arcs range from those which invoke melting of the subducted slab (*e.g.* Wyllie & Sekine, 1982; Brophy & Marsh, 1986), to those in which melting predominantly takes place in the mantle wedge (*e.g.* Tatsumi, 1989; Davies & Bickle, 1991; Arculus, 1994). Most workers currently favour models of the latter type, as the dominant trace element characteristics of arc magmas are more easily explained in these systems (Perfit *et al.*, 1980; Crawford *et al.*, 1987; Hawkesworth *et al.*, 1991; Saunders *et al.*, 1991; Hawkesworth *et al.*, 1994; Elliott *et al.*, 1997). Partial melting of the mantle wedge is facilitated by the release of H_2O from the breakdown of amphibolite in the subducted oceanic lithosphere, which in turn lowers the solidus of mantle peridotite (Tatsumi & Eggins, 1995). Large ion lithophile elements (LILE), derived from both dehydration reactions occurring in the subducting slab and variable contributions from subducted sedimentary material, are preferentially carried in the hydrous fluid and transported to the mantle wedge, and thereby enriched in the source peridotite. Retention of the high field strength elements (HFSE) in a residual refractory eclogite by the same process, may cause relative enrichments of the LILE compared to HFSE (*e.g.* high Ba/Nb) in arc magmas.

The Efaté Island Group lies at the junction between the D'Entrecasteaux collision zone (DEZ) in the central Vanuatu arc, and the 'normal' southern (SVA) part of the arc (see also Chapter Two, Fig. 2.2). Geochemical differences in the Vanuatu arc central chain magmas between the two regions are marked, and reflect the importance of local

tectonics in magma petrogenesis. Seismic studies show that Efaté area is complicated by both a tear in the subducting slab and possibly seamount subduction (Chatelain & Grasso, 1992; Chatelain *et al.*, 1992; Prévot *et al.*, 1994), and this is reflected in the high-Sr, high-P_2O_5 signature of the Efaté basalts. This chapter describes the petrography and geochemistry of the Basalt Volcanoes Formation (BVF) from northern Efaté and the offshore islands of Nguna, Pele and Emau. Essential differences between the BVF lavas and the 'normal' Vanuatu arc lavas, best represented by those in the least complex southern part of the arc, are explored here.

BASALT VOLCANOES FORMATION

Age and distribution

In northern Efaté and the offshore islands of Nguna, Pele and Emau the landscape is dominated by variably degraded volcanic cones. This style of volcano is in marked contrast to the older caldera volcanism, which produced the Efaté Pumice Formation (EPF) and may be a part of a genetically related late-stage, post-caldera event (Chapter Six). The base of the BVF is not exposed since dissection by numerous normal faults and poor exposure obscures the contact relationship between the BVF and the EPF. Previous authors however, have suggested that the BVF appears to unconformably overlie the EPF (Mawson, 1905; Obellianne, 1958; Ash *et al.*, 1978). Lavas and volcaniclastic facies of the BVF from Efaté have an estimated age of ~0.7 Ma determined from geochemical constraints on hot spring waters (Ash *et al.*, 1978). Extensive development of raised limestone terraces on Mount Fatmalapa and Quoin Hill indicate at least 600 m of uplift in northern Efaté over a period of at least 0.3 Ma, giving a minimum age for the volcanoes (Ash *et al.*, 1978; Lecolle *et al.*, 1990). Basalts on the offshore islands are younger, probably not more than a few thousand years old based on the well-preserved, primary constructional morphologies of the volcanic cones, and the general lack of raised onlapping limestone.

Volcano morphology and setting

The topography in the northern part of Efaté and on the offshore islands of Nguna, Pele and Emau is rugged and controlled by the now inactive volcanoes. On Efaté, Mount Fatmalapa and Quoin Hill are deeply dissected, faulted and eroded remnants of basaltic volcanoes. At least seven limestone terraces are cut into, and developed on the Mount Fatmalapa centre (Ash *et al.*, 1978).

Ash *et al.*, (1978) interpreted the Mount Fatmalapa centre as a remnant of a submarine basaltic volcano, citing 'pilloidal' (*sic.*) basalt occurrences and capping limestones as evidence of the submarine environment. The centre is dominated by monomictic basaltic breccia and conglomeratic lithofacies, locally interbedded with thin lavas, and intruded by numerous dykes. Weathered basaltic tuffaceous sands are locally important towards the top of the volcanic succession. In contrast, massive to vesicular, porphyritic basalt lavas, up to 10 m thick, are the principal lithology exposed at Quoin Hill. Both centres are overlapped by raised reef limestone, and this is the only evidence for at least a partially submarine environment for the Quoin Hill centre (Mawson, 1905; Obellianne, 1958; Ash *et al.*, 1978). Lavas, dykes and breccia and conglomerate clasts of these two remnant basalt volcanoes are strongly plagioclase + olivine + pyroxene-phyric basalts.

Volcanic cones on the offshore islands of Pele, Nguna, and Emau are better preserved than the Efaté centres. This characteristic, and the lack of limestone terrace development on these islands attests to their younger age. Degradation of the offshore volcanoes is most severe on Pele Island. Nguna Island is made up of several coalescing cones and the volcanic cone of Marao is easily recognisable in the central part of the island (Fig. 5.1 a). The volcanic centres on all three islands consist of lavas interbedded with subordinate volcanic breccia and conglomerate. In proximal, near-vent areas, bedded fallout ash and surge deposits are common. Bomb-rich spatter beds have also been reported (Ash *et al.*, 1978). In medial areas, thick to very thick (few metres to tens of metres) lavas are the major lithofacies. Volcano flanks are dominated by thin (<1 m) lavas interbedded with coarse, gravelly and minor granular, monomictic basaltic breccia and conglomerate facies. Offshore island lava and volcaniclastic basalt facies are plagioclase + olivine ± pyroxene-phyric and vary from vesicular to non-vesicular.

An arcuate fault scarp trending from northwest and swinging around to northeast in a semicircle, forms the northern coast lines of the three offshore islands (Fig. 1.1). This structure is consistent with a regional structural pattern in the Efaté area, which comprises a series of arcuate, mostly northwesterly-trending, normal faults, that converge to the north. The fault scarp exposes the internal constructional geometry of these small volcanic centres, and records a major collapse event affecting all three islands.

Lithologies of the Basalt Volcanoes Formation

The volcanological attributes of the BVF have not been examined in as much detail as the underlying trachydacitic pumice breccias, as the principal aims of this study are to characterise the deposits and geochemical evolution of the EPF. This chapter focuses primarily on the geochemistry of the BVF, in order to gain a more complete understanding of the volcanic and tectonic evolution of the Efaté Island Group. A summary of the main BVF facies follows. Some problems still remain as to the subaerial versus subaqueous depositional environment of the Mount Fatmalapa and Quoin Hill centres.

Lavas

Porphyritic basalt lavas vary from less than one, up to ten metres thick. Units are massive to vesicular, with well-defined tops and bases, and well-developed flow lobe structures at some localities on the offshore islands (Fig. 5.1 b). At Quoin Hill the surface of a large, locally transported, basalt boulder has polygonal cracks, probably the incipient development of columnar jointing on a flow top (Fig. 5.1 c). Lava tops exposed on the circum-island road, near Mangorango village on Emau have well-developed pahoehoe textures. Vesicle trains in many lavas delineate flow lines (Fig. 5.1 b and d), with single and coalesced vesicles showing some elongation parallel to flow direction. Figure 5.1 (e) shows the 30-40° depositional angle of lava flows along the faulted northeast coast of Nguna Island.

Intrusions

Planar-sided dykes with chilled margins occur on Mount Fatmalapa. The dykes dip steeply with a dominant east-southeast strike, and intrude interbedded basaltic breccias and lavas. They are strongly plagioclase + olivine + clinopyroxene-phyric, texturally similar to Efaté BVF lavas and breccia clasts. Dykes are 0.5 to 2 m wide and principally occur within a small area west of the summit of Mount Fatmalapa.

On the northern coast of Nguna Island, at least two large plug-like intrusions cross-cut the southeast-dipping lavas. One of these plugs juts out from the coast, being more resistant to weathering and erosion than the lavas.

Breccia and conglomeratic facies

Monomictic basaltic conglomerate is interbedded with lavas on the volcano flanks of the offshore islands (Fig. 5.1 d). These beds are up to 0.7 m thick, are commonly lenticular over less than 10 m laterally, and consist of a moderately sorted framework of rounded and subrounded basalt boulders and cobbles with a subordinate matrix of subrounded and subangular basaltic granules and sand.

These facies strongly resemble the deposits currently forming in the modern beach environments on the uneven topographic surfaces of the lavas. The only significant difference between the two is that the modern sediments also contain biogenic components, including limestone fragments and vegetation. It is likely then, that the older lithofacies are the result of normal epiclastic processes causing rapid erosion and deposition of basaltic clasts in earlier beach and/or fluvial environments, in between effusive eruptions. The lack of biogenic material indicates that the basaltic conglomerates formed rapidly, before vegetation or limestone reefs were well established on, and around the active volcanoes.

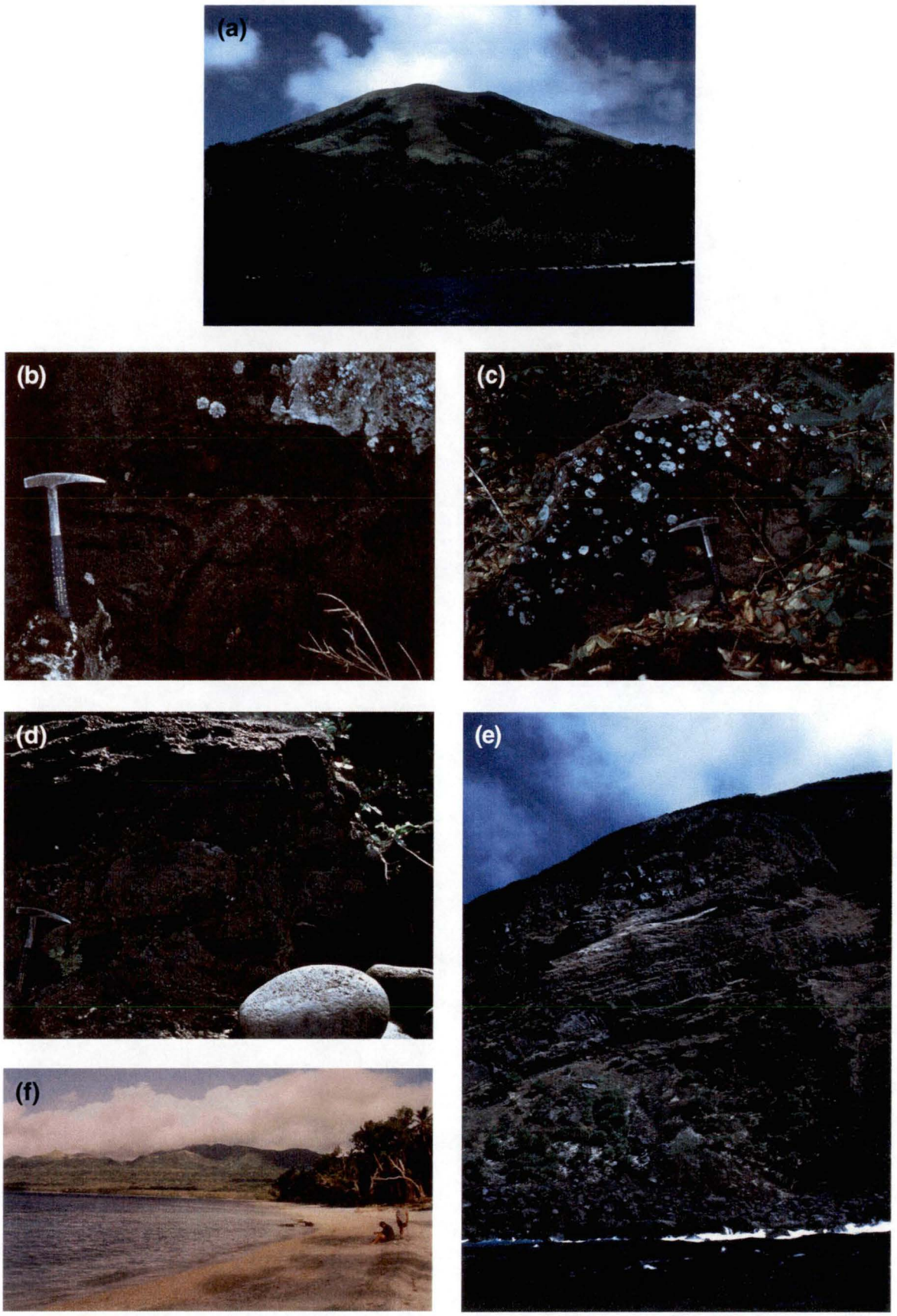

Figure 5.1. (a) Marao basaltic cone on Nguna Island (~475 m high); note well preserved shape; (b) flow lobe structures in vesicular basalt, Nguna Island; hammer is 33 cm long; (c) polygonal joints on flow top (?), basalt boulder, Quoin Hill, Efaté Island; hammer is 33 cm long; (d) basalt boulder conglomerate, overlain by a vesicular basalt lava; hammer is 33 cm long; (e) basalt lavas exposed on sector collapse escarpment, Nguna Island (~400 m high); (f) limestone terraces on Mt Fatamalapa, looking SE from Undine Bay.

Breccia and conglomeratic lithofacies on Mount Fatmalapa are somewhat different. Monomictic, tabular beds of basaltic clasts are up to ~0.5 m thick, and vary from matrix- to clast-supported. Sorting varies from moderate to good, and beds are generally massive, although inverse grading occurs locally. Clast angularity ranges from subangular to well rounded, and clasts up to 50 cm are common. In places, the coarse-grained facies are associated with thin (10 cm) intervals of laminated basalt sand and fine basalt breccia.

The tabular geometries, sorting characteristics and massive nature of the conglomeratic and breccia facies indicates deposition from subaqueous mass-flow processes operating on volcano flanks (Walker, 1993; McPhie, 1995; Stow *et al.*, 1998). Inversely graded units are probably the result of grain flow processes (McPhie *et al.*, 1993). Angular particles are abundant indicating little abrasion during transport and deposition, a feature of some subaqueous sediment gravity flow deposits attributed to particle support mechanisms where grain-grain interactions are minimal (*e.g.* Lowe, 1982; Einsele, 1991; Stow, 1994). Rounding of other particles may be imparted by abrasion of the clasts in fluvial and beach environments, and/or during submarine transport (*e.g.* Pye, 1994). Alternatively rounded particle shapes in some volcaniclastic sediments may reflect weak modification of originally round particle shapes caused by rapid quenching and fragmentation of lavas in subaqueous environments (*i.e.* hyaloclastite development, McPhie *et al.*, 1993). Particles formed by this process might be expected to have chilled margins, but Mount Fatmalapa BVF clasts do not show these features, suggesting that mechanical abrasion was the dominant rounding process.

A submarine setting for the Mount Fatmalapa centre seems very likely based on the occurrence of the 'pilloidal' basalts, overstepping limestones, and conglomeratic and breccia deposit characteristics. However, without more detailed investigation of lithofacies and lithofacies associations, and importantly, the structural constraints in the area, the depositional environment of this centre remains equivocal. The depositional environment at Quoin Hill is even more ambiguous owing to more extensive erosion, and a general lack of definitive submarine facies. Lava tops where exposed, are commonly smooth, or covered with polygonal cracks, features common to subaerially erupted lavas (Cas & Wright, 1987).

PETROLOGY

Petrography

Petrographic characteristics of 25 representative lava samples selected for chemical analysis are outlined in the following section. More complete descriptions are given in

Appendix E. The samples are divided into three groups based on both temporal and geochemical associations: (1) the Mainland Suite (MLS) comprises samples from the Mount Fatmalapa and Quoin Hill centres, the oldest basalts in the Efaté Island Group, (2) samples from Nguna, Pele and Emau islands form the younger Offshore Suite (OSS), and (3) a minor suite of lavas from Emau Island that has distinctively high K_2O and high Rb characteristics (HKRS) relative to all other BVF samples.

Mainland Efaté (MLS) - Older Sequence

These basalts are strongly porphyritic with varying sizes and abundances of plagioclase, clinopyroxene, olivine and Ti-magnetite phenocrysts (Fig. 5.2 a; Table 5.1; Appendix E). Plagioclase occurs as subhedral to euhedral grains, commonly forming polycrystalline aggregates with larger grains showing some zoning at crystal margins. Tabular, discrete phenocrysts are also abundant in some samples. Plagioclase phenocrysts range in size from 0.5-3 mm, and most grains have abundant clear and brown glassy melt inclusions. These may be randomly arranged within the crystals or, more commonly, arranged parallel to crystal rims of the larger crystals (Fig. 5.2 b). Olivine phenocrysts show a wide range of sizes (0.2-3 mm) across the sample population, vary from euhedral to round and cracked, and commonly enclose smaller Ti-magnetite microphenocrysts. The olivine phenocrysts have incipient iddingsite on rims and along fractures, except for sample AR174, which contains two varieties of olivine. In this sample, some crystals have altered rims but in others, the crystal cores are preferentially altered (Fig. 5.2 c). Smectite, chlorite and serpentine, rather than iddingsite, are the alteration products of olivine phenocrysts in most Mount Fatmalapa samples. Euhedral to subhedral clinopyroxene grains (0.2-7 mm) are unaltered and variably zoned, and may host Ti-magnetite inclusions (Fig. 5.2 d). In rare cases, clinopyroxene grains occur in aggregates, and may contain glassy melt inclusions or small olivine or plagioclase inclusions. Euhedral, subhedral and embayed Ti-magnetite phenocrysts and microphenocrysts occur as inclusions in, or in close association with, both olivine and clinopyroxene crystals (Fig. 5.2 e). Groundmasses consist of intergranular larger plagioclase laths, which generally dominate over smaller, equant clinopyroxene and opaque oxide crystals, occurring in variable proportions, with or without minor olivine, and with accessory apatite. MLS basalts also vary from moderately vesicular to non-vesicular.

Two of the analysed samples have different textures. Sample AR172 is dominantly fine-grained (20-40 μm), massive and composed of intergranular lath-shaped plagioclase, clinopyroxene and Ti-magnetite crystals with rare (<1 %), altered olivine microcrysts. Porphyritic domains account for approximately 40 % by volume and occur as irregular-shaped, elongate blebs within the main aphyric body of the rock. These domains have a phenocryst population consisting mostly of plagioclase with minor amounts of

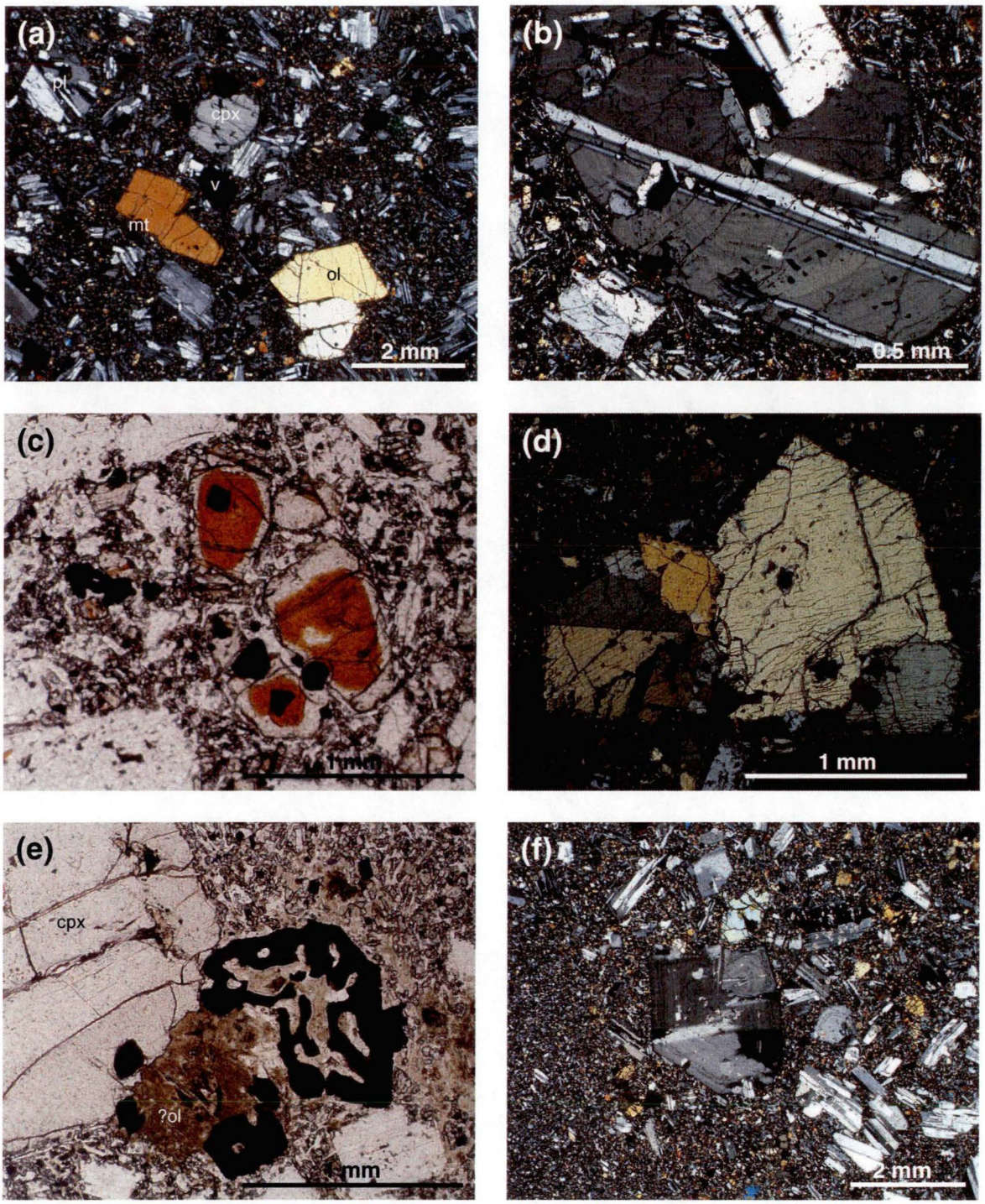

Figure 5.2. Photomicrographs of BVF basalt textures. (a) Porphyritic texture common to most MLS rocks, with plagioclase (pl) aggregates and laths, subhedral clinopyroxene (cpx), euhedral olivine (ol), and small Ti-magnetite (mt) phenocrysts, and round to irregularly shaped vesicles (v); AR158, XPL; (b) detail of zoning and glassy inclusion trails in plagioclase phenocryst; AR158, XPL; (c) olivine phenocrysts with iddingsite altered cores: AR174, PPL; (d) cluster of large, euhedral clinopyroxene phenocrysts, with Ti-magnetite inclusions and twinned crystal in left of view; AR174, XPL; (e) deeply embayed to skeletal Ti-magnetite phenocryst associated with larger clinopyroxene (cpx), and smaller serpentine (?) altered former olivine crystal (?ol); AR179, PPL; (f) boundary between massive aphyric and porhyritic domains in sample AR172, XPL. Abbreviations as follows: MLS=Mainland Suite, PPL=plane polarised light, XPL=cross-polarised light.

clinopyroxene, olivine and Ti-magnetite, in a groundmass that is similar to the intergranular domains (Fig. 5.2 f).

Clinopyroxene crystals are the dominant component of sample AR175 (Fig. 5.3 a). This is a medium- to coarse-, and even-grained rock, with large (3-7 mm) clinopyroxene crystals, commonly containing stubby plagioclase inclusions (rimmed by chlorite) in their crystal margins (Fig. 5.3 b). Plagioclase and Ti-magnetite grains are finer (0.5-1 mm) but overall the large crystals dominate. Subordinate, large (2-5 mm) olivine crystals are also present. Rare interstices between the crystals contain fine-grained (<0.2 mm) equant clinopyroxene and Ti-magnetite microcrysts.

Table 5.1. Phenocryst modal abundances of BVF lavas and intrusions (visual estimations).

SAMPLE	pl	ol	cpx	mt	VESICLES	GROUNDMASS
Mainland (MLS)						
AR172	*24 %*	*4 %*	*8 %*	*4 %*		*60 % pl=cpx=mt±ol*
AR174	15 %	7 %	5 %	3 %	10 %	60% pl>cpx>>mt
AR175	*25 %*	*10 %*	*45 %*	*10 %*	-	*none-coarse grained, massive texture*
AR179	5 %	5 %	15 %	7 %	<1 %	70 % pl=cpx=mt
AR181/AR182	16 %	<2 %	5 %	2 %	-	75 % pl>>mt>cpx>ol
AR153	18 %	5 %	2 %	1 %	-	74 % pl>>cpx>mt>ol
AR157	20 %	5 %	3 %	2 %	3 %	67 % pl>mt>cpx±ol
AR158	20 %	2 %	3 %	3 %	<2 %	70 % pl=cpx=mt
AR161	10 %	5 %	4 %	<1 %	~5 %	76 % pl>>cpx>mt
AR164	15 %	10 %	3 %	1 %	~8 %	63 % pl>cpx>mt±ol
Offshore (OSS)						
AR006	15 %	3 %	-	2 %	7 %	73 % pl>cpx=mt±ol
AR105	20 %	3 %	-	1 %	1 %	75 % pl>cpx>>ol>mt
AR106	15 %	4 %	-	3 %	3 %	75 % pl>cpx=mt>>ol
AR109	12 %	5 %	-	3 %	-	80 % pl=cpx=mt±ol
AR110	7 %	2 %	-	1 %	<1 %	90 % pl>>cpx>mt
AR003	30 %	5 %	-	-	<1 %	65 % pl=cpx=mt
AR114	25 %	5 %	5 %	-	-	65 % mt>pl=cpx
AR184	12 %	8 %	8 %		7 %	65 % pl=cpx=mt
AR185	28 %	<1 %	-	1 %	<1 %	70 % pl>cpx>mt
AR192	12 %	3 %	-	-	<1 %	85 % cpx>>mt>pl±ol
High-K/High-Rb (HKRS)						
AR188	7 %	<1 %	-	1 %	3 %	89 % pl+cpx>mt±ol
AR198	15 %	7 %	-	2 %	-	76 % cpx>>pl>mt±ol
AR199	*50 %*	*2 %*	*35 %*	*12 %*	*<1 %*	*none - dolentic texture*
AR201	10 %	15 %	15 %	-	-	60% pl>>cpx>>mt±ol

Samples in italics are not porphyritic and are described separately in the text. Abbreviations as follows: pl = plagioclase, ol = olivine, cpx = clinopyroxene, mt = Ti-magnetite.

Offshore Islands (OSS and HKRS) - Younger Sequence

Most basalt samples from the offshore islands differ from the mainland rocks in lacking clinopyroxene phenocrysts (see Table 5.1). Only three samples have clinopyroxene phenocrysts. The OSS and HKRS rocks are dominantly plagioclase + olivine ± Ti-magnetite-phyric and variably vesicular (Fig. 5.3 c). As for MLS samples, plagioclase

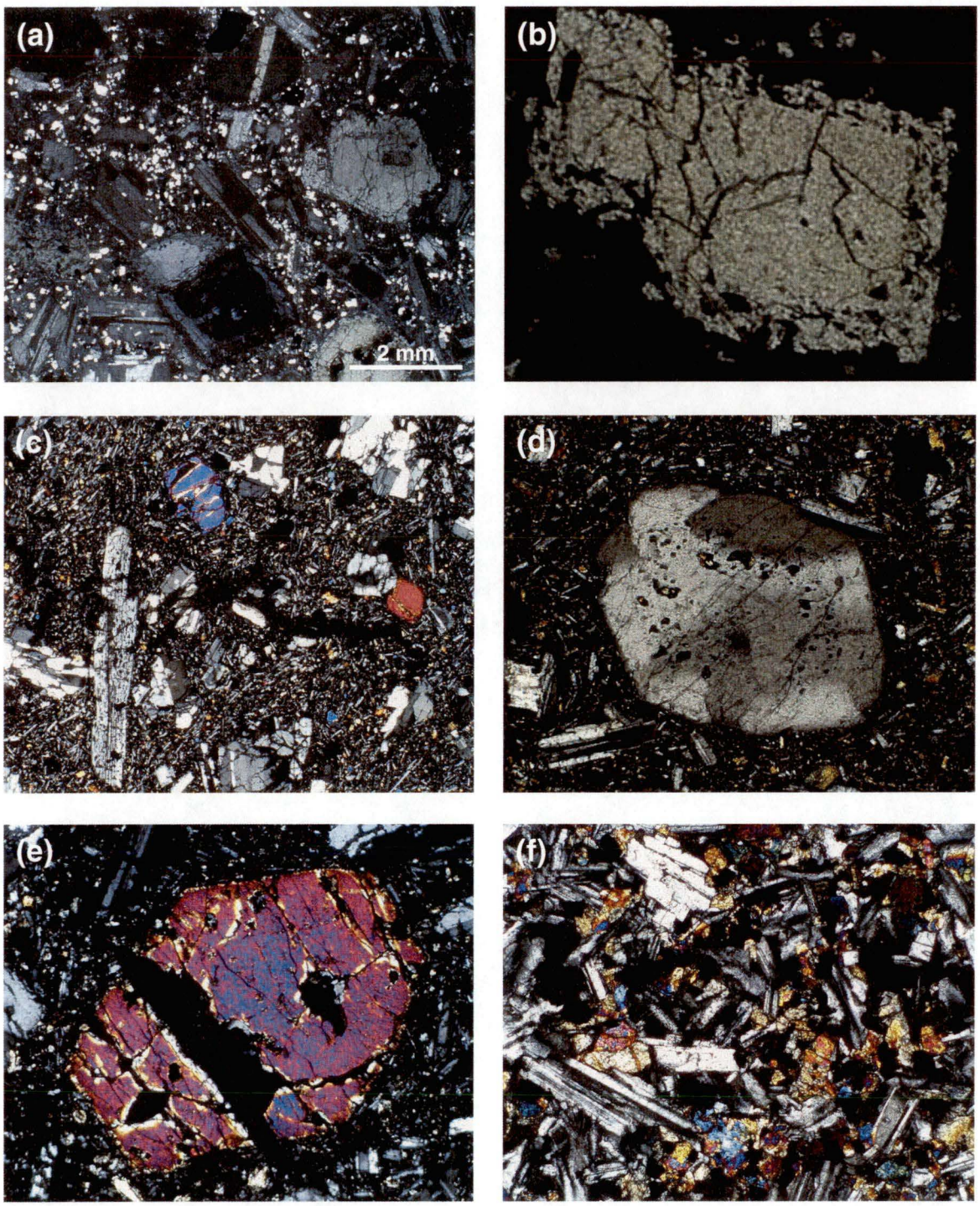

Figure 5.3. Photomicrographs of BVF basalt textures. (a) Coarse-grained, clinopyroxene-rich texture of AR175; note zoning, twinning and ragged margins on clinopyroxene (cpx) crystals, XPL; (b) close-up view of clinopyroxene crystal in AR175; note concentration of stubby plagioclase inclusions, rimmed by cholorite, at crystal margins; XPL; (c) porphyritic texture common to most OSS and HKRS rocks, with plagioclase (pl) aggregates and elongated laths, and euhedral olivine (ol) phenocrysts; Ti-magnetite (mt) microphenocrysts generally associated with olivine phenocrysts; note that clinopyroxene phenocrysts are typically absent from the assemblage; AR106, XPL; (d) rare rounded plagioclase phenocryst in AR157 (MLS sample), similar to rounded plagioclase phenocrysts from some OSS samples; XPL; (e) euhedral but weakly altered olivine phenocryst; AR114, XPL; (f) fine-, even-grained texture in AR199, XPL; Abbreviations as follows: MLS=Mainland Suite, OSS= Offshore Suite, HKRS=High-K/High-Rb Suite, XPL=cross-polarised light.

occurs principally as phenocryst aggregates (0.2-4 mm), and also as discrete, subhedral to euhedral, and rarely, rounded laths (Fig. 5.3 d). Melt inclusion trails parallel to crystal faces are common and some of the larger crystals have weakly zoned rims. Olivine (0.2-1.5 mm) occurs as discrete, paired or rarely clustered phenocrysts, which commonly contain Ti-magnetite inclusions. Olivine phenocrysts are euhedral to subhedral, and less altered to iddingsite compared with the MLS lavas (Fig. 5.3 e). Ti-magnetite phenocrysts vary greatly in size (20 μm-1 mm) and range from subhedral to strongly embayed and even skeletal shapes. They occur as inclusions in, or in close association with olivine phenocrysts. In sample AR198, Fe-oxide forms weak haloes around Ti-magnetite crystals. Rare clinopyroxene (0.2-3 mm) occurs as euhedral to subhedral, typically isolated, strongly coloured phenocrysts. These occur as aggregates enclosing olivine phenocrysts in sample AR201. Unlike the MLS basalts, the groundmass composition of the OSS and HKRS rocks varies from plagioclase-dominant to clinopyroxene-dominant, with highly variable Ti-magnetite and olivine abundances. The groundmass consists of intergranular, generally larger plagioclase laths with smaller clinopyroxene, Ti-magnetite and olivine grains, and ubiquitous accessory apatite.

Sample AR199 has a fine, even-grained rather than porphyritic texture (Fig. 5.3 f). Subhedral plagioclase laths and minor plagioclase crystal aggregates are dominant, with subordinate subhedral to euhedral clinopyroxene crystals. Subhedral to anhedral, and strongly embayed and resorbed Ti-magnetite microcrysts are a minor constituent. The Ti-magnetites are commonly loosely grouped together, and occur in areas close to rare, subhedral, olivine crystals with iddingsite altered rims.

Phenocryst mineral chemistry

Phenocryst compositions are discussed in terms of the three different geochemical groups identified using whole-rock geochemistry. These groups are the Mainland Suite (MLS), the Offshore Suite (OSS) and the High-K/High-Rb Suite (HKRS). Representative mineral analyses are listed in Table 5.2. Analytical methods and a complete list of mineral analyses are given in Appendix G.

Plagioclase

Compositional frequency histograms show that plagioclase phenocrysts in the BVF have strongly calcic cores (Fig. 5.4, Table 5.2). Anorthite contents in phenocryst cores from MLS lavas range from An_{81}-An_{94}, the OSS samples have contents from An_{78}-An_{91}, and the cores of the HKRS group vary from An_{85}-An_{92}. Rim compositions for all groups are generally more sodic than cores with values as low as An_{65} but varying up to An_{92} (Table 5.2, Appendix G). The range of core compositions is always greater than the zoning in single phenocrysts. In all other respects the plagioclase phenocrysts from the

Table 5.2. Representative mineral analyses for phenocrysts from the Basalt Volcanoes Formation (BVF): Mainland (MLS), Offshore (OSS) and High-K/High-Rb (HKRS) Suites.

Plagioclase	MLS								OSS								HKRS					
oxides (wt %)	core	rim	core	rim	core	rim	core	rim	core	rim	core	rim	core	rim	core	rim	core	rim	core	rim	core	rim
SiO_2	46 54	49 56	45.39	48.00	44.73	46 47	45.61	49.43	45 81	47.81	45 82	52.26	47 50	48 35	44 56	49.09	45 20	50 31	44 71	45 61	45.30	50 04
Al_2O_3	33.57	30.84	34 65	32 44	35 43	33.62	34 29	31.31	34.28	31 96	34 47	29.38	33.07	31.73	34 79	31 24	34 50	30.82	35 19	33 08	34 34	31 22
Fe_2O_3	1 14	1.42	1 03	1 05	0 82	1.16	1 06	1 31	0.94	1.13	0 90	1 19	1 16	1.47	1.05	1 65	0 82	1.28	0.96	1 04	1 06	1.41
MgO	0.11	0.13	0 08	0.16	0.08	0.04	0 09	0.14	0.08	0 24	0 09	0.13	0.14	0 08	0 09	0 17	0.08	0.17	0 04	0 06	0.08	0.10
CaO	17.25	14.29	18 20	15.90	19.12	17 46	18 19	14.80	18.01	15 72	18 08	12.80	16.84	15.6	18 46	14 88	17.90	14.00	18.51	18.11	17 84	14 22
Na_2O	1 80	3.43	1 26	2 57	0 99	1.87	1 36	3 08	1.50	2.53	1.42	4 09	2 10	2.78	1 07	2.89	1.22	3 31	1 02	1.20	1.26	3 32
K_2O	0 08	0.22	0.05	0 09	0 07	0.10	0.09	0 19	0 02	0.07	0.07	0 29	0 11	0 16	0 05	0.24	0.08	0 29	0 08	0 10	0 09	0.30
Sr (ppm)	1691	1353	846	1522	1268	2199	1522	1099	338	1438	169	1099	1353	1015	761	592	676	1860	1268	1522	1184	1099
Ba (ppm)	—	—	537	269	—	—	537	806	—	—	627	—	448	—	90	806	—	896	—	179	—	537
Total	100 70	100 09	100.81	100.50	101.46	101 03	100.97	100.61	100 73	99 69	101 06	100 40	101.14	100.42	100.21	100.39	100.07	100 65			100.17	100.87
An (%)	83 29	68 54	88.27	76 60	90 74	82 78	87.13	71.50	86 75	76 78	87 015	62.09	80.66	74.70	90 06	72 72	88 45	68 37	89 93	87.86	87.88	68 76

Olivine	MLS								OSS								HKRS					
oxides (wt %)	core	rim	core	rim	core	rim	core	rim	core	rim	core	rim	core	rim	core	rim	core	rim	core	rim	core	rim
SiO_2	38 38	36.89	38.97	38 48	38 22	36 45	38.23	36.52	38 34	36 32	39 54	36 64	40 01	39.55	40 16	39.69	36.01	35 98	36 00	36.08	36 30	36 33
Cr_2O_3	—	—	—	0.01	—	—	—	0.03	0 02	—	0.05	0 04	0.01	0.01	0 01	0 03	—	0 01	—	—	0.01	—
FeO	20.43	28 97	19.04	19.43	21.42	31.65	21 65	31 10	22 32	33 78	15 33	29.14	12.94	15.17	11 34	13.68	32.14	32.22	32 51	32 17	31 34	31 84
MnO	0 37	0 85	0.39	0 34	0 48	0.78	0 41	0 69	0 40	0.61	0.22	0.63	0.31	0.48	0 23	0.41	0.98	0 94	0 93	0 87	0 96	0.92
MgO	39 75	32 38	41 53	41.30	39.35	31 08	39 52	31.78	38.99	29.62	44 25	32 57	46 09	44 62	47 54	45 62	30 64	30.48	30.27	29.99	30 89	30 80
CaO	0 31	0 25	0 27	0.32	0 30	0 35	0 27	0 28	0.22	0.24	0 27	0 33	0 27	0 20	0 24	0 20	0 20	0 20	0 16	0.17	0.22	0 24
NiO	—	—	0 09	0 10	0.05	—	0.03	—	0 08	0 03	0 12	—	0.23	0 10	0.15	0 16	0.03	0 03	0 05	0 01	0 05	0 03
Total	99 31	99 38	100 16	100.03	99.85	100.36	100 17	100 48	100.43	100.66	99 82	99 44	99.89	100 18	99 72	99 86	100 07	99 87	100 00	99 38	99.81	100.16
Fo (%)	76 6	66.6	79.5	79 1	76 6	63.6	76.5	64 6	75 7	61 0	83 7	66 4	86 4	84 0	88 2	85.6	63.0	62.8	62 4	62 4	63 7	63 3

Clinopyroxene	MLS						OSS					
oxides (wt %)	core	rim	core	rim	core	rim	core	rim	core	rim	core	rim
SiO_2	48 40	46 70	49 55	50 49	51 09	50.74	48 85	48 66	48 47	47 39	48 18	50 15
TiO_2	0.47	0.93	0.47	0 51	0 25	0 50	0.38	0 52	0.52	0.72	0.54	0.36
Al_2O_3	5 79	6 50	3 76	3 10	3 37	2 24	4.98	5.94	5.83	5.75	4 95	3 26
Cr_2O_3	0 23	—	—	—	0.27	0.04	0.29	0 44	0 48	0 14	0 15	0 11
Fe_2O_3(c)	4 94	6 88	6 22	4 80	4 30	4.10	4 85	5 63	5 86	7 66	5 55	5 46
FeO(c)	1.82	3.14	2.15	4 30	0 58	6 13	2 52	2.38	2.07	2.13	2.73	1 97
MnO	0.15	0 16	0 14	0 20	0 10	0 35	0.17	0.15	0.23	0.22	0.15	0.08
MgO	14 47	13 27	14 86	15 40	16 17	14 47	14.86	14.27	14.55	14.19	14 39	15.70
CaO	23.06	22.04	23.13	21 59	24 32	21 10	21 92	22 87	22 46	21.70	22.05	21 76
Na_2O	0.21	0.32	0.28	0 26	0 14	0 39	0 32	0 30	0 30	0 40	0.21	0 22
Total	99 54	99 94	100.56	100.65	100 59	100.05	99 13	101 17	100 78	100 30	98.90	99 08
Wo%	47.84	46.01	46 33	43 30	48 27	42 92	45 60	46 99	46 21	44.60	45 03	43 65
En%	41.73	38 55	41.37	42 94	44 66	40.94	42 99	40 82	41 62	40 57	41 72	44 68
Fs%	10.43	15.44	12.30	13.76	7 06	16 14	11 41	12 19	12 17	14 83	13 25	11 67
Mg_{cpx}	80 40	71 75	77 37	76 15	86 60	72 43	79 40	77.38	77 91	73 71	76 30	79 50

Magnetite	MLS		OSS		HKRS	
oxides (wt %)						
SiO_2	0.12	0 07	0.09	0 09	—	—
TiO_2	4.65	5.04	8 01	4 15	9 27	9 51
Al_2O_3	8 23	6.64	4 67	9 62	2 52	2.69
Cr_2O_3	0 68	—	0 08	1 11	0 61	0 79
Fe_2O_3(c)	50 70	52 37	48 20	50 68	47 89	46 93
FeO(c)	30.68	31.83	36 21	29.85	36 54	36 19
V_2O_3	0 20	0.24	0 18	0 30	0 57	0 60
MnO	0.37	0.46	0.32	0.30	0 57	0 47
MgO	3 71	2 79	1.78	4.31	1.77	2 15
ZnO	—	0 25	0.02	—	0.11	0.05
NiO	—	0 12	—	0 09	—	—
Total	99 34	99 82	99 56	100 49	100 22	99 78

For plagioclase, An%=100[Ca/(Ca+Na+K)]; for olivine, Fo%=100[Mg/(Mg+Fe*)] where Fe* is total Fe; for clinopyroxene, Wo%=100[Ca/(Mg+Fe*+Ca)], En%=100[Mg/(Mg+Fe*+Ca)], Fs%=100[Fe*/(Mg+Fe*+Ca)], where Fe* is (Fe^{2+}+Fe^{3+}+Mn), and Mg_{cpx}=100[Mg/Mg+Fe^{2+})].

three groups show very similar chemistry, with the only distinction being that the HKRS rocks have marginally higher K_2O contents. All plagioclase phenocrysts have extremely high Sr contents (up to 2400 ppm, Table 5.2, Appendix G), with the highest values occurring in phenocryst rims (at values An_{85}-An_{87}). Plagioclase laths from fine-grained sample AR199 have more sodic compositions (An_{58} to An_{69}) than the most sodic BVF phenocryst rims, indicating that plagioclase phenocrysts in samples are more primitive than coexisting groundmass plagioclase (Appendix G).

Olivine

Forsterite contents of olivine phenocryst cores in MLS lavas show weak bimodality, varying from Fo_{63} to Fo_{83} with the majority (~75 %) falling in the range Fo_{75}-Fo_{80}. OSS samples also show a wide variation with values of Fo_{62} to Fo_{89}, again with most samples clustered in the same Fo_{75}-Fo_{80} compositional zone. HKRS rocks however, have much more iron-rich cores with forsterite values ranging from Fo_{62}-Fo_{76} (Fig. 5.4). Rim compositions show a similar spread in values to cores, but extend to lower forsterite contents (*e.g.* Fo_{55}, Appendix G). Calcium contents rapidly increase as Fo decreases to ~Fo_{78}-Fo_{80}, then gradually decline as Fo decreases further (Fig. 5.5). On this diagram inter-suite distinctions are apparent, with HKRS olivines having 0.08-0.10 % lower CaO, compared with MLS and OSS olivines for forsterite contents less than Fo_{70}. NiO shows rapidly decreasing broad trends as forsterite content decreases for all geochemical groups (Fig. 5.5). HKRS olivines again show marked inter-suite differences, defining a separate parallel trend, with higher NiO contents at lower Fo (*i.e.* <Fo_{67}, Fig. 5.5).

Clinopyroxene

Clinopyroxene crystals in the BVF are overwhelmingly dominated by diopside compositions but span a compositional range to Ca-rich augite (Fig. 5.6 a). OSS samples have a higher percentage of augite compositions compared with the MLS samples. The phenocrysts have very weak marginal zoning, with no strong variation between core and rim compositions (Table 5.2). MLS clinopyroxene core compositions have Mg-numbers ($Mg\#_{cpx}=100[Mg^{2+}/Mg^{2+}+Fe^{2+}]$) spanning the range 73-87; less variability exists for OSS samples, whose values range from 76-80 (Fig. 5.4). Rim compositions cluster tightly around core compositions, consistent with the absence of pronounced zoning in the crystals (Table 5.2).

MLS clinopyroxenes are also distinguished from OSS clinopyroxenes by their generally higher CaO contents, and lower Cr_2O_3 values at a given $Mg\#_{cpx}$ (Fig. 5.6 b). Samples from the MLS have better defined trends compared with the significant scatter shown on all diagrams by OSS clinopyroxenes. Al_2O_3 increases with clinopyroxene fractionation (decreasing $Mg\#_{cpx}$) to a maximum of ~7 % Al_2O_3 at $Mg\#_{cpx}$ 77.5. Values between 2.5 and 7.5 % Al_2O_3 are high compared with those in clinopyroxene phenocrysts from normal southern Vanuatu arc basalts, which are generally less than 3 %, but similar compositions

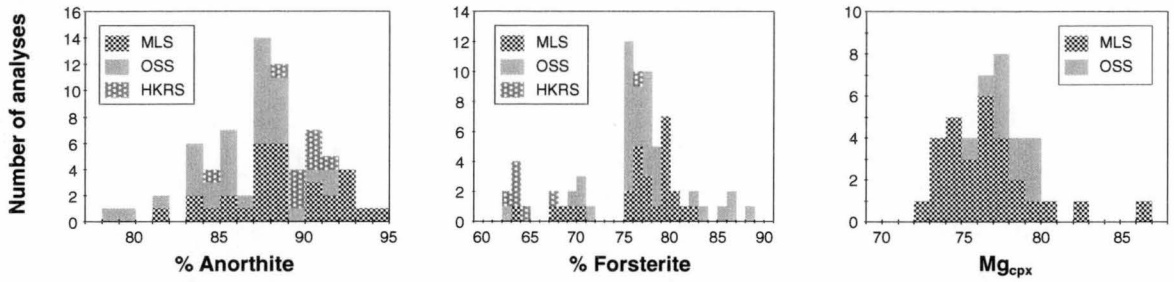

Figure 5.4. Stacked frequency histograms of plagioclase, olivine and clinopyroxene phenocryst core compositions in the MLS, OSS and HKRS.

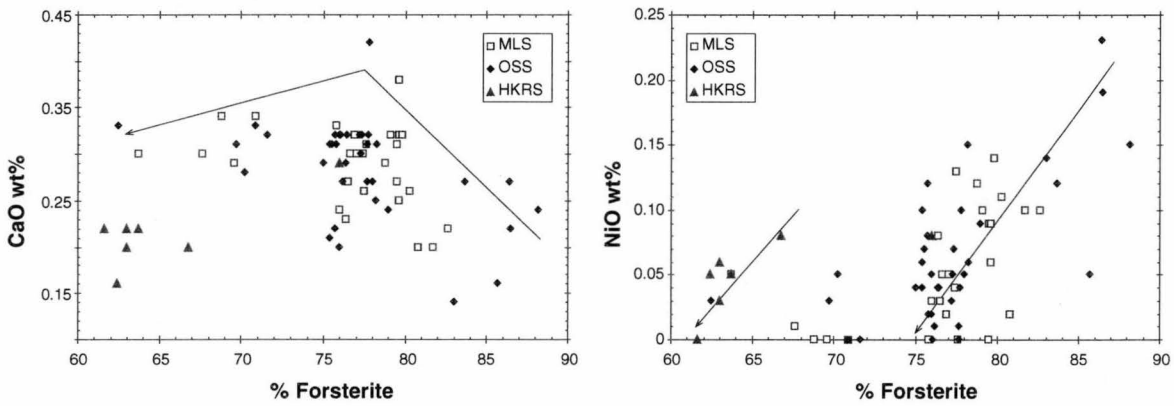

Figure 5.5. Bivariate plots of CaO, and NiO versus forsterite content of olivine cores from MLS, OSS and HKRS basalts. Note lower CaO contents of HKRS lavas at low Fo contents, and separate trend for these lavas on the NiO diagram.

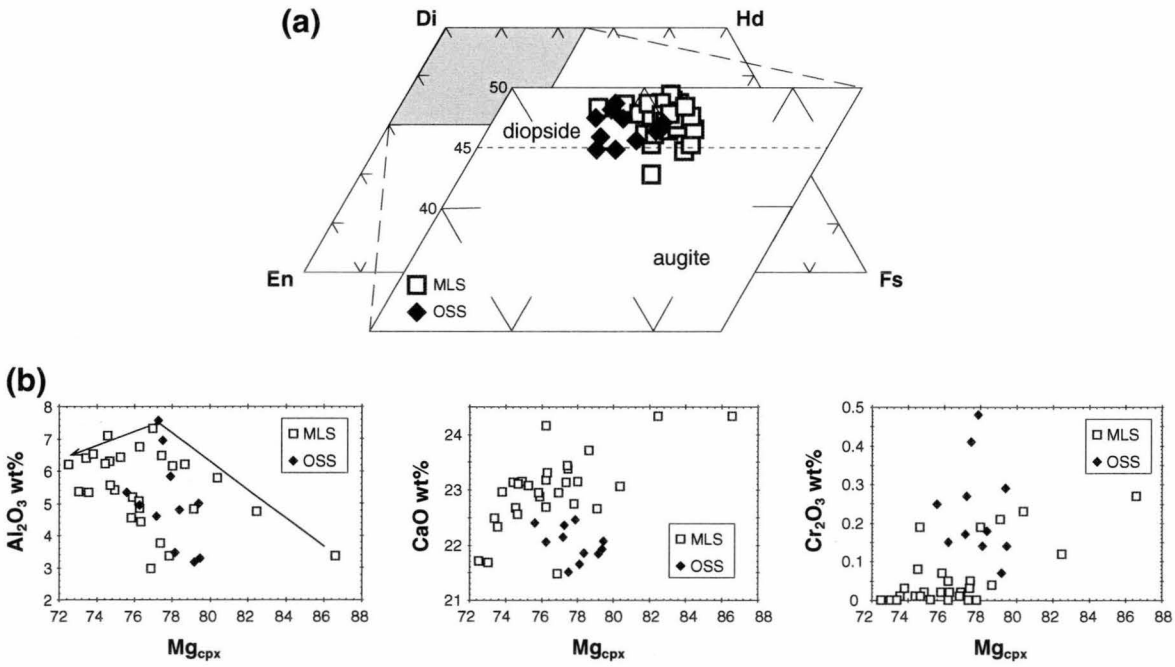

Figure 5.6. (a) Compositions of clinopyroxene cores from MLS and OSS lavas. Quadrilateral pyroxene parameters from Morimoto (1989). Di=diopside, He=hedenbergite, En=enstatite, Fs=ferrosilite; values indicate % wollastonite. (b) Bivariate plots of Al_2O_3, CaO and Cr_2O_3 against clinopyroxene magnesium number (Mg_{cpx}=100[Mg/(Mg+Fe^{2+})]) show the compositional differences between MLS and OSS clinopyroxene core compositions.

occur in augites from basalts on Epi Island to the north (Crawford *et al.*, 1988; Barsdell & Berry, 1990). The high Al_2O_3 contents may result from late crystallisation of plagioclase (Barsdell & Berry, 1990), higher pressure crystallisation of the basalts compared with other Vanuatu arc augite (Green & Ringwood, 1967), or trapping of Al on crystal faces in quench rims (A. Crawford, pers. comm.). No clinopyroxene analyses are available for the HKRS group.

Ti-magnetite

Opaque phenocrysts, microphenocrysts and inclusions in ferromagnesian minerals are all Ti-magnetites, with slightly oxidised compositions lying close to the Ti-magnetite-ulvöspinel solid solution series. TiO_2 content ranges from ~1 % to 10 %, with the HKRS Ti-magnetites having the highest values overall. Consistent with their greater TiO_2 values, FeO contents are likewise highest in the HKRS. For all samples, as the ulvöspinel content increases, so do V_2O_3 and MnO abundances, whereas Al_2O_3, Cr_2O_3 and MgO values decrease (Table 5.2, Appendix G).

GEOCHEMISTRY

A total of 46 whole-rock analyses of basalts from the BVF are investigated below. Twenty-five new analyses are plotted together with previously published data (Ash *et al.*, 1978; Coulon *et al.*, 1979; Dupuy *et al.*, 1982; Melchior, 1989; Peate *et al.*, 1997). All data are recalculated to 100 weight per cent on a volatile-free basis (Table 5.3). Analytical methods are outlined in Appendix F.

Major element geochemistry

Major element covariation diagrams show that lavas of the BVF are transitional to tholeiitic, medium-K basalts with compositions ranging from 45-51 % SiO_2 (Fig. 5.7). On the K_2O versus SiO_2 diagram of Peccerillo and Taylor (1976), all but two basalts (AR188 and AR199) fall broadly within the medium-K field. On the total alkalis versus SiO_2 (TAS) diagram (Le Bas *et al.*, 1986), the same two lavas lie above the proposed transition between alkaline and tholeiitic compositions (parameters from Rickwood, 1989).

Magnesium numbers (Mg#=100[Mg^{2+}/(Mg^{2+}+Fe*)] where Fe* is total iron) vary from 41-57, indicating that these basalts are relatively evolved, contrasting with the adjacent islands of Epi and Aoba, where primitive olivine + clinopyroxene-rich lavas are abundant (Barsdell & Berry, 1990; Eggins, 1993).

Major element abundances (in weight %) are plotted against MgO due to the restricted range of silica values for these basalts (Fig. 5.8). Plotted on the same diagram are

Table 5.3. Whole rock analytical data for Basalt Volcanoes Formation (BVF) Mainland (MLS) and Offshore (OSS) samples.

SUITE	MAINLAND SUITE (MLS)																				OFFSHORE SUITE (OSS)			
SAMPLE	**AR172**	**AR174**	**AR175**	**AR179**	**AR181**	**AR182**	VA76[a]	VA164[a]	Mt Fatma (1)[b]	**AR153**	**AR157**	**AR158**	**AR161**	**AR164**	EA229[a]	EfC1[a]	Quoin H (3)[b]	Q1[c]	Q3[c]	EA143[d]	**AR003**	**AR114**	PeA8[a]	Pele (2)[b]
Major Elements (wt%)																								
SiO_2	46 18	46 90	45 35	45 44	45 58	46 98	46 08	48 18	47 37	47 82	47 79	46 17	47 63	47 21	45 69	47 44	47 37	48 13	48 38	47 78	47 23	46 62	47 06	46 76
TiO_2	0 88	0 84	0 81	0 82	0 85	0 98	0 88	0 82	0 95	0 89	0 92	0 88	0 88	0 89	0 92	0 94	0 95	1 01	0 84	0 90	0 70	0 75	0 81	0 80
Al_2O_3	18 98	20 11	16 13	17 24	18 23	18 04	20 58	18 42	18 65	17 96	19 15	18 50	17 60	18 54	18 46	17 65	17 69	16 70	16 28	17 56	19 97	17 94	19 11	18 93
FeO*	11 17	10 47	11 65	11 46	11 60	11 30	10 75	11 24	10 87	10 75	10 29	10 96	10 82	10 73	11 06	11 57	10 92	11 56	11 01	10 80	9 08	10 17	9 86	9 84
MnO	0 22	0 21	0 19	0 19	0 21	0 23	0 16	0 19	0 21	0 21	0 20	0 21	0 24	0 20	0 20	0 16	0 21	0 20	0 20	0 19	0 16	0 19	0 17	0 17
MgO	5 76	4 73	8 97	8 08	6 67	5 45	6 31	5 70	6 20	5 75	4 88	6 32	6 04	5 99	6 70	5 79	6 61	6 18	7 12	6 03	5 96	7 41	7 07	7 54
CaO	12 19	12 15	13 35	12 99	12 39	11 91	12 58	12 31	11 99	11 49	11 48	12 31	11 79	11 44	13 07	11 77	11 94	11 55	11 78	11 75	12 79	12 46	12 22	12 42
Na_2O	2 20	2 36	1 55	1 75	2 06	2 49	1 24	1 70	2 15	2 74	2 73	2 28	2 66	2 69	2 34	2 84	2 55	2 35	2 19	2 65	2 33	2 43	2 43	2 26
K_2O	0 79	0 65	0 47	0 48	0 68	0 91	0 44	0 44	0 64	0 69	0 81	0 70	0 67	0 65	0 58	0 65	0 70	0 58	0 52	0 68	0 51	0 62	0 61	0,53
P_2O_5	0 39	0 39	0 24	0 27	0 33	0 45	0 48	0 41	0 38	0 47	0 59	0 43	0 45	0 46	0 38	0 43	0 48	0 45	0 46	0 46	0 25	0 26	0 24	0 26
LOI	*1 49*	*0 35*	*1 84*	*1 51*	*1 16*	*2 40*	*2 28*	*2 16*	*2 81*	*0 39*	*0 23*	*-0 09*	*0 09*	*0 70*	*0 36*	*2 06*	*1 68*	*0 20*	*1 72*	*0 55*	*-0 18*	*0 04*	*0 92*	*1 22*
Total	99 53	99 83	99 40	99 57	99 51	99 46	99 42	99 86	100 38	100 20	99 84	99 41	99 62	99 71	100 43	99 80	99 47	99 30	99 91	99 85	99 75	99 58	100 02	99 46
Mg #	47 30	41 46	54 65	55 07	50 34	45 62	50 51	46 87	49 81	48 21	45 20	50 08	49 25	49 25	51 30	46 54	51 27	48 17	52 94	49 27	53 34	55 91	55 53	57 13
Trace Elements (ppm)																								
Rb	12 5	7 9	8 2	6 07	8 34	12 67				7 63	12 2	10 71	8 4	5 4				6	3	8 5	6 9	7 85		
Sr	1164	1266	861	893	1117	1119				1113	1218	1174	1117	1131				967	894	1094	1001	900		
Cs				0 17	0 18	0 21				0 08		0 06								0 12		0 11		
Ba	521	540	353	249	289	429				385	455	294	431	457				254	254	357	222	218		
Sc	27	26	40	33 8	28 1	26 6				27 8	31	27 4	33	29				38	78	30	25	27 7		
V	490	467	522	523	551	578				463	464	506	461	445				456	368	433	367	423		
Cr	18	4	159	107	29	4				56	22	73	65	80				94	139	45	96	215		
Ni	19	10	49	40	23	7				37	20	44	38	44				38	78	33	57	77		
Cu	637	493	143	360	283	517				286	371	436	306	255						269	272	257		
Zn	82	79	69	77	85	96				91	85	83	93	86						85	64	73		
Mo				0 50	0 51	0 52				0 52		0 53										0 32		
Sn				0 10	0 11	0 11				0 29		0 22										0 83		
La				5 98	6 58	10 64				10 76		9 49								9 74		5 68		
Ce				12 78	14 98	22 15				20 78		18 67								21 3		11 91		
Pr				1 90	2 17	3 19				3 16		2 75								3 01		1 80		
Nd				9 78	10 70	15 15				15 93		13 67								14 4		9 06		
Sm				2 52	2 70	3 67				3 77		3 36								3 33		2 41		
Eu				0 87	0 94	1 27				1 33		1 19								1 14		0 88		
Gd				2 42	2 70	3 49				3 82		3 35								3 55		2 41		
Tb				0 36	0 40	0 51				0 55		0 48								0 48		0 38		
Dy				2 09	2 28	2 92				3 16		2 78								2 78		2 22		
Ho				0 43	0 46	0 59				0 66		0 56								0 50		0 46		
Er				1 14	1 26	1 56				1 78		1 50								1 55		1 25		
Tm				0 16	0 17	0 22				0 25		0 20								0 21		0 18		
Yb				0 97	1 04	1 34				1 49		1 24								1 29		1 11		
Lu				0 14	0 15	0 20				0 22		0 18								0 20		0 16		
Y	15 4	33 3	11 1	11 67	12 87	16 00				19 79	19.3	15 51	20 9	17 2						15 3	11 6	12 13		
Zr	25	24	16	21 41	24 23	31 60				28 38	30	29 48	25	25						25 4	20	23 50		
Nb	1 2	<1	1	0 43	0 52	0 77				0 67	1	0 61	1 1	<1						0 63	<1	0 49		
Hf				0 65	0 72	0 97				0 85		0 80								0 86		0 69		
Pb	4 9	3 7	2 4	2 64	3 27	4 66				3 96	4 5	3 51								3 86	2 7	2 70		
Th				0 61	0 74	1 28				0 83		1 00								1 01		0 54		
U				0 20	0 20	0 34				0 19		0 26								0 27		0 19		

Major element data (recalculated to 100 wt.% volatile free) measured by XRF, and trace element data measured by both XRF (Ni, Cr, V, Sc, Zr, Nb, Y, Sr, Ba, Rb, Cu, Zn and Pb), and ICP-MS (Sc, Zr, Nb, Sr, Ba, Rb and Pb and all other trace elements). Data derived by ICP-MS analysis are reported for samples where both methods were used. Bold type denotes new analyses first reported in this thesis, other data sources are: a from Ash *et al.* (1978); b average values from Coulon *et al.* (1979) where numbers in parentheses indicate number of samples from which average is derived; c from Melchior (1989); and d from Peate *et al.* (1997). LOI = loss on ignition; FeO* is total Fe as Fe^{2+}; Mg #=100[Mg^{2+}/(Mg^{2+}+Fe*)] where Fe* is total Fe.

Table 5.3 (cont.). Whole rock analytical data for Basalt Volcanoes Formation (BVF) Offshore (OSS) and High-K/High-Rb (HKRS) samples.

SUITE	OFFSHORE SUITE (OSS)																		HIGH-K/HIGH-Rb SUITE (HKRS)				
SAMPLE	V36[e]	AR006	AR105	AR106	AR109	AR110	NgA7[a]	NgA23[a]	Nguna (6)[b]	ECH14[b]	AR184	AR185	AR192	Mao (5)[b]	ECH55[b]	E9[c]	E6[c]	E1[c]	V20[e]	AR188	AR198	AR199	AR201	V60[e]
Major Elements (wt%)																								
SiO_2	48 61	47 15	46 93	48 42	49 20	50 54	46 19	48 68	48 16	50 27	47 07	48 66	47 01	47 47	47 25	48 38	49 34	49 44	47 84	48 3	47 28	47 95	47 42	48 32
TiO_2	0 79	1 01	0 87	1 00	0 87	0 96	0 73	1 06	0 98	0 97	0 82	0 96	0 80	0 88	0 84	0 89	0 98	1 05	1 12	1 03	0 85	0 94	0 78	0 98
Al_2O_3	18 70	16 70	19 65	18 37	18 08	16 99	18 92	18 09	17 98	17 84	16 93	18 64	16 97	18 12	16 82	15 66	15 54	18 18	17 76	16 83	17 25	17 99	16 98	19 19
FeO*	9 75	12 61	10 78	11 07	11 00	11 26	10 44	11 94	11 29	10 88	11 57	10 89	11 49	10 97	11 40	11 81	12 34	10 98	11 91	11 96	11 53	11 31	11 04	10 54
MnO	0 17	0 24	0 18	0 21	0 22	0 24	0 17	0 24	0 21	0 22	0 22	0 21	0 21	0 20	0 20	0 21	0 22	0 20	0 22	0 24	0 22	0 22	0 20	0 20
MgO	7 53	5 71	5 16	4 45	5 05	4 85	7 53	5 37	5 64	4 99	6 63	4 65	7 00	6 13	7 50	6 90	5 88	4 46	5 32	5 18	6 35	5 05	7 13	4 74
CaO	12 72	11 58	11 71	10 96	10 56	9 58	13 09	10 38	11.46	10 35	12 31	11 06	12 10	12 25	12 26	11 81	10 84	10 35	11 31	10 32	11 54	10 81	11 55	11 22
Na_2O	2 26	2 66	2 60	3 02	2 97	3 33	1 97	3 04	2 75	3 17	2 27	2 81	2 29	2 45	2 25	2 21	2 44	2 61	2 87	2 85	2 28	2 76	2 28	2 75
K_2O	0 54	0 54	0 64	0 88	0 47	0 59	0 40	0 39	0 64	0 53	0 68	0 56	0 63	0 69	0 69	0 55	0 74	1 01	0 64	1 37	1 07	1 28	1 06	1 15
P_2O_5	0 26	0 38	0 27	0 38	0 35	0 42	0 10	0 36	0 33	0 40	0 21	0 33	0 21	0 29	0 23	0 25	0 31	0 51	0 39	0 49	0 36	0 44	0 32	0 46
LOI	*0 42*	*-0 04*	*-0 03*	*0 00*	*-0 29*	*-0 22*	*1 00*	*0 64*	*0 88*	*0 79*	*0 27*	*-0 11*	*-0 34*	*0 73*	*0 77*	*0 54*	*0 49*	*0 45*	*0 76*	*-0 43*	*-0 36*	*-0 42*	*0 03*	*0 42*
Total	99 37	99 42	99 80	99 33	100 07	100 28	100 11	99 94	99 42	99 05	100 27	99 45	99 38	99 34	99 60	99 41	99 36	99 33	99 59	99 82	101 04	99 63	99 40	99 14
Mg #	57 32	44 06	45 43	41 15	44 41	42 80	55 64	43 88	46 51	44 35	49 91	42 62	51 46	49 26	53 36	50 42	45 32	41 39	43 73	42 94	48 94	43 71	52 93	43 91
Trace Elements (ppm)																								
Rb	6 6	6 65	5 8	10 53	5 2	8 8					8 6	7 6	7 03			5	8	11	6 5	29 7	27 5	25 90	26 6	22
Sr	987	901	1026	956	871	861					749	872	727			631	691	810	972	867	821	848	790	989
Cs		0 26		0 37									0 15									0 11		
Ba		234	231	265 8	230	269					274	246	247			215	260	240		312	240	241	223	
Sc	26	34 8	26	25 8	29	30					37	30	36 3						28	33	37	29 5	37	26 5
V	347	608	463	493	420	440					435	465	424			362	376	384	474	460	439	411	400	388
Cr	204	6	39	12	5	2					62	12	69			69	19	7	31	4	25	6	65	18
Ni	88	18	26	15	12	6					27	13	30			30	19	12	17	12	31	23	46	21
Cu		434	403	583	290	380					219	428	212							258	200	250	253	
Zn		104	81	95	94	103					91	92	90							98	88	88	83	
Mo		0 48		0 86									0 63									0 83		
Sn		0 77		0 80									0 31									0 56		
La	4 9	6 17		7 96									7 00						6 7			9 00		7 8
Ce	11	13 39		17 40									14 63						14 8			18 79		18
Pr		2 09		2 50									2 18									2 78		
Nd		10 91		12 60									10 70									13 51		
Sm	2 1	3 05		3 20									2 76						2 9			3 54		3 3
Eu	0 71	1 15		1 15									0 99						1 0			1 24		1 1
Gd		3 15		3 28									2 83									3 61		
Tb	0 33	0 50		0 51									0 44						0 46			0 56		0 55
Dy		2 93		3 01									2 65									3 30		
Ho		0 61		0 63									0 55									0 67		
Er		1 67		1 73									1 52									1 85		
Tm		0 23		0 25									0 22									0 26		
Yb	0 98	1 42		1 54									1 37						1 42			1 68		1 54
Lu	0 16	0 21		0 23									0 20						0 23			0 24		0 26
Y	14	16 76	13 8	17 49	17 4	19 8					15 3	19 4	14 96						23 1	21 7	18 1	18 75	17	22
Zr	29	26 28	28	39 79	24	33					36	29	36 65						37	50	41	46 21	38	47
Nb	2	0 51	<1	0 71	<1	<1					<1	<1	0 75						2 1	1 4	<1	0 95	<1	2 1
Hf		0 83		1 09									1 01									1 20		1 21
Pb		3 23	4 2	4 83	4 4	4 7					3	5	2 90							3 8	4 6	3 71	3 7	
Th	0 42	0 58		0 87									0 92						0 78			0 95		0 84
U		0 20		0 34									0 24									0 36		

Major element data (recalculated to 100 wt.% volatile free) measured by XRF, and trace element data measured by both XRF (Ni, Cr, V, Sc, Zr, Nb, Y, Sr, Ba, Rb, Cu, Zn and Pb), and ICP-MS (all other trace elements and Sc, Zr, Nb, Sr, Ba, Rb and Pb). Data derived by ICP-MS analysis are reported for samples where both methods were used. Bold type denotes new analyses first reported in this thesis, other data sources are: a from Ash *et al.* (1978); b average values from Coulon *et al.* (1979) where numbers in parentheses indicate number of samples from which average is derived; c from Melchior (1989); and e from Dupuy *et al.* (1984). LOI = loss on ignition; FeO* is total Fe as Fe^{2+}; Mg #=100[Mg^{2+}/(Mg^{2+}+Fe*)] where Fe* is total Fe.

representative fields for the 'normal' southern Vanuatu arc basalts (SVA: Tanna and Erromango basalts, Crawford & Eggins, unpublished data), and a suite of island arc tholeiite lavas from the South Sandwich island arc (SSIA: Pearce *et al.*, 1995).

Broad, overlapping trends exist for the three Efaté BVF geochemical groups, over the range 4-10 % MgO. MLS lavas are the most magnesian (MgO > 8 % for AR175 and AR179) and also have the lowest SiO_2 values, only slightly lower than the SVA signature. In contrast to the SVA lavas, appreciable scatter of Al_2O_3 contents occurs for all Efaté groups, indicating that fractionation of plagioclase had little effect on whole-rock geochemistry. CaO contents show some scatter, but broadly follow the SVA trend, with the MLS having the highest values for a given MgO content. On the TiO_2 plot, the OSS ranges up to higher values at low MgO compared with the MLS, which shows a weak inflection point at ~6 % MgO, more consistent with the SVA trend. Similarly, trends on FeO* (total iron as Fe^{2+}) plots for the OSS and HKRS both show inflection (consistent with the SVA trend) at ~6 and ~5 % MgO respectively, except for one group of OSS lavas. A separate and steeper trend occurs for these rocks, having 1-1.5% lower FeO* at 6-8 % MgO than other BVF samples, and also less than those from the SVA. However, no other geochemical differences are apparent for this group. The MLS have higher FeO* contents at high MgO than typical SVA lavas and do not show the same obvious inflection at ~6 % MgO, suggesting earlier onset of Ti-magnetite crystallisation for these basalts. MLS rocks have Na_2O values no different from SVA lavas, but values in the OSS are generally higher. Similarly, K_2O values of the Efaté rocks overlap with the SVA trend, except for the HKRS group. This group shows a marked separation from both the MLS and OSS with greater K_2O contents (1.06-1.37 %), especially at 7-8 % MgO. The biggest differences in major element geochemistry among the groups are apparent on the P_2O_5 - MgO diagram. Except for AR174, the MLS has higher P_2O_5 contents for a given MgO value than the OSS, with HKRS values falling broadly between the two main groups. P_2O_5 contents for BVF lavas are two to three times greater than SVA lavas, and up to twice the levels typically expected for arc rocks, which typically range from 0.05-0.3% (Gill, 1981).

The low SiO_2 values of SVA and BVF basalts contrast starkly with SSIA tholeiites. The SSIA basalts have on average 5 % and 2-3 % higher SiO_2 contents for the same MgO than MLS and OSS lavas respectively. Reversed trends on FeO* and Al_2O_3 plots probably indicate different oxidising, and plagioclase crystallisation conditions, for SSIA magmas compared with Vanuatu arc magmas (Tatsumi & Eggins, 1995). K_2O, Na_2O and particularly P_2O_5 abundances are appreciably higher for BVF rocks compared with SSIA lavas, although a few samples overlap.

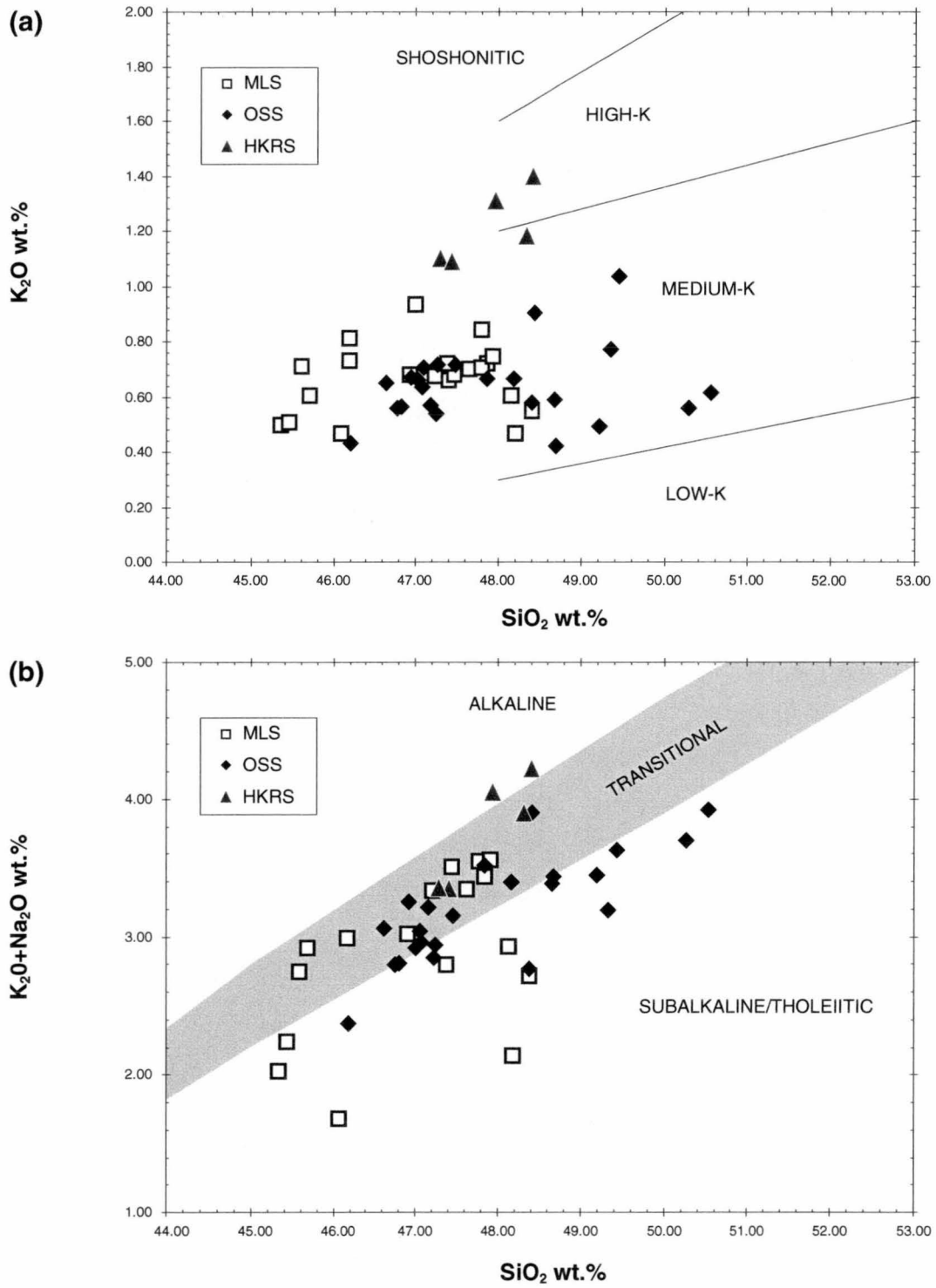

Figure 5.7. Classification of the Efaté Island Group basalts (BVF). (a) K_2O vs. SiO_2 classification diagram of Pecerillo and Taylor (1976) showing medium-K affinities of Efaté rocks. (b) On the total alkalis vs. SiO_2 (TAS) plot of Le Bas *et al.* (1986), the Efaté rocks are clearly subalkaline/tholeiitic to transitional basalts. The shaded band is defined by maximum and minimum limits of series given in Rickwood (1989). MLS = Mainland Suite, OSS = Offshore Suite, HKRS = High-K/High-Rb Suite.

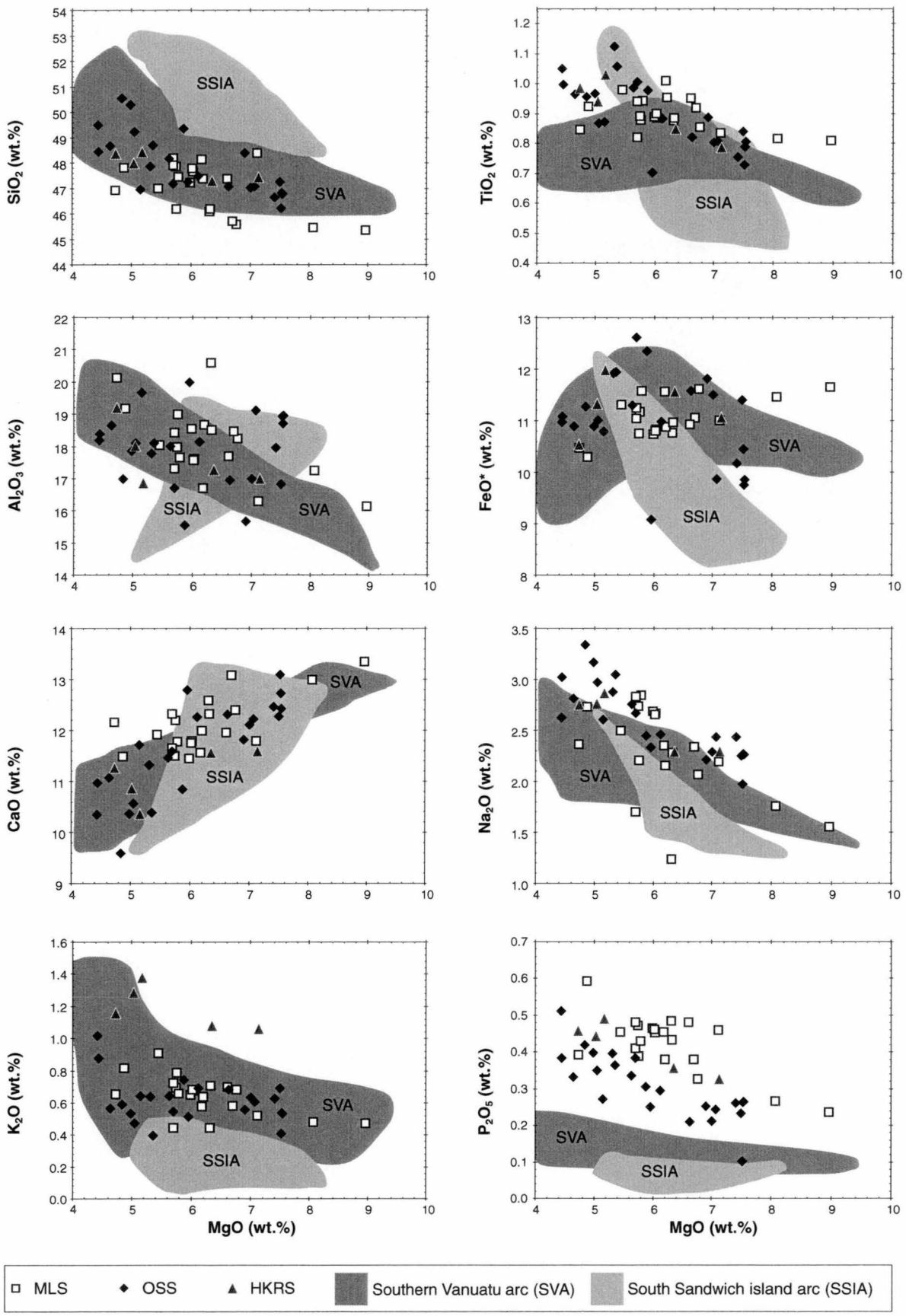

Figure 5.8. Major element covariation diagrams plotted against MgO wt.% for BVF lavas. MLS = Mainland Suite, OSS = Offshore Suite, HKRS = High-K/High-Rb Suite. Plotted for comparison are fields for the southern Vanuatu arc (SVA: Crawford and Eggins, unpublished data) and a typical island arc tholeiite suite from the South Sandwich island arc (SSIA: Pearce *et al.*, 1995).

Trace elements

Selected trace elements (in ppm) are plotted against MgO (in weight %) in Figure 5.9, and some elemental abundance patterns show marked deviation from SVA trends. Zr contents of 50-150 ppm are typically expected for arc lavas (Gill, 1981), and, although they overlap with SSIA values, Efaté BVF (15-52 ppm) and SVA values are strikingly low. The MLS and the HKRS have coherent trends whereas the OSS shows some scatter in Zr values. The HKRS has the highest Zr concentrations of the three suites. SVA basalts form a high- and a low-Y series and all but one of the BVF samples coincide with the low-Y series, and also overlap with SSIA tholeiites. The HKRS and most of the OSS coincide with the main trend for the SVA lavas on the Sc plot, however, MLS rocks have lower concentrations on average for a given MgO, and a group from the OSS having 25-30 ppm Sc forms a flat trend. Sc values (25-40 ppm) are typically lower than SSIA lavas (average 35-50 ppm). BVF lavas have higher V contents (350-650 ppm), and a more scattered distribution than SVA lavas. Trends for V follow FeO* for the HKRS but MLS and OSS patterns are more inconsistent. The SSIA field trends to higher V contents with increasing fractionation whereas the reverse is true for the BVF. Sr values (600-1300 ppm) are extremely high compared with both SVA and SSIA fields and show good separation of the two temporal groups, with some scatter at the higher MgO end for the OSS. Rb is enriched (22-30 ppm) in the few samples having the highest K_2O contents, relative to typical values for BVF (3-13 ppm), SVA and SSIA basalts, characterising the HKRS subset of the OSS. Strong enrichment of Ba at low MgO contents in the MLS contrasts strongly with the flatter pattern shown by the OSS. Between 4-6 % MgO, the MLS has 350-560 ppm Ba compared with 200-280 ppm for the OSS. SVA basalts have a similar trend to the MLS although at a given MgO content their Ba values are much lower. All Vanuatu arc basalts have much higher Ba contents than SSIA basalts. Cu contents (200-700 ppm) are particularly high in BVF rocks compared with both SVA and SSIA lavas.

Rare earth element (REE) patterns normalised to chondrite are given in Figure 5.10. The lavas have fairly flat patterns overall but show a slight to moderate enrichment in the light REE, and depletion in heavy REE relative to N-MORB. The MLS samples have steeper slopes ($[La/Yb]_N$=4.1-5.3) than those of the OSS ($[La/Yb]_N$=2.9-3.5) and both groups show weak positive Eu anomalies (Eu/Eu*=1.07-1.14) and weak but persistent negative Ce anomalies (Ce/Ce*=0.84-0.92). In contrast to a representative Tanna basalt (TA93, Peate *et al.*, 1997), the Efaté basalts are more LREE enriched, have weaker Eu anomalies, and HREE show a consistent depletion. Sample AR199, the HKRS rock, has REE characteristics no different from OSS samples.

Normal mid-ocean ridge basalt (N-MORB) normalised multi-element patterns (Fig. 5.10) for BVF samples show LILE enrichment, strong negative Nb anomalies, and large positive Pb and Sr anomalies, all typical features of island arc rocks (Perfit *et al.*, 1980; Gill,

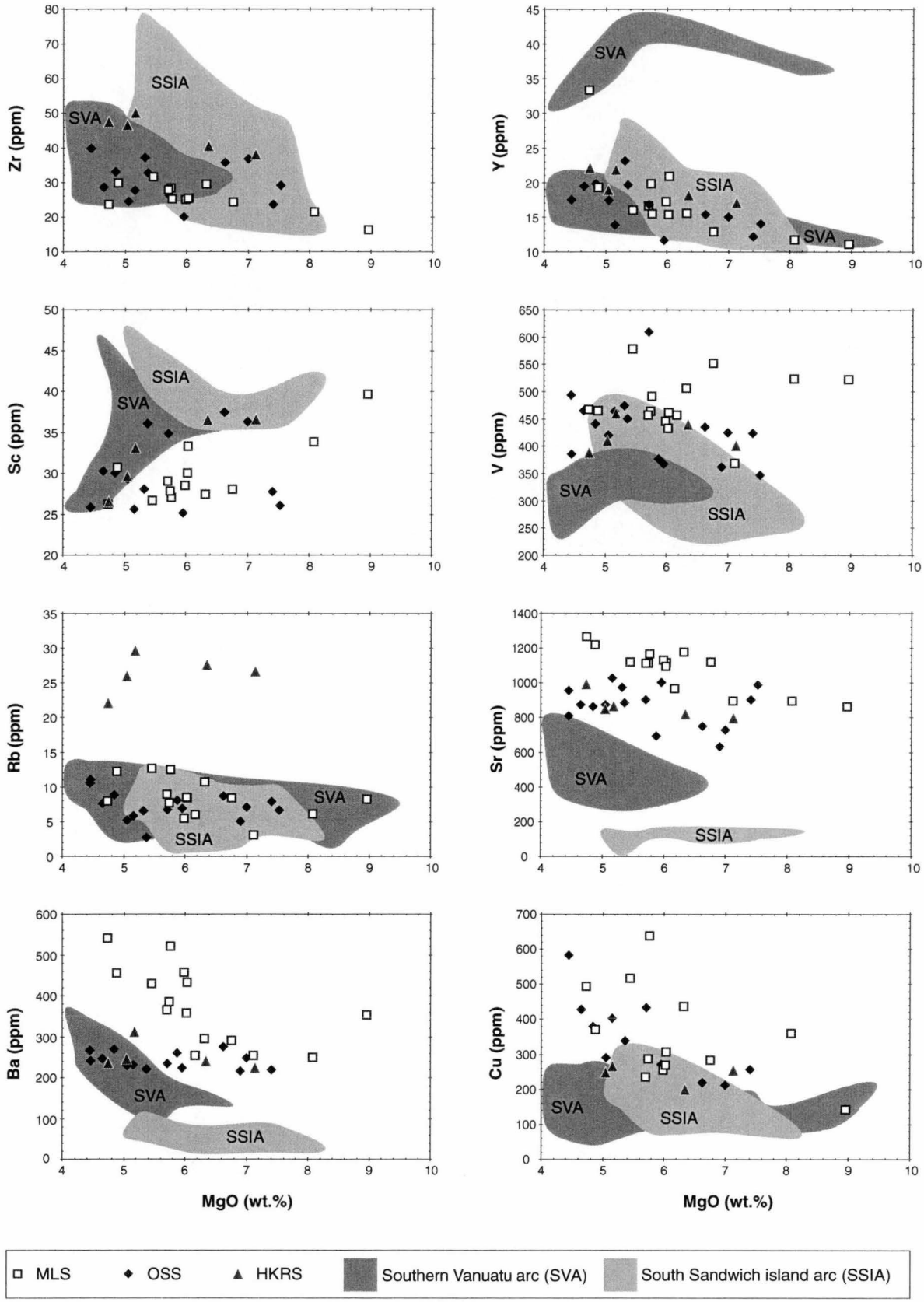

Figure 5.9. Selected trace element covariation diagrams plotted against MgO (wt.%) for Efaté basalts. MLS = Mainland Suite, OSS = Offshore Suite, HKRS = High-K/High-Rb Suite. Fields for southern Vanuatu arc lavas (SVA: Crawford & Eggins, unpublished data), and a typical island arc tholeiite suite form the South Sandwich island arc (SSIA: Pearce *et al.*, 1995) are also plotted for comparison. The SVA fields for Zr, V, Sc, Sr and Ba end at ~7 % rather than ~9 % MgO due to incomplete data sets for these elements.

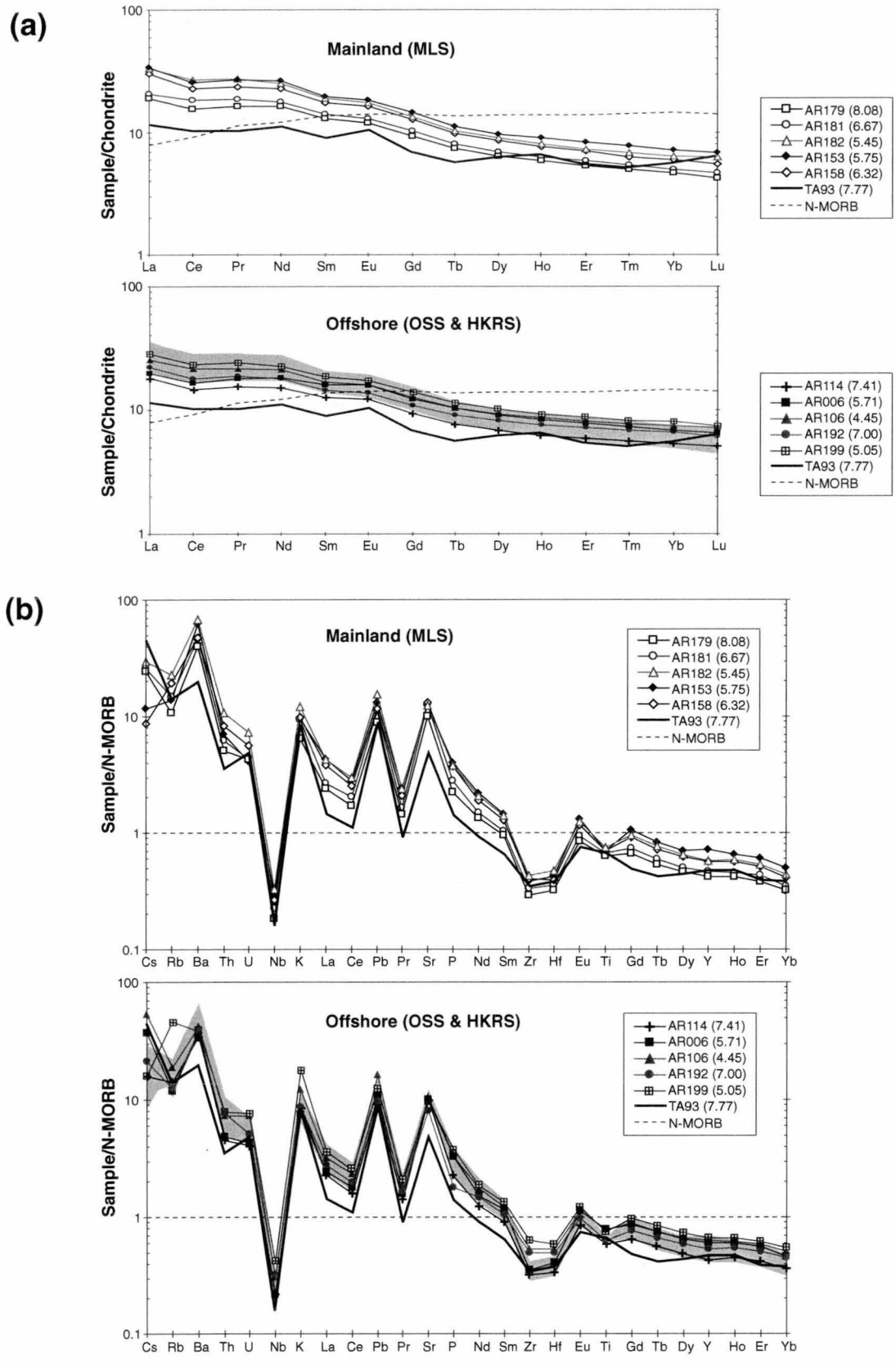

Figure 5.10. (a) Chondrite normalised REE patterns for the BVF lavas; note weak negative Ce anomalies and weak positive Eu anomalies. (b) N-MORB normalised multielement diagrams for BVF lavas; note strong enrichments in Ba and Sr relative to Tanna basalt TA93. Shaded areas on lower diagrams are fields for Mainland (MLS) lavas. MgO values in wt.% given in brackets. Tanna island sample TA93 data from Peate *et al.* (1997). N-MORB compositions and normalising values from Sun and McDonough (1989).

1981). Significant depletion in the HREE is noted for these rocks as seen also on REE plots. Zr and Hf are significantly depleted in these rocks, an unusual feature noted previously for other Vanuatu arc lavas (Peate *et al.*, 1997). The MLS shows more Ba enrichment relative to other LILE, and stronger Zr and Hf depletions than the OSS. The HKRS rock AR199, contrasts with the other groups by showing enrichment rather than depletion of Rb relative to adjacent LILE. The Tanna basalt pattern is lower overall than the BVF lavas, with much lower Ba, Th, La-Ce, Sr, and Gd-Tb, but a positive rather than negative anomaly for Ti.

Sr, Nd and Pb isotope geochemistry

Newly acquired radiometric isotope data are listed together with existing data for the Efaté Island Group in Table 5.4. Figure 5.11 shows Sr, Nd and Pb isotope ratios plotted on standard isotopic covariation diagrams together with fields delineated for the Vanuatu arc, Pacific and Indian MORB (Briqueu *et al.*, 1994; Laporte *et al.*, 1997; Peate *et al.*, 1997), and SSIA (Pearce *et al.*, 1995) for comparison. Also plotted are a local calculated average sediment composition and some actual sediment compositions from the North Loyalty Basin (NLB), expected to represent any subducted sediment component affecting the isotopic signature (Peate *et al.*, 1997). Efaté basalts have among the most radiogenic Sr isotope ratios in the Vanuatu arc, with values at $^{87}Sr/^{86}Sr$=0.70404-0.07042 and restricted $^{143}Nd/^{144}Nd$ (0.51294), a characteristic of the collision-affected, central Vanuatu arc volcanic rocks (Fig. 5.11, Briqueu *et al.*, 1994; Crawford *et al.*, 1995; Peate *et al.*, 1997).

Table 5.4. Sr-Nd-Pb isotope ratios for BVF rocks.

SAMPLE	$^{87}Sr/^{86}Sr$	$^{143}Nd/^{144}Nd$	$^{206}Pb/^{204}Pb$	$^{207}Pb/^{204}Pb$	$^{208}Pb/^{204}Pb$
Mainland (MLS)					
AR158	0.704041	0 512931	18.498	15.526	38.505
EA143*	0.70413	0.512946	18.464	15.520	38.467
EA258*	0.70416	0.512946	18.501	15 558	38.609
Offshore (OSS)					
AR192	0.704244	0.512946	18 482	15.541	38.451
NgA23*	0.70414	-	18.438	15.540	38.436
Undifferentiated samples					
Efaté 7.2	0.70416	-	18.428	15.592	38.730
Efaté 13	0.70407	-	-	-	-
Efaté 20	0.70416	-	-	-	-
Efaté 36	0.70387	-	18.459	15.530	38.463

AR158 and AR192 samples are new data; * denotes samples from Peate *et al.*, (1997); undifferentiated samples from Laporte *et al.*, (1997). New analyses performed at La Tobe University, Melbourne by Roland Maas, standards, analytical techniques and error calculations are given in Appendix F.

Pb isotopic compositions of Vanuatu arc lavas generally fall above the Northern Hemisphere Reference Line (NHRL) of Hart (1984), with a few samples from the southern Vanuatu arc falling into the Pacific MORB field. Efaté basalts have restricted

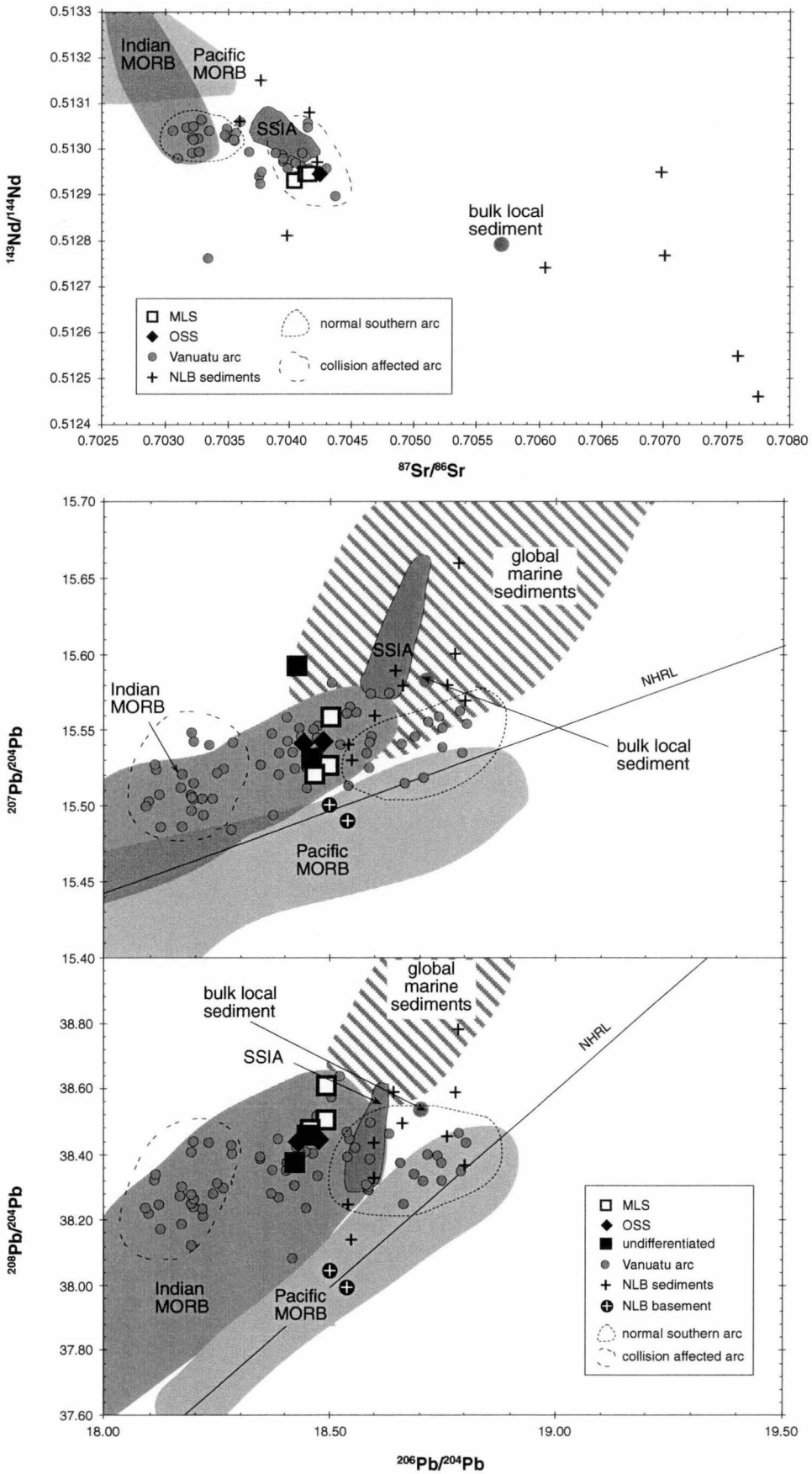

Figure 5.11. Standard Sr-Nd-Pb covariation diagrams for Efaté BVF rocks. Undifferentiated samples are from Laporte *et al.* (1997). Also shown are Vanuatu arc values complete with fields defined for 'normal' and 'collision-affected' lavas, after Briqueu *et al.* (1994), Crawford *et al.* (1995) and Peate *et al.* (1997). Fields for Pacific and Indian Ocean MORB, global marine sediments, and North Loyalty Basin (NFB) sediment compositions and bulk local sediment estimate from Peate *et al.* (1997).

$^{206}Pb/^{204}Pb$ (18.428-18.501), $^{207}Pb/^{204}Pb$ (15.520-15.592) and $^{208}Pb/^{204}Pb$ (38.370-38.609) and fall in the mid-range for Vanuatu arc values, transitional between the collision-affected and normal southern Vanuatu arc Pb isotopic signature (Fig. 5.11, Briqueu *et al.*, 1994; Crawford *et al.*, 1995; Peate *et al.*, 1997).

Summary

The key geochemical features of the BVF arc lavas are:

- SiO_2 contents (especially the MLS lavas) appreciably lower than typical intra-oceanic island arc tholeiitic basalts such as those from the South Sandwich island arc
- slightly elevated TiO_2 and Na_2O contents relative to 'normal' Vanuatu arc lavas
- appreciably elevated P_2O_5 relative to both 'normal' Vanuatu arc lavas and South Sandwich Island arc lavas
- anomalously high Sr contents and variable enrichment in LILE relative to 'normal' Vanuatu arc lavas
- anomalously high Cu values relative to 'normal' Vanuatu arc lavas
- strikingly low Zr contents relative to both 'normal' Vanuatu arc lavas and South Sandwich Island arc lavas at similar MgO contents
- weak but distinct Ce and Eu anomalies on REE diagrams
- Sr-Nd isotopic compositions similar to collision-affected Vanuatu arc lavas
- Pb isotopic compositions transitional between collision-affected and 'normal' Vanuatu arc lavas, corresponding to the spatial location of Efaté between the two zones of the Vanuatu arc

DISCUSSION

Trends on major and trace element plots for the BVF lavas do not show well defined fractionation trends expected for basaltic island arc lavas. This is particularly apparent on the Zr versus MgO plot, which typically shows strong fractionation trends for related magmas. This suggests that BVF lavas, particularly those from the OSS, were erupted from discrete, evolved, magma batches in a crustal magma chamber with rapidly changing parental magma compositions. REE and multi-element patterns are remarkably consistent however, indicating a common mantle source. BVF patterns contrast appreciably with patterns noted for SVA rocks, implying different source and melting

conditions for the Efaté basalts compared with the 'normal' SVA lavas. The enrichments of P_2O_5 and Sr in the Efaté BVF lavas are of particular interest regarding the petrogenesis of these rocks.

Sr enrichment - slab melting?

Mantle wedge peridotite is generally accepted as the source of most subduction zone magmas (*e.g.* Perfit *et al.*, 1980; Tatsumi, 1989; Davies & Bickle, 1991; Woodhead *et al.*, 1993; Arculus, 1994; Hawkesworth *et al.*, 1994). Melting is induced by a metasomatising agent released from the subducting slab into the overlying mantle wedge. Whether this metasomatic agent is a hydrous fluid released from the breakdown of amphibole in the down-going slab, or a silicate melt, or both, is still a matter of debate (Peacock *et al.*, 1994; Sen & Dunn, 1994; Rapp & Watson, 1995; Schiano & Clocchiatti, 1995). The unusual trace element signatures of several suites of arc andesites and dacites, termed adakites, indicate that these geochemically distinctive magmas may be derived by direct melting of subducted slab metabasalt (amphibolite, or more likely eclogite). The most striking geochemical feature of adakites is their high Sr/Y values. This high ratio is generated by melting of the subducting slab in eclogite facies: residual omphacite and garnet do not accept Sr and it is therefore strongly partitioned into the melt, whereas Y is readily retained in garnet and consequently becomes greatly reduced in the resulting magma (Peacock *et al.*, 1994; Sen & Dunn, 1994). For most adakite suites, it can be demonstrated that relatively young and hot lithosphere is being subducted (Defant & Drummond, 1990; Drummond & Defant, 1990; Defant *et al.*, 1991a; Defant *et al.*, 1991b; Verbeeten, 1996).

The high Sr contents and Sr/Y values of the Efaté basalts are akin to levels in adakitic arc suites and BVF data plot in the adakite field of the Sr/Y versus Y discrimination diagram of Defant and Drummond (1990). However, adakites by definition have SiO_2 contents ≥ 56 %, so the extreme Sr enrichments in the Efaté basalts merely indicate adakitic affinities and are quite different in this respect from SVA lavas (Fig. 5.12a). On closer examination, the similarity between the BVF and known adakite suites breaks down. On the $(La/Yb)_N$ against Yb_N discrimination diagram (Drummond & Defant, 1990; Defant *et al.*, 1991b), adakites plot in the field defined for Archean trondhjemite-tonalite-dacite suites believed to have been derived from melting of subducted lithosphere (Jahn *et al.*, 1981; Martin, 1986). On this diagram the Efaté BVF data fall into the post-Archean field, occupied by non-adakitic arc magmas (Fig. 5.12 b). Other element ratios which also reflect the involvement of a slab-derived partial melt include La/Yb>20 and Zr/Sm>50 (Sen & Dunn, 1994; Schiano & Clocchiatti, 1995), but these are much too low (La/Yb<10 and Zr/Sm<15) in the Efaté basalts, and would not generate high enough ratios, even allowing for differentiation of the BVF to more evolved compositions.

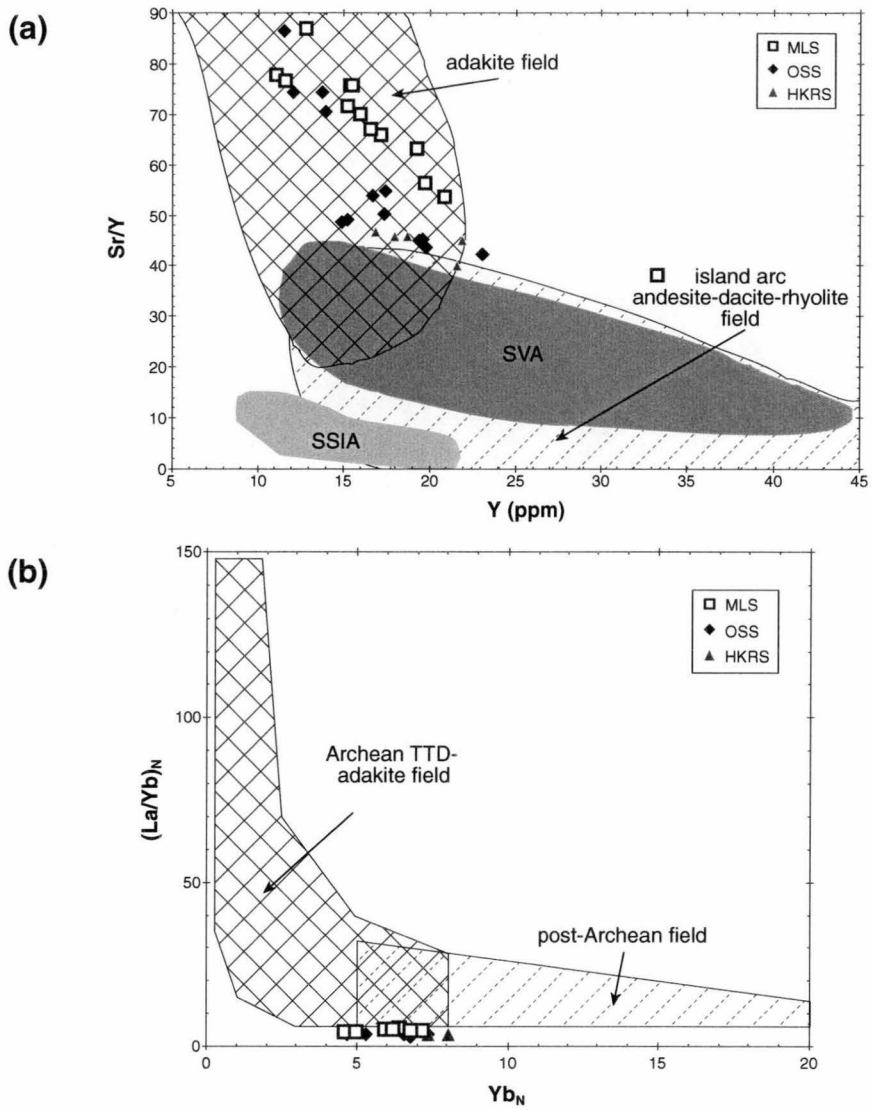

Figure 5.12. Adakite discrimination diagrams after Defant and Drummond (1990) and Defant *et al.* (1991). (a) On the covariation of Sr/Y vs. Y plot, BVF rocks clearly fall in the adakite field, but on (b) the $(La/Yb)_N$ vs. Yb_N plot, the BVF data fall just below the adakite field, in the overlap region for post-Archean rocks. MLS = Mainland Suite, OSS = Offshore Suite, HKRS = High-K/High-Rb Suite. Fields for southern Vanuatu arc (SVA: Crawford & Eggins, unpublished data) lavas, and South Sandwich island arc (SSIA: Pearce *et al.*, 1995) lavas for comparison. Archean trondhjemite-tonalite-dacite (TTD) and post Archean fields after Jahn *et al.* (1981) and Martin (1986).

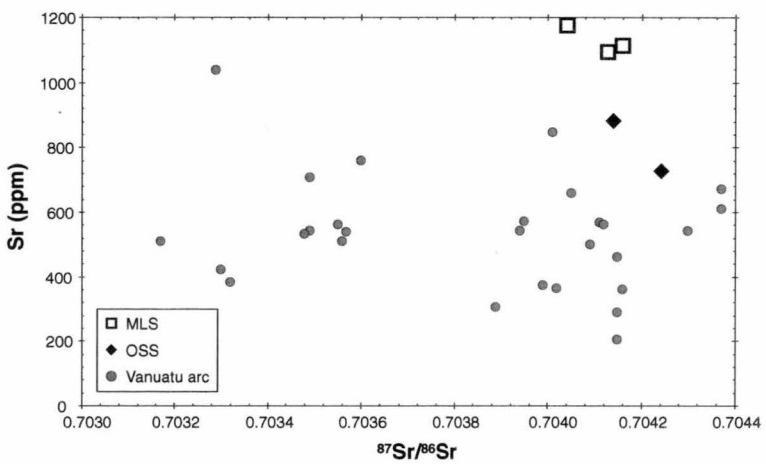

Figure 5.13. Bivariate plot of Sr vs. $^{87}Sr/^{86}Sr$ for Efaté BVF lavas and Vanuatu arc lavas. There is no obvious correlation between Sr-isotope ratio and Sr content for these data. MLS = Mainland Suite, OSS = Offshore Suite.

Perhaps the elevated Sr contents of the BVF can be explained in terms of basalt extraction from a mantle wedge source peridotite previously metasomatised by a slab melt-derived trondhjemitic or tonalitic felsic (adakite) magma. Metasomatism by such a melt would elevate Al_2O_3 and Sr levels in the mantle wedge, thereby causing concentrations in subsequent partial melts *in excess* of those normally imparted by slab-derived hydrous fluid metasomatism. However, felsic slab melts might also be expected to have had significant Zr contents (typically 50-100 ppm, for tonalites in ophiolites, Coleman, 1977; Robson & Cann, 1982; Gass *et al.*, 1984). Subsequent partial melts from a slab melt-metasomatised peridotite should concentrate this extra Zr, but the BVF rocks have strikingly low Zr contents. This mechanism is therefore at odds with BVF Zr contents. This further demonstrates that the BVF lavas are not adakitic in origin, nor did their petrogenesis involve an adakitic component.

Sr enrichment - subducted sediment component?

There is some evidence to support at least partial involvement of a subducted sediment component to the BVF geochemical signature. Hole *et al.* (1984) concluded that small amounts of pelagic sediment (<1 % of the source) incorporated into the subduction component produced high Ba/La (>25) values and negative Ce anomalies in REE patterns for Mariana arc lavas. The addition of such a sediment component might also produce significant enrichment in Sr, which is enriched in pelagic sediment, in turn driving $^{87}Sr/^{86}Sr$ towards more radiogenic (seawater) values. Efaté BVF lavas have Ba/La=26-44, Ce/Ce*=0.84-0.92, extreme Sr enrichments, and some of the most radiogenic Sr isotope ratios in the Vanuatu arc, indicating an important role for subducted pelagic sediment contributions in the petrogenesis of these magmas. Unfortunately, Sr isotope data are frequently strongly affected by other processes occurring during melt generation, transport and storage, and consequently are not good tracers of subducted sediment (see below and also Perfit *et al.*, 1980; Briqueu & Lancelot, 1983; Elliott *et al.*, 1997). If a subducted sediment component was the principal source of Sr enrichment for the BVF (and Vanuatu arc lavas generally) then a strong correlation between Sr contents and $^{87}Sr/^{86}Sr$ should be noted, but this is not the case (Fig. 5.13, Arculus & Johnson, 1981).

Lead isotope characteristics, however, are more sensitive to sediment involvement in subduction-related magmas. Peate *et al.* (1997) concluded that a subducted local sediment component significantly contributed to the variation in Vanuatu arc Pb-isotopic signatures. The Pb-isotopic signature also points to a variation in mantle source between the collision-affected central arc lavas, and 'normal' SVA lavas, the former derived from an Indian MORB mantle source, the latter from a Pacific MORB mantle source (Crawford *et al.*, 1995; Turner *et al.*, 1999). The Efaté basalts are transitional between the two groups, with their Pb-isotope ratios displaced towards local and global marine sediment values. However, these values do not lie on mixing lines between the 'normal' SVA lavas

and local sediment components (either the bulk estimate or any specific analysis), nor do they lie on mixing lines between the Pacific MORB field and the sediments (Fig. 5.11). This indicates a more complex origin for the Pb-isotopic signatures of the Efaté BVF.

Elliott *et al.* (1997) found that a suite of Mariana arc lavas with chemistry that clearly reflects a subducted sediment input had low rather than high Sr and Pb isotope ratios, which are normally expected to accompany high LILE/REE and negative Ce anomalies. This was explained by variability in the type and volume of the subducted sediment component due to local subduction of the Magellan seamounts. The thickness of a seamount edifice and its associated volcaniclastic pile (several kilometres) would overwhelm the isotopic contribution from a few hundred metres of pelagic sediment, resulting in lavas with trace element geochemical signatures reflecting sediment involvement without emphatic corresponding isotopic evidence.

There is good evidence that seamount subduction is also occurring in the Efaté region. The ORSTOM seamount is currently impinging on the South New Hebrides Trench, causing kinking and shoaling of the trench slightly northeast of Efaté (Fig. 2.1, Chatelain & Grasso, 1992; Prévot *et al.*, 1994; Regnier *et al.*, 1997). Furthermore, the central part of the arc is currently colliding with the DEZ, a relict and now submerged Eocene island arc complex, which has been sweeping northwards along the arc for ~3 Ma (Fig. 2.2, Macfarlane *et al.*, 1988; Greene & Collot, 1994; Aitchison *et al.*, 1995). These two current conditions indicate that seamount subduction in the Efaté region during the period of BVF magma generation is highly likely and may have contributed to the anomalous signature of these lavas. Specifically such a process can explain the shift of Sr-Nd isotopes towards more DEZ-like signatures (see below) without a concurrent shift in the Pb isotopes, as this is controlled by the presence of an Indian MORB source in the DEZ.

In conclusion, although a pelagic sediment component was clearly involved in the petrogenesis of the Efaté BVF basalts, isotopic data provide no convincing evidence that this component contributed Sr contents *in excess* of that demonstrated for the main southern section of the Vanuatu arc.

Sr enrichment - plagioclase accumulation?

The strongly porphyritic nature of typical subduction zone volcanic and shallow intrusive rocks complicates the interpretation of whole rock geochemical patterns, as trends cannot be considered to represent liquid lines of descent for related magmas (Tatsumi & Eggins, 1995). Accumulation of phenocryst phases in many arc magmas is increasingly recognised as contributing to some of the particular major and trace element characteristics of arc basalts, in particular high-alumina basalts (Crawford *et al.*, 1987; Blundy & Shimizu, 1991; Vukadinovic, 1993; Lee & Stern, 1998). At least two factors point to accumulation of plagioclase being important in the genesis of the BVF lavas. Plagioclase phenocrysts are abundant and have strongly zoned rims, and scatter on the

Al_2O_3 diagram to values commonly >18 % (Fig. 5.8) may be imparted by variable accumulation of plagioclase, since systematic fractionation of plagioclase (+ clinopyroxene + olivine) should produce a much tighter trend. Additionally, melt inclusion trails indicate a long growth history, and resorption features such as rounding of some crystals, indicate long residence times for plagioclase phenocrysts in these basalts. Careful microprobe analysis has shown that the bulk of the Sr in these rocks clearly resides in both groundmass and phenocrystic plagioclase (Table 5.5, Appendix H). Therefore, perhaps plagioclase accumulation is important in generating such extreme enrichments in Sr.

Table 5.5. Representative and average microprobe analyses of BVF groundmass compositions.

SUITE	MLS			OSS			HKRS		
SAMPLE	AR153-2	AR153-5	*AR153-av*	AR184-1	AR184-2	*AR184-av*	AR198-3	AR198-5	*AR198-av*
Major Elements (wt%)									
SiO_2	48.07	52.05	*49.76*	49.99	50.71	*49.23*	48 98	52 23	*49.57*
TiO_2	1.18	0.16	*0.74*	0.71	0.50	*0.69*	0.70	0.37	*0.75*
Al_2O_3	17.23	25 30	*19.59*	17.40	21.18	*18.94*	17 85	19.83	*18.43*
FeO*	9 92	3 06	*7.38*	9.11	6 98	*8.93*	9.52	5.45	*8.71*
MnO	0.24	0 04	*0.16*	0.18	0.18	*0.21*	0.26	0.18	*0.21*
MgO	5.34	1.91	*4.35*	4 92	3 26	*4.74*	6.41	4 68	*5.26*
CaO	12 45	11.62	*11.95*	11.37	11 30	*11.51*	10 58	11 35	*10.88*
Na_2O	3 27	4.16	*3 61*	3 33	3.46	*3.20*	3.06	3.42	*3.23*
K_2O	0.64	0.62	*0.82*	1.14	1.03	*0.98*	0.86	1.35	*1.25*
P_2O_5	0.31	0.30	*0 47*	0.53	0.27	*0 29*	0.41	0.27	*0.44*
Total	99 31	98.39		98.61	98.83		98.84	98.75	
Mg#	48.97	52 66	*51 43*	49.05	45.44	*43 64*	54.55	60.46	*52.22*
Trace Elements (ppm)									
Cr	9 99	93 18	*72.01*	73.20	2.42	*33 91*	0 69	0.69	*44.70*
Ni	1 58	166.12	*51.44*	124.32	1.59	*53.61*	247.26	1 59	*141.86*
Sr	1574	3104	*2167*	2000	2331	*1802*	1962	2288	*1986*
Ba	507	161	*385*	273	619	*560*	289	2	*171*

Analyses from finest-grained samples, averages calculated from nine spot analyses. Note high values for Sr.

Lever rule mass balance calculations for simple addition of plagioclase to either basaltic, basaltic andesite, or dacite residual melt compositions typical of the southern Vanuatu arc *do not* result in Sr contents that approximate BVF lava compositions, even for 100% addition (Appendix I). There is no evidence for accumulation of plagioclase into an evolved basaltic andesite or dacite magma since measured BVF groundmass compositions are clearly basaltic and very similar to whole-rock compositions, with SiO_2 contents ranging from 46-52 %, and Mg-numbers of 39-60 (Table 5.5, Appendix H). Even though accumulation of plagioclase played a role in generating the BVF rocks, and may be responsible for Al_2O_3 contents between 17-21 % and rather low silica contents in otherwise evolved basalts, this process cannot account for their extremely Sr-rich signature. The abnormally Sr-rich plagioclase compositions simply reflect abnormally Sr-rich parental magmas.

Other possibilities?

Aqueous fluids derived from dehydration of the descending slab in the Efaté region may be enriched in Sr. As stated previously, one of the most important sources of Sr comes from dehydration of seawater-altered ocean crust, and if present, Sr isotope ratios are significantly affected, causing a more radiogenic Sr isotope signature in the magmas generated (Perfit *et al.*, 1980; Pearce, 1982; Arculus, 1994; Kersting *et al.*, 1996). Oceanic lithosphere of the DEZ crust is known to have undergone appreciable seawater alteration both during and subsequent to the active phase of Eocene arc volcanism (Collot *et al.*, 1992; Coltorti *et al.*, 1994). This explains, in part, the shift of Sr isotopes to more radiogenic values in the collision-related lavas (Briqueu *et al.*, 1994). As outlined above, incipient seamount subduction is occurring in the Efaté area, and is also likely to have occurred during the genesis of BVF magmas (Chatelain & Grasso, 1992; Chatelain *et al.*, 1993). Seamount subduction and its attendant interference with the over-riding plate lithosphere, is a source of both hydrothermally altered crust, and seawater infiltration to the mantle wedge (Chatelain *et al.*, 1993; Briqueu *et al.*, 1994), and consequently, will have a significant impact on the physical conditions governing melt generation in the region. Sr enriched fluids released from the descending slab would elevate Sr levels in the mantle wedge above values normally expected for 'normal' SVA mantle wedge source regions. Additionally, the Sr isotope geochemistry of local magmas would be deviated from compositions resembling SVA lavas, towards more radiogenic values similar to the central Vanuatu arc collision zone lavas (*e.g.* Greene *et al.*, 1988a; Macfarlane *et al.*, 1988; Monzier *et al.*, 1997).

Phosphorus enrichments?

Abundances of P_2O_5 in the BVF are much greater than expected for Vanuatu arc lavas and arc basalts in general, and values are even higher than some more evolved andesitic arc magmas (Gill, 1981). The high P content of the BVF magmas is more akin to abundances often reported for Ocean Island Basalt (OIB, Middlemost, 1975; Geist *et al.*, 1995). This may reflect smaller degrees of partial melting and/or deeper partial melting for BVF parental magmas compared with other intraoceanic arc suites (*e.g.* SSIA, Figs 5.8-5.9). However, K_2O and Zr are also strongly partitioned into low degree partial melts and should be elevated as well. Only the HKRS rocks have elevated K_2O, none show Zr enrichment and in fact Zr abundances are strikingly low, and *all* BVF rocks show the P_2O_5 enrichments, so some other mechanism must be responsible.

A hypothesis worth considering, but difficult to prove, is that P_2O_5 and Sr enrichments in the BVF basalts are the result of basaltic melt extraction from a previously carbonatite-metasomatised mantle peridotite. Green and Wallace (1988) suggested that metasomatism of mantle lithosphere by ephemeral and highly reactive carbonatite melts, generated by very low degrees of partial melting of carbonated peridotite, may occur

under relatively oxidising conditions, which could include areas of the mantle wedge in Benioff Zones. This process is increasingly recognised as occurring in subcontinental mantle (Yaxley *et al.*, 1991; Yaxley *et al.*, 1998), but the role of such metasomatising melts in sub-arc mantle is more speculative (Serri *et al.*, 1993; Della-Pasqua, 1997; Schiano *et al.*, 2000).

Arc magmas derived from carbonatite melt-metasomatised mantle wedge lithosphere might be expected to be enriched to varying extents in LILE, LREE and Na_2O. TiO_2 will be strongly decoupled from LILE and LREE showing no concurrent enrichment, and SiO_2 contents of the subsequent magmas will be very little affected. Most importantly, carbonatite melts are extremely effective at transporting both Sr and P_2O_5. Additionally, in the intraoceanic arc environment, such melts need not be enriched in HFSE like rift-zone or hotspot carbonatites generated from ancient, enriched peridotite mantle sources (Dupuy *et al.*, 1989; Woolley & Kempe, 1989; Harmer & Gittins, 1998).

In comparison to 'normal' SVA basalts, and arc basalts generally, the compositions of the Efaté basalts show enrichments in LILE, LREE and Na_2O, and characteristically Sr and P_2O_5, without elevated TiO_2 and SiO_2 (Figs 5.8-5.10). Other chemical fractionations typically affected by carbonatite metasomatism include CaO/Al_2O_3, Na_2O/Al_2O_3 and Zr/Hf. These fractionations are demonstrated for carbonatitic rocks and mantle xenoliths generated above areas of old, enriched mantle sources (Green & Wallace, 1988; Yaxley *et al.*, 1991; Smellie *et al.*, 1995). In the BVF rocks these ratios show little to minor variation from 'normal' SVA or similar arc basalts, suggesting that if the mantle wedge source under Efaté was previously modified by a carbonatite melt, other petrogenetic processes have obscured these chemical fractionations. Alternatively, and more likely, carbonatite generated in sub-arc lithosphere may be significantly different from carbonatite generated in more fertile asthenospheric peridotite.

Key aspects of the unusual geochemical signature of the Efaté basalts suggest that carbonatite metasomatism might have been important in generating BVF magmas. Until experimental data are available on the trace element systematics of carbonatites generated from depleted mantle wedge peridotite, further investigation of this hypothesis is beyond the scope of this study.

Inter-suite variations

Although the signature of the BVF lavas is broadly similar, the HKRS rocks from Emau have a distinctly different pattern of LILE enrichment, with notably higher K and Rb values relative to MLS and OSS basalts (Figs 5.8-5.10). Barsdell *et al.* (1982) showed that variations in the concentration of K-group elements, REE and HFSE in the Banks Islands, systematically decreased with distance from the Vanuatu trench. This is in

direct contrast to the typical across-arc increase (K-h relationship) normally observed for these elements in arc systems (Dickinson, 1975; Hamilton, 1988; Arculus, 1994). The variation was attributed to localised areas of K- and other LILE-enrichment in the mantle wedge source formed from solidified and unerupted partial melts related to early Vitiaz arc volcanism. Subsequent partial melting of such zones (or parts of them) may have generated K-enriched parent magmas (Barsdell *et al.*, 1982). It is likely that similar conditions existed in the Efaté region and HKRS parent magmas may have tapped into K_2O and Rb enriched zones in the mantle wedge.

SPECULATIVE PETROGENETIC MODEL

Prior investigations have emphasised the importance of heterogeneity in the mantle wedge source of Vanuatu arc magmas, particularly with reference to the obvious geochemical changes in lavas noted across the DEZ collision (*e.g.* Gorton, 1977; Crawford *et al.*, 1995; Monzier *et al.*, 1997; Peate *et al.*, 1997; Turner *et al.*, 1999). Efaté sits in a key position between the collision zone and the 'normal' southern section of the arc (Carney *et al.*, 1985; Greene & Wong, 1988; Macfarlane *et al.*, 1988; Robin *et al.*, 1993b). This position also coincides with a point above an interpreted tear in the subducting slab (Chatelain *et al.*, 1992; Prévot *et al.*, 1994; Monzier *et al.*, 1997). Whatever the reason for this tear, the tectonically sensitive position of the island seems to have had a profound effect on the unusual geochemistry of the Efaté basalts.

The element enrichments in the BVF lavas from the Efaté Island Group are probably controlled by a combination of different processes operating both deep in the mantle, and in BVF crustal magma chambers. A slab-derived fluid component, with contributions from both subducted sediments and dehydration reactions of seawater-altered lithospheric amphibolite, contributed in part to some of the features of the BVF geochemistry, particularly isotope ratios more akin to DEZ-affected lavas than the normal SVA rocks. However, this process alone cannot account for the extreme and distinctive enrichments in Sr and P_2O_5 in the BVF basalts. Addition of Sr and P_2O_5 to the mantle wedge peridotite by carbonatite metasomatism prior to BVF parent melt generation, is invoked as a likely source of these anomalous element abundances in the Efaté basalts. The highly reactive carbonatite magmas never reached the surface but modified the mantle wedge source peridotite (specifically enriching Sr and P) from which the BVF parental magmas were subsequently generated. Derivation of the HKRS parental basalts from zones of prior enrichment in the mantle wedge gave rise to the distinctive elevated K_2O and Rb values in the erupted lavas. Figure 5.14 is a schematic representation of the likely multi-component petrogenetic evolution of the Efaté BVF lavas.

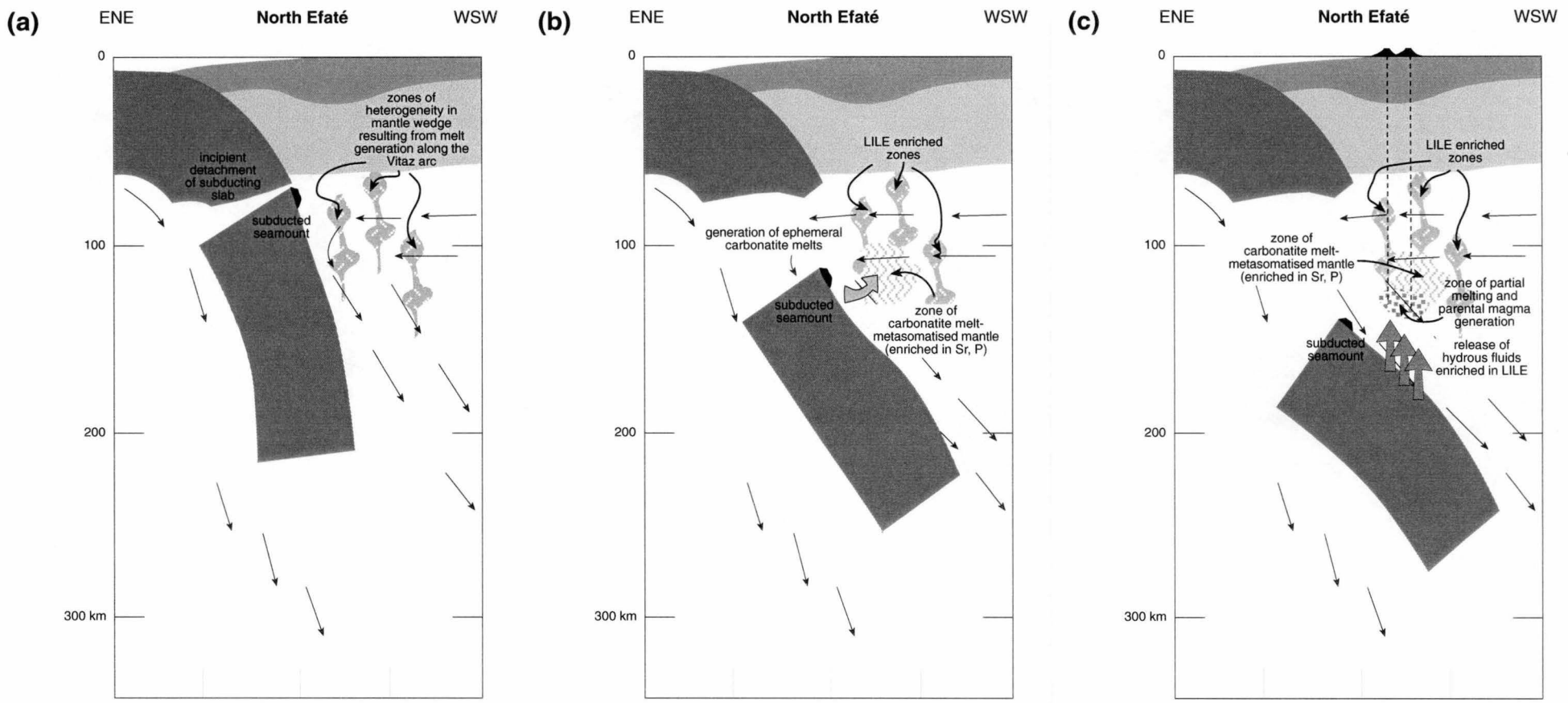

Figure 5.14. Schematic representation of the petrogenesis of Efaté BVF lavas. (a) Incipient detachment of downgoing slab in Efaté region, note areas of hetergeneity (LILE enrichment) in the mantle wedge resulting from prior subduction and melt generation along the Vitiaz arc. (b) Ephemeral carbonatite partial melts metasomatise the mantle wedge source, notably causing local enrichments of Sr and P. (c) Subsequently, hydrous fluids released by the breakdown of amphibolite in the subducting slab initates partial melting of this modified mantle wedge peridotite, generating primitive basaltic magmas. The hydrous fluid is enriched in LILE, which then become concentrated in the partial melts, and impoverished in HFSE which are retained in a refractory eclogite residual. Some parental melts are generated in areas of LILE enriched mantle wedge, further enhancing the K and LILE signature of the HKRS basalts. These processes combine to give the BVF lavas their subduction zone geochemical signature and their characteristic enrichments in Sr and P_2O_5 relative to 'normal' southern Vanuatu arc (SVA) lavas. Modified from Monzier *et al.*, (1997).

Implications

The occurrence of extreme enrichments of Sr in the Vanuatu arc is not unique to the Efaté basalts. North of the collisional DEZ at Santa Maria (Gaua) Island (see Vanuatu arc map, Fig. 2.2), absolute abundances of Sr in basalts range from 860-1030 ppm. Additionally, P_2O_5 values in these lavas reach up to 0.47 % (Robin *et al.*, 1995). Some similarly high Sr and P_2O_5 contents also occur within the collision zone, although on average values are lower (Sr<800 ppm and P_2O_5<0.35 % Monzier *et al.*, 1997). The volcanic and geochemical evolution of these two centres is different, with andesite and basaltic andesite compositions dominating early in the Santa Maria pyroclastic sequence, compared with trachydacites at Efaté (Robin *et al.*, 1995). However, there is a broad correlation between high Sr contents in late stage basalts following the eruption of more differentiated magmas. The West Torres Massif is impinging upon the Vanuatu trench at Santa Maria and, like the Efaté Island Group, this island also sits above a gap in seismicity adjacent to the collision zone (Fig. 2.4). The similarities in local tectonics and geochemistry imply that similar processes caused the enrichments of Sr and P_2O_5 in the Santa Maria lavas.

CONCLUSIONS

The geochemical signature of the Efaté basalts is atypical of normal Vanuatu subduction zone magmas, and intraoceanic arc magmas in general. The Efaté BVF are divided into three suites based on temporal (MLS, OSS) and geochemical differences (HKRS). Enrichments in Sr and P_2O_5 in all three suites are accompanied by variable enrichments in other LILE (Cs, Rb, Ba, Th) and LREE in these low SiO_2 basalts, relative to 'normal' Vanuatu arc basalts, represented by lavas from volcanoes on Tanna and Erromango islands to the south. These characteristics are best explained by the combined effects of carbonatite metasomatism of the mantle wedge prior to melt extraction, together with variable contributions from a local sediment component and seawater-altered crust, generating enriched hydrous fluids which subsequently initiated or facilitated partial melting. Notable enrichment of K and Rb in some rocks from Emau Island is attributed to heterogeneity in the mantle wedge source imparted by magma extraction during the pre-existing Vitiaz arc subduction regime.

Local tectonic conditions are clearly important in controlling the petrogenesis of the BVF magmas. Specifically, the subduction of a seamount in the Efaté region provides firstly, a highly variable sediment component necessary to explain enrichments of some elements and Pb-isotope ratios, and secondly, a source of seawater-altered lithosphere necessary to generate radiogenic $^{87}Sr/^{86}Sr$ values, and further enhance existing Sr enrichments.

Chapter Six

GEOCHEMICAL CHARACTERISTICS OF THE EFATE PUMICE FORMATION, VANUATU

Petrogenesis of a trachydacitic magma chamber in an island arc environment

INTRODUCTION

Although basaltic volcanism is dominant throughout the Vanuatu arc, dacitic magma compositions are known from several centres, particularly in the central islands from Ambrym through to Efaté. Bimodal associations of dacite and basalt only occur at Efaté and off the coast of Epi island, but the composition of the dacites at the two locations are quite different. At all other centres a spectrum of compositions through basaltic andesite and andesite, to dacite is represented. Additionally, the bulk volume of the dacitic volcaniclastics at Efaté is also far in excess of dacitic products elsewhere in the Vanuatu arc, where volumes are generally subordinate to the volume of less evolved basaltic and basaltic andesite products (*e.g.* Robin *et al.*, 1994a).

The volcanic origin and sedimentology of the pumice breccia and sand beds from the Efaté Pumice Formation (EPF) are described in detail in Chapters Three and Four. The EPF deposits are divided into two distinct units: a lowermost unit called the Efaté Pumice Breccias and an upper unit called the Rentabau Tuffs. The Efaté Pumice Breccias are coarse, subaqueous, syn-eruptive, mass-flow deposits generated by a sustained, cataclysmic, caldera-style eruption (Chapter Three). Resulting from the same eruption, the overlying Rentabau Tuffs are syn- and post-eruptively deposited, coarse and fine pumiceous and shard-rich sand and silt facies that contain foraminfera tests (Chapter Four). The geochemical characteristics of the both the Efaté Pumice Breccias and the Rentabau Tuffs are remarkably uniform, in keeping with the syn-eruptive, and immediately post-eruptive nature of these deposits.

One of the difficulties in assessing the petrogenesis of any erupted magma, but particularly with highly evolved magmas, is the variety of processes which have affected the evolution of the magma *en route* to the surface. Although the complications of assimilation of continental crust are removed in oceanic island arc terrains, a variety of other open and closed system processes can occur at any stage during magmatic evolution which in turn impacts the geochemical signature of the erupted magmas. Closed system fractional crystallisation can explain the genesis of some highly evolved

dacitic and rhyolitic magmas in island arcs for which relatively simple geochemical schemes exist. However, fractional crystallisation may be accompanied by processes such as magma mixing, (oceanic) crustal assimilation, phenocryst accumulation and magma chamber tapping and recharge. Furthermore metasomatic processes and/or prior melt extraction may introduce heterogeneity into the trace element signature of the mantle wedge source. All of these processes are increasingly recognised as playing a significant role in the genesis of more geochemically complex magma systems. The following chapter discusses the petrogenesis of the EPF volcaniclastic units, in relation to the dominant processes occurring over the history of this evolving magma batch.

PETROLOGY OF THE EFATÉ PUMICE FORMATION

Petrography

The volcaniclastic sediments are rich in texturally unmodified juvenile volcanic clasts. In the Efaté Pumice Breccias facies, and coarser facies of the Rentabau Tuffs, pumice clasts are hosted in a matrix component of glass shard-rich sand. In the fine-grained facies (interbeds in the Efaté Pumice Breccias and the Rentabau Tuffs sands and silts), glass shard- and crystal-rich sands dominate. Pumices are typically fibrous, tube pumice fragments and range from white to grey. These are typically aphyric but irregular and round vesicle pumice clasts are weakly porphyritic (generally <10 % phenocrysts), and major mineral phases include plagioclase feldspar (3-7 %), ortho- and clinopyroxene (1-2 %), and ubiquitous Ti-magnetite microcrysts and phenocrysts (1-3 %). Accessory phases, which include stubby to prismatic apatite laths and acicular ilmenite, occur as small crystalline inclusions in plagioclase and pyroxene phenocrysts. Discrete apatite laths also occur randomly throughout the samples. Glass shards in the fine-grained facies, and in the matrix component of the pumice breccias, vary from blocky to cuspate to delicate bubble wall shards. In these shard-rich sand and silt facies, crystals commonly occur as discrete and anhedral clasts, commonly with fine glassy mantles. Hydrous phases are notably absent from the mineral assemblage for all units of the EPF. Representative mineral analyses are given in Table 6.1, and a complete data set in Appendix J.

Plagioclase

Plagioclase phenocrysts are euhedral to subhedral, occur as discrete large tabular laths (2-3 mm, up to 7 mm) and glomerocrysts, commonly contain glassy inclusions, and are typically unzoned. Crystal compositions for the Efaté Pumice Breccias span the andesine range from Ab_{49}-Ab_{65} and are fairly evenly spread across the interval (Fig. 6.1). Minor peaks occur at ~Ab_{60}, Ab_{55} and Ab_{50} (Fig. 6.1 a). The plagioclase compositions from the

Table 6.1. Representative mineral analyses for phenocrysts from the Efaté Pumice Formation (EPF): Efaté Pumice Breccias (EPB) and Rentabau Tuffs (RT).

Plagioclase	EPB				RT
oxide (wt%)	core	rim			
SiO_2	56 99	58 44	57 42	59 48	57.53
TiO_2	0 03	0.03	0 04	0 02	0 05
Al_2O_3	26.25	25.30	26 64	25 28	26.03
Fe_2O_3	0 69	0.61	0 75	0 52	0.56
MgO	0.02	0.05	0 06	0 03	0.05
CaO	8 55	7.19	8 28	6 91	8 44
Na_2O	5 87	6 35	6.14	6 91	6 06
K_2O	0 72	1 02	0.78	1.08	0.64
Total	99.34	99 09	100.36	100 71	99 46
Ab (%)	53.03	57 98	54 66	60 40	54 36
An (%)	42 65	36 10	40 73	33 33	41 85
Or (%)	4 32	6 02	4 61	6 27	3 79

Ti-magnetite	EPB			RT
oxide (wt%)				
SiO_2	0.02	0 05	0 08	0.12
TiO_2	13 58	11.94	12.36	11.61
Al_2O_3	2 50	2.30	2 49	2.73
Cr_2O_3	0 02	0.04	0 02	0 02
Fe_2O_3(c)	42 68	43 75	43.06	43 09
FeO(c)	39 24	37 43	38 54	36 15
V_2O_3				0 08
MnO	0 73	1 04	0 82	0.70
MgO	2 23	2 48	2 26	2.54
ZnO	0 10		0.12	0.19
NiO	0 05		0.02	0 06
Total	98 05	99.04	99.76	96.91

Orthopyroxene	EPB							RT			
oxide (wt%)											
SiO_2	53 29	52 84	53 61	53 20	53.15	53.24	52.43	52 65	52 97	52 75	52 90
TiO_2	0 21	0 22	0 18	0 22	0 23	0.20	0 22	0 31	0.25	0 25	0 23
Al_2O_3	0.56	0.42	0.63	0.60	0 82	0.57	0 54	0.60	0.39	0 53	0 63
Cr_2O_3	0 02			0.02	0 03			0 02	0.02		0 02
Fe_2O_3(c)	0 55				1 64	1.97	1 47				
FeO(c)	19 28	21 75	17 59	19 33	17.85	18.11	20 39	20 41	18 66	18 23	17.97
MnO	1.33	1 48	0 94	1 23	1 38	1 56	1.39	1 29	1 70	1 25	1 14
MgO	22 97	21.17	23 83	22 64	23 80	23 49	21.75	21.39	22.33	22 66	22 86
CaO	1.63	1.63	1 63	1 67	1 52	1 61	1 62	1.64	1.61	1.51	1.77
Na_2O	0 04	0.04	0 04	0 04	0 03	0 04	0 05	0.04	0 03	0 02	0 01
K_2O	0.01		0 01			0.01		0 02	0 01		0 02
Total	99 90	99 55	98.48	98.97	100 45	100.82	99.87	98 38	97.98	97 20	97 54
Wo (%)	3.27	3 33	3.32	3 40	3 00	3 14	3.25	3 37	3 31	3 12	3 63
En (%)	63 82	59 82	67 29	63 98	65 17	64 06	60.61	61 57	63 97	65 34	65 58
Fs (%)	32 91	36 85	32 29	32 62	31 83	32 80	36.14	35.06	32.72	31.54	30.79
Mg_{opx}	67 45	63 42	70 70	67 61	68 70	67 81	64 10	65.14	68 10	68 89	69 41

Clinopyroxene	EPB							RT			
oxide (wt%)											
SiO_2	51 03	51 68	51 72	51 30	50.77	51 98	50 35	49.00	49.81	51 51	51 79
TiO_2	0 43	0.44	0 40	0 47	0.50	0 43	0 58	0 45	0.55	0.50	0.43
Al_2O_3	1 88	1.36	1 39	1 27	1.93	1.17	2.21	4 43	3.73	1 59	1.42
Cr_2O_3	0.02					0 01	0.01		0.04	0 04	
Fe_2O_3(c)	4.14	4.09	3 45	3 62	1 79	4 03	3 05	3.81	2.71	1.49	0.65
FeO(c)	5 77	5 28	6.06	7 69	9 14	6 24	7 63	3.98	5 30	8.05	7 91
MnO	0 73	0.74	0.71	1 05	0 68	0 85	0 68	0 19	0.17	0 61	0 65
MgO	15 26	15 26	15.29	14 30	14 55	15 10	14 10	14 19	14 38	14 82	14.66
CaO	20 22	21 21	20 73	20 33	18 63	20 79	20 01	22 28	21.58	19.85	20.21
Na_2O	0 39	0 37	0.35	0.43	0.33	0.40	0.35	0 22	0 28	0 32	0 37
K_2O	0 01	0 02		0 02		0.02				0 01	
Total	99.84	100 47	100 11	100 64	98.32	101 03	98 98	98 54	98.56	98 79	98.09
Wo (%)	40 93	42 40	41 70	40 97	38 97	41 44	41.48	46.46	45 14	41 10	42 33
En (%)	42 91	42 44	42 76	40.11	42 37	41.84	40.61	41.18	41 97	42 69	42 69
Fs (%)	16 16	15 16	15 54	18 92	18 66	16 72	17 91	12.36	12.99	16 21	14.98
Mg_{cpx}	74.10	75.20	74 76	69.10	73.97	73.15	70.77	77.36	76 76	73 76	75.46

For plagioclase, Ab% = 100[Na/(Ca+Na+K)], An% = 100[Ca/(Ca+Na+K)], Or% = 100[K/(Ca+Na+K)]; for pyroxenes, Wo% = 100[Ca/(Mg+Fe*+Ca)], En% = 100[Mg/(Mg+Fe*+Ca)], Fs% = 100[Fe*/(Mg+Fe*+Ca)], where Fe* is (Fe^{2+}+Fe^{3+}+Mn), and $Mg_{opx/cpx}$ = 100[Mg/Mg+Fe)], Fe_2O_3(c) and FeO(c) calculated on the basis of 4 cations for 6 oxygen atoms.

Rentabau Tuffs have a similar distribution, but slightly lower albite contents overall. A single crystal in sample AR101 from the Rentabau Tuffs has high anorthite core and rim contents (An_{86}, An_{77} repectively) and is probably a xenocryst (Fig. 6.1). The plagioclase phenocrysts commonly have glassy mantles, or are hosted in less vesicular glassy patches within pumice clasts. Glass inclusions are large (0.25-0.5 mm), vary from colourless to pale brown, and occur principally as irregular, or cleavage-bounded, blebs in the centre of crystals. Glass inclusions and glassy mantles typically have compositions no different from the host matrix glass, but at least two analyses have trachyandesite compositions (Fig. 6.3; Appendix K).

Pyroxenes

Euhedral to subhedral pyroxene grains may occur as small, pale green-yellow, discrete phenocrysts (~0.5-2 mm), or as a subordinate phase in plagioclase-rich glomerocrysts. Pyroxene grains commonly appear grouped closely together with Ti-magnetite grains, but generally not as glomerocrystic clusters. Clino- and orthopyroxene phenocrysts comprise approximately equal proportions of the pyroxene assemblage, except in sample AR084 in which orthopyroxene dominates. Crystals are unzoned, contain euhedral Ti-magnetite inclusions, acicular ilmenite needles, and, less commonly, apatite inclusions. None of the pyroxenes show any evidence of mineral overgrowths.

Figure 6.2 shows the variation in pyroxene compositions in the EPF. In Efaté Pumice Breccias samples, clinopyroxenes are all augites with Mg_{cpx} = 69-76 with a major peak at Mg_{cpx} = 75. Orthopyroxene crystals have compositions varying from $Wo_3En_{67}Fs_{30}$ to $Wo_3En_{58}Fs_{39}$, and Mg-numbers peaking at Mg_{opx} = 68 and ranging from Mg_{opx} = 62-72. Augitic clinopyroxenes in the Rentabau Tuffs sample show a similar pattern to Efaté Pumice Breccias clinopyroxenes, but with Mg_{cpx} more tightly clustered (Mg_{cpx} = 72-78). Two more Ca-rich diopside analyses ($Wo_{47}En_{41}Fs_{12}$ and $Wo_{45}En_{42}Fs_{13}$) may be xenocrysts. Compositions of Rentabau Tuffs orthopyroxenes are very similar to those from the Efaté Pumice Breccias, and vary from $Wo_4En_{66}Fs_{30}$ to $Wo_3En_{62}Fs_{35}$, with Mg_{opx} = 66-70 (Fig. 6.2; Appendix J).

Ti-magnetite

Small Ti-magnetites (50-500 μm) are principally associated with pyroxenes, occurring as inclusions and along fractures and crystal boundaries. Microphenocrysts of Ti-magnetite occur as euhedral to subhedral polyhedra in most samples and are typically associated with ferromagnesian minerals. Ti-magnetite compositions are restricted to TiO_2 contents around ~12 %, and show little variability (Table 6.1). They are strongly oxidised with compositions falling halfway between the ulvöspinel-magnetite and the ilmenite-hematite solid solutions (Fe_2O_3 contents range from 45-47 %; Appendix J).

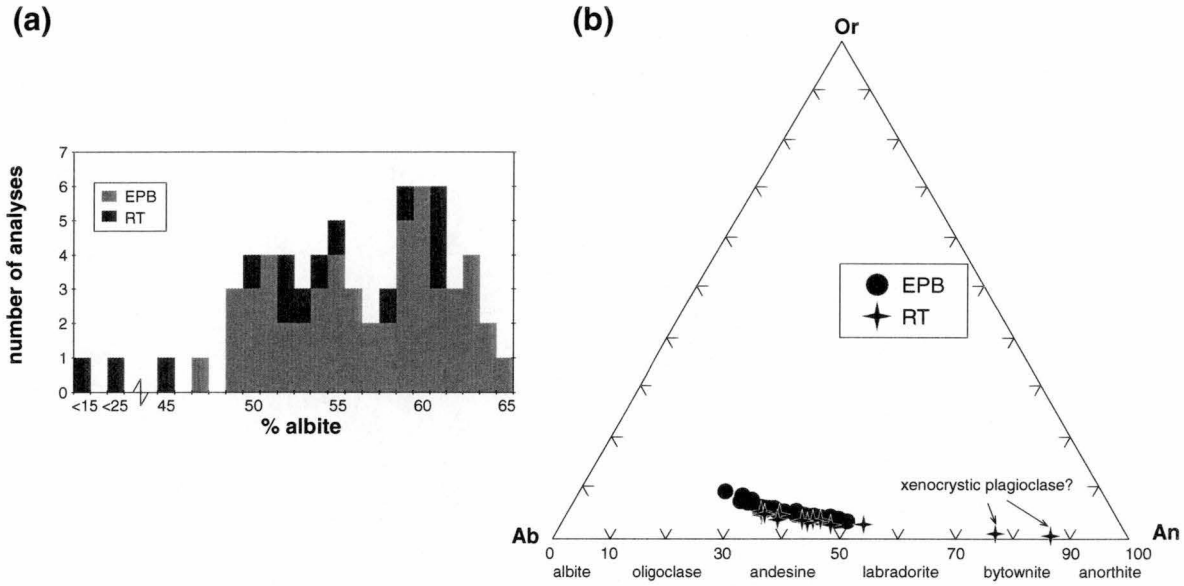

Figure 6.1. Plagioclase feldspar phenocryst compositions for Efaté Pumice Formation, EPB = Efaté Pumice Breccias, RT = Rentabau Tuffs. (a) Frequency histogram showing albite content, and (b) ternary diagram showing feldspar compositional spectrum. Note: two analyses from RT have high anorthite content and are probably from a xenocryst.

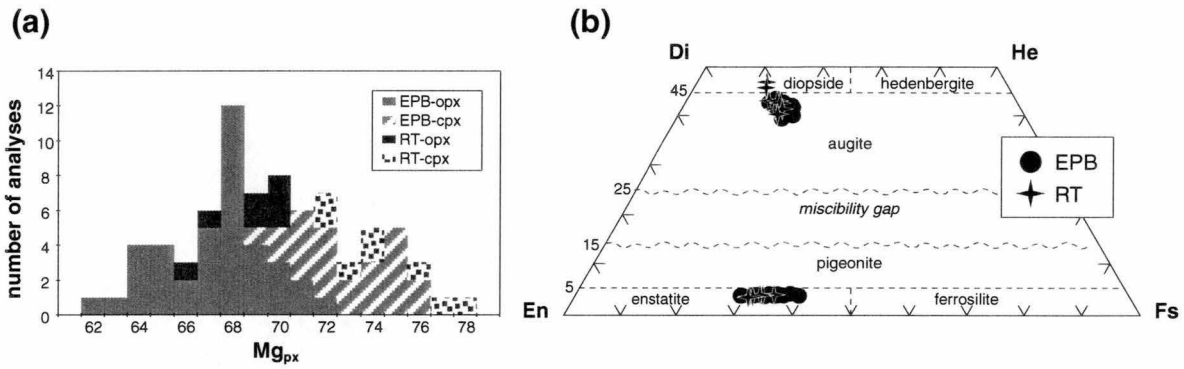

Figure 6.2. Pyroxene phenocryst compositions for Efaté Pumice Formation, EPB = Efaté Pumice Breccias, RT = Rentabau Tuffs. (a) Frequency histogram showing Mg_{px} for both clino- and orthopyroxene. (b) Pyroxene compositions on the pyroxene quadrilateral, after Morimoto (1989). Note diopside compositions for two RT analyses which may be xenocrysts.

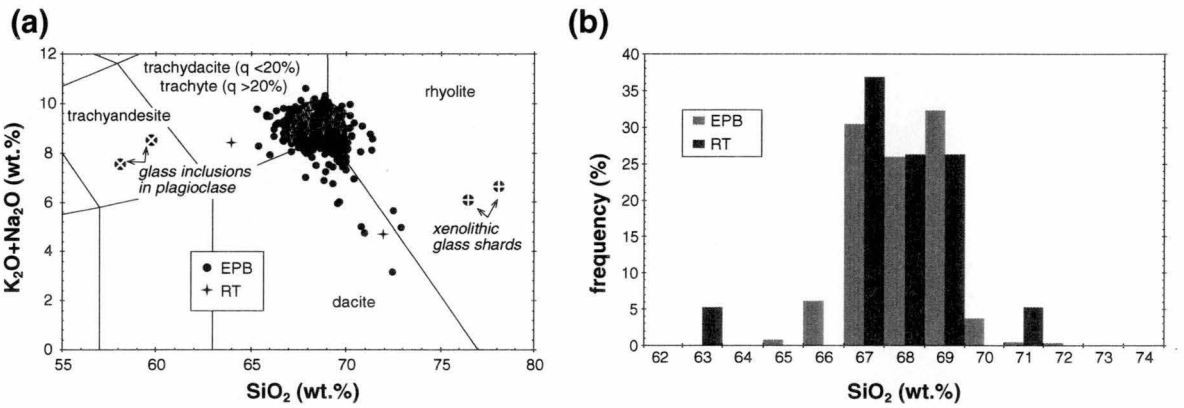

Figure 6.3. Microprobe glass shard compositions for Efaté Pumice Formation, EPB = Efaté Pumice Breccias, RT = Rentabau Tuffs. (a) The majority of compositions fall into the trachydacite field on the total alkali versus SiO_2 diagram of Le Bas *et al.* (1986), with (b) SiO_2 contents clustered around 68 wt.%, and with strong bimodal peaks at 67 and 69 wt.% for the EPB.

Accessory phases

Stubby to elongate apatite needles (~10 μm diameter) occur principally as inclusions within both plagioclase and, less commonly, pyroxene phenocrysts. Very fine (<2 μm diameter) ilmenite needles occur as inclusions in plagioclase phenocrysts.

Geochemistry

Glass chemistry

Figure 6.3 shows the range of compositions of glass shard analyses for EPF sediments. Shards and pumice vary widely in morphology, colour, and size yet show no apparent geochemical grouping. Low totals for glass analyses are attributed to dissolved water content of the glasses as well as less significant effects due to analytical difficulties inherent in electron microprobe analysis of alkaline silicic glasses (Dugmore *et al.*, 1992; Hunt & Hill, 1993; Martel *et al.*, 2000). The field defined by the EPF analyses straddles the boundary between the trachydacite-dacite-rhyolite field and a few samples fall to low $K_2O + Na_2O$ contents (<5 %, Fig. 6.3). Glass compositions have slightly higher SiO_2 contents than representative whole rock data, with the majority of analyses falling into the trachydacite field. Only two departures from trachydacite compositions are noted. Two rhyolitic analyses from sample AR065 with SiO_2 >77 weight % are probably xenolithic shards, demonstrating the pronounced geochemical homogeneity of these volcaniclastic sediments. Also plotted are two trachyandesitic analyses from glass inclusions within plagioclase phenocrysts, which are probably early, trapped melts from the evolving magmatic system (Stamatelopoulou-Seymour *et al.*, 1990; Della-Pasqua, 1997; Lee & Stern, 1998). Most glass inclusions are geochemically indistinguishable from juvenile glass shard compositions. Table 6.2 lists some representative electron microprobe glass analyses; analytical conditions and a complete data set are given in Appendix K.

Table 6.2. Representative electron microprobe analyses for Efaté Pumice Formation (EPF) glasses.

STRATIGRAPHIC UNIT	EPB									RT
SAMPLE	AR024-62	AR037-46	AR062-28	AR063-54	AR064-46	AR076-4	AR077-2	AR084-6	LI961-7	AR101-9
SiO_2	66 58	68 71	69 05	69 05	69 06	67.64	68.10	69.23	68 69	67.15
TiO_2	0.74	0.52	0.48	0 39	0.64	0 54	0.34	0.50	0.53	0 67
Al_2O_3	16.15	16.04	16.26	16.78	16 30	16.12	16.01	16.35	16 12	16.19
FeO*	3.62	2 92	2.48	2.47	2.31	2.52	2.57	2.78	2 86	3.48
MnO	0.16	0.10	0.13	0.14	0.12	0.17	0.09	0.10	0.15	0.09
MgO	0.85	0.62	0.50	0 64	0.51	0.57	0.57	0.57	0.62	0 99
CaO	2.14	1.55	1 34	1.53	1.34	1.66	1.68	1 64	1.70	2 24
Na_2O	4.24	4.08	3 75	3.85	3 90	4.43	4.34	3.35	3.77	4 27
K_2O	4.92	5.07	5 63	4.77	5.47	5.69	5 56	5.15	5.19	4.40
P_2O_5	0.19	0 06	0.11	0.11	0 10	0.13	0 14	0.00	0.05	0.13
Totals	97.34	94 59	95.55	94.79	96.29	96.50	94.98	94 43	97.09	94 96

Major element data recalculated to 100 %. EPB = Efaté Pumice Breccias, RT = Rentabau Tuffs.

Table 6.3. Whole rock analytical data for Efaté Pumice Formation juvenile volcanic clasts.

SAMPLE	AR064	AR066	AR073gs	AR073wr	AR079	AR093	AR098	AR207gs	AR207wr	MI[a]	L51[b]	L52[b]	VA35[c]	VA48[c]	EA303[d]	EA230[d]	EA200[d]	EA310[d]	EfC45[d]	Moy (7)[e]	V12[e]	BOK11[f]
Major Elements (wt%)																						
SiO_2	64 29	64 51	65 63	65 63	65 92	63 92	66 00	66 93	66 93	66 13	67 28	67 67	67 70	66 27	68 25	68 93	62 54	68 13	67 63	67 34	66 67	67 76
TiO_2	0 60	0 64	0 55	0 55	0 56	0 54	0 59	0 56	0 56	0 73	0 77	0 83	0 63	0 52	0 48	0 59	0 74	0 42	0 52	0 58	0 59	0 62
Al_2O_3	16 97	16 83	15 72	15 72	16 28	15 98	15 98	15 92	15 92	16 47	15 64	15 42	16 88	16 32	15 13	15 40	18 24	15 54	14 92	15 76	15 97	15 35
FeO*	4 33	4 41	3 56	3 56	3 41	3 80	3 86	3 26	3 26	1 36	3 71	4 10	3 46	3 79	2 89	2 79	3 76	2 63	3 15	3 20	3 39	3 24
MnO	0 14	0 13	0 11	0 11	0 12	0 16	0 12	0 13	0 13	0 00	0 08	0 10	0 12	0 11	0 12	0 14	0 09	0 10	0 71	0 11	0 11	0 12
MgO	1 42	1 38	1 29	1 29	0 95	1 88	1 23	0 86	0 86	1 19	0 73	0 82	0 68	1 13	1 05	1 00	0 78	0 64	0 62	0 79	0 95	0 74
CaO	3 12	3 03	2 54	2 54	2 11	2 57	2 42	1 83	1 83	3 15	2 05	2 38	3 35	3 09	2 11	1 93	1 63	1 88	1 27	1 81	1 90	1 87
Na_2O	4 20	4 11	5 03	5 03	5 11	6 55	4 36	4 89	4 89	4 50	4 59	3 88	3 77	3 50	2 90	4 10	5 72	4 43	5 28	4 73	2 50	4 62
K_2O	4 23	4 27	4 99	4 99	4 98	4 01	4 87	5 12	5 12	3 39	4 85	4 62	4 63	4 91	6 55	4 90	5 99	6 08	5 63	5 40	7 63	5 09
P_2O_5	0 22	0 21	0 18	0 18	0 17	0 17	0 15	0 14	0 14	0 10	0 09	0 07	0 23	0 17	0 34	0 09	0 15	0 10	0 10	0 16	0 14	0 21
LOI	*5 92*	*6 06*	*5 43*	*5 43*	*1 29*	*10 44*	*6 30*	*5 18*	*5 18*	*4 18*	*1 74*	*3 32*	*3 00*	*4 02*	*5 90*	*6 33*	*1 19*	*1 60*	*1 80*	*2 03*	*6 16*	*3 10*
Totals	99 60	99 54	99 59	99 59	99 64	99 65	99 86	99 64	99 64	100 35	100 23	100 09	98 06	99 73	99 08	99 45	99 97	102 00	100 16	98 74	99 22	99 17
Mg#	36 31	35 25	38 54	38 54	32 52	46 28	35 67	31 40	31 40	33 01	25 51	25 73	25 59	34 12	38 75	38 39	26 52	29 62	25 54	29 91	32 70	28 40
Trace Elements (ppm)																						
Rb	85 6	87 6	103 7	97 7	103 3	79 2	90	96 9	97 8													103
Sr	468	411		325	340	396	295		308													356
Cs	1 41	1 44	1 64	1 54	1 63	1 31		1 46	1 51													
Ba	1052	1055		1068	1176	974	1264		1106													1120
Sc	9 21	8 67	6 40	6 92	7 50	7 64	9	7 15	7 13													
V	60	77		42	47	31	47		32													41
Cr	3	4		4	2	2	7		2													
Ni	2	3		9	1	1	4		1													
Cu	68	61		38	22	35	31		16													
Zn	67	73		62	66	62	69		66													
Mo	4 86	4 85	5 86	5 56	5 85	5 05		5 27	5 56													
Sn	1 61	1.96	2 04	1 65	1 91	1 57		2 32	2 01													
La	23 1	22 7	27 2	24 3	26 1	20 4	22	27 7	26 6													
Ce	46 3	45 5	53 0	48 6	51 7	41 4	54	55 6	51 9													
Pr	5 74	5 59	6 53	5 90	6 16	5 02		6 93	6 44													
Nd	23 21	22 46	26 49	23 58	24 99	20 70	27	28 27	25 69													
Sm	5 04	4 86	5 47	5 04	5 29	4 53		6 10	5 52													
Eu	1 31	1 22	1 19	1 16	1 23	1 23		1 42	1 28													
Gd	4 42	4 17	4 78	4 40	4 55	4 04		5 37	4 85													
Tb	0 71	0 68	0 76	0 70	0 74	0 67		0 85	0 78													
Dy	4 13	4 00	4 58	4 17	4 43	3 95		5 05	4 66													
Ho	0 87	0 85	0 96	0 91	0 95	0 83		1 08	1 01													
Er	2.60	2 57	2 87	2 75	2 86	2 51		3 25	3 07													
Tm	0 40	0 40	0 44	0 43	0 44	0 39		0 50	0 48													
Yb	2 74	2 73	3 10	2 95	3 08	2 64		3 39	3 30													
Lu	0 40	0 41	0 45	0 44	0 47	0 40		0 51	0 49													
Y	23 7	23 4	26 7	24 3	25 9	22 6	26	29 1	27 5													
Zr	183	190	211	201	214	159	207	200	204													
Nb	5 18	5 28	5 99	5 70	6 03	4 17	6 2	5 49	5 55													
Hf	4 82	5 11	5 70	5 55	5 88	4 42		5 49	5 53													
Ta	0 29	0 30	0 33	0 34	0 34	0 24		0 32	0 32													
Tl	0 26	0 27	0 29	0 27	0 29	0 25		0 28	0 28													
Pb	13 2	13 7	15 5	14 9	15 3	11 3	16 0	16 1	16 0													
Th	7 07	7 08	7 59	7 51	7 54	5 30	7 1	7 69	7 81													
U	2 32	2 39	2 27	2 71	2 80	1 94	2 8	2 65	2 66													

Major element data (recalculated to 100 wt.% volatile free) measured by XRF, and trace element data measured by both XRF (Ni, Cr, V, Sc, Zr, Nb, Y, Sr, Ba, Rb, Cu, Zn, Pb, U and Th) and ICP-MS (Sc, Zr, Nb, Sr, Ba, Rb and Pb and all other trace elements). Data derived by ICP-MS are reported for samples where both methods were used. Bold type denotes new analyses first reported in this thesis, other data sources are: a from Mawson (1905); b from Lacroix (1940); c from Obellianne (1958); d from Ash *et al.* (1978); e average values from Coulon *et al.* (1979) where numbers in parentheses indicate number of samples from which average is derived; and f from Melchior (1989). LOI = loss on ignition; FeO* is total Fe as Fe^{2+}; Mg #=100[Mg^{2+}/(Mg^{2+}+Fe*)] where Fe* is total Fe.

Juvenile clast whole-rock chemistry

Nine new whole rock XRF analyses are investigated here together with the few existing analyses of juvenile clasts from the EPF (Table 6.3, Mawson, 1905; Lacroix, 1940; Obellianne, 1958; Ash *et al.*, 1978; Coulon *et al.*, 1979; Melchior, 1989). Trace element concentrations were analysed for both whole rock and glass separates for samples AR073 and AR207. All data are recalculated to 100 weight % on a volatile-free basis. Analytical conditions are outlined in Appendix F. Samples range from individual pumice clasts, to bulk pumiceous sediment, perlitic obsidian clasts and dense porphyritic clasts (Table 6.4). A group of representative electron microprobe major element analyses of fresh glass from shards and pumices from the Efaté Pumice Breccias are presented with the whole rock data, in order to fully characterise the geochemical signature of the EPF.

Table 6.4. Variety of clast types analysed for EPF whole rock geochemistry.

CLAST TYPE	SAMPLE NUMBER
individual pumice clast	AR073, AR098, AR207
bulk pumiceous sediment sample	AR064, AR066, AR093
perlitic obsidian clast	AR079, Mi, L52, VA35, VA48, EA230, Moy (7), V12
dense porphyritic clast	L51, EA200, EfC45, EA310, BOK11
eutaxitic texture/welded tuff?	EA303

Major elements

On the total alkalis versus SiO_2 (TAS) diagram, juvenile clasts from the EPF mostly fall into the trachyte/trachydacite field with a few glass analyses falling into the rhyolite field. The juvenile particles have normative quartz contents consistently less than 15 %, so can be classified as trachydacites. They fall within the boundaries proposed by Rickwood (1989) on the same diagram and can be classed as transitional alkaline/subalkaline magmas (Fig. 6.4 a). The high K_2O content of the trachydacites places them in the shoshonite series on the K-series discrimination diagram of Peccerillo and Taylor (1976), and also among the highest K_2O rocks in the Vanuatu arc (see also Barsdell *et al.*, 1982; Robin *et al.*, 1995; Baker & Condliffe, 1996). Plotted on the same diagram are compositions of the Efaté basalts (Chapter Five) and two other Vanuatu arc suites. A suite of rocks from Tanna in the 'normal' southern part of the arc trend towards high-K/shoshonitic compositions (Crawford and Eggins, unpublished data, Robin *et al.*, 1994a). In contrast, a suite from the Kuwae caldera eruption in the central part of the arc has medium-K trends overall (Monzier *et al.*, 1994; Robin *et al.*, 1994b). Comparing these suites with the Efaté rocks highlights the extreme and unusual bimodality of compositions distinctive at Efaté (Fig. 6.4 b). Major and trace elements are plotted against SiO_2 over the range 44-70 %, in order to show the range of compositions present at Efaté (Fig. 6.5-6.6). Basalts are plotted as the three suites, Mainland Suite (MLS), Offshore Suite (OSS) and High-K/High-Rb Suite (HKRS), identified in Chapter

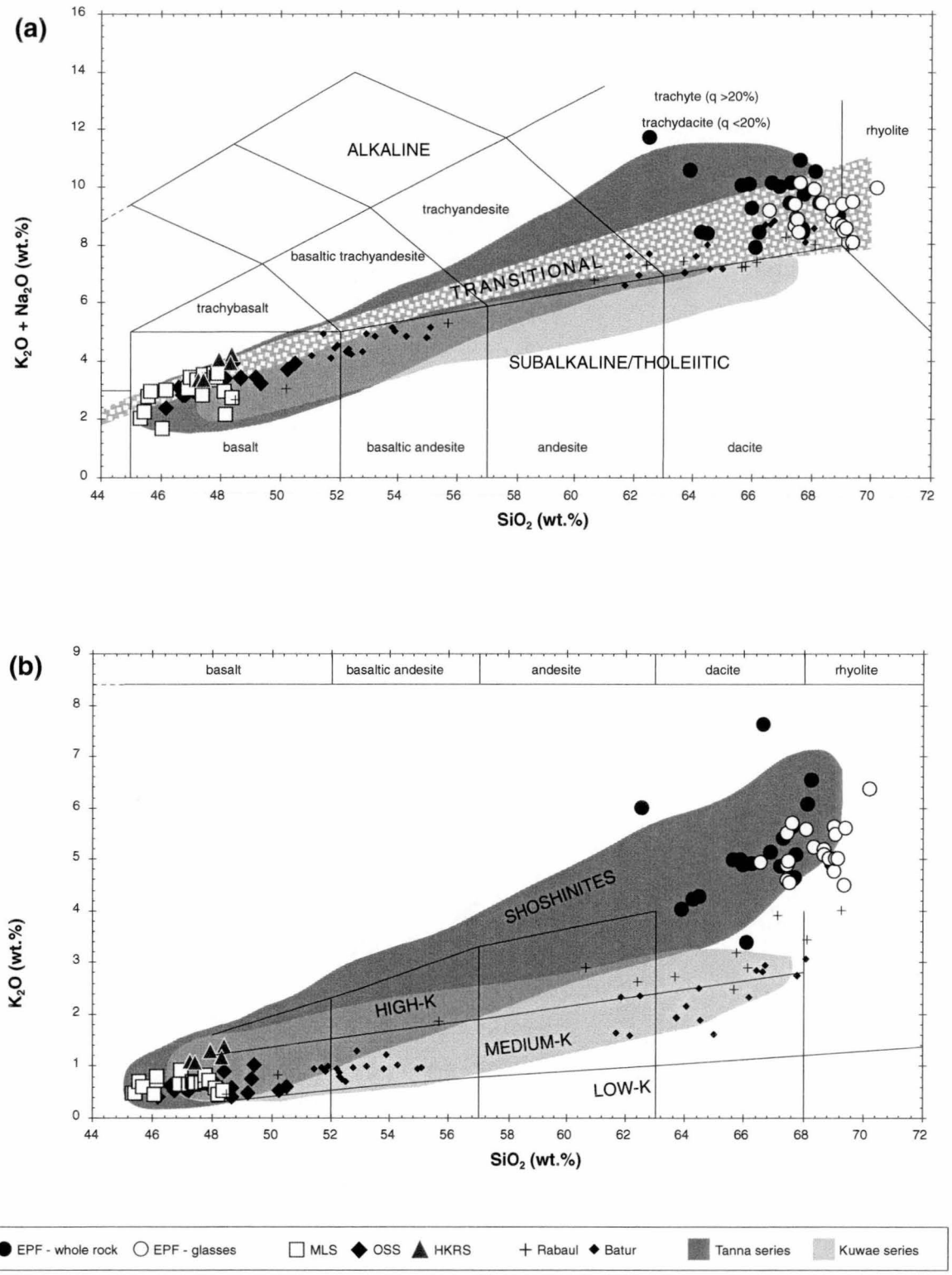

Figure 6.4. Geochemical classification of the Efaté Pumice Formation (EPF) volcaniclastic sediments. (a) The EPF sediments plot in the trachydacite field on the total alkali vs. SiO_2 diagram (TAS, Le Bas *et al.*, 1986), and have (b) shoshonitic characteristics as shown on the K_2O vs. SiO_2 diagram of Peccerillo and Taylor (1976). Note the gap from 51-63 % SiO_2 for the Efaté suite, which contrasts with a much narrower gap from 56-62 % SiO_2 for the bimodal Batur suite.

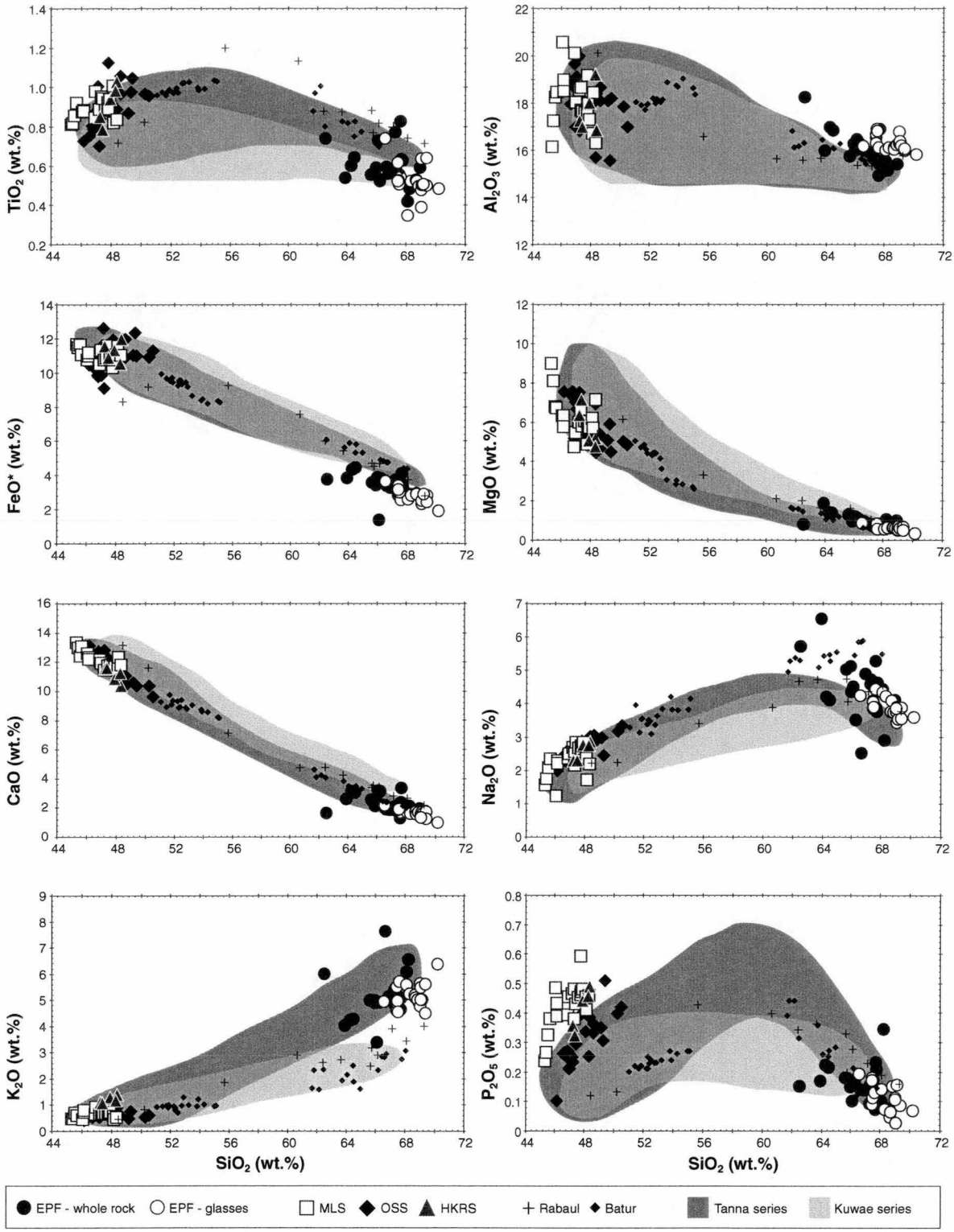

Figure 6.5. Major element covariation diagrams plotted against SiO_2 wt.% for Efaté Pumice Formation (EPF) volcaniclastic sediments, together with the Basalt Volcanoes Formation lavas discussed in Chapter Seven (MLS = Mainland Suite, OSS = Offshore Suite, HKRS = High-K/High-Rb Suite). Plotted for comparison are fields for two suites of Vanuatu arc rocks from Tanna (Crawford and Eggins, unpublished data; Robin *et al.*, 1994a), and the Kuwae caldera eruption (Monzier *et al.*, 1994; Robin *et al.*, 1994b). A suite of normal arc rocks from the Rabaul caldera in New Britain (Wood *et al.*, 1995), and a suite of bimodal rocks from the Batur caldera in Bali (Wheller, 1986) are plotted for comparison.

Five. Fields for suites from both the Kuwae caldera eruption (CVA, Monzier *et al.*, 1994; Robin *et al.*, 1994b), and Tanna (SVA, Crawford and Eggins, unpublished data, Robin *et al.*, 1994a), are also plotted on the diagrams for comparison. Additionally, a suite from a typical island arc caldera volcano (Rabaul caldera, New Britain arc, Wood *et al.*, 1995) and a bimodal arc caldera suite (Batur caldera, East Sunda arc, Wheller, 1986) are also plotted.

Although basaltic compositions are quite variable, fractionation trends for Vanuatu arc rocks in general are fairly well constrained for compositions with SiO_2 >54 % (Fig. 6.5). The Efaté trachydacites broadly conform to this pattern, but a few important exceptions are noted. Extremely variable TiO_2 contents for Efaté trachydacites are in marked contrast to all comparative suites, particularly the Kuwae suite, which shows tight trends for SiO_2 >60 %. Al_2O_3 contents show considerable scatter for SiO_2 contents 45-56 % in the Kuwae (CVA) and Tanna (SVA) series, but trends are much tighter for the EPF trachydacite compositions. This feature probably reflects the importance of plagioclase accumulation in more mafic magmas (see below, Chapter Five). FeO* contents for Efaté trachydacites are ~1.5 times lower for a given SiO_2 content than CVA, SVA, Rabaul or Batur rocks. In contrast, trends for both MgO and CaO show greater coherence with comparison suites. Significant scatter is apparent for Efaté trachydacites on the Na_2O plot and compositions define a broadly negative correlation for these rocks. This contrasts strongly with tighter and dominantly positive trends for all other suites, except for SVA lavas. This feature may be due to incipient, post-depositional, diffusive alteration having affected these submarine emplaced, glassy, volcaniclastic sediments. K_2O contents are notably high for the Efaté trachydacites, having strong similarities to the SVA series. P_2O_5 contents for the EPF fall at the lowest end of the fields defined for Vanuatu suites, and show no strong link to BVF trends.

Trace elements

Efaté trachydacites are notably enriched in the LILE compared with CVA, Batur and Rabaul dacites (Fig. 6.6). Rb contents in Efaté volcaniclastic sediments up to 110 ppm, and Ba up to 1200 ppm, are double and treble those of the three suites respectively. These abundances are similar, however, to those reported for the Tanna series SVA rocks. Pb patterns for the Efaté trachydacites are off-trend from the BVF lavas, but show similar contents to both SVA and Rabaul lavas. Although notably enriched in BVF lavas, Sr contents in the EPF are not very different from those of all the comparison suites. Y contents are slightly low for the EPF compared with all other suites and are also off-trend from the BVF compositions. Sc is also slightly low for the EPF but still on trend with SVA and BVF rocks. Patterns on Zr and V plots are very similar to all comparison suites.

Rare earth element (REE) patterns for EPF rocks normalised to chondrite are plotted together with a representative basalt from each of the three BVF suites (Fig. 6.7 a,

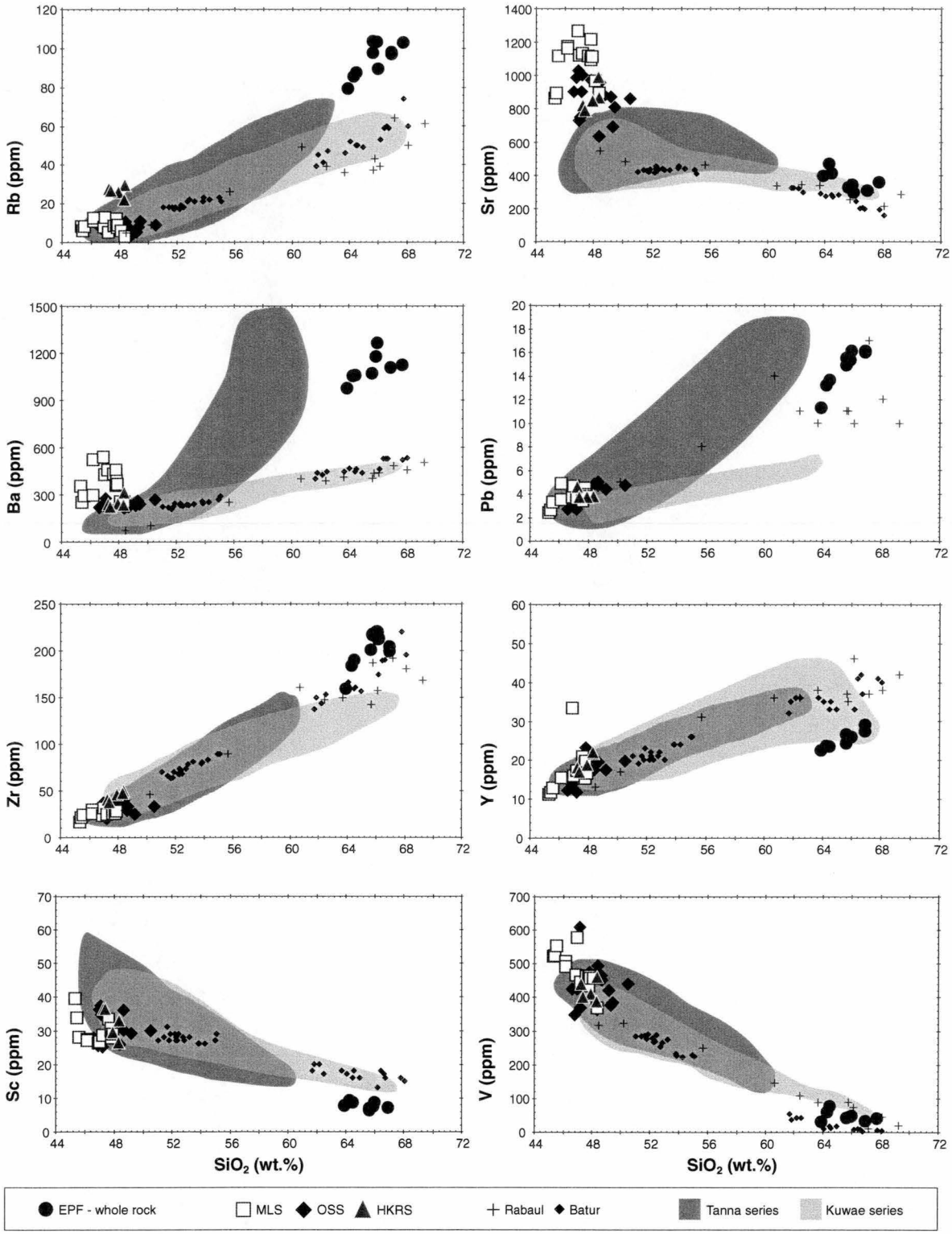

Figure 6.6. Trace element covariation diagrams plotted against SiO_2 wt.% for Efaté Pumice Formation (EPF) volcaniclastic sediments, together with the Basalt Volcanoes Formation lavas discussed in Chapter Seven (MLS = Mainland Suite, OSS = Offshore Suite, HKRS = High-K/High-Rb Suite). Vanuatu arc rocks are represented by fields for rocks from Tanna (Crawford and Eggins, unpublished data; Robin *et al.*, 1994a), and rocks from the Kuwae caldera eruption (Monzier *et al.*, 1994; Robin *et al.*, 1994b); incomplete data sets limit the size of fields. A suite of normal arc rocks from the Rabaul caldera in New Britain (Wood *et al.*, 1995), and a suite of bimodal rocks from the Batur caldera in Bali (Wheller, 1986), are plotted for comparison. Note: not all elements were analysed for both island arc comparative suites, and trace element data for Tanna samples with SiO_2>60% were not available.

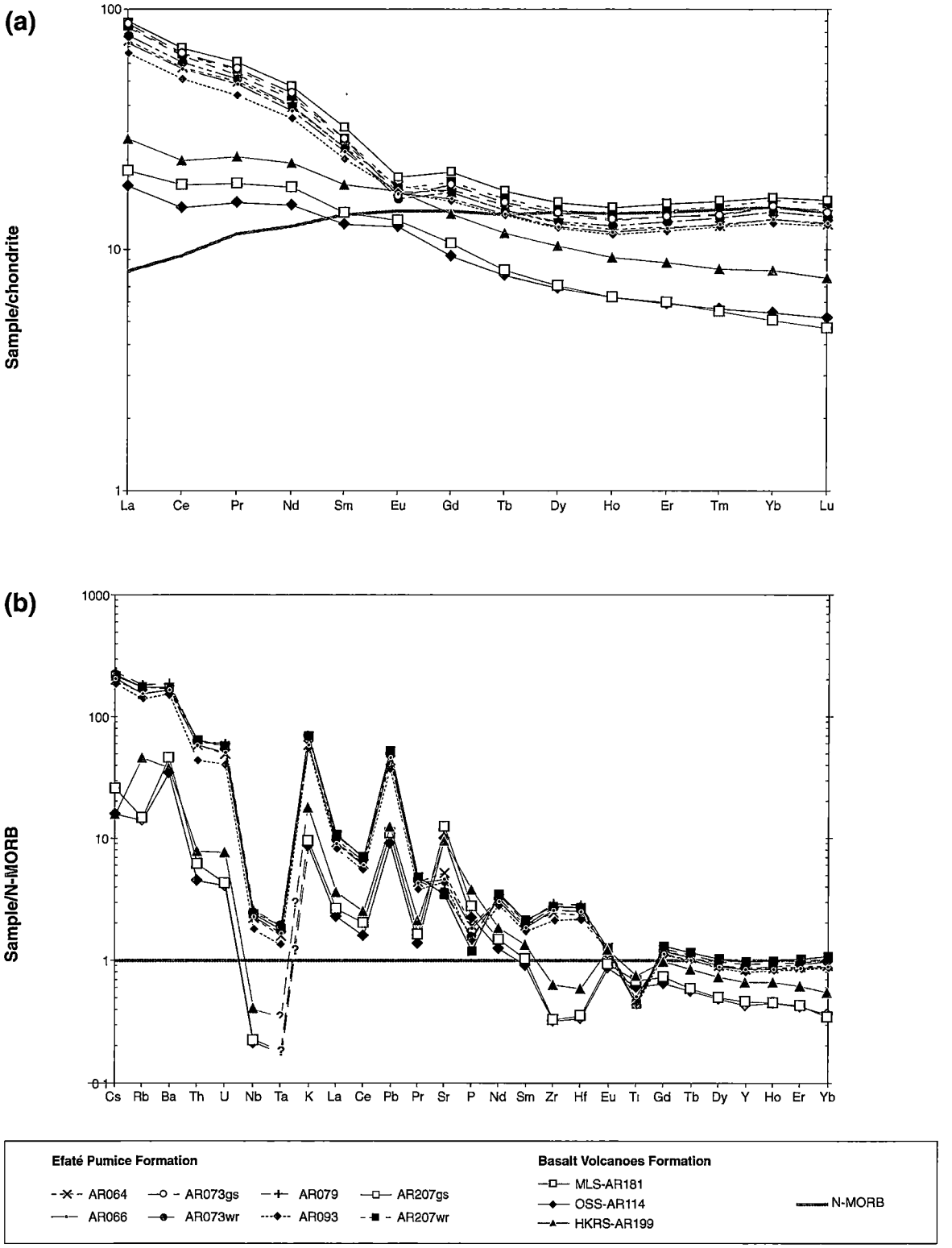

Figure 6.7. Rare earth element and multi-element patterns for Efaté volcanic rocks. (a) Chondrite-normalised REE patterns for trachydacites from the Efaté Pumice Formation (EPF), plotted together with a sample from each of the three basaltic suites from the Basalt Volcanoes Formation (MLS = Mainland suite, OSS = Offshore suite, HKRS = high-K, high-Rb suite). Note negative Eu anomalies for EPF rocks. (b) Multi-element plots for EPF rocks showing BVF lavas for comparison. Dashed lines for BVF rock between Nb and K represent inferred position of Ta which was below ICP-MS analytical detection limits for the basalts. N-MORB composition and normalising values from Sun and McDonough (1989).

Chapter Five). The trachydacite patterns are very weakly U-shaped, caused by relative depletion in the middle REE, and fairly strong relative enrichment in the light REE ($[La/Sm]_N$=2.74-3.03), compared to the Efaté basalts. This is a feature previously noted for dacitic rocks from the Epi submarine volcanoes (Crawford *et al.*, 1988). Patterns also show weak negative Ce-anomalies (Ce/Ce*=0.72-0.89) and stronger negative Eu-anomalies (Eu/Eu*=0.93-0.96), reflecting fractionation of plagioclase.

N-MORB normalised multi-element patterns show the expected overall enrichment in the Efaté trachydacites compared with the BVF basalts (Fig. 6.7 b). In particular, strong enrichments are shown for Rb, and the HFSE Zr and Hf. Stronger Ti depletion in the trachydacites relative to the basalts reflects the presence of Ti-magnetite as an important crystallising phase during magmatic differentiation of these felsic magmas. Extreme Sr and P enrichments in the basalts relative to the trachydacites are a consequence of prolonged plagioclase and apatite fractionation (Chapter Five).

Sr, Nd and Pb isotope geochemistry

The Efaté trachydacites have isotopic characteristics no different from the BVF rocks (Table 6.5). Figure 6.8 shows newly acquired Sr, Nd, and Pb radiogenic isotope data for EPF and BVF volcanics, plotted on standard isotopic covariation diagrams, with the position of the present day bulk earth composition indicated (Rollinson, 1993). Also plotted are fields for Pacific and Indian MORB (Briqueu *et al.*, 1994; Laporte *et al.*, 1997; Peate *et al.*, 1997), the New Britain arc (includes Rabaul caldera, Woodhead & Johnson, 1993), and the East Sunda arc (includes Batur volcano, Stolz *et al.*, 1990) for comparison. Sr isotope ratios fall to the most radiogenic end of the Vanuatu arc field and have restricted low $^{143}Nd/^{144}Nd$, comparable to values for the collision affected rocks in the central Vanuatu arc (Crawford *et al.*, 1995; Laporte *et al.*, 1997; Peate *et al.*, 1997; Turner *et al.*, 1999). Compared with the intraoceanic New Britain arc, the Vanuatu arc rocks span a much broader field, and the Efaté Island Group rocks in particular, extend away from MORB values, towards the bulk earth composition. Values for the East Sunda arc, which are further displaced towards and beyond the bulk earth composition, are explained by Stolz *et al.* (1990) as resulting from complex mixing of multi-component mantle sources. Efaté trachydacite Pb isotopic compositions are likewise similar to BVF values, falling in the transition zone between the collision-affected CVA and the normal SVA (Briqueu *et al.*, 1994; Laporte *et al.*, 1997; Peate *et al.*, 1997). The New Britain arc field shows similar patterns on the Pb covariation diagrams, but has a much more restricted range of $^{206}Pb/^{204}Pb$ values compared with the Vanuatu rocks. East Sunda arc values are more akin to the global marine sediment values and displaced far from the NHRL of Hart (1984). The isotopic signature of the Efaté Island Group rocks can be interpreted to result from the combined affects of a subducted sediment component, and a variable mantle wedge source component with influence from both Pacific- and Indian-MORB mantle sources (see Chapter Five, Peate *et al.*, 1997).

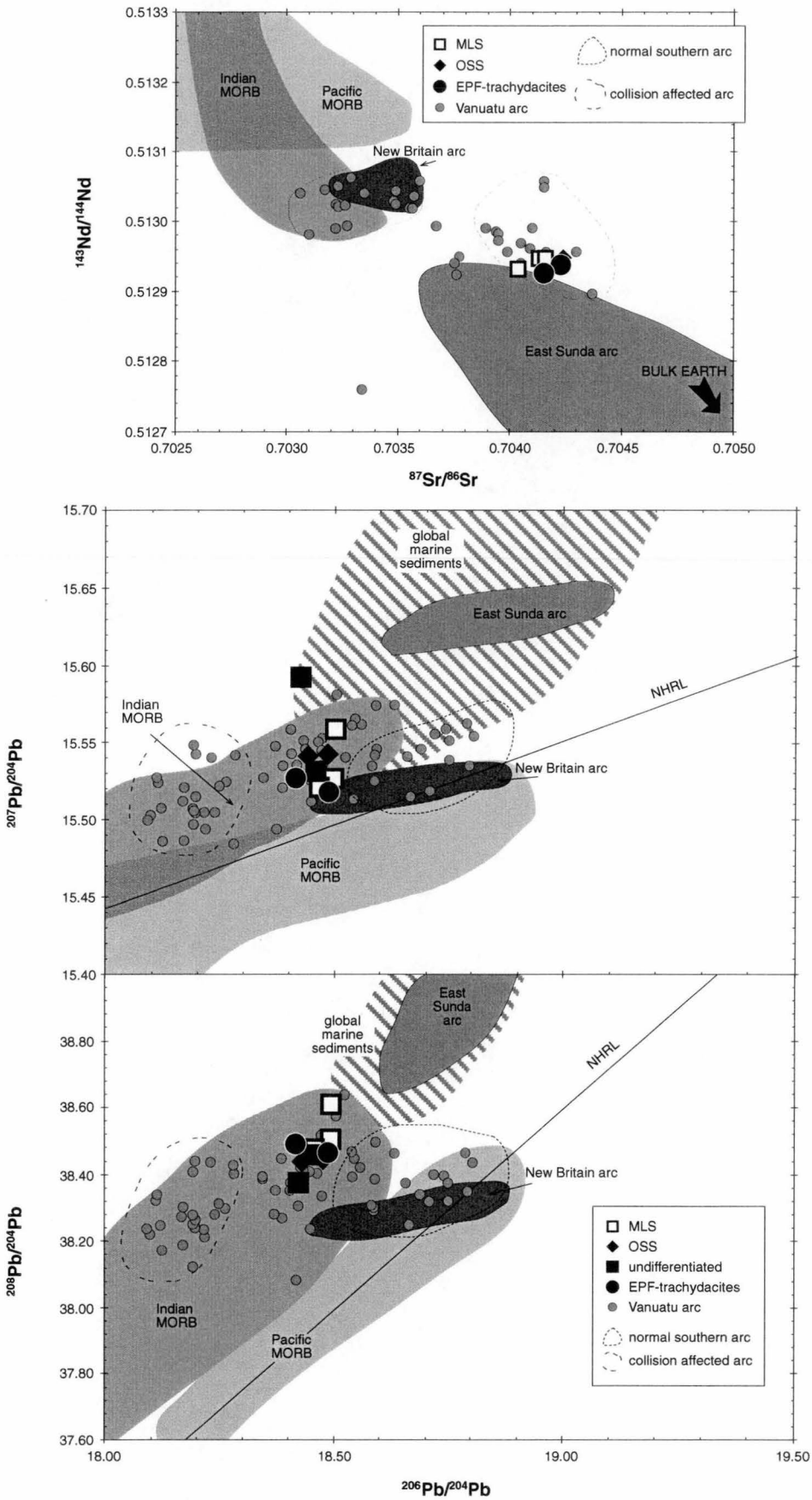

Figure 6.8. Standard Sr-Nd-Pb covariation diagrams for Efaté volcanics. Undifferentiated samples are from Laporte *et al.* (1997). Also shown are Vanuatu arc values complete with fields defined for 'normal' and 'collision-affected' lavas, after Briqueu *et al.* (1994), Crawford *et al.* (1995) and Peate *et al.* (1997). Fields for Pacific and Indian Ocean MORB, and global marine sediment estimate from Peate *et al.* (1997). Fields for East Sunda arc and New Britain arc from Stolz *et al.* (1990) and Woodhead and Johnson (1993).

Table 6.5. Sr-Nd-Pb isotope ratios for Efaté Island Group rocks.

SAMPLE	$^{87}Sr/^{86}Sr$	$^{143}Nd/^{144}Nd$	$^{206}Pb/^{204}Pb$	$^{207}Pb/^{204}Pb$	$^{208}Pb/^{204}Pb$
Efaté Pumice Formation (EPF)					
AR064	0.704156	0.512925	18 407	15.526	38.492
AR073	0.704234	0.512936	18 498	15.519	38.474
Mainland (MLS)					
AR158	0.704041	0.512931	18.498	15.526	38 505
EA143*	0 70413	0 512946	18 464	15.520	38 467
EA258*	0 70416	0 512946	18.501	15.558	38.609
Offshore (OSS)					
AR192	0.704244	0.512946	18 482	15.541	38.451
NgA23*	0 70414	-	18.438	15 540	38.436
Undifferentiated samples					
Efaté 7.2	0.70416	-	18.428	15.592	38.730
Efaté 13	0.70407	-	-	-	-
Efaté 20	0.70416	-	-	-	-
Efaté 36	0.70387	-	18.459	15.530	38.463

AR064, AR073, AR158 and AR192 samples are new data; * denotes samples from Peate *et al.*, (1997); undifferentiated samples from Laporte *et al.*, (1997). New analyses performed at La Trobe University, Melbourne by Roland Maas, standards, analytical techniques and errors are given in Appendix F.

Summary

The Efaté Pumice Formation syn- and post-eruptive volcaniclastic sediments have:

- uniform trachydacitic compositions, with SiO_2 contents averaging ~68 weight %
- elevated K_2O and Rb contents imparting high-K to shoshonitic affinities
- a large compositional gap (51-64 % SiO_2) between the trachydacites and the post-caldera BVF basalts
- greater similarity to SVA (Tanna) rather than CVA (Kuwae) series magmas
- U-shaped REE patterns
- relative enrichments in Zr and Hf on multi-element patterns compared to BVF rocks
- radiogenic isotope signatures effectively identical to BVF basaltic lavas, *i.e.*:
  - Sr-Nd isotopic compositions similar to collision-affected central Vanuatu arc magmas
  - Pb isotopic characteristics transitional between collision-affected and 'normal' southern Vanuatu arc lavas

The single biggest problem to be addressed in the case of the Efaté magmas is the large compositional gap from the low-Si basalts to the shoshonitic trachydacites, which spans the interval from 51.5-62.5 % SiO_2. Crawford *et al.* (1988) demonstrated that a similar compositional gap in magmas from the Epia and Epib submarine volcanoes to the north of Efaté, can be readily explained by fractional crystallisation processes. Fractional crystallisation can also explain the evolution of the basalt-andesite association from Tanna in the southern part of the arc, which bears the strongest geochemical resemblance to the Efaté Island Group magmas (Robin *et al.*, 1994a). For these Tanna lavas, however, modelling breaks down at the dacite end of the spectrum, probably reflecting limited involvement of minor phases such as Na-plagioclase or apatite, not included in the postulated crystallisation scheme for the basalts and andesites (Robin *et al.*, 1994a).

At the Batur caldera complex in the Sunda arc, post-caldera basalts are separated from caldera dacites by a SiO_2 gap from 55-62 %. The dacites are interpreted to have derived from a parent basalt similar in composition to the post-caldera lavas, via fractional crystallisation (Wheller, 1986; Wheller & Varne, 1986). The geological situation at Batur is remarkably similar to that at Efaté, and the possibility that the BVF post-caldera magmas are related to the EPF is explored below.

Fractional crystallisation

The simplest scenario to consider is that closed system fractional crystallisation is the dominant process at work in the production of the high-K to shoshonitic Efaté trachydacites. Several factors suggest that the EPF trachydacites are comagmatic with the BVF basalts. Evidence for a comagmatic relationship includes: (1) the strong spatial and temporal association of the two different magma types; (2) positive correlations of incompatible elements (especially Rb and Zr) between the basalts (particularly the HKRS) and trachydacites on bivariate plots (Fig. 6.6); (3) REE patterns showing overall increasing abundances with increasing SiO_2 content (expected for related magmas); (4) the strong linearity of HKRS basalt-trachydacite associations on log-element versus log-Rb plots (Fig. 6.9); and most importantly, (5) near identical Sr, Nd and Pb isotopic characteristics between the two magmatic groups.

Fractional crystallisation processes for the Efaté magmas were assessed using simple mass balance, least-squares, mixing models determined from GENMIX petrological software (Le Maitre, 1979). Parent liquid compositions for the modelled fractionation sequences are represented by whole-rock analyses from the BVF. These analyses are almost identical to groundmass compositions determined from electron microprobe scans

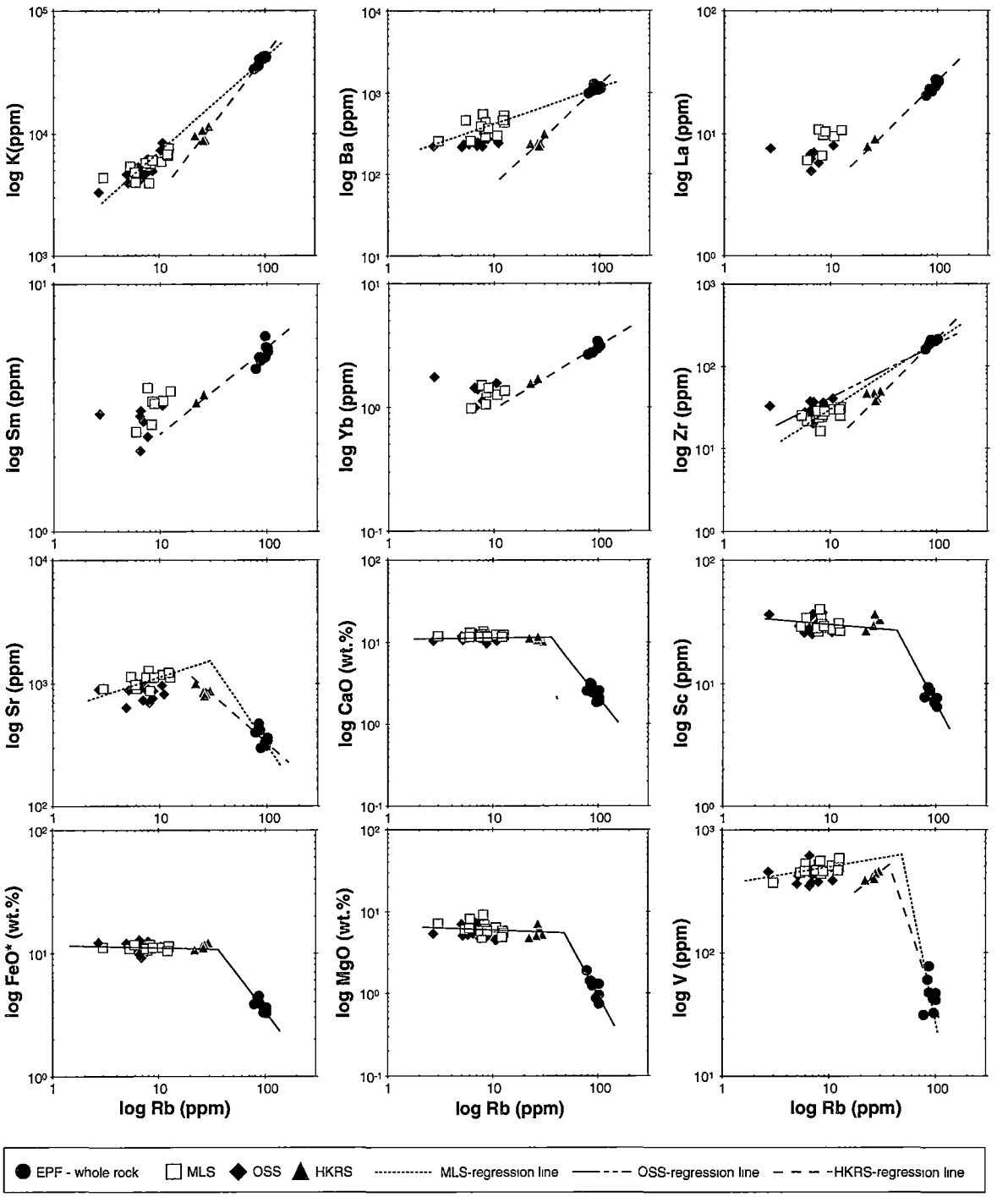

Figure 6.9. Log element versus log Rb plots for selected elements showing the relationships between Efaté trachydacites (EPF) and basalts (BVF): Mainland (MLS), Offshore (OSS) and High-K/High-Rb (HKRS) Suite rocks are plotted. Best fit regression lines drawn between trachydacites and basalts show incompatible (linear) vs. compatible (non-linear) behaviour of elements during fractionation. A single regression line describes the relationship between the basalts and the dacites for all three basaltic suites for the elements CaO, Sc, FeO* and MgO. On both the log K and log Sr versus log Rb plots, the MLS regression line coincides with the OSS line (not drawn). For all plots where regression lines are missing, no satisfactory best fit line can be drawn.

(Table 5.5, Appendix H), and serve as an appropriate initial 'parental' liquid composition. EPF whole-rock analyses that overlap the electron microprobe glass compositional field, were chosen to represent residual liquid compositions.

Models from any of the three BVF geochemical groups produce excellent approximations for fractional crystallisation for major element compositions, with very low sum of squares residuals (Table 6.6, Appendix L). In all models an EPF residual melt is produced after 80-85 % crystallisation, following the scheme andesine + bytownite + augite (Mg_{cpx} ~72) + olivine (Fo_{76})+ Fe-Ti-oxide + apatite, in decreasing order of abundance. This model essentially provides an 'average' fractionate over the basalt to trachydacite spectrum modelled. Interestingly, orthopyroxene cannot be successfully introduced into the fractionation models, indicating that crystallisation of this phase only occurred once the trachydacite residual liquids were established. The absence of orthopyroxene in BVF lavas also indicates late crystallisation.

Trace element tests to establish the validity of the models provide acceptable results for only six of the models (Models A-F, Table 6.6). Even for these six models, trace element test results do not hold for the whole suite of incompatible elements (Tables 6.7-6.8). The mass balance mixing models were tested using the Rayleigh equation for fractional crystallisation,

$$C_L = C_O \cdot F^{(D-1)}$$

where C_L is the concentration of a trace element in the evolving liquid (EPF trachydacite), C_O is the concentration of a trace element in the parental liquid (BVF basalt), F is the fraction of liquid remaining after the crystallisation interval, and D is the bulk partition coefficient for the crystallisation interval (Allègre *et al.*, 1977; Rollinson, 1993; Tatsumi & Eggins, 1995). Trace element concentrations from XRF and ICP-MS analyses were substituted into the equation to determine expected F values. D values were determined in two ways as outlined below.

Assuming that perfect incompatible trace element behaviour applies (*i.e.* D = 0, where the trace element is completely excluded from the crystallising phases and concentrated in the residual melt), the Raleigh fractionation equation can be rewritten such that,

$$F = C_O / C_L$$

The results of this calculation are given in Table 6.7. Calculated Rayleigh fractionation behaviour F values expected for parental magmas similar in composition to OSS rocks only match modelled F value results for Rb, Zr, Th and U. Modelled and calculated F values for the HKRS suite however, show good matches for Rb, Ba, Zr, Hf and U. The lack of good matches overall, however, indicates that perfect incompatible behaviour of these trace elements cannot be occurring for the fractional crystallisation major element models described here.

Table 6.6. Results of GENMIX modelling for fractional crystallisation of Efaté Island Group magmas: BVF parent to EPF daughter.

	Model A - Offshore Suite										Model B - Offshore Suite									
	parent	daughter					Fe-Ti				parent	daughter					Fe-Ti			
	AR106	= AR207wr +	An_{92} +	An_{42} +	Fo_{76} +	augite +	oxide +	apatite =	calc	residuals	AR106	= AR207wr +	An_{92} +	An_{38} +	Fo_{67} +	augite +	oxide +	apatite =	calc	residuals
Vol. %	100%	13%	17%	37%	4%	19%	9%	1%	parent	*r*	100%	13%	21%	33%	4%	18%	9%	1%	parent	*r*
SiO_2	48 42	66 93	44 03	57 33	38 21	51 98	0 00	0 16	48 59	-0 17	48 42	66 93	44 03	58 97	38 21	51 98	0 00	0 16	48 60	-0 18
TiO_2	1 00	0 56	0 04	0 05	0 01	0 44	10 20	0 00	1 10	-0 11	1 00	0 56	0 04	0 03	0 01	0 44	10 20	0 00	1 09	-0 10
Al_2O_3	18 37	15 92	35 11	26 80	0 05	1 23	2 89	0 00	18.52	-0 15	18 37	15 92	35 11	25 54	0 05	1 23	2 89	0 00	18 53	-0 15
FeO*	11 07	3 26	0 89	0 46	22 25	10 78	84 10	0 58	11 22	-0 15	11 07	3 26	0 89	0 50	22 25	10 78	84 10	0 58	11 24	-0 17
MgO	4 45	0 86	0 05	0 05	38 86	14 70	2 30	0 23	4 58	-0 13	4 45	0 86	0 05	0 06	38 86	14 70	2 30	0 23	4 58	-0 13
CaO	10 96	1 83	18 94	8 48	0 22	19 65	0 00	54 10	11 08	-0 12	10 96	1 83	18 94	7 69	0 22	19 65	0 00	54 10	11 08	-0.12
Na_2O	3 02	4 89	0 87	6 07	0 00	0 32	0 00	0 07	3 08	-0 06	3 02	4 89	0 87	6 54	0 00	0 32	0 00	0 07	3 05	-0 03
K_2O	0 88	5 12	0 03	0 70	0 00	0 01	0 00	0 01	0 92	-0 04	0 88	5 12	0 03	0 62	0 00	0 01	0 00	0 01	0 90	-0 02
P_2O_5	0 38	0 14	0 00	0 04	0 00	0 00	0 00	41 95	0 57	-0 19	0 38	0 14	0 00	0 02	0 00	0 00	0 00	41 95	0 59	-0 21
									$\sum r^2$ =	*0 16*									$\sum r^2$ =	*0 17*

	Model C - Offshore Suite										Model D - High-K/High-Rb Suite									
	parent	daughter					Fe-Ti				parent	daughter					Fe-Ti			
	AR106	= AR073wr +	An_{92} +	An_{38} +	Fo_{76} +	augite +	oxide +	apatite =	calc.	residuals	V60	= AR073wr +	An_{92} +	An_{42} +	Fo_{76} +	augite +	oxide +	apatite =	calc	residuals
Vol. %	100%	14%	22%	32%	5%	17%	8%	1%	parent	*r*	100%	20%	25%	25%	6%	15%	8%	1%	parent	*r*
SiO_2	48 42	65 63	44 03	58 97	37 00	51 98	0 00	0 16	48 61	-0 19	48 32	65 63	44 03	57 33	37 00	50 70	0 00	0 16	48 37	-0 06
TiO_2	1 00	0 55	0 04	0 03	0 03	0 44	10 20	0 00	1 03	-0 04	0 98	0 55	0 04	0 05	0 03	0 56	10 20	0 00	1 01	-0 03
Al_2O_3	18 37	15 72	35 11	25 54	0 01	1 23	2 89	0 00	18 53	-0 15	19 19	15 72	35 11	26 80	0 01	3 80	2 89	0 00	19 24	-0 05
FeO*	11 07	3 56	0 89	0 50	29 13	10 78	84 10	0 58	11 25	-0.18	10 54	3 56	0 89	0 46	29 13	7 88	84 10	0 58	10 59	-0 06
MgO	4 45	1 29	0 05	0 06	32 83	14 70	2 30	0 23	4 57	-0 12	4 74	1 29	0 05	0 05	32 83	14 64	2 30	0 23	4 79	-0 04
CaO	10 96	2 54	18 94	7 69	0 20	19 65	0 00	54 10	11 09	-0 13	11 22	2 54	18 94	8 48	0 20	21 97	0 00	54 10	11 27	-0 05
Na_2O	3.02	5 03	0 87	6 54	0 00	0 32	0 00	0 07	3 05	-0 03	2 75	5 03	0 87	6 07	0 00	0 29	0 00	0 07	2 78	-0.03
K_2O	0 88	4 99	0 03	0.62	0 00	0 01	0 00	0 01	0 92	-0.04	1 15	4 99	0 03	0 70	0 00	0 00	0 00	0 01	1 19	-0 03
P_2O_5	0 38	0 18	0 00	0 02	0 00	0 00	0 00	41 95	0 59	-0 21	0 46	0 18	0 00	0 04	0 00	0 00	0 00	41 95	0 51	-0 06
									$\sum r^2$ =	*0 17*									$\sum r^2$ =	*0 02*

Table 6.6. (cont.). Results of GENMIX modelling for fractional crystallisation of Efaté Island Group magmas: BVF parent to EPF daughter.

	Model E - High-K/High-Rb Suite										Model F - High-K/High-Rb Suite									
	parent	daughter					Fe-Ti				parent	daughter					Fe-Ti			
	V60	= AR079	+ An_{92}	+ An_{42}	+ Fo_{76}	+ augite	+ oxide	+ apatite	= calc	residuals	V60	= AR098	+ An_{92}	+ An_{42}	+ Fo_{76}	+ augite	+ oxide	+ apatite	= calc	residuals
Vol %	100%	20%	24%	24%	6%	16%	8%	1%	parent	*r*	100%	19%	23%	27%	6%	16%	8%	1%	parent	*r*
SiO_2	48 32	65 92	44 03	57 33	37 00	50 70	0 00	0 16	48 38	-0 06	48 32	66 00	44 03	57 33	37 00	50 70	0 00	0 16	48 41	-0 09
TiO_2	0 98	0 56	0 04	0 05	0 03	0 56	10 20	0 00	1 01	-0 03	0 98	0 59	0 04	0 05	0 03	0 56	10 20	0 00	1 01	-0.03
Al_2O_3	19 19	16 28	35 11	26 80	0 01	3 80	2 89	0 00	19 24	-0 05	19 19	15 98	35 11	26 80	0 01	3 80	2 89	0 00	19.25	-0 06
FeO*	10 54	3 41	0 89	0 46	29 13	7 88	84 10	0 58	10 59	-0 06	10 54	3 86	0 89	0 46	29 13	7 88	84 10	0 58	10 61	-0 08
MgO	4 74	0 95	0 05	0 05	32 83	14 64	2 30	0 23	4 79	-0 04	4 74	1 23	0 05	0 05	32 83	14 64	2 30	0 23	4 79	-0 05
CaO	11 22	2 11	18.94	8 48	0 20	21 97	0 00	54 10	11 27	-0 05	11 22	2 42	18 94	8 48	0 20	21 97	0 00	54 10	11 27	-0 05
Na_2O	2 75	5 11	0.87	6 07	0 00	0 29	0 00	0 07	2 77	-0 02	2 75	4 36	0 87	6 07	0 00	0 29	0 00	0 07	2 72	0 02
K_2O	1.15	4.98	0 03	0 70	0 00	0 00	0 00	0 01	1 17	-0 02	1.15	4 87	0 03	0 70	0 00	0 00	0 00	0 01	1 10	0 05
P_2O_5	0.46	0.17	0 00	0 04	0 00	0 00	0 00	41 95	0 52	-0 07	0 46	0 15	0 00	0 04	0 00	0 00	0 00	41 95	0 56	-0 11
									Σr^2 =	*0 02*									Σr^2 =	*0 04*

Table 6.7. Trace element F-test results: D = 0

D=0	OSS			HKRS		
	Model A	Model B	Model C	Model D	Model E	Model F
F modelled	13%	13%	14%	20%	20%	19%
Rb	11%	11%	11%	23%	21%	25%
Ba				22%	20%	19%
Zr	20%	20%	20%	23%	22%	23%
La						
Sm						
Yb						
Hf				22%	21%	23%
Pb						
Th	11%	11%	12%			
U	13%	13%	13%	14%	14%	14%
Average	14%	14%	14%	21%	20%	21%
St Dev	4%	4%	4%	4%	3%	4%

Table 6.8. Trace element F-test results: D = calculated

D=calculated	OSS			HKRS		
	Model A	Model B	Model C	Model D	Model E	Model F
F modelled	13%	13%	14%	20%	20%	19%
Rb	10%	10%	10%	21%	20%	23%
Ba	17%	17%	18%	16%	15%	
Zr	14%	13%	14%	17%	16%	16%
La	9%	9%	12%			16%
Sm				23%	19%	17%
Yb						
Hf	10%	11%	11%	14%	13%	14%
Pb				27%	27%	27%
Th	10%	10%	11%			
U	12%	12%	12%	14%	14%	14%
Average	12%	12%	12%	19%	17%	18%
St Dev	3%	3%	3%	5%	5%	5%

In any case, perfect incompatible behaviour is only likely to occur in natural systems over very small crystallisation intervals (*e.g.* Devine, 1995; Gertisser & Keller, 2000). In a magmatic system with a large compositional gap, and therefore a large crystallisation interval, values for D can be determined using established mineral/melt partition coefficients ($Kd = C^i_{mineral}/C^i_{melt}$ where C is the concentration of element i), for the fractionating mineral assemblage. In this case, the bulk partition coefficient (D^i_{bulk}) is given by the equation,

$$D^i_{bulk} = \sum x_{mineral} \cdot Kd^i_{mineral}$$

where D^i_{bulk} is bulk partition coefficient for element i, $x_{mineral}$ is the percentage proportion of a crystallising phase in the system, and $Kd^i_{mineral}$ is the mineral/melt partition coefficient for element i in the crystallising phase (Allègre *et al.*, 1977; Villemant *et al.*, 1981; Rollinson, 1993). Mineral/melt partition coefficients used for modelling the Efaté Island Group system are given in Table 6.9.

Table 6.9. Mineral/melt partition coefficients (*Kd*) used in trace element modelling for fractional crystallisation models.

ELEMENT	$Kd_{Ca\text{-}plag}$	$Kd_{Ca\text{-}Na\text{-}plag}$	Kd_{augite}	Kd_{ol}	$Kd_{Fe\text{-}Ti\text{-}ox}$	Kd_{apa}
Rb	0.071	0.048	0.032	0.010	-	-
Ba	0 23	0 36	0.131	0.010	-	-
Zr	0.48	0.10	0.184	0 012	0.1	0 64
La	0.19	0.38	0.015	0 007	1.5	14.5
Sm	0 067	0.13	0.457	0 007	1.1	46
Yb	0.07	0 06	0.54	0.014	-	23.9
Hf	0.051	0.1	0.247	0.013	2	0.73
Pb	-	-	-	-	-	-
Th	0.01	0.048	0 015	-	-	-
U	0.01	0.093	-	0.002	-	-

Dashes indicate that no data is available and the *Kd* is effectively zero. Data from the compilation of Rollinson (1993).

Calculated F values, using calculated D^i_{bulk} are given in Table 6.8. Results from these calculations provide a better match for modelled F values for both OSS and HKRS parent basalts. Trace element tests for the OSS parent basalts work for Rb, Ba, Zr, La, Hf, Th and U. This result contrasts with log-element versus log-Rb plots where Ba and La do not show linear relationships between EPF trachydacites and OSS basalts (Fig. 6.9). This suggests that the two different magmatic suites are therefore probably unrelated to each other via fractional crystallisation. Furthermore, on incompatible trace element versus SiO_2 bivariate plots, the OSS basalts generally do not show strong positive correlations with EPF trachydacites.

Compared with the OSS, HKRS compositions have strong linear associations with EPF trachydacites on all log-element versus log-Rb plots (Fig. 6.9), and better-defined positive correlations on incompatible element bivariate plots (Figs 6.5 and 6.6). Models D and E with HKRS parental magmas have good matches for Rb, Ba, Zr, Sm, Hf, Pb and U, while Model F works for Rb, Zr, La, Sm, Hf, Pb and U. These results indicate stronger support

for fractional crystallisation processes occurring between these two end-member magmas, although the non-conformable behaviour of some of the elements probably indicates that other processes are also occurring in the evolution of this magmatic system (Allègre *et al.*, 1977; Defant & Nielsen, 1990).

Problems with the closed system fractional crystallisation model

Individual *Kd* values in any natural crystallising system are extremely sensitive to changes in temperature, pressure, oxygen fugacity, and melt composition, and will vary accordingly (Allègre *et al.*, 1977; Rollinson, 1993). This is one reason for limiting fractional crystallisation modelling to small crystallisation steps to avoid the complications of widely varying *Kd* values. In the case of the Efaté magmas, *Kd* values were chosen from published data that most closely approximated the compositions of mineral and melt phases in the system. The chosen partition coefficients used in this analysis may introduce some error into the results calculated for these models.

Although the log-element versus log-Rb plots have impressive linear correlations between basalts and trachydacites for the Efaté magmas, without the intermediate compositions there is no way of assessing whether these correlations are 'real'. The problem of extrapolating regression lines over large compositional gaps is clearly demonstrated on the log-log plots of Villemant *et al.* (1981). Subtle changes in the gradients, and thus the bulk partition coefficients, for several elements, especially the REE La, Ce, Nd, Tb, Yb, and Lu, would not be recognised without the intermediate compositions (Allègre *et al.*, 1977). The results of the modelling over the extreme compositional gap between the Efaté basalts and trachydacites must therefore be viewed as a broad approximation only (see also Allègre *et al.*, 1977; Defant & Nielsen, 1990; Devine, 1995).

Summary

For the EPF trachydacites:

- major element models predict that EPF magmas can be produced by 80-85 % closed system fractional crystallisation from a BVF parental magma
- trace element testing of major element modelling based on the Rayleigh equation for closed system fractional crystallisation shows good results overall, particularly for HKRS-type parent magmas, but
- unreasonable results for a few key trace elements indicate that in addition to perfect fractional crystallisation, other processes may have played a role, albeit minor, in the petrogenesis of EPF magmas

Magma chamber processes

The large volume of trachydacite at Efaté is at odds with dacites erupted from other centres in the Vanuatu arc. The Kuwae caldera ~60 km north of Efaté, has a very similar volcanic history with significant, caldera-related dacite magmatism present. The total bulk volume of caldera-related volcanic products at Kuwae is estimated at ~32-39 km^3, with about two thirds of this volume being dacitic. This is approximately ~30 % as much material as estimated for the EPF trachydacites (Chapter Three, Monzier *et al.*, 1994). Geochemical evolution from basaltic to rhyolitic rocks for related arc magma series, like the Kuwae series magmas, is commonly attributed to the presence of compositionally layered crustal magma chambers (Wheller & Varne, 1986; Robin *et al.*, 1994a; Wood *et al.*, 1995; Mandeville *et al.*, 1996a). The lack of intermediate compositions and the dominance of felsic tephra, indicates that perhaps the trachydacitic magmas at Efaté were effectively separated from more mafic compositions, prior to and during eruption.

Wheller and Varne (1986) proposed a closed-system fractionation model for generation of the bimodal volcanism at Batur (Bali), based on theoretical constraints of fluid dynamics in magma chambers (McBirney, 1980; Turner, 1980; Sparks *et al.*, 1984). In this model, cooling of mafic magmas around the walls of a crustal magma chamber leads to localised fractional crystallisation, not affecting the bulk of the mafic magma in the chamber. The residual felsic liquids collect near the roof of magma chamber due to their lower density compared with the mafic liquids, forming a cap of highly differentiated magma available for eruption. Eruption of the dacites by catastrophic caldera collapse is subsequently followed by late-stage eruption of the genetically related basaltic magmas.

Based on the occurrence of strongly bimodal compositions of glassy melt inclusions in plagioclase and olivine phenocrysts, Lee and Stern (1998) also postulated that Mariana arc magmas may have formed in strongly compositionally zoned magma chambers. In their model, primitive basaltic melts differentiate to more felsic compositions in a shallow level magma chamber, with mafic phases being continually removed from the system by gravitational settling, and with plagioclase accumulating at a boundary layer between mafic and felsic magmas. The principal difference between this model and that of Wheller and Varne (1986) detailed above, is that the system is continually fed from below, eventually allowing a large volume magma chamber to grow in which open system crystal fractionation dominates. This model can account for a bimodal population of magmas within the arc, as well as the frequently observed accumulation of plagioclase in mafic arc magmas.

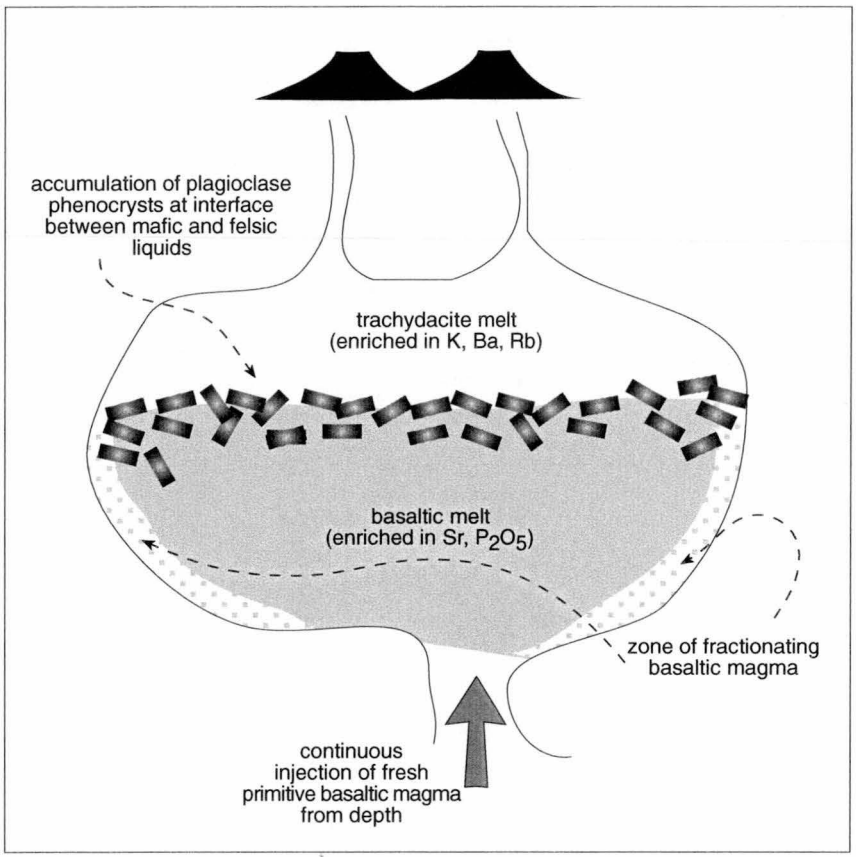

Figure 6.10. Schematic representation of the petrogenesis of the Efaté Pumice Formation magmas. Parental basalts with geochemistry akin to the High-K/High-Rb Suite (HKRS) basalts from the BVF, rise from the mantle wedge and pool in a shallow crustal magma chamber. Fractional crystallisation commences in zones at the margins of the magma chamber, generating low density SiO_2-rich felsic melts which collect at the top of the magma chamber. Prolonged fractionation involving continual recharge from below (open system fractionation) promotes the growth of a large volume, strongly compositionally zoned, magma chamber. The accumulation of floating plagioclase phenocrysts forms a boundary between the felsic and mafic liquids. After Wheller and Varne (1986), Lee and Stern (1998).

PETROGENETIC MODEL

A combination of the principal elements of both the Lee and Stern (1998) and the Wheller and Varne (1986) models can be effectively applied to the magmatic system at Efaté. Figure 6.10 shows schematically a speculative picture of the geochemical evolution of the EPF trachydacite magmas. Primitive basaltic melts related to the present east-dipping subduction regime in the Efaté region are generated by partial melting of the mantle wedge peridotite and continuously rise to pool in shallow crustal magma chambers. Fractional crystallisation of HKRS-like parental basalts occurring near magma chamber margins, results in differentiation to felsic magmas of EPF trachydacite composition. The magma chamber develops a strong chemical zonation as the lighter felsic fractions rise to the top of the chamber while denser, more mafic compositions reside in the lower parts and core. Plagioclase phenocrysts float towards the top of the mafic liquid and accumulate to form a boundary layer, very effectively separating the felsic and mafic liquids. Basaltic parental magmas are continuously fed into the magma chamber from source regions resulting in open-system fractionation, thereby generating non-ideal trace element compositions between mafic and felsic melts, and generating a large volume of felsic magma.

CONCLUSIONS

Geochemical characteristics of the EPF volcaniclastics indicate that they are comagmatic with post-caldera BVF lavas, especially the High-K/High-Rb Suite (HKRS) from Emau Island. These different magma types which are separated by a compositional gap of more than 10 wt.% SiO_2 are closely related in time and space, have generally similar geochemical signatures, and have identical radiogenic isotopic signatures.

Major element modelling shows that closed-system fractional crystallisation can produce EPF trachydacites from HKRS parental basalt compositions after 80-85 % fractionation, following a crystallisation sequence of 24-27 % andesine + 23-25 % bytownite + 15-16 % augite (Mg_{cpx} ~72) + 6 % olivine (Fo_{76}) + 8 % Fe-Ti-oxide + 1 % apatite. The trace element systematics of the system broadly support this general model, however, non-ideal behaviour in these modelled sequences indicates that open-system processes also may have played a limited role in EPF magma genesis.

Prolonged fractional crystallisation from HKRS-like basaltic parent magmas occurred in a shallow crustal magma chamber that became strongly zoned. Felsic and mafic magmas were effectively separated by a boundary layer of accumulating plagioclase phenocrysts prior to eruption of the EPF trachydacites.

Chapter Seven

CONCLUSIONS

Evolution of a trachydacite-dominated island arc centre

The volcanic succession of the Efaté Island Group records a major explosive eruption in the Vanuatu island arc one million years ago that produced at least 82 km^3 of trachydacitic tephra. Following the eruption, basaltic volcanoes (16.5 km^3 total volume subaerial) grew rapidly from effusive eruptions and small-scale explosive events. The Efaté Island Group occurs at the shoulder between the 'normal' southern section and the collisional central section of the Vanuatu arc. Local tectonic conditions clearly had a strong effect on the geochemical evolution of the Efaté Island Group magmas, and in turn, this affected the volcanological evolution of the centre.

IGNEOUS PETROGENESIS

Evolution of the magmatic system involved the growth of a large, shallow crustal magma chamber from parent magmas generated by partial melting of a variably enriched and metasomatised mantle wedge source. These processes were influenced by local tectonics, specifically, tearing of the subducted slab and probably subduction of a seamount. Figure 7.1 summarises the growth of the magma chamber for the Efaté Island Group magmas.

Prior to east-dipping subduction along the Central Chain of Vanuatu arc islands, west-dipping subduction on the now extinct Vitiaz arc ceased. At this time, ascending primitive melts associated with the last stages of Vitiaz arc volcanism, may have frozen in the mantle wedge, resulting in chemical heterogeneity (notably enrichment of K, LILE and REE). These regions became the new mantle wedge source for east-dipping subduction (Barsdell *et al.*, 1982). A tear in the subducting slab in the Efaté region (Chatelain & Grasso, 1992; Chatelain *et al.*, 1992; Chatelain *et al.*, 1993; Regnier *et al.*, 1997), influenced subduction such that ephemeral carbonatite melts were generated. These highly reactive melts never ascended far, and instead metasomatised mantle peridotite elevating Sr and P contents. Hydrous fluids released by the breakdown of amphibole in the descending slab facilitated partial melting of this modified mantle wedge source, generating parental basaltic magmas with characteristic enrichments in Sr and P, and variably in K and Rb, relative to 'normal' southern Vanuatu arc magmas. The

hydrous fluids were also influenced by a variable contribution from subducted sediment and seawater infiltration, leading to Pb-isotope values transitional between the 'normal' and collisional arc signature, and a strongly radiogenic Sr-Nd isotopic signature similar to collision-affected magmas. These parent magmas adiabatically rose and pooled in a shallow crustal magma chamber where fractionation of the basaltic magmas commenced.

Fractional crystallisation occurring mainly at the outer margins of the magma chamber caused differentiation of mafic magmas to more felsic compositions. Early fractionation stages, as elsewhere in the Vanuatu arc, were dominated by olivine and clinopyroxene (Eggins, 1993), whereas, the basaltic andesite to dacite stage, represented on Efaté by the most fractionated basalts and the least fractionated trachydacites, has been effectively modelled by least squares methods, and involves substantial plagioclase and clinopyroxene with minor olivine, Fe-Ti-oxides and apatite. The residual trachydacite liquids floated to the top of the magma chamber forming a cap over the denser mafic liquids. Plagioclase crystals accumulated by flotation in the mafic liquid formed a barrier between the felsic and mafic liquids. Parental basaltic magmas were continually supplied from below allowing a large reservoir of magma to grow, while maintaining basaltic compositions in the lower and central parts of the magma chamber.

ERUPTION STYLE AND DEPOSITIONAL MECHANISMS

The fractionated upper part of the magma chamber was evacuated by a cataclysmic caldera eruption at ~1 Ma, from vents located somewhere north of the Efaté Island Group. Deposition of felsic tephra occurred in submarine environments although whether vent environments were subaerial or submarine remains unresolved. Subsequent eruption of related basalts from the core and lower parts of the same magma chamber probably occurred in both subaerial and submarine environments. Shoaling (?) of basaltic centres at Mount Fatmalapa and Quoin Hill occurred concurrent with uplift in the region commencing around 0.3 Ma (Ash *et al.*, 1978; Lecolle *et al.*, 1990), and activity at Nguna, Pele and Emau Islands occurred more recently in subaerial environments.

The eruption cycle involved three main stages: (1) explosive magmatic eruption of trachydacitic, pumiceous debris, deposited by syn-eruptive, mass-flow processes in submarine environments; followed by (2) a change in eruption style to hydromagmatic fragmentation of the trachydacite magma and submarine deposition of fine-grained shard-rich sediments by turbidity currents; and (3) post-caldera eruptions of more basic magma forming submarine to emergent volcanoes composed of basaltic lavas and volcaniclastic facies. These three stages are outlined below and in Figure 7.2.

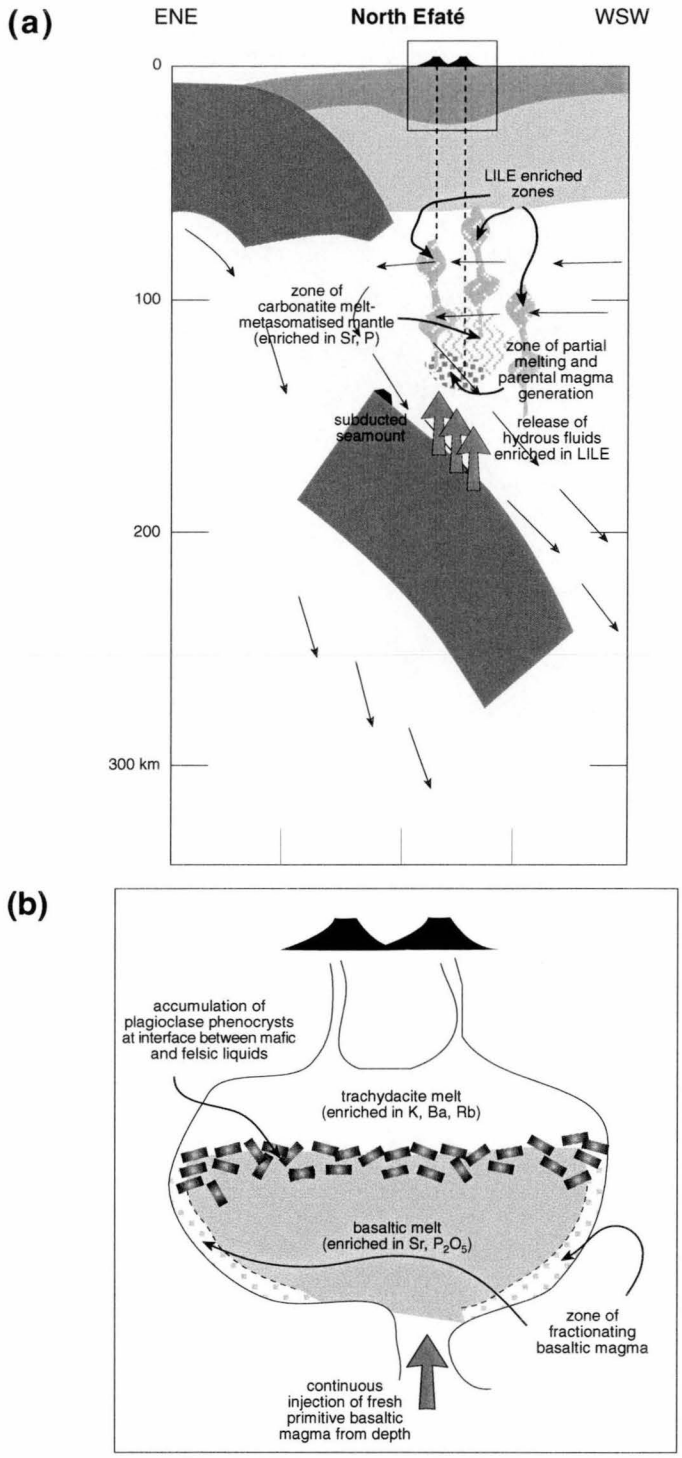

Figure 7.1. Magmatic and geochemical evolution of the Efate Island Group magmas. (a) Summary of processes contributing to geochemical evolution of parental basalts. Partial melting driven by the release of LILE-enriched hydrous fluids from the subducted slab occurs in a zone of modified mantle wedge. Enrichment in Sr and P_2O_5 in this mantle source region is attributed to slightly earlier carbonatite metasomatism. Variable enrichment of K_2O and LILE (notably Rb, Ba) is due to heterogeneity from earlier west-dipping subduction along the Vitiaz arc. (b) The parental basalts rise and pool in a shallow crustal magma chamber and fractional crystallisation commences in zones at the margins of the magma chamber. This generates SiO_2-rich felsic melts which collect at the top of the magma chamber due to density contrasts with the basaltic liquids. Prolonged fractionation and continual recharge from below cause a large volume magma chamber to grow and felsic and mafic liquids are effectively separated by a boundary layer of accumulating plagioclase. Modified from Monzier *et al.* (1997) and Lee and Stern (1998).

Stage 1

Eruption event

The earliest known phase of the eruption sequence in the Efaté Island Group is represented by eruption of the trachydacite magma cap of the shallow crustal magma chamber, leading to deposition of the Efaté Pumice Breccias. Large-scale, explosive eruption of these magmas probably followed some destabilising event occurring in the growing magma chamber, such as a change in the rate of magma supply, or a large seismic event associated with local tectonics (Bonnefoi *et al.*, 1995). Explosive expansion and fragmentation of the trachydacitic magmas followed, producing a plinian eruption column. This probably occurred at shallow submarine vents, and if so, it is likely that the eruption column may have breached the surface. Two or more eruptive episodes of this type are indicated prior to deposition of the Rentabau Tuffs.

Depositional processes

Deposition of the Efaté Pumice Breccias by a succession of high-density, volcaniclastic turbidity currents occurred in a restricted, below-storm-wave base, submarine depocentre. These turbidity currents were generated syn-eruptively from either subaerial pyroclastic flows that transformed to water-supported flows by turbulent mixing near shorelines, or directly from submarine eruptions of the vesiculating trachydacitic magmas. The finest particles were winnowed by turbulence in the high-density currents eventually generating new low-density currents that may have become detached from the parent mass-flow. These low-density currents deposited interbeds of laminated, cross-laminated and massive shard-rich, sand locally. Bottom currents modified the upper parts of some beds. Towards the end of Stage 1 re-deposition of this pumiceous pyroclastic debris by turbidity currents and bottom currents may have occurred.

Stage 2

Eruption event

Eruption of the Rentabau Tuffs represents a change from magmatic to hydromagmatic fragmentation of trachydacite magma, due to flooding of the vent with external water. This probably occurred at submarine vents where seawater gained access as the magmatic explosions that produced the Efaté Pumice Breccias waned, or as the eruption column collapsed. Continual small explosions occurred as available water flashed to steam and ruptured trachydacite foams in the vent. Although submarine vents are favoured, this remains equivocal.

Depositional processes

The fine-grained pyroclast-rich Rentabau Tuffs were deposited in deep submarine environments by quasi-steady turbidity currents generated from contemporaneous hydromagmatic eruptions. Pyroclastic currents were rapidly transformed into cold, water-supported turbidity currents by turbulent mixing with seawater either at shorelines or directly at submarine vents. Turbidity currents were probably also generated by slumping of pyroclastic debris temporarily stored in proximal volcaniclastic aprons. A further source of turbidity currents was from turbulent, vertical sediment plumes developing in the upper parts of the water column from lateral dispersal of a submarine eruption column by ocean currents. The turbidity currents deposited thin to thick, glass shard-rich, dominantly massive, but also laminated and ripple-laminated sand and silt beds. Bottom currents locally reworked some of these turbidites. Seismic activity, probably related to volcanic eruptions, caused local slumping and the development of convolute-bedded intervals within the Rentabau Tuffs stratigraphy. Such events may have also triggered further turbidity currents by remobilisation of this unconsolidated sediment. This unit comprises ~98 % pyroclasts and lacks any significant interbeds of hemipelagic sediment, indicating that deposition occurred penecontemporaneously with explosions, or rapidly following the eruption. The presence of fossil foraminifera in the Rentabau Tuffs constrains the deep marine depositional environment, and deposition over days to weeks following the eruption.

Stage 3

Eruption event

Late stage basaltic magmas, in part related to renewed pulses of primary magma in the shallow crustal magma chamber, ascended to the surface along fractures developed during caldera collapse. The earliest activity was probably dominated by submarine lava emissions occurring at centres in northern Efaté that led to construction of small volume (~3 km^3) volcanic edifices. Continuous eruptive events built small, volcanic cones dominated by volcaniclastic facies at Mount Fatmalapa, and by lavas at Quoin Hill. These volcanoes eventually became emergent, due to both growth and local uplift, and subaerial deposition ensued. Later eruptions further north of these two centres on the islands of Nguna, Pele and Emau followed a similar pattern but the submarine parts of the volcanoes are not uplifted and exposed. Here, volcano flanks are dominated by lavas and summit areas include more pyroclastic facies.

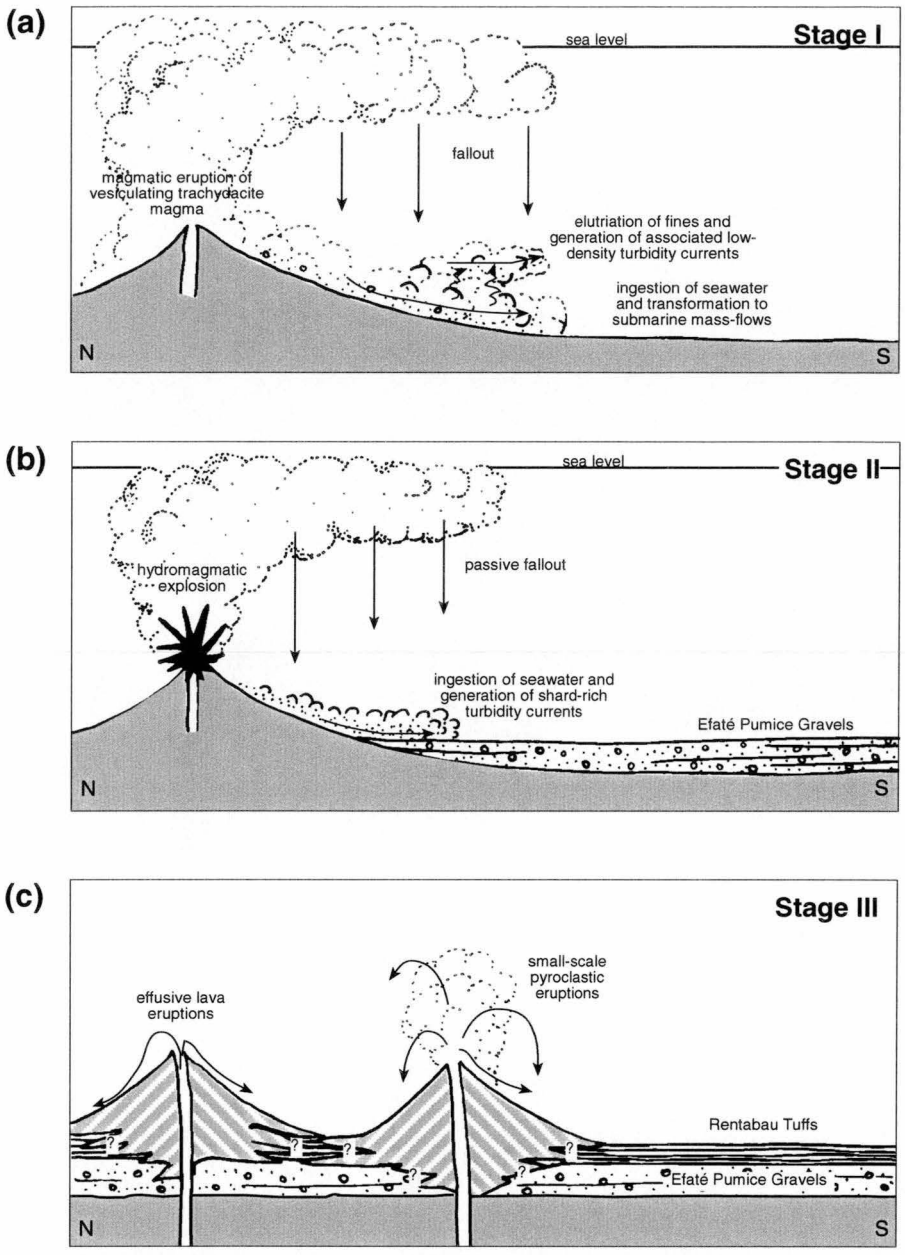

Figure 7.2. Eruption cycle and depositional processes for volcanic deposits of the Efaté Island Group. (a) Stage I: Explosive magmatic eruption of vesiculating trachydacite magma generated coarse pumiceous pyroclastic flows that transformed to cold, water-supported mass-flows after turbulent mixing with seawater by eruption column collapse at vents that were probably submarine. Winnowing of fines from the mass-flows during transport led to the formation of dilute, low-density turbidity currents that may have become detached from the parent mass-flows. These mass flows deposited the Efaté Pumice Breccias in medial to distal below-storm-wave base environments. Deposition occurred concurrently with eruptive activity which probably lasted hours to days. (b) Stage II: Waning of eruption intensity caused flooding of the vent by seawater leading to hydromagmatic explosions that generated much finer-grained pyroclasts. The pyroclastic dispersions turbulently mixed with seawater in proximal areas and sedimentation by quasi-steady turbidity current followed, depositing the Rentabau Tuffs in deep, distal submarine environments. This stage of the cycle probably lasted for several days to weeks following explosive activity. (c) Stage III: Basaltic magma ascended to the surface along crustal fractures generated during caldera collapse and was erupted by passive effusion of lavas, punctuated by periods dominated by small-scale explosive eruptions. Continuous activity led to the growth of steep-sided basaltic volcanic cones, occurring over months to years. The earliest basaltic activity occurred in submarine environments, followed by eventual emergence due to local uplift, and on the islands of Nguna, Pele and Emau by shoaling of the growing volcano.

Depositional processes

Fluid basaltic lavas were emplaced by runout of flows from volcanic vents. At Mount Fatmalapa and Quoin Hill, conglomerate and breccia facies were deposited principally by submarine mass-flow processes operating on volcano flanks. On Nguna, Pele and Emau Islands, pyroclastic fall and surge processes were important in generating volcaniclastic facies in proximal areas. Deposition of conglomerate and breccia facies on island volcano flanks was dominated by normal epiclastic processes operating in beach and/or fluvial environments between effusive eruptions.

IMPLICATIONS AND FUTURE RESEARCH

Geochemistry

The magmas of the Efaté Island Group represent an extreme example of bimodal compositional variation in both the Vanuatu arc and arc magmas generally. Bimodal volcanism occurs sporadically at other island arc centres (*e.g.* Batur caldera, Bali, Wheller & Varne, 1984; Wheller, 1986; Wheller & Varne, 1986), but may be more common than is currently recognised if the sedimentary record is also taken into account (*e.g.* Mariana arc, Lee & Stern, 1998). Silicic volcanic eruptions in arcs are commonly highly explosive, resulting in abundant deposits of unconsolidated tephra that is more easily and rapidly eroded than lavas, and transported to offshore sedimentary environments. Submarine calderas are also increasingly recognised in arcs yet the impact this has on magma petrogenesis and volcanism is not widely appreciated (Cashman & Fiske, 1991; Cas, 1992; Fiske & Naka, 1994; Lloyd *et al.*, 1996). Future studies of silicic pyroclastic deposits in other young island arcs, especially those investigated during the Ocean Drilling Project, may reveal how unusual this style of volcanism is.

Additionally, further investigation of the high-Sr, high-P_2O_5 signature of the Efaté basalts and similar basalts from Santa Maria volcano on the northern shoulder of the DEZ may elucidate the mechanisms for enrichment of these elements. Laser ablation (LA-ICP-MS) studies of melt inclusions in the most primitive olivine phenocrysts from these two centres will contribute substantially to this.

Volcanology

The Efaté Pumice Breccias are an example of syn-eruptive, submarine emplaced, cold volcaniclastic mass-flows generated by ignimbrite-forming (plinian) eruptions. Facies of the Efaté Pumice Breccias show the sedimentary diversity of deposits from the submarine

equivalents of pyroclastic flows related to a major explosive eruption. Recognition of such deposits has important implications for mineral exploration in ancient volcanic successions, as submarine volcanic environments are commonly regions of intense hydrothermal activity leading to base metal deposition and subsequent generation of major ore bodies (Cas, 1992). In addition, such eruptions can have a devastating impact on local civilisations as pyroclastic flows and ignimbrites that enter the sea can generate major tsunamis (Bond & Sparks, 1976; Ninkovich *et al.*, 1978; Carey *et al.*, 1996). Mass movements of sediment on submarine slopes are also known to cause tsunamis and eruptions of submarine caldera volcanoes will have a similar impact (Einsele *et al.*, 1996).

The Rentabau Tuffs represent a rare example of hydromagmatically generated pyroclasts deposited as a thick submarine ash-turbidite sequence. Hydromagmatic activity must occur frequently in island arc caldera eruptions where calderas are commonly breached by the sea, yet the importance of hydromagmatic eruptions leading to submarine deposition of fine ash is largely overlooked (Fiske, 1963; Bond & Sparks, 1976; Nairn *et al.*, 1995; Carey *et al.*, 1996; Mandeville *et al.*, 1996b). A review of some well known subaqueous sequences might demonstrate whether such a phenomenon is also more common than previously recognised.

Although facies characteristics of the Efaté Pumice Formation clearly indicate that deposition of this volcaniclastic sequence occurred in deep submarine environments, definitive criteria for the recognition of sequences generated at subaqueous vents compared with subaerial vents remain unknown.

REFERENCES

ABRARD R. (1947). Fossiles Neogenes et Quaternaires des Nouvelles-Hébrides. *Annals de Palaeontologie* **32**: 5-113.

ABRARD R. AND AUBERT DE LA RUE E. (1938). Note sur les dépôts Quaternaires et les récifs soulevés des Nouvelles-Hébrides. *Bullétin du Societé Géologique de France* **VIII**: 63-66.

ADAMS P. B. (1984). Glass Corrosion. A record of the past? A predictor of the future? *Journal of Non-Crystalline Solids* **67**: 193-205.

AITCHISON J. C., CLARKE G. L., CLUZEL D., AND MEFFRE S. (1995). Eocene arc-continent collision in New Caledonia and implications for regional SW Pacific tectonic evolution. *Geology* **23**: 161-164.

AKIMOTO K. (1994). Cenozoic benthic foraminiferal biostratigraphy, paleobathymetry, paleoenvironments and paleoceanography of the New Hebrides Island Arc and North d'Entrecasteaux Ridge area. In: H. G. Greene, J.-Y. Collot, L. B. Stokking, *et al.* (Eds.), *Proceedings of the Ocean Drilling Program, Scientific Results*. Leg 134. Ocean Drilling Program, College Station, TX. pp. 265-291.

ALLÈGRE C. J., TREUIL M., MINSTER J.-F., MINSTER B., AND ALBARÈDE F. (1977). Systematic use of trace elements in igneous processes. Part I: Fractional crystallisation processes in volcanic suites. *Contributions to Mineralogy and Petrology* **60**: 57-75.

ALLEN J. R. L. (1970). *Physical Processes of Sedimentation. An introduction.* George Allen and Unwin, London. 248 p.

ALLEN J. R. L. (1982). *Sedimentary structures. Their character and physical basis.* Elsevier Scientific Publishing Co, Amsterdam.

ALLEN R. L. AND CAS R. A. F. (1990). The Rosebery controversy: distinguishing prospective submarine ignimbrite-like units from true subaerial ignimbrites in the Rosebery-Hercules Zn-Cu-Pb massive sulphide district, Tasmania. In: *Gondwana: terranes and resources*. Geological Society of Australia-Abstracts volume. Geological Society of Australia. pp. 31-32.

ALLEN S. R. AND MCPHIE J. (2000). Water-settling and resedimentation of submarine rhyolitic pumice at Yali, eastern Aegean, Greece. *Journal of Volcanology and Geothermal Research* **95**: 285-307.

ANCEY M., BASTENAIRE F., AND TIXIER R. (1978). Applications of statistical methods in microanalysis. In: F. Maurice, L. Meny, & R. Tixier (Eds.), *Microanalysis and Scanning Electron Microscopy Summer School.* Les Editions de Physique, Orsay, France. pp. 319-343.

ANDERSON E. B., HARVEY C. C., LOVELOCK B. G., PEARSON C. F., AND USSHER G. N. H. (1986). Factors influencing geothermal exploration of small volcanic Pacific islands. An example from Efaté Island, Vanuatu. *Proceedings of the New Zealand Geothermal Workshop* **8**: 141-146.

AOMINE S. AND WADA K. (1962). Differential weathering of volcanic ash and pumice, resulting in formation of hydrated halloysite. *American Minerologist* **47**: 1024-1048.

ARCULUS R. J. (1994). Aspects of magma genesis in arcs. *Lithos* **33**: 189-208.

ARCULUS R. J. AND JOHNSON R. W. (1981). Island arc magma sources: a geochemical assessment of the roles of slab-derived components and crustal contamination. *Geochemical Journal* **15**: 109-133.

ASH R. P., CARNEY J. N., AND MACFARLANE A. (1978). *Geology of Efaté and Offshore Islands.* Regional Report, New Hebrides Condominium Geological Survey. 49 p.

ASH R. P., CARNEY J. N., AND MACFARLANE A. (1980). *Geology of the northern Banks Islands.* Regional Report, New Hebrides Condominium Geological Survey. 52 p.

ASH R. P., RADFORD N. W., GREENBAUM D., AND MALLICK D. I. J. (1974). Geology of Efaté and offshore islands. British Government's Overseas Development Administration (Directorate of Overseas Surveys). 1:100,000 scale geological map.

AUBERT DE LA RUE E. (1937). Le volcanisme aux Nouvelles Hebrides (Melanesie). *Bullétin Volcanologique* **2**: 79-142.

AUBERT DE LA RUE E. (1939). Les minéraux des Nouvelles-Hébrides. *Bullétin du Musée d'Histoire Naturelle de Paris* **11**: 342-348.

AUBERT DE LA RUE E. (1956). La géologie des Nouvelles-Hébrides. *Journal de Societé des Oceanistes* **12**: 63-98.

AUZENDE J.-M., LAFOY Y., AND MARSSET B. (1988). Recent geodynamic evolution of the North Fiji Basin. *Geology* **16**: 925-929.

AUZENDE J.-M., PELLETIER B., AND EISSEN J.-P. (1995). The North Fiji Basin: geology, structure, and geodynamic evolution. In: B. Tayor (Ed.), *Backarc Basins: Tectonics and Magmatism*. Plenum Press, New York. pp. 139-175.

AYRES L. D., VAN WAGONER N. A., AND FERREIRA W. S. (1991). Voluminous shallow-water to emergent phreatomagmatic basaltic volcaniclastic rocks, Proterozoic (~1886 Ma) Amisk Lake composite volcano, Flin Flon greenstone belt, Canada. In: R. V. Fisher & G. A. Smith (Eds.), *Sedimentation in Volcanic Settings*. SEPM Special Publication No. 45, Tulsa. pp. 175-187.

BAKER P. E. (1968). Comparative volcanology and petrology of the Atlantic island arcs. *Bulletin of Volcanology* **32**: 189-206.

BAKER P. E., COLTORTI M., BRIQUEU L., HASENAKA T., AND CONDLIFFE E. (1994). Volcanic ash layers from sites 828, 830, 831, 832 and 833, New Hebrides Island Arc. In: H. G. Greene, J.-Y. Collot, L. B. Stokking, *et al.* (Eds.), *Proceedings of the Ocean Drilling Program, Scientific Results*. Leg 134. Ocean Drilling Program, College Station, TX. pp. 403-412.

BAKER P. E. AND CONDLIFFE E. (1996). Compositional variations in submarine volcanic ashes from the vicinity of the Vanuatu Island Arc: a response to ridge-arc collision? *Journal of Volcanology and Geothermal Research* **72**: 225-238.

BALLANCE P. F. AND GREGORY M. R. (1991). Parnell Grits - Large subaqueous volcaniclastic gravity flows with multiple particle-support mechanisms. In: R. V. Fisher & G. A. Smith (Eds.), *Sedimentation in Volcanic Settings*. SEPM Special Publication No. 45, Tulsa. pp. 189-200.

BARNES P. M. AND LEWIS K. B. (1991). Sheet slides and rotational failures on a convergent margin: the Kidnappers Slide, New Zealand. *Sedimentology* **38**: 205-221.

BARSDELL M. AND BERRY R. F. (1990). Origin and evolution of primitive island arc ankaramites from Western Epi, Vanuatu. *Journal of Petrology* **31**: 747-777.

BARSDELL M., SMITH I. E. M., AND SPORLI K. B. (1982). The origin of reversed geochemical zoning in the northern New Hebrides Volcanic Arc. *Contributions to Mineralogy and Petrology* **81**: 148-155.

BATH A. H. (1986). Mixed sources and reactions of hydrothermal springs in Efate: Vanuatu island arc. *International Symposium on Water-Rock Interaction* **5**: 39-42.

BERNARD A. AND OBELLIANNE J.-M. (1963). Aperçu métallogénique sur le gisement de manganèse de Forari. *Sciences de Terre* **9**: 123-148.

BIGGER S. E. AND HANSON R. E. (1992). Devitrification textures and related features in the Carlton Rhyolite in the Blue Creek Canyon area, Wichita Mountains, southwestern Oklahoma. *Oklahoma Geology Notes* **52**: 124-142.

BLUNDY J. D. AND SHIMIZU N. (1991). Trace element evidence for plagioclase recycling in calc-alkaline magmas. *Earth and Planetary Science Letters* **102**: 178-197.

BOIANO U. (1997). Anatomy of a siliciclastic turbidite basin: the Gorgoglione Flysch, Upper Miocene, southern Italy: physical statigraphy, sedimentology and sequence-stratigraphic framework. *Sedimentary Geology* **107**: 231-262.

BOND A. AND SPARKS R. S. J. (1976). The Minoan eruption of Santorini, Greece. *Journal of the Geological Society of London* **132**: 1-16.

BONNEFOI C. C., PROVOST A., AND ALBARÈDE F. (1995). The 'Daly Gap' as a magmatic catastrophe. *Nature* **378**: 270-272.

BOUMA A. H. (1962). *Sedimentology of some flysche deposits*. Elsevier, Amsterdam. 168 p.

BRANNEY M. J. AND SPARKS R. S. J. (1990). Fiamme formed by diagenesis and burial-compaction in soils and subaqueous sediments. *Journal of Volcanology and Geothermal Research* **147**: 919-922.

BRIQUEU L. AND LANCELOT J. R. (1983). Sr isotopes and K, Rb, Sr balance in sediments and igneous rocks from the subducted plate of the Vanuatu (New Hebrides) active margin. *Geochimica et Cosmochimica Acta* **47**: 191-200.

BRIQUEU L., LAPORTE C., CRAWFORD A. J., HASENAKA T., BAKER P. E., AND COLTORTI M. (1994). Temporal magmatic evolution of the Aoba Basin, central New Hebrides island arc: Pb, Sr, and Nd isotopic evidence for the coexistence of two mantle components beneath the arc. In: H. G. Greene, J.-Y. Collot, L. B. Stokking, *et al.* (Eds.), *Proceedings of the Ocean Drilling Program, Scientific Results*. Leg 134. Ocean Drilling Program, College Station, TX. pp. 393-401.

BROPHY J. G. AND MARSH B. D. (1986). On the origin of high-alumina arc basalt and the mechanics of melt extraction. *Journal of Petrology* **27**: 763-789.

BULL S. W. AND CAS R. A. F. (1991). Depositional controls and characteristics of subaqueous bedded volcaniclastics of the Lower Devonian Snowy River Volcanics. In: R. Cas & C. Busby-Spera (Eds.), *Volcaniclastic Sedimentation*. (Sedimentary Geology **74**). pp. 189-215.

BURNHAM C. W. (1983). Deep submarine pyroclastic eruptions. In: *The Kuroko and related volcanogenic massive sulfide deposits*. Economic Geology Monographs No. 5. pp. 142-148.

BUSBY-SPERA C. J. (1986). Depositional features of rhyolitic and andesitic volcaniclastic rocks of the Mineral King submarine caldera complex, Sierra Nevada, California. *Journal of Volcanology and Geothermal Research* **27**: 43-76.

CALMANT S., LEBELLEGARD P., TAYLOR F., BEVIS M., MAILLARD D., AND BONNEAU J. R. J. (1995). Geodetic measurements of convergence across the New Hebrides subduction zone. *Geophysical Research Letters* **22**(19): 2573-2576.

CAPACCIONI B. AND CONGLIO S. (1995). Varicolored and vesiculated tuffs from La Fossa volcano, Vulcano Island (Aeolian Archipelago, Italy): evidence of syndepositional alteration processes. *Bulletin of Volcanology* **57**: 61-70.

CAREY S. (1997). Influence of convective sedimentation on the formation of widespread tephra fall layers in the deep sea. *Geology* **25**(9): 839-842.

CAREY S., SIGURDSSON H., MANDEVILLE C., AND BRONTO S. (1996). Pyroclastic flows and surges over water: an example from the 1883 Krakatau eruption. *Bulletin of Volcanology* **57**: 493-511.

CAREY S. N. AND SIGURDSSON H. (1980). The Roseau Ash: deep-sea tephra deposits from a major eruption on Domenica, Lesser Antilles Arc. *Journal of Volcanology and Geothermal Research* **7**: 67-86.

CARNEY J. N. (1988). *Geology of Maewo*. Regional Report, Vanuatu Department of Geology, Mines and Rural Water Resources. 119 p.

CARNEY J. N. AND MACFARLANE A. (1979). *Geology of Tanna, Anneityum, Futuna and Aniwa*. Regional Report, New Hebrides Condominium Geological Survey. 71 p.

CARNEY J. N., MACFARLANE A., AND MALLICK D. I. J. (1985). The Vanuatu Island Arc: an outline of the stratigraphy, structure, and petrology. In: A. E. M. Nairn, F. G. Stehli, & S. Uyeda (Eds.), *The Ocean Basins and Margins*. Plenum Press, New York, London. pp. 683-718.

CAS R. A. F. (1983). Submarine 'crystal tuffs': their origin using a Lower Devonian example from southeastern Australia. *Geological Magazine* **120**: 471-486.

CAS R. A. F. (1992). Submarine volcanism: eruption styles, products, and relevance to understanding the host-rock successions to volcanic-hosted massive sulfide deposits. *Economic Geology* **87**: 511-541.

CAS R. A. F., ALLEN R. L., BULL S. W., CLIFFORD B. A., AND WRIGHT J. V. (1990). Subaqueous, rhyolitic dome-top tuff cones: a model based on the Devonian Bunga Beds, southeastern Australia and a modern analogue. *Bulletin. of Volcanology* **52**: 159-174.

CAS R. A. F. AND WRIGHT J. V. (1987). *Volcanic Sucessions - Modern and Ancient*. Chapman & Hall Publishers, London. 528 p.

CAS R. A. F. AND WRIGHT J. V. (1991). Subaqueous pyroclastic flows and ignimbrites: an assessment. *Bulletin of Volcanology* **53**: 357-380.

CASEY W. H. AND BUNKER B. (1990). Leaching of minerals and glass surfaces during dissolution. In: M. F. Hochella Jr & A. F. White (Eds.), *Mineral-water interface geochemistry*. Reviews in Mineralogy 23. Mineralogical Society of America, Washington DC. pp. 397-426.

CASHMAN K. V. AND FISKE R. S. (1990). Recognition of a submarine pyroclastic deposit - Shirahama Group (Pliocene), Japan. *EOS - Transactions of the American Geophysical Union* **71**(43): 1721.

CASHMAN K. V. AND FISKE R. S. (1991). Fallout of pyroclastic debris from submarine volcanic eruptions. *Science* **253**: 275-280.

CASHMAN K. V. AND MANGAN M. T. (1994). Physical aspects of magmatic degassing II. Constraints on vesiculation processes from textural studies of eruptive products. In: M. R. Carroll & J. R. Holloway (Eds.), *Volatiles in Magmas*. Reviews in Mineralogy 30. Mineralogical Society of America, Washington DC. pp. 447-478.

CHASE T. E. AND SEEKINS B. A. (1988). Submarine topography of the Vanuatu and southeastern Solomon Islands regions. In: H. G. Greene & F. L. Wong (Eds.), *Geology and Offshore Resources of Pacific Island Arcs - Vanuatu Region*. Earth Science Series 8. Circum-Pacific Council for Energy and Mineral Resources, Houston, Texas. pp. 35-39.

CHATELAIN J.-L. AND GRASSO J.-R. (1992). Spatial and temporal seismic energy release in the Efaté region (central New Hebrides Island Arc): evidence for buckling? *Geophysical Research Letters* **19**(11): 1157-1160.

CHATELAIN J.-L., GUILLIER B., AND GRATIER J.-P. (1993). Unfolding the subducting plate in the central New Hebrides island arc: geometrical argument for detachment of part of the downgoing slab. *Geophysical Research Letters* **20**(8): 655-658.

CHATELAIN J.-L., MOLNAR P., PRÉVOT R., AND ISACKS B. (1992). Detachment of part of the downgoing slab and uplift of the New Hebrides (Vanuatu) islands. *Geophysical Research Letters* **19**(14): 1507-1510.

CHESTER D. (1993). *Volcanoes and Society*. Edward Arnold, London. 351 p.

COLEMAN R. G. (1977). *Ophiolites*. Springer-Verlag, Berlin. 229 p.

COLLEY H. AND ASH R. P. (1971). *The Geology of Erromango*. Regional Report, New Hebrides Condominium Geological Survey. 112p.

COLLEY H. AND WARDEN A. J. (1974). Petrology of the New Hebrides. *Geological Society of America Bulletin* **85**: 1635-1646.

COLLOT J.-Y., LALLEMAND S., PELLETIER B., EISSEN J.-P., GLAÇON G., FISHER M. A., GREENE H. G., BOULIN J., DANIEL J., AND MONZIER M. (1992). Geology of the d'Entrecasteaux-New Hebrides Arc collision zone: results from a deep submersible survey. *Tectonophysics* **212**: 213-241.

COLTORTI M., HASENAKA T., BRIQUEU L., BAKER P. E., AND SIENA F. (1994). Petrology and magmatic affinity of the North d'Entrecasteaux Ridge, central New Hebrides Trench, site 828. In: H. G. Greene, J.-Y. Collot, L. B. Stokking, *et al.* (Eds.), *Proceedings of the Ocean Drilling Program, Scientific Results*. Leg 134. Ocean Drilling Program, College Station, Texas. pp. 353-362.

COULON C., MAILLET P., AND MAURY R. C. (1979). Contribution à l'étude du volcanisme de l'arc des Nouvelles-Hébrides: données petrologiques sur les laves de l'ile d'Efaté. *Bullétin du Societé Géologique de France* **21**(5): 619-629.

COULON C. AND MAURY R. C. (1981). Petrology of tholeiitic lavas from Tanna Island (New Hebrides): importance of cumulative processes in island arc magmatism. *Bullétin Volcanologique* **44**: 661-680.

COUSINEAU P. A. (1994). Subaqueous pyroclastic deposits in an Ordovician fore-arc basin: an example from the Saint-Victor Formation, Quebec Appalachians, Canada. *Journal of Sedimentary Research* **A64**: 867-880.

CRAWFORD A. J., BRIQUEU L., LAPORTE C., AND HASENAKA T. (1995). Coexistence of Indian and Pacific oceanic upper mantle reservoirs beneath the central New Hebrides Island Arc. In: B. Taylor & J. Natland (Eds.), *Active Margins and Marginal Basins of the Western Pacific*. 88. American Geophysical Union Monograph. pp. 199-217.

CRAWFORD A. J., FALLOON T. J., AND EGGINS S. (1987). The origin of island arc high-alumina basalts. *Contributions to Mineralogy and Petrology* **97**: 417-430.

CRAWFORD A. J., GREENE H. G., AND EXON N. F. (1988). Geology, petrology and geochemistry of submarine volcanoes around Epi Island, New Hebrides Island Arc. In: H. G. Greene & F. L. Wong (Eds.), *Geology and Offshore Resources of Pacific Island Arcs - Vanuatu Region*. Earth Science Series 8. Circum-Pacific Council for Energy and Mineral Resources, Huston, Texas. pp. 301-327.

CRAWFORD A. J., PRICE R. C., AND MAAS R. (1998). Petrogenesis and geodynamic significance of the Basement Complex ophiolite, Pentecost Island, Vanuatu island arc. *Geological Society of Australia-Abstracts Volume* **49**: 100.

DAVIDSON J. P. (1992). Continental and island arcs. In: *Encyclopedia of Earth System Science*. Volume 1. Academic Press, Inc. pp. 615-626.

DAVIES J. H. AND BICKLE M. J. (1991). A physical model for the volume and composition of melt produced by hydrous fluxing above subduction zones. *Philosophical Transactions of the Royal Society of London* **A 335**: 355-364.

DE' GENNARO M., INCORONATO A., MASTROLORENZO G., ADABBO M., AND SPINA G. (1999). Depositional mechanisms and alteration processes in different types of pyroclastic deposits from Campi Flegri volcanic field (Southern Italy). *Journal of Volcanology and Geothermal Research* **91**: 303-320.

DEFANT M. J. AND DRUMMOND M. S. (1990). Derivation of some modern arc magmas by melting of young subducted lithosphere. *Nature* **347**: 662-665.

DEFANT M. J. AND NIELSEN R. L. (1990). Interpretation of open system petrogenetic processes: Phase equilibria constraints on magma evolution. *Geochimica et Cosmochimica Acta* **54**: 87-102.

DEFANT M. J., CLARK L. F., STEWART R. H., DRUMMOND M. S., DE BOER J. Z., MAURY R. C., BELLON H., JACKSON T. E., AND RESTREPO J. F. (1991a). Andesite and dacite genesis via contrasting processes: the geology and geochemistry of El Valle Volcano, Panama. *Contributions to Mineralogy and Petrology* **106**: 309-324.

DEFANT M. J., RICHERSON P. M., DE BOER J. Z., STEWART R. H., MAURY R. C., BELLON H., DRUMMOND M. S., FEIGENSON M. D., AND JACKSON T. E. (1991b). Dacite genesis via both slab melting and differentiation: petrogenesis of La Yeguada volcanic complex, Panama. *Journal of Petrology* **32**(6): 1101-1142.

DELLA-PASQUA F. N. (1997). Primitive ankaramitic melts in island arcs: evidence from melt inclusions. Unpublished PhD thesis, University of Tasmania.

DEVINE J. D. (1995). Petrogenesis of the basalt-andesite-dacite association of Grenada, Lesser Antilles island arc, revisited. *Journal of Volcanology and Geothermal Research* **69**: 1-33.

DICKINSON W. R. (1975). Potassium-depth (K-h) relations in continental margin and intraoceanic magmatic arcs. *Geology* **3**: 53-56.

DRUITT T. H. (1995). Settling behaviour of concentrated dispersions and some volcanological applications. *Journal of Volcanology and Geothermal Research* **65**: 27-39.

DRUMMOND M. S. AND DEFANT M. J. (1990). A model for trondhjemite-tonalite-dacite genesis and crustal growth via slab melting: Archean to modern comparisons. *Journal of Geophysical Research* **95**(B13): 21,503- 21,521.

DUGMORE A. J., NEWTON A. J., AND SUGDEN D. E. (1992). Geochemical stability of fine-grained silicic Holocene tephra in Iceland and Scotland. *Journal of Quaternary Science* **7**(2): 173-183.

DUPUY C., BARCZUS H. G., DOSTAL J., VIDAL P., AND LIOTARD J. M. (1989). Subducted and recycled lithosphere as the mantle sources of ocean island basalts from southern Polynesia, Central Pacific. *Chemical Geology* **77**: 1-18.

DUPUY C., DOSTAL J., MARCELOT G., BOUGAULT H., JORON J. L., AND TREUIL M. (1982). Geochemistry of basalts from central and southern New Hebrides arc: implications for their source rock composition. *Earth and Planetary Science Letters* **60**: 207-225.

EGGINS S. M. (1993). Origin and differentiation of picritic arc magmas, Ambae (Aoba), Vanuatu. *Contributions to Mineralogy and Petrology* **114**: 79-100.

EINSELE G. (1991). Submarine mass flow deposits and turbidites. In: G. Einsele, W. Ricken, & A. Seilacher (Eds.), *Cycles and Events in Stratigraphy*. Springer-Verlag, Berlin, Heidelberg. pp. 313-339.

EINSELE G. (1996). Event deposits: the role of sediment supply and relative sea-level changes - overview. *Sedimentary Geology* **104**: 11-37.

EINSELE G., COUGH S. K., AND SHIKI T. (1996). Depositional events and their records - an introduction. *Sedimentary Geology* **104**: 1-9.

EISSEN J.-P. AND CALVA SCIENTIFIC TEAM. (1997). New investigations on the 1452 A.D. Kuwae submarine caldera (Vanuatu, SW Pacific). *IAVCEI General Assembly 1997 – Abstracts volume*: 156.

ELLIOT T. (1986). Siliciclastic shorelines. In: H. G. Reading (Ed.), *Sedimentary environments and facies*. Blackwell Scientific Publications, Oxford. pp. 155-188.

ELLIOTT T., PLANK T., ZINDLER A., WHITE W., AND BOURDON B. (1997). Element transport from slab to volcanic front at the Mariana arc. *Journal of Geophysical Research* **102**(B7): 14,991-15,019.

EWART A. (1982). The mineralogy and petrology of Tertiary-Recent orogenic volcanic rocks: with special reference to the andesite-basalt compositional range. In: R. S. Thorpe (Ed.), *Andesites - Orogenic andesites and related rocks.* John Wiley and Sons, Chichester. pp. 26-87.

FEDERMAN B. N. (1984). Hydration of abyssal tephra glasses. *Journal of Non-Crystalline Solids* **67**: 323-332.

FISHER R. V. (1983). Flow transformations in sediment gravity flows. *Geology* **11**: 273-274.

FISHER R. V. (1984). Submarine volcaniclastic rocks. In: B. P. Kokelaar & M. F. Howells (Eds.), *Marginal basin geology; volcanic and associated sedimentary and tectonic processes in modern and ancient marginal basins.* Geological Society of London Special Publication No. 16. pp. 5-27.

FISHER R. V. AND SCHMINCKE H.-U. (1984a). *Pyroclastic Rocks.* Springer-Verlag, Berlin. 472 p.

FISHER R. V. AND SCHMINCKE H.-U. (1984b). Volcaniclastic sedimentation and facies. In: K. Pye (Ed.), *Sediment Transport and Depositional Processes.* Blackwell Scientific Publications. pp. 351-388.

FISHER R. V. AND SCHMINCKE H.-U. (1994). Volcaniclastic sediment transport and deposition. In: K. Pye (Ed.), *Sediment transport and depositional processes.* Blackwell Scientific Publications, Oxford. pp. 351-388.

FISKE R. S. (1963). Subaqueous pyroclastic flows in the Ohanapecosh Formation, Washington. *Geological Society of America Bulletin* **74**: 391-406.

FISKE R. S. (1969). Recognition of pumice in marine pyroclastic rocks. *Geological Society of America Bulletin* **80**: 1-8.

FISKE R. S. AND CASHMAN K. V. (1987). Partitioning of tephra in submarine eruption columns. *Abstracts with Programs – Geological Society of America* **19**(7): 664.

FISKE R. S. AND MATSUDA T. (1964). Submarine equivalents of ash flows in the Tokiwa Formation, Japan. *American Journal of Science* **262**: 76-106.

FISKE R. S. AND NAKA J. (1994). Caldera-forming submarine pyroclastic eruption at Myojin Knoll, Izu-Bonin Arc, Japan. *EOS-Transactions of the American Geophysical Union* **75**(44): 729-730.

FISKE R. S., CASHMAN K. V., SHIBATA A., AND WATANABE K. (1998). Tephra dispersal from Myojinsho, Japan, during its shallow submarine eruption of 1952-53. *Bulletin of Volcanology* **59**: 263-275.

FLOOD R. D. AND SHOR A. N. (1988). Mud waves in the Argentine Basin and their relationship to regional bottom circulation patterns. *Deep Sea Research* **35**: 943-971.

FRIEDMAN I. AND LONG W. (1984). Volcanic glasses, their origins and alteration processes. *Journal of Non-Crystalline Solids* **67**: 127-133.

GARDNER J. E., THOMAS R. M. E., JAUPART C., AND TAIT S. (1996). Fragmentation of magma during Plinian volcanic eruptions. *Bulletin of Volcanology* **58**: 144-162.

GASS I. G., LIPPARD S. J., AND SHELTON A. W. (1984). *Ophiolites and oceanic lithosphere.* Blackwell Scientic Publications, Oxford. 431 p.

GEIST D., HOWARD K. A., AND LARSON P. (1995). The generation of oceanic rhyolites by crystal fractionation: the basalt-rhyolite association at Volcán Alcedo, Galápagos Achipelago. *Journal of Petrology* **36**(4): 965-982.

GERSTENBERGER H. AND HAASE G. (1997). A highly effective emitter substance for mass spectrometric Pb isotope ratio determinations. *Chemical Geology* **136**: 309-312.

GERTISSER R. AND KELLER J. (2000). From basalt to dacite: origin and evolution of the calc-alkaline series of Salina, Aeolian Arc, Italy. *Contributions to Mineralogy and Petrology* **139**: 607-626.

GHIARA M. R. AND PETTI C. (1996). Chemical alteration of volcanic glasses and related control by secondary minerals: experimental studies. *Aquatic Geochemistry* **1**: 329-354.

GHIBAUDO G. (1992). Subaqueous sediment gravity flow deposits: practical criteria for their field description and classification. *Sedimentology* **39**: 423-454.

GILL J. B. (1981). *Orogenic andesites and plate tectonics.* Minerals and Rocks. Springer-Verlag, Berlin. 358 p.

GILL J. B., STORK A. L., AND WHELAN P. M. (1984). Volcanism accompanying back-arc basin development in the southwest Pacific. *Tectonophysics* **102**: 207-224.

GIRSCHIK H. F. (1995). *An assessment of some of the clay deposits of Efaté, Vanuatu, to determine their suitability for the production of bricks, tiles and other ceramics.*

GORTON M. P. (1977). The geochemistry and origin of Quaternary volcanism in the New Hebrides. *Geochimica et Cosmochimica Acta* **41**: 1257-1270.

GOUD COLLINS M. R. (1994). Volcaniclastic sediments of the North Aoba Basin: depositional processes and geologic history. In: H. G. Greene, J.-Y. Collot, L. B. Stokking, *et al.* (Eds.), *Proceedings of the Ocean Drilling Program, Scientific Results.* Leg 134. Ocean Drilling Program, College Station, TX. pp. 97-107.

GREEN D. H. AND RINGWOOD A. E. (1967). The genesis of basaltic magmas. *Contributions to Mineralogy and Petrology* **15**: 103-190.

GREEN D. H. AND WALLACE M. E. (1988). Mantle metasomatism by ephemeral carbonatite melts. *Nature* **336**: 459-462.

GREENBAUM D., MALLICK D. I. J., AND RADFORD N. W. (1975). *Geology of the Torres Islands.* Regional Report, New Hebrides Condominium Geological Survey. 44 p.

GREENE H. G. AND COLLOT J.-Y. (1994). Ridge-arc collision: timing and deformation determined by Leg 134 drilling, central New Hebrides Island Arc. In: H. G. Greene, J.-Y. Collot, L. B. Stokking, *et al.* (Eds.), *Proceedings of the Ocean Drilling Program, Scientific Results*. Leg 134. Ocean Drilling Program, College Station, TX. pp. 609-621.

GREENE H. G., COLLOT J.-Y., FISHER M. A., AND CRAWFORD A. J. (1994a). Neogene tectonic evolution of the New Hebrides Island Arc: a review incorporating ODP drilling results. In: H. G. Greene, J.-Y. Collot, L. B. Stokking, *et al.* (Eds.), *Proceedings of the Ocean Drilling Program, Scientific Results*. Leg 134. Ocean Drilling Program, College Station, TX. pp. 19-46.

GREENE H. G., COLLOT J.-Y., STOKKING L. B., *ET AL.* Eds. (1994b). *Proceedings of the Ocean Drilling Program, Scientific Results Leg 134*. Ocean Drilling Program, College Station, TX. 665p.

GREENE H. G., MACFARLANE A., JOHNSON D. P., AND CRAWFORD A. J. (1988a). Structure and tectonics of the central New Hebrides Arc. In: H. G. Greene & F. L. Wong (Eds.), *Geology and Offshore Resources of Pacific Island Arcs - Vanuatu Region*. Earth Science Series 8. Circum-Pacific Council for Energy and Mineral Resources, Houston, Texas. pp. 377-412.

GREENE H. G., MACFARLANE A., AND WONG F. L. (1988b). Geology and offshore resources of Vanuatu - introduction and summary. In: H. G. Greene & F. L. Wong (Eds.), *Geology and Offshore Resources of Pacific Island Arcs - Vanuatu Region*. Earth Science Series 8. Circum-Pacific Council for Energy and Mineral Resources, Houston, Texas. pp. 1-25.

GREENE H. G. AND WONG F. L. Eds. (1988). *Geology and Offshore Resources of Pacific Island Arcs - Vanuatu Region*. Circum-Pacific Council for Energy and Mineral Resources, Houston, Texas. 442p.

HACKETT W. R. AND HOUGHTON B. F. (1989). A facies model for a Quaternary andesitic composite volcano: Ruapehu, New Zealand. *Bulletin of Volcanology* **51**: 51-68.

HAMILTON W. B. (1988). Plate tectonics and island arcs. *Geological Society of America Bulletin* **100**: 1503-1527.

HAMILTON W. B. (1995). Subduction systems and magmatism. In: J. L. Smellie (Ed.), *Volcanism associated with extension at consuming plate margins*. Geological Society of London Special Publication No. 81. pp. 3-28.

HARMER R. E. AND GITTINS J. (1998). The case for primary, mantle-derived carbonatite magma. *Journal of Petrology* **39**: 1895-1903.

HART S. R. (1984). A large-scale isotope anomaly in the southern hemisphere mantle. *Nature* **309**: 753-757.

HAWKESWORTH C. J., GALLAGHER K., HERGT J. M., AND MCDERMOTT F. (1994). Destructive plate margin magmatism: geochemistry and melt generation. *Lithos* **33**: 169-188.

HAWKESWORTH C. J., HERGT J. M., ELLAM R. M., AND MCDERMOTT F. (1991). Element fluxes associated with subduction related magmatism. *Philosophical Transactions of the Royal Society of London* **A 335**: 393-405.

HEIKEN G. (1987). Textural analysis of tephra from a rhyodacitic eruption sequence, Thira (Santorini), Greece. In: J. R. Marshall (Ed.), *Clastic Particles - Scanning Electron Microscopy and shape analysis of sedimentary and volcanic clasts*. Van Nostrand Reinhold Company, New York. pp. 67-78.

HEIKEN G. AND WOHLETZ K. (1991). Fragmentation processes in explosive volcanic eruptions. In: R. V. Fisher & G. A. Smith (Eds.), *Sedimentation in Volcanic Settings*. SEPM Special Publication No. 45, Tulsa. pp. 19-26.

HEIN J. R., SCHULZ M. S., AND KANG J.-K. (1990). Insular and submarine ferromanganese mineralization of the Tonga-Lau region. *Marine Mining* **9**: 305-354.

HISCOTT R. N. (1994a). Loss of capacity, not competence, as the fundamental process governing deposition from turbidity currents. *Journal of Sedimentary Research* **A64**(2): 209-214.

HISCOTT R. N. (1994b). Traction-carpet stratification in turbidites - fact or fiction? *Journal of Sedimentary Research* **A64**(2): 204-208.

HOCHSTEIN M. P. (1977). *Geothermal reconnaisance, Efaté*. Annual Report for 1975, New Hebrides Condominium Geological Survey. 33 p.

HODDER A. P. W., GREEN B. E., AND LOWE D. J. (1990). A two-stage model for the formation of clay minerals from tephra-derived volcanic glass. *Clay Minerals* **25**: 313-327.

HOLE M. J., SAUNDERS A. D., MARRINER G. F., AND TARNEY J. (1984). Subduction of pelagic sediments: implications for the origin of Ce-anomalous basalts from the Mariana Islands. *Journal of the Geological Society of London* **141**: 453-472.

HOUGHTON B. F. AND WILSON C. J. N. (1989). A vesicularity index for pyroclastic deposits. *Bulletin of Volcanology* **51**: 451-462.

HOUGHTON B. F., WILSON C. J. N., MCWILLIAMS M. O., LANPHERE M. A., WEAVER S. D., BRIGGS R. M., AND PRINGLE M. S. (1995). Chronology and dynamics of a large silicic magmatic system: Central Taupo Volcanic Zone, New Zealand. *Geology* **23**(1): 13-16.

HUNT J. B. AND HILL P. G. (1993). Tephra geochemistry: a discussion of some persistent analytical problems. *The Holocene* **3**: 271-278.

IIZASA K., KAWASAKI K., MAEDA K., MATSUMOTO T., SAITO N., AND HIRAI K. (1998). Hydrothermal sulfide-bearing Fe-Si oxyhydroxide deposits from the Coriolis Troughs, Vanuatu backarc, southwestern Pacific. *Marine Geology* **145**: 1-21.

INGRAM R. L. (1954). Terminology for the thickness of stratification and parting units in sedimentary rocks. *Geological Society of America Bulletin* **65**: 937-938.

IYER S. D. AND KARISIDDAIAH S. M. (1988). Morphology and petrography of pumice from the central Indian Ocean Basin. *Indian Journal of Marine Sciences* **17**: 333-334.

JAHN B. M., GLIKSON A. Y., PEUCAT J. J., AND HICKMAN A. H. (1981). REE geochemistry and isotopic data of Archean silicic volcanics and granitoids from the Pilbara Block, Western Australia: implications for the early crustal evolution. *Geochimica et Cosmochimica Acta* **45**: 1633-1652.

JOHNSON H. D. AND BALDWIN C. T. (1986). Shallow siliciclastic seas. In: H. G. Reading (Ed.), *Sedimentary environments and facies*. Blackwell Scientific Publications, Oxford. pp. 229-282.

JONES J. G. (1967). Clastic rocks of Espiritu Santo Island, New Hebrides. *Geological Society of America Bulletin* **78**: 1281-1288.

JONES P. AND AGSO TIMESCALE CALIBRATION AND DEVELOPMENT PROJECT. (1995). *AGSO Phanerozoic Timescale 1995: Wallchart and Explanatory Notes*. Australian Geological Survey Organisation.

KAMINSKI E. AND JAUPART C. (1998). The size distribution of pyroclasts and the fragmentation sequence in explosive volcanic eruptions. *Journal of Geophysical Research* **103**(B12): 29,759-29,779.

KANO K., YAMAMOTO T., AND ONO K. (1996). Subaqueous eruption and emplacement of the Shinjima Pumice, Shinjima (Moeshima) Island, Kagoshima Bay, SW Japan. *Journal of Volcanology and Geothermal Research* **71**: 187-206.

KAWANO M., TOMITA K., AND SHINOHARA Y. (1997). Analytical electron microscopic study of the noncrystalline products formed at early weathering stages of volcanic glass. *Clays and Clay Minerals* **45**(3): 440-447.

KERSTING A. B., ARCULUS R. J., AND GUST D. A. (1996). Lithospheric contributions to arc magmatism: isotope variations along strike in volcanoes of Honshu, Japan. *Science* **272**: 1464-1468.

KLUG C. AND CASHMAN K. V. (1996). Permeability development in vesiculating magmas: implications for fragmentation. *Bulletin of Volcanology* **58**: 87-100.

KNELLER B. (1995). Beyond the turbidite paradigm: physical models for deposition of turbidites and their implications for reservoir prediction. In: A. J. Hartley & D. J. Prosser (Eds.), *Characterisation of deep marine clastic systems*. Geological Society of London Special Publication No. 94. pp. 31-49.

KNELLER B. C. AND BRANNEY M. J. (1995). Sustained high-density turbidity currents and the deposition of thick massive sands. *Sedimentology* **42**: 607-616.

KOKELAAR P. (1986). Magma-water interactions in subaqueous and emergent basaltic volcanism. *Bulletin of Volcanology* **48**: 275-289.

KOKELAAR B. P., BEVINS R E., AND ROACH R. A. (1985). Submarine silicic volcanism and associated sedimentary and tectonic processes, Ramsey Island, SW Wales. *Journal of the Geological Society of London* **142**: 591-613.

KROENKE L. W. Ed. (1984a). *Cenozoic tectonic development of the southwest Pacific*. UN ESCAP CCOP/SOPAC Technical Bulletin.

KROENKE L. W. (1984b). Vanuatu and the Eastern Outer Solomon Islands - formation of the the New Hebrides and Vitiaz Arcs and development of the North Fiji Basin. In: L. W. Kroenke (Ed.), *Cenozoic tectonic development of the southwest Pacific*. 6. UN ESCAP CCOP/SOPAC Technical Bulletin. pp. 63-75.

LACROIX M. A. (1940). Les charactéristiques des laves des îles situés au sud de l'Equateur, formant la limite du domaine circumpacifique dans la région des Nouvelles-Hébries et de la fosse Tonga Kermadec. *Comptes Rendus de l'Académie des Sciences, Paris* **211**(5): 37-40.

LAPORTE C., BRIQUEU L., CLUZEL D., AND EISSEN J.-P. (1997). Gradients géochimiques et isotopiques le long de l'arc des Nouvelles Hébrides (Vanuatu, Pacifique SW). Collision de la Zone D'Entrecasteaux et hétérogénéité des sources mantelliques. Unpublished.

LE BAS M. J., LE MAITRE R. W., STRECKEISEN A., AND ZANETTIN B. (1986). A chemical classification of volcanic rocks based on the total alkali-silica diagram. *Journal of Petrology* **27**(3): 745-750.

LE MAITRE R. W. (1979). A new generalised pertological mixing model. *Contributions to Mineralogy and Petrology* **71**: 133-137.

LECOLLE J. F., BOKILO J. E., AND BERNAT M. (1990). Soulèvement et tectonique de l'île d'Efaté (Vanuatu) arc insulaire des Nouvelles-Hébrides, au cours du Quaternaire récent. Datations de terrasses soulevées par la méthode U/Th. *Marine Geology* **94**: 251-270.

LEDBETTER M. T. AND SPARKS R. S. J. (1979). Duration of large-magnitude explosive eruptions deduced from graded bedding in deep-sea ash layers. *Geology* **7**: 240-244.

LEE J. AND STERN R. J. (1998). Glass inclusions in Mariana arc phenocrysts: a new perspective on magmatic evolution in a typical intra-oceanic arc. *Journal of Geology* **106**: 19-33.

LLOYD E. F., NATHAN S., SMITH I. E. M., AND STEWART R. B. (1996). Volcanic history of Macauley Island, Kermadec Ridge, New Zealand. *New Zealand Journal of Geology and Geophysics* **39**: 295-308.

LOMAS S. (1992). Submarine mass-flow conglomerates of the Tarentaise Zone, Western Alps: sedimentation processes and depositional setting. *Sedimentary Geology* **81**: 269-287.

LOUGHNAN F. C. (1982). Genesis and synthesis: kaolins in sediments. In: H. van Olphen & F. Veniale (Eds.), *International Clay Conference 1981*. Developments in Sedimentology 35. Elsevier, Amsterdam. pp. 487-494.

LOWE D. R. (1982). Sediment gravity flows: II. Depositional models with special reference to the deposits of high-density turbidity currents. *Journal of Sedimentary Petrology* **52**(1): 279-297.

LOWE D. R. (1988). Suspended-load fallout rate as an independent variable in the analysis of current structures. *Sedimentology* **35**: 765-776.

MACFARLANE A., CARNEY J. N., CRAWFORD A. J., AND GREENE H. G. (1988). Vanuatu - a review of the onshore geology. In: H. G. Greene & F. L. Wong (Eds.), *Geology and Offshore Resources of Pacific Island Arcs - Vanuatu Region*. Earth Science Series 8. Circum-Pacific Council for Energy and Mineral Resources, Huston, Texas. 45-91.

MAHOOD G. (1980). Geological evolution of a Pleistocene rhyolitic centre: Sierra La Primavera, Jalisco, Mexico. *Journal of Volcanology and Geothermal Research* **8**: 199-230.

MAHOOD G. (1981). A summary of the geology and petrology of the Sierra La Primavera, Mexico. *Journal of Geophysical Research* **86**: 10,137-10,152.

MAILLET P., RUELLAN E., GÉRARD M., PERSON A., BELLON H., COTTEN J., JORON J.-L., NAKADA S., AND PRICE R. C. (1995). Tectonics, magmatism, and evolution of the New Hebrides backarc troughs (southwest Pacific). In: B. Tayor (Ed.), *Backarc Basins: Tectonics and Magmatism*. Plenum Press, New York. pp. 177-235.

MALAHOFF A. (1970). *Gravity and magnetic studies of the New Hebrides Island Arc*. Report, New Hebrides Geological Survey. 67 p.

MALLICK D. I. J. (1973). Some petrological and structural variations in the New Hebrides. In: P. J. Coleman (Ed.), *The Western Pacific*. University of Western Australia Press, Nedlands. pp. 193-211.

MALLICK D. I. J. AND ASH R. P. (1975). *Geology of the southern Banks Islands*. Regional Report, New Hebrides Condominium Geological Survey. 33 p.

MALLICK D. I. J. AND GREENBAUM D. (1977). *Geology of southern Santo*. Regional Report, New Hebrides Condominium Geological Survey. 84 p.

MALLICK D. I. J. AND NEEF G. (1974). *Geology of Pentecost*. Regional Report, New Hebrides Condominium Geological Survey. 103 p.

MALONE D. H. (1995). Very large debris-avalanche deposit within the Eocene volcanic succession of the northeastern Absaroka Range, Wyoming. *Geology* **23**(7): 661-664.

MANDEVILLE C. W., CAREY S., AND SIGURDSSON H. (1996a). Magma mixing, fractional crystallisation and volatile degassing during the 1883 eruption of Krakatau volcano, Indonesia. *Journal of Volcanology and Geothermal Research* **74**: 243-274.

MANDEVILLE C. W., CAREY S., AND SIGURDSSON H. (1996b). Sedimentology of the Krakatau 1883 submarine pyroclastic deposits. *Bulletin of Volcanology* **57**: 512-529.

MÁNGANO M. G. AND BUATOIS L. A. (1997). Slope-apron deposition in an Ordovician arc-related setting: the Vuelta de Las Tolas Member (Suri Formation), Famatina Basin, northwest Argentina. *Sedimentary Geology* **109**: 155-180.

MANVILLE V., WHITE J. D. L., HOUGHTON B. F., AND WILSON C. J. N. (1998). The saturation behavior of pumice and some sedimentolgical implications. *Sedimetary Geology* **119**: 5-16.

MARKS R. J. (1983). Hydrogeological development in Vanuatu. *International Contributions to Hydrogeology* **7**: 51-57.

MARTEL C., BOURDIER J.-L., PICHAVANT M., AND TRAINEAU H. (2000). Textures, water content and degassing of silicic andesites from recent plinian and dome-forming eruptions at Mount Pelée volcano (Martinique, Lesser Antilles arc). *Journal of Volcanology and Geothermal Research* **96**: 191-206.

MARTIN A. M. (1988). *11th quartlerly progress report on prospecting licence PL 1417 Mt Fatmalapa, Efaté, for the period ending 30 June 1988*. Open file report. 18 p.

MARTIN H. (1986). Effect of steeper Archean geothermal gradient on geochemistry of subduction-zone magmas. *Geology* **14**: 753-756.

MAWSON D. (1905). The geology of the New Hebrides. *Proceedings of the Linnean Society of NSW* **30**: 400-485.

MCBIRNEY A. R. (1963). Factors governing the nature of submarine volcanism. *Bullétin Volcanologique* **26**: 455-469.

MCBIRNEY A. R. (1980). Mixing and unmixing of magmas. *Journal of Volcanology and Geothermal Research* **7**: 357-371.

MCPHIE J. (1995). A Pliocene shoaling basaltic seamount: Ba Volcanic Group at Rakiraki, Fiji. *Journal of Volcanology and Geothermal Research* **64**: 193-210.

MCPHIE J., DOYLE M., AND ALLEN R. (1993). *Volcanic Textures: a guide to the interpretation of textures in volcanic rocks*. CODES University of Tasmania. 198 p.

MELCHIOR M. (1989). Ambrym et Yasour; volcans actifs du Vanuatu. *L'Association Volcanique Européane* **20**: 17-23.

MELLORS R., CHATELAIN J.-L., ISACKS B. L., HADE G., BEVIS M., AND PREVOT R. (1991). A tilt and seismicity episode in the New Hebrides (Vanuatu) island arc. *Journal of Geophysical Research* **96**(B10): 16,535-16,546.

MIDDLEMOST E. A. K. (1975). The basalt clan. *Earth-Science Reviews* **11**: 337-364.

MITCHELL A. H. G. (1966). *Geology of south Malekula*. Report No. 3, New Hebrides Condominium Geological Survey. p.

MITCHELL A. H. G. (1970). Facies of an early Miocene volcanic arc, Malekula Island, New Hebrides. *Sedimentology* **14**: 201-243.

MITCHELL A. H. G. AND WARDEN A. J. (1971). Geological evolution of the New Hebrides island arc. *Journal of the Geological Society of London* **127**: 501-529.

MONZIER M., DANYUSHESKY L. V., CRAWFORD A. J., BELLON H., AND COTTEN J. (1993). High-Mg andesites from the southern termination of the New Hebrides island arc (SW Pacific). *Journal of Volcanology and Geothermal Research* **57**: 193-217.

MONZIER M., ROBIN C., AND EISSEN J.-P. (1994). Kuwae (≈1425 A.D.): the forgotten caldera. *Journal of Volcanology and Geothermal Research* **59**: 207-218.

MONZIER M., ROBIN C., EISSEN J.-P., AND COTTEN J. (1997). Geochemistry vs. seismo-tectonics along the volcanic New Hebrides Central Chain (Southwest Pacific). *Journal of Volcanology and Geothermal Research* **78**: 1-29.

MONZIER M., ROBIN C., EISSEN J.-P., AND PICARD C. (1991). Découverte d'un large anneau de tufs basaltiques associé à la formation de la caldera d'Ambrym (Vanuatu, SW Pacifique). *Comptes Rendus de l'Académie des Sciences, Paris* **313**(Série II): 1319-1326.

MORIMOTO N. (1989). Nomenclature of pyroxenes. *Canadian Mineralogist* **27**: 143-156.

NAIRN I. A., MCKEE C. O., TALAI B., AND WOOD C. P. (1995). Geology and eruptive history of the Rabaul Caldera area, Papua New Guinea. *Journal of Volcanology and Geothermal Research* **69**: 255-284.

NASH C. AND RANKIN L. (1995). Solid geology interpretation, Efaté Island, Vanuatu. Australian Geological Survey Organisation. 1:100,000 scale geophysics interpretation map.

NEEF G. AND VEEH H. H. (1977). Uranium series ages and late Quaternary uplift in the New Hebrides. *Nature* **269**: 682-683.

NEWHALL C. G. AND SELF S. (1982). The volcanic explosivity index (VEI): an estimate of explosive magnitude for historical volcanism. *Journal of Geophysical Research* **87**: 1231-1238.

NIEM A. R. (1977). Mississippian pyroclastic flow and ash-fall deposits in the deep-marine Ouachita flysch basin, Oklahoma and Arkansas. *Geological Society of America Bulletin* **88**: 49-61.

NINKOVICH D., SPARKS R. S. J., AND LEDBETTER M. T. (1978). The exceptional magnitude and intensity of the Toba eruption, Sumatra: An example of the use of deep-sea tephra layers as a geological tool. *Bullétin Volcanologique* **41**: 286-298.

NISHIMURA A., MARSAGLIA K. M., RODOLFO K. S., COLELLA A., HISCOTT R. N., TAZAKI K., GILL J. B., JANECEK T., FIRTH J., ISIMINGER-KELSO M., HERMAN Y., TAYLOR R. N., TAYLOR B., FUJIOKA K., AND LEG 126 SCIENTIFIC PARTY (1991). Pliocene-Quaternary submarine pumice deposits in the Sumisu Rift area, Izu-Bonin Arc. In: R. V. Fisher & G. A. Smith (Eds.), *Sedimentation in Volcanic Settings*. SEPM Special Publication No. 45, Tulsa. pp. 201-208.

NISHIMURA A., RODOLFO K. S., KOIZUMI A., GILL J., AND FUJIOKA K. (1992). Episodic deposition of Pliocene-Pleistocene pumice from the Izu-Bonin Arc, Leg 126. In: B. Taylor & K. Fujioka (Eds.), *Proceedings of the Ocean Drilling Program, Scientific Results*. 126. Ocean Drilling Program, College Station, TX. 3-21.

NORRISH K. AND CHAPPELL B. W. (1977). X-ray fluorescence spectrometry. In: J. Zussman (Ed.), *Physical methods in determinative mineralogy*. Academic Press, New York. pp. 201-272.

NORRISH K. AND HUTTON J. T. (1969). An accurate X-ray spectrographic method for the analysis of a wide range of geological samples. *Geochimica et Cosmochimica Acta* **33**: 431-453.

O'KEEFE J. A. (1984). Natural glasses. *Journal of Non-Crystalline Solids* **67**: 1-17.

OBELLIANNE J.-M. (1958). *Contribution à la connaissance geologique de l'archipel des Nouvelles-Hébrides (îles Vaté, Pentecote, Maewo, Santo)*. Sciences de la Terre. Foundation Scientifique de la Geologie et de ses Applications, Nancy. 76 p.

PEACOCK S. M., RUSHMER T., AND THOMPSON A. B. (1994). Partial melting of subducting oceanic crust. *Earth and Planetary Science Letters* **121**: 227-244.

PEARCE J. A. (1982). Trace element characteristics of lavas from destructive plate margins. In: R. S. Thorpe (Ed.), *Andesites - Orogenic andesites and related rocks*. John Wiley and Sons, Chichester. pp. 525-548.

PEARCE J. A., BAKER P. E., HARVEY P. K., AND LUFF I. W. (1995). Geochemical evidence for subduction fluxes, mantle melting and fractional crystallization beneath the South Sandwich Island Arc. *Journal of Petrology* **36**(4): 1073-1109.

PEATE D. W., PEARCE J. A., HAWKESWORTH C. J., COLLEY H., EDWARDS C. M. H., AND HIROSE K. (1997). Geochemical variations in Vanuatu Arc lavas: the role of subducted material and a variable mantle wedge composition. *Journal of Petrology* **38**(10): 1331-1358.

PECCERILLO A. AND TAYLOR S. R. (1976). Geochemistry of Eocene calc-alkaline volcanic rocks from the Kastamonu area, northern Turkey. *Contributions to Mineralogy and Petrology* **58**: 63-81.

PELLETIER B., CALMANT S., AND PILLET R. (1998). Current tectonics of the Tonga-New Hebrides region. *Earth and Planetary Science Letters* **164**: 263-276.

PERFIT M. R., GUST D. A., BENCE A. E., ARCULUS R. J., AND TAYLOR S. R. (1980). Chemical characteristics of island-arc basalts: implications for mantle sources. *Chemical Geology* **30**: 227-256.

PICKERING K. T., HISCOTT R. N., AND HEIN F. J. (1989). *Deep marine environments: Clastic sedimentation and tectonics*. Unwin Hyman, London. 416 p.

PICKERING K. T., STOW D. A. V., WATSON M. P., AND HISCOTT R. N. (1986). Deep-water facies, processes and models: a review and classification scheme for modern and ancient sediments. *Earth-Science Reviews* **23**: 75-174.

PIN C., BRIOT D., BASSIN C., AND POITRASSON F. (1994). Concomittant separation of strontium and samarium-neodymium for isotopic analysis in silicate samples, based on specific extraction chromatography. *Analytica Chimica Acta* **298**: 209-217.

PIPER D. J. W. AND STOW D. A. V. (1991). Fine-grained turbidites. In: G. Einsele, W. Ricken, & A. Seilacher (Eds.), *Cycles and Events in Stratigraphy*. Springer-Verlag, Berlin. pp. 361-367.

POSTMA G. (1984). Mass-flow conglomerates in a submarine canyon: Abrioja fan-delta, Pliocene, southeast Spain. In: E. H. Koster & R. J. Steel (Eds.), *Sedimentology of gravels and conglomerates*. Memoir 10. Canadian Society of Petroleum Geologists. pp. 237-258.

POSTMA G. (1986). Classification for sediment gravity-flow deposits based on flow conditions during sedimentation. *Geology* **14**: 291-294.

PRÉVOT R., CHATELAIN J.-L., ROECKER S. W., AND GRASSO J.-R. (1994). A shallow double seismic zone beneath the New Hebrides (Vanuatu): evidence for fragmentation and accretion of the descending plate? *Geophysical Research Letters* **21**(19): 2159-2162.

PYE K. (1994). Properties of sediment particles. In: K. Pye (Ed.), *Sediment transport and depositional processes*. Blackwell Scientific Publications, Oxford. pp. 1-24.

QUANTIN P. (1972). *Vaté*. Archipel des Nouvelles Hebrides; sols et quelques données du milieu naturel. Office de la Recherches Scientifique et Technique Outre-Mer (ORSTOM), Bondy, France. 22p.

QUANTIN P. (1992). *Les sols de l'achipel volcanique des Nouvelles-Hébrides (Vanuatu). Etude de la pedogenèse initiale en milieu tropical*. Editions de l'ORSTOM Institut Français de Recherche scientifique pour le développment en coopération. Collection Etudes et Thèses. ORSTOM, Bondy, France. p.

QUANTIN P., BALESDENT J., BOULEAU A., DELAUNE M., AND FELLER C. (1991). Premiers stades d'altération de ponces volcaniques en climat tropical humide (Montagne Pelée, Martinique). *Geoderma* **50**: 125-148.

QUANTIN P., GAUTHEYROU J., AND LORENZONI P. (1988). Halloysite formation through *in situ* weathering of volcanic glass from trachytic pumices, Vivo's Volcano, Italy. *Clay Minerals* **23**: 423-437.

QUANTIN P., HERBILLON, JANOT, AND SIEFFERMAN. (1984). "L'halloysit" blanche riche en fer de Vaté (Vanuatu). Hypothese d'un edifice interstratifie halloysite-hisingerite. *Clay Minerals* **19**: 629-643.

RAPP R. P. AND WATSON E. B. (1995). Dehydration melting of metabasalt at 8-32 kbar: implications for continental growth and crust-mantle recycling. *Journal of Petrology* **36**(4): 891-931.

REGNIER M., LOUAT R., DECOURT R., AND FROHLICH C. (1997). Seismotectonics of the Efate segment of central New Hebrides subduction zone. *Seismological Research Letters* **68**(2): 317.

REID P. D., MACINTYRE I. G., AND POST J. E. (1992). Micritized skeletal grains in northern Belize lagoon: a major source of Mg-calcite mud. *Journal of Sedimentary Petrology* **62**: 145-156.

REIMER T. O. (1983). Accretionary lapilli in volcanic ash falls: physical factors governing their formation. In: T. M. Peryt (Ed.), *Coated Grains*. Springer-Verlag, Berlin Heidleberg. pp. 56-68.

RICHARD P., SHIMIZU N., AND ALLÈGRE C. J. (1986). $^{143}Nd/^{144}Nd$, a natural tracer: An application to oceanic basalts. *Earth and Planetary Science Letters* **31**: 269-278.

RICKWOOD P. C. (1989). Boundary lines within petrologic diagrams which use oxides of major and minor elements. *Lithos* **22**: 247-263.

RIGGS N. R., HURLBERT J. C., SCHROEDER T. J., AND WARD S. A. (1997). The interaction of volcanism and sedimentation in the proximal areas of a mid-Tertiary volcanic dome field, central Arizona, U.S.A. *Journal of Sedimentary Research* **67**(1): 142-153.

ROBIN C., EISSEN J.-P., AND MONZIER M. (1993a). Giant tuff cone and 12-km-wide associated caldera at Ambrym Volcano (Vanuatu, New Hebrides Arc). *Journal of Volcanology and Geothermal Research* **55**: 225-238.

ROBIN C., EISSEN J.-P., AND MONZIER M. (1994a). Ignimbrites of basaltic andesite and andesite compositions from Tanna, New Hebrides Arc. *Bulletin of Volcanology* **56**: 10-22.

ROBIN C., EISSEN J.-P., AND MONZIER M. (1995). Mafic pyroclastic flows at Santa Maria (Gaua) Volcano, Vanuatu: the caldera formation problem in mainly mafic island arc volcanoes. *Terra Nova* **7**: 436-443.

ROBIN C., MONZIER M., CRAWFORD A. J., AND EGGINS S. M. (1993b). *The geology, volcanology, petrology-geochemistry and tectonic evolution of the New Hebrides Island Arc, Vanuatu*. IAVCEI Pre-conference Excursion Guide A5. 86p.

ROBIN C., MONZIER M., AND EISSEN J.-P. (1994b). Formation of the mid-fifteenth century Kuwae caldera (Vanuatu) by an initial hydroclastic and subsequent ignimbritic eruption. *Bulletin of Volcanology* **56**: 170-183.

ROBINSON G. P. (1969). *The Geology of north Santo*. Regional Report, New Hebrides Condominium Geological Survey. p.

ROBINSON P., TOWNSEND A. T., YU Z., AND MUNKER C. (1999). Determination of scandium, yttrium and rare earth elements in rocks by high resolution inductively coupled plasma-mass spectrometry. *Geostandards Newsletter: The Journal of Geostandards and Geoanalysis* **23**: 31-46.

ROBSON D. AND CANN J. R. (1982). A geochemical model of mid-ocean ridge magma chambers. *Earth and Planetary Science Letters* **60**: 93-104.

ROLLINSON H. (1993). *Using geochemical data: evaluation, presentation, interpretation.* Longman Group UK Limited, London. 352 p.

SAHAGIAN D. (1999). Magma fragmentation in eruptions. *Nature* **402**: 589-591.

SAUNDERS A. D., NORRY M. J., AND TARNEY J. (1991). Fluid influence on the trace element compositions of subduction zone magmas. *Philosophical Transactions of the Royal Society of London* **A 335**: 377-392.

SCHIANO P. AND CLOCCHIATTI R. (1995). Hydrous, silica-rich melts in the sub-arc mantle and their relationship with erupted arc lavas. *Nature* **377**: 595-600.

SCHIANO P., EILER J. M., HUTCHEON I. D., AND STOLPER E. M. (2000). Primitive CaO-rich, silica-undersaturated melts in island arcs: evidence for the involvement of clinopyroxene-rich lithologies in the petrogenesis of arc magmas. *G^3 - Geochemisty Geophysics Geosystems* **1** (Paper number 1999GC000032): 33p.

SCHMINCKE H.-U. AND VAN DEN BOGAARD P. (1991). Tephra layers and tephra events. In: G. Einsele, W. Ricken, & A. Seilacher (Eds.), *Cycles and Events in Stratigraphy.* Springer-Verlag, Berlin. pp. 393-429.

SCHWARTZ H.-U. (1982). Subaqueous slope failures - experiments and modern occurrences. *Contributions to Sedimentology* **11**:

SELF S. AND SPARKS R. S. J. (1978). Characteristics of widespread pyroclastic deposits formed by the interaction of silicic magma and water. *Bulletin of Volcanology* **41**(3): 196-212.

SEN C. AND DUNN T. (1994). Dehydration melting of a basaltic composition amphibolite at 1.5 and 2.0 GPa: implications for the origin of adakites. *Contributions to Mineralogy and Petrology* **117**: 394-409.

SERRI G., INNOCENTI F., AND MANETTI P. (1993). Geochemical and petrological evidence of the subduction of delaminated Adriatic continental lithosphere in the genesis of the Neogene-Quaternary magmatism of central Italy. *Tectonophysics* **223**: 117-147.

SHANMUGAM G. (1997). The Bouma Sequence and the turbidite mind set. *Earth-Science Reviews* **42**: 201-229.

SHANMUGAM G. AND MOIOLA R. J. (1995). Reinterpretation of depositional processes in a classic flysch sequence (Pennsylvanian Jackfork Group), Ouachita Mountains, Arkansas and Oklahoma. *American Association of Petroleum Geologists Bulletin* **79**: 672-695.

SHANMUGAM G., SPALDING T. D., AND ROFHEART D. H. (1995). Deep marine bottom-current reworked sand (Pliocene and Pleistocene), Ewing Bank 826 field, Gulf of Mexico. In: , *Turbidites and associated deep-water facies.* Core Workshop No. 20. SEPM, Houston, Texas. pp. 25-54.

SHERIDAN M. F. AND WOHLETZ K. H. (1981). Hydrovolcanic explosions: the systematics of water-pyroclast equilibration. *Science* **212**: 1387-1389.

SIGURDSSON H. AND CAREY S. (1989). Plinian and co-ignimbrite tephra fall from the 1815 eruption of Tambora volcano. *Bulletin of Volcanology* **51**: 243-270.

SIGURDSSON H., SPARKS R. S. J., CAREY S. N., AND HUANG T. C. (1980). Volcanogenic sedimentation on the Lesser Antilles Arc. *Journal of Geology* **88**: 523-540.

SIMKIN T. AND SIEBERT L. (1994). *Volcanoes of the World.* Geoscience Press, Inc., Tuscon, Arizona. 349 p.

SMELLIE J. L., STONE P., AND EVANS J. (1995). Petrogenesis of boninites in the Ordovician Ballantrae Complex ophiolite, southwestern Scotland. *Journal of Volcanology and Geothermal Research* **69**: 323-342.

SMITH G. A. (1988). Sedimentology of proximal to distal volcaniclastics dispersed across an active foldbelt: Ellensburg Formation (late Miocene), central Washington. *Sedimentology* **35**: 953-977.

SMITH R. L. (1960). Ash flows. *Geological Society of America Bulletin* **71**: 795-842.

SMITH R. T. AND HOUGHTON B. F. (1995). Vent migration and changing eruptive style during the 1800a Taupo eruption: new evidence from the Hatepe and Rotongaio phreatoplinian ashes. *Bulletin of Volcanology* **57**: 432-439.

SMITH W. H. F. AND SANDWELL D. T. (1997). Global seafloor topography from satellite altimetry and ship depth soundings. *Science* **277**: 1956-1962.

SOH W. (1989). Coarse clast dominant submarine debrite, the Mio-Pliocene Fujikawa group, central Japan. In: A. Taira & F. Masuda (Eds.), *Sedimentary Facies in the Active Plate Margin.* Terra Scientific Publishing Company (TERRAPUB), Tokyo. pp. 495-510.

SOH W., TAIRA A., OGAWA Y., TANIGUCHI H., PICKERING K. T., AND STOW D. A. V. (1989). Submarine depositional processes for volcaniclastic sediments in the Mio-Pliocene Misaki Formation, Miura Group, central Japan. In: A. Taira & F. Masuda (Eds.), *Sedimentary Facies in the Active Plate Margin.* Terra Scientific Publishing Company (TERRAPUB), Tokyo. pp. 619-630.

SOHN Y. K. (1995). Geology of Tok Island, Korea: eruptive and depositional processes of a shoaling to emergent island volcano. *Bulletin of Volcanology* **56**: 660-674.

SPARKS R. S. J. (1976). Grain size variations in ignimbrites and implications for the transport of pyroclastic flows. *Sedimentology* **23**: 147-188.

SPARKS R. S. J., HUPPERT H. E., AND TURNER J. S. (1984). The fluid dynamics of evolving magma chambers. *Philosophical Transactions of the Royal Society of London* **A310**: 511-534.

SPARKS R. S. J., SELF S., AND WALKER G. P. L. (1973). Products of ignimbrite eruptions. *Geology* **1**: 115-118.

SPARKS R. S. J., SIGURDSSON H., AND CAREY S. N. (1980). The entrance of pyroclastic flows into the sea, II. Theoretical considerations on subaqueous emplacemant and welding. *Journal of Volcanology and Geothermal Research* **7**: 97-105.

STAMATELOPOULOU-SEYMOUR K., VLASSOPOULOS D., PEARCE T. H., AND RICE C. (1990). The record of magma chamber processes in plagioclase phenocrysts at Thera volcano, Aegean volcanic arc, Greece. *Contributions to Mineralogy and Petrology* **104**: 73-84.

STIX J. (1991). Subaqueous, intermediate to silicic-composition explosive volcanism: a review. *Earth-Science Reviews* **31**: 21-53.

STOLZ A. J., VARNE R., DAVIES G. R., WHELLER G. E., AND FODEN J. D. (1990). Magma source components in an arc-continent collision zone: the Flores-Lembata sector, Sunda arc, Indonesia. *Contributions to Mineralogy and Petrology* **105**: 585-601.

STOW D. A. V. (1994). Deep sea processes of sediment transport and deposition. In: K. Pye (Ed.), *Sediment transport and depositional processes*. Blackwell Scientific Publications, Oxford. pp. 257-291.

STOW D. A. V. AND PIPER D. J. W. (1984). Deep-water fine-grained sediments: facies models. In: D. A. V. Stow & D. J. W. Piper (Eds.), *Fine-Grained Sediments*. Geological Society Special Publication No. 15, Oxford. pp. 611-646.

STOW D. A. V., TAIRA A., OGAWA Y., SOH W., TANIGUCHI H., AND PICKERING K. T. (1998). Volcaniclastic sediments, process interaction and depositional setting of the Mio-Pliocene Miura group, SE Japan. *Sedimentary Geology* **115**: 351-381.

STURCHIO N. C., MUEHLENBACHS K., AND SEITZ M. G. (1986). Element redistribution during hydrothermal alteration of rhyolite in an active geothermal system: Yellowstone drill cores Y-7 and Y-8. *Geochimica et Cosmochimica Acta* **50**: 1619-1631.

SUN S.-S. AND MCDONOUGH W. F. (1989). Chemical and isotopic systematics of oceanic basalts: implications for mantle composition and processes. In: S. A. D & N. M. J (Eds.), *Magmatism in the Ocean Basins*. Geological Society of London Special Publication No. 42. pp. 313-345.

SUTHREN R. J. (1985). Facies analysis of volcaniclastic sediments: a review. In: P. J. Brenchley & B. P. J. Williams (Eds.), *Sedimentology: Recent Developments and Applied Aspects*. Geological Society of London Special Publication No. 18. pp. 123-146.

TATSUMI Y. (1989). Migration of fluid phases and genesis of basalt magmas in subduction zones. *Journal of Geophysical Research* **94**(B4): 4697-4707.

TATSUMI Y. AND EGGINS S. (1995). *Subduction zone magmatism*. Blackwell Science Inc, Cambridge, Massachusetts. 211 p.

TAYLOR F. W. (1992). Quaternary vertical tectonics of the central New Hebrides island arc. In: J.-Y. Collot & H. G. Greene (Eds.), *Proceedings of the Ocean Drilling Program, Initial Reports. Leg 134*. Ocean Drilling Program, College Station, TX. pp. 43-53.

TURNER J. S. (1980). A fluid-dynamical model of differentiation and layering in magma chambers. *Nature* **285**: 213-215.

TURNER S. P., PEATE D. W., HAWKESWORTH C. J., EGGINS S. M., AND CRAWFORD A. J. (1999). Two mantle domains and the time scales of fluid transfer beneath the Vanuatu arc. *Geology* **27**(11): 963-966.

VANUATU DEPARTMENT OF GEOLOGY, MINES AND WATER RESOURCES. (1995). Vanuatu Mineral Exploration Initiative. Vanuatu Department of Geology, Mines and Water Resources.

VERBEETEN A. (1996). Petrology, geochemistry and tectonic implications of magmatism along the northern Hunter Ridge and Kadavu Island Group, Fiji. Unpublished PhD thesis, University of Tasmania.

VESSELL R. K. AND DAVIES D. K. (1981). Nonmarine sedimentation in an active forearc basin. In: F. G. Ethridge & R. M. Flores (Eds.), *Recent and ancient non-marine depositional environments: models for exploration*. SEMP Special Publication No. 31, Tulsa. pp. 31-45.

VILLEMANT B., JAFFREZIC H., JORON J.-L., AND TREUIL M. (1981). Distribution coefficients of major and trace elements; fractional crystallization in the alkali basalt series of Chaîne des Puys (Massif Central, France). *Geochimica et Cosmochimica Acta* **45**: 1997-2016.

VUKADINOVIC D. (1993). Are Sr enrichments in arc basalts due to plagioclase accumulation? *Geology* **21**: 611-614.

WALKER G. P. L. (1982). Eruptions of andesitic volcanoes. In: R. S. Thorpe (Ed.), *Andesites - Orogenic andesites and related rocks*. John Wiley and Sons, Chichester. pp. 403-413.

WALKER G. P. L. (1983). Ignimbrite types and ignimbrite problems. *Journal of Volcanology and Geothermal Research* **17**: 65-88.

WALKER G. P. L. (1993). Basaltic-volcano systems. In: H. M. Prichard, T. Alabaster, N. B. W. Harris, & C. R. Neary (Eds.), *Magmatic processes and plate tectonics*. Geological Society of London Special Publication No. 76. pp. 3-38.

WALKER R. G. (1984a). Shelf and shallow marine sands. In: R. G. Walker (Ed.), *Facies Models*. Geosciences Canada Reprint Series 1. pp. 141-170.

WALKER R. G. (1984b). Turbidites and associated coarse clastic deposits. In: R. G. Walker (Ed.), *Facies Models*. Geosciences Canada Reprint Series 1. pp. 171-188.

WALTER L. M., BISCHOF S. A., PATTERSON W. P., AND LYONS T. W. (1993). Dissolution and recrystallization in modern shelf carbonates: evidence from pore water and solid phase chemistry. *Philosophical Transactions of the Royal Society of London* **A344**: 27-36.

WALTER L. M. AND BURTON E. A. (1990). Dissolution of recent platform carbonate sediments in marine pore fluids. *American Journal of Science* **290**: 601-643.

WALTON A. W. (1975). Zeolitic diagenesis in Oligocene volcanic sediments, Tran-Pecos Texas. *Geological Society of America Bulletin* **86**: 615-624.

WARDEN A. J. (1967). *The geology of the Central Islands*. Report No. 5, New Hebrides Condominium Geological Survey. 108 p.

WARDEN A. J. (1970). Genesis of the Forari manganese deposit, New Hebrides. *Transactions of the Institute of Mining and Metallurgy* **79**: 330-341.

WARDEN A. J. (1971). *Manganese mineralisation in the New Hebrides*. Report, New Hebrides Condominium Geological Survey. 59p.

WATERS J. C. AND BINNS R. A. (1998). Contrasting styles of felsic submarine volcanism, Eastern Manus Basin, Papua New Guinea. *14th Australian Geological Convention - Abstracts volume* **49**. p. 459.

WATERS J. C., BINNS R. A., AND NAKA J. (1996). Morphology of submarine felsic volcanic rocks on Pual Ridge, Eastern Manus Basin, Papua New Guinea. *EOS - Transactions of the American Geophysical Union* **77**(22): W120.

WHELLER G. E. (1986). Petrogenesis of Batur caldera, Bali, and the geochemistry of Sunda-Banda arc basalts. Unpublished PhD thesis, University of Tasmania.

WHELLER G. E. AND VARNE R. (1984). Evolution and petrogenesis of the Batur volcano, Bali. *Geological Society of Australia-Abstracts* **12**: 544-545.

WHELLER G. E. AND VARNE R. (1986). Genesis of dacitic magmatism at Batur Volcano, Bali, Indonesia: implications for the origins of stratovolcano calderas. *Journal of Volcanology and Geothermal Research* **28**: 363-378.

WHITE J. D. L., MANVILLE V., WILSON C. J. N., AND HOUGHTON B. F. (1997). Normal pumice. *1997 IAVCEI General Assembly - Abstracts volume*: 134.

WHITE M. J. AND MCPHIE J. (1997). A submarine welded ignimbrite - crystal-rich sandstone facies association in the Cambrian Tyndall Group, western Tasmania, Australia. *Journal of Volcanology and Geothermal Research* **76**: 277-295.

WHITHAM A. AND SPARKS R. S. J. (1986). Pumice. *Bulletin of Volcanology* **48**: 209-223.

WHITHAM A. G. (1989). The behaviour of a subaerially produced pyroclastic flow in a subaqueous environment: evidence from the Roseau eruption, Domenica, West Indies. *Marine Geology* **86**: 27-40.

WIESNER M. G., WANG Y., AND ZHENG L. (1995). Fallout of volcanic ash to the deep South China Sea induced by the 1991 eruption of Mount Pinatubo (Philippines). *Geology* **23**: 885-888.

WILSON C. J. AND HOUGHTON B. F. (1990). Eruptive mechanisms in the Minoan eruption: Evidence from pumice vesicularity. In: D. Hardy (Ed.), *Thera and the Aegea world III*. 2. Thera Foundation, London. pp. 122-128.

WILSON C. J. N. AND WALKER G. P. L. (1981). Violence in pyroclastic flow eruptions. In: S. Self & R. S. J. Sparks (Eds.), *Tephra Studies*. D. Reidel Publishing Company. pp. 441-448.

WILSON C. J. N. AND WALKER G. P. L. (1982). Ignimbrite depositional facies: the anatomy of a pyroclastic flow. *Journal of the Geological Society of London* **139**: 581-592.

WOHLETZ K. H. (1983). Mechanisms of hydrovolcanic pyroclast formation: grain-size, scanning electron microscopy, and experimental studies. *Journal of Volcanology and Geothermal Research* **17**: 31-63.

WOHLETZ K. H. (1987). Chemical and textural surface features of pyroclasts from hydrovolcanic eruption sequences. In: J. R. Marshall (Ed.), *Clastic Particles - Scanning Electron Microscopy and shape analysis of sedimentary and volcanic clasts*. Van Nostrand Reinhold Company, New York. pp. 79-97.

WOHLETZ K. H. AND SHERIDAN M. F. (1983). Hydrovolcanic explosions II. Evolution of basaltic tuff rings and tuff cones. *American Journal of Science* **283**: 385-413.

WOHLETZ K. H., SHERIDAN M. F., AND BROWN W. K. (1989). Particle size distributions and the sequential fragmentation/transport theory applied to volcanic ash. *Journal of Geophysical Research* **94**(B11): 15,703-15,721.

WOOD C. P., NAIRN I. A., MCKEE C. O., AND TALAI B. (1995). Petrology of the Rabaul Caldera area, Papua New Guinea. *Journal of Volcanology and Geothermal Research* **69**: 285-302.

WOODHEAD J., EGGINS S., AND GAMBLE J. (1993). High field strength and transition element systematics in island arc and back-arc basin basalts: evidence for multi-phase melt extraction and a depleted mantle wedge. *Earth and Planetary Science Letters* **114**: 491-504.

WOODHEAD J. D. AND JOHNSON R. W. (1993). Isotopic and trace-element profiles across the New Britain island arc, Papua New Guinea. *Contributions to Mineralogy and Petrology* **113**: 479-491.

WOODHEAD J. D., VOLKER F., AND MCCULLOCH M. T. (1995). Routine lead isotope determinations using a ^{207}Pb-^{204}Pb double spike: a long-term assessment of analytical precision and accuracy. *The Analyst* **120**: 34-39.

WOOLLEY A. R. AND KEMPE D. R. (1989). Carbonatites: Nomenclature, average chemical compositions, and element distributions. In: K. Bell (Ed.), *Carbonatites - genesis and evolution*. Unwin and Hyman, London. pp. 1-14.

WRIGHT J. V. AND MUTTI E. (1981). The Dali Ash, island of Rhodes, Greece: a problem in interpreting submarine volcanigenic sediments. *Bulletin of Volcanology* **44**(2): 153-167.

WRIGHT J. V., SELF S., AND FISHER R. V. (1981). Towards a facies model for ignimbrite-forming eruptions. In: S. Self & R. S. J. Sparks (Eds.), *Tephra Studies*. D. Reidel Publishing Company. pp. 433-439.

WYLLIE P. J. AND SEKINE T. (1982). The formation of mantle phlogopite in subduction zone hybridization. *Contributions to Mineralogy and Petrology* **79**: 375-380.

YAMADA E. (1973). Subaqueous pumice flow deposits in the Onikobe caldera, Miyagi Prefecture, Japan. *Journal of the Geological Society of Japan* **79**(9): 585-597.

YAMADA E. (1984). Subaqueous pyroclastic flows: their development and their deposits. In: B. P. Kokelaar & M. F. Howells (Eds.), *Marginal basin geology: volcanic and associated sedimentary and tectonic processes in modern and ancient marginal basins.* Geological Society of London Special Publication No. 16. pp. 29-35.

YAMAGISHI H. AND GOTO Y. (1991). Cooling joints of subaqueous rhyolite lavas at Kuroiwa, Yaumo, southern Hokkaido, Japan. *Bulletin of the Volcanological Society of Japan* **37**: 205-207.

YAXLEY G. M., CRAWFORD A. J., AND GREEN D. H. (1991). Evidence of carbonatite metasomatism in spinel peridotite xenoliths from western Victoria, Australia. *Earth and Planetary Science Letters* **107**: 305-317.

YAXLEY G. M., GREEN D. H., AND KAMENETSKY V. (1998). Carbonatite metasomatism in the southeastern Australian lithosphere. *Journal of Petrology* **39**: 1917-1930.

YU Z., ROBINSON P., AND MCGOLDRICK P. (in press). Chemical decomposition of geological materials for trace element determination using ICP-MS. *Geostandards Newsletter: The Journal of Geostandards and Geoanalysis.*

YU Z., ROBINSON P., TOWNSEND A. T., MUNKER C., AND CRAWFORD A. J. (2000). Determination of high field strength elements, Rb, Sr, Mo, Sb, Cs, Tl and Bi at ng g^{-1} levels in geological reference materials by magnetic sector ICP-MS after HF/$HClO_4$ high pressure digestion. *Geostandards Newsletter: The Journal of Geostandards and Geoanalysis* **24**: 39-50.

ZHOU Z. AND FYFE W. S. (1989). Palagonitization of basaltic glass from DSDP Site 335, Leg 37: textures, chemical composition, and mechanism of formation. *American Mineralogist* **74**: 1045-1053.

APPENDIX A

LIST OF SAMPLES AND SAMPLE LOCATIONS

Sample numbers and locations are given in Tables A.1 and A.2. Also provided is a brief description of the sample type, and preparations available for each sample. Grid references refer to positions on the 1:50,000 scale, Efaté series, digital topographic maps published in 1994 by the Government of Vanuatu. These maps are based on the World Geodetic Spheroid 1984, WTM zone 59.

Table A.1. List of Efaté Pumice Formation (EPF) samples.

SAMPLE	GRID REFERENCE	DESCRIPTION	THIN SECTION	POWDER
EFATE PUMICE BRECCIAS (EPB)				
Mele River				
AR041	[Efaté SW] KA133461	polymictic pumice and lithic granule to pebble breccia [from fallen block]	LTS	
AR042	[Efaté SW] KA133461	polymictic granule to pebble breccia, pumice and crystal fragments [from fallen block]		
AR043	[Efaté SW] KA133461	matrix-supported, polymictic breccia, pumice and perlite clasts [float]	LTS	
AR206	[Efaté SW] KA128462	pumice breccia - bulk sample		
AR207	[Efaté SW] KA128462	lithic clasts from pumice breccia (*c f* AR206)	LTS	✓
AR208	[Efate SW] KA128462	pumice clasts from pumice breccia (*c f* AR206)	LTS	
AR211	[Efate SW] KA134471	laminated and cross-bedded volcaniclastic sand [float]		
AR212	[Efaté SW] KA138474	pumice clasts [from landslide deposit]		
AR213	[Efaté SW] KA138474	glassy lithic clasts [from landslide deposits]		
AR214	[Efaté SW] KA138474	dark, dense welded ignimbrite clast? [float]	LTS	
AR215	[Efaté SW] KA138474	dark, dense welded ignimbrite clast? [float]		
AR216	[Efaté SW] KA131467	laminated volcaniclastic sand [float]		
AR217	[Efaté SW] KA131467	poorly sorted, matrix supported pumice pebble breccia fragment [float]		
AR218	[Efaté SW] KA130462	massive (bioturbated?) volcaniclastic sand, with outsize pumice clast [float]		
AR219	[Efate SW] KA130462	laminated volcaniclastic sand [float]		
AR220	[Efaté SW] KA130462	laminated volcaniclastic sand [float]		
AR221	[Efaté SW] KA137457	glassy lithic clast [float]	TS	
AR222	[Efaté SW] KA137457	glassy lithic. Eutaxitic texture with brecciate vein (float)	TS	
AR223	[Efaté SW] KA137457	glassy lithic clast [float]		
AR224	[Efaté SW] KA137457	vesicular glassy lithic clast [float]	TS	
La Colle River				
AR021	[Efaté SW] KA186442	diffusely bedded, medium-grained, shard-rich sand (pumice stringers common)		
AR022	[Efaté SW] KA186442	clast-supported, medium-grained pumice breccia		
AR225	[Efaté SW] KA171434	shard-rich, medium to coarse, indurated volcaniclastic sand [float]		
AR227	[Efaté SW] KA171434	perlitised clasts [float]		
AR228	[Efate SW] KA171434	vesicular clast [float]		
AR229	[Efaté SW] KA171434	glassy, eutaxitic textured, matrix-supported breccia (welded ig?) [float]	TS	
AR230	[Efaté SW] KA171434	massive, porphyrytic lava clast [float]		
AR231	[Efaté SW] KA171434	altered/weathered, light grey porphyritic lava clast [float]		

Abbreviations: TS = thin section, LTS = large thin section.

Table A.1. (cont.). List of Efaté Pumice Formation (EPF) samples.

SAMPLE	GRID REFERENCE	DESCRIPTION	THIN SECTION	POWDER
EFATE PUMICE BRECCIAS (EPB)				
Teouma River				
UT1	[Efaté NE] KA240461	poor to moderately sorted, massive, clast-supported coarse pumice breccia		
UT2	[Efaté NE] KA240461	vesicular and non-vesicular glassy clasts [from fallen block]		
UT3	[Efaté NE] KA240461	massive, clast-supported coarse pumice breccia [from fallen block]		
UT4	[Efaté NE] KA240461	massive, fine-grained volcaniclastic sand		
UT6	[Efate NE] KA240461	poorly sorted, massive medium-coarse pumice breccia with incipient compaction textures		
UT7	[Efaté NE] KA240461	planar bedded, very coarse shard-rich sand		
UT8	[Efaté NE] KA240461	planar laminated, fine shard-rich sand		
Namari River				
AR048	[Efaté SE] KA228442	glassy, eutaxitic welded ignimbrite fragment? (float)	LTS	
AR049	[Efaté SE] KA228442	banded glassy porphyritic fragment (float)	LTS	
Neslep River				
AR050	[Efaté NE] KA343482	pumice granule breccia (fallen block)		
AR051	[Efaté NE] KA343482	sparry calcite cemented pumice breccia (fallen block)	LTS	
AR052	[Efaté NE] KA343482	sparry calcite cemented pumice breccia (fallen block)	LTS	
Tanolui Village				
AR232	[Efaté NW] KA135538	indurated pumice and glassy lithic breccia (float)	LTS	
Lelepa Island				
AR036	[Efaté NW] KA039507	very fine-grained, laminated volcaniclastic sand with pumiceous layers		
AR037	[Efaté NW] KA039507	very fine-grained, laminated volcaniclastic sand		
AR038	[Efaté NW] KA039507	massive volcaniclastic silt	TS	
AR039	[Efaté NW] KA039507	very fine-grained, laminated volcaniclastic sand		
AR040	[Efaté NW] KA039507	reworked eolian detritus		
AR083	[Efaté NW] KA038507	medium-fine-grained, laminated volcaniclastic sand	TS	
AR084	[Efaté NW] KA039507	massive pumice and lithic breccia	PTS+LTS	
AR085	[Efaté NW] KA038507	massive pumice and lithic breccia	LTS	
AR086	[Efaté NW] KA038507	assorted clasts (loose block)		
AR087	[Efaté NW] KA038507	pumice clasts (loose block)		
AR088	[Efaté NW] KA038507	dense lava clasts		
AR089	[Efaté NW] KA038507	glassy clasts		
AR090	[[Efaté NW] KA039507	pumice clasts		
AR091	[Efaté NW] KA039507	assorted clast types		
AR092	[Efaté NW] KA039507 (base)	semi-consolidated medium-grained volcaniclastic sand	PTS	
AR093	[Efaté NW] KA039507 (base)	massive pumice breccia	LTS	✓
AR094	[Efaté NW] KA039507 (base)	massive pumice breccia	LTS	
LI9601	[Efaté NW] KA039507 (base)	compacted pumice lapilli breccia	LTSx2	
LI9602	[Efaté NW] KA039507 (base)	cross-laminated, fine-grained shard-rich sand with massive very fine-grained shard-rich sand/silt drapes	LTS	
LI9603	[Efaté NW] KA039507 (base)	lithified pumice and lithic breccia pebble		
Hat Island				
AR072	[Efaté SW] JA981475	reworked aeolian detritus		
AR073	[Efaté SW] JA981475	pumice clasts from massive pumice and lithic breccia		✓
AR074	[Efate SW] JA981475	lithic clasts from massive pumice and lithic breccia		
AR075	[Efaté SW] JA981475	limestone clasts from massive pumice and lithic breccia		
AR076	[Efaté SW] JA981475	massive pumice and lithic breccia bulk sample		
AR077	[Efaté SW] JA981475	thin bedded, medium-grained pumice breccia· bulk sample		
AR078	[Efaté SW] JA981475	limestone clasts from lithic concentration zone		
AR079	[Efaté SW] JA981475	perlitised obsidian clasts from lithic concentration zone		✓
AR080	[Efaté SW] JA981475	dense lava clasts from lithic concentration zone		

Abbreviations: TS = thin section, PTS = polished thin section, LTS = large thin section.

Table A.1. (cont.). List of Efaté Pumice Formation (EPF) samples.

SAMPLE	GRID REFERENCE	DESCRIPTION	THIN SECTION	POWDER
EFATE PUMICE BRECCIAS (EPB)				
Hat Island				
AR081	[Efaté SW] JA981475	pumice clasts from lithic concentration zone		
AR082	[Efaté SW] JA981475	assorted clast types from lithic concentration zone		
SW coast - waterfall				
EfC4	[Efaté SW] KA023455	very fine pumice breccia/very coarse volcaniclastic sand with weak carbonate cement		
EfC5	[Efaté SW] KA023455	medium-coarse grained pumice breccia		
EfC6	[Efaté SW] KA023455	cross-bedded, coarse volcaniclastic sand		
EfC7	[Efaté SW] KA023455	medium-coarse pumice breccia		
EfC8	[Efaté SW] KA023455	fine-medium grained volcaniclastic sand		
EfC9	[Efate SW] KA023455	massive, poorly sorted, coarse pumice breccia		
EfC10	[Efaté SW] KA023455	semi-consolidated volcaniclastic silt	TS	
Mangalui Quarry				
AR062	[Efaté SW] KA044474	fine pumice lapilli breccia		
AR063	[Efaté SW] KA044474	medium pumice lapilli breccia		
AR064	[Efaté SW] KA044474	medium pumice lapilli breccia	TS	✓
AR065	[Efaté SW] KA044474	very fine volcaniclastic sand		
AR066	[Efate SW] KA044474	coarse pumice lapilli breccia		✓
Creek Ai				
AR023	[Efate NW] KA077504	laminated pumice and vitric rich granular sand with abundant outsize pumice clasts	TS	
AR024	[Efaté NW] KA077504	laminated pumice and vitric rich granular sand	TS	
AR025	[Efaté NW] KA077504	massive, poorly sorted, dominantly clast-supported, coarse pumice breccia	LTS	
AR095	[Efaté NW] KA084505	assorted lithic clasts from fallen boulder of massive pumice breccia		
AR096	[Efaté NW] KA084505	bulk sample of fallen (car-sized) boulder of massive pumice breccia	TS	
AR097	[Efaté NW] KA084505	assorted dark and vesicular lithics from fallen (car-sized) boulder of massive pumice breccia		
AR098	[Efaté NW] KA084505	pumices from fallen (car-sized) boulder of massive pumice breccia		✓
AR099	[Efate NW] KA084505	vitric lithic clasts from fallen (car-sized) boulder of massive pumice breccia		
AR100	[Efaté NW] KA084505	assorted clasts from mega breccia forming river channel (landslide/avalanche deposit)		
AR101	[Efaté NW] KA076505	carbonate cemented vitric-rich, planar bedded coarse sandstone [float]	TS	
AR102	[Efaté NW] KA075506	wavy and cross-bedded, coarse, shard-rich, sand with pumiceous layers [float]	TS	
AR103	[Efaté NW] KA075506	vitric-rich, wavy and cross-bedded coarse sandstone with pumiceous layers [float]		
Interior Cliffs				
AR310	[Efaté NW] KA171514	coarse volcaniclastic sand/very fine pumice breccia		
AR311	[Efaté NW] KA171514	coarse-medium, massive pumice breccia		
RENTABAU TUFFS				
Elu River				
ELUR1	[Efaté NE] KA355474	planar bedded to laminated, fine volcaniclastic sand		
ELUR2	[Efaté NE] KA355474	planar bedded to laminated, fine volcaniclastic sand		
ELUR3	[Efaté NE] KA355474	massive, very fine grained pumice breccia to very coarse volcaniclastic sand		
ELUR4	[Efaté NE] KA355474	massive to locally cross-bedded, very fine grained pumice breccia to very coarse volcaniclastic sand		
ELUR5	[Efaté NE] KA355474	laminated, indurated, very coarse volcaniclastic sand		
ELUR6	[Efaté NE] KA355474	massive, very coarse volcaniclastic sand with internally scoured bedding		
ELUR7	[Efaté NE] KA355474	massive, very coarse volcaniclastic sand with internally scoured bedding		
ELUR8	[Efaté NE] KA355474	massive to diffusely bedded, very fine-grained pumice breccia		
ELUR9	[Efaté NE] KA355474	laminated, medium-fine volcaniclastic sand		
ELUR10a	[Efate NE] KA355474	Mn-altered/cemented fine-very fine-grained pumiceous breccia (rare forams)	LTS	
ELUR10b	[Efaté NE] KA355474	Mn-altered/cemented fine-very fine-grained pumiceous breccia (rare forams)	LTS	
ELUR11	[Efaté NE] KA355474	massive to laminated, fine-very fine-grained, indurated pumice breccia		
ELUR12	[Efaté NE] KA355474	poorly sorted, very fine pumice breccia–coarse volcaniclastic sand with internal scours and irregular cross-bedding		

Abbreviations: TS = thin section, PTS = polished thin section, LTS = large thin section.

Table A.1. (cont.). List of Efaté Pumice Formation (EPF) samples.

SAMPLE	GRID REFERENCE	DESCRIPTION	THIN SECTION	POWDER
RENTABAU TUFFS				
Forari				
AR001	[Efaté SE] KA413429	foram-bearing, very fine-grained pumiceous breccia (rare Mn- and carbonate-altered patches)		
AR002	[Efaté SE] KA413429	Mn-hydroxide altered, fine-grained pumice breccia [spoil from Forari mine export dock site]	LTS	
AR031	[Efaté SE] KA413429	clay altered, laminar bedded, fine and medium volcaniclastic sand		✓
AR032	[Efate SE] KA413429	bedded, poorly sorted, upward coarsening green (chlorite altered?), very fine-grained pumice breccia		✓
AR033	[Efaté SE] KA413429	laminated, clay altered, indurated, medium-grained, volcaniclastic sand		✓
AR034	[Efaté SE] KA413429	fine massive, clay altered, indurated, volcaniclastic sand with coarse, granular Mn-altered patches		✓
AR035	[Efaté SE] KA413429	fine laminated, clay altered, indurated, volcaniclastic sand with coarse granular stringers	TS	✓
Interior Cliffs				
AR302	[Efaté NW] KA171514	cross-bedded indurated, fine volcaniclastic sand		
AR303	[Efaté NW] KA171514	cross-bedded indurated, fine volcaniclastic sand		
AR304	[Efaté NW] KA171514	fine-very fine pumice breccia		
AR305	[Efaté NW] KA171514	pumice clasts from breccia layer (*c f.* AR304)		
AR306	[Efaté NW] KA171514	obsidian clasts from breccia layer		
AR307	[Efaté NW] KA171514	fine-grained volcaniclastic sand		
AR308	[Efaté NW] KA171514	very coarse volcaniclastic sand		
AR309	[Efaté NW] KA171514	massive, fine-grained volcaniclastic sand		
AR312	[Efaté NW] KA171514	folded laminae in convolute bedded, shard- and crystal-rich, coarse sand		
AR313	[Efaté NW] KA171514	Fe-stained, fine to very fine-grained, pumice breccia/very coarse volcaniclastic sand		
Bofua Municipal Tip				
AR026	[Efaté SE] KA225372	hydrated, massive, yellow clay with root fragments/manganese clots		✓
AR027	[Efaté SE] KA225372	hydrated, laminated, yellow and white clay with manganese horizons		✓
AR028	[Efaté SE] KA225372	hydrated, laminated, yellow/ochre clay with minor root fragments/manganese clots		✓
AR029	[Efaté SE] KA225372	hydrated, mottled (bioturbated) clay		✓
AR030	[Efaté SE] KA225372	hydrated, massive, green-brown clay (lateral equivalent of AR029)		✓
Vila Wharf				
AR016	[Efaté SW] KA153357	laminated shard-rich fine-very fine, indurated, volcaniclastic sand with locally common outsize pumice clasts	TS	
AR017	[Efaté SW] KA153357	massive shard-rich very fine indurated, volcaniclastic sand		
AR018	[Efaté SW] KA153357	fossil-bearing, massive, very fine, indurated, volcaniclastic sand (bioturbated?)		
AR019	[Efaté SW] KA153357	laminated (climbing ripple beds), shard-rich, fine-very fine, indurated, volcaniclastic sand with locally common outsize pumice clasts	TS	
AR020	[Efaté SW] KA153357	diffusely thin bedded (rippled) very fine, indurated, volcaniclastic sand with rare rounded outsize pumice clasts	TS	
SW coast - waterfall				
EfC2	[Efaté SW] KA023455	massive, volcaniclastic silt/clay		
EfC3	[Efaté SW] KA023455	laminated, volcaniclastic silt/sand with weak carbonate cement	TS	
Hat Island				
AR068	[Efaté SW] JA981475	semi-consolidated volcaniclastic silt	TS	
AR069	[Efaté SW] JA981475	semi-consolidated volcaniclastic silt		
AR070	[Efaté SW] JA981475	semi-consolidated medium pumice breccia	LTS	
Mangalui Quarry				
AR067	[Efaté SW] KA044474	semi-consolidated volcaniclastic silt	TS	

Abbreviations: TS = thin section, PTS = polished thin section, LTS = large thin section.

Table A.2. List of Basalt Volcanoes Formation (BVF) samples.

SAMPLE	GRID REFERENCE	DESCRIPTION	THIN SECTION	POWDER
Mount Fatmalapa				
AR166	[Efaté NE] KA223569	carbonate-altered, amygdaloidal (carbonate-filled), fine-grained plag-phyric, basaltic lava	TS	
AR167	[Efaté NE] KA223569	med-grained plag and px-phyric dense basalt lava	TS	
AR168	[Efaté NE] KA223569	amygdaloidal (carbonate-, chlorite-? filled) highly plag-phyric basalt lava (close to summit)	TS	
AR169	[Efate NE] KA223569	highly plag-phyric basalt lava (as AR168 but less altered)	TS	
AR171	[Efaté NE] KA223569	altered vesicular plag-phyric basalt lava		
AR172	[Efaté NE] KA216567	massive aphyric (cryptocrystalline) basalt [boulder]	LTS	✓
AR173	[Efaté NE] KA216567	fine-grained glassy basalt (?) with lath-like feldspars [boulder]	TS	
AR174	[Efaté NE] KA216567	vesicular slightly altered ol/px-phyric basalt lava [boulder]	PTS	✓
AR175	[Efaté NE] KA216567	altered ol/px-phyric basalt lava [boulder]	PTS	✓
AR176	[Efaté NE] KA215566	altered coarse-grained plag-phyric basalt [boulder]		
AR177	[Efaté NE] KA215566	hematite altered, plag/px-phyric basalt lava		
AR178	[Efaté NE] KA215566	coarse-grained hematite altered, plag/px-phyric basalt lava		
AR179	[Efaté NE] KA215566	px/ol-phyric basalt lava	PTS	✓
AR180	[Efaté NW] KA210568	olivine basalt dyke-margin	TS	
AR181	[Efaté NW] KA210568	olivine basalt dyke-centre	TS	✓
AR182	[Efaté NW] KA210568	olivine basalt dyke	TS	✓
Quoin Hill				
AR151	[Efaté NE] KA272581	med-grained plag/px-phyric, poorly vesicular basaltic lava	PTS	
AR152	[Efaté NE] KA275581	med-grained plag-phyric, moderately vesicular basaltic lava	TS	
AR153	[Efaté NE] KA278581	med-grained plag-phyric, non-vesicular basaltic lava with some oxidised ol/px	PTS	✓
AR154	[Efaté NE] KA278581	med-grained plag-phyric, very poorly vesicular basaltic lava with some oxidised ol/px	TS	
AR155	[Efaté NE] KA283580	med to coarse-grained oxidised ol+px±minor plag-phyric basaltic lava	PTS	
AR156	[Efaté NE] KA287576	med-grained px-phyric, very poorly vesicular basaltic lava	TS	
AR157	[Efaté NE] KA287574	med-grained plag/px-phyric, poorly vesicular basaltic lava	PTS	✓
AR158	[Efaté NE] KA278568	med to coarse-grained, plag/px-phyric, moderately vesicular basaltic lava	PTS	✓
AR159	[Efaté NE] KA272567	med to coarse-grained, plag/px-phyric, poorly vesicular basaltic lava	TS	
AR160	[Efate NE] KA272570	coarse-grained, plag/px-phyric, poorly vesicular basaltic lava	PTS	
AR161	[Efaté NE] KA277570	med to coarse-grained, plag/px-phyric, poorly vesicular basaltic lava	PTS	✓
AR164	[Efate NE] KA277570	med-grained, plag/px-phyric, poorly vesicular basaltic lava	PTS	✓
Nguna				
AR005	[Efaté NE] KA226654	plag-phyric coarse basalt	PTS	
AR006	[Efaté NE] KA226654	plag-phyric coarse basalt	PTS	✓
AR007	[Efaté NE] KA226654	plag-phyric coarse basalt	PTS	
AR008	[Efaté NW] KA205654	(sheared) vesicular plag-phyric coarse basalt	TS	
AR104	[Efaté NW] KA199652	coarse-grained plag-phyric basalt [float]		
AR105	[Efaté NW] KA199652	vesicular coarse plag-phyric basalt [lava flow top]	PTS	✓
AR106	[Efaté NW] KA197654	coarse plag-phyric basalt [clast from monomict basalt boulder conglomerate]	PTS	✓
AR107	[Efaté NW] KA197654	coarse plag-phyric basalt [loose boulder]	TS	
AR108	[Efaté NW] KA158708	vesicular coarse plag-phyric basalt	LTS	
AR109	[Efaté NW] KA158708	coarse plag-phyric basalt	PTS	✓
AR110	[Efaté NW] KA158708	medium-grained non-vesicular coarse plag-phyric basalt	PTS	✓
AR111	[Efaté NW] KA158708	altered medium-grained non-vesicular coarse plag-phyric basalt		
Pele				
AR003	[Efaté NE] KA238640	coarse plag+ol-phyric basalt	PTS	✓
AR004	[Efaté NE] KA231651	coarse plag-phyric basalt	PTS	
AR112	[Efaté NE] KA234651	hydrothermally altered plag+ol-phyric basalt	TS	

Abbreviations: plag = plagioclase, ol = olivine, px = clinopyroxene, TS = thin section, PTS = polished thin section, LTS = large thin section.

Table A.2. (cont.). List of Basalt Volcanoes Formation (BVF) samples.

SAMPLE	GRID REFERENCE	DESCRIPTION	THIN SECTION	POWDER
Pele				
AR113	[Efaté NE] KA234651	coarse-grained plag-phyric basalt		
AR114	[Efaté NE] KA237651	ol+px-phyric basalt	PTS	✓
AR115	[Efaté NE] KA237651	ol+px-phyric basalt [boulder]		
AR116	[Efaté NE] KA233651	ol+px-phyric basalt		
Emau				
AR183	[Efaté NE] KA328638	plag+px+ol-phyric vesicular basaltic lava		
AR184	[Efaté NE] KA328638	plag+px+ol-phyric vesicular basaltic lava	PTS	✓
AR185	[Efaté NE] KA328638	plag-phyric basalt with subophitic texture	PTS	✓
AR186	[Efaté NE] KA328644	coarse ol+plag-phyric basalt	PTS	
AR187	[Efaté NE] KA326644	plag+ol-phyric basalt	TS	
AR188	[Efaté NE] KA322642	almost aphyric basalt	PTS	✓
AR189	[Efaté NE] KA322642	high-T ol reaction rims in ol+plag-phyric lava	PTS	
AR190	[Efaté NE] KA320645	ol+plag-phyric basalt - iddingsite altered ols	TS	
AR191	[Efaté NE] KA334660	plag+ol-phyric basalt - altered olivines (late magmatic oxidation?)	TS	
AR192	[Efaté NE] KA334660	plag+ol-phyric basalt - vaguely vesicular	PTS	✓
AR193	[Efaté NE] KA334660	strongly altered and degraded ex-plag-phyric basalt - (plag pseudomorphed by calcite?)		
AR194	[Efaté NE] KA321654	highly vesicular, plag+weakly ol-phyric basalt - large opaques	PTS	
AR195	[Efaté NE] KA321654	plag±small px-phyric basalt - dyke texture	PTS	
AR196	[Efaté NE] KA321654	fine-grained ol+plag-phyric basalt [beach pebble]		
AR197	[Efaté NE] KA318654	fine-grained ol+plag-phyric basalt [beach pebble]	TS	
AR198	[Efaté NE] KA317655	fine-grained plag+ol±px-phyric basalt [beach pebble]	PTS	✓
AR199	[Efaté NE] KA317655	holocrystalline, plag+px-rich, doleritic textured basalt [beach pebble]	PTS	✓
AR201	[Efate NE] KA317655	fine-grained, ol+px+plag-phyric basalt [beach pebble]	PTS	✓
AR202	[Efaté NE] KA317655	altered, plag+ol-phyric basalt [beach pebble]	TS	
AR203	[Efate NE] KA317655	vesicular, plag+large opaques+ol-phyric basalt [beach pebble]	PTS	
AR204	[Efaté NE] KA317655	plag+px+minor ol-phyric basalt [beach pebble]	PTS	
AR205	[Efaté NE] KA317655	plag-phyric basalt [beach pebble]	TS	

Abbreviations: plag = plagioclase, ol = olivine, px = clinopyroxene, TS = thin section, PTS = polished thin section, LTS = large thin section.

APPENDIX B

VOLUME CALCULATIONS FOR EFATÉ ISLAND GROUP FORMATIONS

Bulk volume estimates were determined for Efaté Island Group volcanic formations with the parameters outlined in Table B.1. Area estimates were determined from outcrop patterns on the existing 1:100,000 geological map (Ash *et al.*, 1974), and average thicknesses from topography on a combination of 1:100,000 and 1:50,000 scale maps, and known Formation thicknesses (Obellianne, 1958; Ash *et al.*, 1978).

Table B.1. Bulk volume estimates for Efaté Island Group volcanic lithological units.

VOLCANIC LITHOLOGICAL UNIT	AREA	THICKNESS	VOLUME
Efaté Pumice Breccias			
Mount Macdonald summit area	74 km^2	0 50 km	37.8 km^3
Mount Bernier summit area	46 km^2	0.35 km	16 4 km^3
East of Teouma Graben	40 km^2	0.25 km	10.2 km^3
Total volume			*64 4 km^3*
Rentabau Tuffs			
East of Teouma Graben – in contact with EPG	36 km^2	0.05 km	1 84 km^3
East of Teouma Graben – thinning to south of EPG contact	21 km^2	0 03 km	0 64 km^3
West of Teouma Graben	25 km^2	0 015 km	0.38 km^3
Total volume			*2 86 km^3*
Efaté Pumice Formation (EPF) – area under limestone veneer			
Southwest - from Klem's Hill west (including Lelepa and Hat Islands)	47 km^2	*0 15 km	1 05 km^3
Northwest – Mount Erskine area	33 km^2	*0 25 km	8 25 km^3
Southern and eastern coastal areas	276 km^2	*0 02 km	5.52 km^3
Total volume			*14 82 km^3*
Basalt Volcanoes Formation (BVF)			
Mount Fatmalapa and Quoin Hill	15 km^2	0.40 km	6 km^3
Nguna – lowlands (averaged height)	12 km^2	0.25 km	3 km^3
Nguna – highlands (volcano summit areas)	10 km^2	0 50 km	5 km^3
Pele	4 km^2	0.10 km	0.4 km^3
Emau	7 km^2	0 30 km	2 1 km^3
Total volume			*16.5 km^3*

Thicknesses are average thicknesses for units based on average topographic heights and/or measured thickness from mapping. * Thickness determined assuming that the average thickness of the RLF veneer is 50 m.

APPENDIX C

GRANULOMETRIC ANALYSIS

An approximate average grain size for the coarsest facies of the Efaté Pumice Breccias was determined from measuring the longest exposed dimensions of pumice and lithic grains in a ~30x30 cm area on representative beds in key sections. Results are presented in Table C.1.

Table C.1. Average grain sizes and standard deviations for ~30x30 cm areas on representative pumice breccia beds.

SECTION LOCATION	FACIES	AVERAGE CLAST SIZE	STANDARD DEVIATION	n (number)
Section 1(a) (Lelepa Is.)	MLB	32 1 mm	5.24	89
Section 1(a) (Lelepa Is.)	SPB	17.2 mm	1 36	178
Section 1(b) (Lelepa Is)	SPB	12 5 mm	8 90	300
Section 1(b) (Lelepa Is)	XPB	28 0 mm	4 32	103
Section 2 (Hat Island)	MLB	23.1 mm	6 30	132
Section 2 (Hat Island)	SPB	25 3 mm	3 62	120
Section 3 (Mangalui Quarry)	MLB	30 6 mm	1 27	95
Section 6 (Upper Teouma)	MLB	29.4 mm	6 43	92
Section 7 (La Colle R)	MLB	28 2 mm	1.13	102
Section 7 (La Colle R)	MLB	19.5 mm	7 62	290

Granulometric analysis on suitable samples was performed at Monash University and the University of Tasmania. A bulk sample split was dried overnight in an 80°C oven, and then gently hand sieved in a standard set of vertically-aligned metric sieves with mesh openings from –5 ϕ to 4 ϕ (32 mm to $^{1}/_{16}$ mm) with intervals of 1 ϕ. Size fractions collected from each of the sieves were weighed and the fraction reserved for component analysis. Duplicate test runs showed that attrition of particles by dry hand sieving was minimal with standard deviations between runs generally less than 2 % relative (Table C.2). Table C.3 lists the results. Attrition of the bulk sample during the removal of the sample from the deposit, and during transport back to the University of Tasmania cannot be quantified and was assumed to be negligible for the purposes of analysis.

Table C.2. Example of errors on replicate sieve analyses for granulometric analysis of volcaniclastic sediments from the Efaté Island Group.

SAMPLE	AR076											
FRACTION	-5 ϕ	-4 ϕ	-3 ϕ	-2 ϕ	-1 ϕ	0 ϕ	1 ϕ	2 ϕ	3 ϕ	4 ϕ	<4 ϕ	Totals
run 1 (mass in g)	-	13.33	17 77	28 49	38.85	44 29	40 90	46.88	41 61	22 11	13.02	307 26
run 2 (mass g)	-	13 21	17.26	28 37	39 23	43.86	41 49	47.10	40 60	22 41	12 35	305 88
run 3 (mass g)	-	12 84	17 37	27.77	39.63	44 10	41.55	46.12	41 10	23.01	12.98	306 47
average (g)	-	13.13	17 46	28.21	39 24	44.08	41 31	46 70	41.10	22.51	12 78	306 53
standard deviation (g)	-	0.26	0 27	0 39	0 39	0 22	0.36	0.52	0.51	0.46	0.38	0.69
% standard deviation	-	1 95	1 55	1 37	0 99	0 49	0.87	1.11	1.23	2 04	2.94	0 23

Table C.3. Results of granulometric analysis for volcaniclastic sediments, Efaté Pumice Breccias.

SAMPLE	AR062											
FRACTION	-5 ϕ	-4 ϕ	-3 ϕ	-2 ϕ	-1 ϕ	0 ϕ	1 ϕ	2 ϕ	3 ϕ	4 ϕ	<4 ϕ	Totals
mass (g)	-	-	1 58	6.15	23.38	47.14	84 51	79 94	41 91	16 20	7 12	307.93
frequency (%)	-	-	0 51	2 00	7 59	15.31	27.44	25 96	13 61	5 26	2.31	100.00
cum freq (%)	-	-	0.51	2 51	10 10	25 41	52 86	78.82	92.43	97 69	100 00	
	Md_ϕ	0.90			σ_ϕ	1.40			α_ϕ	0 64		

SAMPLE	AR063											
FRACTION	-5 ϕ	-4 ϕ	-3 ϕ	-2 ϕ	-1 ϕ	0 ϕ	1 ϕ	2 ϕ	3 ϕ	4 ϕ	<4 ϕ	Totals
mass (g)	-	-	0 20	5 94	32.83	67.21	111.38	136.00	66 94	19 27	8 23	447 99
frequency (%)	-	-	0 04	1.33	7 33	15.00	24 86	30 36	14 94	4 30	1.84	100 00
cum freq (%)	-	-	0 04	1 37	8 70	23 70	48 56	78 92	93.86	98 16	100 00	
	Md_ϕ	1 00			σ_ϕ	0.95			α_ϕ	1 79		

SAMPLE	AR064											
FRACTION	-5 ϕ	-4 ϕ	-3 ϕ	-2 ϕ	-1 ϕ	0 ϕ	1 ϕ	2 ϕ	3 ϕ	4 ϕ	<4 ϕ	Totals
mass (g)	-	-	0.26	3 36	19.36	52.80	106 99	99 65	52 11	15.73	5.18	355 44
frequency (%)	-	-	0 07	0.95	5.45	14.86	30.10	28 03	14 66	4 42	1 46	100 00
cum. freq (%)	-	-	0 07	1.02	6 46	21.32	51.42	79 46	94 12	98 54	100 00	
	Md_ϕ	0 90			σ_ϕ	1.20			α_ϕ	0.92		

SAMPLE	AR065											
FRACTION	-5 ϕ	-4 ϕ	-3 ϕ	-2 ϕ	-1 ϕ	0 ϕ	1 ϕ	2 ϕ	3 ϕ	4 ϕ	<4 ϕ	Totals
mass (g)				5 88	3 62	30.17	185 91	211.75	103.79	29 76	8 66	579 53
frequency (%)	-	-	-	1 01	0.63	5.21	32 08	36 54	17.91	5.13	1.49	100.00
cum freq. (%)	-	-	-	1.01	1 64	6 85	38 93	75 46	93.37	98.51	100 00	
	Md_ϕ	1 40			σ_ϕ	1 00			α_ϕ	1 40		

SAMPLE	AR066											
FRACTION	-5 ϕ	-4 ϕ	-3 ϕ	-2 ϕ	-1 ϕ	0 ϕ	1 ϕ	2 ϕ	3 ϕ	4 ϕ	<4 ϕ	Totals
mass (g)	-	-	18 13	46 13	80 31	84 05	87.85	83.77	46.31	16 11	6.86	469 52
frequency (%)	-	-	3.86	9 82	17 10	17.90	18.71	17 84	9 86	3 43	1 46	100.00
cum. freq. (%)	-	-	3 86	13.69	30 79	48 69	67 40	85 24	95.11	98.54	100 00	
	Md_ϕ	0 10			σ_ϕ	1 80			α_ϕ	-0 06		

SAMPLE	AR036											
FRACTION	-5 ϕ	-4 ϕ	-3 ϕ	-2 ϕ	-1 ϕ	0 ϕ	1 ϕ	2 ϕ	3 ϕ	4 ϕ	<4 ϕ	Totals
mass (g)	-	-	10.60	16.62	3.97	4.40	13 24	70 37	44.46	5.55	0 25	169 45
frequency (%)	-	-	6.25	9 81	2.34	2 60	7.81	41.53	26.23	3 28	0 15	100 00
cum freq. (%)	-	-	6 25	16.06	18.40	21 00	28 81	70 34	96 58	99 85	100.00	
	Md_ϕ	n/a			σ_ϕ	n/a			α_ϕ	n/a		

SAMPLE	AR037											
FRACTION	-5 ϕ	-4 ϕ	-3 ϕ	-2 ϕ	-1 ϕ	0 ϕ	1 ϕ	2 ϕ	3 ϕ	4 ϕ	<4 ϕ	Totals
mass (g)	-	-	-	4 97	4 32	7.37	13 25	31 12	43.16	27 25	10.39	141 83
frequency (%)	-	-	-	3 51	3.05	5.20	9,34	21.94	30 43	19 21	7 33	100.00
cum. freq (%)	-	-	-	3 51	6.55	11 75	21 09	43 03	73.46	92 67	100.00	
	Md_ϕ	2.30			σ_ϕ	1 45			α_ϕ	1 24		

SAMPLE	AR076											
FRACTION	-5 ϕ	-4 ϕ	-3 ϕ	-2 ϕ	-1 ϕ	0 ϕ	1 ϕ	2 ϕ	3 ϕ	4 ϕ	<4 ϕ	Totals
mass (g)	-	13.13	17 46	28 21	39.24	44.08	41.31	46 70	41 10	22 51	12 78	306.51
frequency (%)	-	4.28	5 70	9.20	12.80	14 38	13 48	15 23	13 41	7 34	4.17	100 00
cum. freq. (%)	-	4.28	9.98	19 19	31 99	46 37	59.84	75 08	88.49	95 83	100.00	
	Md_ϕ	0 30			σ_ϕ	2.40			α_ϕ	0 04		

SAMPLE	AR077											
FRACTION	-5 ϕ	-4 ϕ	-3 ϕ	-2 ϕ	-1 ϕ	0 ϕ	1 ϕ	2 ϕ	3 ϕ	4 ϕ	<4 ϕ	Totals
mass (g)	-	4 88	25 76	38 77	80 37	87.63	87.85	83.77	46 31	16 11	6 86	478 32
frequency (%)	-	1.02	5.39	8 11	16 80	18 32	18.37	17 51	9.68	3 37	1.43	100 00
cum. freq (%)	-	1 02	6.41	14 51	31 32	49 64	68 00	85 52	95.20	98 57	100 00	
	Md_ϕ	0 00			σ_ϕ	1.80			α_ϕ	0.00		

Abbreviations: cum. freq. = cumulative frequency, $Md\phi = \phi 50$ (graphical mean), $\sigma\phi = (\phi 84 - \phi 16)/2$ (graphical standard deviation), $\alpha\phi = [(\phi 84 + \phi 16) - Md\phi]/\sigma\phi$ (first order skewness). Parameters from Inman (1952).

COMPONENT ANALYSIS

Component abundances were calculated from point counting of component types using a standard binocular microscope for grain size fractions from –4 ϕ to 3 ϕ (16 to 0.125 mm). Components from sieved grain size fractions < -2 ϕ (>4 mm) were hand counted up to 300 grains or total abundance, whichever was reached first. Grain size fractions > -2 ϕ (<4 mm) were poured onto glass plates and overlayed with a transparent grid with spacings appropriate for grain size (*e.g.* 4 mm grid for 2 mm grain size fraction). Particle types falling at grid intersections were recorded until 300-400 grains were counted. Table C.4 lists the results of component point count analysis.

Table C.4. Results of point counting for volcaniclastic sediments, Efaté Pumice Breccias.

SAMPLE	AR062															
COMPONENT	-4 ϕ		-3 ϕ		-2 ϕ		-1 ϕ		0 ϕ		1 ϕ		2 ϕ		3 ϕ	
	#	%	#	%	#	%	#	%	#	%	#	%	#	%	#	%
pumice			214	95 11	279	93	353	88.3	378	94 5	362	90.5	229	76.3	228	57
plagioclase			7	3.11	16	5 3	41	10.3	6	1 5						
pyroxene							4	1	1	0 25	17	4 25				
Ti-magnetite											8	2	15	5	9	2 25
lithic			4	1 78	5	1.7							5	1.7		
shard							2	0 5	15	3 75	13	3.25	51	17	163	40.75
Total			225	100	300	100	400	100	400	100	400	100	300	100	400	100

SAMPLE	AR063															
COMPONENT	-4 ϕ		-3 ϕ		-2 ϕ		-1 ϕ		0 ϕ		1 ϕ		2 ϕ		3 ϕ	
	#	%	#	%	#	%	#	%	#	%	#	%	#	%	#	%
pumice			183	92 42	267	89	306	76.5	369	92 25	344	86	280	70	343	85 75
plagioclase			9	4 55	24	8	79	19 8	12	3	3	0.75				
pyroxene							15	3.75	19	4.75	28	7	31	7 75		
Ti-magnetite											4	1	62	15 5	18	4 5
lithic			6	3 03	9	3					2	0 5				
shard											19	4 75	27	6.75	39	9 75
Total			198	100	300	100	400	100	400	100	400	100	400	100	400	100

SAMPLE	AR064															
COMPONENT	-4 ϕ		-3 ϕ		-2 ϕ		-1 ϕ		0 ϕ		1 ϕ		2 ϕ		3 ϕ	
	#	%	#	%	#	%	#	%	#	%	#	%	#	%	#	%
pumice			159	89.83	265	88.33	306	76 5	343	85 75	358	89 5	371	92.75	313	78 25
plagioclase			14	7 91	31	10 33	94	23.5	19	4 75	7	1 75				
pyroxene									22	5 5	21	5.25				
Ti-magnetite											6	1.5	21	5.25	17	4 25
lithic			4	2 26	4	1.333			11	2 75						
shard									5	1.25	8	2	8	2	70	17.5
Total			177	100	300	100	400	100	400	100	400	100	400	100	400	100

SAMPLE	AR065															
COMPONENT	-4 ϕ		-3 ϕ		-2 ϕ		-1 ϕ		0 ϕ		1 ϕ		2 ϕ		3 ϕ	
	#	%	#	%	#	%	#	%	#	%	#	%	#	%	#	%
pumice					277	92 3	299	74 8	330	82.5	366	91 5	303	75.75	210	52 5
plagioclase					23	7 7	92	23	39	9 75	14	3.5				
pyroxene							4	1	10	2 5	3	0 75	7	1.75		
Ti-magnetite													65	16.25	5	1.25
lithic									12	3						
shard							5	1 25	9	2.25	17	4.25	25	6.25	185	46.25
Total					300	100	400	100	400	100	400	100	400	100	400	100

SAMPLE	AR066															
COMPONENT	-4 ϕ		-3 ϕ		-2 ϕ		-1 ϕ		0 ϕ		1 ϕ		2 ϕ		3 ϕ	
	#	%	#	%	#	%	#	%	#	%	#	%	#	%	#	%
pumice			229	76 33	285	95	352	88	376	94	388	97	336	84	398	99 5
plagioclase			71	23.67	11	3 7	42	10.5	2	0.5						
pyroxene							6	1 5	13	3 25	7	1 75	3	0 75		
Ti-magnetite											2	0.5	61	15 25	2	0.5
lithic					4	1 3			7	1 75						
shard									2	0.5	3	0 75				
Total			300	100	300	100	400	100	400	100	400	100	400	100	400	100

Table C.4. Results of point counting for volcaniclastic sediments, Efaté Pumice Breccias.

SAMPLE	AR036															
COMPONENT	-4 ϕ		-3 ϕ		-2 ϕ		-1 ϕ		0 ϕ		1 ϕ		2 ϕ		3 ϕ	
	#	%	#	%	#	%	#	%	#	%	#	%	#	%	#	%
pumice			264	100	276	92.62	298	74.5	343	85 75	303	75 75	312	78	274	68.5
plagioclase					13	4 36	83	20 8	13	3.25						
pyroxene							8	2	25	6 25	12	3	7	1 75		
Ti-magnetite											61	15.25	8	2	5	1.25
lithic					9	3.02										
shard							11	2 75	19	4 75	24	6	73	18.25	121	30 25
Total			264	100	298	100	400	100	400	100	400	100	400	100	400	100

SAMPLE	AR037															
COMPONENT	-4 ϕ		-3 ϕ		-2 ϕ		-1 ϕ		0 ϕ		1 ϕ		2 ϕ		3 ϕ	
	#	%	#	%	#	%	#	%	#	%	#	%	#	%	#	%
pumice					285	95	303	75.7	332	83	373	93 25	329	82 25	285	71 25
plagioclase					12	4	85	21.3	48	12						
pyroxene							5	1 25	13	3.25	7	1.75	2	0.5		
Ti-magnetite											8	2	28	7	63	15 75
lithic					3	1	7	1.75	3	0 75						
shard									4	1	12	3	41	10 25	52	13
Total					300	100	400	100	400	100	400	100	400	100	400	100

SAMPLE	AR076															
COMPONENT	-4 ϕ		-3 ϕ		-2 ϕ		-1 ϕ		0 ϕ		1 ϕ		2 ϕ		3 ϕ	
	#	%	#	%	#	%	#	%	#	%	#	%	#	%	#	%
pumice	27	100	277	92 33	221	73 7	353	88 2	362	90.5	366	91 5	278	69 5	299	74 75
plagioclase			7	2 33	64	21 3	47	11.8								
pyroxene									19	4.75	21	5.25	8	2		
Ti-magnetite													63	15 75	14	3 5
lithic			16	5 33	15	5			8	2						
shard									11	2 75	13	3 25	51	12 75	87	21.75
Total	27	100	300	100	300	100	400	100	400	100	400	100	400	100	400	100

SAMPLE	AR077															
COMPONENT	-4 ϕ		-3 ϕ		-2 ϕ		-1 ϕ		0 ϕ		1 ϕ		2 ϕ		3 ϕ	
	#	%	#	%	#	%	#	%	#	%	#	%	#	%	#	%
pumice	8	100	290	96.67	282	94	289	72 3	345	86.25	331	82.75	301	75 25	283	70 75
plagioclase			2	0 67	11	3 7	102	25 5	9	2 25	4	1				
pyroxene					1	0.3	9	2 25	29	7.25	5	1.25				
Ti-magnetite											25	6 25	13	3 25	18	4 5
lithic			8	2 66	6	2										
shard									17	4 25	35	8 75	86	21 5	99	24.75
Total	8	100	300	100	300	100	400	100	400	100	400	100	400	100	400	100

APPENDIX D

CLAY MINERALOGY IN ALTERED RENTABAU TUFFS

The clay mineralogy of Rentabau Tuffs samples from the Bofua Municipal Tip section (Section 4, Chapter Four) was determined using PIMA spectrometry. Output spectra are presented in Figure D.1. Spectra were analysed and interpreted using The Spectral Geologist software and results are presented in Table D.1.

Spectra for samples AR026 through AR030 show characteristic absorption features of halloysite and were confidently identified. All samples have a well-developed absorption doublet at the low wavelength end of the spectrum (troughs at ~1390 nm and ~1410 nm), a deep asymmetric water (OH^-) feature at ~1920 nm, and the diagnostic, asymmetric kandite doublet, with a shallow trough at ~2170 nm and a deeper trough at ~2210 nm.

The spectrum for AR031 lacks the distinctive kandite clay features and has a much smoother overall shape with low definition in peaks and troughs. It is probably a mixture of opaline silica (unaltered volcanic glass?) and palygorskite (an Mg-bearing, chain lattice clay mineral). AR032 is a mid- to dark green clay-rich sample and did not provide enough reflectance to produce an interpretable spectrum. Spectra for samples AR033, AR034 and AR035 are also clay mixtures. AR033 has a smoother trough at ~1412 nm and is interpreted to be a mixture of halloysite and illite. By contrast, reflectance spectra for AR034 and AR035 have a distinctive shallow trough at ~2250 nm and are interpreted to be mixtures of halloysite and opaline silica (volcanic glass?).

Table D.1. Clay mineral content of samples from Bofua Municipal Tip, Rentabau Tuffs, Efaté Pumice Formation.

SAMPLE	% HALLOYSITE	% PALYGORSKITE	% ILLITE	% OPALINE SILICA	CONFIDENCE IN RESULT
AR026	100				very good
AR027	100				very good
AR028	100				very good
AR029	100				very good
AR030	100				good
AR031		36		64	moderate
AR032					
AR033	63		37		poor
AR034	51			49	moderate
AR035	56			44	moderate

Results are based on calculated estimates from The Spectral Geologist software.

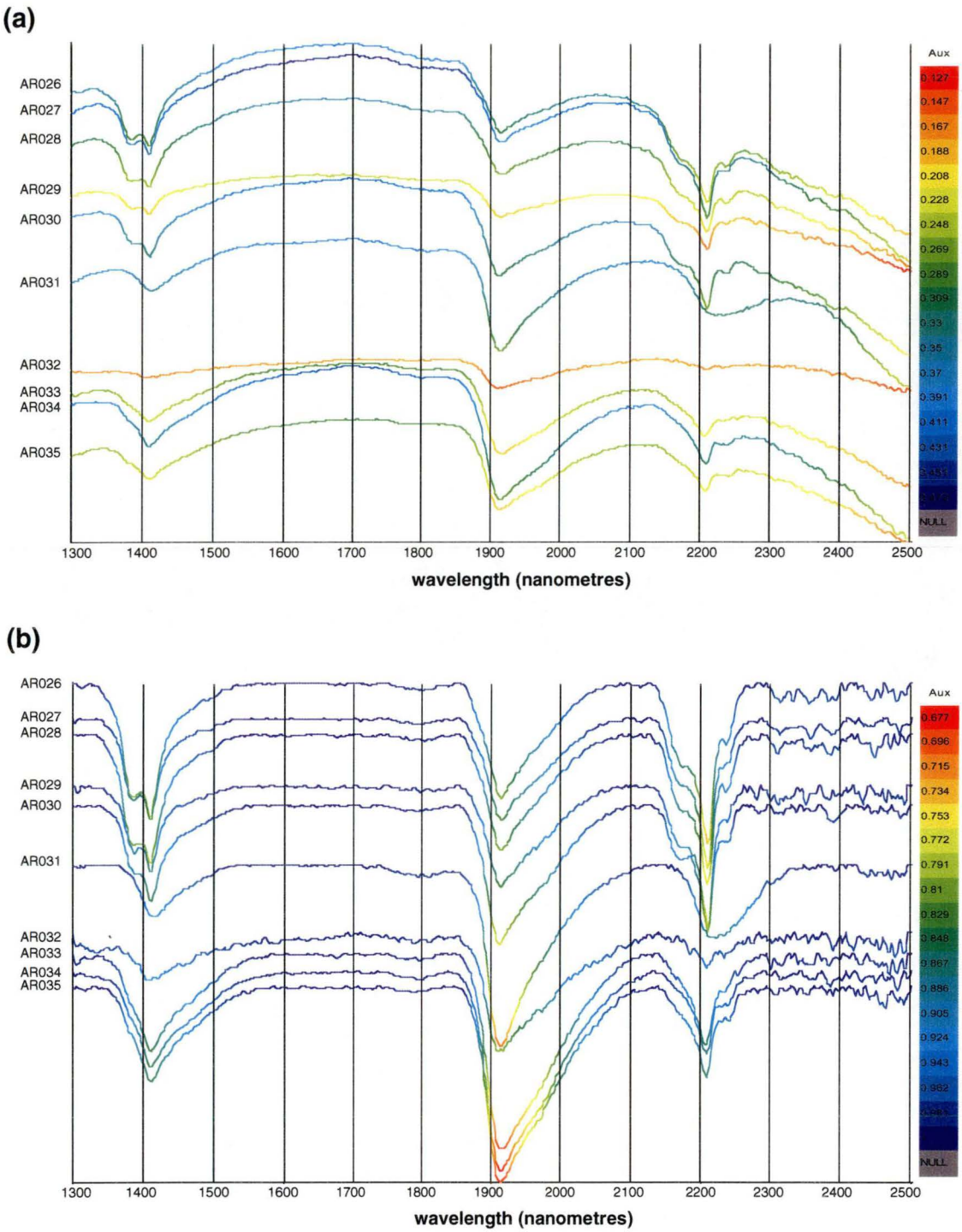

Figure D.1. Stacked (a) reflectance and (b) hull quotient spectra for samples from the Bofua Municipal Tip section, Rentabau Tuffs. Reflectance values are indicated by auxiliary colour values (Aux) at left. Note strongly developed absorption features at ~1400 nm, 1920 nm and 2200 nm.

APPENDIX E

PETROGRAPHY OF THE BASALT VOLCANOES FORMATION

Petrographic descriptions of representative samples from the Basalt Volcanoes Formation are given in Table E.1. All percentages are visual estimates based on microscope work.

Table E.1. Petrographic descriptions for representative basalts of the Basalt Volcanoes Formation, as discussed in Chapter Five.

SAMPLE	TEXTURE	PHENOCRYSTS & MICROPHENOCRYSTS	GROUNDMASS	COMMENTS
Mainland - Mt Fatmalapa				
AR172	fine-grained, massive textured, aphyric rock hosting strongly porphyritic domains	*PORPHYRITIC DOMAINS* *plagioclase* 24 % 0 5-3 mm, euhedral discrete laths & aggregates, melt inclusion trails common, white mica altered cores of phenocrysts, rare clinopyroxene inclusions occurring on twin planes *olivine* 4 % 0 2-0 5 mm, subhedral, associated with large oxide grains, strongly altered to serpentine/chlorite/smectite *clinopyroxene* 8 % 0 5-3 mm, euhedral-subhedral, zoning common, melt inclusion trails in some grains *oxides* 4 % 0 5-1 mm, subhedral & embayed, associated with olivine phenocrysts *vesicles* -	*MASSIVE APHYRIC DOMAINS / GROUNDMASS* pl=cpx=ox±ol pl 20-40 µm, laths cpx 20-40 µm, equant ox 20-40 µm, equant ol <1 % 20-40 µm, equant *ubiquitous accessory apatite*	massive aphyric domains account for 60 % of the rock, & have gradational boundaries into the porphyritic domains porphyritic domains may be cognate lithic fragments from the roof, walls or floor of the same magma chamber as the aphyric material OR aphyric areas may represent residual melt that crystallised in fractures within a more phenocryst-rich cooler magma
AR174	strongly porphyritic	*plagioclase* 15 % 1-3 mm, euhedral to subhedral aggregates, melt inclusion trails common, small clinopyroxene inclusions, commonly zoned at margins *olivine* 7 % 0 5-1 mm, subhedral grains occurring in clusters, iddingsite altered cores *clinopyroxene* 5 % 0 2-0 6 mm (up to 1 mm), subhedral to euhedral, strongly twinned, plagioclase inclusions at crystal margins, occurring as aggregates *oxides* 3 % 0 2-0 4 mm, euhedral to subhedral & embayed, associated with olivine & clinopyroxene phenocrysts *vesicles* 10 % 0 6-2 mm, irregular shapes with rounded bubble wall traces	60 % intergranular pl>cpx>>ox pl 40 % 30-50 µm, laths cpx 35 % 10-15 µm, equant ox 15 % 10-15 µm, equant *ubiquitous accessory apatite*	iddingsite alteration affects cores of olivine phenocrysts rather than rims as typically occurs in other samples - may reflect compositional zoning of grains
AR175	coarse-grained generally massive texture	*plagioclase* 25 % 0 5-1 mm, subhedral discrete grains & clusters, zoned at margins *olivine* 10 % 2-5 mm, subhedral, strongly altered to serpentine/chlorite/smectite *clinopyroxene* 45 % 3-7 mm, subhedral grains with ragged margins marked by plagioclase inclusion trails, oxide inclusions *oxides* 10 % 0 3-1 mm, subhedral, embayed & tatty discrete crystals *vesicles* - *ubiquitous accessory apatite*		< 10 % of the sample comprises interstitial patches of very fine-grained (20-50 µm) equant clinopyroxene & oxide microcrysts chlorite present (with plagioclase inclusions) as alteration product at clinopyroxene grain margins probably from a dyke
AR179	strongly porphyritic	*plagioclase* 5 % 1-3 mm, subhedral aggregates & laths, melt inclusion trails common, zoned at margins *olivine* 5 % 1-3 mm, euhedral, strongly altered to serpentine/chlorite/smectite *clinopyroxene* 15 % 2-4 mm, euhedral, weakly zoned, melt inclusions common, associated with oxide grains, twinning common, some grains with stubby plagioclase inclusions *oxides* 7 % 0 5-1 mm, subhedral & embayed, discrete grains but usually associated with olivine & clinopyroxene *vesicles* <1 % 0 5-1 mm, irregular & rounded shapes, clay mineral(?)/zeolite(?) lining	68 % intergranular pl=cpx=ox pl 5-10 µm, laths cpx 5-10 µm, equant ox 5-10 µm, equant *ubiquitous accessory apatite*	alteration to chlorite at clinopyroxene rims
AR181 & AR182	porphyritic	*plagioclase* 16 % 1-2 5 mm, subhedral aggregates & laths, melt inclusion trails common *olivine* 2 % 0 2-0 5 mm, subhedral, strongly altered to chlorite with minor serpentine/smectite *clinopyroxene* 5 % 0.4-1 mm, subhedral & euhedral, twinning common, weak zoning *oxides* 2 % 0 2-0 6 mm, rarely up to 1 mm, subhedral & embayed, associated with olivine & clinopyroxene *vesicles* -	75 % intergranular pl>>ox>cpx>ol pl 40 % 100-300 µm, laths cpx 20 % 50-100 µm, equant ox 25 % 10-50 µm, equant ol 15 % 50-100 µm, equant, altered (chlorite) *ubiquitous accessory apatite*	sample comes from a dyke with chilled margins localised carbonate altered patches

Table E.1. (cont.). Petrographic descriptions for representative basalts of the Basalt Volcanoes Formation, as discussed in Chapter Five.

SAMPLE	TEXTURE	PHENOCRYSTS & MICROPHENOCRYSTS	GROUNDMASS	COMMENTS
Mainland - Quoin Hill				
AR153	porphyritic	*plagioclase* 18 % ~1 mm, subhedral aggregates & laths, some rounded plagioclase grains, melt inclusion trails common *olivine* 5 % 1-3 mm, euhedral to subhedral & locally embayed, incipient iddingsite alteration at rims & along fractures *clinopyroxene* 2 % 0 2-0 5 mm (up to 1 mm), subhedral to euhedral, very weak iron oxidation causing staining at crystal margins *oxides* 1 % 0 1 mm, subhedral & embayed, associated with olivine phenocrysts *vesicles* -	74 % intergranular pl>>cpx>ox>ol pl 50 % 10-50 µm, laths cpx 20 % 10-50 µm, equant ox 18 % 10-50 µm, equant ol 12 % 10-50 µm, equant, iddingsite altered *ubiquitous accessory apatite*	
AR157	strongly porphyritic	*plagioclase* 20 % 0 5-1 mm, subhedral aggregates & laths with ragged terminations, melt inclusion trails common rare rounded discrete plagioclase grains *olivine* 5 % 1-3 mm, subhedral to rounded shapes, incipient iddingsite alteration at rims, oxide inclusions, occurring as aggregates *clinopyroxene* 3 % 0 3-0 5 mm (rare outsize grains up to 2 mm), euhedral *oxides* 2 % 0 3-0 5 mm, subhedral & embayed, discrete grains & inclusions in olivine phenocrysts *vesicles* 3 % 1-1 5 mm, rounded shapes	67 % intergranular pl>>ox>cpx±ol pl 40 % 50-100 µm, laths cpx 28 % 50 µm, equant ox 30 % 10 µm, equant ol 2 % 50 µm, equant *ubiquitous accessory apatite*	
AR158	porphyritic	*plagioclase* 20 % 0 5-3 mm, subhedral aggregates & laths, melt inclusion trails common, zoned at margins *olivine* 2 % 1-2 mm, subhedral to rounded shapes, incipient iddingsite alteration at rims & along fractures, associated with oxide grains, melt inclusions present *clinopyroxene* 3 % 2-4 mm, euhedral, oxide inclusions *oxides* 3 % 0 2-0 5 mm, subhedral to euhedral, associated with, & as inclusions in olivine & clinopyroxene phenocrysts *vesicles* <2 % 0 5-1 mm, rounded & spherical	70 % intergranular pl=cpx=ox pl 40-50 µm, laths cpx 40-50 µm, equant ox 5-20 µm, equant *ubiquitous accessory apatite*	
AR161	porphyritic	*plagioclase* 10 % 1-2 mm, subhedral to rounded aggregates & laths, melt inclusion trails common *olivine* 5 % 1-3 mm, euhedral to subhedral, incipient iddingsite alteration at rims, some oxide inclusions *clinopyroxene* 4 % 1-3 mm, subhedral & euhedral, rare olivine inclusions *oxides* <1 % ~0 5 mm, subhedral, associated with olivine & clinopyroxene phenocrysts *vesicles* ~5 % 1-3 mm, rounded & spherical	76 % intergranular pl>>cpx>ox pl 50 % 20-30 µm, laths cpx 30 % 10-20 µm, equant ox 20 % 10 µm, equant *ubiquitous accessory apatite*	groundmass plagioclase laths show weak preferred orientation
AR164	porphyritic	*plagioclase* 15 % 1-3 mm, subhedral & euhedral aggregates & laths, melt inclusion trails common in largest grains, zoned at margins, rare clinopyroxene inclusions *olivine* 10 % 0 5-2 mm, euhedral, incipient iddingsite alteration at rims & along fractures, small oxide inclusions *clinopyroxene* 3 % 3-5 mm, embayed & skeletal grains *oxides* 1 % 50-100 µm, subhedral, occurring as inclusions in olivine phenocrysts *vesicles.* ~8 % 0 6-0 8 mm, rounded & spherical	63 % intergranular pl>>cpx>>ox±ol pl 53 % 50 µm, laths cpx 30 % 30 µm, equant ox 15 % 10 µm, equant ol 2% 70 µm, equant *ubiquitous accessory apatite*	

Table E.1. (cont.). Petrographic descriptions for representative basalts of the Basalt Volcanoes Formation, as discussed in Chapter Five.

SAMPLE	TEXTURE	PHENOCRYSTS & MICROPHENOCRYSTS	GROUNDMASS	COMMENTS
Offshore - Nguna				
AR006	porphyritic	*plagioclase* 15 % 0 5-1 2 mm, euhedral to subhedral laths & aggregates, melt inclusion trails common, some zoning at margins	73 % intergranular	
		olivine 3 % 1 2 mm, euhedral to subhedral, discrete & paired grains, incipient iddingsite alteration at rims, small oxide inclusions	pl>cpx=ox±ol	
		clinopyroxene -	pl 35 % 200 µm, laths	
		oxides 2 % 0 1-0 5 mm, euhedral, subhedral & weakly embayed, occurring as inclusions in olivine phenocrysts	cpx 30 % 10-20 µm, equant	
		vesicles 7 % 0 6-1 5 mm, irregular & ovoid	ox 30 % 5-30 µm, equant	
			ol 5 % 30-50 µm, equant, iddingsite altered	
			ubiquitous accessory apatite	
AR105	porphyritic	*plagioclase* 20 % 1 5-4 mm, subhedral to rounded laths & aggregates	75 % intergranular	
		olivine 3 % 0 5-1 5 mm, euhedral to subhedral, discrete phenocrysts, iddingsite altered rims, small oxide inclusions	pl>cpx>>ol>ox	
		clinopyroxene -	pl 48 % 1 mm, laths	
		oxides 1 % 0 5 mm, subhedral, occurring as inclusions in olivine phenocrysts	cpx 35 % 0 5-0 7 mm, equant	
		vesicles 1 % 0 5-1 mm, irregular	ox 7 % 0 5-0 7 mm, equant	
			ol 10 % 0 5-0 7 mm, equant	
			ubiquitous accessory apatite	
AR106	porphyritic	*plagioclase* 15 % 0 5-3 mm, subhedral to rounded aggregates & laths	75 % intergranular	groundmass plagioclase laths show very weak preferred orientation
		olivine 4 % 1 mm, subhedral & cracked, discrete phenocrysts & occurring within plagioclase aggregates, very weakly iddingsite altered rims on some crystals, small oxide inclusions	pl>cpx=ox>>ol	
		clinopyroxene -	pl 36 % 100 µm, laths	
		oxides 3 % 0 3-0 5 mm, embayed & irregular shapes, occurring as inclusions in olivine phenocrysts	cpx 22 % 20-50 µm, equant	
		vesicles 3 % 0 2-0 8 mm, rounded	ox 22 % 20-50 µm, equant	
			ol 10 % 20-50 µm, equant	
			ubiquitous accessory apatite	
AR109	porphyritic	*plagioclase* 12 % 0 5-3 mm, euhedral & subhedral aggregates & laths, zoned at margins	80 % intergranular	
		olivine 5 % 0 5-1 mm, subhedral discrete phenocrysts, small oxide inclusions, rare iddingsite altered rims of some crystals	pl=cpx=ox±ol	
		clinopyroxene -	pl 250 mm, laths	
		oxides 3 % 0 5 mm, subhedral & strongly embayed, associated with, & occurring as inclusions in olivine phenocrysts	cpx 20-50 µm, equant	
		vesicles -	ox 20-50 µm, equant	
			ol <1 % 20-50 µm, equant	
			ubiquitous accessory apatite	
AR110	weakly porphyritic	*plagioclase* 7 % 0 2-1 mm, euhedral & subhedral aggregates & discrete laths	90 % intergranular	
		olivine 2 % 0 2-0 5 mm, subhedral to anhedral discrete phenocrysts, small oxide inclusions	pl>>cpx>ox	
		clinopyroxene -	pl 50 % 50-150 µm, laths	
		oxides 1 % 0 7-1 mm, euhedral, also occurring as smaller (0 05 mm) inclusions in olivine phenocrysts	cpx 30 % 20-30 µm, equant	
		vesicles <1 % 0 2-0 5 mm, rounded & irregular	ox 20 % 5-20 µm, equant	
			ubiquitous accessory apatite	

Table E.1. (cont.). Petrographic descriptions for representative basalts of the Basalt Volcanoes Formation, as discussed in Chapter Five.

SAMPLE	TEXTURE	PHENOCRYSTS & MICROPHENOCRYSTS	GROUNDMASS	COMMENTS
Offshore - Pele				
AR003	strongly porphyritic	*plagioclase* 30 % 5-10 mm, subhedral aggregates, melt inclusions common	65 % intergranular	
		olivine 5 % 0 5-1 5 mm, subhedral & anhedral discrete phenocrysts & occurring within plagioclase aggregates, small (40 µm) oxide inclusions	cpx>pl>>>ox	
		clinopyroxene -	pl: 40 % 100 µm, laths	
		oxides -	cpx 50 % 10-20 µm, equant	
		vesicles. <1 % 0 2-0 5 mm, irregular	ox 10 % 10-20 µm, equant	
			ubiquitous accessory apatite	
AR114	strongly porphyritic	*plagioclase* 25 % 3-5 mm, subhedral to anhedral aggregates, zoned at margins	65 % intergranular	
		olivine 5 % 1-2 mm, subhedral & incipient sieve texture development, small (20-50 µm) oxide inclusions	ox>pl=cpx	
		clinopyroxene 5 % 1-2 mm, subhedral to rounded & incipient sieve texture development	pl: 30 % 20-40 µm, laths	
		oxides -	cpx 30 % 10-20 µm, equant	
		vesicles -	ox 40 % 10-20 µm, equant	
			ubiquitous accessory apatite	
Offshore - Emau				
AR184	porphyritic	*plagioclase.* 12 % 0 5 mm, euhedral & subhedral aggregates & laths	65 % intergranular	groundmass plagioclase laths show very weak preferred orientation, dominantly around phenocrysts
		olivine 8 % 0.5 mm, euhedral & subhedral, small (20-40 µm) oxide inclusions	pl=cpx=ox	
		clinopyroxene 8 % 0.2-0 5 mm, euhedral to subhedral, yellow	pl 15-20 µm, laths	
		oxides. -	cpx 10 µm, equant	
		vesicles 7 % 0 5-1 5 mm, irregular & rounded shapes	ox 10-12 µm, equant	
			ubiquitous accessory apatite	
AR185	porphyritic	*plagioclase* 28 % 2-3 mm, subhedral aggregates & laths, melt inclusion trails common, some zoning at margins	70 % intergranular	
		olivine. <1 % ~1 mm, euhedral & subhedral, small oxide inclusions	pl>>cpx>ox	
		clinopyroxene -	pl: 50 % 50-100 µm, laths	
		oxides 1 % 0 2-0 5 mm, euhedral to subhedral discrete grains & as inclusions in olivine	cpx 30 % 50-100 µm, equant	
		vesicles <1 % 1-1 5 mm, rounded & spherical shapes	ox 20 % 50-100 µm, equant	
			ubiquitous accessory apatite	
AR188	very weakly porphyritic with relatively coarse-grained groundmass	*plagioclase* 7 % 2 mm, subhedral aggregates & 0 2-0 5 mm subhedral laths	89 % intergranular	
		olivine <1 % 1-2 mm, euhedral & subhedral , associated with oxide phenocrysts, incipient iddingsite altered rims	pl=cpx>ox±ol	
		clinopyroxene. -	pl 45 % 200-500 µm, laths	
		oxides 1 % 0.5-0 8 mm, euhedral to subhedral discrete grains & as inclusions in olivine	cpx 45 % 100-500 µm, subhedral	
		vesicles 3 % 0.5-1 mm (up to 5 mm), rounded to spherical but mostly irregular shapes	ox 7 % 20-60 µm, equant	
			ol 3 % 200-400 µm, subhedral	
			ubiquitous accessory apatite	

Table E.1. (cont.). Petrographic descriptions for representative basalts of the Basalt Volcanoes Formation, as discussed in Chapter Five.

SAMPLE	TEXTURE	PHENOCRYSTS & MICROPHENOCRYSTS	GROUNDMASS	COMMENTS
Offshore - Emau				
AR192	weakly porphyritic	*plagioclase* 12 % 2-3 mm, euhedral to subhedral aggregates (5%) & 0 5-1 mm discrete laths, large (0 2 mm) melt inclusion trails common, some zoning at margins *olivine* 3 % 0 2-0 5 mm, subhedral to rounded, occurring in clusters, small (20 µm) oxide inclusions *clinopyroxene* - *oxides* - *vesicles* <1 % 0 2 mm, rounded	85 % intergranular cpx>>ox>pl±ol pl 18 % 100-150 µm, laths cpx 50 % 20-50 µm, euhedral to equant ox 30 % 5-10 µm, euhedral & equant ol 2 % 100 µm, euhedral *ubiquitous accessory apatite*	very weak preferred orientation of phenocrystic plagioclase laths
AR198	porphyritic	*plagioclase* 15 % 1-3 mm, subhedral to euhedral discrete & paired laths & aggregates *olivine* 7 % 0 5 mm, subhedral & broken, discrete or paired grains, small oxide inclusions *clinopyroxene* - *oxides* 2 % 0 1-0 2 mm, subhedral to anhedral, occurring as inclusions in olivine, incipient oxidation causing iron stained haloes *vesicles* -	76 % intergranular cpx>>pl>ox±ol pl 30 % 100 µm, laths cpx 50 % 5-20 µm, equant ox 18 % 10-30 µm, euhedral ol 2 % 50-100 µm, euhedral to subhedral *ubiquitous accessory apatite*	groundmass oxides appear to be 'floating' in the plagioclase/clinopyroxene mosaic hosts patches of coarser grained cognate material (cognate lithics are otherwise compositionally & texturally similar)
AR199	Fine-, even-grained, massive texture	*plagioclase* 50 % 0 2-0 6 mm, subhedral laths, & 10 % 1-2 mm aggregates *olivine* 2 % 0 2-0 4 mm, subhedral, incipient iddingsite altered rims on some grains, associated with oxides, small oxide inclusions *clinopyroxene* 35 % 0 2 mm, subhedral to euhedral, green, isolated crystals *oxides* 12 % 20-40 µm subhedral to anhedral (1 % grains up to 0 5 mm, embayed & resorbed), associated with olivine *vesicles* <1 % 0 5 mm, irregular *ubiquitous accessory apatite*		
AR201	very strongly porphyritic	*plagioclase* 10 % 0 5-1 mm, subhedral aggregates & minor discrete laths *olivine* 15 % 0 5-1 mm, euhedral discrete & paired, iddingsite altered rims & fractures *clinopyroxene* 15 % 1-3 mm, euhedral, occurring as discrete, paired & aggregate crystal clots, small (0 2 mm) olivine inclusions *oxides* - *vesicles* -	60 % intergranular pl>>cpx>>ox±ol pl 50 % 10-50 µm, laths cpx 35 % 10-20 µm, equant ox 15 % 10 µm, euhedral & equant ol <1 % 50-100 µm, equant *ubiquitous accessory apatite*	

APPENDIX F

ANALYTICAL METHODS FOR WHOLE-ROCK GEOCHEMISTRY

Samples collected during field studies in Vanuatu were brought back to the University of Tasmania in Hobart for analysis. Basalt samples selected for analysis were crushed in a hydraulic press between tungsten carbide plates. The fragments were then collected, washed in distilled water, and dried in an 80°C oven overnight. Any fragments with altered or weathered surfaces, or surfaces containing saw marks from thin section preparation, were discarded. The remaining crushed sample was passed through a standard wire mesh sieve with a 2 mm opening. The fragments remaining on the sieve were then passed through a sample splitter until about ~100 g remained (generally two passes). Twenty grams of the ~100 g sample fraction was then ground to a fine powder in a high purity ceramic mill.

Unconsolidated volcaniclastic trachydacite samples were washed in distilled water and dried overnight in an 80°C oven. Samples with maximum grainsizes <4 mm, were passed through a sample splitter until about ~30-50 g remained (generally four passes). Large pumice fragments (>25 mm) selected for individual analysis were crushed by placing the pumice clasts between two sheets of clean, acid-free paper and striking lightly with a rock hammer. Twenty grams of the ~30-50 g sample fraction, or individual pumice clast, was then ground to a fine powder in the high purity ceramic mill.

Powders were reserved for major and trace element analysis at the University of Tasmania. Two crushed basalt samples, a whole pumice fragment and a bulk pumiceous sediment sample were sent to La Trobe University for radiogenic isotope analysis.

Major element analyses

Major element oxide abundances for each sample were measured on a Philips PW 1480 automated X-ray fluorescence (XRF) spectrometer at the University of Tasmania (School of Earth Sciences). Spectrometer calibration was maintained using international and in-house standards and pure silica blanks. Elements were analysed on fused glass discs, made using the method described by Norrish and Hutton (1969). Ignition losses (LOI) were determined by heating ~1 g of powdered sample to 1000°C for twelve hours in a pure vitreosil silica or platinum crucible, followed by cooling the sample to 400°C for five hours, and subsequently calculating the weight percent loss. Net weight gain (positive LOI) for some samples results from the oxidation of FeO to Fe_2O_3 during ignition being

greater than the total volatile loss for the sample. Instrument operating conditions and counting times are outlined in Table F.1.

Table F.1. Instrument operating conditions and counting times for major element oxide analysis on the Philips PW1480 XRF spectrometer.

OXIDE	OPERATING CONDITIONS	EMISSION LINE	COLLIMATOR	X-RAY TUBE	CRYSTAL	COUNTING TIME (s)
SiO_2	40 kV, 70 mA	K-alpha	coarse	Sc-Mo	PE	50
TiO_2	40 kV, 70 mA	K-alpha	fine	Sc-Mo	LiF200	40
Al_2O_3	40 kV, 70 mA	K-alpha	coarse	Sc-Mo	PE	50
Fe_2O_3	90 kV, 30 mA	K-alpha	fine	Sc-Mo	Lif200	10
MnO	90 kV, 30 mA	K-alpha	fine	Sc-Mo	LiF200	20
MgO	40 kV, 70 mA	K-alpha	coarse	Sc-Mo	PX-1	50
CaO	40 kV, 70 mA	K-alpha	fine	Sc-Mo	LiF200	10
Na_2O	40 kV, 70 mA	K-alpha	coarse	Sc-Mo	PX-1	100 + 50(bgd *)
K_2O	40 kV, 70 mA	K-alpha	fine	Sc-Mo	LiF200	20
P_2O_5	40 kV, 70 mA	K-alpha	coarse	Sc-Mo	GE	40

*bgd is background counting time for Na_2O analysis.

Trace element analyses

X-ray fluorescence (XRF)

Trace element abundances were measured on pressed powder pills using the Philips PW 1480 automated X-ray fluorescence (XRF) spectrometer at the University of Tasmania (School of Earth Sciences). Spectrometer calibration was maintained using international and in-house standards and pure silica blanks. Mass absorption coefficients calculated from major element analyses and Compton Scattering were used to correct trace element concentrations. Powdered basalt samples were made into 6 g pressed pellets with a boric acid backing following the method of Norrish and Chappell (1977). Trachydacites pellets were made pressing 10 g of powdered sample mixed with a binding agent in a cylindrical mould. Elements analysed, analytical conditions and detection limits are outlined in Table F.2.

Table F.2. Instrument operating conditions and detection limits for trace element analysis on the Philips PW1480 XRF spectrometer.

ELEMENT	OPERATING CONDITIONS	EMISSION LINE	X-RAY TUBE	DETECTION LIMIT (PPM)
Rb	90 kV, 30 mA	K-alpha	Sc-Mo	1
Sr	80 kV, 35 mA	K-alpha	Au	1
Ba	40 kV, 70 mA	L alpha	Au	4
Sc	40 kV, 70 mA	K-alpha	Au	2
V	40 kV, 70 mA	K-alpha	Au	1.5
Cr	40 kV, 70 mA	K-alpha	Au	1
Ni	90 kV, 30 mA	K-alpha	Sc-Mo	1
Cu	90 kV, 30 mA	K-alpha	Sc-Mo	1
Zn	90 kV, 30 mA	K-alpha	Au	1
La	70 kV, 40 mA	L-alpha	Au	2
Ce	70 kV, 40 mA	L-beta	Au	4
Nd	70 kV, 40 mA	L-alpha	Au	2
Y	90 kV, 30 mA	K-alpha	Sc-Mo	1
Zr	80 kV, 35 mA	K-alpha	Au	1
Nb	90 kV, 30 mA	L-beta	Au	1
Pb	90 kV, 30 mA	L-alpha	Sc-Mo	1 5/2*
Th	90 kV, 30 mA	L-alpha	Sc-Mo	1.5
U			Sc-Mo	1.5

Detection limits are 3σ (99 %) confidence levels. * Detection limits reported for Pb are for basalt/trachydacite.

Inductively coupled plasma mass spectrometry (ICP-MS)

Other trace elements were analysed by inductively coupled plasma mass spectrometry (ICP-MS) on the Finnigan MAT "Element" (Central Science Laboratory, 1998) and the Hewlett Packard HP4500 (School of Earth Sciences, 1999) at the University of Tasmania. Powdered basalt samples were dissolved by PicoTrace digestion methods in a concentrated $HF/HClO_4$ solution for 16 hours at 180°C, with a final digestion run in a $2\%HNO_3/1\%HCl$ solution (Robinson *et al.*, 1999; Yu *et al.*, 2000). To dissolve any resistant minerals (*e.g.* zircon), powdered trachydacite samples were digested by PicoTrace methods in concentrated HF/H_2SO_4 solutions (16 hours at 180°C), followed by evaporation (4-5days) and conversion to perchlorates with a final digestion run in a $2\%HNO_3/1\%HCl$ solution (Yu *et al.*, in press). In-house and international standards, and blanks were run during analysis to ensure spectrometer calibration.

Table F.3. Comparison of analytical results for elements measured by both ICP-MS and XRF for samples from the Efaté Island Group.

ELEMENT	BASALT		TRACHYDACITE	
	AR006 ICP-MS	AR006 - XRF	AR064 ICP-MS	AR064 - XRF
Rb	6 65	6.6	85.6	86
Sr	901 72	922		486
Ba	233 88	256		1052
Sc	34.79	37	9.21	9
La	6.17		23 1	23
Ce	13.39		46 3	50
Nd	10 91		23.2	26
Y	16 76	17	23.7	23
Zr	26 28	24	183	197
Nb	0 51	<1	5.18	5.3
Pb	3.23	2 4	13 2	13
Th	0.58		7.07	7 9
U	0.20		2.32	2.7

Radiogenic isotope analyses

Radiogenic isotope analyses were performed by Roland Maas on a 7-collector Finnigan-MAT262 mass spectrometer at La Trobe University, Victoria. Fresh glass/rock fragments (50-100 mg) were washed in ultrapure Milli-Q water in an ultrasonic bath for 10 minutes. Samples were then were ground to fine powders in-house, and leached in hot 6M HCl for 20 minutes in an attempt to remove any surficial Sr and Pb alteration. After repeated rinsing with Milli-Q water, the samples were dissolved over 2 days on a hotplate, using $HF\text{-}HNO_3$ and $HCl\text{-}HNO_3$.

Pb was isolated using conventional HBr-HCl anion exchange on 0.1 ml columns of AG1-X8 (200-400 mesh). Sr and a LREE-rich fraction were then extracted using 0.15 ml resin beds of Eichrom Sr-spec and TRU.spec resins, respectively, following procedures modified from Pin *et al.* (1994). Nd was further purified on 3 ml beds of HDEHP-coated Kel-F substrate using weak HCl (Richard *et al.*, 1986). Total procedural blanks for Sr, Nd and Pb were <0.2 ng and were negligible.

All isotopic analyses were done in static (Nd-Pb) or dynamic (Sr) mode on the Finnigan-MAT262. Sr was run as a phosphate on single Ta wires, Nd as a nitrate on the Ta side of a Re-Ta double filament, and Pb was run on single Re wires using the Si-gel method (Gerstenberger & Haase, 1997). Sr and Nd isotope ratios were normalised to $^{86}Sr/^{88}Sr = 0.1194$ and $^{146}Nd/^{144}Nd = 0.7219$, respectively, and are reported relative to SRM987, $^{87}Sr/^{86}Sr = 0.710230$ and La Jolla, $^{146}Nd/^{144}Nd = 0.511860$. Pb isotopes were corrected for mass fractionation using the double spike method (Woodhead *et al.*, 1995). Age corrections (based on Rb/Sr, U/Pb ratios derived from ICP-MS) are smaller than the analytical errors in these young samples and are therefore insignificant. Results and external precision for radiogenic isotope analyses are given in Table F.4.

Table F.4. New radiogenic isotope data and calculated error values for Efaté Island Group samples.

SAMPLE	$^{87}Sr/^{86}Sr$	2σ error	$^{143}Nd/^{144}Nd$	2σ error	εNd	$^{206}Pb/^{204}Pb$	$^{207}Pb/^{204}Pb$	$^{208}Pb/^{204}Pb$	error
AR064	0 704156	0 000038	0.512925	0.000020	5 85	18 407	15 526	38.492	≤ ±0.04%
AR073	0.704234	0 000038	0.512936	0.000020	6.15	18 388	15 519	38.474	≤ ±0.04%
AR158	0.704041	0 000038	0.512931	0.000020	5 74	18.498	15 526	38.505	≤ ±0 04%
AR192	0.704244	0 000038	0 512946	0 000020	5 95	18 482	15 541	38 451	≤ ±0 04%

εNd uses present day chondritic mantle $^{143}Nd/^{144}Nd = 0.512631$.

APPENDIX G

MICROPROBE MINERAL ANALYSES: BASALT VOLCANOES FORMATION

Chemical analyses for major and minor element oxides were made on individual mineral grains using polished thin sections and epoxy resin grain mounts. All electron microprobe analyses were collected using the Cameca Camebax SX-50 automated electron microprobe located at the University of Tasmania's Central Science Laboratory. This machine is equipped with four wavelength-dispersive spectrometers, used for quantitative analysis, and one energy-dispersive spectrometer, used for qualitative spectral analysis. X-ray lines used for analyses were calibrated against international and in-house natural minerals, synthetic simple oxides and glass standards.

Operating conditions were set at 15 kV accelerating voltage and a beam current of 25 nA (measured in the Faraday cup). A 10 μm diameter beam was used for all analyses, mainly to overcome Na migration in feldspars. Peak and background counting times, analysing crystal used, and working detection limits for each element are given in Table G.1. Background counting times were measured twice, once on either side of the peak. For elements where peak and background counting times are the same, the background was measured once only, on one side of the peak for analytical reasons.

Table G.1. Peak and background counting times, analysing crystals used and working detection limits for elements analysed during routine mineral analysis on the electron microprobe.

ELEMENT	Si	Ti	Al	Fe	Mn	Mg	Ca	Na	K	P	Rb*	Sr
Analysing crystal	TAP	PET	TAP	LiF	LiF	TAP	PET	TAP	PET	PET	TAP	PET
Peak (s)	10	10	10	10	10	10	10	20	10	10	20	30
Background (s)	5	5	5	5	5	5	5	10	5	10	20	15
Detection limit (wt%)	0 03	0 04	0.03	0.08	0.06	0.03	0 03	0.04	0 03	0 05	0.10	0 12
ELEMENT	Ba	V	Cr	Ni*	Zn*	La*	Ce*	Y*	Zr*	F*	S*	Cl*
Analysing crystal	PET	LiF	LiF	LiF	LiF	LiF	LiF	PET	TAP	PC0	PET	PET
Peak (s)	20	30	15	10	10	30	30	20	10	30	30	20
Background (s)	10	15	8	5	5	15	15	10	10	30	15	10
Detection limit (wt%)	0 17	0 08	0.06	0 12	0 21	0.08	0 05	0.11	0 07	0.15	0 03	0 03

Detection limits were calculated following Ancey *et al.* (1978). * Denotes elements that were not analysed in all sessions or for all minerals.

Structural formulae were calculated using Formula One software installed on the Cameca Camebax SX-50. Mineral analyses of phenocrysts and microphenocrysts from the Basalt Volcanoes Formation are given in Tables G.2 to G.5.

A ternary plot of Ti-magnetite compositions for BVF basalts is given in Figure G.1.

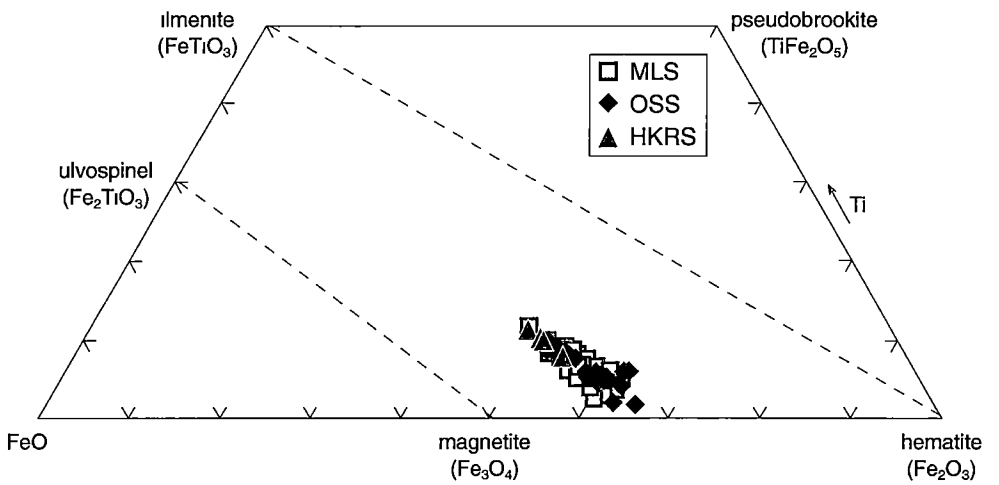

Figure G.1. Ti-magnetite compositions for Basalt Volcanoes Formation (BVF) lavas, Efaté Island Group, Vanuatu arc, southwest Pacific. MLS = Mainland Suite, OSS = Offshore Suite, HKRS = High-K/High-Rb Suite.

Table G.2. Core (C) and rim (R) compositions of plagioclase phenocrysts: Basalt Volcanoes Formation (BVF), Efaté Island Group, Vanuatu arc.

Plagioclase	MAINLAND SUITE (MLS)																						
Analysis number	AR157-1 (C)	AR157-1 (R)	AR157-2 (C)	AR157-2 (R)	AR157-3 (C)	AR157-3 (R)	AR157-4 (C)	AR157-4 (R)	AR157-5 (C)	AR157-5 (R)	AR158-1 (C)	AR158-1 (R)	AR158-2 (C)	AR158-2 (R)	AR158-3 (C)	AR158-3 (R)	AR158-4 (C)	AR158-4 (R)	AR161-1 (C)	AR161-2 (C)	AR161-2 (R)	AR161-3 (C)	AR161-3 (R)
SiO_2	45 8	48 37	44.32	46 14	45 51	47 68	47 2	47 18	46 54	49 56	44.96	45 23	46 26	47.81	46 2	48 29	43 82	45.73	45 42	45 44	47 66	45.39	48
TiO_2	0 02	0 02	0 04	0 02	0	0 02	0 02	0.	0 01	0 03	0 01	0 02	0 03	0 02	0.01	0 06	0 01	0 04	0.03	0 04	0	0.05	0.02
Al_2O_3	34 33	32 46	35 34	34	34 26	32 77	33.01	33.09	33 57	30.84	34 67	34 53	33 85	32.59	33 84	32.08	35 74	33.95	34.55	34 63	32 4	34 65	32 44
Fe_2O_3	0 9	1 2	1	1 1	1 09	0 98	0 93	1 12	1 14	1 42	1 09	1 22	1 1	1 38	1 11	1.32	0 84	1 08	0 98	1 06	1 24	1 03	1 05
MnO	0 04	0	0 03	0	0.03	0 01	0.05	0	0 01	0.01	0	0	0	0	0	0	0	0.03	0.03	0 05	0	0	0.01
MgO	0 09	0 13	0 05	0 08	0.07	0 14	0 12	0.11	0 11	0 13	0 07	0 08	0 13	0.12	0 11	0 1	0 07	0.1	0.11	0 11	0 17	0 08	0.16
CaO	17 74	15 76	19 06	17 25	18 02	16 39	16 7	16.64	17 25	14 29	18 32	18 36	17 61	16 33	17.59	15 82	19 52	17 81	18.2	18 31	16 04	18.15	15 92
SrO	0 23	0 08	0 2	0 16	0 23	0 19	0.16	0.07	0 2	0 16	0 1	0 2	0 1	0.17	0 18	0 12	0 2	0 15	0.21	0 17	0 17	0 1	0 18
BaO	0 15	0 1	0	0	0 03	0	0.03	0 05	0	0	0	0	0	0	0 07	0	0	0	0 03	0 07	0	0 06	0 03
Na_2O	1 39	2 5	0 88	1 59	1 4	2 31	2 1	2 15	1.8	3 43	1 21	1 24	1 65	2 35	1 67	2 57	0 68	1 53	1.34	1.28	2 44	1 26	2.57
K_2O	0 04	0 12	0 03	0 09	0 06	0 1	0 07	0 1	0 08	0.22	0 09	0 04	0 08	0 13	0.07	0 19	0 02	0.06	0.05	0 05	0.11	0.05	0 09
P_2O_5	0.06	0	0	0 04	0 04	0 04	0	0 06	0	0	0.01	0 04	0 03	0	0	0 06	0 03	0 05	0 06	0.04	0 02	0	0 03
Cr_2O_3	n-a	n-a	n-a	n-a	n-a	n-a	n-a	n-a	n-a	n-a	n-a	n-a	n-a	n-a	n-a	n-a	n-a	n-a	n-a	n-a	n-a	n-a	n-a
Total %	100 79	100 74	100 95	100.47	100 75	100 63	100.38	100 57	100.7	100 09	100 52	100.96	100.85	100 9	100.84	100 63	100.91	100 53	101.01	101 26	100 24	100 81	100.5
Sr (ppm)	1945	676	1691	1353	1945	1607	1353	592	1691	1353	846	1691	846	1438	1522	1015	1691	1268	1776	1438	1438	846	1522
Ba (ppm)	1343	896	-	-	269	-	269	448	-	-	-	-	-	-	627	-	-	-	269	627	-	537	269
Si	2.103	2 209	2 04	2 121	2 094	2 183	2 169	2 163	2.136	2 274	2.073	2 078	2 121	2.186	2 121	2.21	2 019	2 106	2 084	2 081	2.191	2 085	2.199
Ti	0 001	0 001	0 002	0 001	0	0.001	0 001	0	0	0.001	0	0.001	0 001	0.001	0	0 002	0	0 001	0.001	0 001	0	0 002	0 001
Al/Al^{IV}	1 858	1 747	1 917	1 842	1 858	1.769	1.787	1 788	1 816	1.668	1.884	1 87	1 829	1.756	1 831	1.73	1 941	1.842	1 868	1 869	1.755	1.876	1.752
Fe^{2+}	0 031	0 041	0 035	0.038	0 038	0.034	0 032	0 039	0 039	0 049	0 038	0 042	0.038	0.047	0 038	0 045	0 029	0 038	0.034	0 036	0 043	0.035	0.036
Mn^{2+}	0 001	0	0 001	0	0 001	0 001	0 002	0	0 001	0	0	0	0	0	0	0	0	0 001	0.001	0.002	0	0	0
Mg	0.006	0 009	0 004	0.006	0 005	0 01	0 008	0.008	0 008	0 009	0 005	0.006	0 009	0 008	0.007	0 007	0 005	0 007	0.007	0.007	0 011	0.006	0.011
Ca	0 873	0 771	0 94	0 85	0 888	0 804	0 822	0 818	0 848	0.703	0 905	0 904	0 865	0 8	0 865	0 776	0.964	0.879	0 895	0.899	0 79	0 893	0.782
Sr	0.006	0.002	0 005	0.004	0 006	0 005	0 004	0 002	0 005	0 004	0.003	0 005	0 003	0 005	0.005	0.003	0.005	0 004	0.006	0 005	0 005	0.003	0.005
Ba	0 003	0 002	0	0	0	0	0.001	0 001	0	0	0	0	0	0	0.001	0	0	0	0 001	0.001	0	0.001	0 001
Na	0 124	0 222	0 078	0 142	0 125	0 205	0 187	0.191	0 16	0.305	0 108	0 11	0 147	0 208	0.148	0 228	0 06	0 137	0 119	0 114	0 217	0 112	0.228
K	0 002	0 007	0.002	0 005	0 004	0 006	0 004	0 006	0 005	0 013	0 005	0 002	0.005	0.008	0 004	0 011	0 001	0.003	0.003	0.003	0 006	0 003	0 005
P	0.002	0	0	0 002	0 002	0 002	0	0 002	0	0	0	0 002	0 001	0	0	0 002	0 001	0 002	0 002	0.002	0.001	0	0 001
Cr																							
Total cation	5 011	5 01	5 023	5.01	5 021	5 018	5.016	5 018	5 018	5.026	5 021	5 019	5 019	5 019	5.021	5 016	5 025	5 02	5.021	5 02	5 02	5 015	5.021
Albite %	12 41	22 20	7 65	14 24	12 29	20 20	18.46	18 82	15 79	29 87	10 61	10 83	14.45	20 47	14 55	22 46	5 85	13.44	11 70	11.22	21.42	11.11	22.46
Anorthite %	87 39	77 10	92 16	85 26	87 32	79 21	81 15	80 59	83 71	68 85	88 90	88 98	85 05	78 74	85 05	76 45	94 05	86 26	88 00	88 48	77 99	88 59	77.04
Orthoclase %	0.20	0 70	0 20	0.50	0 39	0 59	0.39	0 59	0 49	1 27	0 49	0 20	0.49	0 79	0 39	1 08	0.10	0.29	0 29	0.30	0 59	0.30	0.49

Table G.2. (cont.). Core (C) and rim (R) compositions of plagioclase phenocrysts: Basalt Volcanoes Formation (BVF), Efaté Island Group, Vanuatu arc.

Plagioclase	MAINLAND SUITE (MLS)																						
Analysis number	AR161-4 (C)	AR161-4 (R)	AR172-1 (C)	AR172-1 (R)	AR172-2 (C)	AR172-2 (R)	AR172-3 (C)	AR172-4 (C)	AR172-4 (R)	AR172-5 (C)	AR172-5 (R)1	AR172-5 (R)2	AR174-1 (C)	AR174-1 (R)	AR174-2 (C)	AR174-2 (R)	AR174-3 (C)	AR174-3 (R)	AR174-4 (C)	AR174-4 (R)1	AR174-4 (R)2	AR174-5 (C)	AR174-5 (R)
SiO_2	46.38	48 06	45.3	46.14	43 92	44.59	45 01	45.66	45 76	44 73	45 57	46 47	44 2	44 29	45 42	45 22	46 42	54 27	45.61	45 17	49 43	45.9	54 07
TiO_2	0.03	0 05	0.01	0 02	0 01	0.03	0	0 01	0 03	0 01	0 01	0 04	0 02	0 03	0	0 02	0 03	0.08	0 02	0.04	0 07	0.05	0 1
Al_2O_3	33.78	31 98	34.63	33.9	35 51	35.07	34 96	34.28	33 83	35.43	34 41	33.62	35 54	35 33	34 46	34 55	33 86	28.07	34 29	34.22	31 31	34.25	28 38
Fe_2O_3	1 07	1 28	1	1 16	0.94	0 95	0 91	1 13	1 06	0 82	0.93	1 16	0.94	0.94	1 05	1.09	0.95	0.95	1.06	0 97	1.31	0 93	0.95
MnO	0	0	0 01	0	0 02	0 02	0	0	0 01	0 07	0	0 01	0	0 01	0	0.01	0 02	0 02	0	0 01	0	0.02	0
MgO	0.13	0 1	0 05	0 11	0.05	0 05	0 04	0 04	0 04	0.08	0 04	0 04	0.05	0.09	0.09	0.09	0 11	0.09	0 09	0.09	0 14	0 1	0 09
CaO	17 32	15 89	18 28	17 75	19.38	18 74	18 99	18 17	17 89	19.12	18 31	17 46	19 59	19 12	18.51	18 75	17.69	10 87	18.19	18 47	14.8	18.14	11.11
SrO	0 17	0 22	0 16	0 17	0 2	0.11	0 16	0.23	0.18	0.15	0 24	0 26	0 16	0 18	0 07	0 2	0 23	0.27	0 18	0 25	0 13	0.21	0 27
BaO	0 13	0 03	0	0	0 04	0 04	0	0	0 09	0	0 01	0	0	0 06	0 04	0	0	0 02	0.06	0	0 09	0	0 06
Na_2O	1.81	2 51	1 31	1.69	0 85	1 08	1 08	1 42	1 59	0 99	1 45	1 87	0 82	0 94	1 38	1 25	1 82	5 14	1.36	1 3	3 08	1 56	5
K_2O	0.04	0 13	0 09	0.08	0.05	0 05	0 08	0 09	0 11	0 07	0 09	0 1	0 02	0 04	0.07	0 05	0 05	0.53	0 09	0 05	0 19	0.07	0 49
P_2O_5	0.02	0	0 04	0 06	0 01	0 01	0 05	0 06	0 07	0	0.04	0	0.01	0.07	0 02	0.02	0 03	0.08	0 03	0 03	0 05	0	0 06
Cr_2O_3	n-a	n-a	n-a	n-a	n-a	n-a	n-a	n-a	n-a	n-a	n-a	n-a	n-a	n-a	n-a	n-a	n-a	n-a	n-a	n-a	n-a	n-a	n-a
Total %	100 87	100 27	100.87	101 08	100 98	100.74	101 29	101 09	100 66	101 46	101 11	101.03	101 36	101 09	101.11	101.27	101 22	100 39	100.97	100 61	100 61	101 24	100 59
Sr (ppm)	1438	1860	1353	1438	1691	930	1353	1945	1522	1268	2029	2199	1353	1522	592	1691	1945	2283	1522	2114	1099	1776	2283
Ba (ppm)	1164	269	-	-	358	358	-	-	806	-	90	-	-	537	358	-	-	179	537	-	806	-	537
Si	2 127	2 209	2 081	2.114	2 024	2.054	2 063	2 094	2 107	2 047	2.09	2 13	2 028	2 037	2.084	2 074	2 123	2.456	2 094	2.083	2 257	2 101	2.443
Ti	0 001	0 002	0	0 001	0	0 001	0	0	0 001	0	0	0 002	0 001	0 001	0	0.001	0 001	0.003	0 001	0.001	0.003	0.002	0 004
Al/Al ^{IV}	1 826	1 733	1 875	1 83	1.929	1.904	1 888	1 853	1 836	1 911	1 86	1 816	1 922	1.915	1 863	1.868	1 825	1.497	1.855	1 861	1.685	1 848	1 511
Fe^{2+}	0 037	0.044	0 035	0.04	0 032	0 033	0.031	0 039	0 037	0.028	0.032	0.04	0 033	0.033	0.036	0.038	0 033	0 032	0.037	0 034	0 045	0 032	0.032
Mn^{2+}	0	0	0	0	0.001	0 001	0	0	0	0.003	0	0	0	0	0	0 001	0.001	0 001	0	0	0	0.001	0
Mg	0 009	0.007	0 003	0 007	0 004	0 003	0 003	0 003	0 003	0 005	0 003	0 003	0 003	0.006	0 006	0 006	0 008	0.006	0.006	0.006	0 01	0.007	0.006
Ca	0 851	0 783	0.9	0 871	0.957	0 925	0.933	0 893	0 883	0 937	0 9	0 857	0 963	0.942	0 91	0.921	0 867	0.527	0 895	0 913	0.724	0.889	0.538
Sr	0.005	0 006	0 004	0 005	0 005	0 003	0.004	0 006	0 005	0 004	0.006	0 007	0 004	0.005	0.002	0.005	0 006	0.007	0.005	0 007	0 004	0.006	0.007
Ba	0.002	0 001	0	0	0.001	0 001	0	0	0 002	0	0	0	0	0 001	0.001	0	0	0	0.001	0	0.002	0	0 001
Na	0 161	0 224	0.116	0 15	0 076	0.097	0.096	0 126	0 142	0 088	0 129	0 166	0 073	0 083	0 123	0 111	0 161	0.45	0 121	0 117	0.272	0 138	0 438
K	0 003	0 008	0.005	0 005	0 003	0 003	0 004	0.005	0 006	0 004	0 005	0 006	0 001	0.002	0.004	0 003	0 003	0 03	0 005	0 003	0 011	0 004	0 028
P	0 001	0	0.001	0 002	0 001	0	0.002	0.002	0 003	0	0 001	0	0 001	0.003	0 001	0.001	0 001	0.003	0.001	0.001	0.002	0	0 002
Cr																							
Total cation	5 022	5 016	5 022	5 024	5 033	5.025	5.025	5 022	5 025	5 028	5 028	5 026	5.029	5 028	5 029	5 028	5.028	5 013	5.021	5.026	5.014	5 028	5.011
Albite %	15.86	22 07	11 36	14.62	7 34	9 46	9 29	12 30	13 77	8 55	12 48	16 13	7 04	8.08	11 86	10 72	15 62	44.69	11.85	11.33	27 01	13.39	43.63
Anorthite %	83 84	77.14	88 15	84 89	92 37	90 24	90.32	87 21	85.65	91 06	87 04	83.28	92 86	91 72	87 75	88 99	84.09	52.33	87.66	88 38	71.90	86 23	53.59
Orthoclase %	0.30	0 79	0.49	0.49	0 29	0 29	0.39	0 49	0 58	0 39	0.48	0 58	0 10	0 19	0 39	0 29	0 29	2 98	0.49	0 29	1.09	0.39	2.79

Table G.2. (cont.). Core (C) and rim (R) compositions of plagioclase phenocrysts: Basalt Volcanoes Formation (BVF), Efaté Island Group, Vanuatu arc.

Plagioclase	MAINLAND SUITE (MLS)										OFFSHORE SUITE (OSS)												
Analysis number	AR175-1 (C)	AR175-1 (R)	AR175-2 (C)	AR175-3 (C)	AR179-1 (C)	AR179-1 (R)	AR179-2 (C)	AR179-2 (R)	AR179-3 (C)	AR179-4 (C)	AR109-1 (C)	AR109-1 (R)	AR109-2 (C)	AR109-2 (R)	AR109-3 (C)	AR109-3 (R)	AR109-4 (C)	AR109-5 (C)	AR109-5 (R)	AR109-6 (C)	AR109-6 (R)	AR109-7 (C)	AR109-7 (R)
SiO_2	44 76	50 08	45 1	44 96	45 09	49 55	44 61	44.69	43 79	44 43	47 41	48 34	45 81	47 81	45.83	47.33	44.77	45.53	49.57	46.96	51 2	45.99	45 69
TiO_2	0 03	0.07	0	0.07	0.01	0 05	0	0 05	0 01	0 02	0 01	0.07	0 02	0 03	0 01	0.03	0.04	0	0.02	0 03	0	0.01	0 01
Al_2O_3	34 96	30 9	34 03	34 16	35.17	31 64	35.39	35 05	35.62	35 54	33 09	32 36	34 28	31.96	34 57	32 59	35.47	33 99	31.37	33.87	30 56	34.03	34 2
Fe_2O_3	1	1 04	0.95	1 05	1.03	1.13	0 98	1.03	0.8	1 06	1 05	1.06	0.94	1 13	0 79	0.95	0 85	0.86	1 25	1.02	1 34	0.75	0 91
MnO	0.04	0.05	0 02	0.03	0 05	0	0.04	0.02	0 01	0.01	0 1	0 02	0	0	0	0 06	0.01	0	0 04	0	0.02	0.04	0
MgO	0.03	0 05	0 04	0.07	0.09	0 11	0.08	0 07	0 05	0.04	0 06	0 14	0.08	0.24	0.08	0 15	0.09	0 1	0 13	0 08	0 16	0.07	0.04
CaO	18 7	14 26	17 88	17.98	19 13	14.87	19 05	18.9	19 59	19 5	16 7	16 07	18 01	15 72	18 12	16 46	19.06	17 85	15 14	17 37	13 87	17 89	18.09
SrO	0 24	0 27	0 23	0 28	0 16	0 19	0 18	0 2	0 13	0 13	0 11	0 15	0.04	0 17	0.15	0 1	0 2	0.1	0 16	0 18	0 13	0 17	0.09
BaO	0 05	0 02	0 03	0	0	0	0 01	0 07	0 07	0	0	0	0	0	0.06	0 03	0	0 02	0	0	0 02	0 04	0.02
Na_2O	1 09	3 44	1 36	1.28	1 09	3 16	1	1.07	0.69	0 8	2 3	2 64	1 5	2 53	1 38	2 36	1 01	1 42	3 24	1 86	3 74	1 64	1.58
K_2O	0 05	0 33	0 08	0 08	0.03	0 26	0 02	0 04	0.01	0.05	0 11	0.03	0 02	0 07	0 05	0 03	0 01	0.02	0.09	0 06	0.12	0.02	0 04
P_2O_5	0 09	0 02	0.04	0 04	0	0	0	0 02	0	0	0 05	0 01	0 04	0 03	0 03	0 01	0	0 02	0 04	0.1	0	0 09	0
Cr_2O_3	n-a	n-a	n-a	n-a	n-a	n-a	n-a	n-a	n-a	n-a	n-a	n-a	n-a	n-a	n-a	n-a	n-a	n-a	n-a	n-a	n-a	n-a	n-a
Total %	101 04	100.52	99 78	99 99	101.86	100 97	101 36	101 22	100 76	101.58	100 97	100 9	100.73	99 69	101.07	100 1	101 52	99 9	101.04	101 53	101.16	100 75	100.68
Sr (ppm)	2029	2283	1945	2368	1353	1607	1522	1691	1099	1099	930	1268	338	1438	1268	846	1691	846	1353	1522	1099	1438	761
Ba (ppm)	448	179	269	-	-	-	90	627	627	-	-	-	-	-	537	269	-	179	-	-	179	358	179
Si	2 057	2 287	2 094	2.085	2 057	2.255	2 045	2 052	2 022	2 034	2 167	2 206	2 103	2 207	2.098	2 18	2 047	2 107	2.255	2 136	2.316	2 112	2 101
Ti	0 001	0.002	0	0.002	0 001	0 002	0	0.002	0	0 001	0	0.003	0 001	0 001	0	0.001	0.001	0	0 001	0.001	0	0	0
Al/Al^{IV}	1 894	1.663	1.862	1 867	1 891	1 697	1 911	1 897	1 938	1 917	1 782	1 74	1 854	1 739	1 865	1.769	1 912	1 854	1.682	1 816	1 629	1.842	1 854
Fe^{2+}	0 035	0 036	0.033	0 037	0 035	0.039	0.034	0 036	0 028	0.036	0.036	0 036	0 032	0 039	0 027	0.033	0.029	0 03	0.043	0 035	0 046	0 026	0.032
Mn^{2+}	0 002	0 002	0 001	0 001	0 002	0	0.002	0.001	0	0	0 004	0.001	0	0	0	0.002	0 001	0	0.002	0	0 001	0.001	0
Mg	0 002	0.003	0 003	0 005	0 006	0 007	0.006	0.005	0 003	0.003	0 004	0 01	0 006	0.017	0 006	0 01	0 006	0.007	0.009	0 005	0.011	0 005	0.002
Ca	0.921	0.698	0.889	0 893	0 935	0.725	0 935	0 93	0 969	0 956	0 818	0 785	0 886	0 777	0.889	0 812	0.934	0 885	0.738	0 846	0.672	0 88	0 892
Sr	0.006	0 007	0.006	0.007	0 004	0 005	0.005	0 005	0 003	0.003	0 003	0.004	0 001	0.005	0 004	0 003	0.005	0.003	0.004	0.005	0 004	0 005	0.002
Ba	0.001	0	0 001	0	0	0	0	0 001	0.001	0	0	0	0	0	0 001	0	0	0	0	0	0	0.001	0
Na	0 097	0 304	0 123	0 115	0 096	0 279	0.089	0 095	0 062	0 071	0.203	0.234	0.133	0.226	0 123	0 211	0 089	0.128	0 286	0.164	0.328	0 146	0.141
K	0 003	0 019	0 005	0.005	0 002	0 015	0 001	0 003	0 001	0 003	0 006	0.001	0 001	0 004	0.003	0 002	0.001	0.001	0.005	0 003	0.007	0.001	0.003
P	0.003	0 001	0 002	0 002	0	0	0	0 001	0	0	0 002	0 001	0.002	0 001	0.001	0	0	0 001	0 002	0 004	0	0.003	0
Cr																							
Total cation	5 022	5 022	5.019	5 019	5 029	5 023	5.028	5 027	5 026	5.026	5 026	5.021	5 018	5.016	5.016	5 024	5.026	5 015	5.025	5 016	5.014	5 023	5.028
Albite %	9 50	29 77	12 09	11.35	9 29	27 38	8.68	9 24	6 01	6 89	19 77	22.94	13 04	22.44	12 12	20.59	8 69	12 62	27.79	16.19	32 57	14 22	13 61
Anorthite %	90 21	68 36	87 41	88 15	90 51	71.15	91 22	90 47	93.90	92 82	79 65	76 96	86 86	77.16	87 59	79.22	91 21	87.28	71 72	83.51	66 73	85.69	86 10
Orthoclase %	0 29	1.86	0 49	0 49	0 19	1.47	0.10	0 29	0 10	0 29	0 58	0 10	0 10	0 40	0 30	0 20	0 10	0 10	0 49	0 30	0.70	0.10	0 29

Table G.2. (cont.). Core (C) and rim (R) compositions of plagioclase phenocrysts: Basalt Volcanoes Formation (BVF), Efaté Island Group, Vanuatu arc.

Plagioclase	OFFSHORE SUITE (OSS)																						
Analysis number	AR109-8 (C)	AR109-8 (R)	AR109-9 (C)	AR109-10 (C)	AR109-11 (C)	AR105-1 (C)	AR105-1 (R)	AR105-2 (C)	AR105-2 (R)	AR105-3 (C)	AR105-3 (R)	AR105-4 (C)	AR105-4 (R)	AR105-5 (C)	AR105-5 (R)	AR105-6 (C)	AR105-6 (R)	AR114-1 (C)	AR114-2 (C)	AR114-2 (R)	AR114-3 (C)	AR114-3 (R)	AR114-4 (C)
SiO_2	45 19	46 38	45 61	45 74	45 19	46.42	57 09	46 58	46 9	44 73	57.38	45 82	52 26	46.37	54 89	46 87	54 03	45.46	46.13	46 48	46 23	45 64	44.99
TiO_2	0.03	0 03	0.01	0	0	0 04	0 06	0.04	0 01	0 05	0.07	0	0 07	0.03	0.09	0.03	0 09	0 01	0.01	0	0.04	0.03	0.03
Al_2O_3	35.18	34 17	34.69	34 35	34 47	33 97	26 56	33 83	33 55	35 08	26 16	34.47	29 38	34 01	27.85	33 67	28 15	34.58	33.65	33 57	33.82	34.37	34.04
Fe_2O_3	0 78	0.79	0.91	0.84	0 91	1	0.91	1.05	1 08	0.82	1 01	0.9	1.19	0.97	1	1 02	1.03	0.96	1.06	1 21	1 09	1 17	1.24
MnO	0	0 04	0	0 01	0 03	0.03	0	0	0	0	0	0.02	0 01	0.01	0 03	0 07	0 04	0	0	0 04	0	0.03	0 04
MgO	0 06	0 07	0 09	0 1	0.08	0.11	0.04	0.1	0 09	0 09	0 09	0.09	0 13	0 1	0 12	0.1	0.11	0 1	0.16	0 1	0 11	0.06	0 12
CaO	18 85	17 78	18 28	18 33	18 51	17 77	8 7	17 53	17 31	19.04	8 36	18 08	12 81	17 85	10 75	17 27	11 21	18.33	17.72	17 45	17 62	18 33	18.17
SrO	0 1	0.04	0 13	0 03	0 04	0 14	0 18	0.17	0 19	0 17	0 17	0 02	0 13	0 17	0.15	0.19	0 14	0 13	0 14	0.18	0.13	0 06	0.17
BaO	0 1	0 08	0 01	0 05	0 04	0	0 04	0 03	0	0	0	0 07	0	0.11	0	0	0 02	0.01	0	0	0.15	0	0
Na_2O	1.15	1 59	1 38	1 44	1 32	1 68	6 26	1 86	1 89	0 98	6 24	1 42	4 09	1 65	5.33	1 9	4 99	1 34	1 72	1.77	1.82	1 42	1 26
K_2O	0 01	0 05	0 02	0 04	0.02	0 06	0 56	0 08	0.08	0 03	0.7	0 07	0 29	0.06	0.48	0.07	0 43	0 04	0.06	0 06	0 08	0 07	0 06
P_2O_5	0 06	0 04	0.01	0	0	0 01	0 07	0	0 09	0 08	0 03	0 08	0 01	0 03	0 04	0	0 03	0	0 01	0.06	0	0	0 09
Cr_2O_3	n-a	n-a	n-a	n-a	n-a	n-a	n-a	n-a	n-a	n-a	n-a	n-a	n-a	n-a	n-a	n-a	n-a	n-a	n-a	n-a	n-a	n-a	n-a
Total %	101 52	101 05	101.14	100 94	100.62	101 26	100 49	101 26	101 19	101 05	100.2	101.06	100 4	101.34	100.72	101.19	100.28	100 98	100 66	100 92	101.08	101.17	100 22
Sr (ppm)	846	338	1099	254	338	1184	1522	1438	1607	1438	1438	169	1099	1438	1268	1607	1184	1099	1184	1522	1099	507	1438
Ba (ppm)	896	717	90	448	358	-	358	269	-	-	-	627	-	985	-	-	179	90	-	-	1343	-	-
Si	2 064	2.121	2.088	2.098	2 082	2 121	2 561	2 128	2 141	2 054	2 579	2 098	2 374	2 119	2.472	2.141	2 448	2 086	2.121	2.13	2.119	2 091	2 082
Ti	0.001	0.001	0	0	0	0 001	0 002	0 001	0.001	0 002	0 002	0	0 002	0 001	0.003	0 001	0 003	0	0	0	0 001	0 001	0 001
Al/Al^{IV}	1.894	1 841	1 871	1 857	1.871	1.829	1.404	1 822	1 805	1 898	1.385	1.859	1.573	1.831	1 478	1 812	1.503	1.87	1.823	1.814	1 827	1 856	1 857
Fe^{2+}	0 027	0 027	0.031	0 029	0 032	0 034	0.031	0.036	0 037	0.028	0 034	0 031	0 041	0 033	0 034	0.035	0 035	0 033	0.037	0.042	0 037	0 04	0 043
Mn^{2+}	0	0.001	0	0	0 001	0 001	0	0	0	0	0	0 001	0 001	0	0 001	0.003	0.002	0	0	0.001	0	0 001	0.002
Mg	0 004	0 005	0 006	0 007	0 005	0 008	0.003	0 006	0 006	0 006	0.006	0 006	0 009	0.007	0 008	0.007	0 007	0 007	0.011	0 007	0.008	0.004	0 008
Ca	0 923	0.871	0 897	0 901	0 914	0 87	0.418	0 858	0 847	0.937	0.403	0 887	0 624	0 873	0 519	0.845	0.544	0.901	0 873	0 857	0.865	0 9	0 901
Sr	0.003	0.001	0 004	0 001	0 001	0 004	0.005	0 004	0.005	0 004	0.004	0 001	0.003	0.004	0 004	0 005	0 004	0 004	0 004	0.005	0.003	0 001	0 005
Ba	0 002	0 001	0	0 001	0.001	0	0.001	0 001	0	0	0	0.001	0	0 002	0	0	0	0	0	0	0.003	0	0
Na	0 102	0 141	0 123	0 128	0.118	0.149	0 544	0 164	0 167	0 087	0.544	0.126	0 36	0 146	0 466	0.168	0 439	0 119	0.153	0.157	0 161	0 126	0.113
K	0 001	0 003	0 001	0 002	0 001	0 004	0 032	0 005	0 004	0.002	0 04	0.004	0 017	0 004	0 028	0 004	0.025	0.003	0.003	0 004	0.005	0 004	0.004
P	0 002	0 001	0	0	0	0 001	0 003	0	0 003	0 003	0 001	0 003	0 001	0 001	0 001	0	0 001	0	0.001	0 002	0	0	0 004
Cr																							
Total cation	5.022	5 014	5 022	5 024	5 026	5.022	5.004	5.026	5 017	5.021	4 999	5 018	5.005	5.021	5.013	5 021	5 01	5.023	5.026	5.019	5.03	5.025	5 02
Albite %	9 94	13 89	12.05	12.42	11 42	14.57	54.73	15.97	16 40	8 48	55 12	12 39	35 96	14 27	46.00	16.52	43 55	11 63	14.87	15.42	15 62	12.23	11.10
Anorthite %	89 96	85.81	87.86	87.39	88.48	85.04	42.05	83.54	83 20	91 33	40 83	87 22	62 34	85.34	51 23	83 09	53.97	88.07	84.84	84.18	83.90	87.38	88.51
Orthoclase %	0 10	0 30	0.10	0 19	0.10	0 39	3 22	0.49	0 39	0 19	4 05	0 39	1 70	0 39	2.76	0 39	2 48	0 29	0 29	0.39	0 48	0 39	0.39

Table G.2. (cont.). Core (C) and rim (R) compositions of plagioclase phenocrysts: Basalt Volcanoes Formation (BVF), Efaté Island Group, Vanuatu arc.

Plagioclase	OFFSHORE SUITE (OSS)																						
Analysis number	AR114-5 (C)	AR114-5 (R)	AR114-6 (C)	AR114-6 (R)	AR114-7 (C)	AR114-7 (R)	AR003-1 (C)	AR003-1 (R)1	AR003-1 (R)2	AR003-2 (C)	AR003-2 (R)	AR003-3 (C)	AR003-3 (R)	AR003-4 (C)	AR003-4 (R)	AR003-5 (C)	AR003-6 (C)	AR003-6 (R)	AR003-7 (C)	AR003-7 (R)	AR184-1 (C)	AR184-2 (R)	AR184-3 (C)
SiO_2	45 12	45.5	47 87	46.72	47 5	48 35	46 55	46 17	45 62	46 96	48 64	44 94	49 5	45 93	45.31	44 82	46.15	45 9	45.19	45 88	45.12	45 8	45 56
TiO_2	0 04	0 06	0 06	0 02	0 02	0 04	0 01	0	0 03	0 03	0.02	0 03	0 03	0	0 04	0.05	0.04	0 03	0 02	0 05	0 02	0.09	0 04
Al_2O_3	34 81	34 5	32 21	33 23	33.07	31 73	33 57	33.61	34 71	33 2	31 93	34.61	30 89	34 29	34 31	34.89	33 76	34 18	34.76	34 07	34.54	33 74	33 91
Fe_2O_3	0 99	1 09	1 1	1.48	1 16	1 47	1 12	1 19	0 88	0 93	1.03	0 92	1 34	1.06	1 06	0 9	0 97	1.06	0.94	0.95	1 16	1.16	1 02
MnO	0.02	0 05	0.03	0	0	0.06	0 02	0.01	0 01	0.01	0.04	0	0 02	0.04	0 04	0.04	0	0.03	0 01	0	0	0	0
MgO	0 12	0 08	0 15	0.1	0 14	0 08	0 13	0 16	0 11	0 14	0 21	0.09	0 17	0 1	0.11	0 11	0 12	0.12	0 12	0 13	0 13	0.13	0 14
CaO	18.71	18 53	16.39	17.42	16.84	15 6	17.03	17.13	17 92	16 64	15.34	18 1	14.48	17.74	18.18	18 58	17 29	17.53	18 16	17 62	17.95	17 57	17.6
SrO	0 06	0 08	0 24	0.16	0 16	0.12	0.09	0 12	0 14	0 02	0 16	0 17	0 14	0 03	0.12	0 19	0 15	0.18	0 14	0 12	0 16	0.15	0 17
BaO	0	0	0	0	0.05	0	0	0	0 07	0	0 01	0.09	0	0	0	0	0	0 06	0	0	0	0	0
Na_2O	1 24	1 41	2 46	1 85	2 1	2 78	1 82	1 64	1 21	1 99	2.63	1 18	3.04	1.39	1 27	1 06	1 61	1 56	1.13	1 47	1.23	1 38	1 32
K_2O	0.06	0 06	0 09	0 1	0.11	0 16	0 06	0 07	0 03	0.08	0 12	0 06	0 17	0 04	0.04	0 03	0 07	0 09	0 04	0 05	0 05	0 05	0 06
P_2O_5	0 09	0	0	0	0	0	0.06	0 03	0 04	0.02	0 03	0 07	0 02	0.02	0.02	0.04	0 05	0	0 03	0.01	n-a	n-a	n-a
Cr_2O_3	n-a	n-a	n-a	n-a	n-a	n-a	n-a	n-a	n-a	n-a	n-a	n-a	n-a	n-a	n-a	n-a	n-a	n-a	n-a	n-a	0.000	0 000	0.000
Total %	101 28	101.35	100 6	101 1	101.14	100.42	100 47	100 14	100.76	100 02	100 16	100 27	99 79	100 65	100 5	100 72	100.22	100 73	100 53	100 35	100 36	100 07	99 82
Sr (ppm)	507	676	2029	1353	1353	1015	761	1015	1184	169	1353	1438	1184	254	1015	1607	1268	1522	1184	1015	1353	1268	1438
Ba (ppm)	-	-	-	-	448	-	-	-	627	-	90	806	-	-	-	-	-	537	-	-	-	-	-
Si	2 066	2 083	2.196	2 14	2.168	2.219	2 138	2.129	2 093	2 162	2 23	2.076	2 274	2.108	2 088	2 064	2 126	2 109	2 08	2.112	2.118	2 142	2 135
Ti	0.002	0 002	0 002	0 001	0.001	0 001	0	0	0 001	0 001	0.001	0 001	0.001	0	0 001	0 002	0 001	0 001	0.001	0.002	0.001	0 003	0.001
Al/Al ^{IV}	1.879	1.861	1.741	1 794	1.779	1 717	1.817	1 827	1 877	1 801	1 725	1 885	1 673	1.855	1.863	1 893	1 833	1.851	1 885	1.849	1 828	1.805	1.818
Fe^{2+}	0 034	0 037	0 038	0.051	0 04	0 051	0 039	0.041	0 03	0 032	0 035	0 032	0 046	0.036	0.037	0.031	0 034	0.037	0.033	0.033	0 043	0.043	0.038
Mn^{2+}	0 001	0.002	0 001	0	0	0 002	0.001	0	0	0	0 001	0	0 001	0 002	0 001	0 001	0	0.001	0	0	0	0	0
Mg	0 008	0 005	0 01	0 007	0 009	0 006	0.009	0 011	0 008	0.009	0 014	0.006	0 012	0 007	0.007	0 008	0.008	0.008	0 008	0 009	0 009	0 009	0.01
Ca	0 918	0 909	0 805	0 855	0 823	0 767	0 838	0 846	0 881	0 821	0 754	0 896	0.713	0 872	0.898	0 916	0.854	0 863	0.896	0 869	0.903	0.88	0.884
Sr	0.002	0 002	0 006	0 004	0.004	0 003	0 002	0.003	0 004	0.001	0.004	0 005	0 004	0 001	0.003	0 005	0 004	0 005	0 004	0 003	0 008	0.008	0.009
Ba	0	0	0	0	0 001	0	0	0	0 001	0	0	0 002	0	0	0	0	0	0.001	0	0	0	0	0
Na	0 11	0 125	0 219	0.164	0 186	0 247	0 162	0 147	0 107	0 177	0 234	0 105	0 27	0.124	0.113	0.094	0.144	0 139	0.101	0 131	0.11	0.123	0.118
K	0.004	0 003	0.005	0.006	0 006	0 009	0 004	0 004	0.002	0 005	0 007	0.003	0 01	0 003	0.003	0.002	0 004	0.005	0.002	0.003	0 003	0 003	0.004
P	0 003	0	0	0	0	0	0 002	0 001	0 001	0 001	0 001	0.003	0 001	0 001	0.001	0.001	0.002	0	0.001	0			
Cr																							
Total cation	5 027	5 03	5 025	5 022	5 018	5 024	5 013	5 011	5.005	5 01	5.008	5 014	5.004	5.008	5 017	5 018	5 01	5.019	5 01	5 012	5.024	5.016	5 016
Albite %	10 66	12 05	21 28	16 00	18 33	24.14	16 14	14 74	10 81	17.65	23 52	10 46	27 19	12.41	11 14	9 29	14.37	13 80	10.11	13 06	10 82	12 22	11.78
Anorthite %	88 95	87 66	78 23	83.41	81.08	74 98	83 47	84 85	88.99	81 85	75 78	89.24	71 80	87 29	88 56	90.51	85 23	85.70	89.69	86 64	88 85	87 46	87 85
Orthoclase %	0.39	0 29	0.49	0.59	0 59	0.88	0.40	0.40	0 20	0.50	0 70	0 30	1.01	0 30	0 30	0 20	0.40	0 50	0 20	0 30	0.32	0 32	0.37

Table G.2. (cont.). Core (C) and rim (R) compositions of plagioclase phenocrysts: Basalt Volcanoes Formation (BVF), Efaté Island Group, Vanuatu arc.

Plagioclase	OFFSHORE SUITE (OSS)																					
Analysis number	AR184-4 (C)	AR184-4 (R)	AR184-5 (C)	AR184-5 (R)	AR184-6 (C)	AR184-6 (R)	AR184-7 (C)	AR184-7 (R)	AR184-8 (C)	AR184-8 (R)1	AR184-8 (R)2	AR184-9 (C)	AR184-9 (R)	AR185-1 (C)	AR185-1 (C)2	AR185-1 (R)	AR185-2 (C)	AR185-2 (R)	AR185-3 (C)	AR185-3 (R)	AR185-4 (C)	AR185-4 (R)	AR185-5 (C)
SiO_2	45.4	45 69	46.01	45 37	44.74	45.4	45 88	47 28	45 2	45 61	45 51	45 66	46.05	46 76	46 81	46 08	46.04	50.1	46 21	48.14	46 79	47 71	46 31
TiO_2	0 04	0 03	0 04	0	0.02	0 03	0 04	0.03	0 02	0 05	0 03	0.02	0 04	0	0 03	0 02	0 01	0 07	0.04	0.03	0	0	0 01
Al_2O_3	34 17	33 75	33 34	33 8	34 67	33 92	33.47	32 19	33 94	33 61	33 85	33 47	33 34	33.5	33 29	33 67	34.05	30 88	33.63	32.67	33 45	32.75	34 03
Fe_2O_3	0 93	1 17	1 07	0.97	0 94	1 07	1 03	1.33	0 97	0 99	0 91	1 04	1.06	1 26	1 09	1.26	1.16	1 24	1.18	1 23	1.05	1 15	1.13
MnO	0 04	0.06	0	0	0	0	0	0 01	0 01	0	0 06	0	0.02	0	0 05	0 01	0	0	0.02	0	0	0.04	0.03
MgO	0 13	0 15	0.17	0 15	0 11	0 14	0.16	0 2	0 1	0.16	0.13	0 12	0 09	0.11	0.12	0.12	0.12	0 16	0.11	0 14	0.12	0.13	0 1
CaO	17 72	17 79	16 86	17.84	18 1	17 88	17 14	16.18	17.75	17 32	17.69	17 14	16 75	17.05	17 09	17.07	17.5	14.07	17 16	15.93	16 92	16.21	17.3
SrO	0 13	0 12	0 15	0 18	0.09	0.15	0 14	0 16	0 14	0 16	0.16	0 18	0 17	0.16	0 11	0 04	0 05	0 17	0 09	0 17	0.18	0.07	0 11
BaO	0	0 01	0	0.03	0	0.01	0 01	0 01	0	0 01	0	0 01	0	0 1	0.03	0	0	0.03	0	0	0	0.11	0.02
Na_2O	1 34	1 39	1.72	1 31	1 08	1.38	1 62	2 08	1 34	1 47	1 33	1.52	1.65	1 81	1 89	1.83	1 58	3 32	1 74	2 43	1.84	2 21	1 7
K_2O	0.04	0 05	0 08	0.06	0 06	0 05	0 09	0 11	0.06	0 07	0 05	0 1	0 06	0.05	0 04	0 06	0.03	0 12	0 05	0 07	0.04	0 07	0 05
P_2O_5	n-a	n-a	n-a	n-a	n-a	n-a	n-a	n-a	n-a	n-a	n-a	n-a	n-a	0	0	0	0 03	0.07	0 05	0 07	0 01	0 02	0 02
Cr_2O_3	0 000	0 036	0.000	0 021	0 000	0 000	0 036	0 000	0 002	0 000	0 026	0.007	0.000	n-a	n-a	n-a	n-a	n-a	n-a	n-a	n-a	n-a	n-a
Total %	99 94	100 25	99 44	99 73	99.81	100.03	99 61	99 58	99 53	99 45	99.74	99.27	99 23	100.8	100 55	100.15	100 55	100 22	100 27	100 88	100.4	100.46	100 82
Sr (ppm)	1099	1015	1268	1522	761	1268	1184	1353	1184	1353	1353	1522	1438	1353	930	338	423	1438	761	1438	1522	592	930
Ba (ppm)	-	90	-	269	-	90	90	90	-	90	-	90	-	896	269	-	-	269	-	-	-	985	179
Si	2.125	2 136	2 162	2.131	2.099	2 127	2 154	2 216	2.126	2 144	2 135	2 151	2.166	2 143	2 15	2 126	2 115	2 288	2.128	2.196	2 15	2.187	2 122
Ti	0.002	0 001	0.001	0	0 001	0 001	0 001	0.001	0 001	0 002	0 001	0 001	0.001	0	0.001	0.001	0	0 002	0 001	0.001	0	0	0
Al/Al ^{IV}	1 829	1 805	1.791	1.816	1 862	1.817	1 797	1 723	1 826	1 807	1 816	1 803	1 793	1 81	1.802	1.83	1 843	1.662	1 826	1 756	1 811	1.769	1.838
Fe^{2+}	0.034	0.043	0 04	0 036	0.035	0 039	0 038	0.049	0.036	0 037	0.034	0 039	0 039	0.043	0.038	0.044	0 04	0.042	0.041	0.042	0.036	0 04	0.039
Mn^{2+}	0.001	0 002	0	0	0	0	0	0	0	0	0.002	0	0 001	0	0 002	0	0	0	0 001	0	0	0 002	0.001
Mg	0 009	0 01	0.012	0 01	0 008	0 01	0 011	0 014	0 007	0 011	0.009	0.008	0.006	0.008	0 008	0.008	0 008	0 011	0 007	0.009	0 009	0.009	0.007
Ca	0 888	0 891	0 849	0 898	0.91	0.897	0 862	0 813	0 895	0 873	0 889	0.865	0 844	0 838	0 841	0.843	0.861	0.689	0 847	0.779	0 833	0.796	0.849
Sr	0 008	0 007	0 008	0 009	0 007	0 008	0 008	0 008	0 008	0 008	0.009	0.009	0 009	0 004	0 003	0 001	0 001	0.004	0 002	0.005	0.005	0.002	0.003
Ba	0	0	0	0.001	0	0	0	0	0	0	0	0	0	0 002	0.001	0	0	0.001	0	0	0	0.002	0
Na	0.12	0 124	0 155	0 118	0 096	0 123	0.146	0 187	0 12	0.132	0 119	0 137	0 148	0.161	0 168	0 163	0 14	0 294	0 155	0 215	0 164	0.196	0.151
K	0 003	0 003	0 004	0.003	0 004	0.003	0.005	0 007	0 004	0 004	0.003	0.006	0 004	0.003	0 003	0 004	0 002	0 007	0.003	0 004	0.002	0 004	0.003
P														0	0	0	0.001	0.003	0.002	0.003	0	0 001	0.001
Cr																							
Total cation	5 02	5 024	5.022	5 022	5 02	5.027	5.022	5.018	5 023	5 019	5 018	5 019	5.012	5.012	5 015	5 02	5.013	5.004	5.013	5 009	5.009	5 007	5.015
Albite %	11 89	12.20	15.38	11 55	9.53	12 05	14 41	18 61	11.80	13 08	11.81	13.62	14 90	16.07	16 60	16.14	13 96	29 70	15.42	21.54	16.42	19.68	15.05
Anorthite %	87 85	87.49	84.17	88.11	90.11	87 66	85 07	80 71	87.82	86 49	87 88	85 80	84 72	83.63	83 10	83.47	85 84	69 60	84.28	78.06	83 38	79 92	84 65
Orthoclase %	0 26	0 31	0.45	0 34	0 36	0 29	0 52	0 68	0 38	0 43	0.32	0 58	0.38	0 30	0.30	0.40	0 20	0.71	0.30	0 40	0 20	0 40	0 30

Table G.2. (cont.). Core (C) and rim (R) compositions of plagioclase phenocrysts: Basalt Volcanoes Formation (BVF), Efaté Island Group, Vanuatu arc.

Plagioclase	OFFSHORE SUITE (OSS)														HIGH-K/HIGH-Rb SUITE (HKRS)								
Analysis number	AR185-5 (R)	AR185-6 (C)	AR185-6 (R)	AR192-1 (C)	AR192-1 (R)	AR192-2 (C)	AR192-2 (R)1	AR192-2 (R)2	AR192-3 (C)	AR192-3 (R)	AR192-4 (C)	AR192-4 (R)	AR192-5 (C)	AR192-5 (R)	AR188-1 (C)	AR188-1 (R)	AR188-2 (C)	AR188-2 (R)	AR188-3 (C)1	AR188-3 (C)2	AR188-4 (C)1	AR188-4 (C)2	AR188-5 (C)
SiO_2	46.63	46 74	46 3	44 56	49 09	46 14	45 87	45 52	45 74	51.51	45.77	45.61	45 41	45 32	45.2	50.31	47 11	50.56	45 58	44 82	45.12	45 92	46 76
TiO_2	0 02	0 02	0.04	0 04	0.03	0	0 04	0 03	0 05	0 05	0 01	0.02	0 01	0 02	0	0 03	0 01	0.05	0.02	0.02	0.02	0 04	0
Al_2O_3	33 78	33 48	33.43	34 79	31 24	34 08	33 69	34 71	34 35	29 63	34 19	34 26	34 5	34.47	34 5	30.82	33 46	30.62	34 06	34 83	34 51	34 19	33.52
Fe_2O_3	1.11	1 15	1 21	1.05	1 65	1 01	1 2	1 14	1 23	1 74	0 92	1.65	0 91	1.26	0 82	1 28	1 13	1 32	1.11	1 07	0.91	1.08	1
MnO	0 04	0	0 03	0	0 04	0	0	0 02	0 01	0 01	0	0	0	0 03	0.02	0	0	0 01	0	0	0 01	0 02	0
MgO	0 11	0 12	0 14	0.09	0.17	0.13	0.11	0.12	0 14	0 17	0 11	0 09	0 1	0 11	0 08	0.17	0 13	0.18	0 11	0 09	0.08	0 11	0.09
CaO	17 02	16 97	17.13	18 46	14 88	17.59	17.46	18 28	17 85	13.05	17 73	17.54	18 03	18 13	17.93	14.03	16.75	13 81	17.79	18.51	17.92	17 57	17.1
SrO	0.1	0 13	0.1	0 09	0 07	0.13	0 08	0 1	0 05	0 1	0 17	0.08	0 08	0 11	0.08	0 22	0.1	0.07	0.19	0 21	0 2	0 12	0.15
BaO	0.02	0	0 03	0.01	0.09	0 03	0	0	0.03	0 01	0 02	0 13	0	0	0	0 1	0	0.02	0	0	0	0	0.05
Na_2O	1 84	1 79	1.78	1.07	2 89	1.53	1 46	1.2	1.36	3 83	1 38	1 42	1.19	1 28	1 22	3 31	1 9	3 37	1 46	0 99	1 27	1.47	1.76
K_2O	0 04	0 06	0.06	0 05	0 24	0 05	0 07	0 04	0 05	0.31	0 06	0.07	0 05	0 05	0 08	0 29	0 1	0 31	0.09	0 05	0 06	0.11	0.1
P_2O_5	0	0 02	0	0	0	0.01	0 04	0	0 03	0 02	0.02	0	0	0	0 13	0.07	0	0.05	0	0 05	0.01	0.08	0
Cr_2O_3	n-a	n-a	n-a	n-a	n-a	n-a	n-a	n-a	n-a	n-a	n-a	n-a	n-a	n-a	n-a	n-a	n-a	n-a	n-a	n-a	n-a	n-a	n-a
Total %	100 72	100 47	100.24	100 21	100.39	100.71	100.02	101.16	100 91	100 45	100 39	100 86	100 27	100 8	100 07	100.65	100 69	100 36	100.42	100 63	100.13	100.71	100 54
Sr (ppm)	846	1099	846	761	592	1099	676	846	423	846	1438	676	676	930	676	1860	846	592	1607	1776	1691	1015	1268
Ba (ppm)	179	-	269	90	806	269	-	-	269	90	179	1164	-	-	-	896	-	179	-	-	-	- -	448
Si	2 137	2 146	2 134	2 062	2 25	2 117	2.119	2 084	2.097	2 345	2 107	2 095	2 093	2.084	2 088	2 292	2.156	2.305	2 102	2 065	2 086	2 108	2.147
Ti	0 001	0,001	0.001	0 001	0.001	0	0.001	0 001	0.002	0.002	0	0 001	0	0 001	0	0.001	0	0.002	0.001	0.001	0 001	0 001	0
Al/Al ^{IV}	1.824	1.812	1 816	1 897	1 687	1 843	1 834	1 872	1 856	1 59	1 856	1 855	1.875	1 868	1 878	1.655	1 805	1 645	1 851	1.891	1.88	1 849	1 814
Fe^{2+}	0 038	0.04	0 042	0.037	0 057	0 035	0 042	0 039	0 042	0.06	0 032	0.057	0 031	0.044	0.029	0 044	0 039	0.045	0 039	0 037	0.032	0.037	0.035
Mn^{2+}	0 001	0	0.001	0	0 001	0	0	0 001	0	0	0	0	0	0 001	0.001	0	0	0	0	0	0.001	0.001	0
Mg	0 008	0 008	0 01	0 006	0.012	0.009	0.008	0 008	0 009	0 012	0.008	0 006	0 007	0 008	0 005	0.012	0 009	0 012	0 008	0.006	0.006	0 007	0 006
Ca	0 836	0 835	0 846	0.915	0.731	0 865	0.864	0 897	0.877	0 637	0 875	0 863	0 891	0.893	0.887	0.685	0 821	0 674	0.879	0 914	0 888	0 864	0.841
Sr	0 003	0 003	0.003	0 002	0 002	0 003	0 002	0 003	0 001	0 003	0.005	0 002	0 002	0 003	0 002	0 006	0 003	0 002	0 005	0 006	0 005	0 003	0.004
Ba	0	0	0	0	0.002	0	0	0	0 001	0	0	0.002	0	0	0	0.002	0	0	0	0	0	0	0 001
Na	0.163	0 159	0 159	0.096	0.257	0.137	0.131	0.107	0 121	0 338	0 123	0 126	0 107	0 114	0.109	0 292	0 168	0.298	0.13	0.089	0.114	0 131	0.157
K	0.003	0 003	0 004	0 003	0 014	0 003	0 004	0 002	0 003	0 018	0.004	0 004	0 003	0.003	0.005	0.017	0.006	0 018	0 005	0 003	0.004	0.006	0.006
P	0	0 001	0	0	0	0	0 002	0	0 001	0.001	0 001	0	0	0	0.005	0.003	0	0 002	0	0 002	0	0.003	0
Cr																							
Total cation	5 014	5.008	5.017	5 019	5 013	5 013	5.007	5 014	5 012	5 006	5.011	5 013	5 008	5.018	5 008	5 008	5 008	5 003	5.02	5.013	5 016	5.011	5 011
Albite %	16 27	15.95	15.76	9.47	25 65	13.63	13.11	10.64	12.09	34 04	12.28	12 69	10.69	11 29	10 89	29.38	16 88	30.10	12.82	8.85	11.33	13.09	15.64
Anorthite %	83 43	83.75	83.85	90.24	72 95	86.07	86.49	89.17	87.61	64 15	87 33	86 91	89.01	88.42	88.61	68 91	82.51	68.08	86 69	90.85	88 27	86 31	83.76
Orthoclase %	0.30	0.30	0.40	0.30	1.40	0.30	0 40	0 20	0.30	1.81	0 40	0.40	0 30	0 30	0.50	1.71	0 60	1 82	0 49	0 30	0.40	0.60	0.60

Table G.2. (cont.). Core (C) and rim (R) compositions of plagioclase phenocrysts: Basalt Volcanoes Formation (BVF), Efaté Island Group, Vanuatu arc.

Plagioclase	HIGH-K/HIGH-Rb SUITE (HKRS)																					
Analysis number	AR188-5 (R)	AR188-6 (C)1	AR188-6 (C)2	AR188-6 (C)3	AR188-6 (R)	AR198-1 (C)	AR198-1 (R)	AR198-2 (C)	AR198-2 (R)	AR198-3 (C)	AR198-4 (R)	AR198-4 (C)	AR198-4 (R)1	AR198-4 (R)2	AR198-5 (C)	AR198-5 (R)1	AR198-5 (R)2	AR198-6 (C)	AR198-6 (R)1	AR198-6 (R)2	AR198-7 (C)	AR198-7 (R)1	AR198-7 (R)2
SiO_2	51.34	45 53	46.12	47 47	51 27	44 37	44 95	44 93	45 6	44.71	45 61	45 15	44.9	45.37	46 16	45.55	45.6	45 22	45.4	47 83	45.67	45 97	45.41
TiO_2	0.02	0	0 03	0 02	0 07	0 03	0 01	0 04	0.02	0	0 02	0	0.01	0	0	0 02	0 03	0	0 02	0 04	0.02	0	0.01
Al_2O_3	29 88	34 49	34 15	32 39	30 04	34 45	34 57	34.54	34 38	34 69	34.08	34 15	34 63	34 33	33 61	34.52	34 45	34 41	34.66	32 6	34.29	34 36	34.82
Fe_2O_3	1 28	1.03	1 08	1 46	1 32	0.99	1 06	1 08	0.99	0 96	0 99	0 94	0 89	1 14	0.97	0 99	0.93	1 05	0 94	1 11	1.03	0.99	1.03
MnO	0 03	0	0	0.09	0 02	0.01	0 02	0 03	0 02	0	0.02	0	0 07	0 04	0 03	0 05	0.01	0.04	0.03	0.03	0.01	0.01	0
MgO	0.16	0 1	0 12	0 24	0 17	0.03	0.05	0 02	0 05	0 04	0 06	0 05	0 08	0 02	0 02	0 03	0 07	0 06	0 02	0.04	0 11	0 03	0 05
CaO	13 22	18 09	17.57	16 28	13 41	18.55	18 28	18 13	17 97	18 51	18.11	18 07	18 2	17 72	17.22	17 86	17.93	18.38	18.14	16.23	17 93	17.69	18.26
SrO	0 12	0 05	0 1	0 19	0.18	0.22	0 18	0 13	0 15	0 15	0 18	0 18	0 18	0 14	0.17	0 19	0.14	0.18	0 14	0.18	0 15	0.14	0.13
BaO	0	0	0 01	0	0 11	0 03	0.03	0	0	0	0 03	0	0	0 04	0	0	0	0	0.05	0 01	0	0	0.01
Na_2O	3 73	1 27	1 39	2.12	3 72	1.11	1 09	1.19	1.33	1 02	1 22	1 12	1 05	1.19	1 59	1 16	1 29	1.11	1.15	2 03	1.21	1 28	1 17
K_2O	0 38	0 06	0 09	0 14	0 4	0 12	0 08	0 09	0 12	0 08	0 1	0.09	0 07	0 09	0 25	0 11	0.12	0 06	0.09	0 21	0 07	0 13	0 08
P_2O_5	0 04	0.06	0 01	0 04	0	n-a	n-a	n-a	n-a	n-a	n-a	n-a	n-a	n-a	n-a	n-a	n-a	n-a	n-a	n-a	n-a	n-a	n-a
Cr_2O_3	n-a	n-a	n-a	n-a	n-a	0	0	0.06	0	0	0 04	0 01	0	0	0	0	0 02	0.04	0 03	0 04	0 03	0	0
Total %	100 2	100 68	100 67	100 45	100 72	99.91	100 32	100.24	100 63	100 16	100 46	99 76	100 08	100.08	100 02	100 48	100 59	100 55	100 67	100 35	100 52	100 60	100.97
Sr (ppm)	1015	423	846	1607	1522	1860	1522	1099	1268	1268	1522	1522	1522	1184	1438	1607	1184	1522	1184	1522	1268	1184	1099
Ba (ppm)	-	-	90	-	985	269	269	-	-	-	269	-	-	358	-	-	-	-	448	90	-	-	90
Si	2 341	2 092	2 116	2 181	2 332	2 088	2.102	2 102	2 122	2 094	2 128	2.119	2 102	2.123	2 158	2.121	2 122	2.11	2 112	2 221	2 126	2.136	2 107
Ti	0 001	0	0 001	0.001	0 002	0.001	0	0 002	0.001	0	0.001	0	0	0	0	0 001	0.001	0	0.001	0 001	0 001	0	0
Al/Al ^{IV}	1 606	1.867	1.846	1 754	1.61	1.855	1 85	1 85	1.831	1 859	1 818	1 833	1 856	1.838	1 797	1.84	1.834	1.837	1.846	1 73	1.827	1 827	1.85
Fe^{2+}	0 044	0 036	0.037	0.051	0 045	0.037	0 039	0 04	0.037	0.035	0.037	0 038	0 033	0 042	0 036	0 037	0.034	0 039	0.034	0.041	0.038	0 036	0 038
Mn^{2+}	0 001	0	0	0 003	0 001	0	0.001	0 001	0 001	0	0 001	0	0 003	0 001	0.001	0 002	0.001	0.001	0 001	0.001	0	0.001	0
Mg	0 011	0 007	0.008	0 017	0.012	0 002	0.003	0 001	0 003	0 002	0.005	0 003	0 006	0.002	0 002	0 002	0.005	0.004	0.002	0 003	0.007	0 002	0 003
Ca	0.646	0 89	0.864	0 802	0 654	0.935	0 916	0 909	0 896	0.929	0.905	0.908	0 913	0 888	0 863	0 891	0 894	0.919	0.904	0.808	0 895	0.881	0 908
Sr	0 003	0 001	0 003	0.005	0 005	0 01	0 009	0 008	0 008	0 008	0 009	0 009	0 009	0 008	0 009	0 009	0 008	0.009	0.008	0.009	0 008	0 008	0.008
Ba	0	0	0	0	0 002	0 001	0 001	0	0	0	0 001	0	0	0 001	0	0	0	0	0 001	0	0	0	0
Na	0 33	0 113	0.124	0.189	0 328	0.099	0 097	0 107	0 119	0 091	0 109	0.1	0.093	0 106	0 142	0.103	0 115	0 098	0.102	0 181	0 107	0 113	0.103
K	0 022	0 004	0 005	0.008	0 023	0.007	0.005	0 006	0 007	0.005	0 006	0 006	0.004	0 005	0.015	0 006	0 007	0.004	0.005	0 013	0 004	0 008	0.005
P	0 001	0.002	0	0 002	0																		
Cr						0	0	0.002	0	0	0 001	0	0	0	0	0	0 001	0.002	0.001	0 002	0.001	0	0
Total cation	5 007	5 012	5 005	5 012	5.014	5 037	5 023	5 026	5.024	5 024	5 019	5 017	5 019	5.014	5 023	5 013	5.021	5 022	5.017	5.009	5 015	5 011	5.022
Albite %	33 07	11 22	12.49	18.92	32 64	9.55	9.56	10 43	11 61	8.90	10 65	9 85	9 23	10.65	13 97	10 29	11 28	9 62	10.10	18.09	10 67	11.32	10 15
Anorthite %	64 73	88 38	87.01	80 28	65.07	89 77	89 99	89.02	87 71	90 62	88.76	89 61	90 38	88.84	84 54	89 08	88 01	90 04	89.39	80 66	88.91	87 91	89 38
Orthoclase %	2 20	0.40	0 50	0 80	2.29	0.69	0 45	0 55	0 67	0 48	0.58	0 54	0 39	0.51	1 49	0 64	0.71	0 34	0 51	1 26	0 43	0.76	0.47

Table G.2. (cont.). Core (C) and rim (R) compositions of plagioclase phenocrysts: Basalt Volcanoes Formation (BVF), Efaté Island Group, Vanuatu arc.

Plagioclase	HIGH-K/HIGH-Rb SUITE (HKRS)												HIGH-K-HIGH-Rb SUITE (HKRS) GROUNDMASS LATHS					
Analysis number	AR198-7 (R)3	AR198-7 (R)4	AR198-8 (C)	AR198-8 (R)1	AR198-8 (R)2	AR198-9 (C)	AR199-1 (C)	AR199-1 (R)	AR199-2 (C)	AR199-2 (R)	AR199-3 (C)	AR199-3 (R)	AR199-1	AR199-2	AR199-3	AR199-4	AR199-5	AR199-6
SiO_2	45 4	45 54	45 24	45 48	48.62	44.65	45 3	50.04	46 34	49 64	46 54	50 31	51 22	51 61	50.35	51 83	52	52 67
TiO_2	0 04	0 04	0.02	0	0 03	0	0	0.05	0 03	0 05	0.02	0 08	0 04	0 06	0 05	0.08	0.07	0.02
Al_2O_3	34.51	34 19	34.92	34.49	32 3	34 64	34 34	31 22	33 99	31 25	33 79	30 24	30 11	30.05	30.89	29.97	29 85	29 22
Fe_2O_3	0 98	0 93	0.85	1.18	0.97	0 95	1 06	1 41	0 96	1.23	1	1 31	1 21	1.29	1 3	1 32	1 25	1 16
MnO	0	0.08	0 03	0	0	0.05	0	0 03	0	0	0	0.02	0 01	0 01	0 04	0 03	0 01	0.01
MgO	0 05	0 03	0.06	0.04	0.05	0 03	0.08	0.1	0 11	0 15	0 14	0 13	0 12	0 13	0 11	0 09	0 14	0.08
CaO	18 14	17 7	18 59	18 45	15 7	18 42	17 84	14 22	17 21	15 01	17 17	13 38	13 18	13 08	14.16	12 96	13	11.95
SrO	0 13	0.16	0 15	0.19	0 21	0 2	0 14	0 13	0 07	0 05	0 23	0 21	0 13	0 19	0 07	0 15	0 08	0.2
BaO	0 01	0 01	0	0	0.01	0	0	0 06	0	0 04	0	0 03	0	0.11	0	0	0.06	0.02
Na_2O	1 23	1 29	1 04	1 22	2 4	0.98	1 26	3 32	1 62	2 82	1 66	3 52	3 78	3.73	3.26	3.76	3 86	4 37
K_2O	0 1	0.13	0 08	0 12	0 24	0 06	0.09	0.3	0 11	0 23	0 08	0 32	0 37	0 43	0 33	0.38	0.4	0 4
P_2O_5	n-a	n-a	n-a	n-a	n-a	n-a	0.06	0	0 03	0 02	0.03	0 06	0	0 07	0	0	0.02	0
Cr_2O_3	0 06	0	0 01	0	0	0	n-a	n-a	n-a	n-a	n-a	n-a	n-a	n-a	n-a	n-a	n-a	n-a
Total %	100 65	100.10	100.99	101 17	100 53	99.98	100 17	100 87	100 49	100 49	100.66	99.6	100.15	100.75	100.57	100.57	100 72	100 1
Sr (ppm)	1099	1353	1268	1607	1776	1691	1184	1099	592	423	1945	1776	1099	1607	592	1268	676	1691
Ba (ppm)	90	90	-	-	90	-	-	537	-	358	-	269	-	985	-	-	537	179
Si	2.114	2 129	2 099	2.111	2 249	2.095	2.092	2 276	2 127	2 266	2.134	2 312	2.336	2.342	2 293	2 352	2 357	2 396
Ti	0 001	0 001	0 001	0	0.001	0	0	0 002	0 001	0 002	0 001	0.003	0 001	0 002	0.002	0 003	0 002	0 001
Al/Al^{IV}	1 838	1 829	1 855	1 832	1.706	1.86	1 869	1.674	1 839	1 681	1 826	1.638	1.619	1 607	1.658	1 603	1.594	1.567
Fe^{2+}	0 036	0 035	0 031	0 043	0.036	0.035	0 037	0 048	0.033	0 042	0.034	0 045	0 042	0.044	0.045	0.045	0.043	0.04
Mn^{2+}	0	0.003	0 001	0	0	0.002	0	0 001	0	0	0	0 001	0	0.001	0.001	0 001	0.001	0
Mg	0 003	0 002	0 004	0 003	0 004	0 002	0 006	0.007	0 008	0 011	0 01	0 009	0 008	0.009	0 008	0 006	0.009	0.005
Ca	0 905	0 887	0 924	0 918	0.778	0 926	0 883	0 693	0 847	0 734	0 843	0 659	0 644	0 636	0 691	0 63	0.631	0.583
Sr	0 007	0 009	0 008	0.009	0.01	0 009	0 004	0 003	0.002	0 001	0 006	0 006	0 003	0 005	0 002	0 004	0.002	0.005
Ba	0	0	0	0	0	0	0	0 001	0	0.001	0	0 001	0	0 002	0	0	0.001	0
Na	0 109	0.115	0.092	0.108	0 213	0 088	0.113	0 293	0 144	0 249	0.148	0 313	0 334	0 328	0 288	0 331	0.339	0 386
K	0 006	0 008	0 004	0.007	0 014	0.004	0 005	0.017	0 006	0 014	0 004	0 019	0 021	0 025	0 019	0.022	0.023	0 023
P							0 002	0	0 001	0 001	0 001	0.002	0	0 003	0	0	0.001	0
Cr	0.002	0	0	0	0	0												
Total cation	5.022	5 017	5 02	5.03	5.011	5 021	5 01	5.016	5 009	5 001	5 009	5 006	5 01	5.003	5 007	4.998	5 002	5.005
Albite %	10 68	11 37	8.98	10.42	21 23	8 60	11 29	29.21	14 44	24 97	14 87	31 58	33 43	33 16	28 86	33.67	34.14	38.91
Anorthite %	88 74	87.87	90 59	88.92	77 38	91.04	88 21	69 09	84 95	73 62	84.72	66 50	64 46	64 31	69 24	64.09	63 54	58.77
Orthoclase %	0.58	0 76	0 44	0 66	1.39	0.35	0 50	1.69	0 60	1 40	0 40	1 92	2.10	2 53	1 90	2 24	2 32	2 32

Table G.3. Core (C) and rim (R) compositions of olivine phenocrysts: Basalt Volcanoes Formation (BVF), Efaté Island Group, Vanuatu arc.

Olivine	MAINLAND SUITE (MLS)																						
Analysis number	AR157-1 (C)	AR157-2 (C)	AR157-2 (R)	AR157-3 (C)	AR157-3 (R)	AR157-4 (C)	AR157-4 (R)	AR158-1 (C)	AR158-1 (R)	AR158-2 (C)	AR158-2 (R)	AR158-3 (C)	AR158-3 (R)	AR158-4 (C)	AR158-5 (C)	AR161-1 (C)	AR161-1 (R)	AR161-2 (C)	AR161-2 (R)	AR161-3 (C)	AR161-3 (R)	AR161-4 (C)	AR161-4 (R)
	38 55	38 38	36.89	38 39	38 09	38.39	36.60	38.60	36 90	38 86	37.99	38 82	36 89	39.27	38 97	38.79	38.48	38.80	37.24	38 76	35 43	38 67	36.05
TiO_2	0 01	0 00	0 01	0.01	0 01	0 02	0.01	0 00	0 02	0 00	0.02	0 00	0.01	0 00	0 00	0 03	0 03	0.01	0 00	0.00	0 04	0 00	0.08
Al_2O_3	0 06	0 06	0 02	0.04	0 06	0 04	0.02	0.03	0 06	0 06	0 03	0 05	0 05	0 03	0 03	0.01	0 02	0.03	0 11	0 04	0.03	0 04	0.06
Cr_2O_3	0.00	0 00	0 00	0 01	0.00	0 00	0.00	0 03	0 00	0 00	0 00	0.03	0.02	0 00	0 00	0 00	0.01	0.03	0.03	0.00	0 03	0.00	0 01
FeO	20 84	20.43	28 97	20 88	20.91	21.60	27.92	18 97	27 68	18.05	21 56	19 47	27.31	17 24	17.83	19 04	19.43	19.76	27.88	18.93	34.76	18 89	32 26
MnO	0 46	0 37	0 85	0 42	0 52	0 42	0 74	0.40	0 62	0 32	0 41	0 32	0 67	0 21	0 29	0.39	0 34	0 25	0.69	0 31	0.90	0 24	0.90
MgO	40 16	39 75	32 38	40 06	39 10	38 28	33.13	41.51	33 06	41 22	39.30	41 22	34.55	43 25	42 21	41 53	41 30	41.15	32.34	41.47	27 57	41 82	29 41
CaO	0 26	0 31	0.25	0.30	0 41	0 24	0 30	0.32	0 38	0 26	0 27	0 32	0.31	0 20	0 20	0 27	0.32	0 29	0 27	0.38	0 30	0 32	0 33
NiO	0.13	0 00	0 00	0.04	0 04	0 03	0 01	0 06	0.09	0 11	0.13	0 10	0.06	0 10	0 02	0.09	0.10	0.12	0.04	0 09	0 00	0.14	0 03
Total	100 48	99 31	99.38	100 16	99 15	99 02	98 73	99 92	98 82	98 87	99 70	100.33	99 86	100 30	99.55	100 16	100.03	100.45	98 59	99.99	99 06	100.11	99 14
Si	0 993	0 998	1 002	0 992	0 996	1 006	0.996	0 991	1 002	1 003	0.991	0 994	0.989	0 994	0 997	0.993	0 989	0.994	1 012	0.994	0 996	0 990	0 999
Ti	0 000	0 000	0.000	0 000	0 000	0.000	0 000	0 000	0 000	0 000	0 000	0.000	0 000	0 000	0 000	0 001	0.001	0 000	0.000	0 000	0.001	0 000	0.002
Al/Al^{IV}	0 002	0 002	0 001	0 001	0.002	0 001	0 000	0.001	0.002	0 002	0 001	0 002	0 001	0 001	0 001	0.000	0 001	0.001	0 004	0.001	0 001	0 001	0.002
Al^{VI}	0.000	0 000	0.000	0.000	0 000	0.000	0 000	0.000	0 000	0.000	0 000	0 000	0.000	0 000	0 000	0 000	0 000	0 000	0.000	0 000	0.000	0 000	0.000
Cr	0 000	0 000	0.000	0.000	0.000	0.000	0.000	0.001	0 000	0 000	0 000	0 001	0 000	0 000	0 000	0 000	0 000	0 001	0 001	0.000	0 001	0.000	0 000
Fe^{2+}	0 449	0 444	0 000	0.451	0 457	0 473	0.636	0.407	0 628	0 390	0 470	0 417	0 612	0 365	0 382	0 408	0 418	0 423	0.634	0 406	0.818	0 405	0.748
Mn^{2+}	0.010	0 008	0.019	0.009	0.011	0 009	0.017	0.009	0 014	0 007	0 009	0 007	0.015	0 005	0 006	0 009	0.007	0 005	0.016	0.007	0.021	0 005	0 021
Mg	1.542	1.540	1 310	1.543	1 524	1 495	1.344	1 589	1.337	1 586	1.527	1.574	1 381	1 632	1 610	1.586	1 583	1.571	1 310	1.585	1 155	1 596	1 215
Ca	0 007	0 009	0.007	0.008	0 011	0.007	0.009	0 009	0 011	0 007	0 007	0 009	0 009	0 006	0.005	0 008	0.009	0.008	0 008	0.010	0 009	0.009	0.010
Ni	0.003	0 000	0.000	0 001	0 001	0 001	0 000	0 001	0 002	0 002	0.003	0 002	0.001	0 002	0.001	0.002	0 002	0 003	0 001	0 002	0 000	0 003	0.001
Total Cation	3 006	3 001	2.998	3 007	3 003	2 993	3 003	3 008	2 997	2.996	3.009	3.005	3 010	3 005	3.002	3 006	3.010	3 005	2.985	3 005	3.002	3 009	2.998
Fa%	22 50	22 40	33 40	22 60	23 10	24 00	32.10	20 40	32.00	19.70	23 50	20 90	30 70	18 30	19 20	20 50	20 90	21 20	32.60	20 40	41 40	20.20	38 10
Fo%	77 50	77 60	66 60	77.40	76.90	76 00	67.90	79.60	68 00	80 30	76 50	79 10	69 30	81 70	80 80	79 50	79.10	78 80	67.40	79 60	58.60	79 80	61 90

Table G.3. (cont.). Core (C) and rim (R) compositions of olivine phenocrysts: Basalt Volcanoes Formation (BVF), Efaté Island Group, Vanuatu arc.

Olivine	MAINLAND SUITE (MLS)																OFFSHORE SUITE (OSS)				
Analysis number	AR161-5 (C)	AR172-1 (C)	AR172-2 (C)	AR174-1 (R)	AR174-2 (C)	AR174-2 (R)	AR174-3 (C)	AR174-4 (C)	AR174-5 (C)	AR174-6 (C)	AR175-1 (C)	AR175-2 (C)	AR179-1 (C)	AR179-1 (R)	AR179-2 (C)	AR179-3 (C)	AR179-4 (C)	AR109-1 (C)	AR109-1 (R)	AR109-2 (C)	AR109-2 (R)	AR109-3 (C)
	38 80	36 11	36 65	35 44	38 22	36 45	38.18	38 24	38 18	37 15	37 47	37.08	38.23	36.52	38 78	38.40	39 60	38 21	36.79	38 51	38 12	38 34
TiO_2	0 01	0 02	0 00	0.00	0 00	0 01	0.00	0.00	0 00	0 02	0 02	0.02	0 00	0 03	0 03	0.00	0 01	0.02	0.04	0 01	0.03	0 01
Al_2O_3	0.05	0 02	0 01	0 03	0 02	0 04	0.04	0 04	0 05	0.05	0.04	0 04	0 07	0 03	0.03	0 05	0.03	0.03	0.05	0 04	0 03	0 05
Cr_2O_3	0 01	0 00	0 01	0 00	0 00	0 00	0.03	0 04	0 02	0 04	0 04	0 02	0 00	0 03	0 02	0.02	0 06	0.00	0 02	0.00	0 02	0.02
FeO	18 90	31 19	28 56	36.41	21.42	31 65	21.30	22 11	21.40	27 55	25.61	26.70	21 65	31 10	18 80	21.63	16 51	21.92	28.95	22 50	22.48	22 32
MnO	0.39	0 98	0 77	1 07	0 48	0.78	0.35	0 55	0.45	0 69	0 56	0 72	0 41	0 69	0 38	0.39	0.30	0.39	0.45	0 29	0.39	0 40
MgO	41 16	30 74	33 47	26 70	39 35	31 08	40 02	38.84	39 94	34 05	35 04	34 34	39 52	31 78	41 28	39 36	43.88	38 88	32.96	38 67	38 44	38.99
CaO	0 31	0.30	0 30	0 38	0.30	0 35	0 30	0.33	0.32	0 34	0 34	0.29	0.27	0 28	0 25	0.23	0 22	0.20	0.24	0.21	0.22	0 22
NiO	0 00	0 05	0 01	0 00	0 05	0 00	0.05	0.00	0 02	0 00	0 00	0 00	0 03	0.00	0 06	0.08	0.10	0 05	0 05	0.06	0 06	0 08
Total	99 63	99 40	99 78	100 02	99 85	100 36	100.27	100.16	100 37	99.90	99 13	99 22	100 17	100 48	99.63	100 16	100 70	99.70	99 56	100 27	99 78	100 43
Si	0 998	0 994	0 990	0 995	0.994	0.993	0.988	0 995	0.988	0.996	1 002	0 997	0 991	0 991	0 997	0.995	0 995	0.997	0.996	1.000	0 996	0.994
Ti	0 000	0.000	0 000	0 000	0 000	0 000	0 000	0 000	0.000	0.000	0 000	0.000	0.000	0 001	0 001	0.000	0 000	0.000	0 001	0.000	0.001	0.000
Al/Al^{IV}	0 002	0.001	0 000	0 001	0.001	0 001	0 001	0 001	0 001	0 002	0.001	0 001	0.002	0 001	0 001	0.002	0 001	0.001	0.002	0 001	0.001	0 001
Al^{VI}	0 000	0.000	0.000	0 000	0.000	0.000	0.000	0 000	0.000	0.000	0 000	0.000	0 000	0 000	0 000	0.000	0 000	0 000	0.000	0.000	0.000	0.000
Cr	0.000	0 000	0 000	0.000	0.000	0 000	0 001	0 001	0 000	0 001	0.001	0 000	0 000	0 001	0.000	0 000	0 001	0.000	0.001	0.000	0 000	0 000
Fe^{2+}	0.406	0 718	0 645	0 855	0 466	0.721	0 461	0 481	0 463	0 618	0.573	0.601	0 470	0 706	0.404	0.469	0.347	0.478	0 655	0.488	0 491	0.484
Mn^{2+}	0.008	0 023	0 018	0 025	0 011	0 018	0.008	0 012	0 010	0 016	0 013	0 016	0.009	0 016	0.008	0 009	0.006	0.009	0 010	0.006	0 009	0.009
Mg	1.578	1 260	1 348	1 117	1.525	1.262	1 543	1 506	1.540	1 360	1 397	1.377	1.527	1 285	1.582	1 521	1 644	1.511	1.330	1 496	1 497	1.507
Ca	0.009	0 009	0 009	0 011	0 008	0 010	0.008	0.009	0.009	0 010	0.010	0.008	0.007	0 008	0.007	0.006	0 006	0.006	0.007	0 006	0 006	0.006
Ni	0 000	0 001	0 000	0 000	0 001	0 000	0.001	0.000	0.000	0 000	0.000	0.000	0 001	0 000	0 001	0.002	0 002	0.001	0.001	0.001	0 001	0.002
Total Cation	3 001	3 006	3 010	3 005	3 006	3 006	3 011	3 004	3 011	3 002	2 996	3 001	3 007	3 008	3.002	3 004	3.003	3 003	3 002	2 999	3 003	3 004
Fa%	20 50	36 30	32 40	43.30	23.40	36 40	23.00	24 20	23 10	31 20	29 10	30.40	23 50	35 40	20 40	23.60	17 40	24.00	33.00	24 60	24 70	24.30
Fo%	79 50	63 70	67 60	56 70	76.60	63 60	77 00	75 80	76.90	68 80	70.90	69 60	76.50	64 60	79 60	76.40	82.60	76.00	67 00	75 40	75 30	75.70

Table G.3. (cont.). Core (C) and rim (R) compositions of olivine phenocrysts: Basalt Volcanoes Formation (BVF), Efaté Island Group, Vanuatu arc.

Olivine	OFFSHORE SUITE (OSS)																						
Analysis number	AR109-3 (R)	AR109-4 (C)	AR109-4 (R)	AR105-1 (C)	AR105-1 (R)	AR105-2 (C)	AR105-2 (R)	AR105-3 (C)	AR105-3 (R)	AR105-4 (C)	AR105-4 (R)	AR105-5 (C)	AR105-5 (R)	AR105-6 (C)	AR105-7 (C)	AR105-7 (R)	AR006-1 (C)	AR006-2 (C)	AR006-3 (C)	AR006-4 (C)	AR006-5 (C)	AR006-6 (C)	AR006-7 (C)
	36 32	38 85	36.26	38 90	38.34	38 19	35 98	38 21	38.03	38.25	38.08	38 37	35 07	38 24	39.54	36 64	38 17	38 44	38.06	37.81	37.15	37.99	37.72
TiO_2	0 01	0.01	0 01	0 00	0 01	0.00	0.00	0.01	0 00	0.00	0 01	0.00	0.03	0.01	0 00	0 02							
Al_2O_3	0 04	0 00	0 03	0 04	0.04	0 04	0 03	0 05	0 04	0 05	0 05	0 05	0.04	0 05	0 04	0 06							
Cr_2O_3	0.00	0 01	0 03	0 01	0.01	0 01	0.00	0 01	0 00	0 00	0 00	0.00	0 05	0 03	0 05	0.04	0 02	0.00	0.04	0 00	0.00	0.00	0.02
FeO	33.78	19.50	32 20	22 14	22.12	22.43	33.73	22.32	21 82	22 49	23 24	20.15	38.59	22 09	15.33	29.14	20 06	20.49	21.72	21.19	25.59	19.78	19.88
MnO	0.61	0.32	0 68	0 40	0.39	0.51	0.71	0 29	0 38	0 40	0 45	0 34	0 83	0 45	0.22	0.63	0 43	0.32	0.44	0 40	0.58	0.34	0.38
MgO	29.62	41 25	30 47	39 26	39.40	39 27	28 87	38 57	38 96	38 74	38 47	40 61	25 52	38.76	44 25	32.57	39.23	40.16	38 63	38 56	34.93	39 93	39.58
CaO	0 24	0 24	0 23	0 32	0 32	0 32	0 34	0 31	0.30	0 31	0.32	0 25	0 27	0.31	0 27	0 33	0.31	0.32	0 32	0 32	0.33	0 31	0 27
NiO	0.03	0 09	0 05	0 02	0.15	0.12	0 04	0 07	0.08	0 10	0 02	0 15	0 12	0.02	0 12	0 00	0 01	0 04	0 00	0 04	0.00	0 06	0.05
Total	100 66	100 26	99 95	101 09	100 79	100.88	99 70	99 84	99.62	100.35	100 64	99 90	100.51	99.96	99 82	99 44	98.23	99.77	99 21	98 32	98.58	98.41	97.90
Si	0 996	0.995	0 995	1 000	0 991	0 988	0 998	0 997	0.993	0 994	0 991	0.991	0.990	0 996	0 997	0 995	1 002	0 995	0 997	0 998	1.000	0.995	0.994
Ti	0 000	0 000	0.000	0 000	0.000	0 000	0 000	0 000	0 000	0.000	0 000	0.000	0.001	0 000	0 000	0.000							
Al/Al^{IV}	0 001	0.000	0 001	0 001	0.001	0 001	0.001	0 001	0 001	0 001	0 001	0 001	0 001	0 001	0 001	0 002							
Al^{VI}	0.000	0 000	0.000	0 000	0 000	0 000	0 000	0 000	0.000	0 000	0 000	0 000	0 000	0 000	0 000	0 000							
Cr	0 000	0 000	0 001	0.000	0.000	0 000	0 000	0 000	0 000	0 000	0.000	0.000	0 001	0.001	0 001	0.001	0 000	0 000	0.001	0.000	0.000	0.000	0 000
Fe^{2+}	0 774	0 418	0 739	0.476	0.478	0 485	0 782	0 487	0 477	0 489	0.506	0 435	0.911	0.481	0 323	0 662	0 441	0 444	0 476	0.468	0 576	0 433	0 438
Mn^{2+}	0 014	0 007	0 016	0 009	0 009	0 011	0 017	0 006	0 009	0 009	0 010	0.007	0.020	0 010	0.005	0 014	0 010	0.007	0.010	0 009	0 013	0.008	0.008
Mg	1.210	1 576	1 246	1 504	1 518	1 514	1.193	1 500	1.516	1 501	1 491	1.563	1.074	1 504	1 664	1 319	1.536	1 550	1.509	1.517	1.402	1.559	1.555
Ca	0.007	0 007	0.007	0 009	0.009	0 009	0 010	0 009	0.008	0 009	0 009	0.007	0.008	0 009	0.007	0 010	0 009	0 009	0 009	0 009	0 010	0 009	0.008
Ni	0 001	0 002	0 001	0.000	0.003	0 002	0 001	0 002	0.002	0.002	0.001	0 003	0 003	0 000	0.002	0.000	0 000	0.001	0 000	0.001	0.000	0.001	0.001
Total Cation	3 004	3 004	3 004	2 999	3 008	3 011	3 002	3 002	3 006	3 005	3 008	3.008	3.008	3 003	3 001	3 003	2 997	3 005	3 002	3 002	3 000	3 005	3 006
Fa%	39.00	21 00	37 20	24.00	24 00	24 30	39.60	24.50	23.90	24 60	25 30	21 80	45.90	24 20	16 30	33.40	22 31	22.27	23 98	23 58	29 12	21 74	21.98
Fo%	61.00	79.00	62 80	76 00	76 00	75 70	60 40	75 50	76 10	75 40	74 70	78 20	54 10	75.80	83.70	66.60	77 69	77 73	76.02	76 42	70 88	78.26	78 02

Table G.3. (cont.). Core (C) and rim (R) compositions of olivine phenocrysts: Basalt Volcanoes Formation (BVF), Efaté Island Group, Vanuatu arc.

Olivine	OFFSHORE SUITE (OSS)																					
Analysis number	AR006-8 (C)	AR006-9 (C)	AR006-10 (C)	AR006-10 (R)	AR006-11 (C)	AR006-11 (R)	AR006-12 (C)	AR006-12 (R)	AR006-13 (C)	AR006-14 (C)	AR006-14 (R)	AR006-15 (C)	AR006-15 (R)	AR006-16 (C)	AR006-17 (C)	AR006-18 (C)	AR006-18 (R)	AR006-19 (C)	AR006-19 (R)	AR006-20 (C)	AR006-20 (R)	AR114-1 (C)	AR114-1 (R)
	36 70	35 80	37 91	37.26	38.26	37.75	38 12	37.86	36.88	38 08	37 00	38.13	36 73	36.77	37 66	38.01	36 96	37.77	36.08	37.48	35 81	39.51	39.55
TiO_2																						0 02	0.06
Al_2O_3																						0 04	0.00
Cr_2O_3	0 00	0 00	0 00	0.00	0 00	0.00	0 00	0 04	0 00	0 00	0.00	0 05	0 00	0.02	0 00	0.02	0 01	0 00	0 01	0 02	0 00	0.00	0.06
FeO	26 49	31 33	20 17	23 06	20.14	22.85	20.57	20.96	24 81	20 60	24 34	20 67	26 98	25.79	22 22	21.34	25 80	22 10	28.29	21.49	30 27	15.96	15 67
MnO	0 59	0 93	0 32	0.48	0 32	0 50	0 32	0 54	0 40	0.38	0 58	0 45	0.79	0.57	0 49	0.31	0 64	0 53	0.80	0 35	0 66	0.46	0.56
MgO	34 27	29 28	39.71	36 98	39 25	37 37	39.34	39.10	35.07	39 12	35 54	39 55	33 82	34 18	37.46	38.68	34 98	38 03	32 25	38.56	30.22	43.83	44.17
CaO	0 31	0.33	0 42	0.30	0 27	0 27	0 30	0.29	0 32	0 32	0.29	0 32	0.32	0 28	0 29	0.29	0.31	0 31	0.32	0.27	0 29	0.14	0 16
NiO	0.03	0.03	0 10	0 07	0.00	0 01	0.05	0 04	0.00	0 03	0.06	0.07	0.04	0 05	0 04	0.04	0 03	0 04	0.09	0.01	0 00	0.14	0 05
Total	98 39	97.70	98.63	98 15	98.24	98.75	98.70	98 83	97.48	98 53	97.81	99 24	98.68	97 66	98 16	98 69	98.73	98.78	97 84	98 18	97.25	100 10	100.29
Si	0 995	1 004	0 993	0 995	1 004	1 000	0.998	0 994	1 000	0 999	0 999	0 995	0.996	1 001	1.001	0.999	0.995	0.997	0.995	0 993	1 003	0 997	0.996
Ti																						0 000	0.001
Al/Al^{IV}																						0.001	0.000
Al^{VI}																						0.000	0 000
Cr	0 000	0 000	0 000	0 000	0.000	0.000	0 000	0 001	0.000	0 000	0 000	0 001	0 000	0.000	0 000	0 000	0 000	0.000	0 000	0 000	0.000	0 000	0 001
Fe^{2+}	0 601	0 735	0 442	0 515	0.442	0 506	0 451	0 460	0.563	0 452	0 549	0.451	0 612	0.587	0 494	0 469	0.581	0.488	0.653	0 476	0.709	0.337	0 330
Mn^{2+}	0 014	0.022	0 007	0 011	0 007	0 011	0 007	0.012	0 009	0 008	0 013	0.010	0 018	0 013	0.011	0 007	0.015	0.012	0 019	0.008	0 016	0 010	0.012
Mg	1 385	1 224	1.551	1.473	1.535	1 475	1 536	1 530	1.418	1 531	1.430	1 538	1.367	1.387	1 484	1.516	1 404	1 497	1.326	1 522	1.261	1.649	1.657
Ca	0 009	0 010	0 012	0.009	0 008	0 008	0 008	0.008	0 009	0.009	0 008	0.009	0.009	0 008	0 008	0 008	0.009	0 009	0 009	0.008	0.009	0.004	0.004
Ni	0 001	0 001	0.002	0 002	0 000	0 000	0.001	0 001	0.000	0 001	0 001	0.001	0 001	0 001	0.001	0 001	0.001	0.001	0 002	0.000	0.000	0 003	0.001
Total Cation	3 005	2.996	3.007	3 005	2.996	3 000	3.002	3.006	3.000	3 001	3.001	3.005	3 004	2 999	2.999	3 001	3.005	3.003	3.005	3 007	2.997	3.002	3.003
Fa%	30.26	37.52	22 18	25 91	22.36	25.54	22 70	23.12	28.42	22 79	27.74	22.67	30.92	29 74	24.97	23.63	29 27	24 58	33.00	23.82	35 99	17.00	16 60
Fo%	69 74	62 48	77 82	74 09	77.64	74 46	77 30	76 88	71 58	77 21	72 26	77 33	69.08	70 26	75.03	76.37	70 73	75 42	67 00	76.18	64 01	83.00	83 40

Table G.3. (cont.). Core (C) and rim (R) compositions of olivine phenocrysts: Basalt Volcanoes Formation (BVF), Efaté Island Group, Vanuatu arc.

Olivine	OFFSHORE SUITE (OSS)								HIGH-K/HIGH-Rb SUITE (HKRS)													
Analysis number	AR114-2 (C)	AR114-2 (R)	AR114-3 (C)	AR114-3 (R)	AR114-4 (C)	AR114-4 (R)	AR114-5 (C)	AR114-5 (R)	AR198-1 (C)	AR198-1 (R)	AR198-2 (C)	AR198-2 (R)	AR198-3 (C)	AR198-3 (R)	AR198-4 (C)	AR198-4 (R)	AR198-5 (C)	AR198-5 (R)	AR198-6 (C)	AR198-7 (R)	AR198-8 (C)	AR198-8 (R)
	40 01	39.55	39 85	39 34	39 79	40 23	40 16	39.69	36.01	35.98	36 13	35.84	36.00	36 08	37.08	36 71	36.35	35.91	38 56	37 63	36 30	36 33
TiO_2	0 00	0.00	0 04	0 03	0 00	0 06	0 00	0 04	0 04	0.00	0.00	0 00	0 04	0 04	0 03	0 02	0 00	0.01	0 00	0 02	0.00	0 00
Al_2O_3	0.04	0 05	0 04	0 06	0 06	0 10	0.04	0 03	0.03	0.01	0 01	0 04	0 04	0 05	0.01	0 02	0.02	0.00	0 04	0 03	0.04	0 00
Cr_2O_3	0 01	0 01	0 04	0 01	0.02	0 02	0 01	0 03	0 00	0 01	0 01	0.02	0 00	0.00	0.01	0 03	0.04	0.01	0.00	0.00	0.01	0 00
FeO	12 94	15 17	12 89	16 25	13 56	14 72	11.34	13 68	32 14	32 22	33 26	32 62	32 51	32 17	29.19	28 66	31.63	31.80	22.09	26 35	31 34	31 84
MnO	0 31	0 48	0 21	0 57	0 53	0 56	0 23	0.41	0 98	0.94	1 02	0 87	0 93	0.87	0 81	0 82	0 97	0 97	0 43	0 67	0 96	0 92
MgO	46 09	44 62	46 30	43 57	45 52	44 38	47 54	45 62	30 64	30.48	29 92	29 79	30 27	29.99	32 90	32 89	30 23	30 29	39 19	35.50	30 89	30 80
CaO	0 27	0 20	0 22	0 34	0 16	0 35	0 24	0 20	0 20	0 20	0 22	0 17	0.16	0 17	0 20	0 16	0.22	0 17	0 29	0 23	0 22	0 24
NiO	0 23	0 10	0 19	0.07	0 05	0 05	0 15	0 16	0 03	0 03	0 00	0 06	0 05	0.01	0 08	0 02	0 06	0.00	0 08	0 04	0 05	0 03
Total	99.89	100 18	99 79	100.24	99 69	100 46	99 72	99 86	100.07	99 87	100 57	99.41	100 00	99.38	100.31	99 33	99.52	99.16	100.68	100 47	99.81	100 16
Si	0 998	0 994	0 995	0 994	0 998	1.005	0 996	0 994	0 988	0 990	0 991	0 993	0.990	0 996	0.997	0 996	1 000	0.993	0.996	0.996	0.994	0 993
Ti	0 000	0.000	0 001	0 001	0 000	0.001	0 000	0 001	0 001	0 000	0 000	0.000	0.001	0 001	0 001	0.000	0 000	0.000	0 000	0 000	0.000	0.000
Al/Al^{IV}	0.001	0 002	0 001	0.002	0.002	0.003	0 001	0 001	0 001	0 000	0 000	0 001	0 001	0 002	0 000	0.001	0 001	0 000	0 001	0 001	0.001	0.000
Al^{VI}	0 000	0 000	0 000	0.000	0.000	0 000	0.000	0.000														
Cr	0.000	0 000	0.001	0.000	0.000	0 000	0.000	0.001	0 000	0.000	0.000	0 000	0 000	0 000	0.000	0 001	0 001	0 000	0.000	0.000	0.000	0.000
Fe^{2+}	0 270	0 319	0 269	0.343	0 284	0 308	0 235	0.287	0 737	0 741	0 763	0 756	0.748	0 743	0 657	0.650	0 728	0 735	0.477	0.583	0 718	0.728
Mn^{2+}	0 007	0 010	0.005	0.012	0 011	0 012	0.005	0 009	0 023	0 022	0.024	0 020	0 022	0 020	0 019	0 019	0.023	0 023	0 009	0.015	0 022	0 021
Mg	1 714	1 672	1 723	1 641	1.701	1.653	1.757	1.704	1.253	1.250	1 224	1 230	1 241	1 234	1.319	1 330	1 240	1.249	1.509	1 401	1 261	1.255
Ca	0 007	0 005	0 006	0 009	0.004	0.009	0.006	0 005	0.006	0 006	0 006	0.005	0.005	0 003	0 005	0.005	0 006	0 005	0.008	0.006	0.006	0 006
Ni	0 005	0 002	0 004	0 001	0 001	0.001	0.003	0.003	0 001	0 001	0 000	0.001	0 001	0.000	0.002	0.000	0 001	0.000	0 002	0 001	0 001	0 001
Total Cation	3 001	3 005	3 004	3 004	3.001	2 992	3.003	3 004	3 011	3 010	3 009	3 007	3 008	3.000	3 001	3.003	3 000	3.007	3 004	3 003	3 005	3.006
Fa%	13 60	16 00	13 50	17.30	14.30	15 70	11 80	14.40	37.04	37 22	38 40	38 07	37.61	37 58	33 25	32.83	36.99	37 05	24 02	29 39	36.28	36 71
Fo%	86 40	84 00	86 50	82.70	85 70	84 30	88 20	85.60	63 00	62.80	61 60	61 90	62.40	62 40	66 80	67.20	63.00	63.00	76.00	70 60	63.70	63.30

Table G.4. Core (C) and rim (R) compositions of clinopyroxene phenocrysts: Basalt Volcanoes Formation (BVF), Efaté Island Group, Vanuatu arc.

Clinopyroxene	MAINLAND SUITE (MLS)																							
Analysis number	AR157-1 (C)	AR157-1 (R)	AR157-2 (C)	AR157-2 (R)	AR158-1 (C)	AR158-1 (R)	AR158-2 (C)	AR158-3 (C)	AR158-3 (R)	AR158-4 (R)	AR161-1 (C)	AR161-1 (R)	AR161-2 (C)	AR161-2 (R)	AR161-3 (C)	AR161-3 (R)	AR172-1 (C)	AR172-1 (R)	AR172-2 (C)	AR172-2 (R)	AR172-3 (C)	AR172-3 (R)	AR172-4 (C)	AR172-4 (R)
SiO_2	47 52	47.02	47.90	48 87	48.40	46.70	48.61	47.37	49 11	50 23	47 56	48.00	48 37	46 86	49.34	48 92	47.77	49 71	48 11	50.12	48 75	47 61	50.15	48.02
TiO_2	0.86	0 97	0.91	0.70	0.47	0 93	0.61	0.79	0.63	0 57	0 72	0.74	0.51	0 94	0.56	0.60	0 69	0.48	0 71	0.53	0 60	0 76	0.51	0 70
Al_2O_3	6 19	5.88	5.35	4.32	5.79	6.50	5.18	7.09	4 69	2.67	6 30	5.83	6.16	6.17	4 82	5.38	6.40	4.50	5.40	3.62	4.84	5.87	3 37	5.60
Cr_2O_3	0 00	0.05	0 00	0 01	0 23	0 00	0.07	0 08	0.02	0 00	0 19	0 02	0 19	0.11	0.21	0 25	0.00	0 00	0 02	0 02	0.00	0.00	0 00	0.04
Fe_2O_3(c)	6.01	6 69	6 12	4.89	4.94	6 88	5 64	6 20	6 09	4 66	6.56	6 62	5 91	6 21	5 61	5.46	6 59	4.84	6 97	5.45	5 93	6 84	5 47	6 84
FeO(c)	3 76	3 64	3 74	4 86	1.82	3 14	2 86	2 65	2 44	5.43	2.43	2 64	1 81	3 46	2 00	2.04	2 84	3 12	2 08	2 66	2.53	3.45	2.81	2.71
MnO	0.17	0 22	0.17	0 24	0.15	0 16	0 15	0 13	0.17	0 33	0.14	0.12	0 17	0 27	0 19	0.16	0 16	0.15	0.12	0 20	0.12	0 22	0 23	0 17
MgO	13.55	13 50	14.03	14 44	14.47	13 27	14.02	13 55	14.76	14 70	13 78	13 81	14 20	13.40	14 96	14.41	13 59	14.72	14.01	15.03	14.14	13 54	15 25	13.70
CaO	21 71	21.49	21 68	20.91	23.06	22 04	22.87	22 67	22 72	20 94	22.55	22 86	23 15	21.66	22.65	23.15	22 49	22 86	23 15	23 08	23 17	22 14	22 75	22.90
Na_2O	0 37	0 34	0 30	0 31	0 21	0 32	0 29	0 29	0 27	0.38	0 32	0 30	0 28	0 33	0 35	0.33	0 36	0 22	0 29	0 26	0.27	0.31	0 23	0.30
K_2O	0 00	0 02	0 01	0 01	0.00	0 01	0 00	0 01	0.01	0 00	0 00	0 00	0 01	0 00	0 00	0 00	0 01	0.01	0 00	0.00	0 02	0 00	0 00	0 01
Total%	100 15	99 82	100 21	99 54	99.54	99 94	100.33	100.83	100 90	99 91	100 56	100 96	100 76	99 42	100 69	100 69	100 90	100 61	100.85	100 97	100.37	100.74	100 78	100 99
Si	1 769	1 761	1.782	1 827	1 796	1.746	1 801	1 748	1 806	1 874	1 76	1 771	1.778	1 759	1 812	1.799	1.763	1 83	1 776	1.841	1 805	1 766	1.845	1.774
Ti	0 024	0 027	0 026	0 02	0 013	0 026	0 017	0 022	0 017	0 016	0.02	0.021	0 014	0 027	0 016	0.017	0 019	0 013	0 02	0.015	0.017	0 021	0 014	0.019
Al/Al^{IV}	0 231	0 239	0.218	0.173	0 204	0 254	0 199	0 252	0 194	0 118	0 24	0 229	0 222	0 241	0 188	0 201	0 237	0 17	0 224	0.157	0.195	0 234	0.146	0.226
Al^{VI}	0 041	0 02	0	0 018	0.049	0.032	0 027	0 056	0 009	0	0 035	0.025	0 045	0 033	0 021	0.032	0.042	0.026	0.011	0	0.016	0.023	0	0.018
Cr	0	0 002	0	0	0.007	0	0 002	0.002	0 001	0	0 006	0.001	0 006	0.003	0 006	0.007	0	0	0 001	0.001	0	0	0	0 001
Fe^{3+}	0 168	0 188	0 171	0.138	0.138	0.193	0.157	0 172	0 169	0 131	0 183	0.184	0.163	0 175	0 155	0 151	0 183	0 134	0 194	0 15	0 165	0 191	0.151	0 19
Fe^{2+}	0 117	0 114	0.116	0.152	0 057	0.098	0.089	0.082	0 075	0 169	0 075	0.082	0.056	0 109	0.061	0.063	0 088	0 096	0 064	0.082	0 078	0 107	0.087	0.084
Mn^{2+}	0 005	0 007	0 005	0 008	0 005	0 005	0 005	0.004	0 005	0 01	0.004	0.004	0.005	0 009	0 006	0 005	0 005	0.005	0 004	0.006	0.004	0.007	0.007	0.005
Mg	0.752	0 754	0 778	0 805	0 8	0 739	0.774	0.745	0 809	0 817	0 76	0 76	0 778	0 75	0 819	0.79	0.748	0.808	0.771	0.823	0 78	0 749	0 836	0 754
Ca	0.866	0 862	0 864	0.838	0.917	0.882	0 908	0 896	0.895	0.837	0.894	0.904	0 912	0 871	0 891	0 912	0 89	0 902	0 916	0 908	0 919	0 88	0.897	0 906
Na	0 027	0 025	0.022	0 022	0 015	0 023	0.021	0.021	0.019	0.028	0.023	0.021	0 02	0.024	0.025	0.023	0.026	0.016	0.021	0 019	0 019	0 023	0.016	0 022
K	0	0 001	0	0	0	0	0	0 001	0	0	0	0	0.001	0	0	0	0 001	0	0	0	0.001	0	0	0
Total cation	4	4	4	4	4	4	4	4	4	4	4	4	4	4	4	4	4	4	4	4	4	4	4	4
Wo%	45 39	44.78	44.67	43.17	47.84	46 01	46 97	47.18	45 83	42 62	46.66	46.74	47 65	45.51	46 12	47.48	46 50	46.38	47 00	46.11	47.23	45.50	45.35	46 73
En%	39 41	39 17	40 23	41 47	41 73	38 55	40.04	39.23	41 42	41 60	39.67	39.30	40.65	39.18	42.39	41 12	39 08	41 54	39 56	41 80	40 08	38 73	42.26	38 89
Fs%	15.20	16.05	15.10	15.35	10 43	15.44	12.98	13.59	12.75	15.78	13 67	13.96	11.70	15 31	11 49	11.40	14.42	12.08	13.44	12 09	12 69	15.77	12.39	14.39
Mg_{cpx}	72 52	71 40	73.05	73.52	80 40	71 75	75 88	74 57	76 83	73.14	74.66	74.07	78.03	72 53	79.13	78.69	73 41	77 84	74.93	78.01	76 25	71.54	77.84	73.35

Table G.4. (cont.). Core (C) and rim (R) compositions of clinopyroxene phenocrysts: Basalt Volcanoes Formation (BVF), Efaté Island Group, Vanuatu arc.

Clinopyroxene	MAINLAND SUITE (MLS)																								
Analysis number	AR172-5 (C)	AR172-5 (R)	AR174-1 (C)	AR174-1 (R)	AR174-2 (C)	AR174-2 (R)	AR174-3 (C)	AR174-3 (R)	AR174-4 (C)	AR174-4 (R)	AR174-5 (C)	AR174-6 (C)	AR174-6 (R)	AR175-1 (C)	AR175-1 (R)	AR175-2 (C)	AR175-2 (R)	AR175-3 (C)	AR175-4 (C)	AR175-4 (R)	AR175-5 (C)	AR175-6 (C)	AR179-1 (C)	AR179-2 (C)
SiO_2	47.54	47 94	48 22	49 72	49.55	50 49	49 03	49 43	48 28	50 14	50 40	48.98	47 81	51.09	50 74	47 62	50.03	47.77	48.22	49 81	47.60	47 97	47 83	47 91
TiO_2	0 70	0 73	0 45	0 59	0 47	0 51	0 58	0.53	0 70	0 57	0 44	0 58	0 96	0.25	0.50	0.75	0 62	0 71	0 43	0 65	0.55	0 66	0 56	0 50
Al_2O_3	6 51	5 60	7 31	3 36	3 76	3 10	4 43	3 80	5.34	2 58	2 97	4 55	5 13	3.37	2 24	6 42	3.11	6 21	6.19	3 17	6.42	5 55	6.75	6.47
Cr_2O_3	0 03	0.01	0 02	0.00	0 00	0 00	0 02	0 00	0 01	0 00	0 01	0.02	0 06	0 27	0.04	0 00	0 00	0 01	0.04	0.00	0 05	0.01	0 05	0.03
Fe_2O_3(c)	6 73	6.33	3 94	4 84	6 22	4 80	6.40	5 79	5.69	5 18	5 30	6 27	6 88	4 30	4 10	6.10	4.79	5.84	6.28	4 78	5 81	6 43	6.85	6 84
FeO(c)	2 50	3 05	3 36	4.49	2 15	4 30	2 18	3 51	3 67	5 42	3 65	2.54	4 29	0 58	6.13	2 46	5.17	2.94	1 23	4 47	1 94	2 50	1.41	1 18
MnO	0 13	0 18	0 13	0.25	0 14	0 20	0 16	0 26	0 19	0.38	0 24	0 19	0 23	0 10	0 35	0 14	0.31	0.19	0.11	0 25	0.10	0 16	0 13	0 13
MgO	13 52	13 61	12 93	14 87	14 86	15.40	14 37	14 84	13 71	14 65	15 71	14 39	13 46	16 17	14 47	13 55	14.18	13.36	14.25	14.41	13 77	13.73	13.66	14 11
CaO	22.96	22 80	22 95	21.52	23.13	21 59	23 31	21 97	22 32	21 02	21 48	22 95	21 72	24 32	21.10	23 08	21.74	23.13	23.71	21 87	23 38	23 11	24 15	23 44
Na_2O	0 28	0 27	0 43	0 25	0 28	0 26	0 28	0.26	0 31	0 35	0 27	0 27	0.37	0.14	0.39	0 28	0.38	0 24	0.19	0.36	0.18	0 26	0.18	0 26
K_2O	0.01	0 01	0 04	0 00	0 00	0 01	0.00	0 00	0.01	0 00	0 00	0 02	0 00	0.00	0.00	0 00	0.00	0.01	0.01	0.01	0.00	0 00	0.00	0.02
Total%	100 91	100 53	99.78	99.91	100 56	100 65	100.78	100 40	100 25	100 28	100 46	100.76	100 91	100 59	100.05	100 40	100 33	100.41	100.66	99.78	99 83	100.38	101 58	100.88
Si	1 755	1 779	1 789	1 851	1.828	1 862	1.808	1 831	1 795	1 868	1 859	1 808	1 777	1 863	1 893	1.764	1.861	1.772	1.773	1 858	1.769	1 78	1 75	1.761
Ti	0 019	0 02	0 013	0 016	0 013	0 014	0 016	0 015	0 02	0.016	0 012	0 016	0 027	0 007	0 014	0 021	0 017	0 02	0 012	0.018	0 015	0.018	0 015	0.014
Al/Al^{IV}	0 245	0 221	0 211	0.148	0 164	0 135	0.192	0.166	0 205	0 113	0 129	0 192	0 223	0 137	0 098	0 236	0 136	0.228	0 227	0.139	0 231	0 22	0.25	0 239
Al^{VI}	0.038	0.024	0.108	0	0	0	0.001	0	0 029	0	0	0 006	0 002	0.008	0	0 044	0	0.044	0 042	0	0.05	0 023	0.042	0.041
Cr	0 001	0	0 001	0	0	0	0.001	0	0	0	0	0.001	0 002	0 008	0 001	0	0	0	0 001	0	0 002	0	0 001	0 001
Fe^{3+}	0 187	0 177	0 11	0.136	0 173	0.133	0 178	0.161	0 159	0 145	0 147	0 174	0 192	0 118	0.115	0 17	0.134	0.163	0.174	0 134	0.162	0 179	0 189	0.189
Fe^{2+}	0.077	0 095	0.104	0.14	0 066	0 132	0.067	0 109	0 114	0.169	0.113	0 078	0 133	0.018	0 191	0 076	0 161	0.091	0.038	0.14	0.06	0 078	0.043	0.036
Mn^{2+}	0 004	0.006	0 004	0.008	0 004	0 006	0 005	0 008	0 006	0 012	0 008	0.006	0 007	0 003	0.011	0 004	0.01	0 006	0 004	0 008	0.003	0 005	0.004	0.004
Mg	0 744	0 753	0.715	0.825	0 817	0.846	0 79	0.819	0 76	0.813	0 864	0 791	0.745	0 879	0 804	0 748	0 786	0 739	0.781	0.801	0 763	0.759	0 745	0.773
Ca	0 908	0 906	0 912	0 858	0 915	0.853	0 921	0.872	0 889	0.839	0 849	0 908	0 865	0 95	0.843	0 916	0 866	0.919	0.935	0.874	0.931	0 919	0.947	0 923
Na	0 02	0.02	0.031	0.018	0.02	0 018	0.02	0 019	0 022	0.025	0 019	0.019	0 026	0 01	0.028	0 02	0.027	0 018	0.014	0.026	0 013	0.019	0 013	0.018
K	0	0	0 002	0	0	0 001	0	0	0 001	0	0	0 001	0	0	0	0	0	0.001	0	0 001	0	0	0	0.001
Total cation	4	4	4	4	4	4	4	4	4	4	4	4	4	4	4	4	4	4	4	4	4	4	4	4
Wo%	47.29	46 77	49 43	43 62	46 33	43 30	46.97	44 29	46 11	42 42	42 86	46.40	44 54	48 27	42 92	47 86	44 25	47 91	48.40	44.66	48 51	47.37	49 12	47 95
En%	38 75	38.87	38 75	41 94	41.37	42.94	40 29	41.59	39 42	41 10	43.61	40 42	38 36	44 66	40.94	39 08	40.16	38.53	40 42	40.93	39 76	39 12	38.64	40 16
Fs%	13 96	14 35	11.82	14.44	12 30	13.76	12 75	14.12	14 47	16.48	13 53	13.18	17 10	7 06	16 14	13 06	15 59	13.56	11.18	14 41	11 72	13 51	12 24	11.90
Mg_{cpx}	73 81	73.46	76 96	74 93	77.37	76 15	76.33	75.21	73 57	72.14	76 87	75 84	69 63	86.60	72 43	75 25	72 71	74.42	78.65	74.51	77.46	74 70	76 25	77.45

Table G.4. (cont.). Core (C) and rim (R) compositions of clinopyroxene phenocrysts: Basalt Volcanoes Formation (BVF), Efaté Island Group, Vanuatu arc.

Clinopyroxene	MAINLAND SUITE (MLS)				OFFSHORE SUITE (OSS)																	
Analysis number	AR179-3 (C)	AR179-4 (C)	AR179-4 (R)1	AR179-4 (R)2	AR114-1 (C)	AR114-1 (R)	AR114-2 (C)	AR114-3 (C)	AR114-3 (R)	AR114-4 (C)	AR114-4 (R)	AR184-1 (C)	AR184-2 (C)	AR184-2 (R)	AR184-3 (C)	AR184-4 (C)	AR184-4 (R)	AR184-5 (C)	AR184-5 (R)	AR184-6 (C)	AR184-6 (R)	AR184-7 (C)
SiO_2	48 55	49 47	49 92	47.73	48.85	48 66	46 98	47 31	49 56	48 47	47 39	50.06	47.57	47 66	48.42	49 94	47.64	48 18	50.15	48.28	47 04	49.94
TiO_2	0 56	0 31	0 30	0.75	0 38	0 52	0.52	0 55	0 42	0 52	0 72	0.39	0.58	0 49	0.39	0.34	0.54	0.54	0.36	0.48	0 63	0.43
Al_2O_3	5 05	4 74	4 12	5 75	4 98	5.94	6 93	7 55	5 08	5 83	5 75	3.16	5 34	5 23	4.78	3 28	5 33	4 95	3.26	4 60	5 99	3.46
Cr_2O_3	0 00	0 12	0 13	0.00	0 29	0.44	0 41	0 27	0 26	0 48	0.14	0 07	0 25	0 15	0.18	0.14	0 08	0 15	0.11	0.17	0.22	0.14
Fe_2O_3(c)	5 84	6.37	4 26	6 66	4.85	5 63	4.41	6.04	4.75	5 86	7 66	5.36	4.75	4 49	4.43	5 25	5.91	5 55	5 46	5.12	5 50	6 10
FeO(c)	2 69	0 07	1 19	2 59	2 52	2.38	3.11	1 84	2 96	2 07	2.13	2 22	3 69	3 91	3.19	2 11	2 72	2 73	1.97	2 74	3.65	1 80
MnO	0 20	0 04	0 02	0.13	0 17	0 15	0.14	0.16	0 12	0 23	0 22	0 09	0.16	0 14	0.14	0 16	0 23	0 15	0 08	0.12	0 13	0 14
MgO	14 27	15.32	15 31	13 54	14 86	14 27	13.65	13.90	15.05	14 55	14 19	15.71	14 08	14 23	14.83	15 47	13 82	14 39	15 70	14.42	13 80	15 43
CaO	22 68	24.32	23.78	23.19	21.92	22 87	21 50	22 36	22.09	22.46	21.70	21 83	22.39	22 47	21.85	22 06	22.04	22.05	21.76	22 14	21 84	21.65
Na_2O	0 25	0.18	0 21	0 25	0.32	0 30	0 33	0.35	0.30	0.30	0.40	0 20	0 20	0 22	0 24	0.22	0 24	0 21	0 22	0 23	0.25	0.21
K_2O	0.00	0.00	0 01	0.00	0 00	0 00	0 00	0 00	0.01	0 00	0.00	0.00	0 00	0 00	0.00	0 00	0 00	0.00	0 01	0 01	0.00	0 01
Total%	100 09	100.96	99 23	100.59	99 13	101 17	97 98	100.35	100 61	100 78	100.30	99 09	99 02	98 99	98 45	98 96	98 54	98.90	99.08	98 32	99 05	99.31
Si	1 802	1 807	1 848	1 77	1.82	1 784	1.774	1.745	1 82	1 782	1.76	1 87	1.79	1 792	1 821	1 868	1 801	1 812	1 871	1.824	1 772	1 863
Ti	0 016	0 008	0.008	0.021	0 011	0 014	0 015	0.015	0 012	0 014	0 02	0.011	0 016	0 014	0.011	0 01	0.015	0.015	0.01	0.014	0 018	0 012
Al/Al^{IV}	0 198	0 193	0 152	0 23	0.18	0 216	0 226	0 255	0 18	0.218	0 24	0 139	0 237	0 232	0.212	0.145	0 237	0.219	0 143	0.205	0.266	0 152
Al^{VI}	0.022	0.011	0 028	0.021	0 038	0 04	0.083	0 074	0.04	0 035	0.011											
Cr	0	0 004	0 004	0	0 009	0 013	0.012	0.008	0 008	0 014	0 004	0.002	0 007	0 004	0 005	0 004	0 002	0.004	0.003	0.005	0.007	0 004
Fe^{3+}	0.163	0.175	0.119	0.186	0 136	0 155	0.125	0.168	0.131	0 162	0 214	0.062	0 105	0 111	0 09	0.059	0 077	0 077	0.055	0.078	0.104	0 05
Fe^{2+}	0 083	0 002	0.037	0 08	0.078	0 073	0 098	0.057	0 091	0 064	0 066	0 168	0 15	0.141	0 139	0 164	0 187	0 174	0 17	0.162	0.173	0 19
Mn^{2+}	0 006	0 001	0 001	0.004	0 005	0 005	0 005	0.005	0 004	0.007	0 007	0 003	0 005	0 004	0 004	0 005	0 007	0.005	0.003	0.004	0 004	0 004
Mg	0 789	0 834	0 845	0.748	0 825	0.78	0.768	0.765	0 824	0 797	0 785	0 875	0.79	0 798	0 831	0 863	0 779	0.806	0.873	0.812	0 775	0.858
Ca	0 902	0.952	0.943	0 921	0.875	0 898	0 87	0.884	0 869	0.885	0 863	0 857	0 885	0 887	0 867	0 867	0 875	0 87	0 853	0.879	0 863	0.848
Na	0 018	0 013	0 015	0.018	0 023	0 021	0.024	0.025	0 022	0 022	0 029	0 014	0 015	0 016	0 018	0.016	0 017	0 015	0.016	0 017	0 019	0 015
K	0	0	0.001	0	0	0	0	0	0	0	0	0	0	0	0	0	0	0	0.001	0.001	0	0
Total cation	4	4	4	4	4	4	4	4	4	4	4	4	4	4	4	4	4	4	4	4	4	4
Wo%	46 42	48 47	48 48	47 50	45.60	46 99	46 62	47.05	45 28	46 21	44 60	43 61	45 74	45.70	44.90	44 28	45.45	45 03	43.65	45 43	44 97	43.49
En%	40 61	42 46	43.44	38.58	42 99	40 82	41 16	40 71	42.94	41 62	40 57	44.53	40.83	41 11	43.03	44 08	40.47	41.72	44.68	41.96	40 39	44 00
Fs%	12 97	9 06	8 07	13 92	11 41	12.19	12 22	12 24	11 78	12.17	14 83	11 86	13.44	13.19	12 07	11 64	14 08	13.25	11 67	12 61	14.64	12 51
Mg_{cpx}	76 23	82.49	84 42	73 77	79 40	77 38	77 50	77.27	78 78	77 91	73 71	79 19	75 60	76 00	78.40	79.47	74 69	76.25	79 51	77.19	73 67	78.14

Table G.5. Composition of Ti-magnetite microphenocrysts: Basalt Volcanoes Formation (BVF), Efaté Island Group, Vanuatu arc.

Ti-Magnetite	MAINLAND SUITE (MLS)																					
Analysis number	AR157-1	AR157-2	AR157-3	AR157-4	AR158-1	AR158-2	AR158-3	AR158-4	AR161-1	AR161-2	AR161-3	AR161-4	AR172-1	AR172-2	AR172-3	AR172-4	AR172-5	AR172-6	AR174-1	AR174-2	AR174-3	AR174-4	AR174-5
SiO_2	0 14	0 15	0 17	0 42	0.12	0.09	0.10	0.09	0.11	0 08	0 11	0.09	0 08	0.14	0 07	0.11	0.07	0.07	0 13	0.14	0.13	0.12	0.10
TiO_2	7.35	6.26	5 21	8 59	4.65	2 54	3 83	2 97	2 74	4.43	4 83	6 42	10 55	4.31	5 04	4.43	5 15	4.98	5 74	7 34	6 88	7 50	6.70
Al_2O_3	4.60	5 56	6 05	3.79	8 23	10 81	8.80	9.73	11.27	8.09	6 23	6.01	2.58	8.06	6.64	8 99	5 28	4 98	6.56	5.18	5.58	5.24	5.51
Cr_2O_3	0 91	0 36	0 65	0 24	0 68	8 68	0.94	7.45	6 53	4 60	1 09	2.91	0.00	0.02	0.00	0 18	0.10	0.12	0 07	0.06	0.02	0.00	0 00
Fe_2O_3(c)	48 15	49 15	50.82	46 73	50.70	43.72	52.51	46.63	45 40	47.31	51.71	47 20	45 43	53 21	52 37	50 95	53 15	53 39	49 85	49 20	49 61	48 51	50 51
FeO	33.32	31 60	31 13	35 31	30.68	25.69	28 56	26 59	26 13	30 18	31.48	31 47	37.74	28 54	31 83	30.69	32 82	32 43	32 16	34 18	33 67	34 20	33.51
V_2O_3	0 09	0 15	0 15	0.10	0.20	0 12	0 21	0 18	0 11	0 09	0.12	0.15	0 00	0 28	0 24	0.20	0.39	0.37	0.14	0.28	0 27	0.18	0.31
MnO	0.47	0 42	0.41	0.52	0 37	0 31	0 24	0 28	0.32	0 27	0 33	0 50	0 58	0 27	0 46	0 46	0.46	0.41	0.39	0 45	0.33	0.40	0 44
MgO	2 81	3 18	3 21	2.47	3 71	5 69	4 82	5.63	5 68	3 84	2 92	3 68	1.66	5 03	2 79	3 57	2 12	2 10	2 92	2 63	2 82	2 64	2 85
ZnO	0.12	0 16	0 00	0 09	0 00	0 00	0 00	0 10	0 02	0 07	0 06	0 11	0 14	0 03	0 25	0 20	0 25	0 27	0 00	0.16	0 01	0 06	0.00
NiO	0.04	0.07	0 04	0 00	0 00	0 09	0 10	0 01	0 10	0 00	0 10	0 06	0 00	0 05	0 12	0 00	0.00	0 06	0 03	0 00	0.03	0.01	0.01
Total	98.00	97.06	97.85	98.26	99 34	97 74	100 10	99 66	98 41	98 95	98 99	98 59	98 76	99 93	99.82	99 79	99.79	99 18	97 98	99 62	99.35	98 86	99 94
Si	0 01	0 01	0 01	0 02	0.00	0 00	0 00	0 00	0.00	0.00	0 00	0 00	0 00	0 01	0.00	0 00	0.00	0.00	0 01	0 01	0.01	0.00	0.00
Ti	0 21	0 18	0 15	0.24	0.13	0 07	0.10	0.08	0.07	0 12	0 13	0.18	0 30	0 12	0 14	0.12	0.14	0.14	0.16	0.20	0.19	0.21	0 18
Al^{VI}	0.20	0.24	0.26	0.17	0.35	0 45	0.37	0 40	0 47	0 34	0 27	0 26	0.11	0.34	0.28	0.38	0.23	0.22	0.29	0.22	0.24	0 23	0 24
Cr	0 03	0 01	0 00	0 01	0 02	0 24	0 03	0 21	0.18	0 13	0.03	0 08	0.00	0 00	0.00	0 01	0.00	0.00	0.00	0.00	0.00	0 00	0 00
Fe^{3+}	1 35	1 38	1 41	1 31	1 37	1 16	1.39	1.23	1 20	1.28	1 42	1 30	1 28	1.42	1 43	1.37	1.47	1.49	1 38	1.35	1.36	1.34	1.38
Fe^{2+}	1 04	0.99	0.96	1.10	0 92	0 76	0.84	0.78	0.77	0.91	0 96	0 96	1 19	0.84	0 97	0 91	1.01	1.00	0 99	1.05	1 03	1 05	1.02
Fe^{2+}/Fe^{3+}	0 77	0 71	0 68	0.84	0.67	0.65	0 60	0 63	0 64	0.71	0.68	0 74	0.92	0 60	0 68	0.67	0 69	0.67	0.72	0.77	0.75	0.78	0.74
V	0.00	0 01	0.00	0 00	0.01	0.00	0 01	0 01	0 00	0 00	0.00	0 00	0 00	0 01	0 01	0.01	0.01	0.01	0 00	0 01	0.01	0.01	0.01
Mn^{2+}	0 02	0 01	0.01	0 02	0.01	0.01	0.01	0.01	0.01	0 01	0.01	0.02	0 02	0.01	0 01	0 01	0.01	0 01	0.01	0.01	0.01	0.01	0 01
Mg	0 16	0 18	0 18	0 14	0.20	0 30	0 25	0 29	0 30	0 21	0 16	0 20	0 09	0.27	0 15	0.19	0 12	0.12	0.16	0 14	0 15	0 15	0 15
Zn	0 00	0 00	0 00	0 00	0.00	0.00	0 00	0.00	0 00	0.00	0.00	0 00	0 00	0 00	0.01	0 01	0.01	0.01	0.00	0.00	0 00	0.00	0 00
Ni	0 00	0.00	0.00	0 00	0 00	0 00	0.00	0 00	0.00	0 00	0 00	0 00	0 00	0 00	0 00	0 00	0.00	0 00	0.00	0 00	0.00	0 00	0 00
Total Cation	3 00	3.00	3.00	3 00	3.00	3 00	3 00	3 00	3 00	3 00	3 00	3 00	3.00	3.00	3.00	3.00	3.00	3.00	3.00	3.00	3 00	3 00	3.00
TiO_2 %	8 28	7 19	5 98	9 48	5.41	3 53	4.51	3 90	3.69	5 41	5 49	7.54	11 26	5 01	5 65	5.15	5 65	5 48	6.54	8 09	7.63	8.31	7.39
Fe_2O_3 %	54 21	56 49	58 31	51.56	58 93	60.76	61.85	61 20	61.13	57.75	58 75	55 47	48 47	61 83	58.68	59 20	58 33	58 80	56.81	54.23	55 02	53.77	55.68
FeO %	37 51	36 32	35 72	38 96	35 66	35 71	33 64	34 90	35.18	36.84	35 76	36.98	40 27	33 16	35 67	35 66	36 02	35 72	36 65	37.68	37.34	37.91	36.94

Table G.5. (cont.). Composition of Ti-magnetite microphenocrysts: Basalt Volcanoes Formation (BVF), Efaté Island Group, Vanuatu arc.

Ti-Magnetite	MAINLAND SUITE (MLS)											OFFSHORE SUITE (OSS)										
Analysis number	AR174-6	AR174-7	AR174-8	AR174-9	AR174-10	AR175-1	AR175-2	AR175-3	AR175-4	AR175-5	AR175-6	AR006-1	AR006-2	AR006-3	AR006-4	AR006-5	AR006-6	AR006-7	AR006-8	AR006-9	AR006-10	AR006-11
SiO_2	0.12	0 14	0 15	0.13	0 14	0 07	0.06	0.31	0 21	0 18	0 11	n-a	n-a	n-a	n-a	n-a	n-a	n-a	n-a	n-a	n-a	n-a
TiO_2	7 11	5 18	7 76	4 83	7 69	8 11	8.18	6 46	7.84	6 82	4.60	4.32	3.39	7 50	4.31	3.51	4 99	4 52	4.94	8 42	8 93	8.12
Al_2O_3	5 41	6 73	4.76	8.19	5 51	3 21	3 08	2 28	4 27	5 60	7 91	6 95	8 42	4 29	7 00	7 82	7 09	6 96	6 57	3.42	2 88	3 74
Cr_2O_3	0.01	0 38	0 07	0.07	0 06	0.37	0.30	0 11	0.23	1 17	1 11	0 42	0 34	0 15	0 48	0 37	0.44	0.42	0 13	0 18	0 10	0.10
Fe_2O_3(c)	49.48	50 41	48.07	51 43	48.44	49 24	49.36	51 95	48.46	49 24	50.93	54.04	54.29	51 85	53 61	56.51	53.14	53.65	53 63	49.40	48.94	50.30
FeO	34 05	30 46	34 76	29 87	34 42	34 65	34.98	33.95	34 49	33 90	31 02	31 16	28.31	35 15	30 68	29.54	31 38	31 02	31 71	35 55	36.01	35 46
V_2O_3	0 31	0 14	0 26	0 30	0 24	0 22	0.27	0.36	0 24	0 25	0 23	0 44	0 42	0 73	0 47	0 46	0 54	0.50	0 53	0.82	0.82	0.74
MnO	0.42	0 42	0.46	0 27	0 36	0 57	0.40	0.42	0 39	0 38	0 32	0 37	0.30	0 49	0 42	0.28	0 36	0.41	0 36	0 58	0 46	0.56
MgO	2 70	3.52	2 35	4 40	2 88	2.35	2 27	1 72	2 66	2 88	3.49	3 17	4 50	2 40	3 32	4 27	3.55	3 33	3 16	2 09	2 07	2.18
ZnO	0 00	0.19	0.02	0 07	0 00	0 00	0.00	0 13	0 00	0 00	0 12	0.01	0 10	0 11	0.08	0.03	0.04	0.07	0 00	0 05	0 00	0 15
NiO	0.00	0 01	0 03	0 04	0.08	0 03	0 07	0.00	0.03	0 06	0 00											
Total	99 62	97 58	98 69	99 61	99.83	98 83	98 97	97 67	98 82	100 47	99.85	101 16	100 34	103.16	100.69	103 10	101.88	101.22	101.37	101.04	100 75	101 84
Si	0 00	0.01	0.01	0 01	0.01	0 00	0 00	0.01	0 01	0 01	0.00											
Ti	0 20	0 14	0 22	0 13	0 21	0 23	0.23	0.19	0 22	0 19	0 12	0.12	0.09	0 20	0 12	0 09	0 13	0 12	0 13	0.23	0 25	0 22
Al^{VI}	0.23	0 29	0 21	0 34	0.24	0 14	0 14	0 10	0 19	0 24	0.33	0 29	0.35	0 18	0 30	0 32	0 29	0 29	0.28	0 15	0.12	0 16
Cr	0 00	0 01	0 00	0.00	0.00	0 01	0 01	0 00	0 01	0 03	0 03	0 01	0 01	0.00	0 01	0 01	0 01	0.01	0.00	0.01	0.00	0.00
Fe^{3+}	1.36	1.40	1.34	1 38	1.32	1.38	1 39	1 49	1 35	1 34	1 37	1 45	1.45	1 39	1 44	1 47	1 41	1 44	1.44	1 36	1.35	1.37
Fe^{2+}	1 04	0.94	1 08	0 89	1.05	1.08	1 09	1 08	1 07	1 02	0.93	0 93	0 84	1.05	0 92	0 86	0 93	0.92	0.95	1 09	1.11	1.07
Fe^{2+}/Fe^{3+}	0 76	0 67	0 80	0 65	0.79	0 78	0 79	0 73	0 79	0 77	0 68	0.64	0.58	0 75	0.64	0.58	0 66	0.64	0 66	0 80	0 82	0 78
V	0.01	0 00	0.01	0 01	0.01	0 01	0 01	0 01	0 01	0 01	0 01	0 02	0 02	0 03	0 02	0 02	0 02	0 02	0 02	0 03	0.03	0 03
Mn^{2+}	0 01	0 01	0 02	0 01	0.01	0 02	0 01	0 01	0 01	0 01	0 01	0.01	0.01	0 01	0 01	0 01	0 01	0.01	0 01	0 02	0 01	0 02
Mg	0 15	0.19	0.13	0 23	0 16	0.13	0 13	0 10	0 15	0 16	0.19	0 17	0 24	0 13	0 18	0 22	0.19	0.18	0 17	0 11	0.11	0 12
Zn	0 00	0 01	0 00	0 00	0 00	0 00	0.00	0 00	0 00	0 00	0 00	0 00	0.00	0 00	0 00	0.00	0.00	0 00	0 00	0.00	0.00	0 00
Ni	0 00	0 00	0 00	0 00	0.00	0.00	0 00	0.00	0.00	0 00	0 00											
Total Cation	3.00	3 00	3 00	3 00	3.00	3 00	3 00	3 00	3 00	3 00	3 00	3 00	3 00	3.00	3 00	3 00	3.00	3.00	3.00	3.00	3 00	3 00
TiO_2 %	7 84	6 02	8 57	5 61	8 49	8 82	8 84	6 99	8 64	7 58	5 31	4 82	3 94	7 94	4.86	3 92	5.57	5.07	5.47	9 02	9 51	8 65
Fe_2O_3 %	54 59	58 58	53 06	59 71	53.50	53 52	53 35	56 25	53.38	54 74	58 84	60 37	63.14	54.87	60 51	63.09	59.37	60 15	59 41	52.91	52.14	53.58
FeO %	37.57	35 40	38 37	34 68	38.01	37.66	37 81	36 76	37.99	37 68	35.84	34 80	32.92	37 19	34 63	32.98	35.06	34 78	35.12	38 07	38 36	37.77

Table G.5. (cont.). Composition of Ti-magnetite microphenocrysts: Basalt Volcanoes Formation (BVF), Efaté Island Group, Vanuatu arc.

Ti-Magnetite	OFFSHORE SUITE (OSS)													HIGH-K/HIGH-Rb Suite (HKRS)			
Analysis number	AR006-12	AR006-13	AR109-1	AR109-2	AR109-3	AR109-4	AR105-1	AR105-2	AR105-3	AR105-4	AR105-5	AR114-1	AR114-2	AR198-1	AR198-2	AR198-3	AR198-4
SiO_2	n-a	n-a	0 14	0 13	0 09	0 13	0 14	0 12	0 11	0 15	0 09	0.04	0.01	n-a	n-a	n-a	n-a
TiO_2	6 97	4 23	7 03	1.38	8 01	4 68	4 60	4.17	3.99	4 25	4.15	5.15	4 90	9 27	9.51	10 46	7.40
Al_2O_3	4.70	6 79	6 20	5 40	4 67	7.39	9 91	9 28	9 20	9.86	9 62	2.76	2 56	2.52	2 69	2 40	3.58
Cr_2O_3	0 12	0 08	0 17	0.07	0.08	0.12	1 26	1 15	1.90	1 28	1 11	1 40	3 79	0.61	0.79	0.71	0 90
Fe_2O_3(c)	51 64	55 30	47.97	60.94	48.20	52.55	48.67	50 80	50 39	49.60	50 68	56.34	54.24	47.89	46 93	46 27	51.00
FeO	33 81	31.02	34 72	30 37	36 21	32 50	30 22	28 94	29 78	28.64	29 85	28 14	27 82	36.54	36 19	37 61	35 04
V_2O_3	0 68	0 45	0 20	0.56	0.18	0.25	0 32	0 31	0 25	0 33	0 30	0.06	0.02	0.57	0 60	0.62	0 42
MnO	0 50	0.41	0 38	0 22	0 32	0 25	0 18	0 32	0 26	0 28	0 30	0 52	0 48	0.57	0.47	0.54	0.48
MgO	2 71	3.30	2.20	2 03	1.78	2 76	4 37	4 76	4 17	5 06	4 31	4 78	4 64	1.77	2.15	1 96	2.06
ZnO	0 06	0 03	0.08	0.07	0.02	0.06	0 04	0 06	0 09	0 04	0 00	0 13	0.22	0 11	0.05	0 07	0 13
NiO			0 00	0 04	0 00	0 03	0 01	0 08	0 07	0 02	0 09	0 03	0 06				
Total	101.63	101 90	99 09	101 21	99 56	100 73	99 71	99 99	100 22	99 50	100 49	99 35	98 75	100 22	99.78	101 03	101 26
Si			0 01	0 01	0 00	0 01	0.01	0.00	0 00	0 01	0 00	0 00	0 00				
Ti	0 19	0 11	0 19	0 04	0 22	0 13	0.12	0 11	0 11	0 11	0.11	0 14	0.14	0 26	0 27	0 29	0.20
Al^{VI}	0 20	0 28	0 27	0.23	0 20	0 31	0 41	0.39	0 38	0 41	0.40	0.12	0.11	0 11	0 12	0 10	0.15
Cr	0 00	0 00	0 01	0 00	0.00	0 00	0 04	0.03	0 05	0 04	0 03	0 04	0.11	0 02	0 02	0 02	0 03
Fe^{3+}	1 40	1 48	1 32	1 67	1 34	1 42	1 29	1 35	1 34	1.31	1.34	1 55	1 51	1 34	1 31	1 28	1 40
Fe^{2+}	1 02	0 92	1 07	0 92	1.12	0 97	0.89	0 85	0 88	0.84	0.88	0.86	0 86	1.13	1.12	1 15	1 07
Fe^{2+}/Fe^{3+}	0 73	0 62	0 80	0.55	0.83	0·69	0.69	0 63	0.66	0.64	0 65	0.56	0 57	0 85	0 86	0 90	0 76
V	0.03	0.02	0 01	0 02	0.01	0 01	0 01	0 01	0 01	0 01	0 01	0 00	0 00	0 02	0 02	0.03	0 02
Mn^{2+}	0.02	0 01	0 01	0 01	0.01	0.01	0.01	0 01	0 01	0 01	0.01	0 02	0 02	0 02	0 01	0 02	0 01
Mg	0 15	0 17	0 12	0 11	0 10	0.15	0 23	0 25	0 22	0 27	0 23	0 26	0 26	0 10	0.12	0.11	0.11
Zn	0 00	0 00	0.00	0.00	0 00	0.00	0 00	0.00	0 00	0 00	0.00	0 00	0 01	0 00	0 00	0 00	0 00
Ni			0 00	0 00	0 00	0.00	0.00	0.00	0.00	0 00	0 00	0 00	0 00				
Total Cation	3 00	3 00	3 00	3.00	3 00·	3 00	3 00	3 00	3.00	3 00	3 00	3 00	3 00	3 00	3 00	3 00	3 00
TiO_2 %	7.54	4 67	7 84	1 49	8 67	5.22	5 51	4 97	4 74	5 15	4 90	5 75	5 63	9 89	10 27	11 08	7 91
Fe_2O_3 %	55.88	61 07	53 47	65 75	52 15	58.56	58.29	60 54	59 87	60 13	59 85	62 86	62 37	51 11	50 66	49 05	54.59
FeO %	36 58	34 26	38 70	32 77	39 18	36 22	36 20	34.49	35.38	34.72	35 25	31 40	31 99	39 00	39.07	39.87	37.50

APPENDIX H

MICROPROBE GROUNDMASS ANALYSES: BASALT VOLCANOES FORMATION

Major element (and some trace element) oxide contents were determined for BVF groundmasses by electron microprobe analysis on polished thin sections. All electron microprobe analyses were collected using the Cameca Camebax SX-50 automated electron microprobe located at the University of Tasmania's Central Science Laboratory. This machine is equipped with four wavelength-dispersive spectrometers, used for quantitative analysis, and one energy-dispersive spectrometer, used for qualitative spectral analysis. X-ray lines used for analyses were calibrated against international and in-house natural minerals, synthetic simple oxides and glass standards.

Groundmass scan analyses were collected with operating conditions set at 20 kV accelerating voltage, and 10 nA beam current, with a 120 μm diameter beam. Peak and background counting times, analysing crystal used, and working detection limits for each element are given in Table H.1. Background counting times were measured twice, once on either side of the peak. For elements where peak and background counting times are the same, the background was measured once only, on one side of the peak for analytical reasons.

Table H.1. Peak and background counting times for elements analysed during analysis of BVF groundmasses on the electron microprobe.

ELEMENT	Si	Ti	Al	Fe	Mn	Mg	Ca	Na	K	P	Sr	Ba	Cr	Ni
Analysing crystal	TAP	PET	TAP	LiF	LiF	TAP	PET	TAP	PET	PET	TAP	PET	LiF	LiF
Peak (s)	10	10	10	10	10	10	10	20	10	10	20	20	15	10
Background (s)	10	5	5	5	5	5	5	10	5	10	20	10	8	5
Detection limit (wt%)	0.09	0 04	0 05	0 07	0.07	0.05	0 04	0 09	0.04	0.07	0.06	0.08	0 06	0 08

Detection limits were calculated following Ancey et al. (1978).

Analyses of the finest grained groundmasses from samples of each of the three BVF suites are given in Tables H.2 to H.4. All analyses were normalised to 100 wt% to account for beam and spectrometer defocussing artefacts.

Table H.2. Groundmass compositions of Mainland Suite (MLS) sample AR153.

SUITE	MAINLAND SUITE (MLS)									
	AR153-1	AR153-2	AR153-3	AR153-4	AR153-5	AR153-6	AR153-7	AR153-8	AR153-9	*AR153-av*
Major Elements (wt%)										
SiO_2	50.82	48 07	49.10	48 99	52 05	49 96	49.64	50.54	48.85	*49.78*
TiO_2	0.53	1 18	0 67	1 36	0 16	0.69	0 80	0.62	0.64	*0.74*
Al_2O_3	21 79	17 23	18.86	16 01	25 30	20.75	17 28	17.95	21.15	*19.59*
FeO*	5 22	9 92	6 53	10 15	3 06	8.27	8 13	7 06	8 05	*7.38*
MnO	0 10	0 24	0 11	0 22	0 04	0 20	0 13	0 21	0.21	*0 16*
MgO	3 48	5 34	5 72	4.56	1 91	4 15	5 35	5.05	3 59	*4 35*
CaO	12 51	12 45	14 19	11.34	11 62	8 95	12 71	12.41	11 36	*11 95*
Na_2O	3 63	3 27	2 99	3.55	4 16	4 14	3 39	3 67	3.75	*3 61*
K_2O	0 74	0.64	0 49	1.47	0 62	1 08	0.85	0 83	0.65	*0 82*
P_2O_5	0 25	0 31	0 28	0 98	0 30	0 60	0 51	0 51	0.44	*0.47*
Total	98 51	99 31	98 64	98 79	98 39	99 01	99.03	98.91	98 91	
Mg#	54 30	48 97	60 96	44 50	52.66	47.19	53 99	56 03	44 31	*51 43*
Trace Elements (ppm)										
Sr	2506	1574	1954	1625	3104	2005	1891	2168	2672	*2167*
Ba	428	507	471	351	161	552	212	477	334	*388*
Cr	0.7	10.0	103 0	0 7	93 2	0 7	93 3	132 5	214.1	*72.0*
Ni	1 6	1.6	1.6	20.7	166.1	1 6	247 6	1.6	20 7	*51 4*

Major element oxides determined from electron microprobe scans using a large (120 μm) diameter beam.

Table H.3. Groundmass compositions of Offshore Suite (OSS) sample AR184.

SUITE	OFFSHORE SUITE (OSS)									
	AR184-1	AR184-2	AR184-3	AR184-4	AR184-5	AR184-6	AR184-7	AR184-8	AR184-9	*AR184-av*
Major Elements (wt%)										
SiO_2	49.99	50.71	48 58	48.19	50 49	48 59	47 50	50.74	48 28	*49 23*
TiO_2	0 71	0.50	0 65	0.62	0 65	0.84	0 99	0.55	0 71	*0 69*
Al_2O_3	17 40	21.18	17.94	20.46	18.00	19.71	18 91	19 17	17 67	*18.94*
FeO*	9 11	6.98	9 51	9.16	8.24	9.13	10 77	7 10	10 34	*8 93*
MnO	0.18	0 18	0 16	0 27	0.21	0 14	0 17	0 25	0 29	*0 21*
MgO	4.92	3 26	5 83	4 96	4.88	3 95	4.40	4 40	6.04	*4 74*
CaO	11.37	11 30	12 09	10 85	11.56	11 72	11 41	12 24	11 01	*11 51*
Na_2O	3.33	3.46	2.90	3 07	3 24	3 31	3.28	3.22	3 02	*3 20*
K_2O	1.14	1 03	0.78	0 89	1 23	0 98	0 87	0.97	0 91	*0.98*
P_2O_5	0.53	0 27	0.26	0 20	0 36	0 31	0 24	0.18	0 28	*0.29*
Total	98 61	98 83	97.69	100 11	99 24	98 91	99 42	97.10	97.59	
Mg#	49.05	45 44	52.21	49.12	51 33	43.54	42 15	52 51	51 02	*43.64*
Trace Elements (ppm)										
Sr	2000	2331	1457	1845	1635	1871	1556	2007	1515	*1802*
Ba	273	619	578	667	308	325	513	1035	718	*560*
Cr	73.2	2.4	6.7	0.7	0.7	5 9	62 6	103 6	49 4	*33 9*
Ni	124 3	1 6	20.9	102 0	1 6	227 2	1.6	1.6	1.6	*53 6*

Major element oxides determined from electron microprobe scans using a large (120 μm) diameter beam.

Table H.4. Groundmass compositions of High-K/High-Rb Suite (HKRS) sample AR198.

SUITE	HIGH-K/HIGH-RB SUITE (HKRS)									
	AR198-1	AR198-2	AR198-3	AR198-4	AR198-5	AR198-6	AR198-7	AR198-8	AR198-9	*AR198-av*
Major Elements (wt%)										
SiO_2	50 88	51 25	48.98	49 13	52 23	48 78	49 44	49.28	46 18	*49.57*
TiO_2	0.69	0 42	0.70	0 60	0 37	0.97	0.88	0.74	1.39	*0.75*
Al_2O_3	17 18	20.58	17.85	17.71	19 83	19.31	17.77	17.86	17 82	*18.43*
FeO*	9 20	6.04	9.52	9 00	5.45	8 73	9 23	8.29	12 92	*8.71*
MnO	0.25	0.14	0.26	0.18	0.18	0 18	0 22	0.21	0 23	*0.21*
MgO	6.45	4 36	6 41	6.02	4.68	3 95	5 32	5 38	4.80	*5.26*
CaO	9 22	11 15	10.58	11.28	11.35	11 55	10.76	12 59	9 46	*10 88*
Na_2O	3 05	3.61	3 06	3.18	3.42	3.45	3 26	2 99	3 05	*3 23*
K_2O	1 55	1 18	0.86	0 93	1.35	1 16	1.55	1 10	1 59	*1 25*
P_2O_5	0 23	0.29	0.41	0 62	0.27	0.59	0.26	0 42	0 90	*0 44*
Total	99 58	100.66	98.84	99.74	98.75	99.12	99 89	98 65	100 49	
Mg#	55 55	56 24	54.55	54.40	60.46	44.62	50 69	53.66	39 85	*52.22*
Trace Elements (ppm)										
Sr	1741	2161	1962	2048	2288	2482	1726	1728	1735	*1986*
Ba	165	78	289	445	2	404	148	2	2	*171*
Cr	88 6	109.4	0.7	48.7	0.7	52 1	46.9	54 4	0.7	*44.7*
Ni	164.1	81 2	247.3	409.7	1.6	1 6	368.2	1.6	1.6	*141 9*

Major element oxides determined from electron microprobe scans using a large (120 μm) diameter beam.

APPENDIX I

PLAGIOCLASE ADDITION CALCULATIONS AND RESULTS: BVF

The possibility of deriving the BVF rocks from a 'normal' southern Vanuatu arc magma composition by accumulation of plagioclase was investigated. The results of addition of a calcic plagioclase to (1) a basaltic, (2) a basaltic andesitic, and (3) an andesitic composition from the 'normal' southern part of the Vanuatu arc are presented in Figures I.1–I.3. The plagioclase was added to each composition in stepwise increments at 5, 10, 15, 20, 25, 30, 35, 40, 50, 60, 70, 80, 90, and 100%. These initial rock compositions, and the added plagioclase composition are given in Table I.1.

Table I.1. Initial rock compositions and added plagioclase composition from Tanna Island used in plagioclase addition calculations.

COMPOSITION	BASALT	BASALTIC ANDESITE	ANDESITE	PLAGIOCLASE
Sample number	TA93	Tan5C	Tan3B	An_{80} in TA93
Major Elements (wt%)				
SiO_2	47.51	56.05	60.31	48.38
TiO_2	0.82	0.76	0.78	0.01
Al_2O_3	16.08	17.48	16.70	31.62
FeO*	11.30	8.21	7.25	0.92
MnO	0.22	0.23	0.19	0.00
MgO	7.77	3.06	2.06	0.10
CaO	12.46	6.62	4.84	16.41
Na_2O	1.83	4.33	4.34	2.22
K_2O	0.59	1.89	3.23	0.09
P_2O_5	0.16	0.47	0.50	
L.O.I.	0.80	0.19	0.18	
Totals	100.27	100.64	99.34	99.75
Trace Elements (ppm)				
Rb	7.70	31	47	1
Sr	424	547	476	300
Cs	0.31			
Ba	120	580	765	900
Sc	26	18	15	
V	349	238	157	
Cr	81	22	5	
Ni	30	16	6	
Cu	148			
Zn	67			
La	3.54	15.25	15.25	0.16
Ce	8.13			0.40
Pr	1.16			
Nd	6.47	21.00	23.00	0.14
Sm	1.67			0.05
Eu	0.74	1.45	1.55	0.16
Gd	1.74			0.04
Tb	0.27			0.03
Dy	1.97	4.40	5.10	0.04
Ho	0.47			
Er	1.14	3.00	3.10	0.03
Tm	0.16			
Yb	1.12	2.65	3.05	0.05
Lu	0.20			0.01
Y	12.90	27.0	30.5	0.36
Zr	25.10	101	122	
Nb	0.36	1.4	1.5	0.02
Hf	0.76			
Pb	2.60			
Th	0.41			0.01
U	0.22			0.01

TA93 analysis from Peate *et al.* (1997). Tan3B and Tan5C analyses from Robin *et al.* (1994a). TA93 plagioclase analysis from Coulon *et al.* (1981).

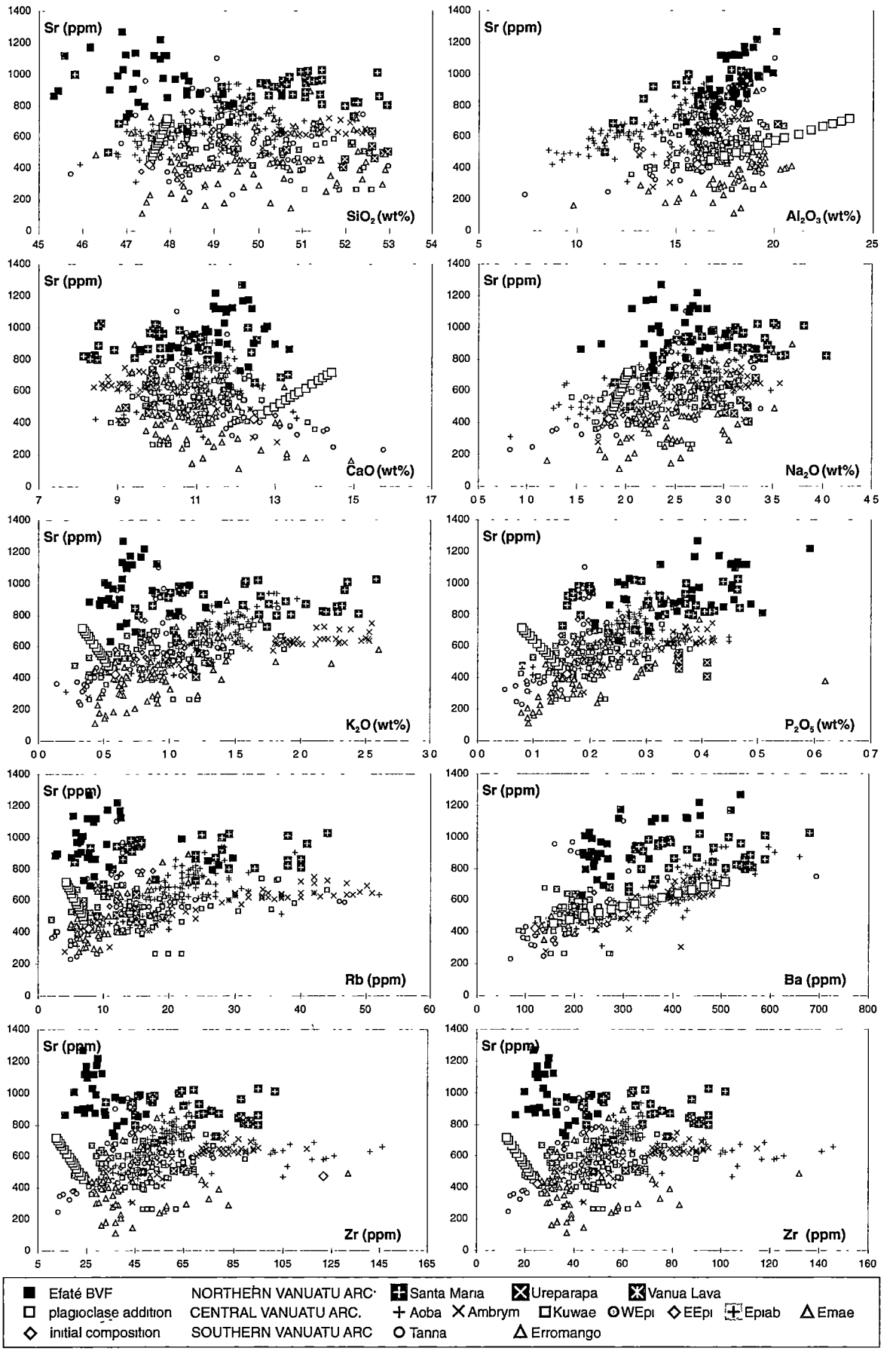

Figure I.1. Results of plagioclase addition to Tanna basalt TA93. Note that addition of plagioclase cannot produce rocks/magmas with a BVF composition, even for 100% addition. Vanuatu arc basalt data source is ORSTOM database from Monzier *et al.* (1997).

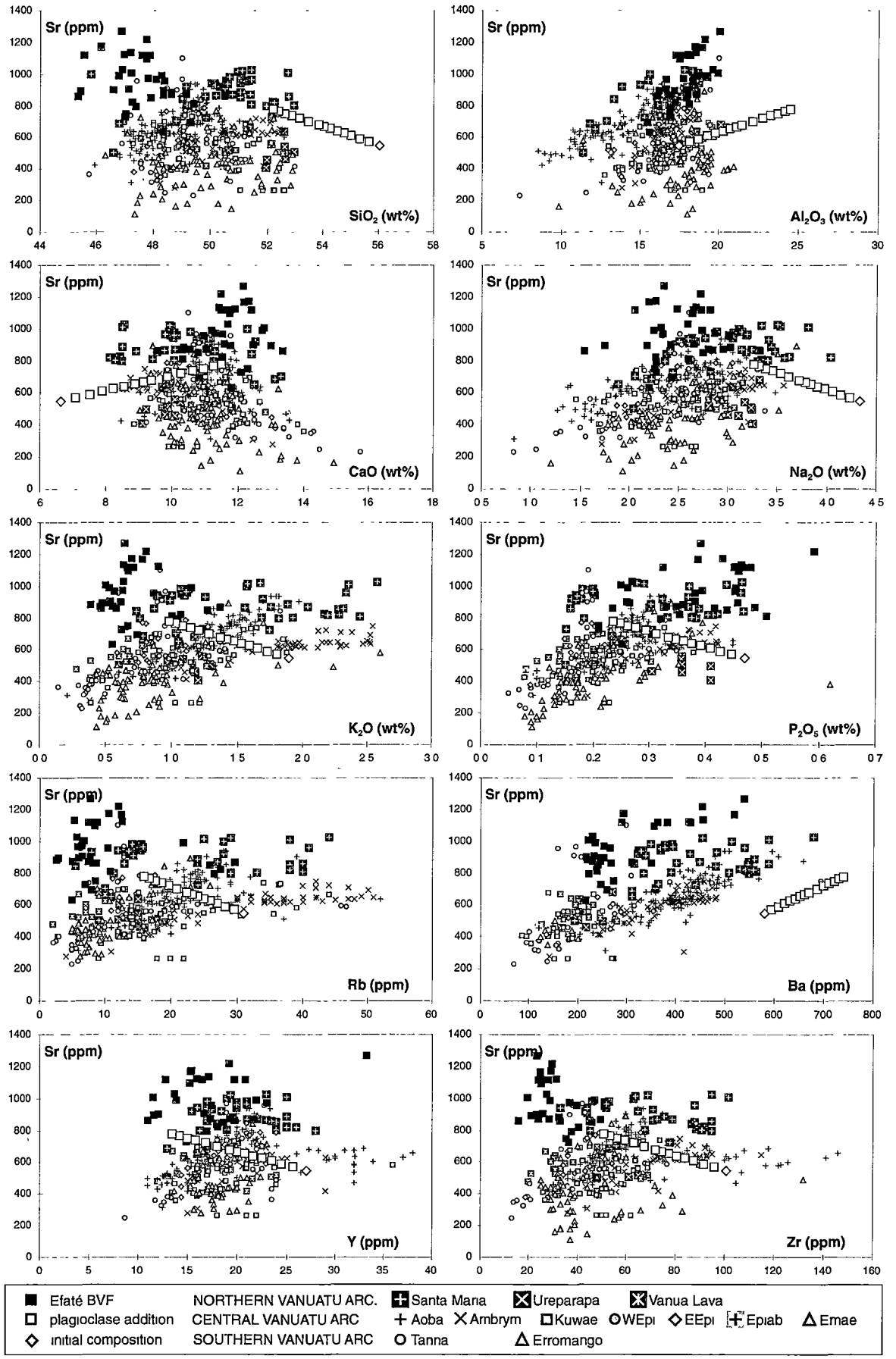

Figure I.2. Results of plagioclase addition to Tanna basaltic andesite Tan5C. Note that addition of plagioclase cannot produce rocks/magmas with a BVF composition, even for 100% addition. Vanuatu arc basalt data source is ORSTOM database from Monzier *et al.* (1997).

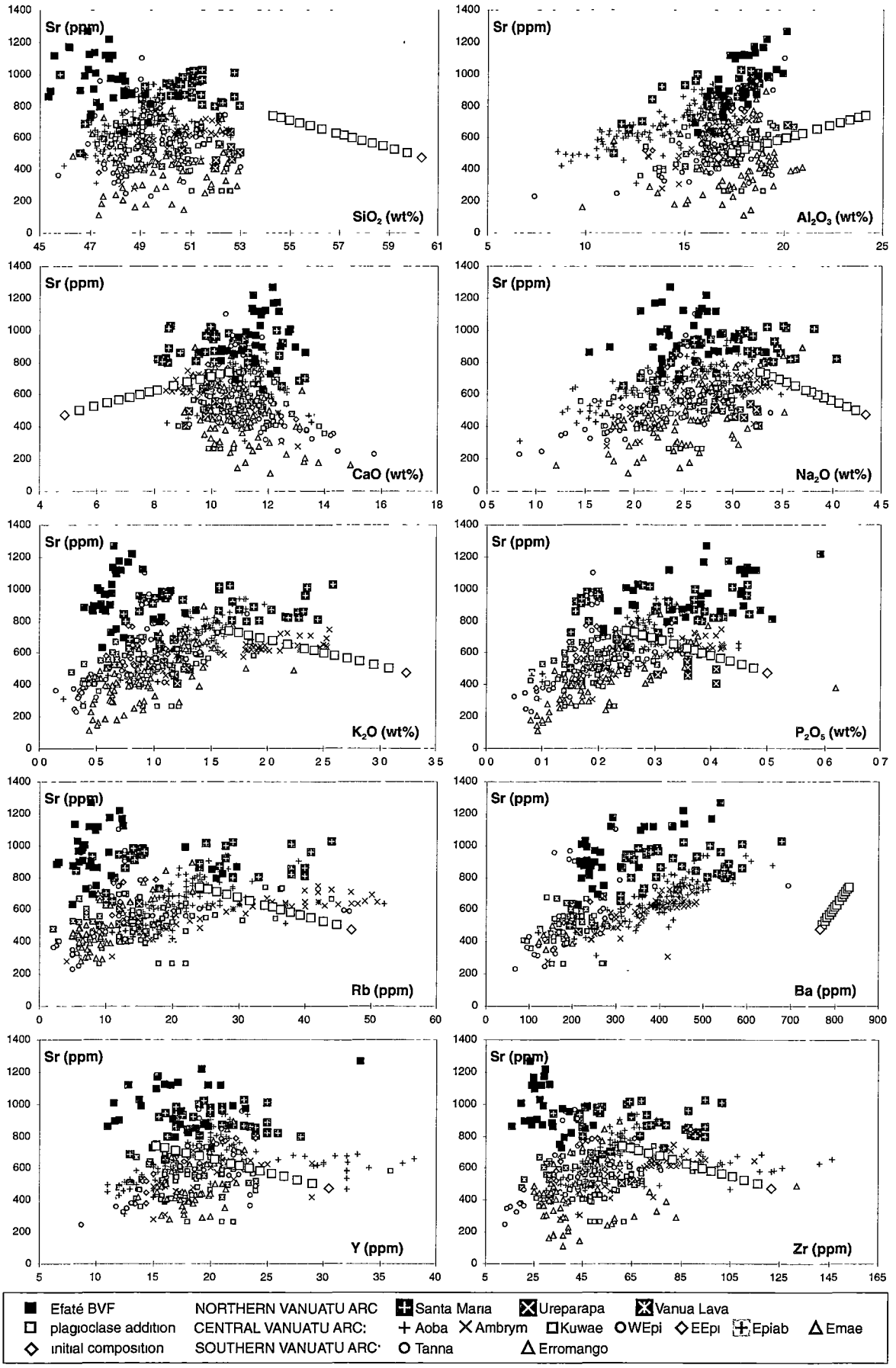

Figure I.3. Results of plagioclase addition to Tanna andesite Tan3B. Note that addition of plagioclase cannot produce rocks/magmas with a BVF composition, even for 100% addition. Vanuatu arc basalt data source is ORSTOM database from Monzier *et al.* (1997).

APPENDIX J

MICROPROBE MINERAL ANALYSES: EFATÉ PUMICE FORMATION

Chemical analyses for major and minor element oxides were made on individual mineral grains using polished thin sections and epoxy resin grain mounts. All electron microprobe analyses were collected using the Cameca Camebax SX-50 automated electron microprobe located at the University of Tasmania's Central Science Laboratory. This machine is equipped with four wavelength-dispersive spectrometers, used for quantitative analysis, and one energy-dispersive spectrometer, used for qualitative spectral analysis. X-ray lines used for analyses were calibrated against international and in-house natural minerals, synthetic simple oxides and glass standards.

Operating conditions were set at 15 kV accelerating voltage and a beam current of 25 nA (measured in the Faraday cup). A 10 μm diameter beam was used for all analyses, mainly to overcome Na migration in feldspars. Peak and background counting times, analysing crystal used, and working detection limits for each element are given in Table J.1. Background counting times measured twice, once on either side of the peak. For elements where peak and background counting times are the same, the background was measured once only, on one side of the peak for analytical reasons.

Table J.1. Peak and background counting times, analysing crystals used and working detection limits for elements analysed during routine mineral analysis on the electron microprobe.

ELEMENT	Si	Ti	Al	Fe	Mn	Mg	Ca	Na	K	P	Rb*	Sr
Analysing crystal	TAP	PET	TAP	LiF	LiF	TAP	PET	TAP	PET	PET	TAP	PET
Peak (s)	10	10	10	10	10	10	10	20	10	10	20	30
Background (s)	5	5	5	5	5	5	5	10	5	10	20	15
Detection limit (wt%)	0 03	0.04	0 03	0.08	0 06	0.03	0.03	0 04	0.03	0 05	0.10	0.12
ELEMENT	Ba	V	Cr	Ni*	Zn*	La*	Ce*	Y*	Zr*	F*	S*	Cl*
Analysing crystal	PET	LiF	LiF	LiF	LiF	LiF	LiF	PET	TAP	PC0	PET	PET
Peak (s)	20	30	15	10	10	30	30	20	10	30	30	20
Background (s)	10	15	8	5	5	15	15	10	10	30	15	10
Detection limit (wt%)	0 17	0.08	0 06	0 12	0 21	0.08	0.05	0 11	0 07	0.15	0 03	0.03

Detection limits were calculated following Ancey *et al.* (1978). * Denotes elements that were not analysed in all analytical runs.

Structural formulae were calculated using Formula One software installed on the Cameca Camebax SX-50. Mineral analyses of phenocrysts and microphenocrysts from the Efaté Pumice Formation are given in Tables J.2 to J.5.

A ternary plot of Ti-magnetite compositions for EPF trachydacites is given in Figure J.1.

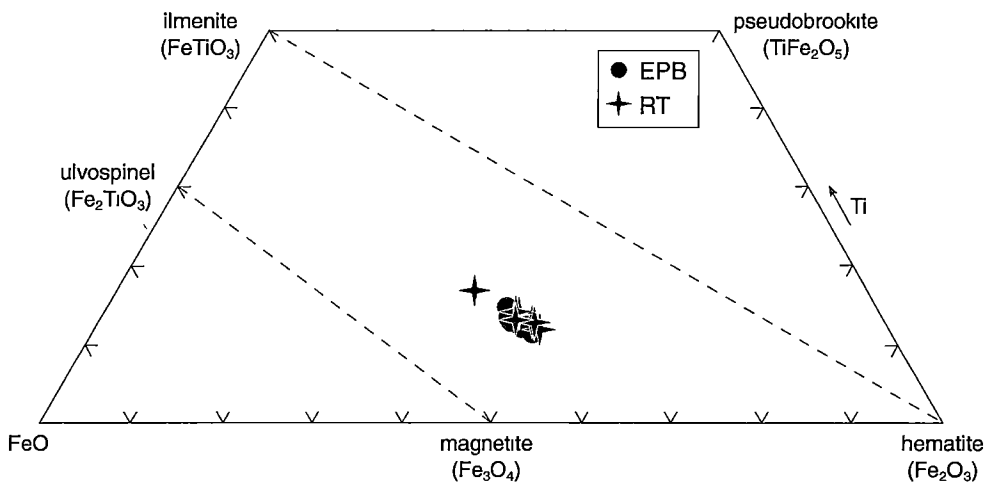

Figure J.1. Ti-magnetite compositions for Efaté Pumice Formation (EPF) trachydacites, Efaté Island Group, Vanuatu arc, southwest Pacific. EPB = Efaté Pumice Breccias, RT = Rentabau Tuffs.

Table J.2. Compostion of plagioclase phenocrysts: Efaté Pumice Formation (EPF), Efaté Island Group, Vanuatu arc.

Plagioclase	EFATE PUMICE BRECCIAS (EPB)																								
Analysis	AR208-	AR208-	AR208-	AR208-	AR208-	AR208-	AR208-	AR208-	AR208-	AR208-	AR208-	AR208-	AR207-	AR207-	AR207-	AR207-	AR207-	AR207-	AR207-	AR207-	AR207-	AR207-	AR207-	AR207-	AR207-
number	1	2	3	4	5	6	7	8	9	10	11	12	1	2	3	4	5	6	7	8	9	10	11	12	13
SiO_2	55 70	58 59	60.43	60.15	59 74	59,45	60 00	58 87	59 58	57 87	58.40	59.31	59 48	59 65	57 11	57 52	58 33	58 88	55.76	55.62	55 02	54.88	58 40	57 34	58.08
TiO_2	0 01	0 06	0 03	0 03	0 02	0 05	0 03	0 03	0 05	0 06	0 02	0 03	0 02	0 05	0.04	0 05	0 02	0.06	0 06	0.04	0 05	0.05	0 04	0 04	0 05
Al_2O_3	27 28	25.70	24 19	24.70	24 75	24 55	24 67	25 67	24 66	25 83	25 48	25 00	25 28	24 79	26.65	25.81	25 39	24 57	27 34	27.37	27 51	27 80	25.46	25.90	25.22
Fe_2O_3	0 64	0 59	0 37	0 52	0 50	0.43	0.40	0 48	0.54	0 46	0 47	0.48	0 52	0 51	0 49	0.42	0 53	0 47	0 64	0.65	0 62	0 61	0.55	0.63	0 55
MnO																									
MgO	0 05	0 03	0 02	0 02	0 03	0 03	0 03	0.03	0.02	0 04	0 04	0 03	0.03	0 05	0 03	0 05	0 02	0 03	0.03	0.04	0.05	0.04	0.04	0 04	0 04
CaO	9 27	7 27	5 52	6 28	6 29	6 14	6.17	7 02	6 54	8 00	7 35	6 99	6 91	6 44	8 56	7 94	7 25	6 59	9 64	9 86	9.91	9.96	7 35	7.96	7 15
SrO	0 30	0 29	0 29	0.26	0 26	0 27	0 23	0.30	0 25	0 27	0 30	0.30	0 24	0 27	0.28	0.30	0 33	0.28	0 32	0.33	0 32	0.34	0 28	0 30	0.25
BaO	0 10	0 19	0 27	0 19	0 24	0 23	0.28	0 23	0 20	0.12	0 18	0 23	0 23	0.24	0 14	0 16	0 17	0 24	0 09	0 08	0.15	0 04	0 16	0 20	0.16
Na_2O	5.92	6 89	7 56	7 17	7 18	7 24	7 29	6.91	7 02	6.63	6.80	6.96	6 91	7.14	6 24	6 60	6 83	6 94	5.80	5 69	5.63	5 47	6 89	6.46	6 71
K_2O	0 64	0 94	1 59	1 32	1 30	1 26	1 29	1 03	1 27	0 89	1 01	1 08	1 08	1.20	0 79	0 84	0.96	1 17	0 60	0 57	0.60	0 51	1.00	0.88	0 88
P_2O_5																									
Rb_2O	0 02	0 00	0 00	0.00	0.00	0 00	0 00	0 00	0.00	0 00	0 00	0 00	0 00	0 00	0 00	0 00	0.00	0 01	0 01	0 01	0.01	0 03	0.00	0 00	0 00
Total %	99 93	100.54	100 27	100.63	100 31	99 65	100 40	100 58	100 13	100.17	100.05	100.42	100.71	100.34	100 32	99.70	99.82	99 24	100 29	100 25	99 87	99 72	100 18	99.76	99 08
Sr (ppm)	2537	2452	2452	2199	2199	2283	1945	2537	2114	2283	2537	2537	2029	2283	2368	2537	2790	2368	2706	2790	2706	2875	2368	2537	2114
Ba (ppm)	896	1702	2418	1702	2150	2060	2508	2060	1791	1075	1612	2060	2060	2150	1254	1433	1523	2150	806	717	1343	358	1433	1791	1433
Si	2.521	2 623	2 706	2 683	2 675	2 679	2 683	2 633	2 673	2 603	2 627	2.656	2 653	2 671	2 568	2 6	2.63	2 666	2.516	2 512	2.498	2 491	2 625	2.593	2 634
Ti	0	0 002	0.001	0 001	0 001	0 002	0 001	0 001	0 002	0.002	0 001	0.001	0 001	0 002	0 001	0 002	0.001	0 002	0 002	0.001	0 002	0.002	0 001	0.001	0.002
Al/Al^{IV}	1.455	1.356	1 277	1 298	1 306	1.303	1.3	1 353	1.304	1.369	1.351	1.319	1 329	1 308	1 412	1.375	1.349	1.311	1.454	1.457	1.472	1 487	1.349	1.38	1 348
Al^{VI}	1.455	1 356	1 277	1 298	1 306	1.303	1 3	1 353	1 304	1.369	1.351	1.319	1 329	1 308	1 412	1.375	1.349	1 311	1 454	1 457	1.472	1.487	1.349	1.38	1 348
Fe^{3+}	0.022	0 02	0 012	0 017	0 017	0 015	0 013	0 016	0 018	0 016	0 016	0 016	0 017	0 017	0 017	0 014	0.018	0 016	0.022	0 022	0 021	0 021	0.019	0.022	0 019
Mn^{2+}																									
Mg	0 004	0 002	0 001	0 001	0 002	0 002	0 002	0.002	0 001	0 003	0 003	0.002	0 002	0 003	0 002	0.003	0 001	0 002	0.002	0 003	0.003	0 003	0.003	0 003	0 002
Ca	0 45	0.349	0 265	0 3	0 302	0 297	0 296	0.336	0 315	0 386	0.354	0.335	0.33	0 309	0 412	0.385	0.35	0 32	0 466	0 477	0.482	0 485	0.354	0 386	0.347
Sr	0.008	0 007	0.008	0 007	0.007	0 007	0 006	0 008	0.007	0 007	0.008	0.008	0 006	0 007	0.007	0.008	0.009	0 007	0.008	0 009	0.009	0 009	0.007	0.008	0.007
Ba	0 002	0 003	0 005	0 003	0 004	0 004	0.005	0 004	0 004	0 002	0 003	0 004	0.004	0 004	0 003	0.003	0.003	0 004	0 002	0 001	0.003	0 001	0.003	0.003	0.003
Na	0 52	0 598	0.656	0 62	0 624	0 632	0 632	0 599	0.611	0 578	0.593	0.605	0 598	0 62	0 544	0 579	0.597	0 609	0.507	0 498	0.496	0 481	0.601	0.567	0 59
K	0 037	0 054	0 091	0 075	0 074	0 073	0.074	0 059	0.073	0.051	0.058	0 062	0.062	0 069	0.046	0.049	0.055	0 068	0.034	0 033	0 035	0.03	0.058	0.051	0.051
P																									
Rb	0.001	0	0	0	0	0	0	0	0	0	0	0	0	0	0	0	0	0	0	0	0	0.001	0	0	0
Total cation	5.019	5 013	5.022	5 006	5.011	5 013	5 012	5 011	5.006	5 017	5 014	5 009	5 003	5 009	5 011	5 017	5 012	5.007	5.014	5.013	5 02	5.009	5 019	5.014	5 002
Albite %	51 64	59.74	64.82	62.31	62.40	63.07	63 07	60 26	61.16	56.95	59.00	60.38	60.40	62 12	54 29	57 16	59.58	61.08	50.35	49.40	48 96	48.29	59 33	56.47	59.72
Anorthite %	44 69	34 87	26.19	30 15	30 20	29 64	29.54	33 80	31 53	38 03	35 22	33.43	33.33	30 96	41 12	38 01	34 93	32.10	46 28	47 32	47 58	48.69	34.95	38.45	35 12
Orthoclase %	3 67	5.39	8 99	7 54	7.40	7 29	7 39	5.94	7.31	5 02	5.77	6.19	6.26	6 91	4 59	4 84	5.49	6 82	3 38	3 27	3.46	3 01	5.73	5 08	5 16

Table J.2. (cont.). Compostion of plagioclase phenocrysts: Efaté Pumice Formation (EPF), Efaté Island Group, Vanuatu arc.

Plagioclase	EFATE PUMICE BRECCIAS (EPB)																								
Analysis	AR207-	AR024-	AR024-	AR024-	AR024-	LI961-	LI961-	LI961-	LI961-	LI961-	LI961-	LI961-	LI961-	LI961-	LI961-	AR084-	AR084-	AR084-	AR084-	AR084-	AR084-	AR084-	AR084-	AR084-	AR084-
number	14	1	2	3	4	1	2	3	4	5	6	7	8	9	10	1(C)	1(R)	2	3(C)	3(R)	4	5	6	7	8
SiO_2	58 37	58 54	55.57	57.42	57 11	57 58	55.78	58 79	57.47	55.34	56.92	56.88	56.77	56.58	56 04	56 99	58.44	58.85	55.22	58 82	56 31	55 83	57.72	59 48	56.95
TiO_2	0 04	0 03	0 04	0.04	0 05	0 02	0 05	0.03	0 05	0 03	0 05	0 06	0.07	0.04	0 03	0.03	0 03	0 02	0 01	0.04	0 04	0.03	0.03	0.02	0.05
Al_2O_3	25 67	25 80	28 08	26.64	26.70	26 20	27 53	25 44	26.40	27.42	26.33	26.98	26 53	26 64	27 37	26 25	25.30	25 21	27 86	24 79	26.70	26.93	25 67	24 77	26 27
Fe_2O_3	0 58	0 49	0 56	0 75	0 51	0 53	0.65	0 59	0 55	0.51	0 63	0 55	0 60	0 57	0.63	0 68	0.61	0 65	0.60	0 65	0.69	0.67	0.67	0 60	0 68
MnO		0 13	0.00	0.05	0.01	0.01	0 04	0 00	0 00	0 00	0.01	0 00	0 00	0 00	0 06	0.05	0 00	0 00	0 01	0.00	0 00	0.04	0.00	0.03	0.03
MgO	0 04	0.03	0 06	0 06	0 05	0 02	0 05	0 05	0.03	0 01	0 03	0.04	0 05	0 05	0 07	0 02	0 05	0 03	0 05	0.02	0 07	0 05	0.04	0.03	0 05
CaO	7 66	7 17	9 69	8.28	8.45	7 95	9 28	7 10	8.08	9.22	8 41	8 88	8.73	8 64	9 21	8.55	7 19	7.03	10 07	6.80	9 07	9.23	7 84	6.30	8 40
SrO	0 29	0 18	0 16	0 17	0 13	0.23	0 13	0 30	0 20	0 22	0 18	0 19	0 23	0.17	0 18	0 00	0 00	0 00	0 00	0.00	0 00	0.00	0 00	0 00	0.00
BaO	0 16	0 07	0 10	0 02	0.18	0 13	0 17	0 18	0 17	0 16	0 13	0 16	0 08	0.04	0 07	0.14	0 09	0 19	0 08	0 14	0 10	0.08	0 17	0.23	0.17
Na_2O	6 75	6 48	5.34	6 14	6 05	6.09	5 46	6 39	5 97	5 58	5 89	5 70	5 82	5.86	5.58	5.87	6.35	6.52	5 20	6.49	5 54	5.42	6 03	6.82	5 81
K_2O	0.96	1 02	0.56	0.78	0.70	0.86	0 60	0.95	0 84	0 62	0 77	0 75	0 73	0 69	0.64	0 72	1.02	1.05	0 53	1.06	0 69	0 66	0 89	1 30	0.71
P_2O_5		0 01	0.00	0 02	0 04	0 01	0 07	0 00	0 01	0 02	0.04	0 00	0 06	0 00	0 00	0 04	0 01	0.01	0 01	0 02	0 03	0 09	0 04	0.02	0 08
Rb_2O	0 00	-	-	-	-	-	-	-	-	-	-	-	-	-	-	-	-	-	-	-	-	-	-	-	-
Total %	100.51	99 95	100.16	100 36	99.98	99 64	99 81	99 82	99 76	99.15	99 37	100.19	99 67	99 27	99 88	99.34	99 09	99 56	99.63	98.82	99 25	99 02	99.10	99 60	99 20
Sr (ppm)	2452	1522	1353	1438	1099	1945	1099	2537	1691	1860	1522	1607	1945	1438	1522	0	0	0	0	0	0	0	0	0	0
Ba (ppm)	1433	627	896	179	1612	1164	1523	1612	1523	1433	1164	1433	717	358	627	1273	818	1727	727	1273	909	727	1545	2091	1545
Si	2 616	2.628	2.503	2 574	2.57	2 598	2 52	2 642	2.59	2 519	2 578	2 557	2 565	2 564	2 53	2 583	2 645	2.653	2.503	2.667	2 557	2.541	2 617	2.679	2 583
Ti	0 001	0 001	0 001	0.001	0.002	0.001	0 002	0.001	0 002	0.001	0.002	0 002	0.002	0 001	0 001	0.001	0 001	0.001	0	0.001	0 001	0.001	0 001	0.001	0 002
Al/Al ^{IV}	1 356	1.365	1 49	1.408	1 416	1.393	1.466	1 348	1 402	1.471	1.405	1 43	1 413	1.423	1 456	1.402	1 35	1.339	1.489	1 325	1 429	1.445	1 372	1.315	1 404
Al ^{VI}	1 356	0	0	0	0	0	0	0	0	0	0	0	0	0	0	0	0	0	0	0	0	0	0	0	0
Fe^{3+}	0 02	0 016	0 019	0 025	0 017	0 018	0.022	0.02	0 019	0 018	0 021	0.019	0 02	0 019	0.021	0 016	0.014	0 015	0.014	0 015	0 017	0.016	0 016	0 014	0 016
Mn^{2+}		0 005	0	0 002	0 001	0	0 001	0	0	0	0	0	0	0	0 002	0.002	0	0	0 001	0	0	0 001	0	0.001	0 001
Mg	0 002	0 002	0 004	0 004	0 003	0 002	0.004	0.003	0.002	0 001	0 002	0 003	0 003	0.003	0 004	0 002	0 003	0.002	0 004	0 001	0 005	0 003	0 003	0 002	0 004
Ca	0 368	0 345	0 468	0 398	0 408	0 384	0 449	0 342	0.39	0 45	0 408	0.428	0 423	0 419	0.445	0 415	0 348	0.34	0.489	0 33	0 442	0 45	0.381	0 304	0 408
Sr	0 008	0.005	0 004	0.005	0.003	0 006	0 003	0 008	0 005	0 006	0 005	0 005	0 006	0 005	0 005	0	0	0	0	0	0	0	0	0	0
Ba	0.003	0 001	0 002	0	0.003	0.002	0 003	0.003	0 003	0.003	0 002	0.003	0.001	0 001	0.001	0 003	0 002	0.003	0.001	0 002	0.002	0.001	0 003	0.004	0.003
Na	0.586	0 564	0.466	0 534	0 528	0.532	0.478	0 557	0 522	0 492	0 517	0 497	0 51	0 515	0.489	0.516	0 558	0 569	0.457	0.57	0.488	0 479	0 53	0.595	0 51
K	0.055	0 058	0.032	0.045	0 04	0.05	0.034	0.054	0 048	0.036	0 044	0 043	0.042	0 04	0.037	0 042	0.058	0 06	0.031	0 061	0.04	0 038	0.052	0 075	0.041
P		0 001	0	0 001	0 002	0 001	0 003	0	0	0.001	0 002	0	0 002	0	0	0 001	0	0 001	0.001	0.001	0 001	0 004	0 002	0.001	0.003
Rb	0	-	-	-	-	-	-	-	-	-	-	-	-	-	-	-	-	-	-	-	-	-	-	-	-
Total cation	5 015	4 991	4 99	4.996	4 993	4 986	4 987	4 978	4.983	4 998	4 986	4.986	4 988	4.99	4 993	4 983	4 98	4.983	4 989	4 975	4.981	4 98	4.976	4.99	4.976
Albite %	58 08	58 32	48 24	54 66	54.10	55 07	49 74	58.45	54.38	50 31	53 35	51.34	52.31	52 87	50.36	53 03	57 88	58.72	46.78	59.31	50.31	49 53	55.04	61.09	53.18
Anorthite %	36 47	35.68	48 45	40 74	41 80	39 75	46 72	35 89	40.63	46 01	42 11	44.21	43.38	43 02	45 83	42 65	36 10	35.09	50.05	34.34	45 57	46.54	39.56	31.21	42 54
Orthoclase %	5.45	6.00	3 31	4 61	4.10	5.18	3.54	5 67	5.00	3 68	4 54	4 44	4.31	4 11	3 81	4 32	6.02	6.19	3 17	6.35	4.12	3 93	5 40	7.70	4 28

Table J.2. (cont.). Compostion of plagioclase phenocrysts: Efaté Pumice Formation (EPF), Efaté Island Group, Vanuatu arc.

Plagioclase	EPB			RENTABAU TUFFS (RT)													
Analysis	AR084-	AR084-	AR084-	AR101-	AR101-	AR101-	AR101-	AR101-	AR101-	AR101-	AR101-	AR101-	AR101-	AR101-	AR101-	AR101-	AR101-
number	9	10	11	1(C)	1(R)	2(C)	2(R)	3	4	5	6	7	8	9	10	11(C)	11(R)
SiO_2	58 70	59 91	57 88	57 00	56.73	57 53	56.23	55 92	59 91	58 96	57.02	54 36	59.48	58.97	59 09	45.51	48 25
TiO_2	0 06	0 06	0 02	0 05	0.04	0 05	0 04	0.04	0 11	0.05	0 07	0 06	0 04	0.03	0 02	0 05	0.04
Al_2O_3	25 01	24 15	25.92	26.80	26.64	26 03	26 78	27 13	24.71	24 76	26.21	27 88	24 93	25 54	25 41	32.76	31 00
Fe_2O_3	0 62	0 61	0 67	0 61	0.54	0.56	0.61	0 61	0.49	0 59	0 54	0.64	0 42	0 56	0 55	1.09	1 35
MnO	0.00	0 02	0 06	0.00	0 01	0.00	0.05	0.00	0.02	0.02	0.03	0.00	0.02	0 02	0 01	0.01	0 00
MgO	0.04	0 00	0 05	0 05	0.07	0 05	0.05	0.06	0.04	0 04	0 04	0.05	0 03	0 06	0.04	0 14	0 18
CaO	7 05	5 74	7 97	8.86	9.10	8.44	9 09	9.66	6 87	7.01	8 70	10.67	6 85	7 69	7.62	17 23	15 48
SrO	0 00	0 00	0 00	0.00	0 00	0 00	0 00	0.00	0 00	0.00	0.00	0.00	0 00	0 00	0 00	0 00	0 00
BaO	0 16	0 26	0.13	0 10	0 15	0 06	0 02	0 15	0 13	0.14	0.08	0 00	0 20	0 11	0.11	0 01	0 02
Na_2O	6.47	6 74	6 10	5.80	5 72	6 06	5.68	5.59	6 72	6.63	6.02	4.91	6.71	6 54	6.44	1.43	2 50
K_2O	1 02	1.42	0 78	0 61	0 57	0 64	0 55	0.46	0 79	0 81	0 52	0 38	0.82	0.62	0 75	0 11	0 18
P_2O_5	0 00	0 03	0 00	0 06	0 00	0 04	0.06	0.04	0.05	0.00	0.00	0 00	0 00	0 02	0 00	0 08	0 03
Rb_2O	-	-	-	-	-	-	-	-	-	-	-	-	-	-	-	-	-
Total %	99 12	98 94	99 58	99.94	99.57	99.46	99 17	99.66	99.84	99 02	99 24	98 96	99 51	100 16	100 05	98 40	99 03
Sr (ppm)	0	0	0														
Ba (ppm)	1455	2364	1182	896	1343	537	179	1343	1164	1254	717	0	1791	985	985	90	179
Si	2 656	2 71	2 612	2 564	2 563	2 596	2.55	2.53	2.68	2 664	2 582	2 48	2 672	2 636	2.644	2.135	2 24
Ti	0 002	0 002	0 001	0 002	0.002	0 002	0 001	0 002	0 004	0 002	0 002	0 002	0 001	0 001	0 001	0.002	0 001
Al/Al^{IV}	1 334	1 288	1 379	1 42	1 419	1 384	1.432	1 446	1 303	1 319	1 398	1 499	1 32	1 346	1 34	1.811	1.696
Al^{VI}	0	0	0	0	0	0	0	0	0	0	0	0	0	0	0	0	0
Fe^{3+}	0 014	0 014	0 016	0 02	0.019	0 019	0 021	0 021	0 017	0 02	0.018	0 022	0 014	0 019	0.019	0.038	0 047
Mn^{2+}	0	0 001	0 002	0	0	0	0 002	0	0 001	0 001	0 001	0	0 001	0 001	0	0	0
Mg	0.003	0	0.003	0.003	0.005	0.003	0 003	0.004	0.003	0 003	0.003	0.003	0.002	0 004	0 002	0 01	0 012
Ca	0 342	0 279	0 385	0 427	0.441	0 408	0 442	0 468	0 329	0 34	0.422	0.522	0 33	0 368	0.365	0.866	0 77
Sr	0	0	0	0	0	0	0	0	0	0	0	0	0	0	0	0	0
Ba	0 003	0.005	0 002	0 002	0.003	0 001	0	0.003	0 002	0 002	0 001	0	0 004	0.002	0.002	0	0
Na	0 567	0.591	0 534	0 506	0.501	0 53	0 5	0.49	0 583	0.581	0.528	0.434	0.585	0 567	0 559	0 13	0 225
K	0 058	0 082	0 045	0 035	0.033	0 037	0.032	0.026	0 045	0 047	0 03	0 022	0.047	0 035	0 043	0.006	0.011
P	0	0 001	0	0.002	0	0.002	0.002	0 002	0 002	0	0	0	0	0.001	0	0 003	0 001
Rb	-	-	-	-	-	-	-	-	-	-	-	-	-	-	-	-	-
Total cation	4 98	4 972	4.98	4 981	4 984	4 982	4.985	4 991	4.968	4.978	4 987	4 985	4.975	4 98	4 976	5 002	5.003
Albite %	58.63	62.08	55.39	52 27	51.38	54 36	51 33	49.80	60 92	60 02	53.88	44 38	60 81	58.45	57.81	12.97	22.37
Anorthite %	35.37	29.31	39.94	44.11	45.23	41.85	45.38	47.56	34 38	35.12	43.06	53.37	34.30	37 94	37 75	86.43	76.54
Orthoclase %	6 00	8.61	4.67	3 62	3 38	3.79	3.29	2.64	4 70	4 86	3.06	2 25	4 89	3 61	4.45	0 60	1 09

Table J.3. Composition of orthopyroxene pheoncrysts: Efaté Pumice Formation (EPF), Efaté Island Group, Vanuatu arc.

Orthopyroxene	EFATE PUMICE BRECCIAS (EPB)																						
Analysis	AR024-	AR024-	AR024-	AR084-	AR084-	AR084-	AR084-	AR084-	AR084-	AR084-	AR084-	AR084-	AR084-	AR084-	AR207-	AR207-	AR207-	AR207-	AR207-	AR207-	AR207-	AR207-	AR207-
number	1	2	3	1	2	3	4	5	6	7	8	9	10	11	1	2	3	4	5	6	7	8	9	10
SiO_2	52 33	52 52	53 29	52 59	53 25	53 28	52 84	52.92	53 61	52 80	52 51	53 37	53 20	52 48	52.55	52 71	52 78	52.88	53.15	53 11	53 51	53 21	52 23	52 81
TiO_2	0 20	0 24	0 21	0 29	0 26	0.20	0 22	0 28	0 18	0 23	0 18	0.22	0 22	0 27	0.30	0 27	0 20	0.18	0.23	0 23	0 24	0 16	0.25	0 27
Al_2O_3	0 48	0 72	0 56	0 51	0.62	0.45	0 42	0.81	0 63	0 69	0 33	0 60	0 60	0 98	0.75	0 52	0 46	0.38	0.82	0.75	0 68	0 57	0.73	0 75
Cr_2O_3	0 05	0 00	0 02	0.00	0.00	0.00	0 00	0 00	0 00	0 00	0.02	0 05	0 02	0 01	0.00	0 02	0.00	0.01	0.03	0 00	0.02	0 02	0 00	0.00
Fe_2O_3(c)	2 33	1 72	0 55	0 00	0 00	0.00	0 00	0.00	0 00	0 23	0 00	0 00	0 00	0 12	2 09	2 36	1.08	0 89	1.64	1.27	1 95	1 28	3.36	1 47
FeO(c)	20 55	18 71	19 28	20 90	19 15	19 35	21 75	19.25	17 59	19 15	21 00	19 30	19 33	19 34	18.84	18 43	19 12	18.87	17.85	16.73	16 30	17.64	16.30	17 27
MnO	1 60	1 33	1.33	1 47	1 12	1 34	1 48	1 15	0 94	1 26	1 57	1.36	1 23	1.14	1 90	1 68	1.89	1 68	1 38	1.31	1.32	1.41	1.48	1 37
MgO	21 31	22.58	22.97	21 34	22 99	22 21	21 17	22.78	23 83	22 83	21 35	22.85	22 64	22.55	22 40	22.99	22 47	22.72	23.80	24 30	24 90	23.84	23.95	23 90
CaO	1 72	1.75	1.63	1.72	1 72	1.71	1 63	1 73	1.63	1 62	1 50	1.60	1 67	1 66	1 72	1 55	1 61	1.68	1 52	1 61	1 58	1.63	1.61	1.59
Na_2O	0 08	0 07	0 04	0 02	0 03	0.03	0.04	0 03	0.04	0 03	0.03	0 04	0 04	0 03	0 04	0 03	0.03	0 03	0.03	0.05	0 04	0.03	0.03	0.02
K_2O	0 01	0 04	0.01	0 01	0.01	0 02	0 00	0 00	0 01	0 00	0 02	0 00	0 00	0 01	0 02	0 01		0 01		0 02				
Total%	100 66	99 69	99.90	98.84	99 16	98 57	99 55	98.95	98.48	98 83	98 53	99 39	98 97	98 61	100 59	100.58	99 65	99.33	100 45	99.37	100 53	99.79	99.93	99 45
Si	1 953	1 957	1.976	1 986	1.983	1.999	1.987	1 977	1 993	1.976	1 991	1 985	1.987	1 97	1 948	1.949	1 97	1 975	1.954	1.962	1.953	1.966	1.931	1 956
Ti	0 006	0 007	0 006	0.008	0.007	0 006	0 006	0 008	0 005	0 007	0 005	0 006	0 006	0.008	0.008	0 007	0 006	0.005	0 006	0.006	0.007	0 004	0 007	0 007
Al/Al^{IV}	0 021	0 031	0.024	0 014	0 017	0.001	0 013	0 023	0 007	0.024	0 009	0 015	0 013	0.03	0.033	0.023	0 02	0 017	0 036	0.033	0.029	0 025	0 032	0 033
Al^{VI}				0.008	0.01	0.019	0 006	0 013	0 02	0 006	0 005	0.012	0 014	0 013										
Cr	0 002										0 001	0 001							0 001			0.001		
Fe^{3+}	0 065	0.048	0.015							0 007				0.003	0 058	0.066	0 03	0 025	0.045	0.035	0.054	0 036	0.093	0.041
Fe^{2+}	0 641	0 583	0 598	0 66	0 597	0 607	0 684	0.601	0 547	0 599	0 666	0 6	0 604	0 607	0 584	0 57	0 597	0.589	0 549	0 517	0.498	0.545	0 504	0 535
Mn^{2+}	0 051	0 042	0.042	0 047	0 035	0.042	0 047	0 037	0 03	0 04	0 05	0 043	0 039	0.036	0.06	0 052	0 06	0 053	0 043	0.041	0 041	0 044	0.046	0.043
Mg	1 186	1 254	1 27	1 201	1 277	1 242	1.186	1 269	1 32	1 274	1 206	1 267	1 261	1 262	1 238	1 267	1.25	1 265	1 304	1.338	1.354	1.313	1 32	1 32
Ca	0 069	0 07	0 065	0 07	0 069	0 069	0 066	0 069	0.065	0 065	0 061	0 064	0 067	0 067	0.068	0 062	0 065	0 067	0 06	0 064	0.062	0 064	0 064	0.063
Na	0 006	0.005	0 003	0 001	0 002	0 002	0.003	0 002	0 003	0.002	0 002	0 003	0 003	0.002	0 003	0 002	0.002	0 003	0 002	0.003	0.002	0 002	0 002	0 002
K	0 001	0 002	0 001		0.001	0 001					0 001				0.001					0.001				
Total cation	4	4	4	3 996	3 998	3 987	3 999	3 998	3.99	4	3 998	3 996	3 994	4	4	4	4	4	4	4	4	4	4	4
Wo%	3 43	3 51	3.27	3.54	3 49	3 52	3 33	3.49	3 31	3 27	3.08	3 24	3 40	3 39	3.39	3 07	3 25	3.35	3 00	3.21	3.09	3.20	3.16	3 15
En%	58 95	62 79	63.82	60.72	64.56	63 37	59 81	64.22	67 28	64.18	60.82	64.18	63 98	63 90	61 65	62 82	62 44	63.28	65.17	67 07	67 40	65 58	65.12	65.93
Fs%	37 62	33 70	32.91	35.74	31 95	33 11	36 86	32.29	29 41	32 54	36 11	32 57	32 62	32 71	34 96	34 11	34 32	33.37	31.83	29 72	29.52	31 22	31 72	30.92
Mg_{opx}	62 68	66 53	67.45	64 54	68 14	67 17	63.42	67 86	70 70	67.77	64 42	67 86	67 61	67 41	65 85	66 58	66 60	67 32	68.70	70 79	71.04	69 32	68 86	69.62

Table J.3. (cont.). Composition of orthopyroxene pheoncrysts: Efaté Pumice Formation (EPF), Efaté Island Group, Vanuatu arc.

Orthopyroxene	EFATE PUMICE BRECCIAS (EPB)															RENTABAU TUFFS (RT)						
Analysis	AR207-	AR208-	AR208-	LI961-	LI961-	LI961-	LI961-	LI961-	LI961-	LI961-	LI961-	LI961-	LI961-	LI961-	LI961-	AR101-	AR101-	AR101-	AR101-	AR101-	AR101-	AR101-
number	11	1	2	1	2	3	4	5	6	7	8	9	10	11	12	1	2	3	4	5	6	7
SiO_2	52 90	53 24	50 94	53 04	52.33	50 85	52 58	51 77	52 27	52 43	52 59	52.90	52.16	53 03	52.43	52 65	52.69	52.97	52.84	52 75	52 22	52.90
TiO_2	0 21	0 20	0.22	0 23	0.26	0 25	0 16	0.23	0 23	0 22	0 25	0 20	0 24	0 20	0.18	0.31	0.24	0 25	0 23	0.25	0 30	0.23
Al_2O_3	0 74	0 57	4.07	0 67	0 52	0 57	0 49	0 73	0 55	0 54	0 65	0 67	0 94	0 43	0 61	0 60	0.56	0.39	0 55	0 53	0 53	0.63
Cr_2O_3	0 00	0.00	0.00	0 04	0.01	0 00	0.00	0 00	0 00	0.00	0.00	0 00	0.00	0 02	0 00	0.02	0.00	0 02	0.00	0 00	0 03	0.02
Fe_2O_3(c)	2 26	1.97	0 93	0 55	1 07	1.03	1 44	0.84	1 07	1 47	1 14	0.70	1 62	0 19	0 94	0 00	0 00	0.00	0 00	0.00	0.00	0.00
FeO(c)	16 66	18 11	17.77	18.70	21 05	21 75	19 86	20 82	20 77	20 39	20 21	18.93	18 83	19 70	19 13	20 41	18 32	18.66	18 12	18 23	19.47	17 97
MnO	1 29	1 56	1.51	1 28	1 36	1.55	1 25	1 26	1.42	1 39	1 28	1.15	1 20	1.15	1 27	1 29	1 10	1 70	1.37	1 25	1 06	1 14
MgO	24 26	23 49	22 18	23 09	21 29	19.91	22 25	21.18	21 42	21 75	21 97	23 11	22 64	22.68	22 49	21.39	23 22	22.33	22.83	22.66	21 79	22 86
CaO	1 61	1.61	1 46	1.74	1.68	1 58	1 61	1 57	1 67	1.62	1.71	1 60	1 62	1.70	1 64	1 64	1 58	1.61	1.61	1 51	1.71	1 77
Na_2O	0 04	0 04	0 06	0 05	0 05	0 04	0 04	0.05	0 04	0.05	0 05	0.02	0 02	0 03	0.04	0.04	0.03	0 03	0.05	0.02	0 04	0 01
K_2O		0 01	0 04		0.01			0.01			0 01		0 01		0 01	0 02	0.01	0 01	0 01	0 00	0.01	0.02
Total%	99 97	100 82	99 19	99 39	99 63	97.53	99 68	98 46	99 43	99 87	99 86	99.29	99 28	99.13	98 76	98 38	97 75	97 98	97.61	97.20	97 17	97 54
Si	1 948	1 956	1 895	1 973	1 968	1.966	1 966	1.967	1 968	1 963	1 965	1 971	1 951	1 983	1.97	1.991	1.984	1 997	1 993	1.997	1.991	1 993
Ti	0 006	0 006	0 006	0 006	0.007	0 007	0 004	0.007	0.006	0.006	0 007	0.006	0 007	0 006	0 005	0.009	0.007	0 007	0.006	0.007	0 008	0.006
Al/Al^{IV}	0.032	0.025	0.105	0.027	0 023	0.026	0.022	0.033	0 024	0 024	0 029	0 029	0 041	0.017	0 027	0 009	0 016	0.003	0 007	0 003	0.009	0.007
Al^{VI}			0.073	0 002										0.002		0.017	0.009	0.015	0 017	0 02	0.014	0.021
Cr				0 001										0.001		0.001		0 001			0 001	0 001
Fe^{3+}	0.063	0 054	0 026	0.015	0.03	0 03	0.041	0 024	0 03	0.041	0.032	0 02	0 046	0 005	0.027							
Fe^{2+}	0 513	0 557	0 553	0.582	0 662	0 703	0.621	0 662	0 654	0 639	0 631	0 59	0 589	0 616	0 601	0 645	0 577	0 588	0.571	0.577	0.621	0 566
Mn^{2+}	0 04	0.048	0.048	0 04	0 043	0 051	0.04	0 041	0 045	0.044	0.041	0 036	0.038	0 036	0.041	0.041	0.035	0.054	0.044	0 04	0.034	0 037
Mg	1 332	1 287	1 229	1 28	1 194	1.148	1.24	1.199	1 202	1 214	1 223	1.283	1 262	1 264	1 26	1 205	1 304	1 255	1 283	1.278	1.238	1 284
Ca	0 064	0 063	0.058	0 069	0 068	0 065	0 064	0.064	0 067	0 065	0 068	0 064	0 065	0 068	0 066	0 066	0 064	0.065	0 065	0.061	0 07	0 071
Na	0 003	0.003	0 005	0 004	0 004	0 003	0.003	0 003	0 003	0.004	0.004	0.002	0.001	0 002	0.003	0.003	0 002	0 002	0.004	0 002	0 003	0 001
K		0 001	0 002		0 001			0.001					0.001		0 001	0 001		0.001			0.001	0.001
Total cation	4	4	4	4	4	4	4	4	4	4	4	4	4	4	4	3 989	3 998	3.988	3.991	3 985	3.99	3 987
Wo%	3 18	3.14	3 03	3 47	3 41	3 25	3 19	3.22	3 35	3 25	3 41	3 21	3.25	3.42	3 31	3 37	3.23	3 31	3 31	3.12	3.57	3 63
En%	66.20	64 06	64 21	64.45	59 79	57.49	61 81	60 25	60.16	60 61	61 30	64.38	63 10	63.55	63 16	61 57	65 86	63.97	65.36	65 34	63.07	65.58
Fs%	30 62	32.80	32 76	32.07	36 81	39.26	35 00	36.53	36.49	36 15	35 29	32 41	33 65	33.03	33.53	35 05	30 91	32.72	31 33	31 54	33.37	30.80
Mg_{opx}	69 81	67 81	67 98	68.19	63.31	61.03	65.19	63.61	63 73	64 10	64 85	67 78	66 53	67 06	66.74	65 14	69 32	68.10	69 20	68.89	66 59	69 41

Table J.4. Composition of clinopyroxene phenocrysts: Efaté Pumice Formation (EPF), Efaté Island Group, Vanuatu arc.

Clinopyroxene	EFATE PUMICE BRECCIAS (EPB)																						
Analysis	AR024-	AR024-	AR024-	AR024-	AR084-	AR207-	AR207-	AR207-	AR207-	AR207-	AR207-	AR207-	AR207-	AR207-	AR207-	AR208-	AR208-	AR208-	AR208-	LI961-	LI961-	LI961-	LI961-
number	4	5	6	7	12	12	13	14	15	16	17	18	19	20	21	3	4	5	6	13	14	15	16
SiO_2	51.40	51.60	51 56	51 83	51.63	51 63	51 98	51 51	51 11	50.54	51 03	51 68	51.69	51 11	51.72	51.89	51 30	51.66	51.75	50.77	51.17	51 36	50 35
TiO_2	0 47	0 38	0 44	0 40	0 45	0.37	0 43	0 38	0 41	0 54	0.43	0 44	0 41	0 46	0 40	0.34	0.47	0 34	0 32	0 50	0.46	0 40	0.58
Al_2O_3	1 64	1 11	1 22	1.50	1 42	0.92	1 17	1 44	1 55	2 04	1 88	1 36	1 40	1 75	1.39	0.97	1 27	0.92	0.98	1 93	1 64	1 14	2 21
Cr_2O_3	0 00	0 00	0.01	0.00	0 00	0 00	0 01	0 03	0.02	0 02	0.02	0 00	0 01	0 00	0 00	0.00	0 00	0 00	0.01	0.00	0 00	0 00	0 01
Fe_2O_3(c)	2 26	1 64	2 27	0 78	1.73	4 12	4 03	4 05	3 95	4 58	4 14	4 09	3 63	4 47	3 45	3 62	3 29	2.50	3 04	1 79	2.41	1 43	3 05
FeO(c)	7 73	10 18	8.65	9 67	7 89	6 26	6 24	5 42	5 86	5 29	5 77	5 28	5 61	5 16	6 06	7.69	8 22	8.15	7 44	9.14	8.44	9 28	7.63
MnO	0 67	1 02	0 88	0.77	0 59	1 06	0.86	0 72	0 81	0 61	0 73	0 74	0 68	0 81	0.71	1 05	0 90	0 99	0.99	0 68	0 76	0 79	0.68
MgO	14.74	14.01	14 58	14.39	14 74	14 68	15 10	15 18	15 01	14 71	15 24	15.26	15 42	15 19	15.29	14.30	14 02	14 41	14.41	14.55	14.62	14 11	14.10
CaO	20 01	18 98	19 49	19 27	20 29	20.84	20 79	21 01	20 53	20 97	20 22	21 21	20 85	20 80	20.73	20.33	20 10	19.94	20 54	18.63	19.32	19 56	20 01
Na_2O	0 33	0 33	0.32	0 32	0 30	0 40	0.40	0 39	0 38	0 41	0.39	0 37	0 36	0 39	0.35	0 43	0 40	0.36	0.37	0.33	0.34	0 32	0.35
K_2O	0 01		0 01	0 02	0.00		0 02				0 01	0.02				0.02	0 01	0 01					
Total%	99 25	99 25	99.45	98 95	99 04	100.28	101 03	100 13	99 63	99 71	99 84	100 47	100 06	100 15	100.11	100 64	99 98	99 29	99.85	98.32	99.16	98 38	98.98
Si	1.931	1 953	1 94	1.956	1 942	1 926	1.921	1 915	1 912	1 89	1 903	1.915	1.92	1 9	1 922	1.935	1 927	1 948	1.94	1.929	1.929	1 954	1.904
Ti	0 013	0 011	0 012	0.011	0 013	0.01	0 012	0 011	0.012	0 015	0 012	0.012	0.011	0 013	0 011	0 009	0 013	0 01	0.009	0 014	0.013	0 011	0.016
Al/Al^{IV}	0 069	0 047	0.054	0.044	0.058	0.04	0.051	0 063	0.068	0 09	0 083	0 059	0 061	0.077	0 061	0.043	0 056	0 041	0 043	0 071	0.071	0 046	0.096
Al^{VI}	0 003	0.003		0 023	0 005															0 016	0 002	0 005	0.002
Cr								0 001	0.001	0 001	0.001												
Fe^{3+}	0 064	0 047	0 064	0.022	0.049	0.116	0 112	0.113	0.111	0 129	0 116	0 114	0.102	0 125	0.097	0.102	0.093	0 071	0 086	0 051	0 068	0.041	0.087
Fe^{2+}	0 243	0.322	0 272	0 305	0 248	0.195	0.193	0.169	0.183	0 165	0 18	0.164	0 174	0 16	0 189	0 24	0 258	0 257	0 233	0 29	0.266	0 295	0 241
Mn^{2+}	0 021	0 033	0.028	0.025	0.019	0.034	0 027	0.023	0.026	0 019	0 023	0 023	0.021	0.026	0 022	0.033	0.029	0.032	0 031	0 022	0.024	0 026	0.022
Mg	0 826	0 79	0.818	0 81	0.826	0.816	0.831	0 841	0.837	0 82	0 847	0.843	0 854	0.842	0 847	0.795	0.785	0 81	0 805	0 824	0 822	0 8	0.794
Ca	0 805	0 77	0 786	0 779	0 818	0.833	0 823	0 837	0 823	0.84	0 808	0.842	0 83	0 829	0 826	0.812	0 809	0 806	0 825	0.758	0 78	0 797	0.811
Na	0 024	0 024	0 024	0 024	0 022	0 029	0.029	0 028	0 027	0 03	0 028	0 027	0 026	0 028	0.025	0 031	0 029	0 026	0 027	0.024	0 025	0.023	0 026
K			0 001	0 001			0 001				0 001	0.001				0 001							
Total cation	4	4	4	4	4	4	4	4	4	4	4	4	4	4	4	4	4	4	4	4	4	4	4
Wo%	41 09	39 25	39 94	40.13	41.73	41.78	41 44	42.21	41 57	42 57	40 93	42 40	41 90	41 83	41 70	40.97	40 98	40.79	41.67	38.97	39 80	40 68	41.48
En%	42 16	40 27	41 57	41.73	42 14	40 92	41 84	42.41	42 27	41 56	42 91	42 45	43 11	42.48	42.76	40.11	39.77	40 99	40.66	42.37	41.94	40.84	40 61
Fs%	16.74	20.49	18 50	18 13	16 12	17.30	16 72	15.38	16 16	15 86	16 16	15 16	14 99	15 69	15 55	18 92	19 25	18.22	17.68	18 66	18 27	18.48	17 90
Mg_{cpx}	72 90	68 16	70 88	71.24	73.55	72 40	73 15	74.89	74 01	73 61	74 10	75 20	75 58	74 71	74.76	69 92	69.10	71 18	71.62	70 73	71 11	70.42	70.77

Table J.4. (cont.). Composition of clinopyroxene phenocrysts: Efaté Pumice Formation (EPF), Efaté Island Group, Vanuatu arc.

Clinopyroxene	RENTABAU TUFFS (RT)							
Analysis	AR101-	AR101-	AR101-	AR101-	AR101-	AR101-	AR101-	AR101-
number	8	9	10	11	12	13	14	15
SiO_2	49.00	51.72	49.81	50 61	51.51	51 32	51.36	51.79
TiO_2	0 45	0 46	0 55	0 48	0.50	0.39	0 38	0.43
Al_2O_3	4 43	1 10	3 73	1.91	1.59	1 31	1.33	1 42
Cr_2O_3	0 00	0 04	0.04	0.00	0.04	0.02	0 00	0.00
Fe_2O_3(c)	3.81	0.58	2.71	2 04	1 49	1 42	1 14	0 65
FeO(c)	3 98	9 61	5 30	7 49	8 05	8 58	8 80	7 91
MnO	0 19	0 63	0.17	0.58	0.61	0.59	0.70	0.65
MgO	14.19	14 14	14 38	14 24	14 82	14 18	14 67	14 66
CaO	22 28	19.68	21 58	20 20	19 85	20.05	19 21	20 21
Na_2O	0 22	0 33	0 28	0 34	0.32	0.33	0 32	0.37
K_2O	0 00	0 02	0.00	0 00	0 01	0.01	0 00	0.00
Total%	98.54	98.32	98 56	97 90	98.79	98.22	97.91	98.09
Si	1.843	1 966	1 873	1.927	1 941	1 951	1.955	1.96
Ti	0 013	0 013	0 016	0 014	0 014	0 011	0.011	0 012
Al/Al^{IV}	0 157	0 034	0 127	0.073	0 059	0 049	0 045	0.04
Al^{VI}	0 039	0 015	0 039	0 013	0.011	0 01	0 015	0.024
Cr		0.001	0.001		0 001	0 001		
Fe^{3+}	0 108	0.017	0 077	0.058	0 042	0.041	0 033	0.019
Fe^{2+}	0.125	0.306	0 167	0 239	0 254	0 273	0 28	0 25
Mn^{2+}	0 006	0.02	0 006	0 019	0 02	0.019	0.022	0.021
Mg	0 796	0 801	0 806	0 808	0 832	0 803	0.832	0 827
Ca	0 898	0 802	0 869	0 824	0 801	0 817	0.783	0.82
Na	0.016	0.024	0.02	0 025	0.024	0 025	0.024	0.027
K		0.001				0 001		
Total cation	4	4	4	4	4	4	4	4
Wo%	46 46	41 21	45 14	42 30	41 10	41 83	40 15	42 33
En%	41 18	41 16	41 87	41 48	42.69	41.12	42 67	42.69
Fs%	12.36	17.63	12.99	16.22	16 21	17.05	17 18	14.97
Mg_{cpx}	77.36	71 26	76 76	73.12	73 76	71 89	72 66	75.46

Table J.5. Composition of Ti-magnetite phenocrysts and mircophenocrysts: Efaté Pumice Formation (EPF), Efaté Island Group, Vanuatu arc.

Ti-magnetite	EFATE PUMICE BRECCIAS (EPB)																					RENTABAU TUFFS (RT)						
Analysis	AR024	AR084-	AR084-	AR084-	AR084-	AR084-	AR207-	AR207-	AR207-	AR207-	AR207-	AR207-	AR207-	AR207-	AR207-	AR207-	AR207-	LI961-	LI961-	LI961-	LI961-	AR101-	AR101-	AR101-	AR101-	AR101-	AR101-	AR101-
number	1	1	2	3	4	5	1	2	3	4	5	6	7	8	9	10	11	1	2	3	4	1	2	3	4	5	6	7
SiO_2	0 05	0 06	0 07	0 02	0 08	0 07	0 08	0 08	0 09	0.05	0 08	0 09	0 08	0 07	0 07	0 07	0 05	0 11	0 11	0 10	0 08	0.07	0.12	0 09	0 08	0.09	0.08	0 05
TiO_2	11 96	13 54	13 57	13 58	13 51	13.52	11.86	11.97	11 89	11 94	12.12	11 97	12.23	12.15	12.27	12 23	12 09	12 17	12.41	12 45	12.35	11.87	11.16	12.21	12.34	14 28	11 85	12 34
Al_2O_3	2 76	2 56	2 49	2.50	2.55	2.51	2 21	2.31	2.32	2 30	2.38	2 24	2 28	2 26	2 22	2 28	2 28	2.51	2.45	2.51	2 49	2.44	2 73	2 50	2 20	1.98	2.64	2.33
Cr_2O_3	0 04	0 00	0 00	0 02	0.00	0 04	0.04	0 03	0.03	0 04	0 00	0 05	0 03	0 00	0 00	0.00	0 01	0 04	0.00	0.00	0 02	0.01	0 02	0.00	0 00	0.04	0.01	0.06
Fe2O3(c)	43 80	42 19	42 30	42 68	42 92	42 89	43.53	43 04	43 21	43 75	43 26	43 21	43.26	42.67	42 92	42 51	43 30	42.46	41.95	42.46	43 06	43 13	43.09	41.43	41.28	37.86	42.36	41.57
FeO	37 85	38.71	39.00	39.24	39 18	39 13	37 06	37 24	37 30	37 43	37 56	37 45	37 82	37.47	37 80	37 54	37 53	38 11	38.27	38 64	38 54	36.74	36.15	37.21	36.72	39.20	36.56	37 16
V_2O_3	0 00	0 00	0 00	0.00	0 00	0.00	0 00	0 00	0 00	0 00	0.00	0.00	0 00	0 00	0 00	0 00	0.00	0 00	0 00	0.00	0 00	0.00	0.08	0.04	0 00	0 00	0.00	0.00
CaO		0 02	0.01	0 01	0 00	0 02																0 08	0.08	0.10	0.15	0.09	0 07	0.05
MnO	0 80	0 89	0 68	0 73	0.82	0.79	1 06	0 97	1.03	1.04	1 04	1.07	1 01	1 00	1 04	0 98	1.02	0 74	0.84	0.73	0.82	1 03	0 70	0 71	1.00	0.99	0.81	0.85
MgO	2 52	2 32	2.32	2 23	2 27	2 31	2 55	2 53	2.44	2.48	2 54	2.38	2 48	2 43	2.39	2.45	2.47	2.29	2 21	2.32	2.26	2 67	2.54	2 46	2.43	2 22	2.66	2.44
ZnO	0.16	0 19	0 20	0 10	0 23	0 13	-	-	-	-	-	-	-	-	-	-	-	0 12	0 13	0 00	0.12	0 00	0 19	0 12	0 27	0 03	0.16	0.22
NiO	0 00	0 00	0 00	0 05	0.00	0 02	-	-	-	-	-	-	-	-	-	-	-	0 00	0 00	0.00	0.02	0.00	0.06	0 05	0 01	0 03	0 07	0 07
Total	99 95	97.37	97.52	98 05	98 41	98 30	98 40	98.18	98.31	99.04	98 97	98 47	99 19	98 05	98 71	98 06	98.75	98 55	98 36	99 21	99.76	98 04	96 91	96.92	96 48	96.82	97.28	97.12
Si	0 002	0 002	0 003	0 001	0.003	0 003	0.003	0.003	0.003	0.002	0 003	0.003	0 003	0 003	0.003	0.003	0 002	0.004	0.004	0.004	0.003	0 003	0 005	0 003	0.003	0.003	0 003	0.002
Ti	0.331	0 384	0 385	0 383	0.38	0 38	0 334	0.338	0.335	0 334	0.339	0 337	0 342	0 344	0 345	0 346	0 339	0 342	0 35	0 348	0.343	0 335	0 318	0.349	0.354	0.409	0.336	0.352
Al/Al^{IV}																												
Al^{VI}	0.12	0 114	0.111	0.111	0 113	0 111	0 098	0.102	0 103	0.101	0.104	0 099	0.1	0 1	0 098	0 101	0.101	0 111	0.108	0 11	0.109	0.108	0 122	0.112	0.099	0.089	0.117	0 104
Cr	0.001	0	0	0.001	0	0 001	0.001	0.001	0.001	0.001	0	0 001	0 001					0 001			0.001					0.001		0 002
Fe^{3+}	1.213	1.113	1.115	1 12	1.122	1 123	1 227	1.215	1.219	1 226	1.211	1 218	1.21	1 207	1 207	1 202	1 217	1.195	1.184	1 187	1.198	1.217	1 229	1.183	1.186	1.085	1 203	1.187
Fe^{2+}	1.165	1 222	1 229	1 231	1 224	1.224	1 161	1 168	1 169	1 166	1 169	1 174	1 175	1.178	1.181	1 18	1 172	1 192	1 2	1.2	1 192	1 152	1 146	1 181	1 173	1.249	1.154	1.179
V																							0.002	0.001				
Ca		0 001		0 001		0.001																0.003	0.003	0 004	0 006	0 004	0 003	0 002
Mn^{2+}	0 025	0.028	0 022	0.023	0.026	0 025	0.034	0.031	0.033	0.033	0 033	0 034	0.032	0 032	0.033	0 031	0 032	0 023	0 027	0 023	0 026	0.033	0.023	0.023	0 032	0.032	0.026	0.027
Mg	0.138	0.131	0.13	0.125	0.127	0.129	0.142	0.142	0.137	0 138	0.141	0.133	0 137	0 136	0 133	0 137	0 137	0.127	0 123	0 128	0.125	0.149	0.144	0.139	0.138	0.126	0 15	0.138
Zn	0 004	0 005	0.006	0.003	0.006	0 004	-	-	-	-	-	-	-	-	-	-	-	0 003	0 004		0.003		0.005	0.003	0 008	0.001	0 004	0 006
Ni				0.002		0.001	-	-	-	-	-	-	-	-	-	-	-						0.002	0 002		0.001	0.002	0.002
Total Cation	3	3	3	3	3	3	3	3	3	3	3	3	3	3	3	3	3	3	3	3	3	3	3	3	3	3	3	3
TiO_2 %	12 78	14 34	14 31	14 22	14 13	14 15	12.83	12 98	12.87	12.82	13 04	12.92	13 11	13.17	13.19	13 25	13 01	13 12	13 40	13 31	13.15	12.94	12.35	13.44	13.66	15.63	13.05	13.55
Fe_2O_3 %	46 79	44 68	44 58	44 69	44 89	44.89	47 08	46 66	46 76	46 98	46 55	46 65	46.36	46.23	46.16	46.07	46.60	45 78	45.29	45 39	45.83	47.01	47.67	45.60	45.69	41 45	46 67	45 65
FeO %	40 43	40 98	41 11	41 09	40 98	40 95	40 09	40 37	40 37	40 20	40 41	40 43	40 53	40.60	40.65	40 68	40 39	41.09	41.31	41.30	41 02	40 05	39 99	40 96	40.65	42 92	40.28	40 80

APPENDIX K

MICROPROBE GLASS ANALYSES: EFATÉ PUMICE FORMATION

Major element glass chemistry was determined from analyses on individual glass shards mounted in polished epoxy resin blocks and polished thin sections. All electron microprobe analyses were collected using the Cameca Camebax SX-50 automated electron microprobe at the University of Tasmania's Central Science Laboratory. This machine is equipped with four wavelength-dispersive spectrometers, used for quantitative analysis, and one energy-dispersive spectrometer, used for qualitative analysis. All analyses were calibrated against international and in-house natural mineral and glass standards.

Instrument operating conditions were 20 kV accelerating voltage, 10 nA current, with a 2 μm diameter, defocussed beam. Sodium was analysed first to minimise the effects of sodium migration under the electron beam. Peak and background counting times, analysing crystal used, and working detection limits for each element are given in Table K.1. Background counting times measured twice, once on either side of the peak. For elements where peak and background counting times are the same, the background was measured once only, on one side of the peak for analytical reasons. Glass standards used to verify primary line calibrations were a basaltic mid-ocean ridge (MORB) glass (VG2) and a rhyolitic obsidian glass (AOBS).

Table K.1. Peak and background counting times, analysing crystals used and working detection limits for elements analysed during analysis of EPF trachydacite shards on the electron microprobe.

ELEMENT	Si	Ti	Al	Fe	Mn	Mg	Ca	Na	K	P	Cr*	Ni*	Cl*
Analysing crystal	TAP	PET	TAP	LiF	LiF	TAP	PET	TAP	PET	PET	LiF	LiF	PET
Peak (s)	10	10	10	10	10	10	10	20	10	10	15	10	20
Background (s)	10	5	5	5	5	5	5	10	5	10	8	5	10
Detection limit (wt%)	0 09	0.04	0 05	0 07	0 07	0.05	0.04	0 09	0 04	0.07	0.06	0 08	0.05

Detection limits were calculated following Ancey *et al.* (1978). * Denotes elements that were not analysed in all sessions.

Glass shard analyses for the Efaté Pumice Formation (Efaté Pumice Breccias and Rentabau Tuffs) are given in Tables K.2 and K.3.

Table K.2. Major element chemistry of juvenile glass shards: Efaté Pumice Formation (EPF), Efaté Island Group, Vanuatu arc. All data recalculated to 100%.

SUITE	EFATE PUMICE BRECCIAS (EPB)																					
Analysis	AR024/1	AR024/2	AR024/3	AR024/4	AR024/5	AR024/6	AR024/7	AR024/8	AR024/9	AR024/10	AR024/11	AR024/12	AR024/13	AR024/14	AR024/15	AR024/16	AR024/17	AR024/18	AR024/19	AR024/20	AR024/21	AR024/22	AR024/23
SiO_2	68 89	69 67	69.75	69 81	69 76	68 09	68 06	68 00	69 36	67 35	69 58	67 77	67 31	67 21	66.94	66.86	67 49	69 23	68.38	66 72	66 87	67 18	67.16
TiO_2	0.71	0.76	0 35	0 36	0.51	0 48	0 56	0 58	0 62	0 51	0.63	0 54	0 55	0 50	0 63	0 58	0.53	0.59	0.47	0 77	0.51	0.70	0.51
Al_2O_3	16 85	16.53	16 10	16.11	16 07	16.36	16 34	16 20	16 19	16 20	16 80	16 19	16 20	16 26	16.13	16.16	16 42	16 77	16.86	16 16	16.14	16 07	16 03
FeO*	3 64	3.60	2 42	2 61	2.34	3 06	3 10	3 11	3 49	3 44	3 50	3 12	3 21	3 22	3 52	3 51	3 02	2.07	2.04	3 41	3.54	3.61	3 76
MnO	0.18	0 22	0 10	0.08	0 11	0.16	0 19	0 10	0 14	0.15	0 17	0 17	0 19	0 15	0 20	0 21	0 12	0.11	0.09	0 17	0.15	0.15	0.16
MgO	0 63	0 75	0.43	0 42	0.42	0 69	0 68	0 71	0 82	0 80	0 83	0 71	0 74	0.69	0.85	0 90	0 72	0 24	0 34	0 85	0.86	0 90	0.94
CaO	1 52	1 84	1 18	1 19	1 19	1.84	1 75	1 81	2 06	1 96	1 90	1 85	1 85	1 89	2.03	2.03	1 81	1 02	1.27	2 06	2.10	2 19	2.08
Na_2O	1 25	1 06	3 98	3.81	3 86	3 88	4 00	3 92	1 71	4.17	1 40	4 26	4 11	4 52	4 21	4 54	3 18	3.82	3 83	4.13	3 99	3 16	3.97
K_2O	5.62	4 91	5 33	5 25	5 45	4 93	4 84	5 03	5.02	4 83	4 54	4 92	5 33	5 01	4 91	4.66	6.17	5 80	6.34	5 14	5.27	5 47	4.74
P_2O_5	0 30	0 24	0 08	0.08	0 03	0.15	0.13	0 19	0.21	0 20	0 25	0 12	0 15	0 18	0 20	0.16	0 19	0 12	0 15	0.21	0 18	0.17	0.22
Cl																							
Cr_2O_3																							
NiO																							
Totals	95.00	93 62	94 92	94 71	95.72	95 11	95 92	95 91	95.06	96.00	94 90	96 58	97 26	97 98	96 78	97 44	96 61	96.19	96.07	97 07	97.37	95 46	96.44
Mg#	23 13	26.63	23 44	21.76	23 78	28 32	27.54	28 57	29 05	28 83	29 21	28.46	28 72	27 16	29.46	30 79	29.37	16.58	22.48	30.27	29 65	30 24	30 39

SUITE	EFATE PUMICE BRECCIAS (EPB)																						
Analysis	AR024/24	AR024/25	AR024/26	AR024/27	AR024/28	AR024/29	AR024/30	AR024/31	AR024/32	AR024/33	AR024/34	AR024/35	AR024/36	AR024/37	AR024/38	AR024/39	AR024/40	AR024/41	AR024/42	AR024/43	AR024/44	AR024/45	AR024/46
SiO_2	66 93	67 53	67.31	67 67	69 24	68.04	67 88	67 19	66.43	66.81	66.84	67.18	67.04	67.55	67 84	67.75	68.01	67.83	67.04	68 44	67 76	67.89	66 28
TiO_2	0.90	0.68	0.49	0.59	0 52	0.56	0 49	0 56	0 57	0 53	0 65	0 53	0.59	0.58	0 69	0 75	0 52	0.56	0.67	0 56	0 55	0 64	0 64
Al_2O_3	16.11	16 00	16 18	16 29	16 03	16 22	16 43	16 31	16 25	16.47	16.42	16.31	16.11	16 09	16 05	16.02	16.11	16.25	16 10	16 26	16 24	16 55	16 40
FeO*	3 66	3 41	3 38	3 11	2 64	3 10	3 06	3 26	3.71	3.66	3.48	3 45	3 22	3 20	3 22	3.22	3 11	3.07	3.28	2 97	3.14	3 79	3 60
MnO	0 18	0 17	0 17	0 11	0 13	0.15	0 07	0 16	0 22	0 17	0.13	0 14	0 21	0 13	0.13	0 12	0 16	0.19	0 18	0.20	0.20	0.19	0 20
MgO	0 91	0.78	0.84	0.69	0.51	0 77	0.82	0 93	0 88	0.92	0 88	0 85	0 79	0 72	0.75	0 67	0.64	0.65	0.76	1.05	0 80	0 97	0.98
CaO	1 66	1 94	2 06	1.74	1 38	1.89	1.98	2 06	2 08	2.17	2 16	2.17	2 19	1 77	1.75	1 68	1.70	1.56	1 76	2.48	1 92	2.30	2 13
Na_2O	4 00	4 09	4 14	4.45	4 24	3.88	3 86	4 32	4 21	4 08	4.22	4 10	4 29	3.96	4.18	3.85	4 29	4.27	3 68	3 12	3 75	2 09	4.48
K_2O	4 93	4.87	4 92	4 87	4 87	4 93	4 98	4.60	4.98	4 51	4 65	4 64	5.04	5.45	4 87	5 40	4 96	5 16	6 01	4 34	5 13	4 88	4.64
P_2O_5	0 30	0.16	0.14	0 13	0 14	0 13	0 08	0 25	0 25	0 27	0 19	0 26	0.16	0 18	0.16	0.19	0 15	0.12	0 15	0.25	0 18	0.26	0 23
Cl																							
Cr_2O_3																							
NiO																							
Totals	96 49	97.15	97 66	97 17	97.32	95 55	96.04	97.05	97 69	96 50	96.52	96 19	97.05	96.79	96.36	97 21	97.26	97.70	97.62	94.75	95.58	97.84	97 65
Mg#	30.16	28 41	30.04	27 86	25.26	30 21	31 90	33.24	29 19	30 38	30 55	30 13	30.01	28 22	28.98	26 48	26 32	27.02	28.88	38.00	30 63	30.75	32 16

Table K.2. (cont.). Major element chemistry of juvenile glass shards: Efaté Pumice Formation (EPF), Efaté Island Group, Vanuatu arc. All data recalculated to 100%.

SUITE	EFATE PUMICE BRECCIAS (EPB)																					
Analysis	AR024/47	AR024/48	AR024/49	AR024/50	AR024/51	AR024/52	AR024/53	AR024/54	AR024/55	AR024/56	AR024/57	AR024/58	AR024/59	AR024/60	AR024/61	AR024/62	AR024/63	AR024/64	AR024/65	AR024/66	AR024/67	AR024/68	AR024/69
SiO_2	66.91	67 48	66.19	66.23	66 69	67.81	66.92	67 43	68 35	67 96	67 40	67 61	67 70	66 72	67 04	66 58	66.94	67 90	67.47	67 49	67 32	67 23	67.62
TiO_2	0 69	0 54	0 63	0 72	0 77	0 56	0.60	0 71	0 52	0 59	0 69	0 56	0.57	0.72	0 85	0 74	0.71	0 44	0 53	0.74	0 55	0 65	0.59
Al_2O_3	16 20	16 29	16.48	16 21	16 36	16.02	16 47	16 18	16.10	15 88	16 04	16 11	16 15	16 13	16 08	16.15	16 02	16 38	16 09	16.11	16 56	15.96	15.80
FeO*	3 46	3 36	3 82	3.74	3 77	2.38	3.60	3 18	2 82	3 06	3 31	3 05	2 97	3 71	3.44	3.62	3 56	2 24	3.37	3.50	3 31	3.32	3 41
MnO	0.12	0.17	0 17	0.17	0 16	0.12	0 16	0 15	0 16	0.16	0 18	0 21	0 19	0 13	0 17	0 16	0.14	0 08	0 17	0.16	0 17	0.18	0 21
MgO	0 81	0 76	0 98	1 01	0 93	0 66	0 94	0 82	0 62	0 67	0 65	0 67	0 85	0 94	0 89	0.85	0 87	0.43	0 85	0 82	0 88	0 75	0.72
CaO	2 13	1.94	2 39	2.38	2 17	2 12	2.17	2 11	1 60	1 69	1.85	1 66	2 05	2 28	2 26	2.14	2 17	1 45	2.02	1 87	1.97	1 79	1.81
Na_2O	4.37	4 04	4 29	3.96	3 91	4 58	4 03	4.11	4 23	4.08	4 37	4.21	4 17	4.08	4.14	4 24	4.23	4 69	3.99	3.66	3 93	4.31	4.51
K_2O	4 70	4 87	4.36	4 96	4.59	5 29	4.54	4 73	5 22	5 42	4 92	5 32	4 83	4.69	4 57	4.92	4 75	5 92	4.92	5 06	4 77	5 23	4 74
P_2O_5	0 23	0 17	0 26	0 20	0 24	0 21	0.19	0.23	0 07	0 13	0 23	0 26	0.18	0.17	0 18	0 19	0.22	0 23	0 21	0 20	0 18	0 21	0 21
Cl																							
Cr_2O_3																							
NiO																							
Totals	97 35	95 83	96 43	97 63	96 27	97 27	96.51	96.63	96 80	97 43	97 24	97 17	95 37	96 16	96.91	97 34	96 57	97 14	97 32	97 05	95.55	97 50	97 11
Mg#	28.85	28 28	30 83	31.99	29 90	32 75	31 16	30 96	27 68	27 64	25 39	27 68	33 29	30 61	31.10	29 13	29.84	25.18	30 42	28.98	31 71	28.12	26 82

SUITE	EFATE PUMICE BRECCIAS (EPB)																						
Analysis	AR024/70	AR024/71	AR024/72	AR024/73	AR024/74	AR024/75	AR024/76	AR024/77	AR024/78	AR024/79	AR024/80	AR024/81	AR024/82	AR024/83	AR024/84	AR024/85	AR024/86	AR024/87	AR024/88	AR024/89	AR024/90	AR024/91	AR036/1
SiO_2	67 68	67 25	67.74	65.99	67.96	66 85	66 83	66.68	66 87	66 00	65 82	65 82	66.82	66 75	67.09	66.99	67.89	67.73	68 20	67.85	65 32	68.90	69 39
TiO_2	0.47	0 72	0.58	0 45	0 75	0 60	0.59	0.77	0 66	0.65	0.63	0.79	0 73	0.77	0.59	0.51	0.59	0 67	0.55	0 81	0.61	0.55	0.64
Al_2O_3	16 00	15 89	16.08	18 01	16 19	16 12	16.24	16 16	15.95	15 97	16 20	15 95	16.06	16 08	16.37	16 41	16.24	16 16	16.06	15 80	15 64	16.35	15.98
FeO*	3 39	3 56	3.15	2 78	3 10	3 44	3.56	3.55	3 51	3.79	3 69	3 72	3.52	3 69	3 36	3.46	2 92	2.95	3.02	3 36	3.87	2.40	2.81
MnO	0 13	0 15	0.14	0 06	0.11	0.17	0.14	0 20	0 13	0 15	0 19	0 21	0 17	0 14	0 16	0 18	0 15	0 16	0.09	0 18	0 22	0.12	0.09
MgO	0 83	0 87	0 73	0 62	0 72	0 92	0.89	0.92	0.86	0 98	1 09	1 00	0 94	0 98	0 87	0 85	0.68	0.66	0 60	0.78	1 25	0.23	0 66
CaO	1 89	2 02	1 69	3 70	1 65	2 13	2.15	1.97	2.12	2 33	2 28	2 32	2 18	2.28	2 09	2 03	1.65	1 76	1.55	2 02	2.69	0.76	1.71
Na_2O	4 36	4 31	4.28	4 14	4 25	4 05	4 33	4.50	4 30	3 55	3 76	3 84	3 67	3.68	3 98	4 08	4 34	4.36	4 43	3 67	3 60	3 44	3.55
K_2O	4 69	4 69	5.03	3.75	4 81	5 18	4 62	4 64	5 01	5 92	5.71	5 67	5.30	4 97	4 89	4 92	5 06	5.15	5 06	5.02	6 17	6.86	4 50
P_2O_5	0.17	0 15	0.22	0 18	0 12	0.14	0 25	0 21	0 20	0 24	0 23	0 27	0 21	0 26	0.23	0 17	0 14	0.09	0 10	0 15	0 21	0.12	0 09
Cl																							0 27
Cr_2O_3																							
NiO																							
Totals	97.64	97 26	97.63	97 51	96 84	96 12	97.17	97 39	96.93	97.66	97.50	97 53	96 42	96 07	96 52	96.97	97.50	97.66	97.01	96.56	97.50	96.42	94.10
Mg#	29.83	29.73	28 68	27.98	28 70	31 74	30 36	31 13	29.93	31 15	33.93	31 88	31 74	31 53	31 08	29.89	28.74	28 03	25.81	28.81	35.99	14 32	29.10

Table K.2. (cont.). Major element chemistry of juvenile glass shards: Efaté Pumice Formation (EPF), Efaté Island Group, Vanuatu arc. All data recalculated to 100%.

SUITE	EFATE PUMICE BRECCIAS (EPB)																					
Analysis	AR036/2	AR036/3	AR036/4	AR036/5	AR036/6	AR036/7	AR036/8	AR036/9	AR036/10	AR036/11	AR036/12	AR036/13	AR036/14	AR036/15	AR036/16	AR036/17	AR036/18	AR036/19	AR036/20	AR036/21	AR037/1	AR037/2	AR037/3
SiO_2	69.13	69 18	68 80	68 72	69.33	69 30	68.70	69.10	68 80	69.48	68.62	69.34	68.94	68 89	69 73	69 16	68.96	69 18	68 82	68 90	69 21	69.38	68.64
TiO_2	0 54	0.47	0 45	0 51	0 39	0.36	0.65	0 53	0 69	0 65	0 48	0.56	0 70	0 53	0 51	0 47	0 66	0 30	0 55	0.44	0 44	0 42	0 55
Al_2O_3	16 39	16 21	15 82	16 13	16 36	16.28	16 24	16.01	16 11	15 93	16 04	16 39	15 86	16 15	15 89	16 05	16.16	16 12	16.19	16 18	16 13	15 90	16 07
FeO*	3 02	2 97	2 99	2 95	2 87	2.92	2 99	2 98	2 92	2 83	3 15	3 01	2 98	2 94	3.09	3 12	2 96	2 97	2 98	3.09	2 80	2 87	2.90
MnO	0 15	0.08	0 15	0 11	0 17	0 15	0 15	0 10	0 08	0 11	0 13	0.08	0 19	0 12	0.12	0.10	0 15	0 14	0 11	0 09	0 14	0 14	0.13
MgO	0 66	0.64	0 62	0 62	0 59	0 62	0 58	0 61	0 56	0.49	0 59	0.63	0.54	0.55	0.60	0.61	0 57	0 65	0 62	0 60	0 64	0 61	0 65
CaO	1 84	1 71	1 71	1 62	1 62	1 78	1 74	1.86	1 73	1 42	1.83	1 80	1 64	1.60	1 71	1 66	1 65	1 70	1.70	1.60	1 65	1 64	1 59
Na_2O	3 47	3.62	3 84	3 89	3.63	3 65	3 63	3 58	3 58	3 75	3.73	3 48	3.77	3.76	3 47	3 71	3.62	3 67	3 72	3.76	3.60	3 74	3 96
K_2O	4 06	4 42	4.94	4.76	4.40	4 31	4.71	4 46	4 71	4 69	4 65	3 92	4 73	4 74	4 17	4 44	4.53	4 56	4 64	4 56	4 86	4 61	5 04
P_2O_5	0.12	0 08	0 12	0 09	0.05	0.03	0.03	0.14	0 19	0 07	0 12	0 13	0 08	0 11	0 12	0 08	0.12	0 10	0.13	0.13	0 21	0 12	0 15
Cl	0 28	0 28	0 23	0 26	0.27	0 26	0.24	0 29	0 29	0.26	0 31	0 31	0 26	0 29	0 25	0 25	0 30	0.28	0.22	0.30		0 24	
Cr_2O_3																							
NiO																							
Totals	92 36	92 95	93 45	94 25	92 28	93 48	93 36	93.08	93 44	93.60	92 73	92 88	93.69	94 06	93.97	95 02	95 05	93.89	94.49	94 24	94 00	94.70	95.24
Mg#	27 46	27 21	26.47	26.82	26 29	26.98	25 32	26.38	25 05	23 20	24.41	26 62	24 04	24 65	25 18	25 43	25.11	27.53	26.60	25 41	28.46	27 17	27 95

SUITE	EFATE PUMICE BRECCIAS (EPB)																						
Analysis	AR037/4	AR037/5	AR037/6	AR037/7	AR037/8	AR037/9	AR037/10	AR037/11	AR037/12	AR037/13	AR037/14	AR037/15	AR037/16	AR037/17	AR037/18	AR037/19	AR037/20	AR037/21	AR037/22	AR037/23	AR037/24	AR037/25	AR037/26
SiO_2	68 88	69 33	69 34	69 84	70 78	69.85	69 87	68 96	68 81	69.60	69 51	68 49	68 80	69 17	69 76	70 25	70 02	69 07	68 96	69.56	69.13	70.43	70.03
TiO_2	0 50	0 59	0 48	0 52	0 45	0 46	0 45	0 54	0 39	0 55	0 49	0 57	0 58	0 54	0 45	0 40	0 58	0 50	0.52	0 54	0.46	0.44	0 50
Al_2O_3	15 87	16.07	16 03	16.03	15 63	16 09	15 86	16.14	16.15	15 96	16 15	16 25	16.02	16.19	15 70	15 50	16.03	16.38	16 29	16 13	16.32	16 14	16.01
FeO*	3 12	2 76	3 04	2 62	2 56	2 90	2 85	3 01	2.99	2 97	2 74	2 95	2 89	2 99	2 57	2 45	2.83	2.84	2.77	2.97	2 83	2 89	2 67
MnO	0.14	0 10	0 12	0 12	0 09	0 10	0.13	0 08	0.09	0.12	0 11	0 12	0 10	0.10	0.10	0 12	0 12	0 10	0 08	0 09	0 14	0 08	0.08
MgO	0 62	0 59	0 59	0.46	0.46	0.60	0.58	0.66	0 58	0 56	0 63	0.65	0 69	0 51	0 48	0 40	0.61	0.68	0.60	0.61	0.62	0 66	0.61
CaO	1 55	1.53	1 68	1 18	1 31	1.76	1 75	1 63	1 58	1 64	1.69	1 67	1.59	1 68	1 24	1.25	1.74	1 65	1 76	1 70	1 65	1.65	1.62
Na_2O	3 82	3.61	3 52	3 56	3.53	3.34	3.49	3 36	3 60	3.51	3.48	3 59	3 58	3 57	3 78	3 74	3 25	3 44	3 53	3.45	3.22	3.17	3.34
K_2O	4 74	4.95	4 40	5 31	4 51	4.07	4 26	5 12	5 37	4.40	4.50	5.22	5.32	4 54	5.59	5 25	4.05	5.00	5 06	4.25	5 17	3.76	4.48
P_2O_5	0 11	0 15	0 19	0 07	0 08	0.19	0 15	0 18	0 11	0 06	0 11	0 16	0.12	0 08	0.05	0.09	0.17	0 03	0 11	0 09	0 13	0.14	0 09
Cl	0 30		0 27		0.32	0.30	0.29			0 29	0 29			0 30		0 28	0.28			0.28		0.31	0 27
Cr_2O_3																							
NiO																							
Totals	95.42	93.92	95 15	94.67	94.77	93 03	93 94	93.95	93 52	94 21	93 81	95.06	93.48	94 74	94 81	95.97	92.74	93.15	93.06	94 42	93 47	94 02	95.02
Mg#	25 61	27 20	25 31	23.54	24 01	26 39	26 08	27 70	25.13	24.85	28 51	27 65	29 33	22 72	24 51	22 29	27.40	29.25	27.31	26.34	27.56	28 54	28 44

Table K.2. (cont.). Major element chemistry of juvenile glass shards: Efaté Pumice Formation (EPF), Efaté Island Group, Vanuatu arc. All data recalculated to 100%.

SUITE	EFATE PUMICE BRECCIAS (EPB)																						
Analysis	AR037/27	AR037/28	AR037/29	AR037/30	AR037/31	AR037/32	AR037/33	AR037/34	AR037/35	AR037/36	AR037/37	AR037/38	AR037/39	AR037/40	AR037/41	AR037/42	AR037/43	AR037/44	AR037/45	AR037/46	AR037/47	AR037/48	AR037/49
SiO_2	68 54	69.33	68.82	69 37	68.73	69.57	69.82	69 32	69 69	68 47	69 66	68 86	68.95	70 45	71.37	68 86	69.21	69.00	68.75	68 71	69 02	68.92	69 58
TiO_2	0 48	0.59	0 46	0 57	0.47	0 47	0 55	0 47	0.46	0.57	0 35	0 38	0 50	0 43	0 40	0.50	0 53	0 49	0.50	0.52	0.45	0.49	0.54
Al_2O_3	16 21	15.77	16 18	15.89	16 21	16 02	15 24	16 29	16 22	16.13	16 15	16 21	16 02	15 92	15.71	16 14	16.09	16 10	16.08	16.04	16.06	16.14	15 78
FeO*	2 99	2.87	2 89	2 86	2.94	2 80	2 64	2 77	2.95	3.04	2 82	2 85	2 72	2 20	2 24	3 08	2.94	2.90	2 80	2.92	2.92	2 93	2.86
MnO	0 13	0 10	0.11	0.11	0 17	0.08	0.12	0.16	0 13	0.14	0.13	0.08	0.11	0.13	0 16	0.09	0 12	0 06	0.12	0.10	0.14	0 14	0.15
MgO	0 60	0 56	0 66	0.63	0 65	0 61	0.36	0 61	0 57	0 63	0 62	0 63	0.58	0 36	0 35	0.60	0 59	0 68	0.64	0 62	0.55	0 69	0.61
CaO	1 49	1 65	1 67	1 75	1 57	1 68	0 93	1 58	1 66	1.64	1 67	1 56	1 72	1 05	1 05	1 57	1 58	1 66	1 58	1 55	1 50	1.60	1 73
Na_2O	3 75	3 71	3 56	3 59	3 63	3 56	3 90	3 46	3 42	3 60	3 59	3 80	3 82	3 55	3 46	3 48	3.50	3 68	3 84	4 08	3 84	3.51	3.50
K_2O	5 33	4 75	5 13	4 52	5 16	4 47	5 98	4 94	4.18	5 28	4 30	5 20	4 91	5 64	4.62	5.21	4 65	4.97	4 97	5 07	4 82	5.11	4.50
P_2O_5	0 14	0 07	0 20	0 06	0 15	0.12	0 17	0 09	0 11	0.17	0.12	0 11	0 10	0 03	0 06	0.12	0 16	0.15	0 13	0 06	0 11	0 15	0.12
Cl		0 28		0 33		0 29			0 27		0 27		0 28		0.31		0 30		0 27		0.26		0.30
Cr_2O_3																							
NiO																							
Totals	95.13	95.78	94 25	94.73	94 33	94.64	95 91	93 51	94 53	94.97	95 00	94 71	96 10	93.84	95.42	94.43	94.98	94.14	96 32	94.59	96.48	94.15	94.45
Mg#	25 98	25.41	28 48	27 84	27.71	27 52	18 97	27.72	25.27	26 55	27.63	27 86	27 06	22 15	21.51	25.35	26 02	28 85	28 46	27.03	24.52	29.06	26 93

SUITE	EFATE PUMICE BRECCIAS (EPB)																						
Analysis	AR037/50	AR037/51	AR037/52	AR037/53	AR037/54	AR037/55	AR037/56	AR037/57	AR062/1	AR062/2	AR062/3	AR062/4	AR062/5	AR062/6	AR062/7	AR062/8	AR062/9	AR062/10	AR062/11	AR062/12	AR062/13	AR062/14	AR062/15
SiO_2	68.93	68 90	68 98	68 90	69 88	70 12	68.80	69 93	69.04	69 26	68 21	69 15	69 09	69.21	67 71	67 71	67 24	67 15	68 20	69 36	69.28	69.94	69.94
TiO_2	0 47	0 66	0 46	0 54	0.41	0 42	0 43	0 48	0 49	0.32	0.50	0 43	0 45	0.27	0 62	0 62	0 64	0 60	0 53	0 45	0.50	0.44	0.44
Al_2O_3	16 16	16 18	16 14	16 01	15.95	15 87	16.21	16.08	16.37	16 30	16 51	16.19	16 39	16.47	16 79	16 79	16.64	16.56	16 38	16.35	16.11	16 35	16 35
FeO*	2 85	3 03	2.92	3 00	2.75	2 58	3 05	2 91	2.45	2 40	2 54	2.46	2.38	2.42	2.88	2 88	2 89	2.92	2 63	2.37	2.38	2 40	2.40
MnO	0 12	0 12	0.14	0.10	0 12	0 08	0 09	0.16	0.12	0 08	0 13	0.04	0.12	0.11	0 14	0 14	0 11	0 16	0.11	0.10	0 13	0.13	0.13
MgO	0 63	0.63	0.66	0 64	0 47	0 44	0.65	0 64	0.40	0 45	0.56	0 50	0 56	0 50	0.78	0.78	0 81	0.78	0 64	0 51	0 47	0 54	0 54
CaO	1 71	1 79	1 79	1.63	1 27	1 44	1 66	1.74	1 23	1 24	1 41	1 40	1 18	1 43	1.85	1 85	1 92	2 04	1 74	1 21	1 20	1 24	1 24
Na_2O	3 61	3.61	3.35	3 80	3.40	3.46	3 51	3 29	3 97	4 00	4.37	3.93	3 96	3 76	3 70	3.70	4 22	4.13	3.58	3 85	4.11	3.22	3 22
K_2O	5 05	4 35	5 08	4.70	5 36	4.93	5.06	4 17	5 56	5.59	5 45	5 55	5 51	5 47	5 08	5 08	5 09	5 12	5 75	5.48	5.50	5 36	5 36
P_2O_5	0 15	0.11	0 15	0 08	0.07	0 06	0 21	0.03	0.08	0.08	0.03	0 08	0 10	0 09	0.13	0.13	0 11	0.21	0.15	0 06	0 07	0 11	0 11
Cl		0 29		0 27		0 32		0 26															
Cr_2O_3																							
NiO																							
Totals	93 76	94.98	94 35	95 38	94 51	94.56	93 85	94.32	95 63	95 67	96 16	95 74	95 59	94.76	97.30	97 30	96 18	96 79	94 55	95 81	95.72	95 21	95 21
Mg#	27.66	26.44	28 27	27.23	22 82	22 76	27.00	27 56	22.23	24.77	27 66	26 07	28.96	26.28	31.96	31.96	32.78	31.64	29.64	27.12	25 46	28.00	28 00

Table K.2. (cont.). Major element chemistry of juvenile glass shards: Efaté Pumice Formation (EPF), Efaté Island Group, Vanuatu arc. All data recalculated to 100%.

SUITE	EFATE PUMICE BRECCIAS (EPB)																						
Analysis	AR065/16	AR065/17	AR065/18	AR065/19	AR065/20	AR065/21	AR065/22	AR065/23	AR065/24	AR065/25	AR065/26	AR065/27	AR065/28	AR065/29	AR065/30	AR065/31	AR065/32	AR065/33	AR065/34	AR065/35	AR065/36	AR065/37	AR065/38
SiO_2	69.27	68 95	69 22	69 13	69 38	69.55	69 29	68 15	67 97	67 93	67 92	68.53	69 05	67 62	69 29	69.40	68.68	68 91	68 84	69.28	68 77	67.53	67 62
TiO_2	0 37	0 57	0 51	0 29	0 40	0 47	0 48	0 50	0.48	0 43	0 54	0 58	0 48	0 57	0 52	0.53	0.55	0.57	0.56	0 38	0 59	0 50	0 47
Al_2O_3	16 48	16 56	16 22	16 52	16.30	15 98	16 06	16.62	16 88	16 75	16 40	16 26	16 26	16.69	16 16	16 34	16 19	16.16	16.18	16.40	16 51	16 41	16 71
FeO*	2 33	2.50	2 38	2 31	2 36	2 31	2 41	2 76	2 77	2.77	2 58	2 45	2 48	2 66	2 34	2.30	2 48	2.36	2.36	2 43	2.53	2.86	2 68
MnO	0.11	0 12	0 05	0 13	0.08	0 16	0.11	0 16	0 12	0 12	0.11	0.12	0.13	0 06	0.12	0 12	0.07	0.12	0.15	0.08	0.11	0 14	0 09
MgO	0 51	0.52	0.45	0.55	0.51	0.42	0.44	0 68	0 73	0.65	0 73	0 54	0 50	0 66	0 45	0.47	0 50	0.54	0.54	0.49	0.52	0 72	0 66
CaO	1 35	1 29	1.18	1.32	1 25	1.23	1.17	1.68	1 83	1 70	1 68	1 38	1.34	1.65	1 24	1 27	1.36	1 30	1.29	1.41	1 36	1 78	1.80
Na_2O	3 69	3 69	4 00	3.95	3 86	3.80	3.87	4 01	3 98	3 60	4 32	3 91	3 75	3.82	3 91	3 58	4.03	4 07	3.96	3.75	3 65	4.00	4 03
K_2O	5 53	5.47	5 66	5.47	5.49	5 80	5.85	4.96	4 89	5 58	5 29	5 90	5 63	5.82	5 60	5 63	5.86	5.60	5.79	5 46	5 60	5 61	5.54
P_2O_5	0 10	0 05	0 08	0 08	0.09	0.03	0.06	0 17	0.06	0 16	0 15	0 06	0 11	0 16	0.10	0 09	0 01	0.11	0.07	0.08	0 07	0 14	0 10
Cl																							
Cr_2O_3																							
NiO																							
Totals	94 36	94 13	95 22	94 58	94.51	95 50	95.72	95 59	94 82	94.46	96.67	96 45	95 55	95 62	95.62	95 54	95 24	95 25	95.65	94 81	94.76	96 19	95 53
Mg#	27 59	26.52	24 79	29 20	27.47	23.95	23 99	29 91	31.31	29 09	33 07	27 80	26 16	30.09	25 17	26 12	25.95	28 62	28 63	25 88	26 34	30.34	29.86

SUITE	EFATE PUMICE BRECCIAS (EPB)																						
Analysis	AR062/39	AR062/40	AR062/41	AR062/42	AR062/43	AR062/44	AR062/45	AR062/46	AR062/47	AR062/48	AR062/49	AR062/50	AR062/51	AR062/52	AR062/53	AR062/54	AR062/55	AR062/56	AR062/57	AR062/58	AR062/59	AR062/60	AR062/61
SiO_2	67 65	68 81	68 94	68 79	67 68	67 68	68 00	69.01	68 88	68 74	68 87	68 66	68 54	69.05	68 74	69 45	69 28	68 42	68.08	67.70	68.18	69 92	68 92
TiO_2	0 50	0.50	0 66	0 40	0 59	0.36	0 44	0 46	0 49	0 50	0 42	0 46	0 53	0 59	0 58	0 50	0 50	0.52	0.45	0 56	0.49	0 28	0 35
Al_2O_3	16 58	16 36	16 53	16 38	16 74	16.68	16 74	16 29	16 27	16 47	16 57	16 19	16 46	16 46	16.41	16 21	16 40	16 76	16.77	16 63	16.64	16.33	16 21
FeO*	2 78	2 38	2.51	2 50	2 70	2 84	2 85	2 43	2 48	2 39	2 41	2 52	2 36	2 27	2.47	2 37	2.32	2.61	2.72	2.68	2.63	2 32	2.47
MnO	0 13	0 10	0 11	0 14	0 12	0 15	0 11	0 08	0 09	0 08	0 15	0.14	0.10	0 12	0.08	0.08	0.11	0 12	0.13	0.14	0 10	0 10	0.11
MgO	0.68	0 56	0 50	0 53	0 73	0 68	0 70	0 58	0 59	0 51	0.53	0.49	0 54	0 54	0 52	0 46	0.55	0.67	0.70	0.71	0.71	0.46	0.52
CaO	1 70	1 43	1.42	1 41	1.68	1 63	1 63	1 39	1.35	1.30	1 36	1.38	1.44	1.38	1.45	1 32	1.35	1.74	1.70	1 73	1 59	1 20	1 34
Na_2O	4 02	3 89	3.75	3 89	4 11	4 14	4.01	3 92	4 00	4.21	3 97	4 10	3 84	3.86	3.64	3.68	3.67	3 58	3 74	4 03	3 90	3 62	4 05
K_2O	5.51	5.58	5 24	5 55	5 21	5.34	5 09	5.55	5 54	5.45	5 39	5 69	5.86	5.49	5.76	5.56	5 46	5 18	5.30	5 40	5 29	5.39	5.65
P_2O_5	0 15	0.13	0 07	0 14	0 13	0 20	0 11	0.02	0.06	0.07	0.06	0 08	0 07	0.01	0.07	0 11	0.10	0 11	0 11	0.12	0.17	0.11	0 11
Cl																							
Cr_2O_3																							
NiO																							
Totals	95 46	94 89	93.85	94 24	95.14	95.74	94.96	95 02	95 63	95.50	95.12	96 44	95.77	94 65	93.48	94.18	94.19	96 31	94 70	94 33	94 84	96 03	95.21
Mg#	29 99	28 94	25 74	26.89	32 02	29 29	29 96	29.51	29.14	27.23	27 52	25.19	28 32	29 37	26.69	25.35	29 28	30.81	31.01	31.64	31 81	25.44	26 86

Table K.2. (cont.). Major element chemistry of juvenile glass shards: Efaté Pumice Formation (EPF), Efaté Island Group, Vanuatu arc. All data recalculated to 100%.

SUITE	EFATE PUMICE BRECCIAS (EPB)																						
Analysis	AR062/62	AR062/63	AR062/64	AR062/65	AR062/66	AR062/67	AR062/68	AR062/69	AR062/70	AR062/71	AR062/72	AR062/73	AR062/74	AR062/75	AR062/76	AR062/77	AR062/78	AR062/79	AR062/80	AR062/81	AR062/82	AR062/83	AR062/84
SiO_2	68 93	68.70	68 27	69 95	69 03	69 23	68.76	68 35	69 38	69.47	69.49	69 32	68 83	68 97	68 68	69.18	69.10	68 99	68 68	69.29	69 13	69 45	69.13
TiO_2	0 40	0.54	0 45	0 34	0 46	0.63	0.56	0.51	0.50	0.57	0 44	0 56	0 49	0.47	0 61	0 35	0.50	0 51	0.69	0.26	0 51	0.31	0.50
Al_2O_3	16 32	16 29	16 37	16.58	16.19	16.38	16 24	16 90	16 07	16 19	16 25	16 29	16 46	16 46	16 41	16 08	16 32	16.16	16 16	16 36	16 30	16.25	16 34
FeO*	2 34	2.47	2 75	2 46	2.44	2 48	2 48	2 78	2 62	2 26	2 50	2.44	2.40	2.37	2 56	2 60	2.43	2 30	2 48	2 30	2.31	2 42	2 42
MnO	0 12	0 15	0.09	0.09	0.06	0 10	0 14	0 10	0.07	0.06	0.09	0 09	0.07	0.11	0 10	0.12	0 10	0 08	0 12	0 11	0.08	0.15	0.13
MgO	0 50	0 49	0 57	0 43	0 44	0.51	0 50	0 61	0 50	0 48	0 50	0 67	0.52	0 53	0 52	0 50	0.49	0 51	0.51	0.53	0 45	0.46	0.49
CaO	1 24	1 34	1 49	1 33	1 21	1 47	1 44	1 68	1 39	1 25	1 31	1 68	1.37	1.37	1 40	1 33	1 20	1.29	1 28	1 29	1 19	1.30	1 28
Na_2O	4 06	4 11	3.90	3 56	3 93	3.69	3 88	3 61	3 77	3 91	3 75	3 72	3.88	3 70	3.74	3 75	3.92	4.08	3 93	3 93	3 99	3.67	3 67
K_2O	5.75	5 58	5 38	4 53	5 58	4 82	5 32	4 79	4.98	5 06	4 98	4 47	5.66	5.65	5 65	5 69	5 53	5 80	5.82	5 57	5 69	5.63	5.63
P_2O_5	0 08	0 07	0 11	0 11	0 09	0 06	0 11	0.10	0.11	0 15	0 06	0 06	0.06	0.11	0 06	0 11	0 13	0 02	0 06	0 12	0 10	0 07	0 14
Cl			0 32	0 34	0 31	0 35	0 28	0 25	0.31	0 35	0 34	0 43											
Cr_2O_3																							
NiO																							
Totals	95 77	96 81	93 94	92 71	94 67	93.88	94 63	93 30	94.36	95 14	94 63	93 29	95 34	94 80	94 62	94 64	95 52	94 99	95 63	94 92	94 77	95.15	94 57
Mg#	26 91	25 78	26 58	23 12	23.93	26 37	26 03	27.75	25.04	27 07	25 75	32.33	27 39	27 96	25.98	24 94	25.93	27 93	26.33	28.47	25 44	24 93	26.11

SUITE	EFATE PUMICE BRECCIAS (EPB)																						
Analysis	AR062/85	AR062/86	AR062/87	AR062/88	AR062/89	AR062/90	AR062/91	AR062/92	AR062/93	AR062/94	AR062/95	AR062/96	AR062/97	AR062/98	AR062/99	AR062/100	AR062/101	AR062/102	AR062/103	AR062/104	AR062/105	AR062/106	AR062/107
SiO_2	68 58	69 19	68 89	69.04	68 90	68.67	69 09	68 79	68 57	68 98	68 06	67 81	67.87	67 64	68 05	67 72	67.62	67 59	68 68	68.76	68.73	68 77	68 82
TiO_2	0 47	0 46	0 63	0 52	0.52	0 57	0 39	0 54	0 49	0 46	0 44	0 60	0.48	0 54	0 53	0.65	0 63	0 44	0 48	0.42	0.51	0.49	0.46
Al_2O_3	16.37	16 34	16.27	16 26	16 32	16.48	16.17	16 25	16 54	16 27	16 67	16.45	16 47	16.60	16.73	16 54	16.74	16 71	16 37	16.54	16.45	16 41	16.29
FeO*	2 50	2 48	2 40	2.35	2 54	2 44	2 43	2 52	2.48	2 43	2 50	2 74	2.68	2.75	2.90	2.91	2.90	3 07	2 34	2 41	2 48	2.37	2.40
MnO	0.13	0 16	0.14	0 11	0 14	0 16	0 09	0.14	0 09	0 10	0.13	0 14	0.11	0.12	0 19	0 11	0 14	0 12	0 10	0.07	0 09	0.14	0.13
MgO	0 54	0 54	0 50	0 53	0.52	0.56	0 55	0 54	0.51	0 54	0 74	0 63	0.62	0 70	0 79	0 78	0 75	0.77	0 49	0.58	0 55	0 56	0.54
CaO	1 41	1.37	1 29	1.29	1 40	1 33	1 42	1 26	1.30	1 33	1.50	1 60	1 71	1.66	1.97	1 85	1 85	1 87	1 49	1 38	1 38	1 41	1.32
Na_2O	3 63	3 63	3.87	3 75	3 81	3 90	3 76	3 78	3 77	3 91	3 81	3.81	3 92	3.84	3 37	3.90	3 92	3.93	3 99	4 00	3 99	3 92	4 01
K_2O	5 93	5.45	5 71	5 80	5 49	5.56	5 75	5 77	5 88	5 60	5 72	5.76	5.74	5.73	5 04	4.99	4 98	5 02	5.71	5.46	5.43	5 59	5 65
P_2O_5	0 16	0.10	0 03	0 09	0.08	0 06	0 09	0 13	0.10	0 11	0 15	0 16	0 10	0 11	0 11	0 23	0 14	0.14	0 08	0.11	0 12	0.08	0.11
Cl																							
Cr_2O_3																							
NiO																							
Totals	93 47	94 05	95 42	94 50	95.04	94.77	95 10	94 87	94 13	94 58	94 42	95 25	94 11	95 39	95.92	95 09	95.34	94.92	96.02	95.26	95.92	95 81	95.35
Mg#	27.11	27 46	26.66	28.33	26 24	28.65	28 25	27.22	26 51	27.96	33 86	28.58	28.60	30.83	32.10	31.81	31.02	30.47	26.70	29.52	27.79	29.26	28 02

Table K.2. (cont.). Major element chemistry of juvenile glass shards: Efaté Pumice Formation (EPF), Efaté Island Group, Vanuatu arc. All data recalculated to 100%.

SUITE	EFATE PUMICE BRECCIAS (EPB)																					
Analysis	AR062/10	AR062/10	AR062/11	AR062/11	AR062/11	AR062/11	AR062/11	AR062/11	AR062/11	AR062/11	AR062/11	AR062/11	AR062/12	AR062/12	AR062/12	AR062/12	AR062/12	AR062/12	AR062/12	AR062/12	AR062/12	AR062/130
SiO_2	68 89	69.18	68.77	68 96	69 03	69 42	69 74	70 86	68 44	69.51	69 71	69 40	69.15	69.22	69.81	69 26	67 71	68.97	68.04	67 39	67.51	68.79	68.64
TiO_2	0.49	0 49	0 49	0 53	0 59	0 50	0 62	0.44	0 59	0.52	0 46	0 63	0.42	0.60	0.45	0.37	0 38	0 50	0 52	0 57	0.57	0.47	0 58
Al_2O_3	16.24	16.37	16.30	16 24	16 34	16 28	16 38	15.40	16 22	16.15	16.43	16.25	16 32	16.07	16.11	15.98	16 58	16.82	16 82	16 75	16.86	16.38	16.24
FeO*	2.51	2.34	2 44	2 28	2 48	2 58	2 26	2 14	2 60	2.46	2.51	2 21	2.44	2 54	2 42	2.42	2.87	3.15	3.02	3.06	2 86	2.40	2.46
MnO	0 09	0 10	0.11	0 10	0.06	0 09	0 11	0 13	0.08	0.12	0.12	0 12	0.14	0 08	0 11	0 13	0 09	0.09	0 10	0.16	0 18	0.16	0.17
MgO	0.48	0 45	0 54	0 51	0.57	0.51	0 46	0 27	0.52	0 50	0 50	0.37	0 52	0.51	0.50	0 52	0.71	0.83	0.80	0 81	0 81	0 51	0.54
CaO	1 36	1 19	1 32	1.42	1 23	1.45	1.15	0 93	1.42	1.26	1 44	1.12	1.49	1 42	1 30	1.35	1.79	1 93	1 92	1 94	1.85	1 45	1.47
Na_2O	3.92	3 60	4 07	4.03	3 88	3.76	3.53	3 59	3 81	3.83	3 56	3 26	3 98	3 88	3 58	3.96	3.80	2.07	3 37	4.00	3.83	3 79	3 92
K_2O	5.73	5 93	5 62	5.60	5 42	4.71	5.07	5 48	5.72	4 99	4 61	5.98	4 87	4.97	5 00	5 42	5 26	5.15	4 85	4 87	5 02	5 70	5.64
P_2O_5	0.01	0 09	0 06	0 09	0.13	0 13	0 07	0 10	0.06	0 06	0 05	0 07	0 05	0 12	0 13	0 00	0 20	0 15	0 21	0.11	0.18	0.08	0 06
Cl						0.29	0.35	0 42	0 26	0.33	0 32	0.34	0 35	0.31	0.31	0 35	0 30						
Cr_2O_3																							
NiO																							
Totals	94.88	94 25	95 20	94 73	94.40	93 83	93 03	94 45	92.61	94 28	92.85	92.65	94.31	94.70	93 75	94 67	94 37	93.08	95 44	95.41	94 34	95 02	94.44
Mg#	25 09	24.90	27.87	27 82	28 74	25 71	26 07	18 15	25 82	26 06	25.80	22.56	27.01	26 07	26 38	27 11	29.99	31.50	31 63	31 50	33 06	27.10	27.55

SUITE	EFATE PUMICE BRECCIAS (EPB)																					
Analysis	AR062/131	AR062/13	AR062/13	AR062/13	AR062/13	AR062/13	AR062/13	AR062/13	AR062/13	AR062/14	AR062/141	AR062/14	AR062/14	AR062/14	AR062/14	AR062/14	AR062/14	AR062/14	AR062/14	AR062/15	AR062/151	AR062/15	AR062/153
SiO_2	68.62	68.30	68.76	69 09	69.36	69.31	69.78	68.74	69 14	69.33	69 37	68 99	69 79	68 98	69 05	69 29	69.05	69 33	69 30	68.77	68 58	68.57	68 59
TiO_2	0 70	0 47	0.47	0 41	0.58	0.54	0.48	0.56	0 41	0.31	0 57	0 44	0 48	0 47	0.44	0 36	0.49	0 22	0.39	0.68	0 58	0 55	0.62
Al_2O_3	16 37	16.42	16.31	16 30	16.10	16 32	16 14	16.31	16.43	16 17	16 02	16.35	16 47	16.40	16 35	16 14	16.22	16.31	16.24	16.20	16 27	16.21	16.48
FeO*	2 44	2 57	2 47	2 45	2.42	2.33	2 38	2 45	2 31	2.38	2 47	2 54	2 38	2 36	2 38	2.29	2.39	2 47	2 37	2.34	2.63	2.41	2 48
MnO	0 09	0.10	0.08	0 12	0 10	0 15	0 09	0.11	0 11	0 13	0.10	0.12	0 07	0.09	0 09	0 14	0 15	0.10	0.14	0.09	0 11	0 15	0.08
MgO	0 50	0 50	0.60	0 46	0.48	0.51	0 44	0 50	0 46	0 48	0.47	0.50	0 47	0 53	0.55	0 53	0 48	0.49	0 51	0.43	0.53	0 53	0 52
CaO	1 30	1 33	1 43	1 27	1 29	1 20	1 26	1 33	1 32	1 25	1.26	1 28	1.31	1 27	1 40	1 29	1 29	1 23	1.28	1.27	1.35	1.56	1 26
Na_2O	4 02	4 04	3 99	3.74	3 64	3.60	3 50	3 93	3.89	3.84	3.73	3.57	3.53	4.01	4 08	3.92	4 02	3.88	3.69	4.06	3 88	3 99	4 02
K_2O	5.59	5.87	5 55	5 82	5 73	5 71	5.58	5.66	5.60	5 72	5.67	5.87	5 11	5 54	5.35	5 69	5 59	5 61	5 80	5.81	5.70	5.66	5 61
P_2O_5	0.10	0.12	0 06	0.06	0 03	0.07	0.09	0.14	0 07	0.12	0 06	0.05	0 12	0.08	0 06	0.09	0.06	0.09	0 03	0 09	0 08	0.09	0.07
Cl																							
Cr_2O_3																							
NiO																							
Totals	95.71	95 82	95 26	95 21	93 71	94.35	93 88	94.97	94 38	94 19	94 69	93.59	96 52	94.56	95.70	94.52	95.41	94.98	94 91	95.39	95 51	95 53	94.61
Mg#	26.22	25.34	29 69	24.53	25 44	27.78	24 39	26 03	25 65	26.00	24 96	25.31	25.56	28.29	28.49	28 63	25 90	25.77	27.09	24.04	25 78	27.57	26.54

Table K.2. (cont.). Major element chemistry of juvenile glass shards: Efaté Pumice Formation (EPF), Efaté Island Group, Vanuatu arc. All data recalculated to 100%.

SUITE	EFATE PUMICE BRECCIAS (EPB)																						
Analysis	AR062/154	AR062/155	AR062/156	AR062/157	AR062/158	AR062/159	AR062/160	AR062/161	AR062/162	AR062/163	AR062/164	AR062/165	AR062/166	AR062/167	AR062/168	AR062/169	AR062/170	AR062/171	AR062/172	AR062/173	AR062/174	AR062/175	AR062/176
SiO_2	68 42	69.02	68 80	68.62	69 25	68 81	69 30	69.22	68 87	67 49	67 61	67.60	67.17	68.69	68.91	68.97	68.67	68 78	68.52	69 00	67.37	67 57	67.07
TiO_2	0 51	0 42	0 51	0 57	0 43	0.42	0 32	0.42	0.49	0 66	0 44	0 54	0 51	0 52	0 54	0 48	0.59	0 33	0.56	0.44	0 59	0.46	0.42
Al_2O_3	16.39	16 17	16 17	16 40	16 56	16 46	16 63	16 36	16 16	16.42	16 59	16 66	16.78	16 40	16 29	16.25	16.49	16.53	16.32	16.23	16 68	16 52	16.90
FeO*	2 42	2 42	2 38	2 54	2 38	2 44	2 40	2 14	2 42	2.65	2 74	2 87	2 93	2 56	2 44	2.51	2 53	2 51	2.58	2.46	2.85	2 95	2 80
MnO	0 09	0.09	0.08	0 12	0 10	0.14	0 07	0 14	0.11	0 16	0.10	0.11	0 12	0 14	0.07	0 11	0 06	0.09	0.15	0 08	0 07	0 11	0.16
MgO	0 49	0 53	0.56	0 52	0 54	0.59	0.49	0 51	0 51	0 71	0 78	0 70	0 72	0 55	0 52	0 57	0.50	0.51	0.54	0 55	0 81	0.70	0 72
CaO	1 40	1.39	1 40	1 36	1 45	1 43	1 42	1 31	1 37	1 86	1 77	1 79	1 86	1 33	1 34	1 32	1.36	1 36	1 41	1 44	1 75	1 68	1 82
Na_2O	4 17	3.86	4 19	4 23	3.64	3 74	3 57	3 94	4 07	4 09	3 96	3 72	3 90	3 57	3 88	3.91	4 02	3.88	3 96	3.62	3.86	3.94	3 90
K_2O	5.75	5.69	5 55	5 29	5 32	5 61	5 35	5 64	5 62	5.48	5 54	5 58	5 62	5 92	5.65	5.58	5.45	5 63	5 53	5.79	5.55	5.61	5 72
P_2O_5	0 10	0 15	0 10	0 08	0 06	0 09	0 17	0 09	0 11	0.19	0.18	0 11	0.07	0 03	0 07	0.02	0 05	0.11	0.14	0.12	0 16	0.12	0.19
Cl																							
Cr_2O_3																							
NiO																							
Totals	95.90	95.84	96.22	95.47	94 54	94.64	92.71	94.66	95.25	95 66	95 65	95 23	95.25	95 27	94.35	95.55	94 54	94.30	94.77	94 63	95.81	95 44	94 97
Mg#	25 93	27 54	28.97	26 37	28 33	29.70	26 42	29 35	26.92	31.67	33 11	29 94	29.83	27 33	27 11	28 27	25 55	26.12	26 74	27 89	32 99	29 22	31 04

SUITE	EFATE PUMICE BRECCIAS (EPB)																						
Analysis	AR062/177	AR062/178	AR062/179	AR062/180	AR062/181	AR062/182	AR062/183	AR062/184	AR062/185	AR062/186	AR062/187	AR062/188	AR062/189	AR062/190	AR062/191	AR062/192	AR062/193	AR062/194	AR062/195	AR062/196	AR062/197	AR062/198	AR063/1
SiO_2	67 45	68 98	69 23	68 94	68 01	68.31	67 75	67 64	69 75	68.85	68 65	68 96	68 89	69 14	70 21	68.82	69 57	68 70	69.34	68.99	70.23	69.05	67.54
TiO_2	0 54	0.36	0.45	0 46	0 56	0.43	0 50	0.41	0 46	0 39	0 49	0 43	0 43	0 54	0.48	0.39	0.48	0.44	0.46	0.53	0.38	0 51	0 55
Al_2O_3	16.78	16 36	16 35	16 52	16 72	16 49	16 66	16.69	16 27	16 35	16 58	16 47	16 28	16 27	15 82	16 23	16.60	16.49	16 34	16 60	16 13	16 41	16 58
FeO*	2 83	2 51	2 32	2 48	2 55	2.68	2 68	2.74	2 51	2 45	2 54	2.41	2.40	2.22	1.90	2 63	2.36	2.27	2.25	2.32	2.00	2 29	2 79
MnO	0 16	0 14	0.10	0 13	0 12	0 13	0 14	0 14	0 11	0 10	0.16	0 09	0.12	0 11	0 06	0 10	0.07	0.10	0.13	0 14	0.07	0 09	0 11
MgO	0 68	0 46	0 52	0.49	0 67	0 66	0.65	0.63	0 51	0.55	0 56	0 48	0.50	0 37	0 34	0.64	0 55	0.48	0.53	0.57	0.43	0 60	0 81
CaO	1 82	1.30	1 18	1 18	1 56	1.65	1.61	1.54	1.33	1 45	1 37	1 34	1.39	1 14	0.95	1.40	1.31	1 29	1 25	1 37	0 97	1 35	1.93
Na_2O	3 81	3.90	3 83	3 84	4.14	4 09	4 19	4 29	3.12	3 63	3 81	3 91	4 12	3.77	3.59	3 80	3 02	4.04	3 66	3.91	3.60	3 66	4 27
K_2O	5 52	5 62	5 70	5 61	5 31	5 14	5 36	5.51	5.53	5 88	5 40	5 57	5.48	6.16	6 36	5 55	5.67	5 89	5.79	5.26	5.89	5.71	4.97
P_2O_5	0 08	0 08	0.08	0.08	0.08	0 12	0.15	0.11	0.15	0 08	0 17	0 07	0.12	0.03	0 07	0 14	0 11	0 05	0.00	0.05	0 08	0 08	0.14
Cl																							
Cr_2O_3																							
NiO																							
Totals	95 19	95 05	95 11	94.92	95 07	95 34	95 57	96 04	96 12	94 41	95 26	94.92	96 44	95.83	96 26	95.34	96.49	97 01	95 61	95.21	95.40	96.68	95.11
Mg#	29 42	24 20	28 00	25 64	31.46	30.15	29 75	28.68	26 24	27 90	27 58	25 94	26 48	22.31	23 99	29 70	28.73	26 84	29 06	29 88	27.30	31.26	33.44

Table K.2. (cont.). Major element chemistry of juvenile glass shards: Efaté Pumice Formation (EPF), Efaté Island Group, Vanuatu arc. All data recalculated to 100%.

SUITE	EFATE PUMICE BRECCIAS (EPB)																					
Analysis	AR063/2	AR063/3	AR063/4	AR063/5	AR063/6	AR063/7	AR063/8	AR063/9	AR063/10	AR063/11	AR063/12	AR063/13	AR063/14	AR063/15	AR063/16	AR063/17	AR063/18	AR063/19	AR063/20	AR063/21	AR063/22	AR063/23	AR063/24
SiO_2	69 37	70.31	69.20	67 50	70 83	67.72	67 61	67.82	67 72	67 99	67 94	68 87	68 73	67.54	67.77	69 29	69 18	68.99	67 62	67 94	68.70	69 32	67 41
TiO_2	0.51	0 52	0 58	0.42	0 63	0 58	0 44	0.50	0 54	0 68	0 43	0 37	0 60	0 41	0.55	0 37	0 43	0.55	0.51	0.62	0 49	0 43	0 60
Al_2O_3	16 23	16 71	16 58	16 85	17 21	16 96	16 98	16 82	16 61	16 62	17 10	16 28	16.26	16 85	16 66	16.67	16 44	16 35	16.96	16.50	16 23	16 43	16 54
FeO*	2 40	1 71	2 35	3 03	3 00	2 80	2 87	2 81	2 71	2 93	2 88	2 34	2 44	2 85	2 74	2.18	2 49	2 45	2 75	2 83	2.56	2.30	3 09
MnO	0 13	0.04	0 06	0 15	0 11	0 12	0 12	0.10	0 13	0 11	0 11	0.11	0 14	0 17	0 11	0.12	0 14	0 11	0 11	0.08	0 13	0 11	0.18
MgO	0 50	0 70	0 53	0.80	0 78	0.78	0 75	0 74	0 72	0 79	0 79	0.51	0 60	0 78	0.81	0 54	0 51	0.50	0 80	0 83	0.55	0 46	0 74
CaO	1 27	0.88	1 25	1.90	1 99	1 94	1 94	1 77	1 89	1 90	1.89	1 45	1.40	1 88	1 92	1 33	1.32	1.45	1.96	2 03	1 47	1 33	1 98
Na_2O	3 83	3 59	4.00	3 93	0 74	3 84	4.02	4 27	4 12	3 75	3 63	4 14	3.96	4.15	4.27	3 82	3 99	3 92	3 95	3 81	4 04	3 87	4 03
K_2O	5.42	5 08	5 11	4.91	4 23	4 76	4 78	4 72	5 15	4 77	4 69	5 55	5 49	4.85	4 81	5 31	5 16	5 29	4 90	4.60	5 12	5.06	4.68
P_2O_5	0.08	0 27	0 09	0 17	0 15	0.20	0 16	0.12	0 10	0 13	0 21	0.10	0.10	0 21	0 07	0 10	0 06	0.12	0 13	0.12	0.12	0.08	0 13
Cl																				0.32	0 31	0.36	0 27
Cr_2O_3																							
NiO																							
Totals	95 21	94.16	95 49	95 24	92 80	93 51	94 84	96.01	96 37	94 20	93 36	95 01	96 09	94.75	95.65	94 43	94 84	95.39	94 82	94.12	94.58	94.06	94.87
Mg#	26 52	41 60	28 11	31.41	31 09	32 75	31 16	31 36	31 59	31 83	32 17	27 70	29 87	32 32	34 01	30.00	26 29	26.16	33.63	33 70	27 08	25 82	29 49

SUITE	EFATE PUMICE BRECCIAS (EPB)																						
Analysis	AR063/25	AR063/26	AR063/27	AR063/28	AR063/29	AR063/30	AR063/31	AR063/32	AR063/33	AR063/34	AR063/35	AR063/36	AR063/37	AR063/38	AR063/39	AR063/40	AR063/41	AR063/42	AR063/43	AR063/44	AR063/45	AR063/46	AR063/47
SiO_2	68 51	67.63	66 35	67 00	69.98	68.52	68 03	68.26	67 58	69 35	68 25	69 54	67 89	67.81	67.98	67.82	67 72	69.15	69.57	67.95	67 09	67 40	67 55
TiO_2	0.50	0 60	0 50	0 52	0.41	0 71	0.49	0 56	0 58	0 36	0 56	0 43	0.42	0.42	0.63	0 51	0 65	0 58	0.36	0.35	0.66	0 57	0 46
Al_2O_3	16 64	16.65	16 66	16 61	16 44	16.07	16.50	16 71	16 67	15 93	16 61	16 38	16 81	16 92	16.78	16 69	16.87	16.13	16.40	16.63	16.54	16.59	16.68
FeO*	2 81	3.11	3 15	2.97	2 31	2 55	3.12	2 91	3 02	2.46	2 91	2 43	3 22	3 00	2.72	3.06	2 74	2 34	2.47	2.72	2.92	2.85	2 88
MnO	0 12	0 12	0 16	0 12	0.10	0.09	0 11	0 15	0 13	0.13	0 10	0.09	0.15	0 15	0.13	0 17	0 13	0.08	0.07	0.14	0 13	0.13	0 07
MgO	0 65	0.77	0 80	0 80	0 51	0 50	0 80	0 88	0.80	0 48	0.70	0 52	0 81	0 78	0 76	0 78	0 84	0.48	0.47	0 73	0.80	0 83	0 81
CaO	1 71	1 89	1.88	2 13	1 31	1.35	2 19	1 96	1 93	1 28	1 59	1 48	1.93	1.85	1 87	1 96	1.95	1 26	1.28	1.98	1 82	1.90	1 89
Na_2O	3 53	3 85	4.57	4 11	3.63	4 24	3 71	3 48	3 85	3.95	3 86	3.65	3.68	3.98	4 10	4 05	3.76	3 99	3.97	4.13	4.27	4 19	4 21
K_2O	4.75	4.63	5 11	4.95	4 71	5.26	4 25	4 33	4 68	5 37	4 82	4 81	4.32	4 64	4.60	4 52	4.90	5.65	5.04	4.94	5 25	5 07	4.98
P_2O_5	0 22	0 14	0 18	0 16	0.04	0 13	0 14	0 18	0 12	0.05	0.06	0 11	0.15	0 12	0 13	0.11	0.14	0.08	0.10	0 12	0 18	0 15	0 15
Cl	0 24	0 27	0 30	0 30	0 32	0 31	0 32	0 26	0 29	0 37	0 22	0 30	0 25										
Cr_2O_3																							
NiO																							
Totals	92 96	93 45	96.19	94 33	92 40	94.56	93.05	93 46	93.78	93 29	94.05	93 88	93 77	95 62	94.93	94 75	93.84	95.72	94.64	94.73	95.75	96.27	94 80
Mg#	28 77	30 04	30.57	32.02	27 64	25 36	30.78	34.58	31 45	25 18	29 42	27.15	30.54	31 18	32 63	30 67	34 74	26.22	24 77	31.75	32 35	33.57	32.85

Table K.2. (cont.). Major element chemistry of juvenile glass shards: Efaté Pumice Formation (EPF), Efaté Island Group, Vanuatu arc. All data recalculated to 100%.

SUITE	EFATE PUMICE BRECCIAS (EPB)																						
Analysis	AR063/48	AR063/49	AR063/50	AR063/51	AR063/52	AR063/53	AR063/54	AR063/55	AR063/56	AR063/57	AR063/58	AR063/59	AR063/60	AR063/61	AR063/62	AR063/63	AR063/64	AR063/65	AR063/66	AR063/67	AR063/68	AR063/69	AR063/70
SiO_2	69 11	69 91	69 26	69 53	68 71	68 93	69.05	68 65	67 83	67 87	67 84	68 33	68.62	69 00	68 42	68 86	67 87	68.05	67.72	69.11	69 23	69 33	67 11
TiO_2	0.52	0 32	0 54	0 46	0 42	0.45	0.39	0.41	0 39	0 47	0 50	0 51	0.51	0.45	0 48	0 49	0.48	0 52	0.49	0.44	0.49	0.40	0.61
Al_2O_3	16 38	16 27	16 40	16.23	16 53	16 46	16 78	16 76	16 65	16.73	16 86	16 58	16 45	16 91	16.36	16 24	16 50	16 74	16.73	16 20	16 16	16 16	16 88
FeO*	2 42	2.29	2 37	2 24	2 55	2 50	2.47	2 48	2.76	2 63	2.94	2 74	2 59	2 58	2 37	2 32	2 83	2 80	2 76	2 44	2 38	2 41	2 97
MnO	0 11	0 09	0 08	0 06	0 08	0.10	0 14	0.09	0.08	0.10	0.12	0.07	0 08	0.11	0 13	0 13	0.17	0.10	0.10	0.14	0 14	0 17	0 15
MgO	0 49	0 49	0 49	0 48	0 61	0 61	0 64	0 63	0 72	0.67	0 80	0.69	0 65	0 63	0.53	0.49	0 72	0 77	0.80	0.50	0.51	0 50	0.83
CaO	1 22	1 22	1 15	1 31	1 50	1.49	1 53	1 52	1 74	1 74	1.95	1 64	1 64	1.63	1 44	1 34	1 89	1.83	1.87	1 22	1 21	1 20	1 88
Na_2O	3.71	3 60	3 62	3 74	4 00	3.98	3.85	3 99	4 13	4 11	3 90	3.59	3 63	2.69	4 18	4 13	3 88	3.85	3.95	4 07	3 86	3 92	4 09
K_2O	5 58	5.44	5.69	5 63	5 25	5.12	4 77	5.06	5 20	5 26	4.60	5 44	5 36	5.54	5.71	5 56	5.17	4 96	5.14	5.53	5 65	5 56	4 99
P_2O_5	0.19	0 10	0 14	0 07	0 07	0 09	0 11	0 12	0 18	0 13	0 17	0 12	0 18	0 15	0 11	0.18	0 18	0 06	0.12	0.09	0.11	0 08	0 15
Cl																							
Cr_2O_3																							
NiO																							
Totals	94 47	95.90	94 73	94 15	95 19	94.81	94.79	95 25	95 98	95 63	95 60	95.16	95 14	93.50	95.18	96 01	93.76	94 77	94 68	96.17	96 04	95.65	95.60
Mg#	26 04	27 02	26.34	27 01	29 43	29 63	31 07	30.63	31 13	30.57	32 24	30 33	30 31	29 99	28 00	26.93	30 54	32 33	33 50	26.15	27.26	26.56	32.66

SUITE	EFATE PUMICE BRECCIAS (EPB)																						
Analysis	AR063/71	AR063/72	AR063/73	AR063/74	AR063/75	AR063/76	AR063/77	AR063/78	AR063/79	AR063/80	AR063/81	AR063/82	AR063/83	AR063/84	AR063/85	AR063/86	AR063/87	AR063/88	AR063/89	AR063/90	AR063/91	AR063/92	AR063/93
SiO_2	69 44	67 75	70.97	72 46	68 37	69 37	68 11	67.55	67.41	69.54	69 64	69.73	67.73	67.53	67 47	68 34	68 69	68.65	69.13	69.28	69.37	67.43	67.51
TiO_2	0 43	0.49	0 58	0 53	0.48	0 41	0.66	0 32	0 48	0.59	0 50	0 41	0.47	0 53	0 52	0 50	0.35	0.48	0 45	0 47	0 39	0.46	0 69
Al_2O_3	16 31	16 74	17 35	17 43	16 92	16 11	16 74	16 93	16 85	16 12	16 08	16 29	16 29	16 62	16.67	16.35	16.07	16 31	16.29	16.16	16 14	16 68	16.58
FeO*	2 46	2 83	2 97	3 09	2 60	2.28	2 82	3 22	3.06	2 27	2 29	2 18	2 88	2 64	2.81	2 53	2 50	2 48	2.30	2.36	2 18	2 87	2.90
MnO	0 10	0 11	0 11	0 11	0 10	0.10	0 13	0 14	0.09	0 10	0 14	0 06	0.04	0.11	0.14	0 07	0.11	0.12	0 12	0.04	0 11	0 15	0 08
MgO	0 48	0.71	0 79	0 74	0.73	0 49	0.69	0.85	0 90	0 50	0.48	0 48	0 76	0.73	0.71	0.53	0.55	0 52	0 48	0 45	0 47	0 80	0 85
CaO	1 34	1 95	2 00	2 01	1.93	1 21	1.63	1 97	2 02	1.19	1 24	1 21	1 68	1 79	1 82	1.40	1.37	1 40	1.24	1.18	1.13	1 83	1 89
Na_2O	3 87	3 98	0.63	0.26	3 67	4 19	3 63	3 95	4.05	4.04	4.11	4 09	4.06	3.87	3.85	4.31	4.49	4.32	3 76	3.72	3.84	4.02	3.90
K_2O	5.21	4.99	4.08	2 85	4.81	5 52	5 16	4 57	4 70	5 36	5 20	5.20	5 70	5 72	5 51	5 62	5 53	5.37	5.91	5.96	5 96	5 28	5 12
P_2O_5	0 09	0.12	0.18	0 18	0 10	0.06	0 10	0.13	0.09	0.04	0.07	0 10	0.08	0 17	0.18	0.07	0.06	0 08	0 05	0.13	0.16	0.17	0.15
Cl																							
Cr_2O_3																							
NiO																							
Totals	95 10	95 40	92.87	93.34	93.95	95 72	93 62	94 12	95.08	95.37	96 36	96.01	94.51	95 70	96.79	96.93	97.54	97 17	93.47	94.40	93.49	95.51	94.79
Mg#	25.48	30.51	31.68	29 50	32 95	27.31	29.78	31.43	33.94	27 61	26.71	27 81	31 48	32 56	30.53	26 66	27 69	26 72	26.80	24.96	27.34	32 66	33 75

Table K.2. (cont.). Major element chemistry of juvenile glass shards: Efaté Pumice Formation (EPF), Efaté Island Group, Vanuatu arc. All data recalculated to 100%.

SUITE	EFATE PUMICE BRECCIAS (EPB)																					
Analysis	AR063/94	AR063/95	AR063/96	AR063/97	AR063/98	AR063/99	AR063/10(	AR063/101	AR063/10	AR063/10	AR063/104	AR063/10	AR063/106	AR063/107	AR063/10	AR063/109	AR063/11(	AR063/111	AR063/11	AR063/11	AR063/114	AR063/11	AR063/116
SiO_2	67 69	67 46	67 64	67 55	67.69	67.91	67 70	67 67	67 77	67 90	67 56	67 52	67 67	67 67	67.90	67.89	67 56	67.58	69 39	68.87	69 23	69.00	67 45
TiO_2	0 46	0 51	0.50	0.48	0 61	0 49	0 53	0.48	0 45	0 61	0 57	0 64	0 51	0 63	0 62	0 54	0.41	0.70	0.46	0 48	0 52	0.37	0 54
Al_2O_3	16.96	16.87	16 63	16 89	17.00	16.69	16 96	16 97	16 89	16 80	16 70	16 80	16 86	16 68	16.75	16 96	16 73	16.85	16.45	16.40	16.35	16 45	16.68
FeO*	2 90	2.93	2 94	2 95	2.73	2 88	2.71	2 79	2 79	2 86	2.84	2 87	2.91	2 76	2 72	2.68	3 18	2.95	2.27	2.49	2.47	2.53	3.06
MnO	0.10	0.10	0.10	0 07	0 13	0.10	0.09	0 06	0 15	0 12	0 20	0 08	0.14	0.13	0.13	0.10	0 14	0.10	0.19	0 09	0.15	0 10	0.12
MgO	0 76	0 86	0 82	0.78	0 73	0 69	0 75	0.80	0 78	0 83	0 85	0 82	0 78	0.72	0.74	0.72	0 83	0.84	0.54	0.57	0.50	0.54	0.75
CaO	1 92	2 07	1.81	1 83	1 78	1 80	1.83	1 85	1 99	1 78	1 86	1 93	1 87	1 77	1.74	1.79	1 84	1 83	1.34	1.47	1 40	1 34	2 05
Na_2O	3.89	3 80	3 93	4.11	3 83	3.98	4 02	4 01	3 93	3 84	3 94	3 98	3 90	4.06	3 93	3.86	4 10	4 03	3 83	4 01	3.90	3 89	4 01
K_2O	4 86	4.87	5 07	4.90	5.05	5.01	4 97	4 92	4.82	4 80	5 06	4.90	4.94	5 15	5 06	5 06	4.70	4.59	5 20	5.24	5.19	5 47	4.55
P_2O_5	0.15	0 21	0.22	0 11	0 14	0.14	0.12	0.13	0.12	0 14	0.11	0.15	0.10	0 12	0.10	0 10	0.15	0 20	0.08	0.09	0 03	0.03	0 18
Cl																							0 27
Cr_2O_3																							
NiO																							
Totals	94 34	94 87	95 21	95 50	95 09	96 02	94 34	94 72	94.64	95 37	95 86	94 40	96 57	95 13	95 01	95.32	94 95	95.40	94.50	94.65	94.16	95.27	94 58
Mg#	31 22	33.84	32.73	31 44	31 82	29.36	32 38	33.38	32 74	33 59	34 35	33.09	31 69	31 22	32 02	31.90	31.31	33 22	29 13	28 60	25 96	27.15	29 91

SUITE	EFATE PUMICE BRECCIAS (EPB)																						
Analysis	AR063/117	AR063/11	AR063/11	AR063/12(	AR063/121	AR063/122	AR063/12	AR063/124	AR063/125	AR063/12	AR063/127	AR063/12	AR063/12	AR063/13(	AR063/131	AR063/132	AR063/13	AR063/134	AR063/13	AR063/13	AR063/137	AR063/13	AR063/139
SiO_2	69 34	66 86	67 53	67 82	69.36	68.27	67 66	69.65	68.41	67.20	67 46	69 48	68 83	67.57	67 94	67.63	69.45	67.48	68.82	67 22	68.89	69.20	67 29
TiO_2	0.43	0 58	0 46	0.70	0 50	0 49	0.31	0 52	0 50	0 59	0.56	0 38	0 50	0 52	0.66	0 49	0.42	0 60	0.44	0.45	0 41	0.47	0 66
Al_2O_3	15 95	16.66	16.69	16 60	16 10	16.58	16 67	16 08	16 65	16 83	16 96	16 35	16 34	16.87	16 94	16 76	16.59	16 78	16.40	16 67	16 43	16.33	16.75
FeO*	2 48	3 06	2.95	2.95	2 45	3.00	3 05	2 44	2 44	3.08	3.11	2 30	2 63	2 90	2.69	2 83	2.10	2 86	2.41	2.99	2 45	2.50	2 84
MnO	0 13	0 08	0 10	0 10	0.13	0.12	0 17	0 12	0 08	0 16	0 14	0 09	0 12	0.11	0 10	0 13	0.09	0 07	0.10	0.12	0 13	0.15	0.09
MgO	0 46	0 83	0 73	0 72	0.52	0.72	0.80	0.44	0 55	0 79	0 86	0 50	0.63	0.84	0.85	0.81	0 51	0 84	0.52	0 84	0.54	0 50	0 89
CaO	1 34	1 90	1 99	2 01	1.32	1.95	1 99	1.28	1 52	1 90	1 98	1 25	1 41	1.81	1 82	1 81	1.38	1 88	1.40	1 99	1 34	1.29	1 92
Na_2O	3 75	4 24	3.73	3.83	3 93	3 78	3.80	3 73	4 08	4 20	3.75	4.07	4 05	4.03	3 66	4 23	3 74	4 09	4.07	4 21	4 15	4.06	4 24
K_2O	5 45	4.98	5.12	4 48	5 06	4.32	4 73	5 11	5 10	4 75	4.70	5.21	5.10	4.79	4 85	4.83	5 41	4.99	5.52	5 02	5.26	5.21	4.87
P_2O_5	0 10	0 20	0 09	0 15	0.10	0.15	0 22	0 05	0.07	0 16	0 12	0.12	0 10	0 22	0.19	0.16	0.09	0.11	0.06	0.17	0.14	0.03	0.14
Cl	0 28	0 27	0 27	0.30	0 26	0 27	0.27	0.32	0.33														
Cr_2O_3																							
NiO																							
Totals	94 20	95 67	93.88	93.24	94 49	92 79	93.70	93.38	93.16	96 71	95.58	97.01	96 33	95 27	96.42	97 23	96.01	96.47	96 85	96.87	96.65	97.11	96.54
Mg#	24 53	32.07	30.06	29.88	27.11	29.36	31.25	23.85	28 29	30 85	32.42	27 29	29 50	33 51	35.57	33 26	29.51	33 79	27.31	32.72	27 62	26.00	35.40

Table K.2. (cont.). Major element chemistry of juvenile glass shards: Efaté Pumice Formation (EPF), Efaté Island Group, Vanuatu arc. All data recalculated to 100%.

SUITE	EFATE PUMICE BRECCIAS (EPB)																						
Analysis	AR063/14(	AR063/141	AR063/142	AR063/14(	AR063/144	AR063/14E	AR063/14E	AR063/147	AR064/1	AR064/2	AR064/3	AR064/4	AR064/5	AR064/6	AR064/7	AR064/8	AR064/9	AR064/10	AR064/11	AR064/12	AR064/13	AR064/14	AR064/15
SiO_2	67.89	68.89	67 54	66.96	69 41	69 56	68.05	67 35	67.18	67 30	67 90	67.47	67 20	67.55	69 36	69.47	69.35	69 67	69 65	72 52	69 40	69 37	69 50
TiO_2	0 43	0 52	0 59	0.56	0 24	0 60	0 39	0.56	0 48	0.61	0.60	0.36	0 56	0.56	0 49	0 57	0.54	0.61	0 39	0.48	0.54	0.57	0 37
Al_2O_3	16 68	16.48	16.62	16 95	16 02	16 31	16 67	16 62	16 68	16.75	16.72	16 78	16 49	16 52	16.09	15 98	16.05	16.44	16.09	16.65	16.25	16.28	16.27
FeO*	2 96	2 44	2.98	2 88	2.51	2 19	2.87	2 98	3 00	3.01	2.97	2 92	2.88	2.88	2 30	2 23	2.37	2.36	2 37	2.43	2.14	2.18	2 15
MnO	0 13	0.07	0.11	0 09	0 10	0 12	0.12	0 14	0 13	0.15	0 13	0 17	0 10	0.15	0.11	0 11	0 12	0.07	0.09	0 08	0 10	0.10	0.10
MgO	0 81	0 60	0.79	0 85	0.46	0 42	0.77	0 79	0 88	0 86	0.82	0 83	0 82	0 79	0 53	0 51	0.52	0 44	0 48	0.53	0.52	0 44	0.41
CaO	1 84	1.35	1.87	2 02	1 27	1 21	1 77	1 97	2 05	1.99	1 97	1.88	2 03	1 95	1 25	1.25	1 21	1 17	1.22	1.32	1 16	1 08	1.19
Na_2O	4 11	3.98	4 11	4 31	4 20	3 69	4 03	4 35	4 25	4.05	3 53	3 97	4 37	4 06	4 13	4 28	4.19	3.41	3 87	0.84	3.93	3 88	4.09
K_2O	4 71	5.30	4 93	4 89	5 45	5.63	4 91	4 76	4.84	4 80	4 88	5 09	5 12	5 07	5 30	5.30	5 26	5 47	5.51	4.78	5.64	5 81	5 59
P_2O_5	0 11	0.09	0 12	0.18	0 07	0.03	0.11	0.14	0.19	0.15	0.14	0 22	0 11	0 15	0.17	0.06	0.11	0 09	0.06	0.09	0.09	0 05	0.10
Cl																							
Cr_2O_3																							
NiO																							
Totals	96 84	96 17	96 78	96 05	96 46	96.31	96.76	97 18	96 77	95.63	96 35	96 63	97 73	95 50	96.05	96 44	96 61	96 41	95.39	93.82	95.44	95 64	96 59
Mg#	32 21	29 82	31.54	33 92	24.07	24.78	31.83	31 48	33 71	33 25	32 52	32 94	33 08	32 31	28 42	28 28	27 76	24.52	26.04	27 67	29.54	26 11	25.16

SUITE	EFATE PUMICE BRECCIAS (EPB)																						
Analysis	AR064/16	AR064/17	AR064/18	AR064/19	AR064/20	AR064/21	AR064/22	AR064/23	AR064/24	AR064/25	AR064/26	AR064/27	AR064/28	AR064/29	AR064/30	AR064/31	AR064/32	AR064/33	AR064/34	AR064/35	AR064/36	AR064/37	AR064/38
SiO_2	69 62	67.40	67 20	69.17	69 19	69 46	69 46	69.57	69.13	67 50	67.42	67 50	67.46	67.46	67 58	66 99	70.30	69.52	69 26	69 26	69.29	66.85	66 81
TiO_2	0 42	0 54	0.45	0 49	0 53	0.39	0 50	0 43	0.51	0.46	0.64	0.44	0.41	0 55	0 61	0.68	0 39	0.46	0.46	0 42	0 47	0.58	0 47
Al_2O_3	16 25	16.81	16 92	16.09	16.01	15.95	16 10	16.05	16.13	16.85	16.67	16 93	16 70	16 77	16.55	16 55	16 08	16.06	16.03	16 27	16.27	16.65	16 95
FeO*	2 10	3 04	2.88	2 24	2 42	2.20	2.43	2 26	2 37	2 82	2 87	2.89	2.91	2.77	2 90	2 85	2.47	2 42	2 52	2.32	2.31	3 07	2.96
MnO	0 11	0 10	0.11	0 16	0.08	0.15	0 10	0 13	0 13	0.10	0 12	0.15	0.11	0.12	0 11	0 13	0.09	0 09	0.08	0.12	0.10	0 12	0 14
MgO	0.44	0 81	0.82	0.54	0.47	0 53	0.48	0.53	0 50	0 73	0.83	0 81	0 73	0 75	0.78	0.73	0 48	0.47	0.47	0.46	0.48	0 87	0 87
CaO	1 13	2 01	1.98	1 17	1.18	1.21	1.18	1 19	1 29	1.77	1 81	1 92	1 78	1 89	1.77	1 90	1 20	1.19	1.12	1 22	1 23	2 04	1 97
Na_2O	3 98	3 67	4 12	3 97	4.12	4.04	3.93	3 90	3 95	4 09	4 25	3.81	4.38	4.16	4 14	4.59	3.34	3 99	4 09	3.97	3 92	4 37	4.16
K_2O	5 66	5.08	5 07	5 87	5 66	5.72	5.49	5 65	5 62	5.18	4 97	5.04	5.05	5.12	5.06	5.16	5.32	5 46	5.63	5 64	5 62	4 95	5.15
P_2O_5	0.07	0.20	0 12	0.05	0.06	0.11	0 06	0 05	0 11	0.18	0 11	0.18	0.14	0.11	0 17	0 10	0 06	0.07	0.06	0 06	0.05	0.14	0.18
Cl																							
Cr_2O_3																							
NiO																							
Totals	96 11	95.45	95 61	95 01	96 34	96.36	96 57	95 57	95 22	95.89	95 99	94.89	96 21	96 29	96.40	97 52	95.25	95.52	95 91	94.70	95.65	97 65	97.18
Mg#	26.61	31 59	33 24	29 61	25.21	29.52	25 71	28.93	26 74	31.00	33.42	32.67	30 47	31.95	31 83	30 76	25.12	25 10	24.53	25.83	26.74	33.06	33 79

Table K.2. (cont.). Major element chemistry of juvenile glass shards: Efaté Pumice Formation (EPF), Efaté Island Group, Vanuatu arc. All data recalculated to 100%.

SUITE	EFATE PUMICE BRECCIAS (EPB)																						
Analysis	AR064/39	AR064/40	AR064/41	AR064/42	AR064/43	AR064/44	AR064/45	AR064/46	AR064/47	AR064/48	AR064/49	AR064/50	AR064/51	AR064/52	AR064/53	AR064/54	AR064/55	AR064/56	AR064/57	AR064/58	AR064/59	AR064/60	AR064/61
SiO_2	67 11	67 79	67.84	68 04	67 80	67 81	69.62	69.06	69.17	68 92	69 62	69 43	69 44	69.46	69 18	69.03	69.32	69.08	69.38	68.97	69 40	69.13	69 36
TiO_2	0 62	0.52	0 52	0.31	0.48	0.58	0 52	0 64	0 52	0 51	0 30	0 63	0.42	0.38	0 45	0.53	0 48	0.50	0.38	0.56	0 49	0.51	0 51
Al_2O_3	16.76	16 61	16 64	16.70	16 56	16.47	16 22	16.30	16.56	16.61	16 34	16 27	16.12	16.18	16.41	16 33	16.12	16.29	16.06	16 17	16.07	16 31	16 22
FeO*	3 06	2 68	2 61	2 59	2 84	2 61	2 39	2 31	2 26	2.40	2 36	2.21	2 38	2 38	2 26	2.23	2 38	2 47	2 45	2 49	2.33	2 38	2 27
MnO	0 15	0 12	0 15	0 12	0.06	0.10	0.13	0.12	0 11	0 18	0.12	0 12	0.07	0.07	0.11	0 08	0.04	0.05	0 12	0 05	0 12	0 11	0.11
MgO	0 84	0 74	0 67	0.61	0 73	0.67	0.51	0 51	0 56	0 53	0.46	0 53	0.52	0 48	0 43	0 49	0.53	0.44	0.53	0 50	0 44	0 54	0 50
CaO	2.11	1.71	1.70	1 66	1.56	1.65	1.30	1.34	1.39	1 37	1 27	1 21	1 17	1 15	1 14	1 19	1 20	1.28	1.27	1.28	1.25	1.30	1.24
Na_2O	4 08	3 84	3 73	3.84	3 92	3 92	3 37	3 90	4 06	3 92	3 62	3 82	4 07	3 90	3 69	3.77	3.94	3 94	4 01	3.91	3 87	4.03	3.76
K_2O	4 79	5 60	5 75	5 73	5 60	5 72	5 61	5 47	5 06	5 25	5 56	5 41	5 43	5 71	6.03	6 04	5.59	5 60	5.44	5 72	5.67	5.37	5 65
P_2O_5	0 13	0.10	0 11	0 10	0 13	0 17	0 08	0 10	0 07	0.05	0 09	0.12	0 10	0 03	0.04	0.05	0.13	0.08	0.09	0.08	0.10	0 04	0 12
Cl																							
Cr_2O_3																							
NiO																							
Totals	96 46	95 26	94 70	96 49	96 59	96 13	95 43	96 29	95 53	96 15	97.18	96.04	96 23	95 62	95 92	96 48	96.34	95.88	96.25	96.64	95 84	95 87	95.78
Mg#	32 25	32 57	30 72	29 17	30 94	30 90	26 92	27.93	30 05	27 65	25 24	29.59	27 67	26 07	24 90	27 73	27.91	23 69	27.22	25.98	24.89	28 24	27.89

SUITE	EFATE PUMICE BRECCIAS (EPB)																						
Analysis	AR064/62	AR064/63	AR064/64	AR064/65	AR064/66	AR064/67	AR064/68	AR064/69	AR064/70	AR064/71	AR064/72	AR064/73	AR064/74	AR064/75	AR064/76	AR064/77	AR064/78	AR064/79	AR064/80	AR064/81	AR064/82	AR064/83	AR064/84
SiO_2	67 98	67 53	67.46	69.14	69 27	68.94	67.70	67.75	67.76	68 66	69 18	69.58	69 58	69 01	69 42	69 27	67.48	67.25	67.69	67.60	67.59	69 29	69 20
TiO_2	0 43	0 64	0 44	0.47	0 45	0 49	0 45	0.52	0 50	0 43	0.36	0.49	0.43	0 34	0.53	0.48	0.57	0 62	0 47	0 41	0 60	0 49	0 39
Al_2O_3	16 78	16 71	16 61	16.16	16.06	16 23	16 74	16.73	16 76	16 36	16 19	16 57	16.25	16.34	16.03	16 08	16.67	16.68	16 66	16 78	16 53	16 06	16.01
FeO*	2 72	2 77	2 92	2 34	2 33	2 23	2 91	2.76	2 81	2 48	2 33	2 55	2.34	2.30	2 21	2.48	2 83	3.03	2.95	2 61	2 75	2 28	2 41
MnO	0 09	0 13	0 12	0 13	0 14	0 11	0 13	0.13	0 12	0 09	0 15	0.10	0 13	0 12	0 10	0.08	0 16	0 11	0 17	0.08	0 12	0 09	0 08
MgO	0 76	0 77	0.76	0 51	0 50	0 52	0 81	0 84	0.73	0 60	0 50	0.52	0.50	0.49	0 53	0.46	0 87	0.86	0.83	0.63	0.72	0 49	0.48
CaO	1.76	1 96	1.88	1 15	1.31	1 29	1 89	2.00	1.89	1 36	1 35	1 33	1 26	1 30	1 25	1 12	2 00	2.00	1.95	1.70	1.73	1.24	1.21
Na_2O	4 03	4 08	4.13	4 03	3 99	4 12	3.86	3 80	3 85	4.07	3.95	2.79	3 90	3 98	4.01	4 09	4.08	3.94	3.95	3.99	3.87	3.93	4.02
K_2O	5 01	4 94	5 19	5.68	5 57	5.75	5 02	5 01	5 10	5.55	5.67	5.68	5.30	5 75	5.66	5.53	4.89	4.97	4.88	5.73	5.59	5.75	5.86
P_2O_5	0 15	0.18	0.17	0.12	0.11	0 08	0 16	0 17	0 15	0 12	0 07	0 12	0 04	0.09	0 02	0 13	0.13	0 21	0 13	0 17	0 18	0 14	0.07
Cl																							
Cr_2O_3																							
NiO																							
Totals	96 03	96 41	96 35	96 34	96 08	96.14	95 32	95 18	96 20	97 02	95.93	95.97	96 27	96.37	96 20	96.76	95.62	96 34	96.15	96 20	96.41	95 85	96 23
Mg#	32 55	32.49	31.06	27.52	27.33	28.98	32.70	34 69	31 16	29.54	27 20	26 15	27 14	27 13	29 22	24 29	34.90	32.99	32.96	29.54	31.23	27 09	25 74

Table K.2. (cont.). Major element chemistry of juvenile glass shards: Efaté Pumice Formation (EPF), Efaté Island Group, Vanuatu arc. All data recalculated to 100%.

SUITE	EFATE PUMICE BRECCIAS (EPB)																						
Analysis	AR064/85	AR064/86	AR064/87	AR064/88	AR064/89	AR064/90	AR064/91	AR064/92	AR064/93	AR064/94	AR064/95	AR064/96	AR064/97	AR064/98	AR064/99	AR064/10(	AR064/101	AR064/10:	AR064/10:	AR064/10-	AR064/10[	AR064/10[	AR064/107
SiO_2	69 58	67 52	69 76	69 33	66 92	67 17	67 51	69 28	69 10	69 82	69 85	68 93	69 01	72 95	68 88	69 14	68.95	69.13	69.08	67 73	69 12	69.36	69.23
TiO_2	0.44	0 52	0 36	0 26	0 62	0 61	0 57	0 56	0 42	0 44	0.40	0 50	0.42	0 50	0.35	0.46	0.53	0 47	0.34	0.59	0.57	0.43	0.46
Al_2O_3	16 26	16.89	15 94	16 12	16 70	16 64	16 72	16 14	16 10	16 15	16.14	16.25	16.27	16 63	16.49	16.36	16 25	16 17	16.13	16 53	16.40	16 17	16 17
FeO*	2 38	2 92	2.25	2 32	3 09	3 01	2 81	2 32	2 45	2 30	2 09	2.35	2 34	2.54	2.53	2 27	2 23	2.36	2 29	3.04	2.38	2.36	2 41
MnO	0 06	0 15	0 07	0 13	0 13	0.16	0.16	0.10	0.12	0 12	0 06	0 14	0 14	0.13	0.13	0.11	0 14	0.12	0 11	0.14	0.12	0 08	0 07
MgO	0 48	0 82	0 45	0 49	0 77	0 76	0 79	0 48	0.47	0 45	0 40	0.55	0.55	0 53	0 56	0 42	0.48	0 47	0.48	0 83	0 48	0.50	0.55
CaO	1 32	1 88	1 17	1 20	1 99	2 00	1 97	1 15	1 21	1 15	1 10	1 37	1.37	1 44	1 32	1.17	1.13	1.12	1.14	2 11	1 24	1.29	1 29
Na_2O	3 59	3 89	3 79	3 91	4.09	3.99	3 84	3 68	3 81	2 83	3.49	3 91	4.04	0 61	3 82	3.71	3.75	3 82	3.68	3.64	3 68	3.67	3.89
K_2O	5 56	4 96	5.82	5 90	5 17	5 18	5.14	5 96	5 98	6 34	6 18	5 63	5 49	4.32	5 57	6 07	6 25	6 01	6 38	4.98	5 71	5 82	5 57
P_2O_5	0 08	0 11	0.13	0.08	0 16	0 14	0 17	0 07	0 05	0 13	0 05	0 12	0 12	0 07	0 05	0.03	0 03	0 07	0.11	0 08	0 04	0.05	0.10
Cl																							
Cr_2O_3																							
NiO																							
Totals	97 18	95 13	94 12	96 58	96 18	96 28	95 87	95.62	96 03	95 08	95 80	95.80	96 65	93 36	96 94	96.23	95 82	96 74	96 53	97.54	96.29	95.52	96.04
Mg#	26 05	32 91	26 00	26 78	30 24	30 59	32.79	26.35	24.98	25 58	24 83	28 74	28 88	26 54	27 93	24 37	27.27	25 65	26.70	32.09	25 94	26 87	28.53

SUITE	EFATE PUMICE BRECCIAS (EPB)																						
Analysis	AR064/10E	AR064/10:	AR064/11(	AR064/111	AR064/11:	AR064/11:	AR064/11-	AR064/11[	AR064/11E	AR064/11E	AR064/11:	AR064/11:	AR064/12(	AR064/121	AR064/12:	AR064/12:	AR064/12-	AR064/12E	AR064/12E	AR064/127	AR064/12E	AR064/12E	AR064/130
SiO_2	69 40	68 91	69 08	67 38	67 22	67 51	67 53	67.46	67.58	67 22	67 28	67 76	67 54	67 95	69 02	67 30	67.56	67.28	67 62	69.79	68 31	69.91	67.34
TiO_2	0 50	0.37	0.31	0.50	0 57	0 45	0 50	0.58	0.55	0 66	0 50	0 31	0 60	0 61	0 46	0 39	0 49	0.50	0 60	0 53	0 38	0.36	0.58
Al_2O_3	16 06	16.31	16 30	16 77	16 72	16 65	16 87	16 81	16 64	16 70	16.90	16 81	16.45	16.73	16 06	16 94	16.79	16.86	16 52	16 37	16 69	16.09	16 56
FeO*	2 44	2.35	2 28	3 11	3 06	2 99	2 88	2 94	2 93	2.95	2 94	2 89	2 98	2 75	2 48	2 88	2 87	2 74	2 87	2.46	2.95	2 26	3.24
MnO	0 08	0 12	0 08	0 13	0.13	0.12	0 13	0.13	0.12	0 09	0 09	0 12	0 13	0 08	0 12	0.13	0.13	0.12	0.13	0 06	0.13	0 09	0 09
MgO	0 49	0 57	0 53	0 85	0 87	0 82	0 73	0.86	0 82	0 86	0 86	0.74	0.82	0 75	0.53	0.78	0 82	0.81	0.72	0 56	0 72	0.48	0.82
CaO	1 21	1 36	1.37	2 05	2 15	2 07	1 98	1.84	1.96	1 92	1 91	1 88	1 89	1 77	1 44	1.95	1.81	2.06	1.95	1 35	1.70	1 23	1 87
Na_2O	3 88	3 80	4 06	4 12	4 09	4 03	4 02	3.94	3 94	4 04	4.00	4.16	3 95	3 99	3 89	4.07	4.03	4.15	4.08	3 63	3 56	3 52	3 93
K_2O	5 59	5 79	5 62	4 67	4 65	4 88	4 91	4 95	5 02	5 09	5 06	4 91	5 12	4 89	5 62	5.13	5 11	5.14	5.04	4.61	4 80	5.44	4 82
P_2O_5	0 08	0.15	0 11	0 09	0.21	0.15	0.13	0.16	0.12	0 15	0 14	0 11	0 19	0.17	0.10	0 10	0 08	0.04	0.14	0.09	0.11	0.02	0 14
Cl																				0 29	0 32	0 34	0.25
Cr_2O_3																							
NiO																							
Totals	95 70	96.39	96 28	95.80	95 88	95 91	96.32	96.53	96.06	95.98	96 17	96.34	95 93	96 37	94 71	96.73	95.97	95.70	95.95	94 19	93 11	93 05	94.45
Mg#	25 93	29 72	28 66	32 13	33.05	32.44	30 67	33.58	32 65	33.81	33 75	30 80	32 39	32 11	27 07	31.85	33.16	33 82	30 43	28 25	29 81	27 16	30.55

Table K.2. (cont.). Major element chemistry of juvenile glass shards: Efaté Pumice Formation (EPF), Efaté Island Group, Vanuatu arc. All data recalculated to 100%.

SUITE	EFATE PUMICE BRECCIAS (EPB)																						
Analysis	AR064/131	AR064/132	AR064/133	AR064/134	AR064/135	AR064/136	AR064/137	AR064/138	AR064/139	AR064/140	AR064/141	AR064/142	AR064/143	AR064/144	AR064/145	AR064/146	AR064/147	AR064/148	AR064/149	AR064/150	AR064/151	AR064/152	AR065/1
SiO_2	67 65	69.11	68 68	67 60	69 30	69.56	67.99	67 84	67 49	67.55	68.86	70.09	68 78	67 13	67 50	67.74	67.19	67 35	69 73	69 42	68.08	68 22	67 19
TiO_2	0 54	0.51	0.48	0.49	0 46	0 44	0.55	0.46	0.64	0.63	0 30	0 46	0.48	0.66	0.58	0 35	0.57	0 48	0.41	0.41	0 43	0.44	0.64
Al_2O_3	16 80	16.13	16 46	16 35	15.96	16 16	16.70	16.85	16.74	16 45	16 04	16 42	16 38	16 81	16 79	16.87	16.36	16 71	16 21	16 03	16.45	16 52	16 61
FeO*	3 03	2 46	2.94	2 83	2 42	2 34	2.89	3 03	3.00	2 71	2 22	2 32	2.55	3 19	3.16	2.91	2.91	3 20	2 59	2.17	2.72	2.75	2.94
MnO	0 11	0 14	0.13	0 13	0 15	0.12	0.09	0 14	0.08	0.12	0 09	0.11	0.10	0 08	0.13	0 13	0.14	0.16	0 10	0.09	0.13	0.12	0.13
MgO	0 76	0 59	0 68	0 67	0.40	0.45	0.77	0 77	0 83	0.66	0 49	0.49	0.51	0.90	0 78	0 76	0.63	0 79	0 51	0.48	0.70	0.70	0.83
CaO	1 96	1 49	1 76	1 72	1 26	1.26	2 02	2 08	2 13	1 74	1 22	1 29	1 47	2.09	1.98	1.92	1.62	2 04	1 19	1 33	1.77	1.84	2 00
Na_2O	3 84	3 86	3 30	3.90	3 97	3.84	3.77	3 80	3 99	3 76	4 50	3 52	3 77	3 95	3.77	3.98	4 24	3.79	3 74	4 01	3 77	3 68	4 07
K_2O	4 55	5 02	4 87	5 54	5 37	5.13	4 51	4 27	4 34	5 68	5 68	4 62	5 23	4 41	4 56	4 61	5 53	4 63	4 88	5 42	5.25	5 01	4 90
P_2O_5	0 15	0 15	0.06	0 15	0 10	0.13	0.08	0 16	0 15	0 09	0 09	0 05	0 12	0 19	0.13	0 15	0 19	0 17	0.04	0.10	0 11	0.10	0 10
Cl	0 27	0 29	0 31	0.29	0 34	0.32	0.30	0 27	0 28	0 31	0 26	0 36	0 33	0 24	0 27	0.25	0 29	0.31	0 31	0.30	0 29	0.31	0 27
Cr_2O_3																							
NiO																							
Totals	94 16	94.09	92 69	93.42	93 25	93 13	92 64	93 05	94.33	95 19	95.13	93.31	92.62	93.25	94 12	94 65	96.77	94 11	93 70	94 69	94.99	93.35	93.50
Mg#	30 45	29 50	28 84	29 12	22 24	25 12	31 59	30 64	32 42	29.62	27.72	26 82	25 80	32 80	30 01	31 20	27.37	30.04	25 57	27.67	30 87	30.61	32 89

SUITE	EFATE PUMICE BRECCIAS (EPB)																						
Analysis	AR065/2	AR065/3	AR065/4	AR065/5	AR065/6	AR065/7	AR065/8	AR065/9	AR065/10	AR065/11	AR065/12	AR065/13	AR065/14	AR065/15	AR065/16	AR065/17	AR065/18	AR065/19	AR065/20	AR065/21	AR065/22	AR065/23	AR065/24
SiO_2	67 68	67 97	68.39	67.65	67 55	67 29	70.03	70.10	69.88	69 60	69 04	67 57	67.13	66.72	67.47	68 04	67.54	69.40	68.62	67 52	67.80	67 82	71 29
TiO_2	0.52	0 67	0 56	0 61	0 50	0 69	0.58	0 37	0 47	0 60	0.54	0 50	0.56	0.59	0 71	0.42	0.61	0 56	0.39	0 45	0.47	0.46	0.31
Al_2O_3	16 56	16 57	16.42	16.57	16 47	16 66	16 32	16.33	16.18	16 30	16.34	16 82	16 95	16 47	16 66	16.61	16 51	16 19	16.12	16 71	16 63	16 65	15.56
FeO*	2 84	2 96	2 90	3.06	3 06	2 99	2 42	2 45	2 30	2 42	2 47	2 98	3 35	3 05	3 14	2 98	2 84	2 52	2.61	3 04	2 78	3.00	2.07
MnO	0 14	0 08	0.11	0.13	0.09	0.10	0 12	0 10	0.13	0.11	0.12	0 13	0 10	0 11	0 11	0.11	0 14	0.11	0 11	0.13	0.13	0.14	0.09
MgO	0 72	0 69	0.68	0.77	0.79	0.80	0 45	0 50	0.53	0 47	0 54	0 82	0.89	0.75	0.78	0 73	0 76	0.47	0 56	0 71	0 70	0.77	0.33
CaO	1 83	1.77	1 62	1.99	1.98	2 10	1 29	1 37	1 27	1.33	1 41	2 01	2.19	1 78	1.97	1 93	2 06	1 33	1 46	2.01	1 66	1.99	0.94
Na_2O	3 84	3 72	3 68	3.52	4 03	4 07	3 51	3 46	3 63	3.62	3.74	3.89	3.82	4.29	3 80	3 81	4 16	3.85	4.18	3 74	3.99	3.80	3.59
K_2O	5 19	4 75	4 85	4 85	4 74	4 53	4 58	4 67	4 92	4 85	5 09	4.53	4 20	5.50	4.59	4 64	4 73	4.98	5.20	4 95	5.15	4 61	5 17
P_2O_5	0.07	0.18	0 16	0.25	0 17	0.15	0 11	0 06	0 12	0 09	0.12	0 17	0 15	0 14	0.14	0 12	0 09	0.03	0.14	0.16	0.10	0 15	0 00
Cl	0 29	0 32	0.30	0 25	0 28	0 28	0 33	0.31	0.32	0 35	0.32	0 25	0 27	0 26	0 27	0.27	0 24	0 29	0.30	0.26	0.29	0 27	0.41
Cr_2O_3																							
NiO																							
Totals	93 86	93.67	94 04	92.28	94 09	93 98	93 21	92.68	93.37	92 42	94 21	94.65	94 02	95.58	93 78	93 66	94.53	93.76	94.97	93.40	94.04	94.83	92 84
Mg#	30 70	28.82	29 10	30 52	30 86	31 88	24 55	26.23	28.52	25 41	27.49	32 25	31 59	29 99	30.27	29 91	31 78	24 40	27.31	28.83	30 34	30.97	21.72

Table K.2. (cont.). Major element chemistry of juvenile glass shards: Efaté Pumice Formation (EPF), Efaté Island Group, Vanuatu arc. All data recalculated to 100%.

SUITE	EFATE PUMICE BRECCIAS (EPB)																					
Analysis	AR065/25	AR065/26	AR065/27	AR065/28	AR065/29	AR065/30	AR066/1	AR066/2	AR066/3	AR066/4	AR066/5	AR066/6	AR066/7	AR066/8	AR066/9	AR066/10	AR066/11	AR066/12	AR066/13	AR066/14	AR066/15	AR066/16	AR066/17
SiO_2	71 40	66 97	69 26	67.15	69 66	69.15	67 17	67 52	67 72	68.92	67 60	69 57	68 21	67 93	67.37	68 63	66.96	67 16	67 39	67.54	66.72	67.16	67 31
TiO_2	0.41	0 56	0 46	0 55	0 46	0 39	0 38	0 51	0 57	0 43	0 48	0 56	0.49	0 64	0 44	0.36	0 59	0 47	0 53	0.46	0.63	0 61	0 68
Al_2O_3	15.53	16.26	16 23	16 94	16 24	15.92	16 40	16.86	16 29	16 46	16 40	16.26	16.42	16 60	16 21	16 16	16.87	16.72	16.71	16.85	16.81	16.71	16 60
FeO*	2 08	3 04	2 33	3 12	2 41	2.45	3.15	2.98	3 12	2 67	2 99	2 40	2 92	3 18	2 76	2 34	3.08	3 06	3 09	3 06	3.26	2 94	2 98
MnO	0 06	0.18	0 15	0.09	0 10	0 09	0 12	0.13	0 14	0 10	0 10	0 06	0.13	0 15	0 10	0 12	0.13	0 15	0 12	0 16	0.13	0.13	0 10
MgO	0 31	0 76	0 48	0 81	0 44	0 46	0 80	0 77	0 77	0 44	0 83	0 51	0.74	0.90	0 73	0 50	0 81	0.76	0 74	0 80	0 84	0.77	0 74
CaO	0 94	1 96	1 34	2 06	1 30	1 33	2 07	1 95	1 95	1 36	2 03	1 38	1 68	1 91	1 83	1 38	1.94	2.03	1 92	2.03	2.25	1 98	1.87
Na_2O	3 34	4.56	3 91	3 73	3.46	4.05	4 13	3 99	3 99	3 73	4 09	3 64	3 78	3 55	4 26	4.48	3 90	4 16	4.07	3.88	3 84	4 07	4.09
K_2O	5 23	4.95	5 19	4 71	5.27	5.54	4 95	4 49	4 66	5.11	4 71	4 96	4 92	4 41	5.58	5 44	4 79	4 70	4.73	4 51	4 60	4 88	4.85
P_2O_5	0 06	0 16	0 06	0 20	0 11	0.08	0 19	0 16	0.15	0 14	0 15	0 06	0 09	0 10	0 10	0 06	0.23	0 17	0 09	0.15	0.24	0 10	0 12
Cl	0 41	0 27	0 34	0 30	0 27	0 27	0 29	0.30	0 30	0 34	0 31	0.34	0 29	0.27	0.30	0 27	0.34	0.28	0.25	0 22	0 33	0.32	0 33
Cr_2O_3																							
NiO																							
Totals	94 52	96.32	93.51	92.62	93 37	94 12	94.94	93 88	94.66	94.32	94.04	92 83	93 68	93.41	93 87	93 91	94 34	94.95	95 17	93.42	94.13	94 73	93.85
Mg#	20.60	30 24	26 59	31 16	23 98	24.69	30 59	31 09	29 97	22 17	32.48	27 01	30 56	32 95	31 61	27 04	31 40	30 03	29.46	31.15	30 99	31.35	30.07

SUITE	EFATE PUMICE BRECCIAS (EPB)																					
Analysis	AR066/18	AR066/19	AR066/20	AR066/21	AR066/22	AR066/23	AR066/24	AR076/1	AR076/2	AR076/3	AR076/4	AR076/5	AR076/6	AR076/7	AR076/8	AR076/9	AR076/10	AR076/11	AR076/12	AR076/13	AR076/14	AR077/1	AR077/2
SiO_2	67 46	67.53	66.79	66.98	67 40	69.08	69 64	68 61	68 97	68 66	67 64	68 45	67 91	68 71	68 66	69.40	70 17	68 90	68.33	68.28	68 28	69.52	68.10
TiO_2	0 61	0.65	0.53	0 44	0 46	0 49	0.39	0 53	0 58	0 52	0 54	0 44	0 37	0 45	0 36	0.39	0 48	0 49	0.50	0 63	0 51	0.57	0.34
Al_2O_3	16 54	16 69	16.83	16.44	16 76	16 41	16 17	16 19	16 25	16 28	16 12	16 22	16 26	16.14	16 15	16 08	15.98	16.23	16 26	16.32	16 40	16.03	16 01
FeO*	3 15	3.19	3 31	3 08	3 05	2 53	2 66	2 54	2 57	2 58	2 52	2 58	2 70	2 61	2 59	2 24	2 13	2 48	2.79	2 66	2.70	2 46	2 57
MnO	0 09	0 19	0 16	0 15	0.11	0 10	0.13	0 13	0.10	0 09	0 17	0.10	0 10	0 10	0 05	0 13	0.10	0.08	0 14	0 12	0.12	0 09	0 09
MgO	0 78	0 74	0 88	0 76	0.71	0.54	0 55	0.58	0 55	0 57	0.57	0.59	0.51	0 56	0.60	0 44	0 45	0.58	0.53	0 61	0 57	0 50	0 57
CaO	1 95	2 05	2 11	1.98	2 03	1.36	1 42	1 54	1 54	1 47	1 66	1 61	1 56	1 53	1.55	1 19	1 14	1 41	1 51	1 53	1.44	1.31	1 68
Na_2O	4 08	3 59	4.08	4.28	4 06	3.85	3 63	3 93	3 83	3.91	4 43	4 09	4 50	3 87	4 29	3.85	3 70	3 94	4 10	4.05	4.12	4 09	4 34
K_2O	4 58	4 60	4 60	5 15	4 68	4.98	4 72	5 23	4 96	5 22	5 69	5 33	5 41	5.37	5 10	5 64	5 26	5 24	5.20	5.10	5 19	4 87	5.56
P_2O_5	0 09	0 15	0 12	0.13	0.13	0.06	0 11	0 14	0 10	0 11	0.13	0 02	0 12	0 08	0 09	0.09	0 10	0 06	0 05	0.12	0.10	0 05	0.14
Cl	0 31	0 27	0 22	0 26	0.26	0.32	0.28	0.30	0 26	0 30	0.26	0 28	0 24	0.31	0 28	0 29	0.25	0 30	0.28	0.28	0.29	0.23	0 29
Cr_2O_3																							
NiO																							
Totals	94 73	94 32	93 86	95 00	93.69	94.00	93 52	94 25	92 91	94 44	96.50	93 85	96 81	93.38	94.87	95.08	93.96	94.84	94 49	94 71	94.36	92 63	94 98
Mg#	30 08	28 64	31.62	30.12	28 93	27.04	26.59	28 28	27 15	27 88	28 34	28 27	24 78	27.06	28 61	25 65	26.90	28 82	24 97	28.64	26 73	26.15	27.98

Table K.2. (cont.). Major element chemistry of juvenile glass shards: Efaté Pumice Formation (EPF), Efaté Island Group, Vanuatu arc. All data recalculated to 100%.

SUITE	EFATE PUMICE BRECCIAS (EPB)																					
Analysis	AR077/3	AR077/4	AR077/5	AR077/6	AR077/7	AR077/8	AR077/9	AR077/10	AR077/11	AR084/1	AR084/2	AR084/3	AR084/4	AR084/5	AR084/6	AR084/7	AR084/8	AR084/9	AR084/10	LI961/1	LI961/2	LI961/3	LI961/4
SiO_2	68.68	68.75	68 54	69.50	69.55	68.79	68.90	68 26	68.99	68 39	69 02	70.03	69.18	68.96	69 23	69 02	68.76	68 98	68 99	69.53	68 89	69 62	69.52
TiO_2	0 32	0 50	0 56	0.73	0 45	0 38	0 55	0 55	0.61	0 46	0.48	0.51	0.53	0.51	0.50	0.55	0.51	0 51	0 53	0.52	0.53	0.46	0 53
Al_2O_3	16.01	16 47	16 14	16 13	16 03	16 15	16 28	16.29	16 31	16 27	16.26	15 83	16.38	16.27	16.35	16 12	16.19	16 14	16 14	16.17	16.30	15.89	16.05
FeO*	2 48	2 85	2 61	2 62	2 51	2 56	2 49	2 70	2 66	2 72	2 85	2 46	2 62	2 63	2.78	2 78	2 87	2 89	2 84	2.70	2.80	2 87	2 72
MnO	0 13	0 12	0 14	0 12	0.13	0.11	0 11	0 12	0.12	0.11	0 05	0 11	0.09	0 10	0 10	0 08	0.09	0 08	0 15	0 18	0 14	0.14	0.10
MgO	0 56	0 58	0 58	0.48	0 38	0.59	0.59	0.56	0.65	0 58	0 53	0 41	0 60	0 66	0 57	0.64	0 66	0 63	0 64	0 54	0 62	0.53	0.59
CaO	1 71	1.47	1 53	1 36	1 32	1 51	1.49	1 60	1 41	1 69	1 61	1 27	1.60	1 57	1 64	1 60	1 68	1.60	1.68	1 52	1 62	1.47	1.55
Na_2O	4 15	3 71	4 13	3.78	3.78	4 07	3.89	4 18	3 73	4 02	3 49	3 71	3.40	3.45	3 35	3 46	3.70	3.66	3 29	3 42	3.56	3 45	3.26
K_2O	5 24	4 83	5 08	4 59	5.20	5.18	5.04	5 02	4 87	5 28	5 28	5 38	5 26	5 31	5 15	5.11	5 14	5.13	5 25	5 02	5 06	5.12	5.20
P_2O_5	0 13	0 13	0 09	0 09	0 07	0.09	0 09	0 11	0 07	0 18	0 11	0 00	0 04	0 24	0 00	0 29	0.07	0 05	0 17	0.11	0.17	0.12	0.15
Cl	0 29	0 26	0.31	0.29	0.30	0.28	0.29	0.30	0.30														
Cr_2O_3										0 0002	0 0002	0 0043	0.0103	0.0015	0 0233	0 0525	0.0087	0 0002	0 0002	0.0002	0 0002	0.0002	0.0274
NiO																							
Totals	93 06	92 71	94 16	93.89	93 71	94.24	94 11	94 74	93 16	95 04	94 06	94.48	93.02	94 09	94.43	93.71	94.63	94.94	93 90	96 69	95 99	96.44	95.40
Mg#	28 22	26 18	28 00	24 18	21 06	28 55	29 17	26.53	29.84	26 93	24 25	22 64	28 60	30 27	26 45	28.51	28.54	27.42	28.07	25 74	27 76	24 46	27 53

SUITE	EFATE PUMICE BRECCIAS (EPB)				RENTABAU TUFFS (RT)												EPB -XENOLITHS	
Analysis	LI961/5	LI961/6	LI961/7	LI961/8	AR101/1	AR101/2	AR101/3	AR101/4	AR101/5	AR101/6	AR101/7	AR101/8	AR101/9	AR101/10	AR101/11	AR101/12	AR065/31	AR065/32
SiO_2	69 26	70 03	68 69	69 17	68 06	69.38	68 02	68 85	69 95	69 07	71 97	69 31	67.15	67.37	67.87	63.98	78 12	76 51
TiO_2	0.49	0 54	0 53	0 51	0.55	0 53	0 58	0.61	0 49	0 58	0 65	0.57	0.67	0.67	0 63	0 76	0.93	0 89
Al_2O_3	16.16	16 11	16 12	16 20	16 45	15 86	16 04	15.95	15.65	15 87	16.41	15.83	16 19	16 05	15 87	16.33	11.65	14 04
FeO*	2.93	2.94	2.86	2 88	2 47	2 34	3.16	2.69	2.28	2.64	3.06	2.52	3 48	3 20	2.97	4.43	0 44	0 45
MnO	0 10	0 16	0 15	0.08	0 08	0.06	0 14	0 16	0.14	0 12	0 18	0 11	0.09	0.16	0 16	0 20	0.05	0 01
MgO	0.64	0 64	0 62	0 61	0.63	0.51	0.75	0 63	0 43	0 53	0.68	0 61	0 99	0 81	0 69	1 48	0 52	0 19
CaO	1 68	1 60	1.70	1 56	1.54	1 23	1 87	1 62	1.19	1 33	1 79	1 45	2 24	2 01	1 77	3 45	1 05	0.59
Na_2O	3 42	2.67	3 77	3 53	4.05	4.45	4 28	4.63	4 68	4.69	2 00	4 61	4 27	4.73	4.87	4.79	1 56	2 68
K_2O	4.98	4 98	5 19	5 01	5 69	5.19	4 64	4 39	4 92	4 74	2 67	4 66	4 40	4 56	4.71	3 64	5.09	3.40
P_2O_5	0.01	0 00	0 05	0 15	0 19	0.14	0.07	0.15	0 00	0 14	0.16	0.05	0.13	0.06	0 13	0.37	0.21	0.81
Cl																	0.34	0.37
Cr_2O_3	0 0002	0.0002	0 0104	0 0002	0 0243	0 0222	0 0631	0 0339	0 0163	0 0039	0 0433	0 0002	0 0002	0 0002	0.0002	0 0526		
NiO					0.0002	0 0167	0 0333	0 0002	0 0002	0.0002	0.0305	0 0002	0.0002	0.0027	0 0054	0 0296		
Totals	95 99	94.83	97 09	96.35	93 5372	93.8856	93.9128	93 9166	94 0343	94.3274	94.4525	94 5151	94 9546	95.0797	95 9926	96 8933	93 33	92.40
Mg#	27 52	27 47	27.37	26 79	30 67	27 48	29.17	28 76	24 64	25 89	28 00	29.52	33 19	30 67	28.86	36.71	67.47	43 08

Table K.3. Major element chemistry of glass inclusions in plagioclase phenocrysts: Efaté Pumice Formation (EPF), Efaté Island Group, Vanuatu arc. All data recalculated to 100%.

SUITE	EFATE PUMICE BRECCIAS (EPB) - INCLUSIONS											RENTABAU TUFFS (RT) - INCLUSIONS					
Analysis	AR084/11	AR084/12	*AR084/13*	LI961/9	LI961/10	LI961/11	LI961/12	LI961/13	LI961/14	LI961/15	LI961/16	AR101/13	AR101/14	AR101/15	AR101/16	AR101/17	*AR101/18*
SiO_2	66.47	69 76	*59.76*	69 51	69.40	68 86	68.99	70 04	70 08	69.39	65 39	67 77	67 10	69.76	68.16	68.03	*58 08*
TiO_2	0 26	0 49	*0.04*	0.50	0 45	0.50	0 50	0 49	0 48	0.52	0.41	0.62	0 63	0 49	0.62	0.65	*0.04*
Al_2O_3	19.95	16 19	*24.88*	16.24	16.23	16 20	16.18	16 15	16.06	16.11	19 23	15 81	16 48	15.95	15 60	15.66	*26 00*
FeO*	1.51	2.44	*0 30*	2.91	2 78	2.79	2 69	2 46	2.71	2 82	1 98	3.01	3.15	2 29	2.92	3.16	*0.48*
MnO	0 06	0.07	*0 00*	0.14	0 10	0.17	0.07	0.11	0 17	0.08	0.08	0.16	0.13	0.15	0.13	0.15	*0.00*
MgO	0.34	0.46	*0.06*	0 65	0.58	0 59	0.62	0.49	0 49	0 61	0 39	0 76	0 96	0 57	0.68	0.66	*0 04*
CaO	4.02	1.33	*6 38*	1 68	1.49	1 67	1 59	1.49	1.42	1 56	3.96	1 98	2 07	1 35	1.42	1.78	*7 62*
Na_2O	3.75	3 36	*7 15*	2 91	3 50	3 75	3 71	3 24	3 06	3 37	4 64	4.90	4 63	4.56	5.09	4.75	*6 79*
K_2O	3 45	5.50	*1 38*	4 98	5 09	5 00	5 16	5 16	5 05	5.11	3.61	4 62	4 30	4 46	4.95	4.68	*0.76*
P_2O_5	0 03	0 11	*0.00*	0.15	0.06	0 15	0 19	0 08	0 18	0.05	0 10	0 04	0 20	0 10	0 10	0 10	*0.05*
Cl																	
Cr_2O_3	0 0042	0.0237	*0.0244*	0 0024	0.0002	0 0002	0 0002	0 0002	0 0002	0 0653	0 0007	0 0002	0.0002	0.0002	0.0002	0.0002	*0.0201*
NiO			*0 0000*									0 0028	0.0002	0.0612	0.0002	0 0218	*0 0710*
Totals	93.39	94.01	*99 30*	94.61	95.86	96 93	96 28	95 18	94 07	95.97	98.04	93 23	94.05	94 10	95 61	95.72	*98 30*
Mg#	28.11	24.71	*24.27*	28.07	26 56	26.94	28 46	25.70	23 98	27 38	25 61	30 51	34 63	30.04	28.72	26 50	*11.82*

Andesitic compositions in italics.

APPENDIX L

RESULTS OF MAJOR ELEMENT MODELLING

Major element modelling for basalt → trachydacite fractionation for the Efaté Island Group magmas was carried out using GENMIX petrological software (Chapter Six, Le Maitre, 1979). Results of the modelling are presented in Table L.1.

Table L.1. Major element fractionation models, Efaté Island Group magmas: basalt → trachydacite

MODEL A - OFFSHORE SUITE (OSS)

	parent		daughter																	
	AR106	=	AR207wr	+	An_{92}	+	An_{42}	+	Fo_{76}	+	augite	+	Fe-Ti oxide	+	apatite	=	calc	residuals		
Volume %	100%		13%		17%		37%		4%		19%		9%		1%		parent	r		
SiO_2	48 42		66 93		44 03		57 33		38 21		51 98		0 00		0 16		48 59	-0 17		
TiO_2	1 00		0 56		0 04		0 05		0 01		0 44		10 20		0 00		1 10	-0 11		
Al_2O_3	18 37		15 92		35 11		26 80		0 05		1 23		2 89		0 00		18 52	-0 15		
FeO*	11 07		3 26		0 89		0 46		22.25		10 78		84 10		0 58		11 22	-0 15		
MgO	4 45		0 86		0 05		0 05		38 86		14 70		2 30		0 23		4 58	-0 13		
CaO	10 96		1 83		18 94		8 48		0 22		19 65		0 00		54 10		11 08	-0 12		
Na_2O	3 02		4 89		0 87		6 07		0 00		0 32		0 00		0 07		3 08	-0 06		
K_2O	0 88		5 12		0 03		0 70		0 00		0 01		0 00		0 01		0 92	-0 04		
P_2O_5	0 38		0 14		0 00		0 04		0 00		0 00		0 00		41 95		0 57	-0 19		
																	$\sum r^2=$	0 16		

MODEL B - OFFSHORE SUITE (OSS)

	parent		daughter																	
	AR106	=	AR207wr	+	An_{92}	+	An_{38}	+	Fo_{67}	+	augite	+	Fe-Ti oxide	+	apatite	=	calc	residuals		
Volume %	100%		13%		21%		33%		4%		18%		9%		1%		parent	r		
SiO_2	48 42		66 93		44 03		58 97		38 21		51 98		0 00		0 16		48 60	-0 18		
TiO_2	1 00		0 56		0 04		0 03		0 01		0 44		10 20		0 00		1 09	-0 10		
Al_2O_3	18 37		15 92		35 11		25 54		0 05		1 23		2 89		0 00		18 53	-0 15		
FeO*	11 07		3 26		0 89		0 50		22 25		10 78		84 10		0 58		11 24	-0 17		
MgO	4 45		0 86		0 05		0 06		38 86		14 70		2 30		0 23		4 58	-0 13		
CaO	10 96		1 83		18 94		7 69		0.22		19 65		0 00		54 10		11 08	-0 12		
Na_2O	3 02		4 89		0 87		6 54		0 00		0 32		0 00		0 07		3 05	-0 03		
K_2O	0 88		5 12		0 03		0 62		0 00		0 01		0 00		0 01		0 90	-0 02		
P_2O_5	0 38		0 14		0 00		0 02		0 00		0 00		0 00		41 95		0 59	-0 21		
																	$\sum r^2=$	0 17		

MODEL C - OFFSHORE SUITE (OSS)

	parent		daughter																	
	AR106	=	AR073wr	+	An_{92}	+	An_{38}	+	Fo_{76}	+	augite	+	Fe-Ti oxide	+	apatite	=	calc.	residuals		
Volume %	100%		14%		22%		32%		5%		17%		8%		1%		parent	r		
SiO_2	48 42		65 63		44 03		58 97		37 00		51 98		0 00		0 16		48 61	-0 19		
TiO_2	1 00		0 55		0 04		0 03		0 03		0 44		10 20		0 00		1 03	-0 04		
Al_2O_3	18 37		15 72		35 11		25 54		0 01		1 23		2 89		0 00		18 53	-0 15		
FeO*	11 07		3 56		0 89		0 50		29 13		10 78		84 10		0 58		11 25	-0 18		
MgO	4.45		1.29		0 05		0 06		32 83		14 70		2 30		0.23		4 57	-0 12		
CaO	10 96		2 54		18 94		7 69		0 20		19 65		0 00		54 10		11 09	-0 13		
Na_2O	3 02		5 03		0 87		6 54		0 00		0 32		0 00		0 07		3 05	-0 03		
K_2O	0 88		4 99		0 03		0.62		0 00		0 01		0 00		0 01		0 92	-0 04		
P_2O_5	0 38		0 18		0 00		0 02		0 00		0 00		0 00		41 95		0.59	-0 21		
																	$\sum r^2=$	0 17		

MODEL D - HIGH-K/HIGH-Rb SUITE (HKRS)

	parent		daughter																	
	V60	=	AR073wr	+	An_{92}	+	An_{42}	+	Fo_{76}	+	augite	+	Fe-Ti oxide	+	apatite	=	calc	residuals		
Volume %	100%		20%		25%		25%		6%		15%		8%		1%		parent	r		
SiO_2	48 32		65 63		44 03		57 33		37 00		50 70		0 00		0 16		48 37	-0 06		
TiO_2	0 98		0 55		0 04		0 05		0 03		0 56		10 20		0 00		1 01	-0 03		
Al_2O_3	19 19		15 72		35 11		26 80		0 01		3 80		2 89		0 00		19 24	-0 05		
FeO*	10 54		3 56		0 89		0 46		29 13		7 88		84 10		0 58		10 59	-0 06		
MgO	4 74		1.29		0 05		0 05		32 83		14 64		2 30		0 23		4 79	-0 04		
CaO	11 22		2 54		18 94		8 48		0.20		21 97		0 00		54 10		11 27	-0 05		
Na_2O	2 75		5 03		0 87		6 07		0 00		0.29		0 00		0 07		2.78	-0 03		
K_2O	1 15		4 99		0 03		0 70		0 00		0 00		0 00		0 01		1 19	-0 03		
P_2O_5	0 46		0 18		0 00		0 04		0 00		0 00		0 00		41 95		0 51	-0 06		
																	$\sum r^2=$	0 02		

Table L.1. (cont.). Major element fractionation models, Efaté Island Group magmas: basalt → trachydacite

MODEL E – HIGH-K/HIGH-Rb SUITE (HKRS)

	parent		daughter																	
	V60	=	AR079	+	An_{92}	+	An_{42}	+	Fo_{76}	+	augite	+	Fe-Ti oxide	+	apatite	=	calc	Residuals
Volume %	100%		20%		24%		24%		6%		16%		8%		1%		parent	r
SiO_2	48 32		65 92		44 03		57 33		37 00		50 70		0 00		0 16		48 38	-0 06
TiO_2	0 98		0 56		0 04		0 05		0 03		0 56		10 20		0 00		1 01	-0 03
Al_2O_3	19 19		16 28		35 11		26 80		0 01		3 80		2 89		0 00		19 24	-0 05
FeO*	10 54		3 41		0 89		0 46		29 13		7 88		84 10		0 58		10.59	-0 06
MgO	4 74		0 95		0 05		0 05		32 83		14.64		2 30		0 23		4 79	-0 04
CaO	11 22		2 11		18 94		8 48		0.20		21 97		0 00		54 10		11 27	-0 05
Na_2O	2 75		5 11		0 87		6 07		0 00		0 29		0 00		0 07		2 77	-0 02
K_2O	1 15		4 98		0 03		0 70		0 00		0 00		0 00		0 01		1 17	-0 02
P_2O_5	0 46		0 17		0 00		0 04		0 00		0 00		0 00		41 95		0 52	-0 07
																	$\sum r^2$=	0 02

MODEL F – HIGH-K/HIGH-Rb SUITE (HKRS)

	parent		daughter															
	V60	=	AR098	+	An_{92}	+	An_{42}	+	Fo_{76}	+	augite	+	Fe-Ti oxide	+	apatite	=	calc	Residuals
Volume %	100%		19%		23%		27%		6%		16%		8%		1%		parent	r
SiO_2	48 32		66 00		44 03		57 33		37 00		50 70		0 00		0 16		48 41	-0 09
TiO_2	0 98		0 59		0 04		0 05		0 03		0 56		10 20		0 00		1 01	-0 03
Al_2O_3	19 19		15 98		35 11		26 80		0 01		3 80		2 89		0 00		19 25	-0 06
FeO*	10 54		3 86		0 89		0 46		29 13		7 88		84 10		0 58		10 61	-0 08
MgO	4 74		1.23		0 05		0 05		32 83		14 64		2 30		0 23		4 79	-0 05
CaO	11 22		2 42		18 94		8 48		0 20		21 97		0 00		54 10		11 27	-0 05
Na_2O	2 75		4 36		0 87		6 07		0 00		0 29		0 00		0 07		2 72	0 02
K_2O	1 15		4 87		0 03		0 70		0 00		0 00		0 00		0 01		1 10	0 05
P_2O_5	0 46		0 15		0 00		0 04		0 00		0 00		0 00		41 95		0 56	-0 11
																	$\sum r^2$=	0 04

MODEL G – OFFSHORE SUITE (OSS)

	parent		daughter															
	AR106	=	AR073wr	+	An_{92}	+	An_{38}	+	Fo_{76}	+	augite	+	Fe-Ti oxide	+	apatite	=	calc.	Residuals
Volume %	100%		14%		22%		32%		4%		18%		9%		1%		parent	r
SiO_2	48 42		65 63		44 03		58 97		38 21		51 98		0 00		0 16		48 59	-0 17
TiO_2	1 00		0 55		0 04		0 03		0 01		0 44		10 20		0 00		1 09	-0 10
Al_2O_3	18 37		15 72		35 11		25 54		0 05		1 23		2 89		0 00		18 52	-0 15
FeO*	11 07		3 56		0 89		0 50		22 25		10 78		84 10		0 58		11.23	-0 16
MgO	4 45		1.29		0 05		0 06		38 86		14 70		2 30		0.23		4 58	-0 13
CaO	10 96		2 54		18 94		7 69		0.22		19 65		0 00		54 10		11 08	-0 12
Na_2O	3 02		5 03		0 87		6 54		0 00		0 32		0 00		0 07		3 07	-0 05
K_2O	0 88		4 99		0 03		0 62		0 00		0 01		0 00		0 01		0 93	-0 05
P_2O_5	0 38		0 18		0 00		0 02		0 00		0 00		0 00		41 95		0 57	-0 19
																	$\sum r^2$=	0 15

MODEL H – OFFSHORE SUITE (OSS)

	parent		daughter															
	AR106	=	AR079	+	An_{92}	+	An_{38}	+	Fo_{76}	+	augite	+	Fe-Ti oxide	+	apatite	=	calc	Residuals
Volume %	100%		14%		22%		32%		4%		18%		9%		1%		parent	r
SiO_2	48 42		65 92		44 03		58 97		38 21		51 98		0 00		0 16		48 59	-0 17
TiO_2	1 00		0 56		0 04		0 03		0 01		0 44		10 20		0 00		1 09	-0 10
Al_2O_3	18 37		16 28		35 11		25 54		0 05		1 23		2 89		0 00		18 52	-0 15
FeO*	11 07		3 41		0 89		0 50		22 25		10 78		84 10		0 58		11 23	-0 16
MgO	4 45		0 95		0 05		0 06		38 86		14 70		2 30		0 23		4 58	-0 13
CaO	10 96		2 11		18 94		7 69		0 22		19 65		0 00		54 10		11 08	-0 12
Na_2O	3 02		5 11		0 87		6 54		0 00		0 32		0 00		0 07		3 06	-0 04
K_2O	0 88		4 98		0 03		0 62		0 00		0 01		0 00		0 01		0 92	-0 04
P_2O_5	0 38		0 17		0 00		0 02		0 00		0 00		0 00		41 95		0 58	-0 20
																	$\sum r^2$=	0 16

MODEL I – OFFSHORE SUITE (OSS)

	parent		daughter															
	NgA23	=	AR098	+	An_{92}	+	An_{38}	+	Fo_{76}	+	augite	+	Fe-Ti oxide	+	apatite	=	calc	Residuals
Volume %	100%		8%		16%		41%		6%		19%		9%		1%		parent	r
SiO_2	48 68		66 00		44 03		58 97		38 21		51 98		0 00		0 16		48 63	0 06
TiO_2	1 06		0 59		0 04		0 03		0 01		0 44		10.20		0 00		1 11	-0 05
Al_2O_3	18 09		15 98		35 11		25 54		0 05		1.23		2 89		0 00		18 08	0 01
FeO*	11 94		3 86		0 89		0 50		22 25		10 78		84 10		0 58		11 92	0 03
MgO	5 37		1 23		0 05		0 06		38 86		14 70		2 30		0 23		5 39	-0 03
CaO	10 38		2 42		18 94		7 69		0 22		19 65		0 00		54.10		10 43	-0 05
Na_2O	3 04		4 36		0 87		6 54		0 00		0 32		0 00		0 07		3 25	-0 21
K_2O	0 39		4 87		0 03		0 62		0 00		0 01		0 00		0 01		0 64	-0 24
P_2O_5	0 36		0 15		0 00		0 02		0 00		0 00		0 00		41 95		0.25	0 11
																	$\sum r^2$=	0 12

MODEL J - OFFSHORE SUITE (OSS)

	parent		daughter															
	NgA23	=	AR207wr	+	An_{92}	+	An_{38}	+	Fo_{76}	+	augite	+	Fe-Ti oxide	+	apatite	=	calc.	residuals
Volume %	100%		7%		17%		41%		6%		19%		-9%		1%		parent	r
SiO_2	48 68		66 93		44 03		58 97		38 21		51 98		0 00		0 16		48 62	0 06
TiO_2	1 06		0 56		0 04		0 03		0 01		0 44		10 20		0 00		1 11	-0 05
Al_2O_3	18 09		15 92		35 11		25 54		0 05		1.23		2 89		0 00		18 07	0 01
FeO*	11 94		3.26		0 89		0 50		22.25		10 78		84 10		0 58		11 91	0 03
MgO	5 37		0 86		0 05		0 06		38 86		14 70		2 30		0.23		5 40	-0 03
CaO	10 38		1 83		18 94		7 69		0.22		19 65		0 00		54 10		10 44	-0 06
Na_2O	3 04		4 89		0 87		6 54		0 00		0 32		0 00		0 07		3 27	-0 23
K_2O	0 39		5 12		0 03		0 62		0 00		0 01		0 00		0 01		0 64	-0 25
P_2O_5	0 36		0 14		0.00		0 02		0 00		0 00		0 00		41.95		0.24	0 12
																	$\sum r^2$=	0.14

Table L.1. (cont.). Major element fractionation models, Efaté Island Group magmas: basalt → trachydacite

MODEL K - HIGH-K/HIGH-Rb SUITE (HKRS)

	parent		daughter																	
	V60	=	AR207wr	+	An_{92}	+	An_{42}	+	Fo_{67}	+	augite	+	Fe-Ti oxide	+	apatite	=	calc	residuals
Volume %	100%		19%		23%		26%		6%		17%		8%		1%		parent	r
SiO2	48 32		66 93		44 03		57 33		37 00		50 70		0 16		0 16		48 44	-0 12
TiO2	0 98		0 56		0 04		0 05		0 03		0 56		6 85		0 00		0 78	0 20
Al2O3	19 19		15 92		35 11		26 80		0 01		3 80		6 08		0 00		19 27	-0 08
FeO*	10 54		3 26		0 89		0 46		29 13		7 88		82 96		0 58		10 66	-0 13
MgO	4 74		0 86		0 05		0 05		32 83		14 64		3 48		0 23		4 79	-0 05
CaO	11 22		1 83		18 94		8 48		0 20		21 97		0 00		54 10		11 31	-0 09
Na_2O	2 75		4 89		0 87		6 07		0 00		0 29		0 00		0 07		2 76	-0 02
K_2O	1 15		5 12		0 03		0 70		0 00		0 00		0 00		0 01		1 16	-0 01
P_2O_5	0 46		0 14		0 00		0 04		0 00		0 00		0 00		41 95		0 57	-0 12
																	$\sum r^2=$	0 10

MODEL L - HIGH-K/HIGH-Rb SUITE (HKRS)

	parent		daughter															
	V60	=	AR207wr	+	An_{92}	+	An_{42}	+	Fo_{67}	+	augite	+	Fe-Ti oxide	+	apatite	=	calc	residuals
Volume %	100%		19%		24%		26%		6%		16%		8%		1%		parent	r
SiO_2	48 32		66 93		44 03		57 33		37 00		50 70		0 00		0 16		48 40	-0 08
TiO_2	0 98		0 56		0 04		0 05		0 03		0 56		10 20		0 00		1 01	-0 03
Al_2O_3	19 19		15 92		35 11		26 80		0 01		3 80		2 89		0 00		19 24	-0 06
FeO*	10 54		3 26		0 89		0 46		29 13		7 88		84 10		0 58		10 60	-0 07
MgO	4.74		0 86		0 05		0 05		32 83		14 64		2 30		0 23		4 79	-0 05
CaO	11 22		1 83		18 94		8 48		0 20		21 97		0 00		54.10		11 27	-0 05
Na_2O	2 75		4 89		0 87		6 07		0 00		0.29		0 00		0 07		2 75	0 00
K_2O	1 15		5 12		0 03		0 70		0 00		0 00		0 00		0 01		1 14	0 01
P_2O_5	0 46		0 14		0 00		0 04		0 00		0 00		0 00		41 95		0 54	-0 09
																	$\sum r^2=$	0 03

MODEL M - MAINLAND SUITE (MLS)

	parent		daughter															
	AR153	=	AR098	+	An_{92}	+	An_{42}	+	Fo_{67}	+	augite	+	Fe-Ti oxide	+	apatite	=	calc	residuals
Volume %	100%		11%		17%		36%		8%		20%		7%		1%		parent	r
SiO_2	47 85		66 00		44 03		57 33		37 00		50 70		0 00		0 16		48 01	-0 16
TiO_2	0 89		0 59		0 04		0 05		0 03		0 56		10 20		0 00		0 96	-0 07
Al_2O_3	17 96		15 98		35 11		26 80		0 01		3 80		2 89		0 00		18 11	-0 14
FeO*	10 75		3 86		0 89		0 46		29 13		7 88		84 10		0 58		10 91	-0 16
MgO	5 75		1 23		0 05		0 05		32 83		14 64		2 30		0 23		5 88	-0 13
CaO	11 49		2 42		18 94		8 48		0 20		21 97		0 00		54 10		11 63	-0 14
Na_2O	2 74		4 36		0 87		6 07		0 00		0 29		0 00		0 07		2 84	-0 10
K_2O	0 69		4 87		0 03		0 70		0 00		0 00		0 00		0 01		0 78	-0 09
P_2O_5	0 47		0 15		0 00		0 04		0 00		0 00		0 00		41 95		0 63	-0 16
																	$\sum r^2=$	0 16

MODEL N - MAINLAND SUITE (MLS)

	parent		daughter															
	AR153	=	AR073wr	+	An_{92}	+	An_{42}	+	Fo_{67}	+	augite	+	Fe-Ti oxide	+	apatite	=	calc	residuals
Volume %	100%		12%		17%		34%		8%		20%		7%		1%		parent	r
SiO_2	47 85		65 63		44 03		57 33		37 00		50 70		0 00		0 16		47 99	-0 14
TiO_2	0 89		0 55		0 04		0 05		0 03		0 56		10 20		0 00		0 96	-0 07
Al_2O_3	17 96		15 72		35 11		26 80		0 01		3 80		2 89		0 00		18 10	-0 13
FeO*	10 75		3 56		0 89		0 46		29 13		7 88		84 10		0 58		10 89	-0 14
MgO	5 75		1.29		0 05		0 05		32 83		14 64		2 30		0 23		5 88	-0 13
CaO	11 49		2 54		18 94		8 48		0 20		21 97		0 00		54 10		11 63	-0 14
Na_2O	2 74		5 03		0 87		6 07		0 00		0 29		0 00		0 07		2 87	-0 14
K_2O	0 69		4 99		0 03		0 70		0 00		0 00		0 00		0 01		0 83	-0 14
P_2O_5	0 47		0 18		0 00		0 04		0 00		0 00		0 00		41 95		0 60	-0 13
																	$\sum r^2=$	0 15

MODEL O - MAINLAND SUITE (MLS)

	parent		daughter															
	EA258	=	AR066	+	An_{85}	+	An_{42}	+	Fo_{67}	+	diopside	+	Fe-Ti oxide	+	apatite	=	calc	residuals
Volume %	100%		13%		11%		35%		6%		25%		8%		1%		parent	r
SiO_2	47 91		64 51		45 78		57 33		37 00		47 31		0 00		0 16		48 05	-0 14
TiO_2	0 94		0 64		0 01		0 05		0 03		0 79		10 20		0 00		1 09	-0 15
Al_2O_3	17 31		16 83		33 88		26 80		0 01		7 08		2 89		0 00		17 44	-0 13
FeO*	11 04		4 41		0 67		0 46		29 13		8 22		84 10		0 58		11 17	-0 13
MgO	5 71		1 38		0 07		0 05		32 83		13 53		2 30		0 23		5 84	-0 13
CaO	11 65		3 03		17 81		8 48		0 20		22 64		0 00		54 10		11 78	-0 13
Na_2O	2 83		4 11		1 63		6 07		0 00		0 29		0 00		0 07		2 94	-0 11
K_2O	0 72		4 27		0 02		0 70		0 00		0 01		0 00		0 01		0 82	-0 10
P_2O_5	0 48		0 21		0 09		0 04		0 00		0 00		0 00		41 95		0 62	-0 14
																	$\sum r^2=$	0 15

MODEL P - MAINLAND SUITE (MLS)

	parent		daughter															
	EA258	=	AR064	+	An_{85}	+	An_{42}	+	Fo_{67}	+	diopside	+	Fe-Ti oxide	+	apatite	=	calc	residuals
Volume %	100%		14%		11%		35%		6%		25%		8%		1%		parent	r
SiO_2	47 91		64 29		45 78		57 33		37 00		47 31		0 00		0 16		48 04	-0 13
TiO_2	0 94		0 60		0 01		0 05		0 03		0 79		10 20		0 00		1 08	-0 14
Al_2O_3	17 31		16 97		33 88		26 80		0 01		7 08		2 89		0 00		17 44	-0 13
FeO*	11 04		4 33		0 67		0 46		29 13		8 22		84 10		0 58		11 17	-0 13
MgO	5 71		1 42		0 07		0 05		32 83		13 53		2 30		0 23		5 84	-0 13
CaO	11 65		3 12		17 81		8 48		0 20		22 64		0 00		54 10		11 78	-0 13
Na_2O	2 83		4 20		1 63		6 07		0 00		0 29		0 00		0 07		2 95	-0 12
K_2O	0 72		4 23		0 02		0 70		0 00		0 01		0 00		0 01		0 83	-0 11
P_2O_5	0 48		0 22		0 09		0 04		0 00		0 00		0 00		41 95		0 62	-0 14
																	$\sum r^2=$	0 15

Table L.1. (cont.). Major element fractionation models, Efaté Island Group magmas: basalt → trachydacite

MODEL Q - OFFSHORE SUITE (OSS) - GROUNDMASSES

	parent OSS	=	daughter EPF-GL1	+	An_{82}	+	An_{42}	+	Fo_{76}	+	augite	+	Fe-Ti oxide	+	apatite	=	calc parent	residuals r
Volume %	100%		17%		14%		36%		4%		22%		7%		1%			
SiO_2	49 98		65 58		44 03		57 33		37 00		48 61		0 00		0 00		49 97	0 01
TiO_2	0 70		0 41		0 04		0 05		0 03		0 52		10 20		0 00		0 88	-0 18
Al_2O_3	19 22		19 28		35 11		26 80		0 01		5 85		2 89		0 00		19 21	0 01
FeO*	9 06		1 98		0 89		0 46		29 13		7 36		84 10		0 27		9 02	0 04
MgO	4 81		0.39		0 05		0 05		32 83		14 59		2 30		0 04		4 80	0 01
CaO	11 68		3 97		18 94		8 48		0 20		22 53		0 00		57 10		11 64	0 04
Na_2O	3 25		4 65		0 87		6 07		0 00		0 30		0 00		0 00		3 17	0 08
K_2O	0 99		3 62		0 03		0 70		0 00		0 00		0 00		0 00		0 87	0 13
P_2O_5	0 30		0 10		0 00		0 04		0 00		0 00		0 00		42 59		0 31	-0 02
																	$\sum r^2$=	**0.06**

MODEL R - OFFSHORE SUITE (OSS) - GROUNDMASSES

	parent OSS	=	daughter EPF-GL1	+	An_{86}	+	An_{42}	+	Fo_{76}	+	augite	+	Fe-Ti oxide	+	apatite	=	calc parent	residuals r
Volume %	100%		17%		14%		35%		3%		23%		7%		1%			
SiO_2	49 98		65 58		45 70		57 33		37 00		48 61		0 14		0 00		50 04	-0 06
TiO_2	0 70		0 41		0 04		0 05		0 03		0 52		4 93		0 00		0 55	0 15
Al_2O_3	19 22		19 28		34 03		26 80		0 01		5 85		7 78		0 00		19 25	-0 02
FeO*	9 06		1 98		0 97		0 46		29.13		7 36		83 99		0 27		9 12	-0 05
MgO	4 81		0 39		0 11		0 05		32 83		14 59		2 91		0 04		4 81	0 00
CaO	11 68		3 97		17 49		8 48		0 20		22 53		0 00		57 10		11 70	-0 02
Na_2O	3 25		4 65		1 46		6 07		0 00		0 30		0 00		0 00		3 19	0 06
K_2O	0 99		3 62		0 11		0 70		0 00		0 00		0 00		0 00		0 87	0 12
P_2O_5	0 30		0 10		0 08		0 04		0 00		0 00		0 00		42 59		0 36	-0 07
																	$\sum r^2$=	**0 05**

MODEL S - HIGH-K/HIGH-Rb SUITE (HKRS) - GROUNDMASSES

	parent HKRS	=	daughter EPF-GL1	+	An_{86}	+	An_{42}	+	Fo_{76}	+	augite	+	Fe-Ti oxide	+	apatite	=	calc parent	residuals r
Volume %	100%		21%		15%		31%		7%		19%		6%		1%			
SiO_2	50 31		65 58		45 70		57 33		37 00		48 61		0 00		0 00		50 38	-0 07
TiO_2	0 76		0 41		0 04		0 05		0 03		0 52		10 20		0 00		0 78	-0 02
Al_2O_3	18 71		19 28		34 03		26 80		0 01		5 85		2 89		0 00		18 73	-0 02
FeO*	8 84		1 98		0 97		0 46		29 13		7 36		84 10		0 32		8 88	-0 04
MgO	5 34		0 39		0 11		0 05		32 83		14 59		2 30		0 05		5 33	0 01
CaO	11 05		3 97		17 49		8 48		0 20		22 53		0 00		55 08		11 04	0 01
Na_2O	3 28		4 65		1 46		6 07		0 00		0 30		0 00		0 04		3 14	0 13
K_2O	1.27		3 62		0 11		0 70		0 00		0 00		0 00		0 01		1 01	0 26
P_2O_5	0 45		0 10		0 08		0 04		0 00		0 00		0 00		42 40		0 55	-0 10
																	$\sum r^2$=	**0 11**

MODEL T - HIGH-K/HIGH-Rb SUITE (HKRS) - GROUNDMASSES

	parent HKRS	=	daughter EPF-GL2	+	An_{86}	+	An_{42}	+	Fo_{76}	+	augite	+	Fe-Ti oxide	+	apatite	=	calc parent	residuals r
Volume %	100%		14%		13%		40%		6%		20%		6%		1%			
SiO_2	50 31		66 38		45 70		57 33		37 00		48 61		0 00		0 00		50 33	-0 03
TiO_2	0 76		0 65		0 04		0 05		0 03		0 52		10 20		0 00		0 79	-0 03
Al_2O_3	18 71		16 07		34 03		26 80		0 01		5 85		2 89		0 00		18 70	0 00
FeO*	8 84		3 81		0 97		0 46		29 13		7 36		84 10		0 32		8 84	-0 01
MgO	5 34		0 99		0 11		0 05		32 83		14 59		2 30		0 05		5 33	0 01
CaO	11 05		2 34		17 49		8 48		0.20		22 53		0 00		55 08		11 03	0 02
Na_2O	3 28		3 57		1 46		6 07		0 00		0 30		0 00		0 04		3 18	0 09
K_2O	1 27		5 96		0 11		0 70		0 00		0 00		0 00		0 01		1 15	0 12
P_2O_5	0 45		0 24		0 08		0 04		0 00		0 00		0 00		42 40		0 49	-0 04
																	$\sum r^2$=	**0 03**